

---

---

# Unsaturated Flow and Transport Through Fractured Rock Related to High-Level Waste Repositories

Final Report - Phase II

---

---

Compiled by T. C. Rasmussen, D. D. Evans

Department of Hydrology and Water Resources  
University of Arizona

Prepared for  
U.S. Nuclear Regulatory  
Commission

HYDROLOGY DOCUMENT NUMBER 526

870615 6101

## NOTICE

This report was prepared as an account of work sponsored by an agency of the United States Government. Neither the United States Government nor any agency thereof, or any of their employees, makes any warranty, expressed or implied, or assumes any legal liability of responsibility for any third party's use, or the results of such use, of any information, apparatus, product or process disclosed in this report, or represents that its use by such third party would not infringe privately owned rights.

## NOTICE

### Availability of Reference Materials Cited in NRC Publications

Most documents cited in NRC publications will be available from one of the following sources:

1. The NRC Public Document Room, 1717 H Street, N.W.  
Washington, DC 20555
2. The Superintendent of Documents, U.S. Government Printing Office, Post Office Box 37082,  
Washington, DC 20013-7082
3. The National Technical Information Service, Springfield, VA 22161

Although the listing that follows represents the majority of documents cited in NRC publications, it is not intended to be exhaustive.

Referenced documents available for inspection and copying for a fee from the NRC Public Document Room include NRC correspondence and internal NRC memoranda; NRC Office of Inspection and Enforcement bulletins, circulars, information notices, inspection and investigation notices; Licensee Event Reports; vendor reports and correspondence; Commission papers; and applicant and licensee documents and correspondence.

The following documents in the NUREG series are available for purchase from the GPO Sales Program: formal NRC staff and contractor reports, NRC-sponsored conference proceedings, and NRC booklets and brochures. Also available are Regulatory Guides, NRC regulations in the *Code of Federal Regulations*, and *Nuclear Regulatory Commission Issuances*.

Documents available from the National Technical Information Service include NUREG series reports and technical reports prepared by other federal agencies and reports prepared by the Atomic Energy Commission, forerunner agency to the Nuclear Regulatory Commission.

Documents available from public and special technical libraries include all open literature items, such as books, journal and periodical articles, and transactions. *Federal Register* notices, federal and state legislation, and congressional reports can usually be obtained from these libraries.

Documents such as theses, dissertations, foreign reports and translations, and non-NRC conference proceedings are available for purchase from the organization sponsoring the publication cited.

Single copies of NRC draft reports are available free, to the extent of supply, upon written request to the Division of Information Support Services, Distribution Section, U.S. Nuclear Regulatory Commission, Washington, DC 20555.

Copies of industry codes and standards used in a substantive manner in the NRC regulatory process are maintained at the NRC Library, 7920 Norfolk Avenue, Bethesda, Maryland, and are available there for reference use by the public. Codes and standards are usually copyrighted and may be purchased from the originating organization or, if they are American National Standards, from the American National Standards Institute, 1430 Broadway, New York, NY 10018.

---

---

# Unsaturated Flow and Transport Through Fractured Rock Related to High-Level Waste Repositories

Final Report - Phase II

---

---

Manuscript Completed: October 1986  
Date Published: May 1987

Compiled by  
T. C. Rasmussen, D. D. Evans

T. J. Nicholson, NRC Project Manager

Department of Hydrology and Water Resources  
University of Arizona  
Tucson, AZ 85721

Prepared for  
Division of Engineering  
Office of Nuclear Regulatory Research  
U.S. Nuclear Regulatory Commission  
Washington, DC 20555  
NRC FIN B7291  
Under Contract No. NRC-04-81-224

## ABSTRACT

In response to high-level radioactive waste repository licensing needs of the U.S. Nuclear Regulatory Commission, this report examines and provides insights into physical characteristics and methodologies for performance assessment of candidate sites in unsaturated fractured rock. The focus is on the ability of the geologic medium surrounding an underground repository to isolate radionuclides from the accessible environment. Media of interest are consolidated rocks with variable fracturing, rock matrix permeabilities, contained water under negative pressure, and air-filled voids. Temperature gradients are also of interest. Studies present conceptual and theoretical considerations, physical and geochemical characterization, computer modeling techniques, and parameter estimation procedures. Radionuclide transport pathways are as solutes in ground water and as vapor through air-filled voids. The latter may be important near a heat source. Water flow and solute transport properties of a rock matrix may be quantified using rock core analyses. Natural spatial variation dictates many samples. Observed fractures can be characterized and combined to form a fracture network for hydraulic and transport assessments. Unresolved problems include the relation of network hydraulic conductivity to fluid pressure and to scale. Once characterized, the matrix and fracture network can be coupled. Reliable performance assessment requires additional studies.

## ACKNOWLEDGEMENTS

This report was compiled and written by Todd C. Rasmussen and Daniel D. Evans. Drafting and technical editing was performed by Marie Engle. Contributions from the following individuals are acknowledged:

Dr. James G. McCray	Dept of Nuclear and Energy Engineering
Dr. Eugene S. Simpson	Dept of Hydrology and Water Resources
Dr. Shlomo P. Neuman	Dept of Hydrology and Water Resources
Dr. Arthur W. Warrick	Dept of Soils and Water Science
Dr. Chi-hua Huang	Dept of Hydrology and Water Resources

In addition, the following graduate students within the Department of Hydrology and Water Resources substantially contributed to the material presented:

Steve Amter	Bill Davies	Andy Messer
Rikki Amutis	Douglas Earp	Khayyun Rahi
Ingrid Anderson	Tim Goering	Mary Roberts
John Andrews	Ron Green	Todd Shrauf
Steve Brown	Richard Kilbury	Robert Trautz
Steve Cullinan	Dan Matthews	Dan Weber

The NRC project technical monitor was Mr. Thomas J. Nicholson, Division of Radiation Programs and Earth Sciences, U.S. Nuclear Regulatory Commission, 7915 Eastern Avenue, Silver Spring, MD, 20910, phone (301)-443-7672.

TABLE OF CONTENTS

	<u>Page</u>
ABSTRACT . . . . .	iii
ACKNOWLEDGEMENTS . . . . .	iv
TABLE OF CONTENTS . . . . .	v
LIST OF TABLES . . . . .	xii
LIST OF FIGURES . . . . .	xv
0. EXECUTIVE SUMMARY . . . . .	1
0.1 Measurement of Radionuclide Transport . . . . .	2
0.1.1 Conduction in the Liquid Phase . . . . .	2
0.1.1.1 Matrix Transport . . . . .	3
0.1.1.2 Fracture Transport . . . . .	4
0.1.1.3 Determination of Liquid Velocities . . . . .	5
0.1.1.4 Geochemical Factors . . . . .	7
0.1.2 Conduction in the Vapor Phase . . . . .	8
0.2 Influence of Thermal Loading on Solute Transport . . . . .	8
0.3 Limitations and Recommendations for Further Research . . . . .	10
1. INTRODUCTION . . . . .	11
1.1 Scope . . . . .	11
1.2 Organization . . . . .	12
1.3 Field Study Areas . . . . .	14
1.3.1 Patagonia Mountains Study Area . . . . .	14
1.3.1.1 Santo Nino Mine Site . . . . .	16
1.3.1.2 Patagonia Field Site . . . . .	23
1.3.2 Superior Study Area . . . . .	29
1.3.2.1 Apache Leap Field Site . . . . .	35
1.3.2.2 Queen Creek Road Tunnel Site . . . . .	35
1.3.2.3 Magma Site . . . . .	42
1.4 Laboratory Facilities . . . . .	42
1.5 Computer Facilities . . . . .	42

**TABLE OF CONTENTS (Continued)**

	<u>Page</u>
<b>2. ROCK CHARACTERIZATION . . . . .</b>	<b>45</b>
<b>2.1 Rock Matrix Characterization . . . . .</b>	<b>45</b>
<b>2.1.1 Matrix Porosity Determination . . . . .</b>	<b>45</b>
2.1.1.1 Paraffin Method . . . . .	46
2.1.1.2 Water Saturation Method . . . . .	47
2.1.1.3 Gravimetric and Gamma Ray Attenuation Methods . . . . .	48
2.1.1.4 Comparison of Techniques . . . . .	48
<b>2.1.2 Pore-Size Distribution . . . . .</b>	<b>52</b>
2.1.2.1 Mercury Infusion . . . . .	52
2.1.2.2 Nitrogen Gas Adsorption . . . . .	53
2.1.2.3 Comparison of Methods . . . . .	54
2.1.2.4 Recommended Improvements . . . . .	59
<b>2.1.3 Specific Surface . . . . .</b>	<b>59</b>
<b>2.2 Fracture Characterization . . . . .</b>	<b>60</b>
2.2.1 Orientation . . . . .	61
2.2.2 Density and Spacing . . . . .	68
2.2.2.1 Fracture Centroids . . . . .	71
2.2.2.2 Areal Extent . . . . .	71
2.2.3 Fracture Aperture . . . . .	74
2.2.4 Fracture Porosity . . . . .	76
2.2.5 Fracture-Surface Characterization . . . . .	79
2.2.5.1 Specific Surface . . . . .	79
2.2.5.2 Aperture Variability . . . . .	80
<b>3. ISOTHERMAL HYDROLOGIC CHARACTERIZATION . . . . .</b>	<b>81</b>
<b>3.1 Water Potential Measurement . . . . .</b>	<b>81</b>
3.1.1 Thermocouple Psychrometer . . . . .	82
3.1.1.1 Field Psychrometer . . . . .	86
3.1.1.2 Thermocouple Psychrometer Sample Changer . . . . .	98
3.1.2 Tensiometer . . . . .	98
3.1.3 Osmotic Tensiometer . . . . .	100
3.1.4 Absorber Method . . . . .	103
<b>3.2 Water Content Measurement . . . . .</b>	<b>104</b>

TABLE OF CONTENTS (Continued)

	<u>Page</u>
3.3 Rock Matrix Hydraulic Conductivity . . . . .	117
3.3.1 Mathematical Development . . . . .	118
3.3.2 Numerical Implementation . . . . .	119
3.3.3 Materials and Methods . . . . .	120
3.3.4 Results and Discussion . . . . .	124
3.4 Fracture Permeability Using a Heat-Pulse Flowmeter . . .	131
3.4.1 Operation . . . . .	131
3.4.2 Field Investigation . . . . .	136
3.4.3 Results and Conclusions . . . . .	138
3.5 Water and Air Intake on Surface-Exposed Rock Fractures .	142
3.5.1 Water Intake Method . . . . .	144
3.5.2 Air Intake Method . . . . .	156
3.5.3 Discussion and Conclusions . . . . .	163
3.6 Determination of Fracture Aperture Using Air Injection .	163
3.6.1 Single Hole Flow Test . . . . .	168
3.6.2 Fracture Aperture Test Procedure . . . . .	171
4. NONISOTHERMAL HYDROLOGIC CHARACTERIZATION . . . . .	177
4.1 Laboratory Experiments Using Gamma Attenuation . . . . .	178
4.1.1 Equipment and Procedures . . . . .	179
4.1.2 Results and Conclusions . . . . .	186
4.2 Field Heating Experiment . . . . .	200
4.2.1 Equipment and Procedures . . . . .	200
4.2.2 Results and Conclusions . . . . .	203
4.3 Numerical Simulation . . . . .	208
4.3.1 Assumptions . . . . .	209
4.3.2 Results and Conclusions . . . . .	212

TABLE OF CONTENTS (Continued)

	<u>Page</u>
5. SOLUTE TRANSPORT . . . . .	221
5.1 Sampling Techniques . . . . .	223
5.1.1 Volatile Compounds . . . . .	223
5.1.1.1 Selection of Fluorocarbon Tracers . . . . .	227
5.1.1.2 Experimental and Computer Results . . . . .	229
5.1.1.3 Summary and Conclusions . . . . .	237
5.1.2 Vacuum Lysimeter . . . . .	239
5.1.2.1 Proposed Methodology . . . . .	241
5.1.2.2 Computer Simulation . . . . .	243
5.1.2.3 Conclusions and Applications . . . . .	251
5.1.3 Vapor Condensation . . . . .	256
5.1.3.1 Principles of Thermoelectricity . . . . .	257
5.1.3.2 Application to Vapor Condensation . . . . .	262
5.1.3.3 Testing and Application . . . . .	264
5.1.4 Fluorescent Tracers . . . . .	268
5.1.4.1 Use in Fractured Rock . . . . .	268
5.1.4.2 Preliminary Testing in Tuff . . . . .	274
5.1.4.3 Recommendations . . . . .	275
5.2 Hydrogeochemistry of Unsaturated Fractured Rock . . . . .	276
5.2.1 Variation of Environmental Isotopes and Hydration of Authigenic Minerals . . . . .	276
5.2.1.1 Stable Isotopes of Oxygen and Hydrogen as Tracers of Water/Rock Interactions . . . . .	277
5.2.1.2 Radiogenic Isotope of Strontium ( <sup>87</sup> Sr/ <sup>86</sup> Sr) as a Tracer of Water/Rock Interactions . . . . .	278
5.2.2 Field Investigations Involving Isotopic and Hydration Analyses of Unsaturated Fractured Tuff . . . . .	280
6. CONTAMINANT TRANSPORT AS VAPOR . . . . .	283
6.1 Introduction . . . . .	283
6.1.1 Radioactive Species of Interest . . . . .	283
6.1.2 Physical Setting . . . . .	284

## TABLE OF CONTENTS (Continued)

	<u>Page</u>
6.2 Gas Movement in a Fractured Medium . . . . .	285
6.2.1 Ordinary Diffusion . . . . .	289
6.2.1.1 Self and Binary Diffusion . . . . .	290
6.2.1.2 Knudsen Flow . . . . .	296
6.2.1.3 Surface Diffusion . . . . .	304
6.2.1.4 Total Contribution by Ordinary Diffusion . . . . .	307
6.2.2 Viscous Flow . . . . .	310
6.2.2.1 Pressure Flow . . . . .	310
6.2.2.2 Slip Flow . . . . .	313
6.2.2.3 Diffusion-Viscous Flow Transition . . . . .	314
6.2.2.4 Ordinary Diffusion: Effects at Longer Distances . . . . .	314
6.3 Forced Diffusion . . . . .	321
6.4 Aerosol Transport . . . . .	335
6.4.1 Nucleation and Solubility . . . . .	338
6.4.2 Aerosol Formation . . . . .	339
6.4.3 Analysis of Aerosol Formation at Repository Conditions . . . . .	343
6.5 Free Convection . . . . .	344
6.6 Thermal Diffusion and Thermophoresis . . . . .	349
6.7 Discussion and Summary . . . . .	353
7. DISCUSSION AND CONCLUSIONS . . . . .	361
8. LIST OF PUBLICATIONS . . . . .	367
8.1 Published Articles . . . . .	367
8.2 Papers Accepted for Publication . . . . .	368
8.3 Presented Papers . . . . .	368
8.4 Theses Completed . . . . .	369
8.5 Dissertations Completed . . . . .	370
8.6 Theses in Progress . . . . .	370
8.7 Dissertations in Progress . . . . .	370

TABLE OF CONTENTS (Continued)

	<u>Page</u>
9. REFERENCES . . . . .	371
 <u>Appendices</u>	
A. THERMOCOUPLE PSYCHROMETERS . . . . .	397
A.1 Equipment . . . . .	397
A.2 Procedures . . . . .	400
A.2.1 Dew Point Method . . . . .	400
A.2.2 Psychrometric Method . . . . .	405
A.2.3 Combined Method . . . . .	406
A.3 Data Analysis . . . . .	406
A.4 Thermocouple Psychrometer Sample Changer: Calibration . .	407
A.4.1 Calibration Procedure at Low Water Potential . . .	407
A.4.2 Calibration Procedure at High Water Potential . . .	408
A.4.3 Calibration Equations and Curves . . . . .	411
B. OSMOTIC TENSIOMETER . . . . .	415
B.1 Membranes . . . . .	415
B.2 Solutes . . . . .	417
B.2.1 Polystyrene Sulfonic Acid (PSSA) . . . . .	417
B.2.2 Polyethylene Glycol (Carbowax) . . . . .	418
B.2.3 Polyvinyl Pyrrolidone (PVP) . . . . .	420
B.2.4 Polyethylene Oxide (PEO) . . . . .	420
B.3 Experimental Apparatus . . . . .	421
B.3.1 Osmometer . . . . .	421
B.3.2 Concrete . . . . .	421
B.3.3 PVC pipe . . . . .	423
B.3.4 Cloth tube . . . . .	423
B.3.5 Ceramic pipe . . . . .	424
B.4 Laboratory Experiments . . . . .	424
B.5 Field Experiments . . . . .	434
B.5.1 Field Test of Carbowax . . . . .	434
B.5.2 Field Test of PVP . . . . .	434
B.5.3 Field Test of PEO . . . . .	437

**TABLE OF CONTENTS (Continued)**

	<u>Page</u>
<b>C. ABSORBER METHOD FOR MOISTURE POTENTIAL DETERMINATION . . . . .</b>	<b>441</b>
C.1 Ceramic Plate Extractor Method . . . . .	441
C.2 Equilibration of Filter Papers with Soil Samples . . . . .	443
C.3 Moisture Release Curve for Filter Papers . . . . .	447
C.4 Equilibration of Filter Papers with Rock Samples . . . . .	449
<b>D. LABORATORY DETERMINATION OF MOISTURE RELEASE CURVES . . . . .</b>	<b>453</b>
<b>E. DRILLING TECHNIQUES . . . . .</b>	<b>455</b>
E.1 Santo Nino Mine and Queen Creek Road Tunnel Sites . . . . .	455
E.2 Apache Leap Site . . . . .	457
<b>F. LABORATORY METHODS INVESTIGATING VOLATILE TRACERS . . . . .</b>	<b>459</b>
F.1 Gas Chromatography . . . . .	459
F.2 Batch Test Procedure . . . . .	463
F.3 Column Test Procedure . . . . .	463
F.4 Computer Modeling of Laboratory Experiment . . . . .	467
F.5 Field Experiment and Conclusions . . . . .	468
<b>G. ISOTOPE GEOCHEMISTRY IN LOW TEMPERATURE WATER/ROCK INTERACTIONS . . . . .</b>	<b>471</b>
G.1 General Characteristics of Isotopes . . . . .	471
G.2 Stable Isotopes . . . . .	471
G.3 Stable Isotope Variations in Water . . . . .	472
G.4 Radiogenic Isotopes . . . . .	473
G.5 Isotope Geochemistry and Rock/Water Interactions . . . . .	473

## LIST OF TABLES

	<u>Page</u>
1.1 Mineralogy of Santo Nino Quartz Monzonite, after Baker (1962). . . . .	16
1.2 Mineralogy of the Magma Quartz Latite, after Peterson (1961). . . . .	33
1.3 Results of fracture survey at Apache Leap tuff site . . . .	38
2.1 Porosity measurements of the slightly-welded Apache Leap tuff. . . . .	50
2.2 Porosity measurements of the densely-welded Apache Leap tuff. . . . .	51
2.3 Result of bulk density and grain density determinations of granodiorite samples. Percent porosity determination was made using mercury-infusion (Hg) and grain-density ( $\rho_g$ ) measurements . . . . .	56
3.1 Summary of thermocouple psychrometer measurements in Pride-of-the-West mine. . . . .	90
3.2 Summary of thermocouple psychrometer measurements in Santo Nino mine . . . . .	95
3.3 Moisture potential as measured using thermocouple psychrometers in the dew point (DP) and psychrometric (PS) modes in welded tuff at the Queen Creek road tunnel. .	97
3.4 Selective properties of rock samples. . . . .	121
3.5 Computed parameters of rock samples using three models. . .	125
3.6 Observed flow rates versus depth of observation for Boreholes X-1, X-2, and X-3 at the Apache Leap site . . . .	139
3.7 Steady-state water intake ( $Q_w$ ), fracture aperture ( $e_w$ ), final depth to wetting front ( $h_1$ ), and fluid velocity ( $v$ ) for 21 FRI experiments. . . . .	151

**LIST OF TABLES (Continued)**

	<u>Page</u>
3.8 Comparison of final depth to wetting front and fracture aperture not considering the capillary effect ( $h_1$ and $e_w$ , respectively) with values computed considering the capillary effect ( $h_1'$ and $e_w'$ , respectively). . . . .	155
3.9 Fracture apertures for FRI air experiments. . . . .	160
3.10 Sample flow test. . . . .	174
3.11 Summary of the single-hole pneumatic testing procedure. . . . .	176
4.1 Sand column countercurrent experimental results . . . . .	190
4.2 Sandstone core countercurrent experimental results. . . . .	191
4.3 Tuff core countercurrent experimental results . . . . .	197
5.1 Properties of possible fluorocarbon tracers . . . . .	228
5.2 Partial list of published expressions relating tortuosity to air-filled and total porosity of medium (From Weeks et. al., 1982). . . . .	235
6.1 Attributes of various gases, from Kennard (1938). . . . .	291
6.2 Functions for predictions of transport properties of gases at low densities, from Hirschfelder et al. (1949). . . . .	295
6.3 Coefficient of Diffusion - Isothermal Case. . . . .	309
6.4 Equations describing viscous flow . . . . .	315
6.5 Summary of gamma spectrum (photons/sec) per fuel assembly (structural materials + actinides + fission products) (From Sutherland and Bennett, 1979) . . . . .	327
6.6 Coefficients for Equation (6.68) to determine the solubility of gases in water (from Cleaver and Han, 1980). . . . .	339

LIST OF TABLES (Continued)

	<u>Page</u>
6.6 A list of values assigned to the variables needed to determine the Rayleigh number (from Wang et al., 1983). . .	347
A.1 Water potentials and water activities of selected saturated solutions at 20°C. To find water activities at other temperatures, see Greenspan (1975). . . . .	409
A.2 Water potentials-activities of KCl and NaCl solutions at 20°C. To find water potentials at other temperatures use $OP_T = OP_{293} T/293$ . . . . .	409
F.1 Properties of possible fluorocarbon tracers . . . . .	460
F.2 Underwriters' laboratories' classification of comparative life hazard of gases and vapors. (From Handbook of Chemistry and Physics, Chemical Rubber Company, 1979-80). .	461
F.3 Procedure for batch test determination of distribution coefficients. . . . .	464
F.4 Sieve size analysis for the sand used in the column study .	464
F.5 Procedure for soil column test. . . . .	466

## LIST OF FIGURES

	<u>Page</u>
1.1 Location map of the Patagonia and Superior study areas. . .	15
1.2 Location map of the Santo Nino mine, the Pride-of-the- West mine and the Patagonia field sites . . . . .	17
1.3 Photograph of entrance to the Santo Nino mine . . . . .	18
1.4 Plan view of Santo Nino mine adit (after Baker, 1962) . . .	20
1.5 Schmidt stereonet of fracture orientation . . . . .	21
1.6 Plan view location, strike and dip for each fracture detected on the video log . . . . .	22
1.7 Cross-section of the Santo Nino mine. . . . .	24
1.8 Relative water levels in Borehole 6.0a. . . . .	25
1.9 Borehole temperatures (line graph) and mean monthly surface temperatures (bar graph) at the Santo Nino field site. . . . .	26
1.10 Cross-section perpendicular to the Santo Nino mine adit showing the location of boreholes and ponded water levels . . . . .	27
1.11 Partial stratigraphic section (A), structural cross- section (B), and site location map (C) of the Patagonia study area . . . . .	28
1.12 Photograph of the Patagonia study area welded tuff outcrop. . . . .	30
1.13 Photograph of the Patagonia study area surface . . . . .	31
1.14 Photograph showing a vertical fracture plane area at the Patagonia study area . . . . .	32
1.15 Physical characteristics of the dacitic ash-flow sheet . .	34

LIST OF FIGURES (Continued)

	<u>Page</u>
1.16 Location map of Superior field sites . . . . .	36
1.17 Borehole diagram, Apache Leap field site . . . . .	37
1.18 View perpendicular to the Magma haulage tunnel . . . . .	43
1.19 Flow rates from the lower borehole (line graph) and precipitation (bar graph) versus time at Magma field site . . . . .	44
2.1 Range of primary porosities for samples of partially-welded tuff using the paraffin method (A), partially-welded tuff using the water saturation method (B), and granodiorite using the water-saturation method (C). . . . .	49
2.2 Pore-size distribution results from mercury infusion for granodiorite samples. . . . .	55
2.3 Pore-size distribution results from gas-adsorption for the same granodiorite sample shown in Figure 2.2. . . . .	57
2.4 Pore-size distribution results combining two measurement techniques for a granodiorite sample obtained from the Santo Nino Mine . . . . .	58
2.5 Diagrams showing strike, dip direction, and dip angle for three different fractures . . . . .	62
2.6 Measurements used to calculate strike, dip direction and dip angle of a fracture intersecting a borehole core. . . . .	64
2.7 Plot of normals to discontinuities on a Schmidt polar equal area net. . . . .	65
2.8 Contour plot of fracture data from Santo Nino mine. . . . .	67
2.9 Map of fractures intersecting boreholes at the Apache Leap Tuff site. . . . .	69

## LIST OF FIGURES (Continued)

	<u>Page</u>
2.10 Inclination of fractures intercepted by boreholes at the Apache Leap Tuff site. . . . .	70
2.11 Fracture spacing histogram . . . . .	72
2.12 Reynolds number diagram for fracture flow. . . . .	77
2.13 Typical curve of flow rate against hydraulic gradient. . .	78
3.1 Thermocouple psychrometer response curve for dewpoint (1), psychrometric (2), and combined modes (3). Water potential is 25 bars suction. Temperature is 32.8°C. . . .	85
3.2 Average cooling rate curves for eight screen cage psychrometers under saturated (0 bar) and very dry (76 bar suction) conditions. Vertical bars about the mean values indicate the one standard deviation confidence region. . . . .	87
3.3 Median longitudinal section of a screen-enclosed thermocouple psychrometer (after Meyn and White, 1972). . .	88
3.4 Moisture potentials measured in Borehole 3 of the Pride-of-the-West mine using Thermocouple Psychrometer 150. . . .	92
3.5 Average cooling rate curves for eight screen cage psychrometers under wet (0 bars suction) and very dry (76 bars suction) conditions. . . . .	93
3.6 Thermocouple psychrometer sample changer, sample cups and microvoltmeter (Decagon Devices, Inc., Pullman, WA) . . . .	99
3.7 Diagram of the prototype osmotic tensiometer in a borehole in fractured rock . . . . .	102
3.8 Variation in the normalized neutron data with time and space in Borehole 5.2 at the Santo Nino field site. . . . .	106
3.9 Variation in the normalized neutron data with time and space in Borehole 5.8 at the Santo Nino field site. . . . .	107

LIST OF FIGURES (Continued)

	<u>Page</u>
3.10 Variation in the resistivity data with time and space in Borehole 5.8 at the Santo Nino field site. . . . .	108
3.11 Variation in the normalized neutron data with time and space in the upper borehole at the Magma field site. . . .	109
3.12 Resistivity (lower) profile and normalized neutron (upper) profile for Borehole 5.2 at the Santo Nino field site . . . . .	110
3.13 Resistivity (lower) profile and normalized neutron (upper) profile for Borehole 5.8 at the Santo Nino field site . . . . .	111
3.14 Cross-section perpendicular to the Santo Nino mine adit showing the location of boreholes and ponded water levels . . . . .	113
3.15 Relative water levels in Borehole 6.0a . . . . .	114
3.16 Resistivity (lower) profile and normalized neutron (upper) profile at a depth of 5.2 meters in the top borehole at the Magma field site . . . . .	115
3.17 Resistivity (lower) profile and normalized neutron (upper) profile at a depth of 11.3 meters in the top borehole at the Magma field site . . . . .	116
3.18 Modified Tempe pressure cell for measuring saturated conductivity, $K_s$ . Water is forced through a saturated sample by applying air pressure. Outflow is collected and used to compute $K_s$ by using Darcy's law. Sealant is used to prevent flow along the sides of the sample. Clay and tissue are used to improve the contact between the sample and the porous plate . . . . .	122

**LIST OF FIGURES (Continued)**

	<u>Page</u>
3.19 Cross-sectional view of Tempe pressure cell used to measure unsaturated hydraulic conductivity, K, by the outflow method. A saturated sample is placed in the cell and, after assuring good contact between the sample and the ceramic plate, a small increment of pressure is applied. Outflow is measured using a graduated tube after an air bubble is introduced into the system. K is calculated by plotting the flow rate against time, and then using a set of type curves. . . . .	123
3.20 Moisture content by volume ( $\theta$ ) versus suction for the Apache Leap Tuff sample T1 . . . . .	127
3.21 Moisture content by volume ( $\theta$ ) versus suction for the Coconino Sandstone sample T4 . . . . .	128
3.22 Moisture content by volume ( $\theta$ ) versus suction for the Coconino Sandstone sample S1 . . . . .	129
3.23 Moisture content by volume ( $\theta$ ) versus suction for the tuff sample GU4 (from Peters et al., 1984) . . . . .	130
3.24 View of heater grid and thermistor inside flow tube of heat-pulse flowmeter . . . . .	132
3.25 Diagram of electronic circuit used for recording temperature pulse in flowmeter . . . . .	132
3.26 Temperature response curve showing electric pulse to heater and peak temperature difference between the two thermistors. . . . .	134
3.27 Calibration curve for the heat-pulse flowmeter . . . . .	134
3.28 View of heat-pulse flowmeter and packer assembly. Wall roughness exaggerated . . . . .	135
3.29 Measured flow rates and calculated flow losses for Boreholes X-1, X-2, and X-3 at the Apache Leap site. . . .	137

LIST OF FIGURES (Continued)

	<u>Page</u>
3.30 Measured downhole flows for Boreholes X-1, X-2, and X-3, plotted against vertical depth . . . . .	140
3.31 Cross-sectional diagram of the FRI, showing the apparatus as used for water intake measurements. . . . .	145
3.32 Photograph of the FRI set up over a mock fracture. . . . .	146
3.33 Water intake rate <u>vs.</u> time for a representative FRI water experiment (setup 16W) . . . . .	149
3.34 Cumulative water intake volume (A), fluid velocity (B), and depth to wetting front (C) <u>vs.</u> time graphs . . . . .	152
3.35 Log-probability plot of fracture apertures computed for the FRI water method . . . . .	154
3.36 Cross-sectional diagram of the FRI as used for air intake measurements (A), and FRI geometry represented in the real plane (B) . . . . .	157
3.37 Air intake rate <u>vs.</u> time for a representative FRI air experiment (setup 1A). . . . .	159
3.38 Log-probability plot of fracture apertures computed using the air and water methods on the same fractures. . . . .	161
3.39 Plot of fracture apertures calculated using the water method ( $e_w$ ) <u>vs.</u> apertures calculated using the air method ( $e_a$ ) for the same fracture. . . . .	162
3.40 Sequential air-intake (A), water-intake (B), and air-intake (C), curves for a single fracture at the Patagonia study area . . . . .	164
3.41 Fracture-borehole interaction angle, $\alpha$ . . . . .	166
3.42 Geometric relations between injection and observation boreholes. . . . .	166

LIST OF FIGURES (Continued)

	<u>Page</u>
3.43 $r_{ave}$ versus $a_2/b_2$ for different borehole-fracture plane interaction angle, $\alpha$ . . . . .	167
3.44 Geometric relations between radius of influence for a known case (left) and for an unknown case (right). . . . .	170
3.45 Pressure drop versus volumetric flow rate for different apertures, e. Theoretical equations using $r_2 = 2$ m, $r_1 = 0.05$ m and $\alpha = 0^\circ$ . . . . .	172
3.46 Pressure drop versus volumetric flow rate for different apertures, e. Theoretical equations using $r_2 = 2$ m, $r_1 = 0.05$ m and $\alpha = 60^\circ$ . . . . .	173
3.47 Arrangement of valves for packer system. . . . .	175
4.1 Heating experimental carriage . . . . .	180
4.2 Gamma attenuation equipment . . . . .	183
4.3 Comparison of initial and steady state water content changes for sand column . . . . .	188
4.4 Comparison of initial and steady state water content changes for sandstone core. . . . .	189
4.5 Water content of sandstone sample after application of 2/3 bar suction . . . . .	192
4.6 Sandstone core tracer distribution. . . . .	194
4.7 Tuff core heating experiment initial and final water content distribution. . . . .	195
4.8 Tuff core heating experiment water content changes with time. . . . .	196
4.9 Temperature distribution at the end of tuff and sandstone heating experiments . . . . .	198

LIST OF FIGURES (Continued)

	<u>Page</u>
4.10 Diagram of heating element and thermocouple located behind packer (right borehole), and packers isolating psychrometers (left borehole) at Queen Creek . . . . .	201
4.11 Diagram of 500 watt (short element) and 1500 watt (long element) heating units, and wiring to control box. . . . .	202
4.12 Water content against time for heating experiment in the Queen Creek road tunnel. . . . .	204
4.13 Suction against time plot for heater experiment in Queen Creek road tunnel. . . . .	206
4.14 Temperature against time plot for heater experiment in Queen Creek road tunnel. . . . .	207
4.15 The heat and moisture flow domain. . . . .	210
4.16 Saturated vapor density versus calculated vapor density. The shaded area represents a zone of evaporation and the hashed area a zone of condensation . . . . .	214
4.17 Qualitative plot of rock water flux versus time illustrating the drying process. . . . .	216
4.18 Illustration of how a set of natural microfractures is replaced by an effective microfracture. The single fracture takes into account all gravity drainage for a given node space . . . . .	217
5.1 Breakthrough curves for BCF (A) and SF <sub>6</sub> (B) . . . . .	230
5.2 Breakthrough curves for Freon-22 test . . . . .	231
5.3 Breakthrough curves for BCF (A), SF <sub>6</sub> (B), and Freon-22 (C). . . . .	232
5.4 Computed breakthrough curves for fluorocarbon tracer in the soil gas and in the liquid. The close agreement between the curves indicates the suitability of vapor phase concentration as a surrogate measure of fluid concentration . . . . .	236

**LIST OF FIGURES (Continued)**

	<u>Page</u>
5.5 Observed and computed soil gas breakthrough curves for a fluorocarbon tracer in a column test. The two curves agree except for the last data point . . . . .	238
5.6 Schematic view of vacuum lysimeter parts and installation. In sufficiently wet media a water sample is collected by clamping shut the discharge tube and pumping the air out of the sampler. Water flows from the soil into the sampler through the porous cup. To bring this sample to the surface, air is pumped into the lysimeter with the discharge tube open. Positive pressure forces the water to the surface through the open tube. (Figure is modified from Soilmoisture Equipment Corp. Instruction Manual) . . . . .	240
5.7 Finite element mesh. The flow field contains triangular and quadrilateral elements which are defined by the numbered corner nodes. The lysimeter shown forms part of the left side boundary, along an axis of symmetry. The region simulated is the right side of a mirrored pair . . .	245
5.8 Plot of injection rate against time. The injection rate is initially rapid, then quickly decreases toward a steady state value of approximately 6 ml/sec. The area under curve is equal to the cumulative injection volume . .	248
5.9 Expansion of the wetted region. Three positions of the 20 percent volumetric water content isobar corresponding to T = 30, 100, and 720 sec are shown. Each isobar defines an area of 20 percent or greater water content about the cup. Antecedent moisture content was 12.7% . . .	249
5.10 Applied pressure against time during the simulated injection phase. The magnitude of applied pressure inside the cup required to generate the simulated injection rate was calculated for different times using Darcy's law. Although pressures which may exceed the breaking strength of ceramic cups were required at times before 45 sec, this interval accounts for only 18 percent of the total flow . . . . .	250

LIST OF FIGURES (Continued)

	<u>Page</u>
5.11 Moisture profile for three times during redistribution. The vertical axis corresponds to volumetric water content and the horizontal axis is a scale plot of node distance along a horizontal line from the midpoint of the cup. At T = 1 sec after the end of injection, the gradient of moisture content is steep. With time the gradient decreases as water is drawn into unwetted areas. Given sufficient time the moisture profile would approach the shape corresponding to the antecedent moisture condition. . . . .	252
5.12 Applied vacuum during the recovery phase. The magnitude of vacuum inside the cup required to generate the simulated sample recovery rate was calculated for different times using Darcy's law. All calculated values fall within practical limits. Recovery began at 720 sec. . . . .	253
5.13 Cumulative volume of recovered water against time during the simulated recovery phase. Recovery began at 720 sec and the rate at which water drained from the soil rapidly decreased with time, as indicated by the decrease in slope. The maximum volume of recovered water was 146 ml. At times after 1216 sec, matric suction exceeded the applied suction and previously recovered water was drawn from the cup back into the soil. By 2016 sec all recovered water had been lost. It is important to collect the water sample before the gradient reverses . . . . .	254
5.14 Schematic cross section of Thermoelectric Cooling Module. Semiconductor materials of dissimilar properties (n-type and p-type) are connected thermally in parallel and electrically in series so that heat is absorbed on one surface and carried to the other. The junction is formed by welding the p- and n-type semiconductor materials together. The reduction of temperature at the cold junction results in condensation of vapor on the ceramic surface. Actual size of the module used in these experiments is (3 x 3 x .4) cm. . . . .	261

**LIST OF FIGURES (Continued)**

	<u>Page</u>
<p><b>5.15 Thermoelectric Cooling System:</b> Current is run through leads so as to create a reduction in temperature on the exposed surface, resulting in vapor condensation. The opposite surface of the module is attached to an aluminum block heat sink. In addition, copper tubing is attached to the block and used to circulate cold water to dissipate heat. . . . .</p>	265
<p><b>5.16 Schematic Diagram of Proposed Field Application:</b> The thermocooling system is inserted into a nearly horizontal borehole attached to one end of an inflatable packer assembly, which is used to isolate the section of interest. Tubing for water circulation and for drawing off the sample are run through the center of the packer. Electrical leads run between the borehole wall and the packer and fit snugly when the packer is fully inflated. When operated, the condensate formed on the thermocooler cold side will drip off into the sample collecting trough and be carried through tubing to the sample container at the surface . . .</p>	266
<p><b>5.17 Effect of pH on fluorescence of tracer dyes . . . . .</b></p>	271
<p><b>5.18 Effect of various materials on solubility of tracers . . . . .</b></p>	272
<p><b>5.19 Excitation spectra of amino G acid, lissamine FF, and rhodamine WT and transmission characteristics using secondary filters (A) and primary filters (B) . . . . .</b></p>	273
<p><b>5.20 Schematic representation of <math>\delta D</math> and <math>\delta^{18}O</math> correlation of clay minerals (or other minerals such as diagenetic quartz which contains both hydrogen and oxygen) and a meteoric water source . . . . .</b></p>	279
<p><b>6.1 Schematic of high-level waste repository located in fractured media illustrating thermally induced zone of lower saturation enveloped by zone of higher saturation . . . . .</b></p>	286

LIST OF FIGURES (Continued)

	<u>Page</u>
6.2 Representation of molecule-molecule interaction according to (a) simplified kinetic theory and (b) rigorous kinetic theory. Molecule A travels toward molecule B along trajectory (dotted line) (adapted from Hirschfelder et al., 1954). . . . .	294
6.3 Diffusion coefficient (cm <sup>2</sup> /sec) for carbon dioxide versus temperature (°K). The top curve is determined by the Bird-Slattery method, the bottom curve is determined by the Chapman-Enskog method. . . . .	297
6.4 Diffusion coefficient (cm <sup>2</sup> /sec) for hydrogen versus temperature (°K). The top curve is determined by the Bird-Slattery method, the bottom curve is determined by the Chapman-Enskog method. . . . .	297
6.5 Diffusion coefficient (cm <sup>2</sup> /sec) for methane versus temperature (°K). The top curve is determined by the Bird-Slattery method, the bottom curve is determined by the Chapman-Enskog method . . . . .	298
6.6 Diffusion coefficient (cm <sup>2</sup> /sec) for krypton versus temperature (°K). The top curve is determined by the Bird-Slattery method, the bottom curve is determined by the Chapman-Enskog method . . . . .	298
6.7 Diffusion coefficient (cm <sup>2</sup> /sec) for iodine versus temperature (°K). The top curve is determined by the Bird-Slattery method, the bottom curve is determined by the Chapman-Enskog method . . . . .	299
6.8 Parallel plate model (a) and capillary tube model (b) used to represent flow through an idealized fracture and an idealized porous medium, respectively . . . . .	300
6.9 Experimental permeability, k, for different pore geometries: (1) bed of spheres; (2) short capillary (l = 5a); (3) long capillary; and (4) parallel plates. k <sub>K</sub> and k <sub>S</sub> are Knudsen and slip permeabilities (from Massignon, 1979) . . . . .	303

LIST OF FIGURES (Continued)

	<u>Page</u>
6.10 Velocity profiles of idealized gas flow through either parallel plates or capillary tube: (a) total viscous flow-no slip flow; (b) viscous and slip flow; and (c) total slip flow-no viscous flow. . . . .	311
6.11 Transition from Knudsen to viscous flow through a long capillary tube as Knudsen number decreases: (1) total flow rate; (2) viscous flow; (3) slip flow; and (4) Knudsen flow (from Massignon, 1979) . . . . .	316
6.12 Diffusive flux versus normalized concentration for a 300 m long cylindrical conduit at time 1 to 75 years . . .	319
6.13 Effective range of electrons in tuff versus electron energy level . . . . .	324
6.14 Electric current density in tuff from a 0.30 MeV photon emitted from an infinite line source. Values for e indicate accuracy relative to magnitude of current density. . . . .	326
6.15 Electric current density in tuff from a 1.55 MeV photon emitted from an infinite line source. Values for e indicate accuracy relative to magnitude of current density. . . . .	329
6.16 Electric field intensity (left axis) and ion drift velocity (right axis) in tuff at 100, 300, 1000, 10,000 and 100,000 years versus radial distance from an infinite line source. Resistivity of tuff is $10^6$ ohm-cm, mobility is $2 \text{ cm}^2/\text{V-sec}$ . . . . .	330
6.17 Effective range of electrons in air versus electron energy level . . . . .	332
6.18 Electric current density in air from a 1.55 MeV photon emitted from an infinite line source. Values for e indicate accuracy relative to magnitude of current density. . . . .	333

LIST OF FIGURES (Continued)

	<u>Page</u>
6.19 Electric field intensity (left axis) and ion drift velocity (right axis) in air at 100, 300, 1000, 10,000 and 100,000 years versus radial distance from an infinite line source. Resistivity of air is $10^{15}$ ohm-cm and mobility is 2 cm/V . . . . .	334
6.20 Schematic of countercurrent (or heat pipe). Liquid film moves toward heat source in response to gradient in negative pressure and vaporizes. The vapor moves away from heat source in response to pressure or concentration gradient and condenses at lower temperature. . . . .	337
6.21 Mole fraction solubility of oxygen and nitrogen in water versus temperature. . . . .	340
6.22 Three idealized cases of free convective flow: (a) homogeneous equivalent porous medium; (b) layered equivalent porous medium; and (c) zone of fractures or piped flow model. Arrows denote direction of gas flow. $k$ is intrinsic permeability and $x$ is thermal conductivity. . . . .	346
6.23 Chart of major gradients and fluxes with off diagonal phenomenological coefficients (from de Marsilly, 1985) . . . . .	358
A.1 Thermocouple psychrometer response curve for dewpoint (1), psychrometric (2), and combined modes (3). Water potential is 25 bars suction. Temperature is 32.8°C. . . . .	401
A.2 Equilibration curves for four initially dry screen cage psychrometers placed in calibration chambers containing a 25 bar NaCl solution . . . . .	404
A.3 Calibration curve for low water potential readings using saturated salts for calibration . . . . .	412
A.4 Calibration curve for high water potential readings using saturated salts for calibration. . . . .	413

LIST OF FIGURES (Continued)

	<u>Page</u>
B.1 Calibration curve for 70,000 mw Polystyrene sulfonic acid . . . . .	418
B.2 Diagram of plexiglass cells used to determine osmotic potentials of aqueous solutions . . . . .	422
B.3 Diagram of apparatus used to assess osmotic tensiometer response characteristics under variable external potentials. . . . .	425
B.4 Summary of water potentials measured in lab experiments in which soil samples were previously brought to a specified moisture potential by applying a known pressure for 48 hours. . . . .	427
B.5 Diagram of the prototype osmotic tensiometer in a borehole located in fractured rock. . . . .	429
B.6 Tensiometer response curve for an experiment in which the prototype containing a Carbowax solution was inserted in a simulated borehole made of cloth and submerged in water. . . . .	430
B.7 Tensiometer response in saturated concrete with manual pressure adjustments to facilitate equilibrium . . . . .	431
B.8 Tensiometer response in saturated concrete for three different internal osmotic potentials . . . . .	433
B.9 Tensiometer response in PVC pipe submerged in water . . . . .	435
B.10 Tensiometer response curve in fractured granodiorite at the Santo Nino mine. Tensiometer contained a Carbowax solution . . . . .	436
B.11 Response curve for osmotic tensiometer in Borehole 28.3 at the Santo Nino mine. Tensiometer contained a 40,000 mw PVP solution with an osmotic potential equal to 1 bar suction. . . . .	438

LIST OF FIGURES (Continued)

	<u>Page</u>
B.12 Response curve for osmotic tensiometer in fractured granodiorite at the Santo Nino mine, Borehole 28.3. Tensiometer was filled with a 200,000 mw PEO solution having an osmotic potential equal to 2.41 bars suction. Pressure drop at 18.5 hours was manually induced . . . . .	439
C.1 Results using Schleicher and Schwell filter papers with buffers on a ceramic plate extractor . . . . .	442
C.2 Cross sectional diagram of experiment used to measure matric potential of soil or rock using a filter paper in good contact (lower), and matric plus osmotic potential using a filter not in direct contact (upper). . . . .	444
C.3 Results using soils equilibrated on a ceramic plate extractor and filter papers sealed in a sample can in vapor. . . . .	445
C.4 Moisture release curves obtained from: (•) Fawcett and Collis-George curve; (x) psychrometer; and (o) ceramic plate . . . . .	448
C.5 Three types of filter paper; (x) Millipore, (•) Whatman No. 42, and (o) Scheicher and Schuel, were placed between sandstone or welded tuff slabs. The rock slabs ere saturated and placed on a ceramic plate extractor to induce a matric potential. The applied potential is noted by (- -). The rocks were placed in sample cans with filter papers between the rocks. 22 to 36 days were allowed for equilibration. The filter papers were removed and placed in the thermocouple psychrometer to evaluate their water potential.	450
F.1 Sample chromatogram showing the three fluorocarbon tracers used in study. Analyses were performed using a Hewlett-Packard 5700A series gas chromatograph with a Carbopack, 1% SP1000 column at 60°C . . . . .	462
F.2 Diagram of soil column test apparatus . . . . .	465

## EXECUTIVE SUMMARY

In response to the need of the U.S. Nuclear Regulatory Commission (NRC) to review characterizations of candidate sites for the ability of geologic media to isolate high-level nuclear waste (HLW), this report provides elements of the conceptual, theoretical, methodological and technological tools which are appropriate for use at sites located in unsaturated fractured rock. The ability to characterize fluid flow and solute transport in the medium surrounding a repository stems from a number of legislative acts, in particular 10CFR60.

This report documents work performed for the NRC by the Department of Hydrology and Water Resources of the University of Arizona in Tucson. Provided in this report are methods to characterize physical properties of geologic media, including the porosity, pore-size distribution, specific surfaces, as well as fracture characteristics, such as densities, orientations, apertures, lengths and centers. Also provided are techniques for characterizing hydraulic and pneumatic properties of geologic media. The measurement of moisture potential and water release curves are two important parameters necessary for the determination of the direction and magnitude of groundwater flow. Downhole, as well as surface, testing techniques are presented which are used to estimate hydraulic and pneumatic conductivities of rock masses.

The influence of heat on fluid flow may be appreciable in the vicinity of a high-level waste repository. This influence results in two-phase flow, i.e., simultaneous liquid and vapor flow. Laboratory and field evidence of counter-current flow is presented. Counter-current flow may result in the formation of a natural barrier to the movement of soluble contaminants in the event of a failure of the waste package and engineered barriers in the near-field.

Tools useful for the characterization of solute transport in unsaturated, isothermal media environment are also presented. Because removing a liquid sample in the unsaturated zone is restricted to only the wet range, the development of effective tracers and recovery techniques is paramount. Presented methods include the use of both volatile and fluorescent tracers. Recovery techniques using thermoelectric cooling elements and vacuum lysimeters are presented.

Movement of contaminants in the vapor phase is a secondary pathway for radionuclide escape. Governing equations describing the forces which influence the movement of wastes away from a repository in unsaturated fractured media are presented.

This report summarizes knowledge gained during the four previous years with regard to the physical and chemical properties of unsaturated, fractured rock. The knowledge was obtained using theoretical investigations, computer simulations, laboratory experiments, and field observations. In addition, professional meetings and special symposiums were conducted to evaluate and disseminate conclusions and observations.

### 0.1 Measurement of Radionuclide Transport

The assessment of the potential of a geologic medium to transmit HLW from a repository constructed for the permanent storage of those wastes is an important component of site characterization. Hydrogeologic and hydrogeochemical studies of the unsaturated zone are used to interpret rates and magnitudes of ground-water flow and the ability of ground water to transport high-level nuclear waste (HLW) over time periods of thousands of years.

The transport of HLW may occur in the liquid phase as a solute, or in the vapor phase as a gas or aerosol. The relative importance of transport rates in each phase is largely dependent upon the degree of saturation of the medium. It is also dependent upon the size and degree of connection between voids such as fractures, pores, and shafts.

#### 0.1.1 Conduction in the Liquid Phase

Water flow in the liquid phase through unsaturated rock may be the dominant mechanism for the transport of contaminants from a repository to the biosphere. The characterization of flow through an unsaturated formation requires the understanding of liquid flow through the pores and micro-fractures within the rock mass, as well as the movement through larger fractures.

Fluid flow is site and depth dependent. Important determinants of the water intake at the upper surface of the lithosphere include:

- o Surface properties, such as depressions, fracture densities, etc.;
- o Climatic properties, such as evaporation rates, surface temperatures, relative humidity, and rainfall duration and intensity; and
- o Vegetation properties, such as canopy coverage, plant densities, and rooting depth.

In addition, the subsequent redistribution of water originating at the atmosphere-earth interface is strongly dependent upon percolation

characteristics, including:

- o Stratification of geologic materials;
- o The relative permeabilities of the rock matrix and fractures; and
- o The ability of the rock matrix to act as a buffer for fracture flow.

Near the atmosphere-earth interface, ground water will move primarily through fractures as discrete pulses. This plug flow will be damped out with depth, however. Depending upon the degree of saturation of the geologic media, part of the fracture flow will either move into the rock matrix, into smaller, drained fractures, or drain into lower fractures.

#### 0.1.1.1 Matrix Transport

Within the matrix of unfractured geologic material, existing soil physics techniques, with modifications as described in this report, can be used to estimate the following parameters from drilled core samples:

- o Moisture release curves;
- o Hydraulic conductivity and diffusivity;
- o Total and effective porosities;
- o Pore size distributions;
- o Air entry potentials; and
- o Geochemical and thermal properties.

In situ techniques can also be used to obtain parameters important for the characterization of the rock matrix. These parameters include:

- o Air permeabilities; and
- o Water contents, using the neutron method.

#### Determination of Moisture Release Curves

Moisture release curves relate the unsaturated matrix hydraulic conductivity to the water content and/or the potential at which water is held within the porous medium. Parameters such as total and effective porosities, and the pore size distribution are important determinants of the moisture release curve. Several equations have been proposed to calculate moisture release curves from experiments performed on drilled core samples. These equations have primarily been used to estimate the hydraulic conductivity of unconsolidated materials. The application to consolidated and/or fractured media have not been widely tested.

A recent study (Peters et al., 1984) applied the Mualem model (1976) to tuff samples, but because of the difficulty in obtaining field estimates of the conductivity, the models could not be validated. Direct measurement of the unsaturated hydraulic conductivity in situ is a

difficult and inexact task because of long measurement times and the spatial variability of the parameter.

### Determination of Water Potentials

In addition to unsaturated hydraulic conductivity, water potentials in the geologic media are required. This need is twofold. Spatial changes in the total water potential drive fluid movement. Also, the rock water content, an important parameter for determining the unsaturated hydraulic conductivity, is a direct function of the water potential.

In the zone above the region water table, water potentials are generally negative. Water moves from areas where the potential is higher (less negative) to areas of lower potential (more negative). Various field methods have been developed for measuring rock water potentials in situ. The methods include an osmotic tensiometer and filter papers used in conjunction with a thermocouple psychrometer.

The osmotic tensiometer is composed of a steel cylinder core on which a semi-permeable membrane is sealed. The osmotic tensiometer is designed for emplacement in a borehole. When in place, the annular space between the core and the membrane is filled with an osmotic solution. The rock-water flows into or out of the device in response to relative changes in the total potential on either side of the membrane.

The osmotic tensiometer works on the principle that osmotic pressures and hydraulic pressure differences are equally effective in moving water through a membrane when the solutes are completely restricted. Thus, a proper combination of solute and membrane is essential for obtaining data about the rock-water potential.

The filter paper method in conjunction with a thermocouple psychrometer has been evaluated as a method for measuring in situ rock-water potential. Use of the method assumes that a filter paper in liquid or vapor contact with fractured rock will exchange moisture until equilibrium is achieved.

#### 0.1.1.2 Fracture Transport

At high suctions, fluid flow and solute transport through the rock matrix will be more significant than fracture flow, resulting from the size difference between fracture apertures and matrix pores. Vugs and larger apertures will drain first, followed by smaller fractures, and then micro-fractures and pores. In highly-fractured geologic media,

drained fractures may impede flow from matrix block to matrix block. Flow from block to block will occur at fracture asperities and in zones where pendular water is present within a fracture.

In highly-fractured geologic media at low suctions, fractures may provide the principal pathway for fluid flow and solute transport. Film flow will also become important at lower suctions, yet the magnitude of film flow is small relative to flow through saturated fractures.

Flow and solute transport through fractures requires the determination of rock-fracture parameters, such as:

- o Fracture densities, from spacing data along boreholes or from surface exposures;
- o Fracture orientations, also from borehole and surface exposure data;
- o Fracture lengths, using connections between boreholes and surface exposure data;
- o Fracture apertures, using apparent hydraulic or pneumatic aperture for existing water contents; and
- o Fracture shapes, using surface exposures.

A direct means for estimating flow through saturated fractures is to use a relation which combines Poiseuille's law with Darcy's law. This relation can be applied to unsaturated fractures by including capillary theory, which relates the aperture of the fracture to the potential at which the fracture will drain (or fill). Pneumatic and hydraulic methods to estimate the fracture aperture are presented.

#### 0.1.1.3 Determination of Liquid Velocities

A major difficulty associated with monitoring the velocity of water and solutes in unsaturated porous media is the necessity of removing samples of the rock water at different times for analysis. Several solutions are proposed. One is to use a tracer which is transported in a soluble form, and can also be measured in a gaseous state. The advantage of measuring the tracer in the gaseous state is that gas samples can be easily obtained. The suitability of using volatile fluorocarbons for this purpose is currently under investigation.

Gaseous sampling of a fluorocarbon tracer in equilibrium with the liquid phase can be used to predict the rate of liquid redistribution, thus eliminating the need for direct sampling of the liquid phase. Gas monitoring offers a low cost, reliable method for monitoring travel times of soluble constituents at sites located in the unsaturated zone.

To determine travel times of water within unsaturated geologic media, laboratory soil column studies have been conducted to test the suitability of fluorocarbon tracers. Modeling of the fluorocarbon tracer in both the gaseous and liquid phases has been performed using computer simulations. Results from laboratory column tests have been used to test the accuracy and validity of the computer model. The experimental approach and computer simulation have also been extended to a fractured rock field setting.

A second technique for determining travel times in unsaturated media is to modify vacuum lysimeter use. The modification is composed of:

- o An injection phase, in which a known quantity of fluid is injected into the media surrounding a lysimeter to provide sufficient fluids to bring the potential of the water in the media to near saturation;
- o A redistribution phase, in which the injected fluids mix with the native fluids; and
- o A recovery phase, in which injected and native fluids are recovered by applying a partial vacuum within the lysimeter.

A third technique uses fluorescent tracers to identify visually the arrival of a tracer front. Various tracers are evaluated and the suitability of these tracers is discussed.

Finally, a technique which uses Peltier cooling of a thermopile is used to recover samples from the gas phase. The method uses an electric current to provide a cooling surface upon which water vapor condenses and is collected. The objectives of this investigation have been:

- o The assesement of a laboratory procedure making use of the Peltier effect, which once established could be adapted into an in situ field method; and
- o The evaluation of the usefulness of tritium in its vapor state as a tracer, and other possible tracers should tritium prove ineffective or impractical.

The Peltier effect is produced when a current is passed through a junction of two different metals of a thermopile, resulting in a rising or lowering of temperature depending on current direction. If a current is induced in the direction such that the temperature is reduced, and the thermopile is placed in a humid environment, continuation of cooling to the dewpoint will result in condensation of water vapor onto the thermopile. The condensate, which initially might consist of tritium enriched water, can then be collected for analysis.

#### 0.1.1.4 Geochemical Factors

Identifying mineralogic changes and measuring isotopic variations may help establish the history of climatic and geomorphologic processes that might affect the isolation properties of a repository site. Previous work in this area for unsaturated fractured rock is sparse. Field work has been performed to assess mineralogic and isotopic techniques for obtaining information on flow regimes in unsaturated rock of low permeability.

Careful selection of the particular hydrogeochemical parameters and interpretation of the data can help characterize a representative site's unsaturated zone hydrology. Mineralogic and isotopic analyses can yield important information on how the system has behaved in the past and predict how it will behave in the future.

A field site near Superior, Arizona, where the predominant geologic material is a partially welded tuff (or, quartz latite), has been selected to conduct this assessment. The information that has been targeted for mineralogic and isotopic analysis includes:

- o Origins of pore waters;
- o Distinction of flow paths, mixing, and variability;
- o Age and age gradients of bound water;
- o Paleoclimatic information; and
- o Natural water-rock interactions.

Understanding site-specific parameters is important for proper selection and interpretation of the hydrogeochemical data. A program has been performed for evaluating existing techniques for fracture-filling mineral assemblages with regard to:

- o Sampling;
- o Initial treatment (e.g., filtration, nonfiltration, acidification, addition of precipitating salts); and
- o Preservation (e.g., isolation, temperature control).

Analysis and influence of drilling methods and drilling fluids will also be important.

Mineralogical indicators that are the most important to distinguish in fracture zones are the silica and clay assemblages. The key isotopes to be determined include  $^3\text{H}$ ,  $^{14}\text{C}$ ,  $^2\text{H}$ ,  $^{18}\text{O}$ ,  $^{13}\text{C}$ ,  $^{36}\text{Cl}$ , and  $^{87}\text{Sr}/^{86}\text{Sr}$ . A high concentration of tritium ( $^3\text{H}$ ) is an indication of recent water either by contamination or infiltration. The carbon, oxygen, and

strontium isotopes are useful for dating and for inferring the origins of pore and bound waters. Disequilibrium of uranium and radium isotopes can provide information on age and natural interactions. Isotopic analysis of uranium and thorium of fracture fillings can be used to date those minerals.

### 0.1.2 Conduction in the Vapor Phase

Vapor phase transport may be significant when large driving forces are present and suitable voids exist within the geologic media. The voids may be open shafts, or drained fractures and pores. The movement of gas in an unsaturated, non-isothermal, fractured medium which is located near a radioactive source can take place as a result of several different driving forces. The driving forces present in this setting include those resulting from:

- o A concentration or partial pressure gradient;
- o A total pressure gradient; or
- o A liquid or surface concentration gradient;

Each driving force results in an associated transport mechanism. A concentration gradient can cause ordinary diffusion. Diffusion includes Knudsen flow, self-diffusion, binary diffusion and surface flow. A gradient in the total pressure can result in viscous flow which includes Poiseuille (or Couette) and slip flow. An electric field can result in forced diffusion. And finally, a thermal gradient can cause a mechanism called thermal diffusion. A brief review of the equations governing gas movement in a fractured medium are presented.

Possible pathways for migration include direct transport in the vapor phase to the accessible environment, or to a zone of higher saturation where the contaminant is further transported in the liquid phase. An important conclusion drawn from this analysis is that because the potential influence of the driving forces are strongly dependent upon parameters unique to each application, the importance of vapor transport must be assessed for each site and engineering design.

### 0.2 Influence of Thermal Loading on Solute Transport

Heat released by the radioactive decay of HLNW in an underground repository will cause a long-term thermal disturbance in the host rock containing it (Wang et al., 1979). Therefore, non-isothermal moisture flow must be considered. Experiments have shown that a counter-current is established when a thermal gradient is applied to a sealed rock core. The counter-current is composed of movement in the vapor phase away from

the heat source, and a compensating movement in the liquid phase toward the heat source.

To date, little research has been conducted with regard to non-isothermal unsaturated water transport through fractured media. If, however, an unsaturated fracture can be considered to be analogous to a single pore, having both an air phase and a water film, then a significant amount of literature on non-isothermal moisture movement in unsaturated porous media (i.e. the air-filled volume of the granular media and the associated film absorbed to the pore forming particles) can be applied.

Philip and de Vries (1957) provided the first comprehensive work dealing with moisture movement in granular materials under temperature gradients. Their work is a water content formulation and took into account both liquid and vapor flowing response to both soil-water pressure and thermal gradients.

Taylor and Cary (1964) developed flow equations which were based on the laws of irreversible thermodynamics, and considers the heat flux. Both the Philip-de Vries and the Taylor-Cary theories involve the use of soil-water diffusivities. Milly (1982) developed a matric head, as opposed to water content, model of moisture and heat flow in a porous media. This change in dependent variable made possible the incorporation of hysteresis and soil heterogeneities.

All of the mathematical models proposed consider simultaneous heat, liquid water, and water vapor transfer. At the elevated temperatures expected in the vicinity of the HLNW repository, vapor transfer will presumably be greater than liquid water transfer. In addition, the resulting latent heat storage and advection of sensible heat by the vapor phase will be small when compared to heat conduction through the rock matrix. This fact allows for indirect coupling of heat and mass transfer rather than direct coupling.

Heating experiments have been performed to establish a vapor liquid counter-current in a sealed rock core. After a temperature gradient is established along the rock core, the core is monitored to determine changes in water content, temperature, and electrical resistivity. With this information, the ion movement caused by the counter-current is determined. Water soluble ions will move with liquid water toward the heat source but will not move away in the water vapor.

In fractured media, fracture flow may dominate in the zone of

condensation around the repository. The lower suction in the zone of condensation will allow larger fractures to saturate, establishing a zone of higher fluid conductivity.

### 0.3 Limitations and Recommendation for Further Research

Limitations with current theories and techniques include the inadequate testing of measurement techniques over a wide range of suctions, especially the dry range which may be of particular interest. Also, accurate methods for measuring matrix suction, or the hydraulic head, are not currently available.

The sampling of pore or fracture fluids is difficult at high suctions. Thus, samples for examining travel times of tracers or for investigating geochemical processes are difficult to obtain.

The conductivity of fractures as a function of fluid suction is an area for additional research. Little empirical evidence has been obtained with regard to the moisture release curve for an individual fracture. Also, the lack of data has impeded the calibration of conceptual and computer models.

It is recommended that further research be performed, specifically with regard to large-scale field facility for testing of a well-instrumented heating experiment. In addition, it is recommended that a natural analog be identified for use in model calibration and validation.

## CHAPTER 1 INTRODUCTION

This document describes field, laboratory and numerical methodologies for judging the contaminant isolation capabilities of unsaturated fractured rock. The focuses are on the hydrologic and transport issues stated in the revisions to 10 CFR 60 formulated to include unsaturated media as potential repository sites for high level waste disposal (Hackbarth, Nicholson and Evans, 1985). The research which this document summarizes is generic in nature, having application to the characterization of specific unsaturated fractured rock sites.

### 1.1 Scope

Of primary interest to regulatory reviewers will be the ability to demonstrate the potential for a geologic setting to isolate a wide assortment of nuclear wastes from the accessible environment. Of primary interest is high-level radioactive waste from commercial sources. By showing that the geologic media, in conjunction with engineered barriers, adequately prevents harmful levels of radioactive materials from reaching the biosphere, the regulators and general public can be more assured of the safety of nuclear waste disposal. The scope, therefore, is the ability to accurately determine fluid and solute movement within the zone around the waste canisters, and also at greater distances.

To provide a quantitative understanding of the rate and amount of fluid and solute transport through the geologic media surrounding proposed repositories within unsaturated zones, an integrated package of research topics has been undertaken. The research topics have provided new, substantial information which is critical to the successful design and understanding of the hydrogeologic environment at a proposed repository site.

The research topics are of interest because of the potential difficulty of quantifying fluid and solute movement through unsaturated fractured rocks of low permeability. Previous to the current research, the understanding of movement of fluids and solutes was limited to saturated and unsaturated media composed of uniformly porous material with moderate to high permeability, or to saturated rock of low permeability.

Thus, the topics of interest incorporate theory, experimental and statistical methods, and laboratory and field data, which differ from classical studies on several points. In particular, transport through

discrete fractures, as opposed to continuous porous media transport, requires new sampling techniques and procedures. The interpretation of data from discrete points is more difficult when averaging over space. Also, there is a major difficulty associated with the application of fluid and vapor transport theories in the unsaturated zone. This results from the paucity of empirical support to provide a consistent and universally acceptable basis for consensus.

To overcome these and other difficulties, the present program has generated data, information, and techniques which are useful for resolving issues central to successful site characterization for the isolation of nuclear waste materials.

The research has been conducted by the Department of Hydrology and Water Resources, College of Engineering and Mines, University of Arizona. The program has been closely coordinated with a parallel, NRC-funded project at the University of Arizona focused on contaminant transport through saturated fractured rock, with Drs. S. P. Neuman and E. S. Simpson as co-principal investigators. The methods and results obtained for saturated conditions are directly applicable to the special case of a combined unsaturated-saturated system.

## 1.2 Organization

A general overview of the project is presented in this first chapter, along with a description of the field sites and available computer and laboratory resources. Following this introductory chapter, an assessment of the information required to describe the physical and chemical nature of the rock matrix and fractures located within a rock matrix is presented. The chapter focuses on techniques to describe the physical properties of both the rock matrix and fracture systems within the rock body. Methods to determine the porosity, pore size distribution and fracture parameters such as density, orientation, etc., are also presented.

Chapter 3 describes the current status of the ability to provide data about the energy distribution of fluids within geologic media. Because fluids flow from regions of higher energy potential to regions of lower potential, the knowledge of energy levels will indicate the direction of fluid flow. Also necessary is the rate at which fluid flow occurs. By knowing the potential distribution and estimating the hydraulic conductivity of each medium, one may obtain an estimation of the flux and velocity of the fluid. A technique which is useful for determining the conductivity as a function of the energy potential is described.

Stored high-level waste will generate heat and cause a thermal gradient to develop in the media surrounding the waste. The determination of fluid flow and solute transport through geologic media where non-isothermal conditions are present requires the application of coupled process analysis. A coupled approach for simultaneous fluid, vapor, solute, and heat is presented in Chapter 4. Numerical, laboratory and field experiments are presented which support the hypothesis that a counter-current flow regime may develop near the heat source.

A counter-current flow regime will result in liquid and solutes moving toward the heat source while vapor and heat are transported away from the heat source. It is possible that heat generated by a repository will result in the net migration of dissolved constituents back to the repository. If this process is confirmed, then even if radionuclides escape engineered structures, then natural mechanisms will prevent the migration of the soluble nuclides away from the repository. This fail-safe mechanism has been demonstrated.

Chapter 5 presents solute transport research which is useful for confirming calculated velocities. Sampling the rock water for chemical analysis is a major difficulty associated with solute transport assessment. Several approaches have been explored and preliminary results are presented.

A field technique is described which utilizes a volatile tracer (i.e., a chemical compound which vaporizes easily) to monitor the progress of a fluid as it moves through the unsaturated zone. This technique is useful because obtaining a gas sample from unsaturated rock with low water content and with the liquid under negative pressure is easier than obtaining a liquid sample.

Another technique to examine fluid and solute movement through unsaturated media considers the possibility of recovering water vapor which would be in equilibrium with liquid water within the rock. The testing of water vapor for the presence of an isotope of water can indicate the source and/or age of the water. This may lead to an understanding of the past and present movement of the water.

The total flux and solute movement through unsaturated media might be estimated by utilizing geo-chemical mixing at or near the water-table. By identifying the reaction kinetics and the mixing process of two dissimilar water components, a more accurate assessment of the through-flow of solutes and fluids can be made. In addition, the reaction

kinetics will provide a more detailed understanding of the migration of escaped radionuclides.

Chapter 6 investigates the potential influence nuclear materials will have on liquid, vapor and solutes in the zone immediately surrounding a repository. This analysis explores the possibility that gamma radiation may provide a mechanism for the dispersal of positively-charged ions away from a repository. The mechanism is considered to be near-field effect resulting from the decay of nuclear materials in the repository.

A final, summary chapter reviews the procedures presented in this report for evaluating the capacity of unsaturated media to isolate wastes. Appendices are also included which more specifically describe laboratory and field procedures described in this report.

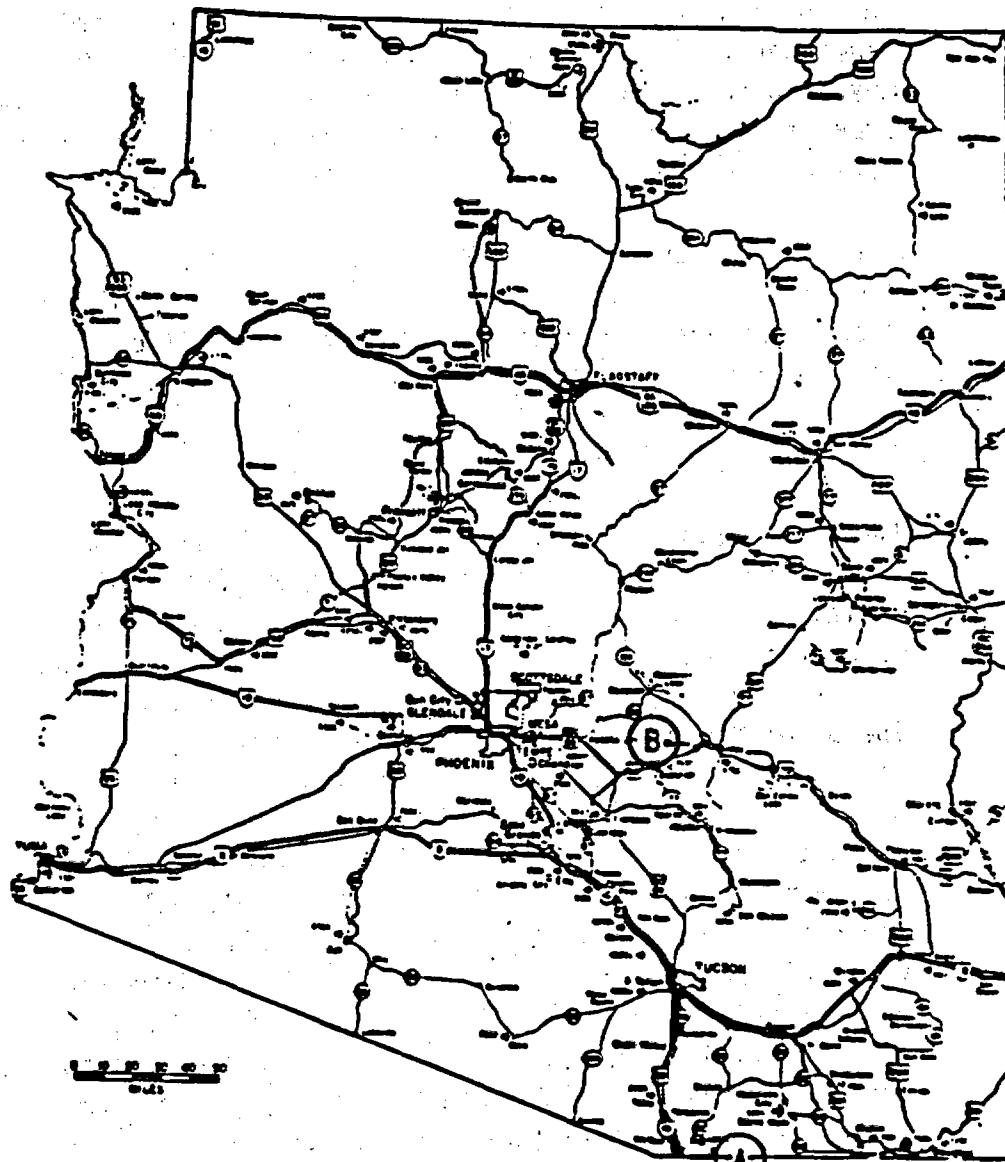
### 1.3 Field Study Areas

Two field study areas have been developed for the assessment of methods to measure fluid flow and solute transport in unsaturated geologic media. Both study areas (Figure 1.1) are located in unsaturated, fractured rock. One study area is located near Patagonia, Arizona, in the region surrounding the Patagonia Mountains in southeast Arizona. The other study area is located near Superior, Arizona, on the western edge of the Pinal Mountains in central Arizona.

The climate at the study areas is semi-arid, receiving less than 510 mm of rain per year. Rainfall varies seasonally, with the majority occurring during two periods, July through September, and December through March. Thunderstorms produce localized, high-intensity precipitation events during the summer months, and frontal storms produce widespread, but low-intensity, precipitation during the winter months. Summer temperatures typically range from 10 to 40°C, while winter temperatures range from -5 to 15°C.

#### 1.3.1 Patagonia Mountains Study Area

The Patagonia Mountains are a north-northwesterly trending range lying east of Nogales and south of Patagonia in southeastern Arizona. The mountains consist in large part of Mesozoic volcanic and sedimentary rocks. The layered rocks comprise six stratigraphic units of known or strongly inferred Mesozoic age and two units of uncertain but probable Late Cretaceous or early Tertiary age. The aggregate total thickness is unknown, but may be as much as 4500 m. Volcanic rocks of silicic to intermediate composition make up 75 percent or more of the Mesozoic



- A - PATAGONIA STUDY AREA
- B - SUPERIOR STUDY AREA

Figure 1.1 Location map of the Patagonia and Superior study areas.

stratigraphic column; the remainder is sedimentary rocks and some interlayered volcanic beds.

Three field sites have been developed in the Patagonia Mountains. The locations of sites are presented in Figure 1.2. One site, the Santo Nino mine, is located in quartz diorite. A second site, the Patagonia field site, is located in bedded, welded tuff. The third site, at the Pride-of-the-West Mine, is not described. A description of the other two sites is summarized below.

#### 1.3.1.1 Santo Nino Mine Site

The Santo Nino mine site lies at an elevation of approximately 1800 m in the extreme southern section of Arizona, 3 km directly north of the Mexican border. The mine is located in section 9, township 24 south, range 16 east on the eastern slope of the Patagonia Mountains. The mine penetrates the Patagonia range batholith, a tertiary intrusive underlying the Patagonia mountains. The rock is described as a gray quartz monzonite. The principal ore-bearing formation was described by Kirkemo et al. (1965) as a pink feldspar-rich medium-grained granitic rock.

The contact between the pink feldspar rock and the granitic monzonite is gradational and irregular, suggesting the ore body has replaced the surrounding country rock. Copper and molybdenite disseminated throughout the ore body were the principal ores mined. Specific mineralogy is presented in Table 1.1 (Baker, 1962). The bulk density of the quartz monzonite matrix is  $2.63 \pm 0.06 \text{ g/cm}^3$  and the grain density is  $2.67 \pm 0.04 \text{ g/cm}^3$  (Evans, 1983a). Thus, the matrix porosity is  $1.7 \pm 0.8$  percent.

-----  
Table 1.1 Mineralogy of Santo Nino Quartz Monzonite, after Baker (1962).  
-----

<u>Mineral</u>	<u>Percent</u>
Albite-orthoclase	32 - 38
Potassium feldspar	26 - 29
Quartz	20 - 33
Biotite	6 - 8
Hornblend	0 - 3

-----

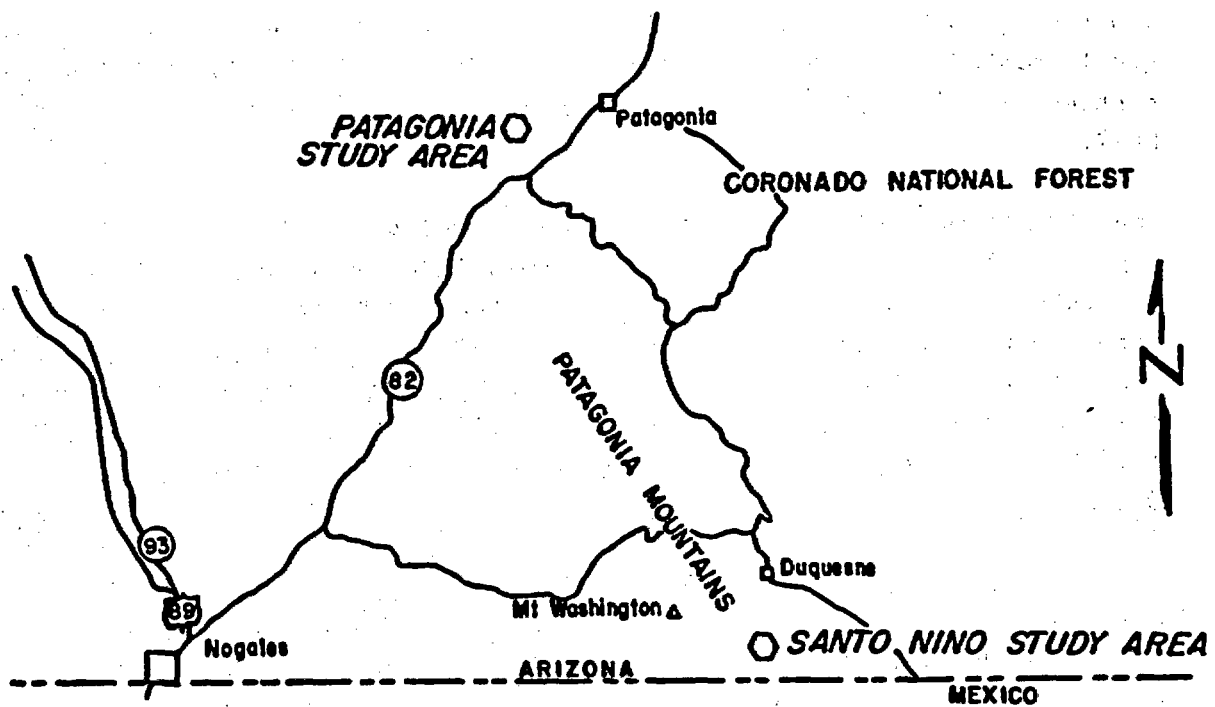


Figure 1.2 Location map of the Santo Nino mine, the Pride-of-the-West mine and the Patagonia field sites.



Figure 1.3 Photograph of entrance to the Santo Nino mine.

Three prominent fracture sets, both mineralized and unmineralized, are found inside the mine and at the surface (Figure 1.3). These three joint sets are nearly perpendicular to one another, thus forming an orthogonal fractured rock system. Even though conventional blasting techniques were employed in constructing the drift, all three sets can be still be distinguished from the fractures caused by blast damage.

A fracture survey was conducted along the first 100 m of the adit (Figure 1.4). Sampling was conducted along a scanline taken at approximately 1.2 m above the floor and along the western rib of the adit. All fractures which had a regular trace and intercepted the scanline were noted. Fracture data recorded included:

- |                         |                                  |
|-------------------------|----------------------------------|
| (1) orientation;        | (5) fracture filling;            |
| (2) spacing;            | (6) weathering;                  |
| (3) length of trace;    | (7) seepage characteristics; and |
| (4) surface regularity; | (8) shear displacement.          |

The fracture orientation data were plotted on a Schmidt stereonet and contoured for fracture density (Figure 1.5). The data indicate that two prominent fracture sets were present. The most pervasive set runs parallel to several major faults and gouge zones. Its apparent dominance is primarily due to the near perpendicular orientation of the fracture relative to the axis of the adit. The third fracture set is not evident because it lies parallel to the adit and is difficult, if not impossible, to sample.

The poles of the second fracture set almost plot in the center of the Schmit net, thus indicating this set is nearly horizontal. The density is slightly diminished in comparison to the first set because the second set is parallel to the survey scanline. A third, less-pronounced set also runs parallel to the survey scanline. The existence of the third set is made evident by the large exposures of these fracture planes along the adit walls.

Eight holes, each with a diameter of 4.75 cm were drilled into the walls of the Santo Nino mine. Of these, two horizontal holes in the east wall were logged for this study. They are located 5.2 and 5.8 m from the portal and six meters below the surface. Borehole 5.2 is 5.6 m long and Borehole 5.8 is 6.4 m long. The spatial location of fractures detected using a video logger in Boreholes 5.2 and 5.8 are presented in Figure 1.6. The fracture density calculated from the core data is three fractures per meter.

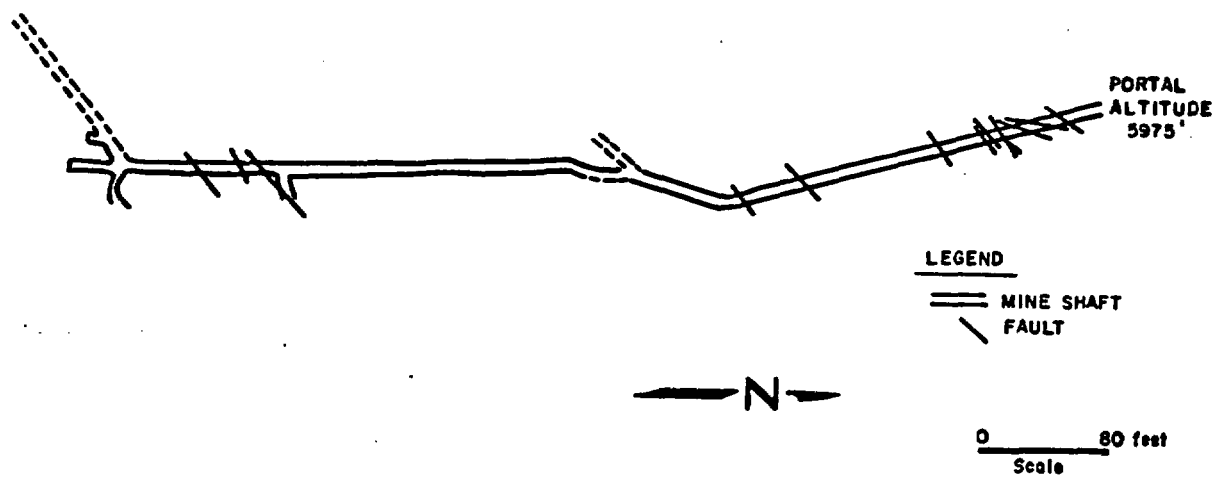


Figure 1.4 Plan view of Santo Nino mine adit (after Baker, 1962).

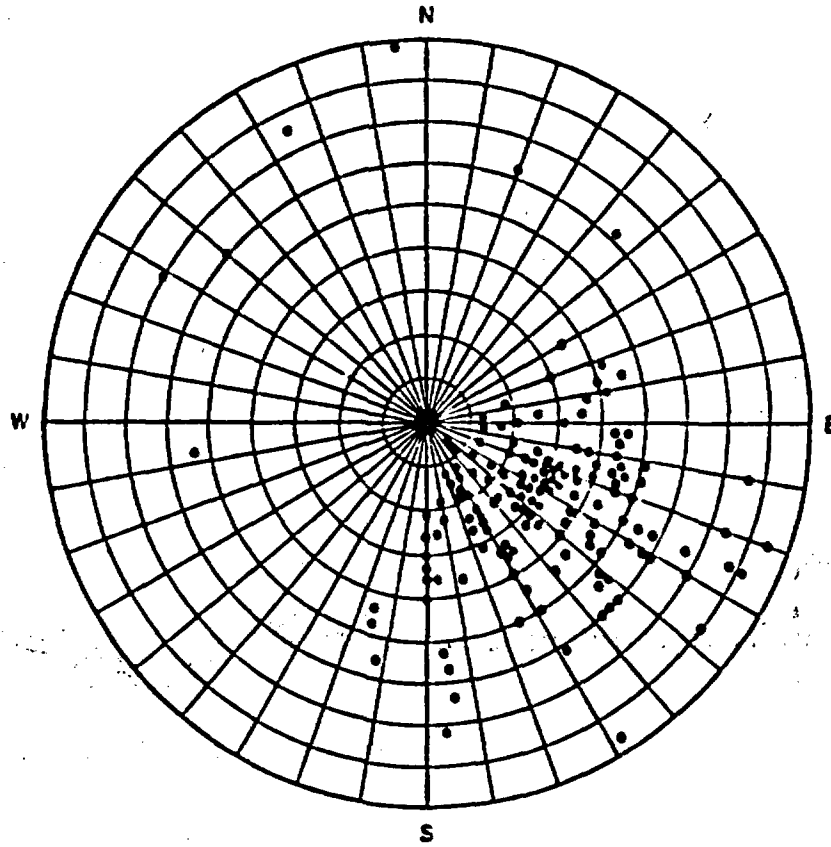


Figure 1.5 Schmidt stereonet of fracture orientation.

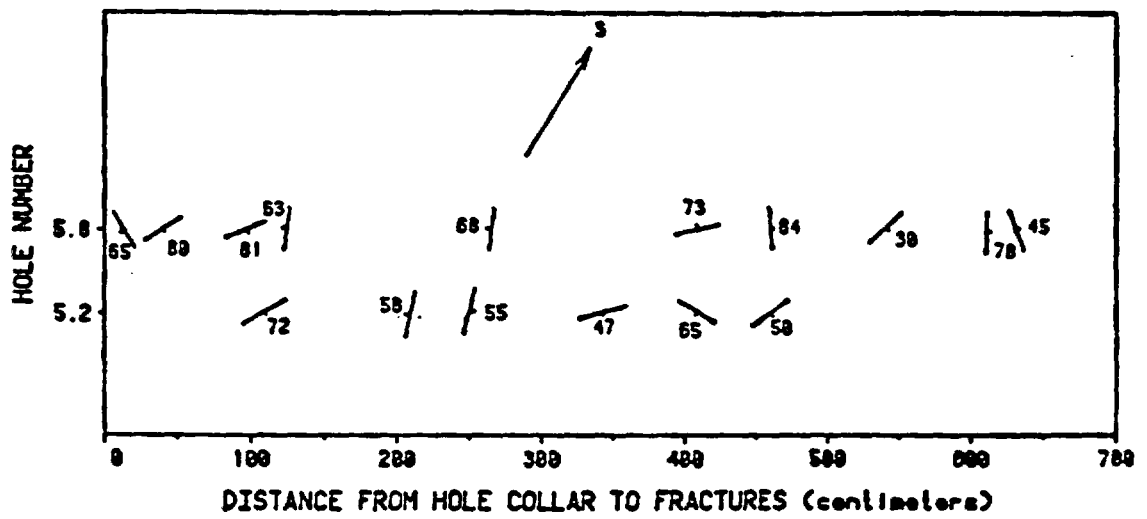


Figure 1.6 Plan view location, strike and dip for each fracture detected on the video log.

Figure 1.7 provides a cross-section of the Santo Nino mine. Two slightly inclined holes ( $10^\circ$  below horizontal) in the west wall six meters from the portal have standing water. Water levels in the upper hole (Borehole 6.0a) measured between October 1982, and August 1983, are presented in Figure 1.8 (Evans, 1983c). Precipitation data collected in the Patagonia Mountains between September 1982 and August 1983 from a rain gage situated above the Santa Nino mine are also presented in Figure 1.8. Mean monthly surface and recorded borehole temperatures for the Santo Nino mine are presented in Figure 1.9. The mean monthly data, from the Nogales weather station, have been corrected for an elevation difference of 640 m using an adiabatic lapse rate of  $2^\circ\text{C}$  per 300 m.

By comparing the precipitation histogram with the the borehole water level profile, it appears that the response time between the surface and Borehole 6.0a is approximately eight weeks when the overburden is initially dry, and less than four weeks when the overburden is nearly saturated. The water levels for Borehole 6.0b are not included because the standing water on the mine floor flooded this hole in February and again in July. Although a drain was installed at the portal, flow into the mine exceeded the capacity of this pipe. Unexpectedly, standing water above the pipe level remained through the dry spring months. A diagram of the location of these boreholes and the standing water levels is presented in Figure 1.10.

#### 1.3.1.2 Patagonia Field Site

The Patagonia field site (Figure 1.11) is located approximately two miles southwest of the town of Patagonia, 1.2 km north of Sonoita Creek, between Goat Canyon to the west and Temporal Canyon to the east, Santa Cruz County, Arizona. Its formal location description is Patagonia, Arizona, U.S. Geological Survey 17-minute quadrangle. The study area lies on the privately-owned land bounded on the south by the Patagonia Bird Sanctuary and the north by the Coronado National Forest. Across Sonoita Creek to the southeast are Alum and Flux Mountains. The Santa Rita Mountains are approximately eight kilometers to the north.

The Patagonia study area is a flat-topped butte approximately 1.4 hectares in area, at an approximate elevation of 1,280 m above sea level. Geology of the local area has been studied in detail by Drewes (1972). The butte which comprises the study area is capped by a Paleocene aged (60 to 65 million years) welded ash-flow tuff. This rhyolitic tuff, described as the basal unit of the upper member of the Gringo Gulch Volcanics, is the unit characterized by this investigation. It was deposited largely by airfall and fluvial processes. The welded

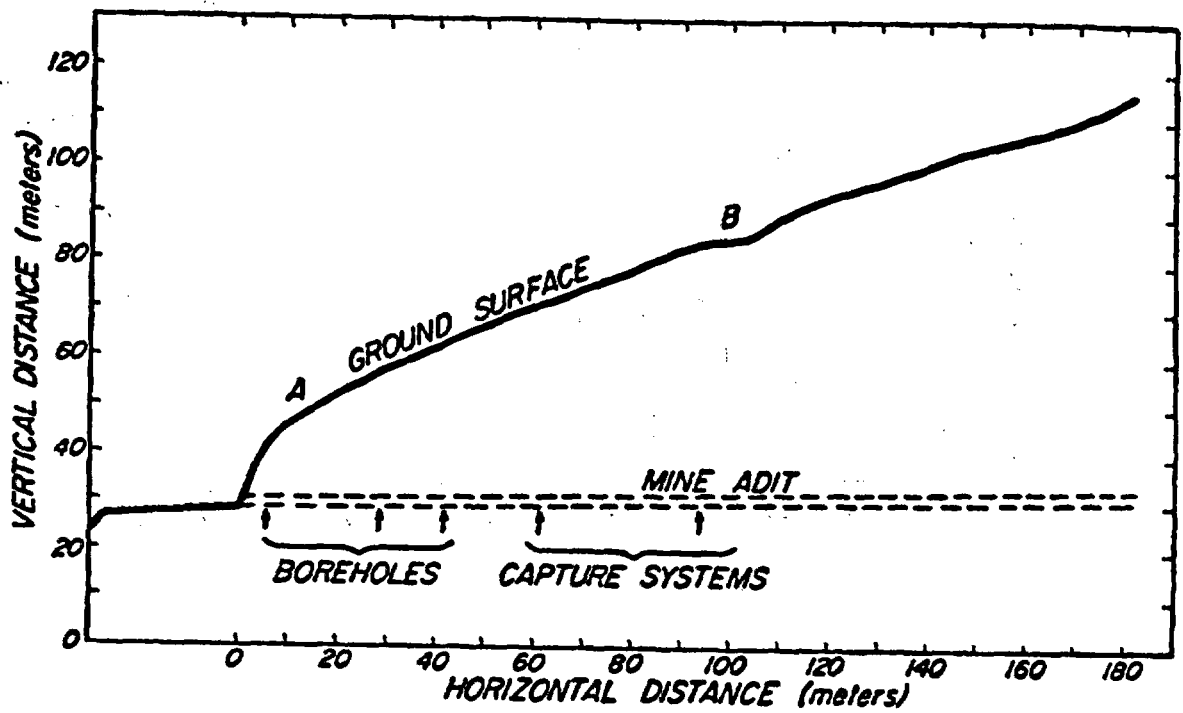


Figure 1.7 Cross-section of the Santo Nino mine.

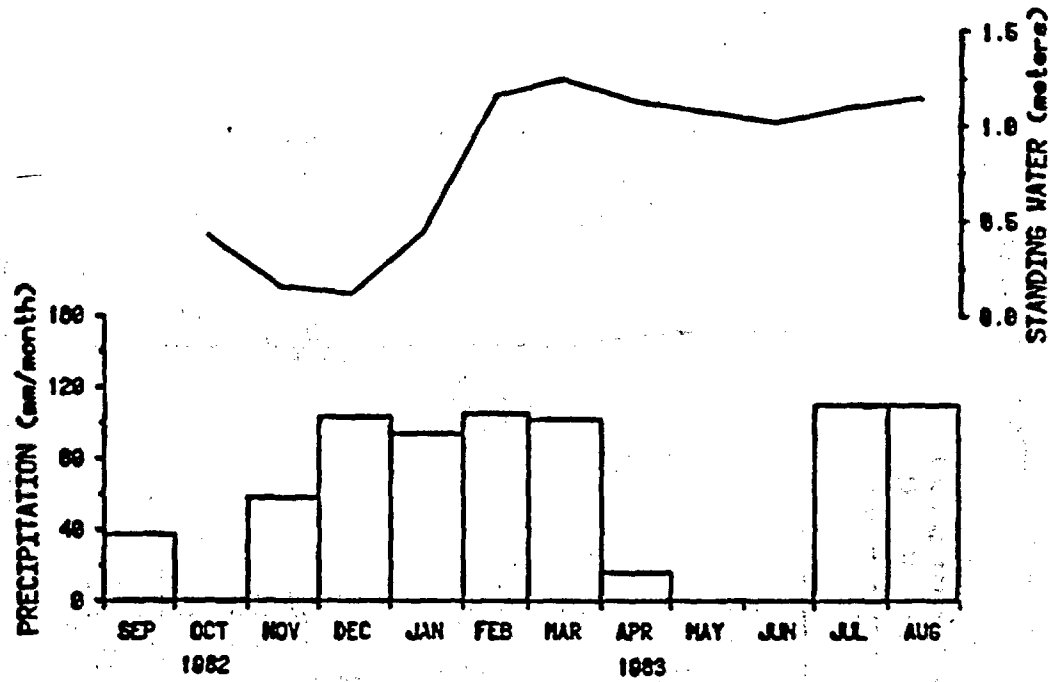


Figure 1.8 Relative water levels in Borehole 6.0a.

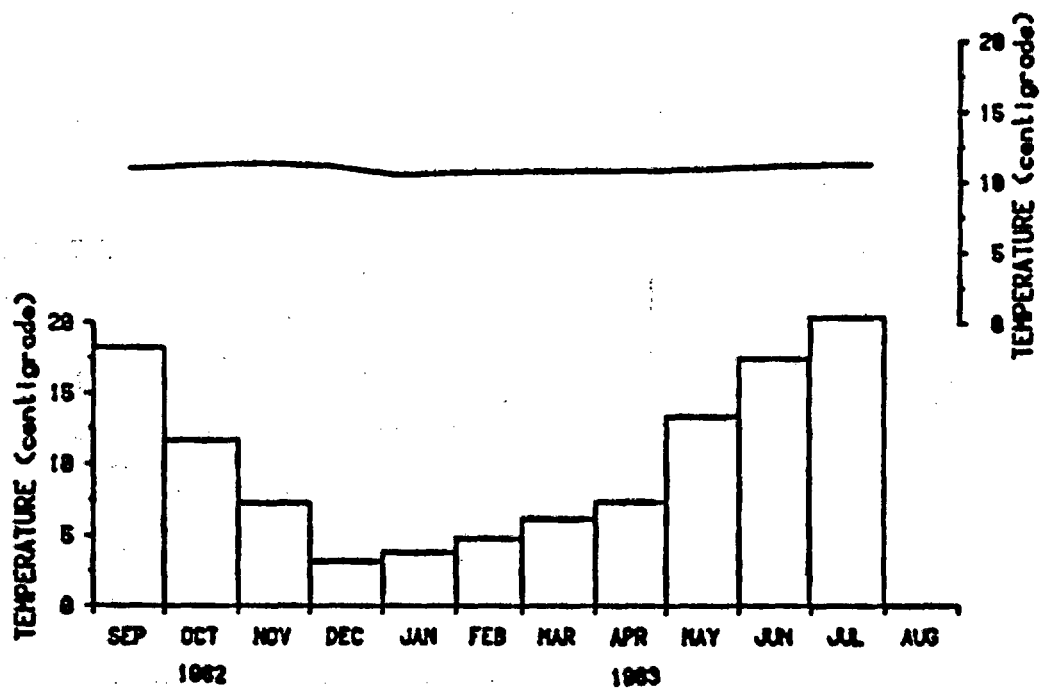


Figure 1.9 Borehole temperatures (line graph) and mean monthly surface temperatures (bar graph) at the Santo Nino field site.

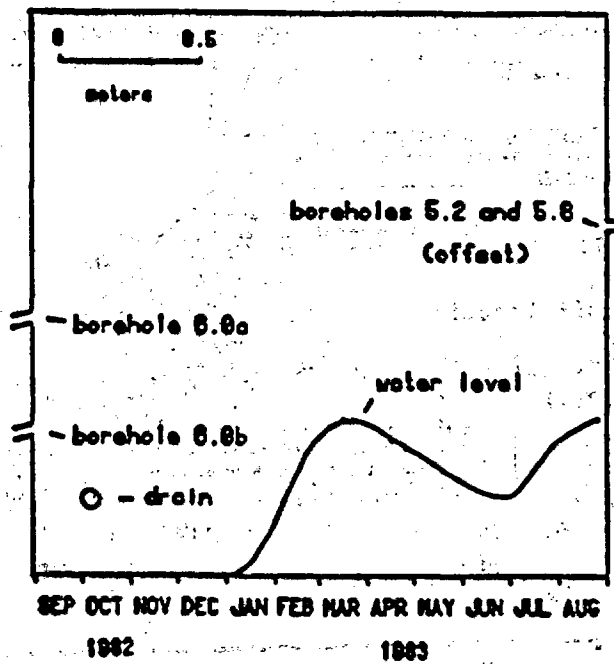


Figure 1.10 Cross-section perpendicular to the Santo Nino mine adit showing the location of boreholes and ponded water levels.

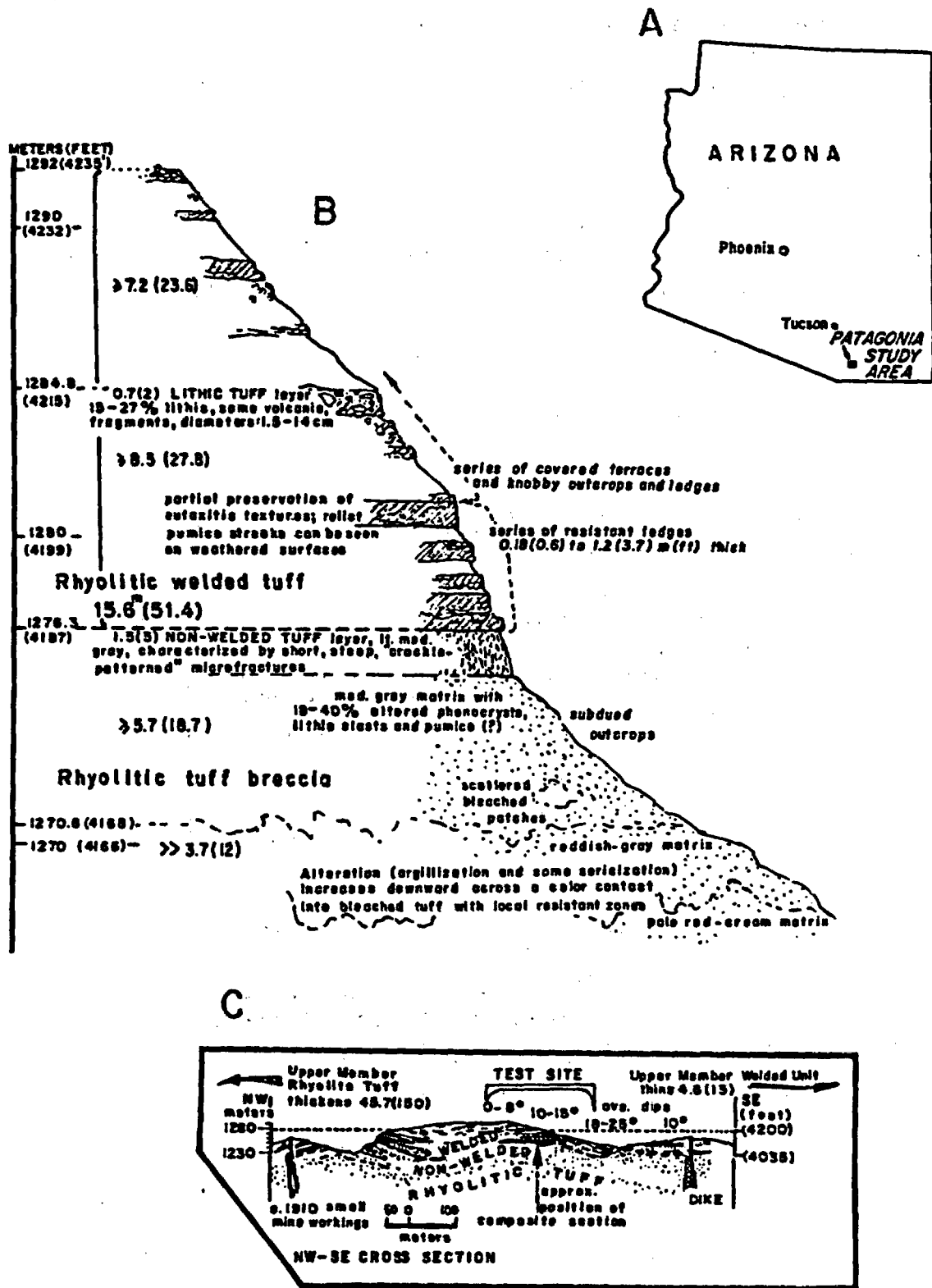


Figure 1.11 Site location map (A), partial stratigraphic section (B), and structural cross-section (C) of Patagonia study area.

tuff is approximately 15 m thick (Figure 1.12). It overlies the lower member of the Gringo Gulch Volcanics, a non-trending undifferentiated rhyolitic tuff, and is dissected by a northwest-trending fault (Drewes, 1971). The Gringo Gulch Volcanics lies unconformably upon the upper Cretaceous Josephine Canyon Diorite, whose youngest member is 65 million years old (Drewes, 1972).

The welded tuff at the Patagonia study area is relatively flat. Dips range from 5 to 9° striking an approximate north to northwest direction. Horizontal fractures in the tuff are evidenced by a series of terraces and ledges (Figure 1.13) which produce an obvious bedded appearance. The tuff matrix is microcrystalline, dark blue-gray in color, and contains less than 10 to 20 percent phenocrysts of altered biotite and plagioclase. Flattened, subparallel, aligned pumic fragments, with an estimated 15:1 length-width ratio, are evidence of a high degree of welding.

Vertical fractures in the tuff are considered to be the major form of recharge through the unsaturated zone. The large number of fractures present in the tuff is likely the result of the brittle nature of the rock. No single dominant vertical fracture strike pattern is apparent. It is likely that a combination of fracture-inducing events, such as contraction due to cooling and tectonic events, produced the random strike pattern at the Patagonia study area. Near the perimeter of the study area large blocks break off the ledges revealing the nature of the vertical fracture planes at depth. The planes are surprisingly smooth, free of fracture waviness and abnormalities (Figure 1.14).

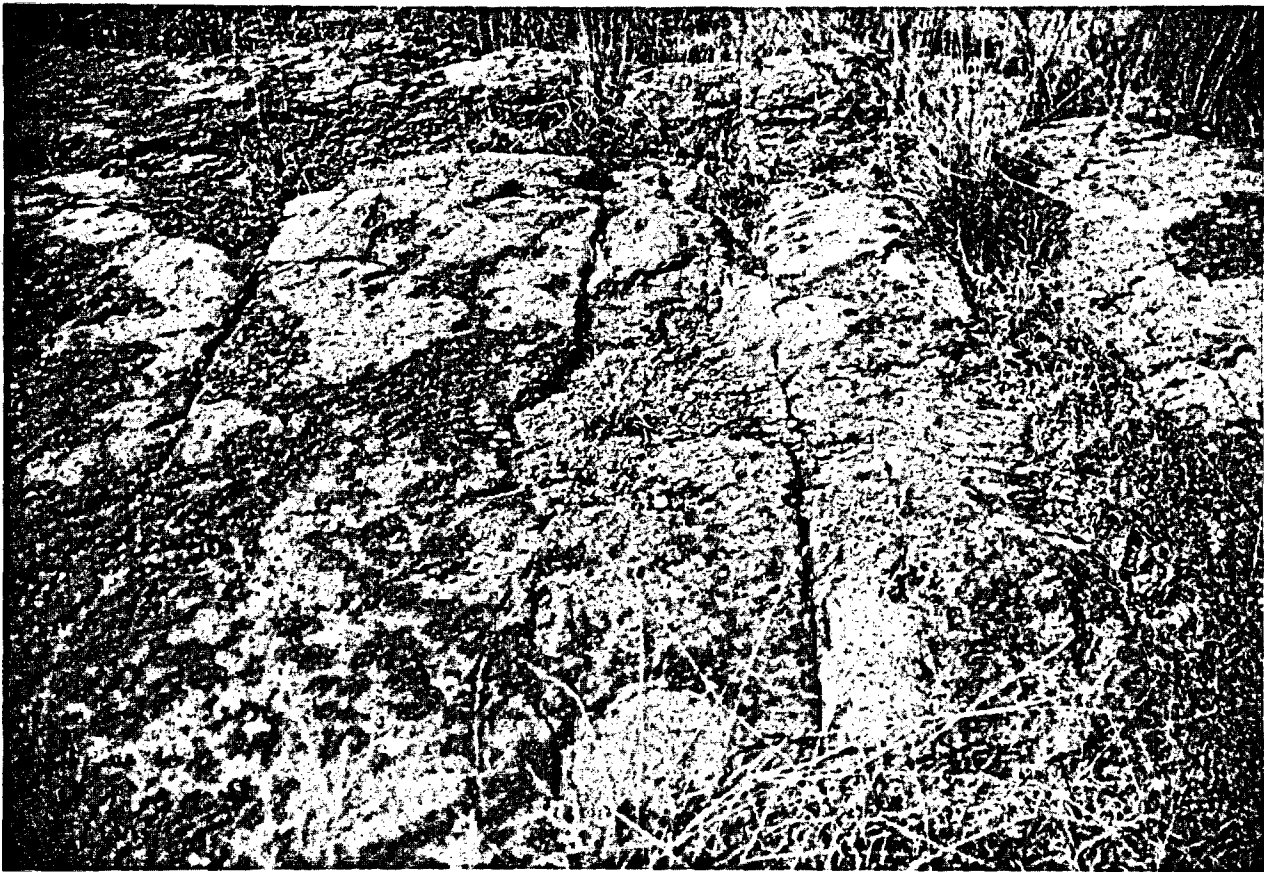
### 1.3.2 Superior Study Area

The Superior study area is located near the extreme western edge of the Pinal mountains of central Arizona. Elevations rising above 2100 m are found in the Mazatzal Mountains, 50 km to the north-northwest, in the Sierra Ancha Mountains, 56 km to the north-northwest, and in the Pinal Mountains, 25 km to the east (Sellers, 1974).

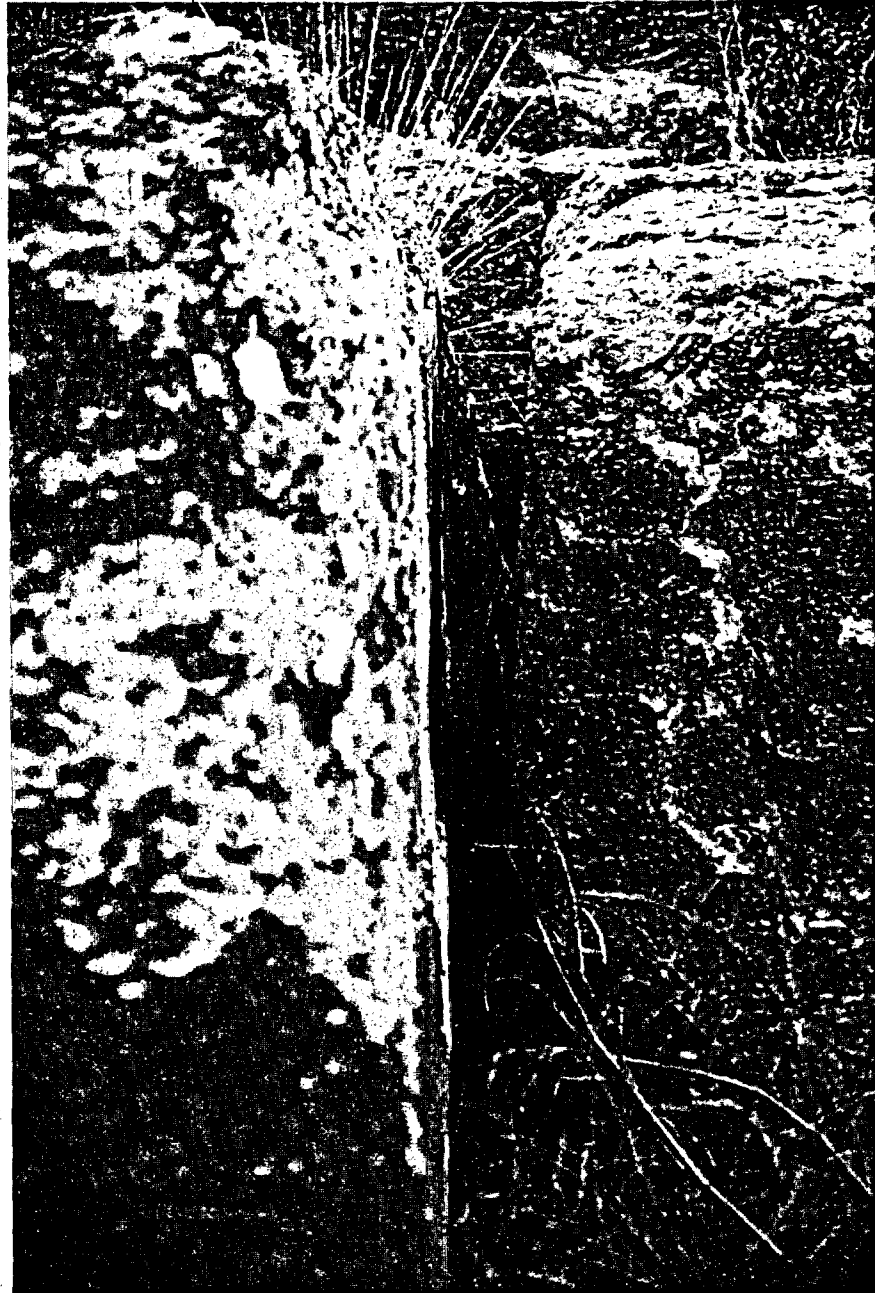
Dacitic ash-flow deposits at one time covered an area of approximately 1000 km<sup>2</sup> in the region. Presently, this area has been reduced by erosion to 250 km<sup>2</sup>. Although the average thickness of the ash flow is about 150 m, its thickness exceeds 600 m east of Superior (Peterson, 1961). Ash-flow tuffs are consolidated deposits of volcanic ash (diameter less than 0.4 mm) resulting from a turbulent mixture of gas and pyroclastic materials of high temperature, ejected from a crater, that have traveled rapidly down the slope of a volcano. The beds



Figure 1.12 Photograph of the Patagonia study area welded tuff outcrop.



**Figure 1.13** Photograph of the Patagonia study area surface.



**Figure 1.14** Photograph showing a vertical fracture plane area at the Patagonia study area.

resulting from this flow mechanism may or may not be completely or partially welded (Ross, 1961).

The geologic deposit in the which the Superior study area is located is a dacitic ash-flow sheet made up of an undetermined number of separate ash flows. The ash flows have been dated to  $19.9 \pm 0.9$  million years (middle Miocene age). It is believed they were erupted in rapid succession to form a single ash-flow sheet, which represents a single cooling unit. In places, the individual units cannot be recognized.

Part of the ash flow is composed of densely-welded tuff, other parts are slightly-welded. Peterson (1968) divided the ash-flow sheet into five different units based upon the degree of welding (Figure 1.15). Peterson also determined, on the basis of chemical composition, that the volcanic ash-flow sheet is a quartz latite. Although classified as a quartz latite, dacite is a genetically more descriptive term because the tuff units consist of large phenocrysts embedded in a groundmass. The mineralogy of the phenocrysts (ranging in diameter from 0.5 to 3.0 mm) and the crypto- and micro-crystalline groundmass is presented in Table 1.2 for the brown zone.

-----  
 Table 1.2 Mineralogy of the Magma Quartz Latite, after Peterson (1961).  
 -----

<u>Phenocrysts</u> (0.5 - 3 mm)		<u>Groundmass</u> (< 0.5 mm)	
Plagioclase	75 %	Cristobalite	-
Quartz	10 %	Potassium feldspar	-
Biotite	10 %	Quartz	-
Sanidine	-	Plagioclase	-
Magnetite	< 5 %		
<b>TOTAL</b>	<b>35 - 45 %</b>	<b>TOTAL</b>	<b>55 - 65 %</b>

-----

Three test sites have been developed in the tuff deposit. The highest site both stratigraphically and elevationally is the Apache Leap site, located in slightly-welded tuff. Lower in the column are two densely-welded tuff sites. The Queen Creek road tunnel site is located approximately 200 m below the Apache Leap site in an abandoned road tunnel on U.S. Route 60, below the new road tunnel. The main haulage tunnel in the Magma Mine is the third site, located approximately 200 m below the Queen Creek road tunnel site.

ZONES OF WELDING	ZONES OF CRYSTALLIZATION	FIELD UNITS
Upper nonwelded	<div style="display: flex; flex-direction: column; align-items: center;"> <div style="margin-bottom: 10px;">↑</div> <div style="margin-bottom: 10px;">↑</div> <div style="margin-bottom: 10px;">↓</div> <div style="margin-bottom: 10px;">↓</div> <div style="margin-bottom: 10px;">↑</div> <div style="margin-bottom: 10px;">↓</div> </div>	White
Upper partly welded		Gray
Densely welded		Brown
Lower partly welded		Vitrophyre
Lower nonwelded		Basal tuff

Figure 1.15 Physical characteristics of the dacitic ash-flow sheet.

### 1.3.2.1 Apache Leap Field Site

Three boreholes have been placed in slightly-welded volcanic tuff at the Apache Leap site near Superior, Arizona (Figure 1.16). The 10-cm diameter boreholes are inclined at an angle of  $45^\circ$  from the vertical and are offset from each other by a vertical distance of 10 m (Figure 1.17). The boreholes vary in length from 18.3 m for the uppermost (X-1), to 46.6 m for the lowermost (X-3), with the intermediate borehole (X-2) having a length of 32.6 m. This design allows for the monitoring of fluid and solute flow in both the horizontal and vertical directions.

Scribed cores with a diameter of 6.35 cm were also obtained from the borehole. The scribing tool provided an orientation mark every 3.05 m. The cores have been logged to provide information regarding the location and orientation of fractures within the boreholes, and the composition and occurrence of fracture fillings. This information is presented in Table 1.3. X-ray diffraction and thin sections of the host rock and the fracture fillings are also being made.

To determine the alignment of the boreholes, photographs of a downhole gyroscope have been obtained. The photographs indicate that the total displacement of the boreholes from design specifications amounted to less than  $1.5^\circ$ . Additionally, downhole televiewer images have been obtained. Due to instrument difficulties only one borehole was viewed.

### 1.3.2.2 Queen Creek Road Tunnel Site

The Queen Creek road tunnel site is located in the unit with the highest degree of welding. Because the unit is noticeably darker than the overlying unit, the unit is also referred to as the brown unit. The site is developed in an abandoned road tunnel on U.S. Route 60, below the new road tunnel.

The bulk density of the brown zone, calculated from core samples, is approximately 2.41 grams per cubic centimeter, and the matrix porosity is about 9.0 percent. The fracture density, also from core data, is three fractures per meter. Estimating an average aperture of 300 micrometers, a crack porosity of 0.1 can be calculated. An estimate of total porosity for the Magma brown zone is, therefore, 9.1 percent.

Jointing at the Queen Creek road tunnel site is not as conspicuous in the dacite as it is in the quartz monzonite at the Santo Nino mine site. Blast damage resulting from the construction of the road tunnel helped to mask natural fractures in the dacite, making mapping difficult.

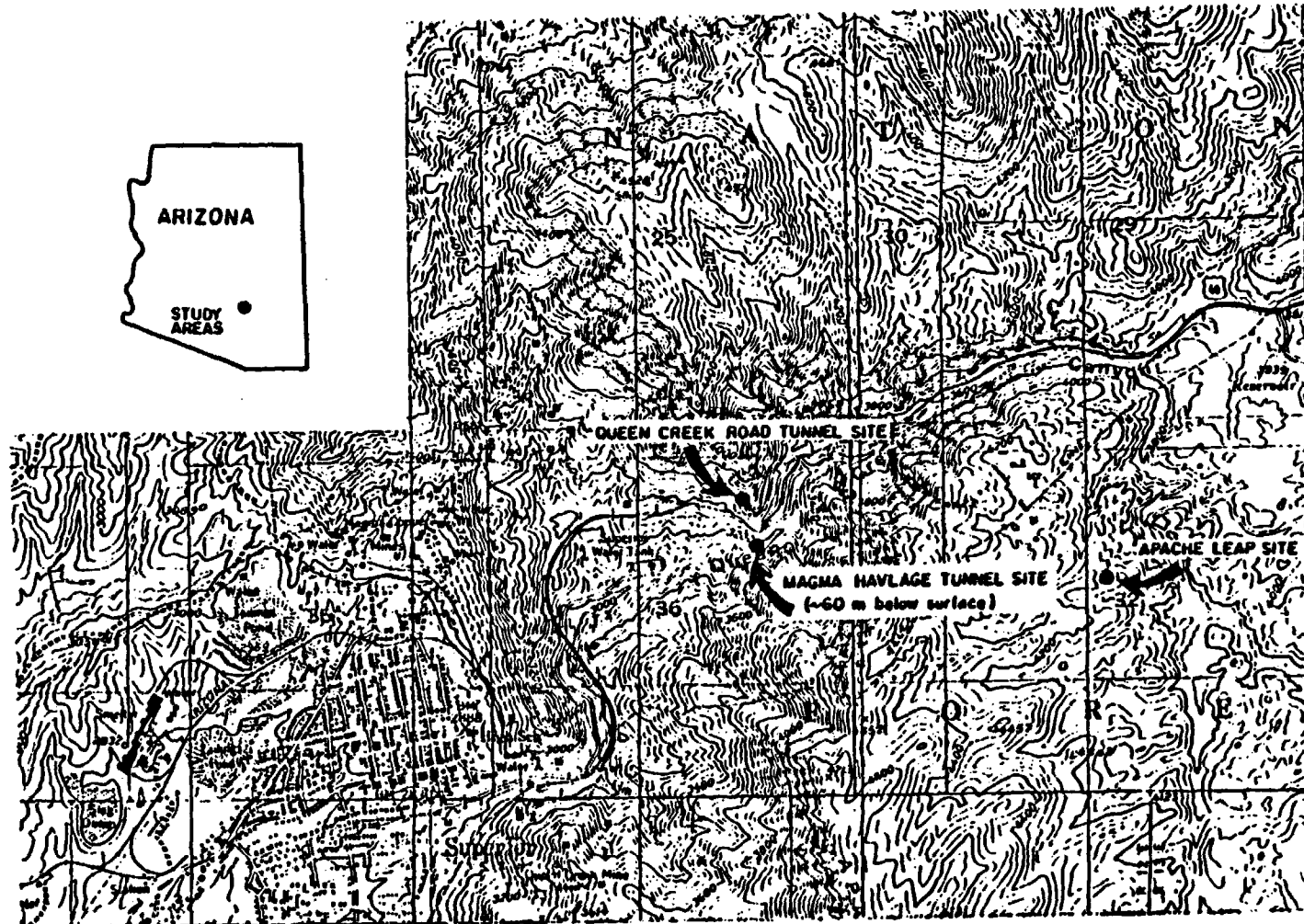


Figure 1.16 Location map of Superior field sites.

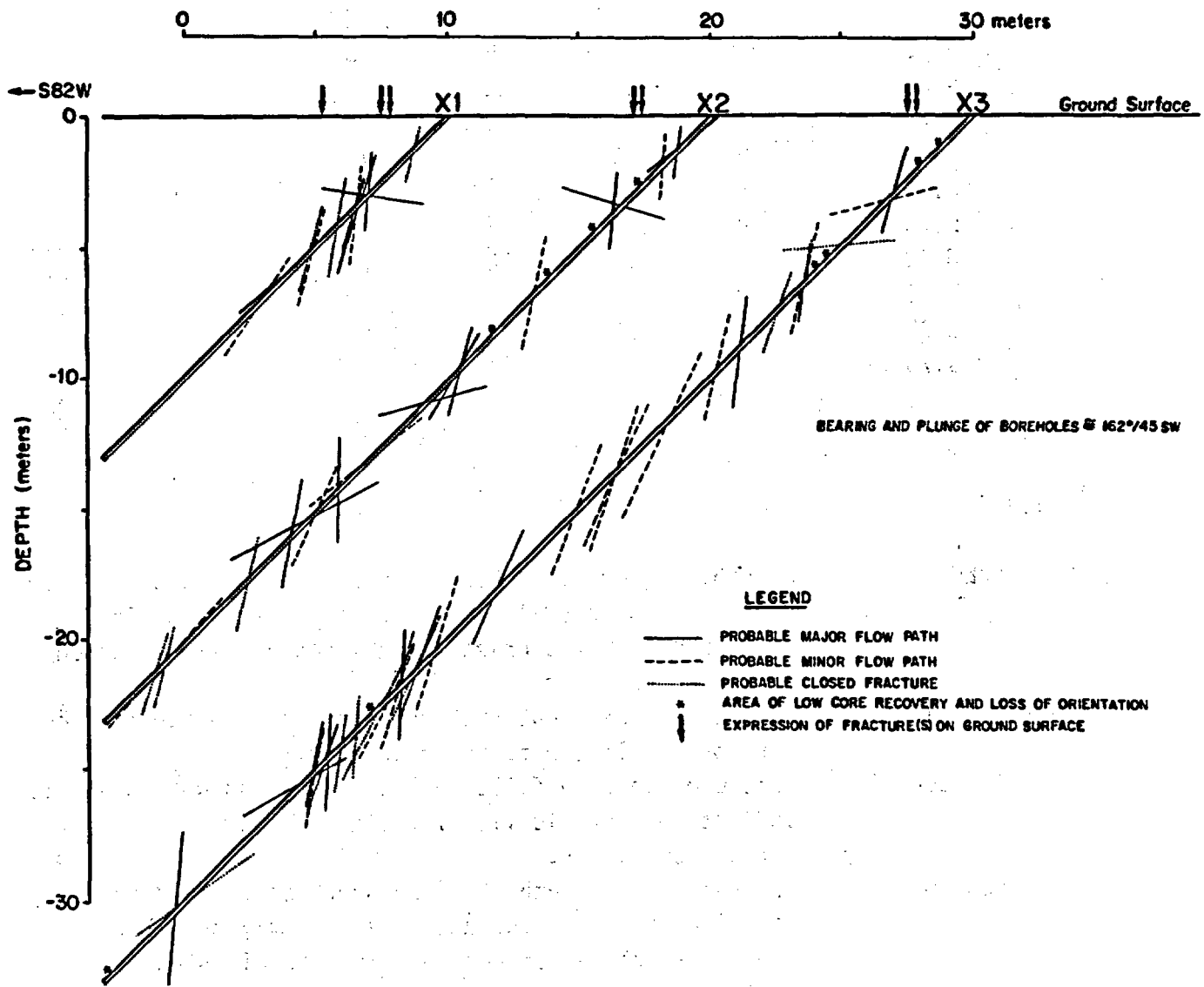


Figure 1.17 Borehole diagram, Apache Leap field site.

Table 1.3 Results of fracture survey at Apache Leap tuff site.

Borehole X-1 (Total Borehole Length 18.44 m)

Distance from Surface (m)	Class <sup>1</sup>	Strike	True Dip	Apparent <sup>2</sup>
1.77	*	345°	75°	75°
4.15	****	352°	85°	85°
4.33	****	215°	12°	171°
4.36	****	346°	73°	73°
4.63	****	329°	76°	75°
4.79	***	336°	84°	84°
5.73	*	326°	82°	81°
6.92	***	359°	75°	75°
7.13	*	358°	69°	69°
8.93	****	031°	48°	40°
9.78	***	035°	64°	56°

<sup>1</sup> Class:

- \*\*\*\* OPEN Probable major flow channel, fracture surfaces separate easily upon removal from core barrel and was clearly open when in situ. Fracture surfaces highly weathered and friable.
- \*\*\* PARTLY OPEN Same as above except that exposed fracture surface shows portions of little to no weathering.
- \*\* POSSIBLY OPEN Fracture aperture filled or nearly filled with minerals indicating historic flow but limited flow at present. Surface subplanar.
- \* CLOSED Fracture remains unbroken when core is removed from core barrel or fracture surfaces mesh tightly together. Exposed fracture surfaces show no visible sign of weathering; some display trace minerals.

<sup>2</sup> Apparent dip of fractures aligned with bearing of borehole (262°)

Table 1.3 (Continued)

Borehole X-2 (Total Borehole Length 32.61 m)

Distance from Surface (m)	Class <sup>1</sup>	Strike	True Dip	Apparent <sup>2</sup>
1.77	****	359°	82°	82°
2.32	****	300°	56°	42°
2.38	***3	-	-	-
2.47	-	359°	85°	85°
3.63	** 3	-	-	-
3.69	** 3	-	-	-
3.75	** 3	-	-	-
4.85	***	191°	17°	164°
5.18	****	354°	84°	84°
6.07	***3	-	-	-
8.50	** 3	-	-	-
9.14	***	347°	78°	78°
10.67 to 12.19	----	low core recovery	----	----
13.38	****	331°	75°	74°
13.56	****	342°	59°	59°
15.49	****	20°	17°	15°
15.51	****	20°	17°	15°
18.68	***	032°	47°	39°
20.27	***	327°	89°	89°
21.03	***	334°	67°	66°
21.67	****	16°	30°	28°
22.49	****	347°	79°	79°
24.78	*	339°	76°	76°
28.47	***	303°	60°	49°
28.56	* 3	-	-	-
28.65	***	44°	63°	50°
29.23	*	318°	78°	76°
29.38	*	3°	72°	72°

<sup>1</sup> See note on initial page of table.

<sup>2</sup> See note on initial page of table.

<sup>3</sup> No orientation possible either due to very subplanar fracture, high degree of mineralization closing fracture, or loss of orientation during drilling.

Table 1.3 (Continued)

Borehole X-3 (Total Borehole Length 46.64 m)

Distance from Surface (m)	Class <sup>1</sup>	Strike	True Dip	Apparent <sup>2</sup>
1.62	**** <sup>3</sup>	-	-	-
2.74	** 3	-	-	-
4.15	****	356°	74°	74°
4.60	***	338°	14°	14°
5.52	* 3	-	-	-
7.01	***	19°	6°	5°
7.01 to 7.62	*	---- low core recovery ----		
7.62	* 3	-	-	-
7.62 to 8.53	*	---- low core recovery ----		
8.83	**	5°	79°	79°
9.02	***	337°	76°	76°
10.12	*	20°	73°	71°
12.44	****	332	83°	82°
13.32	***	343°	76°	76°
15.85	***	336°	66°	65°
18.62	***	11°	67°	66°
18.90	***	6°	71°	71°
21.03	***	334°	71°	70°
25.60	***	10°	67°	66°
25.73	****	336°	66°	65°
28.68	***	8°	74°	73°
29.66	****	329°	72°	71°
29.81	**	11°	66°	65°
30.54	****	312°	87°	86°
30.60	***	336°	78°	76°
31.21	***	328°	66°	64°
31.58	**	336°	64°	63°
31.70 to 32.52	**	---- low core recovery ----		

(Borehole X-3 continued on next page)

- <sup>1</sup> See note on initial page of table.
- <sup>2</sup> See note on initial page of table.
- <sup>3</sup> See note on initial page of table.

**Table 1.3 (Continued)**

**Borehole X-3 (Continued)**

Distance from Surface (m)	Class <sup>1</sup>	Strike	---- True	Dip Apparent <sup>2</sup>
32.64	*	332°	85°	85°
33.65	*	337°	82°	82°
34.47	****	339°	87°	87°
34.45	****	342°	72°	72°
35.14	***	324°	81°	80°
35.23	****	323°	80°	79°
35.97	****	316°	36°	29°
42.25	*	52°	55°	35°
42.55	****	309	86°	85°
46.30	* 3	-	-	-

<sup>1</sup> See note on initial page of table.

<sup>2</sup> See note on initial page of table.

<sup>3</sup> See note on initial page of table.

Moisture conditions in the dacite at the road tunnel site are measured using two sets of two boreholes drilled approximately 0.9 meters apart. In addition to measurements of moisture conditions, heater experiments have been performed to determine the movement of water in the presence of a strong thermal driving force.

### 1.3.2.3 Magma Site

The Magma field site is located inside Magma Copper Company's "Never Sweat" haulage tunnel in Superior, Arizona. Two horizontal holes were drilled where the densely-welded tuff intersects the "Never Sweat" haulage tunnel. These holes, 4.75 centimeters in diameter, are located 1800 meters from the portal and 80 meters below the surface (Figure 1.18). The 15-meter top hole was logged periodically with the resistivity and neutron probes between March and August 1983. Water did not stop flowing from the 22-meter bottom hole until June 1983. Therefore, this hole was not logged. Flowrates for the lower borehole are presented in Figure 1.19.

## 1.4 Laboratory Facilities

In addition to the field sites identified above, laboratories have been developed which provide facilities for the analysis of materials obtained from field sampling. These facilities include a constant temperature laboratory which is necessary for the isolation of samples from the effects of variable thermal influences. In addition, laboratory space is available for determining the porosity and moisture content of rock samples.

Available facilities also include four Tempe pressure cells, a rock-coring bit, a 5-bar and a 15-bar pressure plate extractor. This equipment is used for obtaining moisture release curves. Drilling equipment is also available to provide 5-cm rock cores. X-ray diffraction equipment is available for determining the composition of rock samples.

## 1.5 Computer Facilities

Simple numerical problems are solved using IBM-PC microcomputers equipped with 8087 numeric co-processors. For larger problems, a VAX 11/780 computer operating under VAX/VMS 4.1 is available. In applications where the VAX system is inadequate to arrive at a solution in a cost-effective manner, a CYBER 175 operating under NOS/BE 1.7 is used.

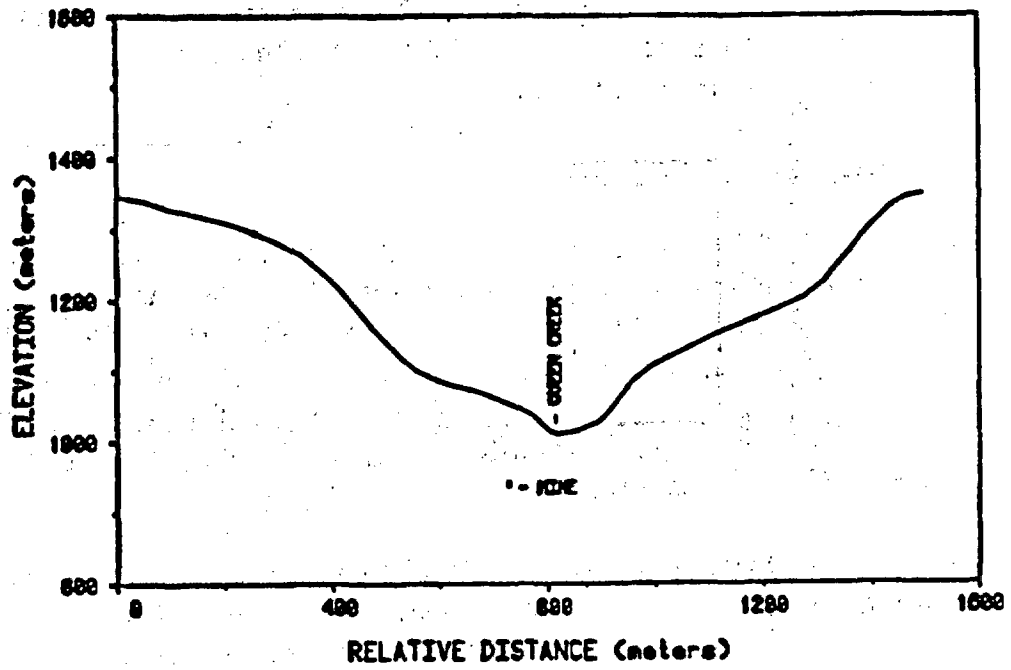


Figure 1.18 View perpendicular to the Magma haulage tunnel.

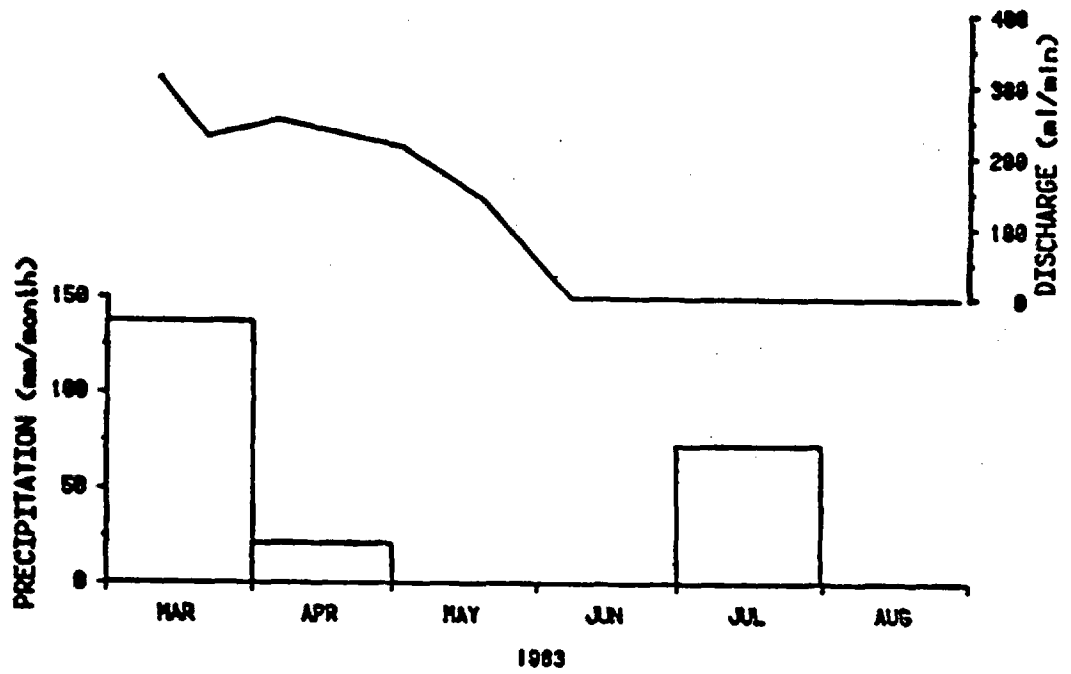


Figure 1.19 Flow rates from the lower borehole (line graph) and precipitation (bar graph) versus time at Magma field site.

## CHAPTER 2 ROCK CHARACTERIZATION

Fluid fluxes and transport of solutes in geologic media are dependent on the physical and hydraulic properties of the media. The transport of solutes is also strongly dependent upon the degree of interaction between the medium and the solute. Of particular interest is the assessment of parameters which determine fluid and solute travel times and fluxes over space and time. By knowing the physical relations between measurable parameters, an improved understanding of factors which affect the travel times and fluxes are obtained, and quantification of processes are possible.

An important factor affecting ground-water travel times and fluxes is the hydraulic conductivity. At any point in the geologic media, the saturated hydraulic conductivity generally remains constant, only changing due to variable stress loading and temperatures. Unsaturated hydraulic conductivity, however, can vary with water content over time at a point, even at constant stress levels and temperatures.

Emphasis in this chapter is placed on the measurement techniques for physical parameters important in determining the unsaturated hydraulic conductivity, specifically in relation to the low permeability rocks in which a high-level nuclear waste repository site might be located. The use of these parameters for the purpose of determining the hydraulic conductivity is discussed in Chapter 3.

This chapter focuses on the characterization of rock-matrix properties, followed by a characterization of rock-fracture properties.

### 2.1 Rock Matrix Characterization

To characterize the capacity of a rock matrix for fluid fluxes and solute transport, several parameters must be evaluated:

- Total and matrix porosities, for determining total water holding capacity;
- Pore-size distribution, for determining the unsaturated hydraulic conductivity and the fluid content as a function of potential; and
- Matrix-specific surface areas, for determining sorption capacities.

#### 2.1.1 Matrix Porosity Determination

The total porosity of a rock mass is the percentage of the total volume of a rock sample which is not occupied by the solid matrix. The matrix

porosity of a geologic medium is the amount of pore space within a rock mass, exclusive of fractures and sizable solution openings. The matrix porosity might include pores which are isolated from other pores or which dead-end. Both dead-end and isolated pores do not normally provide a conduit for the movement of fluids.

The effective matrix porosity refers specifically to interconnected pores, and is always less than the total matrix porosity. It is important to note that most techniques used to measure matrix porosity actually measure the total matrix porosity. Yet, the effective porosity is perhaps the more relevant parameter for predicting flow and diffusion rates within geologic media.

Porosities can be evaluated using four experimental techniques:

- (1) Paraffin method;
- (2) Water saturation method;
- (3) Gravimetric method; and
- (4) Gamma ray attenuation.

These techniques have been applied to rock samples obtained at the field study areas described in Chapter 1. A description of each technique is given in the following sections.

#### 2.1.1.1 Paraffin Method

The paraffin method measures the total matrix porosity by weighing an oven-dried sample, then coating the sample with paraffin and measuring its buoyancy in water. The technique first requires that samples be oven-dried at 104°C and weighed daily to determine the total moisture loss. Once all interstitial moisture has evaporated, the samples are removed from the oven and cooled to room temperature. They are then dipped in molten paraffin heated to slightly above the melting temperature of the paraffin. After the paraffin coating solidifies and cools, the samples are weighed to determine the total amount of paraffin added to the sample. The volume of paraffin added can be calculated by dividing the weight of paraffin by the its density.

The samples are then suspended in water with thread, and reweighed to determine their buoyancy. The volume of rock plus paraffin can be calculated from the buoyancy, and from this, the bulk volume of sample can be determined. The bulk density can be calculated using:

$$(2.1) \quad \rho_b = \rho_w W_d / (W_d - W_w + W_p(1 - \rho_w/\rho_p))$$

where

$\rho_b$  is the dry bulk density;  
 $\rho_w$  is the density of water;  
 $\rho_p$  is the density of paraffin, approximately 0.9;  
 $W_d$  is the weight of the oven-dried sample;  
 $W_w$  is the weight of the paraffin-coated sample in water; and  
 $W_p$  is the weight of the paraffin coat.

The porosity is then determined by:

$$(2.2) \quad n = 1 - \rho_b / \rho_s$$

where

$n$  is the matrix porosity;  
 $\rho_b$  is the dry bulk density; and  
 $\rho_s$  is grain density.

An advantage of the paraffin method lies in the fact that any shaped sample may be used. A disadvantage of the technique is that fore-knowledge of the grain density is required.

Four rock samples have been collected from the Magma Mine Number Nine Shaft vicinity, near Superior Arizona. These samples were of the slightly-welded unit of the Apache Leap tuff. Each rock was split into two sub-samples of approximately 5 cm diameter, and the paraffin technique was used to determine the total matrix porosity.

#### 2.1.1.2 Water Saturation Method

The water saturation measures the effective matrix porosity by determining the volume of a regularly-shaped sample, such as a cylindrical core, then saturating the previously oven-dried sample under a vacuum and determining the saturated water content. The method yields the effective porosity,

$$(2.3) \quad n_e = V_w / V_s$$

where

$n_e$  is the effective matrix porosity;  
 $V_w$  is the volume of water required to saturate the sample; and  
 $V_s$  is the volume of the sample.

The porosity is determined by de-gassing the core samples in a vacuum and saturating them with water. Assuming full saturation, the volume of interconnected voids is calculated by weighing the water within the

cores. The difference between the matrix porosity and the effective porosity determined using this method is an indicator of the relative ratio of interconnected to isolated pores.

#### 2.1.1.3 Gravimetric and Gamma Ray Attenuation Methods

The gravimetric method uses the same technique as the water saturation method, except the dry weight is used to calculate the bulk density and Equation (2.2) is used to calculate the total matrix porosity.

A gamma ray attenuation method has also been used to determine the range of total matrix porosity of slightly-welded tuffs. The method is described in detail in Section 4.1. Briefly, the method employs a radiation beam which is attenuated as it passes through a sample. The magnitude of the attenuation is a direct function of the water content of the sample.

#### 2.1.1.4 Comparison of Techniques

The porosity ranges of slightly-welded and densely-welded tuffs, and granodiorites have been measured and are presented as Figure 2.1. Table 2.1 contains data for the slightly-welded Apache Leap tuff obtained using the four methods described above. The water saturation results indicate an average effective matrix porosity of 18.1 percent for 6 samples obtained from cores removed from a tuff boulder. The paraffin technique was used on 7 rock chips with a resulting average total matrix porosity of 15.5 percent.

The results from the gamma-ray technique are from one core which measures 6.35 cm in diameter by 12.5 cm in length, with the measurement sites distributed 1 cm apart along the core. The range in total porosity over the core is 18.6 to 21.7 percent. The overall average for the twelve values is 20.0 percent. The same core was used to determine the total porosity using the gravimetric technique, which yielded an identical estimate of 20.0 percent. Table 2.2 presents results for densely-welded Apache Leap tuff. The results from two methods provide an average total porosity of approximately nine percent.

These preliminary results indicate a large spatial variation in the bulk density and porosity, as well as a sizable variation within a single core. A grain density of  $2.65 \text{ g/cm}^3$  (used in the calculations) is tentative, based on the rock mineralogy. The density of rock powder can be used to determine the grain density, yet results for the tuff give unreasonably low values.

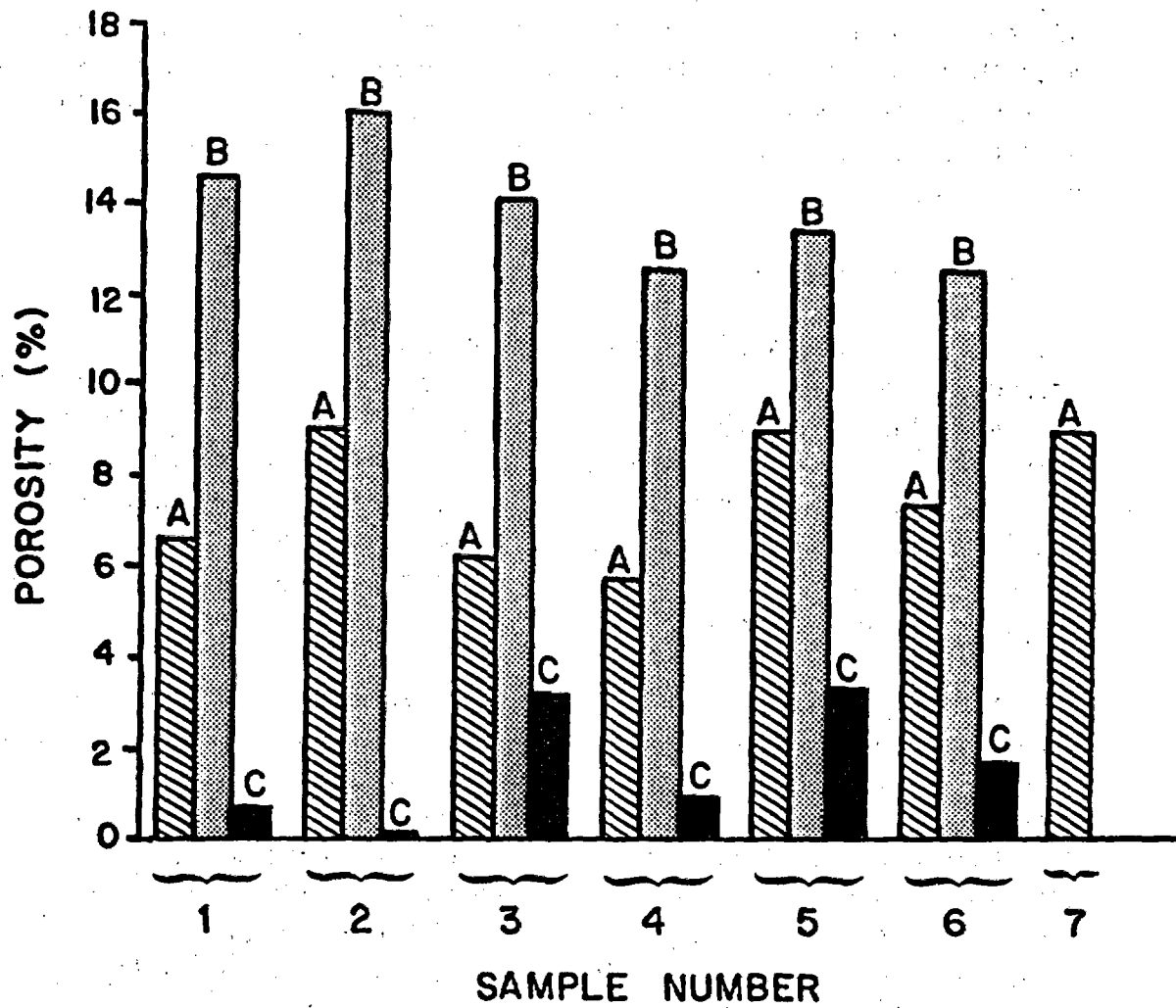


Figure 2.1 Range of primary porosities for samples of partially-welded tuff using the paraffin method (A), partially-welded tuff using the water saturation method (B), and granodiorite using the water-saturation method (C).

Table 2.1 Porosity measurements of the slightly-welded Apache Leap tuff.

**Water Saturation Method**

Sample Number	Bulk Density (g/cm <sup>3</sup> )	Effective Porosity	Total Matrix * Porosity
1	2.07	17.3 %	21.9 %
2	2.03	19.1	23.4
3	2.08	17.8	21.5
4	2.11	17.8	20.4
5	2.09	18.6	21.1
6	2.12	17.8	20.0
Mean	2.08	18.1	21.4

**Paraffin Method**

Sample Number	Bulk Density (g/cm <sup>3</sup> )	Effective Porosity	Total Matrix * Porosity
1	2.26	-	14.7 %
2	2.20	-	17.0
3	2.27	-	14.3
4	2.28	-	14.0
5	2.20	-	17.0
6	2.24	-	15.5
7	2.20	-	17.0
Mean	2.24	-	15.5

**Gamma Ray Attenuation Method**

Sample Number	Bulk Density (g/cm <sup>3</sup> )	Effective Porosity	Total Matrix * Porosity
Range	-	-	18.5 to 21.7 %
Mean	-	-	20.0

\* Using  $\rho_s$  of 2.65 g/cm<sup>3</sup>

-----  
**Table 2.2 Porosity measurements of the densely-welded Apache Leap tuff.**  
 -----

**Paraffin Method**

Sample Number	Bulk Density (g/cm <sup>3</sup> )	Effective Porosity	Total Matrix * Porosity
-----	-----	-----	-----
1	2.42	-	8.75 %
2	2.43	-	8.49
3	2.41	-	9.02
4	2.41	-	8.94
5	2.40	-	9.55
Mean	2.41	-	8.95

**Gravimetric Method**

Sample Number	Bulk Density (g/cm <sup>3</sup> )	Effective Porosity	Total Matrix * Porosity
-----	-----	-----	-----
1	2.41	-	9.06 %
2	2.41	-	9.06
Mean	2.41	-	9.06

\* Using  $\rho_s$  of 2.65 g/cm<sup>3</sup>

## 2.1.2 Pore-Size Distribution

Determination of the pore-size distribution is also critical to understanding unsaturated flow and solute transport. Mercury infusion (Gregg and Sing, 1967) and nitrogen gas adsorption (Norton and Knapp, 1977) are two commonly used techniques for determining the pore-size distribution of porous materials.

### 2.1.2.1 Mercury Infusion

A mercury porosimeter was constructed from a pycnometer and Ruska mercury pump, and a pore-size distribution for pores greater than 0.1  $\mu\text{m}$  in radius was determined (Walter, 1982). The apparatus is comparable to available standardized mercury porosimeters, and is capable of supplying pressures of up to 140 bars. This enabled pores greater than 0.1  $\mu\text{m}$  in radius to be mercury-intruded, as calculated by Washburn's equation:

$$(2.4) \quad r = 2 T \cos \alpha / P$$

where

$r$  is the pore radius;

$T$  is the surface tension;

$\alpha$  is the contact angle of mercury, equal to  $140^\circ$ ; and

$P$  is the applied pressure.

The mercury infusion method involved placing two to three grams of rock sample in a mercury-filled pycnometer, incrementally increasing the pressure within the chamber, and recording the volume of mercury intruded. Approximately 40 pressure intervals were used to establish the pressure/volume relationship, with readings taken every 0.14 bars for the range of 0 to 0.7 bars, every 0.7 bars from 0.7 to 7.0 bars, and every 7 bars from 7 to 140 bars.

The chamber expanded due to increasing pressures. This expansion was measured by repeating the experiment with an empty pycnometer. The blank run was used to calibrate the pressure/volume relationship of the system prior sample testing. Due to the extremely low porosities, a blank was also run using two silica marbles in the pycnometer.

Six granodiorite samples from the Santo Nino mine and two welded tuff samples from near Kingman, Arizona were analyzed using these techniques. Each rock sample weighed 3 to 6 kg, and showed little apparent weathering. The samples were crushed using the U.A. Department of Mines ore crushing machines, and then sieved for ten minutes into five

fractions ranging from less than 1 mm to greater than 9.4 mm in diameter. The four larger fractions were washed to remove smaller particulates and then oven dried at approximately 105 °C. The smallest fraction was used for grain density measurements, the 1 to 2 mm fraction was used for gas adsorption analysis, and the largest fraction was used for mercury infusion analysis.

#### 2.1.2.2 Nitrogen Gas Adsorption

This method involves physically sorbing and then desorbing nitrogen gas at different pressure intervals onto a sample at the temperature of liquid nitrogen (76.8 °K). The total quantity of gas sorbed and desorbed onto the particle surfaces at various pressures is measured, and related to the pore radius through Kelvin's equation (Gregg and Sing, 1967):

$$(2.5) \quad \ln(p/p_0) = - 2 T V \cos \alpha / (r R t)$$

where

- $p_0$  is the saturated vapor pressure;
- $p$  is the vapor pressure of the system;
- $T$  is the surface tension;
- $V$  is the molar volume of adsorbate;
- $\alpha$  is the contact angle of liquid and solid;
- $r$  is the pore radius;
- $R$  is the gas constant; and
- $t$  is the temperature.

The sample is placed in a flask of known volume and weight, then weighed and degassed overnight to a pressure of about  $1.33 \cdot 10^{-7}$  bars. During the adsorption and desorption process the flask is submerged in a bath of liquid nitrogen to maintain a constant temperature of 76.8 °K. Using a manifold system of known volume ( $28.99 \text{ cm}^3$ ) and a second chamber ( $131.3 \text{ cm}^3$ ), the volumes and quantities of gas used in the experiment are measured using the equation of state for an ideal gas.

To determine the total volume of the sample, a known quantity of helium in the manifold is allowed to equilibrate with the sample in the flask. Helium is used because it is a non-adsorbing gas. After this determination is made, the flask is again degassed.

An adsorption isotherm is determined by sorbing nitrogen in a quasi-liquid state onto the surface of the material at different partial pressures. After complete saturation at one bar, a desorption isotherm

is determined. The resulting complete adsorption-desorption isotherm with hysteresis is then known. The initial sorption curve up to 0.2 ( $P/P_0$ ) can be used to determine the specific surface area of the sample using the BET equation (Gregg and Sing, 1967). The surface area determined in this manner is a summation of external surface areas plus surface areas on the interior of pores.

The specific surface area of the samples, while valuable information in itself, is not directly used in the determination of the pore-size distribution. The desorption portion of the isotherm (from 1.0 to about 0.5  $P/P_0$ ) is instead used for this analysis. The volume of nitrogen drained from the pores is measured for each decrement of pressure. The total pore volume of the samples with radii relating to the decremental pressures measured is determined using Kelvin's equation.

Desorption of the sample results in the determination of the pore-size distribution for the sample, as well as the specific surface area of the interiors. The adsorption-desorption isotherm has been determined for one sample of granodiorite and one sample of densely-welded tuff from near Kingman, Arizona. The 1- to 2-mm sieve fraction was used for these analyses. Analyses were performed on samples weighing 13 to 14 grams because a five gram sample failed to provide an accurate measurement.

#### 2.1.2.3 Comparison of Methods

The two techniques were used to estimate the pore-size distribution for granodiorite from the Santo Nino Mine. For the low porosity rock (less than 2 percent) and the equipment available, the techniques were applicable over different pore-size ranges. Consequently, an integrated procedure has been devised using mercury infusion for determining the size distribution of pores with radii greater than 0.1  $\mu\text{m}$  and nitrogen gas adsorption for pores of radii between 0.1 and 0.0001  $\mu\text{m}$ .

The pore-size distributions of seven granodiorite samples were determined using the mercury-infusion technique (Figure 2.2). The shape of the distributions are variable among samples, all samples indicating a range of pore-size distributions. Results in the range from 80 to 100 percent are inconclusive due to equipment limitations.

The results of mercury infusion experiments, as well as the bulk density and grain-density measurements for the seven granodiorite samples, are presented in Table 2.3. In general, the porosity values calculated with grain density measurements exceeded values determined by mercury infusion. This reflects the fact that mercury-infusion methods measure

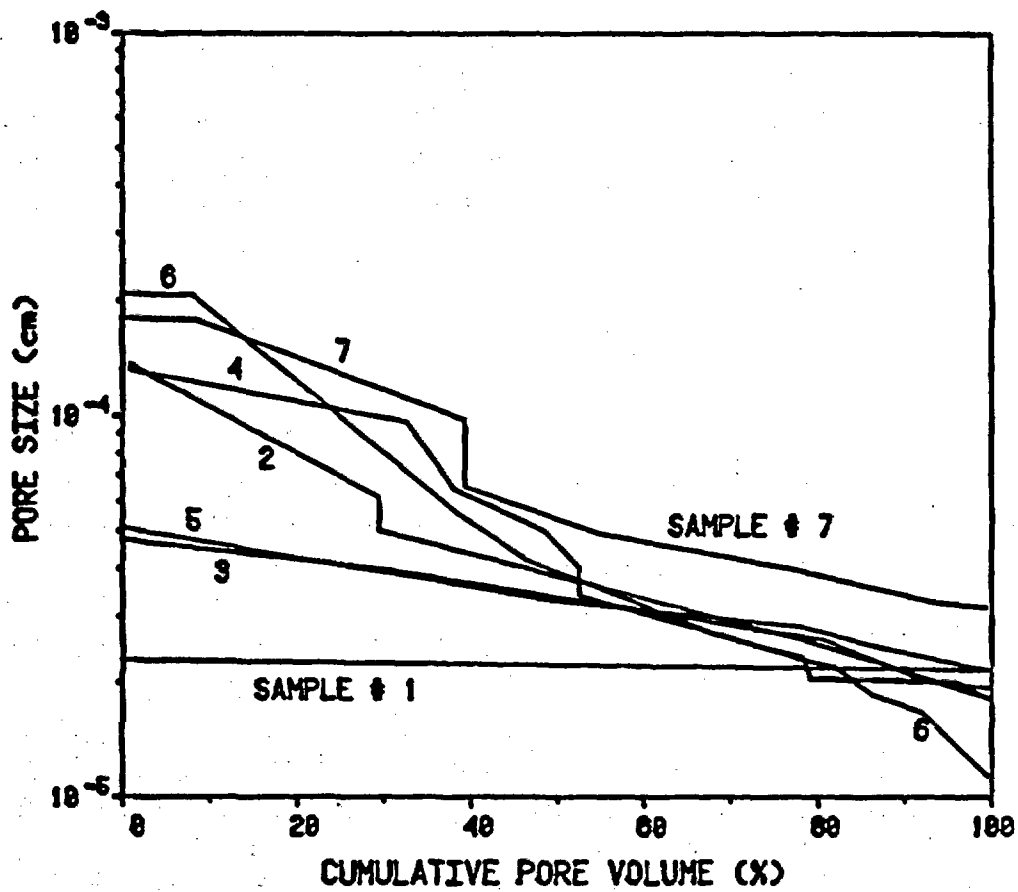


Figure 2.2 Pore-size distribution results from mercury infusion for granodiorite samples.

-----  
**Table 2.3** Result of bulk density and grain density determinations of granodiorite samples. Percent porosity determination was made using mercury-infusion (Hg) and grain-density ( $\rho_g$ ) measurements.  
 -----

Sample	Bulk Density (g/cm <sup>3</sup> )	Porosity (Hg) (%)	Grain Density (g/cm <sup>3</sup> )	Porosity ( $\rho_g$ ) (%)
1	2.665	0.05	-	-
2	2.636	0.29	2.654	0.68
3	2.696	0.43	2.697	0.04
4	2.609	1.44	2.697	3.26
5	2.676	0.84	2.703	1.01
6	2.522	4.50	2.610	3.37
7	2.615	0.81	2.663	1.83

-----

effective porosity, while grain-density calculations yield the total porosity. In addition, the mercury-infusion technique did not measure pores with radii smaller than 0.1  $\mu\text{m}$ .

Nitrogen gas adsorption techniques have been used to determine the pore-size distributions for pores ranging from 0.1 to 0.0001  $\mu\text{m}$  in radius. Figure 2.3 presents the pore-size distributions determined with nitrogen gas adsorption methods for one of the granodiorite samples (Sample 5). The effective porosities determined by gas adsorption were 0.55 percent for the fraction between 0.1 and 0.0001  $\mu\text{m}$  of the granodiorite samples. Pores with a radius greater than 0.1  $\mu\text{m}$  are not measured by gas adsorption. As seen in Figure 2.3, only about 10 percent of the pore volume is composed of pores larger than 0.1  $\mu\text{m}$  in radius. Figure 2.4 is a graph combining the mercury infusion and gas adsorption pore-size distribution results for a granodiorite sample from the study site at the Santo Nino mine.

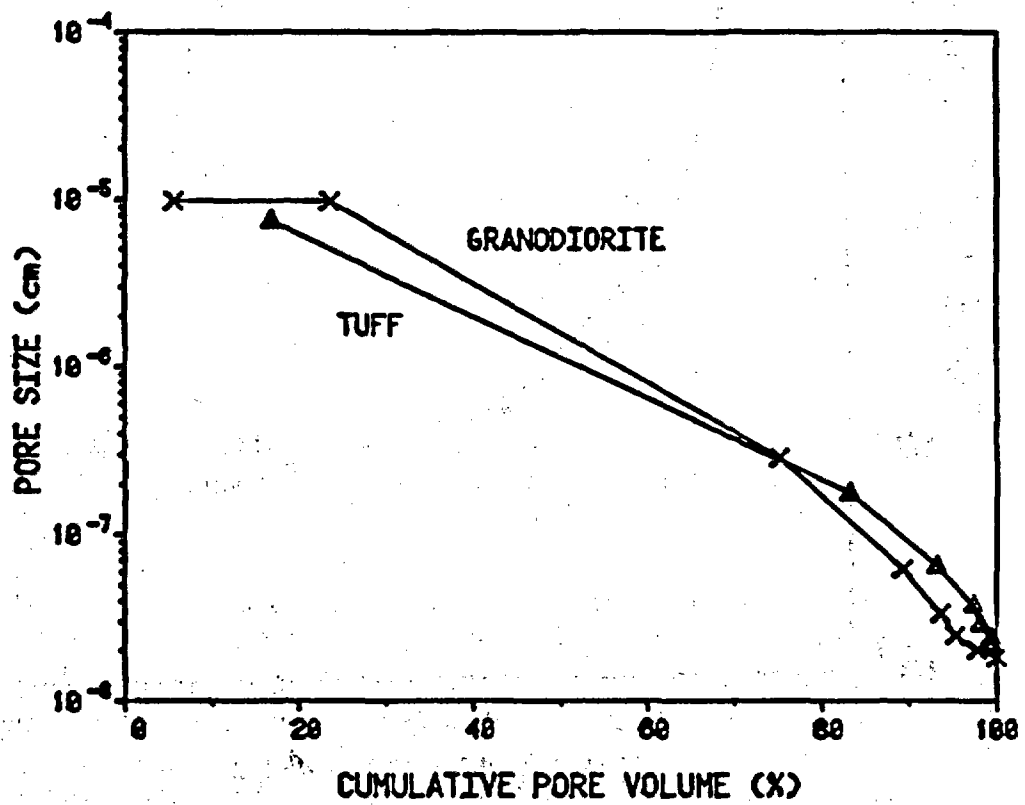


Figure 2.3 Pore-size distribution results from gas-adsorption for the same granodiorite sample shown in Figure 2.2.

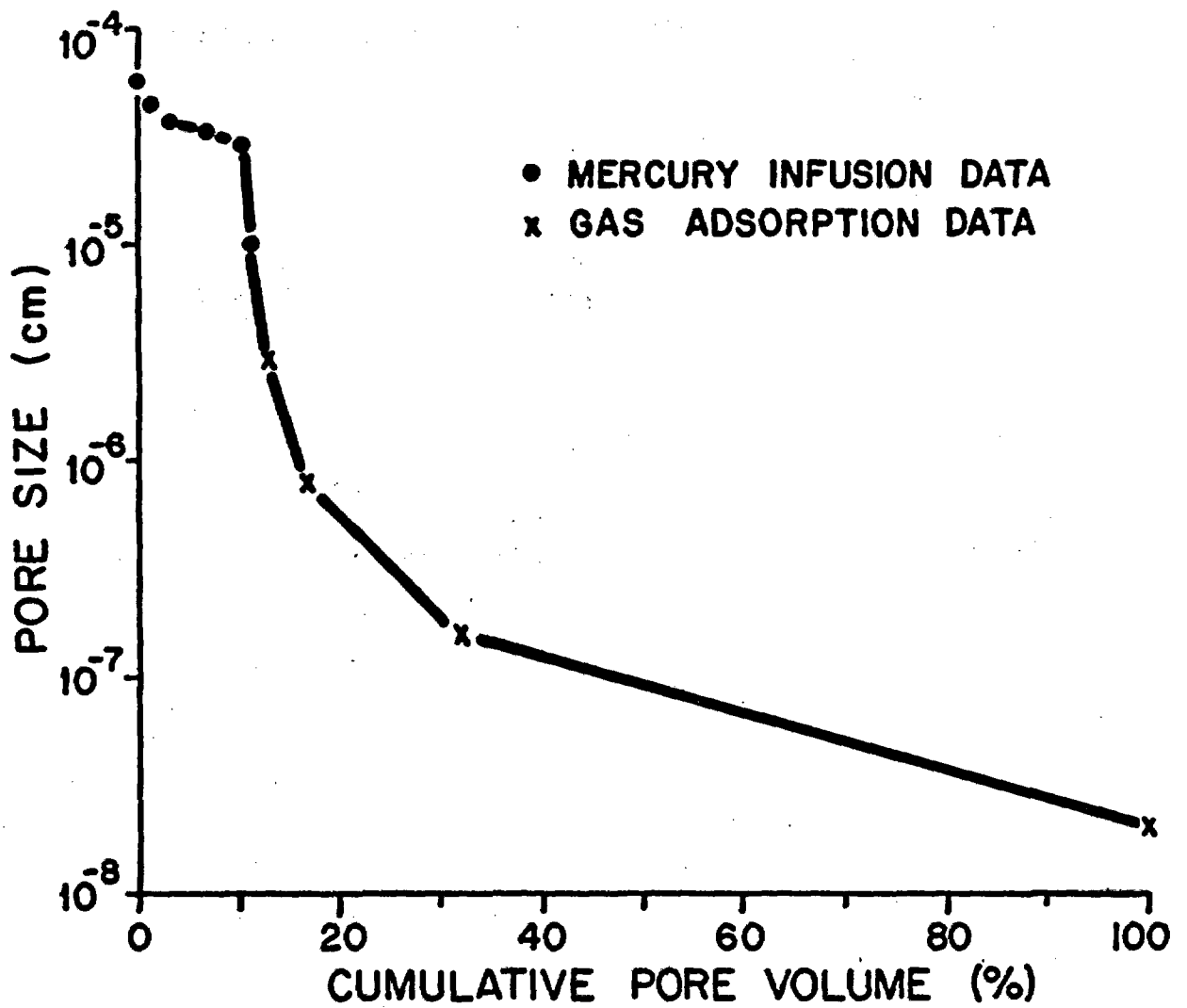


Figure 2.4 Pore-size distribution results combining two measurement techniques for a granodiorite sample obtained from the Santo Nino Mine.

#### 2.1.2.4 Recommended Improvements

Three refinements are suggested to improve the mercury infusion and gas adsorption techniques:

- Krypton gas is better suited for gas adsorption on materials with low specific surface areas (due to the ability of Krypton gas to adsorb into smaller pores), and should be used in future tests on rocks of low porosity;
- More complete desorption isotherms should be used for determining pore-size distributions; and
- There is a gap between the effective range of pores measured by mercury infusion and that measured by gas adsorption. This could be eliminated by conducting mercury infusion at pressures greater than 138 bars, if possible. When continuous porosity measurements are available, a comprehensive pore-size distribution from  $10^{-4}$  to  $10\ \mu\text{m}$  can then be determined using a combined laboratory technique of mercury infusion and gas adsorption.

In conclusion, the mercury-infusion technique yields information on the pore-size distribution for pores of radii larger than  $0.1\ \mu\text{m}$ , while the nitrogen gas adsorption method provides information on the pore-size distribution for pores with radii ranging from  $0.1$  to  $0.0001\ \mu\text{m}$ . (Equipment is commercially available which extends this range.) These two methods can be combined to provide a more complete pore-size distribution diagram.

#### 2.1.3 Specific Surface

Specific surface is another important measurement that aids in the hydrologic and geochemical characterization of a rock matrix. The matrix specific surface of a rock is defined as the total solid/pore surface area per unit, bulk, volume, or mass.

The standard procedure for determining the matrix specific-surface area is to measure the amount of gas or liquid required to form a monomolecular layer over the entire solid/pore surface area. Although a matrix specific-surface value may be measured using the nitrogen gas adsorption technique for a crushed rock sample, the resultant estimate may be higher than that for the uncrushed rock due to microfractures formed during the crushing operation. In order to obtain a more valid estimation of the matrix specific surface, the nitrogen gas adsorption method should be performed on larger sample fragments.

## 2.2 Fracture Characterization

In rocks of low matrix hydraulic conductivity, fracture systems may form the principal pathways for water and contaminant transport. Important fracture properties are fracture apertures, densities, and orientations. Specifically with regard to unsaturated flow, fracture system properties control:

- The relationship between water content and potential within the fractures;
- The preferred direction of flow pathway; and
- The corresponding rates of water or contaminant transport along these pathways.

The approaches to be discussed pertain to fracture systems which have sufficient regularity and continuity to be considered discrete systems. As fracturing increases in density and randomness, the individual fracture characteristics are masked by the averaged characteristics and an equivalent porous medium or continuum approach is applicable. While the contribution of the countless individual pores within a porous medium is physically averaged in a continuum sense, even on a very small scale, larger scale systems of discrete fractures are not so readily averaged. Even though it is not plausible to completely describe the geometry or hydrological behavior of an entire fracture system in a deterministic sense, a range of behaviors may be observed by using the statistical distributions of its parameters to obtain simulated behaviors.

Sources of data for analyzing rock masses are limited due to both the cost and destructive effects of sampling. As data sources are limited, selective sampling of fractures along cylinders (i.e., boreholes and mine shafts) and along planes (e.g., surface exposures) provide only a small base upon which to infer the total fracture system. Hence, additional information, such as that obtained from indirect measurements, must often be used to supplement data obtained by direct sampling.

While large geologic structures (dikes, faults, bedding planes, and large shear zones) can often be modeled individually using deterministic models because of their continuity and visibility, the minor structures (shrinkage joints, tectonic joints, stress-release joints, and cooling joints near margins of igneous bodies) usually cannot be mapped individually from one borehole or exposure to another. In the latter case, a statistical model must be developed which accurately simulates the fracture system and its response to some imposed condition.

To quantify a fracture system, particular attention must be placed on the types of data which can be obtained from the exposed rock mass. Such information would normally consist of (1) fracture strike and dip, (2) fracture spacing, (3) degree of fracture continuity (or areal extent), and (4) fracture aperture. In addition the presence of coatings and fillings within fractures can be noted.

Once the basic data have been obtained, statistical distributions can be developed which describe fracture characteristics. The following section discusses the measurement and statistical distribution of pertinent fracture parameters and the physical nature of fracture surfaces. The geochemistry of fracture surfaces is covered in Chapter 6.

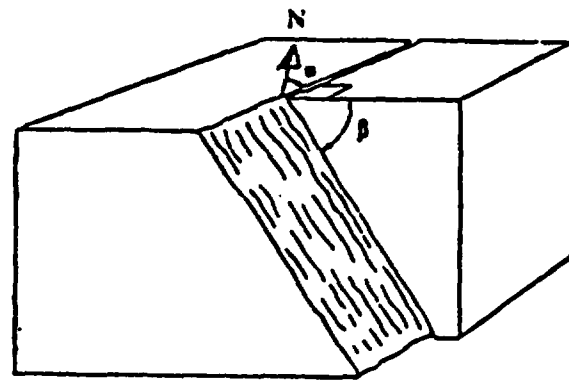
### 2.2.1 Orientation

Fracture orientation is one of the more easily and widely measured fracture parameters. Spatial orientation of a fracture plane is characterized by two measurements; the dip direction and the dip angle (Figure 2.5). The dip direction is the azimuthal bearing of the line of steepest declination (as measured from the horizontal) in the plane of the fracture. The dip angle is the inclination of this line from the horizontal. Strike (dip direction plus or minus  $90^\circ$ ) is sometimes used instead of dip direction since it is often measured directly; although a compass direction must then be specified with the dip angle.

Commonly, fracture strikes and dips are obtained from a large number of measurements of discontinuities. These features can be treated statistically and plotted on stereographic nets. Zanback (1977) has used the stereographic projections to develop two-dimensional normal distributions of fracture poles in a rock media. (A pole is the vector normal to the fracture plane surface). Because the poles of each fracture set tend to vary about some mean value, Zanback was able to obtain confidence intervals about the mean by assuming no correlation between the deviations in dip directions and dip angles.

Fracture orientations can be measured directly from surface exposures such as outcrops or mines using a compass and clinometer. Determination of fracture orientations from boreholes is also feasible using oriented core logging, borehole viewing, or acoustic-televiewer logging.

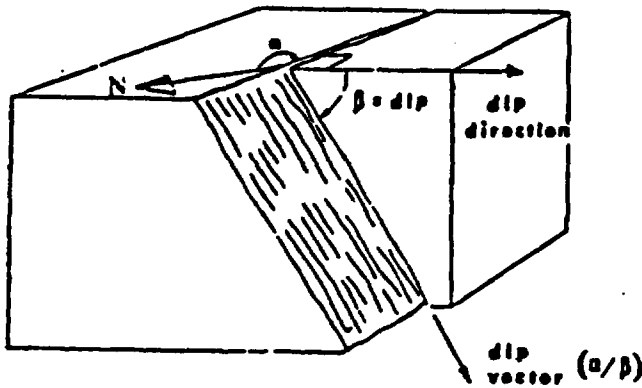
Oriented core is obtained from core-orientation devices which either mark the core at the end of each segment or scribe the core during drilling (Goodman, 1976). Determination of fracture orientation can then be analyzed by graphical or mathematical methods (McClellan, 1948).



strike =  $\alpha^\circ$

dip =  $\beta^\circ$

dip  
directions  $\alpha^\circ + 90^\circ$   
(=  $\alpha^\circ$ )



strike =  $\alpha^\circ$

dip =  $\beta^\circ$

dip  
directions  $\alpha^\circ + 90^\circ$   
(=  $\alpha^\circ$ )

Figure 2.5 Diagrams showing strike, dip direction, and dip angle for three different fractures.

Direct viewing of the borehole wall is achieved using a borehole periscope (sometimes called borescope or stratascope) or a borehole television camera. Camera viewing is generally preferable as it can be used at greater depths, permits greater magnifications, and allows for video recording of the borehole surface for later viewing.

Fracture orientation is measured by either directly observing fracture dip and dip direction or by measuring intercept locations of the fracture trace at three locations along the borehole wall. Direct measurements of fracture dip and dip direction must be corrected for inclined boreholes.

The acoustic televiewer is a recently developed geophysical logging tool which delineates a fracture trace from seismic P-wave attenuation. Fracture dip and dip direction are measurable from these logs.

Fracture orientation data are commonly presented using a stereonet on which the poles (i.e., normals to fracture planes) are plotted (Figure 2.6). Generally, an equal area or Schmidt net is used to facilitate contour density plotting of the data (Figure 2.7). Contouring of the data aids in the identification of fracture sets or clusters (groupings of parallel fractures), while the peak contour densities are used to determine the density and mean orientation of each fracture set. An alternate means of identifying fracture sets is to cluster data points using specially designed computer programs (Shanley and Mahtab, 1974). The mean orientation of each cluster set is then computed as the vectorial sum of the cluster component orientations.

The spherical normal distribution has been applied to statistically characterize the variability of orientation within individual joint sets (Mahtab et al., 1972), but does not always accurately represent the variation which may be present. A bivariate normal distribution has also been suggested (Zanbak, 1977), which may be more appropriate due to the inclusion of an additional parameter. The bivariate normal distribution may be biased, however, due to two principal errors associated with contour diagrams. The errors are:

- Fracture surfaces which are perpendicular to the sampling surfaces (i.e., borehole or surface exposure) are more frequently encountered than those which are subparallel, thus biasing density contour plots. This bias can be removed by either sampling enough differently oriented surfaces or weighting the observed frequency by the sine of the angle between the observed feature and the orientation of the sampling line (Terzaghi, 1965).

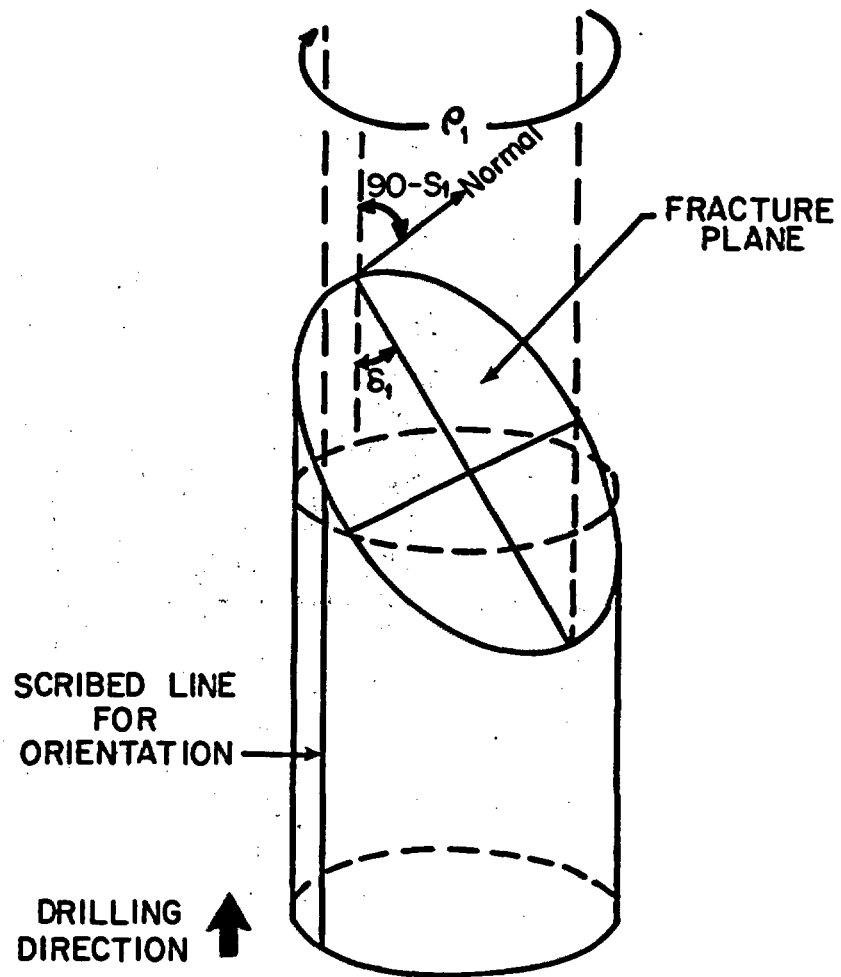


Figure 2.6 Measurements used to calculate strike, dip direction and dip angle of a fracture intersecting a borehole core.

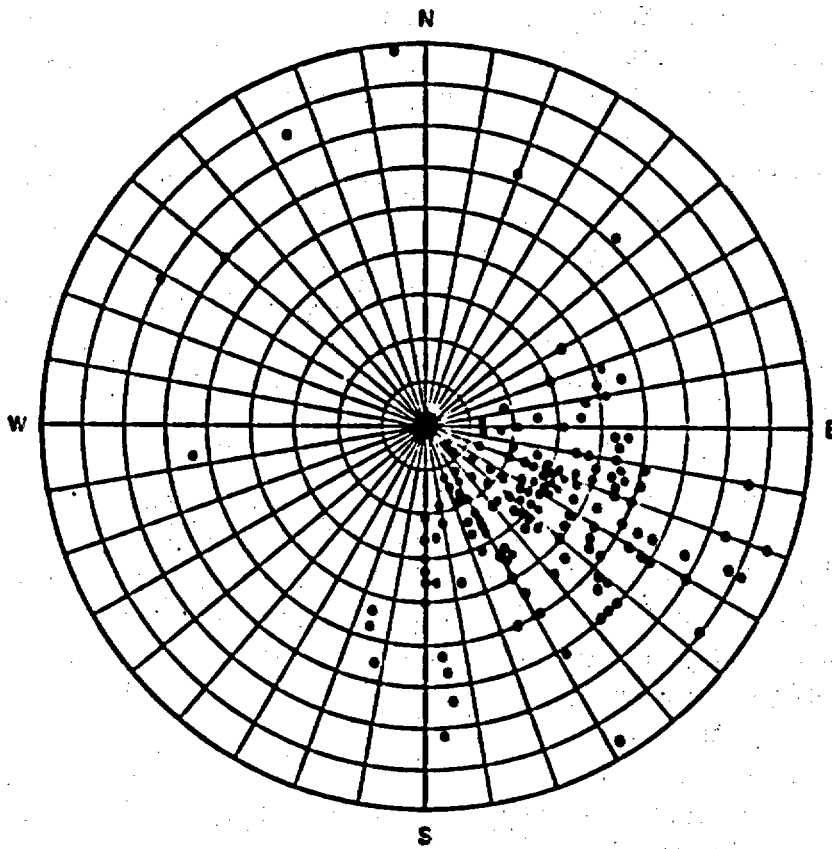


Figure 2.7 Plot of normals to discontinuities on a Schmidt polar equal area net.

- Individual poles may be double-counted if the same fracture is measured at two different boreholes, thereby violating the probability theory (ISRM, 1978)

Despite these limitations, however, stereonet density contouring remains a valuable tool for the identification of joint sets and their mean orientation.

A fracture survey was made along the first 100 m of the main adit of the Santo Nino mine. Sampling was conducted along a scanline at midheight along the right (western) rib of the adit. All fractures with a regular trace intercepting the scan line were noted.

The orientation data taken have been plotted on a Schmidt net and contoured (Figure 2.8). These data indicate that the existence of two predominant fracture sets and suggest the existence of a third set as shown. Set number one is the most pervasive and parallels several faults and mineralized or altered zones. Its apparent dominance in Figure 2.8 is due partially to the fact that the set is nearly perpendicular to the main adit.

Set number two also appears to be a major fracture set, but is diminished slightly in the contour plot due to its near parallel orientation to the sampling line. Set number three appears to be more widely spaced than the other two fracture sets as it is only faintly suggested by the contour plot. This set also parallels the main adit, and therefore the number of intercepts are considerably fewer. The existence of this set, however, is supported by its large fracture surface exposures which define the adit walls along certain sections, and its numerous traces exposed in the bedrock surrounding the mine entrance (not included in the survey).

The data taken during this survey have been used to orient drillholes so as to perpendicularly intercept two of the major fracture sets. Unfortunately space and time constraints limited the number of drillholes. Only a few locations of overbreak along the adit provided the space required to drill. In all, a total of 18 holes were core drilled; 16 perpendicular to Fracture Set 3, and 2 perpendicular to Fracture Set 2. Although the holes were too small in diameter to permit the use of core-orientation devices, some oriented core was obtained by marking of the core stub at the start of each hole. This method provided 1.5 to 4.5 m of oriented core by matching successive pieces.

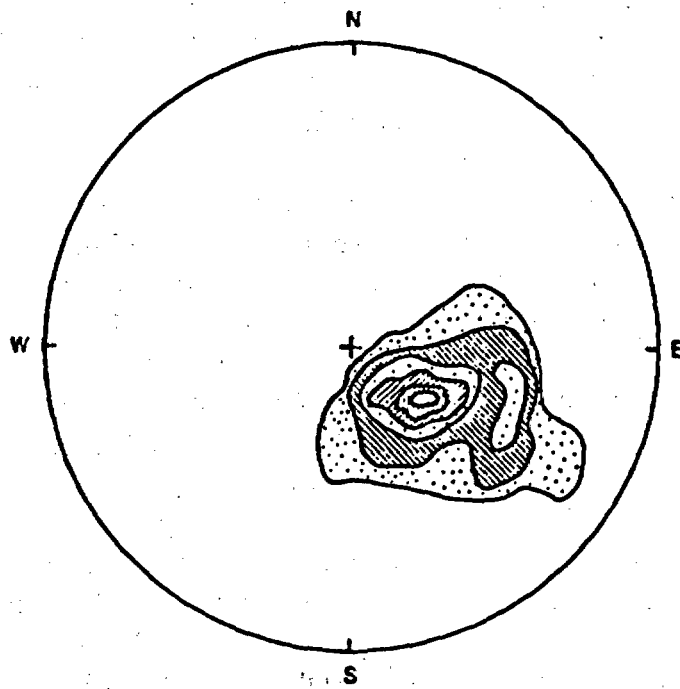


Figure 2.8 Contour plot of fracture data from Santo Nino mine.

A small diameter (32 mm) TV logging camera was used to measure sixteen of the eighteen drillholes to investigate nominal aperture widths. The method showed great potential although use of the camera for fracture orientation purposes was limited by lack of proper orientation rods and a measurement reference.

The field site in the slightly-welded unit of the Apache Leap tuff provides for many experiments that study how a fractured rock system controls unsaturated flow. Scribed cores with a diameter of 6.35 cm were obtained from each of the three inclined boreholes. The scribing tool provided an orientation mark every 3.05 meters. The cores have been logged in the laboratory regarding the location and orientation of fractures within the boreholes. A cross-sectional view along the bearing of the boreholes of these fractures and their intersection with the boreholes is presented as Figure 2.9.

To determine the alignment of the boreholes, photographs of a down-hole gyroscope were taken after the completion of drilling. The photographs indicated the total displacement of the boreholes deviate at the most 1° laterally and 3° vertically from design specifications.

The orientations of fractures within the boreholes have been determined with the aid of a goniometer designed for oriented core and a geometric solution given by Zimmer (1963) and McClellan (1948). These data, given in Figure 2.10, indicate the presence of many fracture sets that dip steeply to the southwest and northwest. The existence of these sets is supported by fracture surface exposures in surrounding outcrops of the study area. However, the apparent dominance of these trends is also due to the fact that the boreholes are nearly perpendicular to the fracture sets.

The orientation data in the fracture survey are used to identify fractures which are continuous between boreholes. This information is then used to help locate injection and monitoring equipment within the boreholes, which in turn provide data on such parameters as fluid and solute travel times, fracture apertures, rock moisture content, and chemistry of fracture-filling minerals.

### 2.2.2 Density and Spacing

An estimate of fracture spacing is dependent on two factors: the number of unique fractures per unit volume; and the mean area, or areal extent, of the fractures. Fracture spacing can be estimated by determining the number of fractures which intersect a line. If a line transect is used,

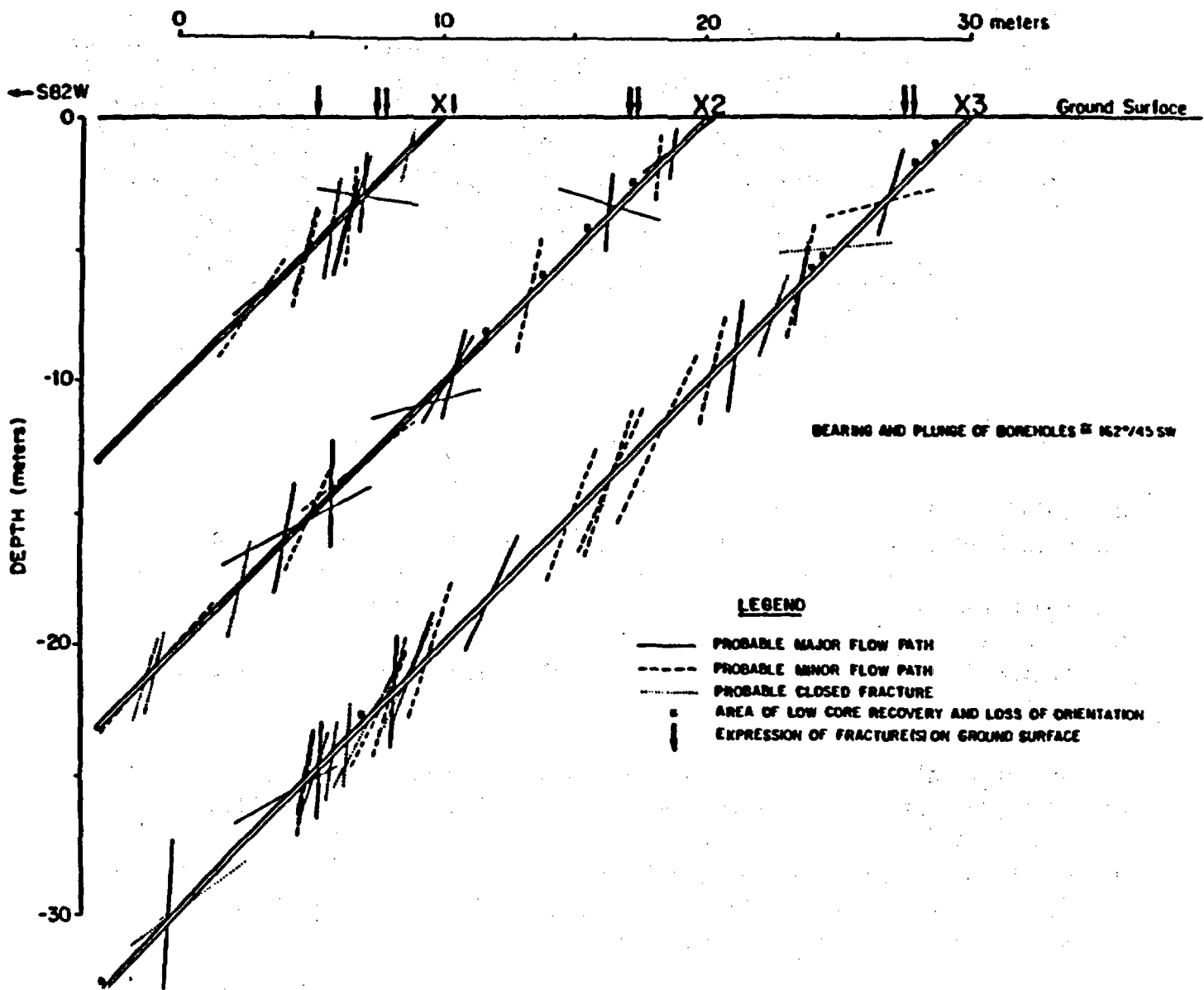
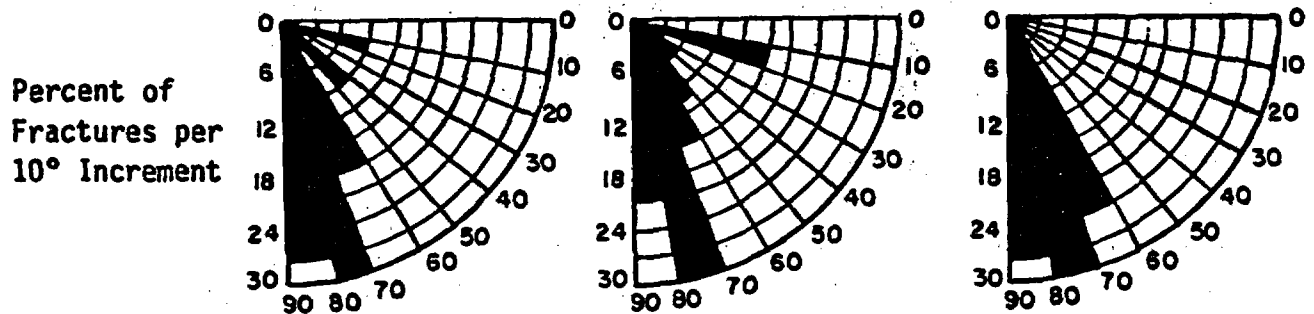


Figure 2.9 Map of fractures intersecting boreholes at the Apache Leap Tuff site.

Borehole Number Interval (meter)	X-1 0.0-18.44	X-2 0.0-32.61	X-3 0.0-46.64
-------------------------------------	------------------	------------------	------------------



Number of Measured Fractures	11	20	30
Average Number of Measured Fractures per 3-Meter Interval	1.8	1.8	1.9
Percent of Total Measured Fractures	18.0	32.8	49.4
Number of Examined Fractures	11	27	38
Percent of Closed Fractures	27.3	14.8	23.7

Figure 2.10 Inclination of fractures intercepted by boreholes at the Apache Leap Tuff site.

then the average spacing is the length of the transect divided by the number of observed fractures. This technique is appropriate when no preferred fracture direction is present.

This technique is biased, however, if distinct fracture sets are present. To avoid the bias, transects are established normal to the preferred direction of each fracture set. Fracture spacing is obtained by dividing the transect length by the number of fractures belonging to the set of interest which intersect the transect. The scan line should be at least ten times the length of the average measured spacing. Spacing data are plotted on a histogram (Figure 2.11) from which the spacing frequency distribution can be estimated.

#### 2.2.2.1 Fracture Centroids

The number of unique fractures per unit volume can be determined if the center of each fracture can be located. Ideally, the spacing of fracture centroids should follow some fixed rule; assuming a random distribution of centroids within a rock mass yields a Poisson rule for the density of the centroids. Without empirical evidence, such an assumption would seem untenable. Snow (1968) indicates that observed fracture spacings along a sample line can be found to belong to a negative exponential distribution. Such a distribution would be expected for a Poisson process. Baecher et al., (1977) supports this conclusion.

Other researchers (Priest and Hudson, 1976) have demonstrated that an evenly spaced set of centroids would result in a distribution which cannot be described by the negative exponential distribution. They observe, however, that a mix of random, clustered, and evenly-spaced centroids would tend to result in a distribution which can be statistically described by the negative exponential distribution.

#### 2.2.2.2 Areal Extent

The areal extent of fractures is difficult to measure chiefly due to the limited rock surface exposures available. As a result, no standardized methods have been developed. In theory, fracture surfaces could be delineated from surface exposures or by correlation between borehole-fracture logs. In actuality, neither method is entirely successful. Most exposed rock surfaces are of limited extent and generally smaller than the linear fracture traces (intercept of the fracture surface with the exposed rock surface) being measured.

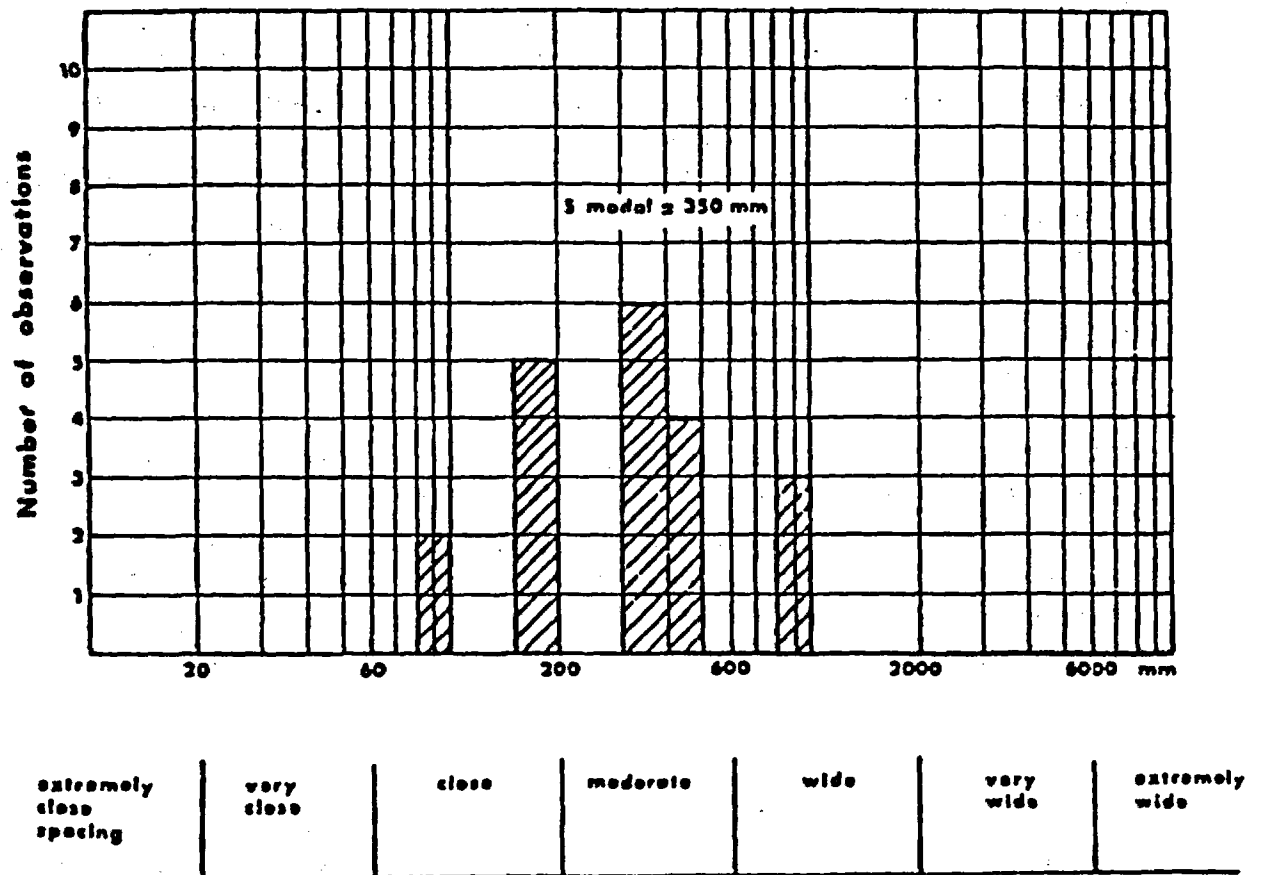


Figure 2.11 Fracture spacing histogram.

Additionally, only one chord across the fracture surface is generally measurable and this trace must be abstractly related to the dimensions of the entire fracture surface.

Use of borehole-fracture logs suffers from the limited ability to correlate fracture intercepts between all but closely-spaced boreholes. Hence, a large number of boreholes are required to delineate the areal extent of fractures. The analysis of fracture extent from fracture trace measurements is possible if certain simplifications can be made:

- The distribution of fracture centroids is assumed, usually random;
- Fractures have an assumed shape, usually circular; and
- The distribution of fracture lengths is assumed, usually lognormal or exponential.

While existing data cannot contradict these assumptions, only limited data are available to support the assumptions. In particular, the assumption of circular-fracture geometry is only an approximation.

If the validity of these simplifications is assumed, the distribution of trace lengths along any sampling line can be predicted. Field measurements of trace length represent a censored and truncated sample of this distribution, because larger trace lengths exceed the exposed measurement surface and very small trace lengths are often ignored during mapping. To account for the limited sample, the parameters of the complete trace distribution are first calculated. From this distribution, the parameters of the true-size distribution are obtained.

Robertson (1970) showed that fracture shape (plan view) is equi-dimensional (or the major axes are uncorrelated). Using this result, the effective centroid can be determined for each fracture. The centroid can then be used as a representative point which describes the position of a fracture in relation to the entire rock mass.

For assumed circular fractures, fracture lengths have been described by a lognormal distribution (Baecher et al., 1977) which was shown to pass the goodness-of-fit test. The gamma distribution did not provide as good a fit as the lognormal, while the exponential and normal distributions performed poorly. Baecher et al., (1977) cite MacMahon (1974), Bridges (1976), and Barton (1977) to support their observations. Other authors (Robertson, 1970; Stetten et al., 1970; Call et al., 1976), however, report obtaining better results using the exponential distribution.

### 2.2.3 Fracture Aperture

Aperture refers to the perpendicular distance between adjacent walls of a fracture in which the intervening space is air- or water-filled. This definition distinguishes fracture aperture from filled fracture widths. Fracture aperture is not a constant but varies from zero aperture at points of contact (which may exist to transmit stress), to some maximum value.

Apertures can be measured by direct and indirect methods. Larger apertures can be crudely measured along exposed rock surfaces using a millimeter scale while narrower apertures can be accurately measured with a feeler gauge. A very accurate method (<10  $\mu\text{m}$  absolute error) has been developed (Snow, 1969) using a penetrant dye and camera. The difficulty with measurements at surface exposures is that stress relief, weathering, and blast damage tend to alter fracture apertures from those in undisturbed rock.

Boreholes provide another means of direct measurement. Under certain conditions a grouted rod may be overcored and removed to preserve fracture apertures in the core. More commonly, borehole surfaces are inspected directly using borescopes or borehole television cameras.

Indirect methods of measuring fracture apertures have been developed based on the hydraulic characteristics of fractures. Liquid- and gas-injection tests in both saturated and unsaturated rock have been used to measure changes in individual fracture apertures (Pratt et al., 1977; Hardin et al., 1981), to assess fracture aperture changes associated with blast damages (Montezer, 1982; Jakubick and Korompany, 1982), and to assess fracture porosity and aperture distribution (Snow, 1968, 1969).

The principal advantage of indirect methods is that the aperture over greater fracture surface areas are measured. The principal disadvantage is their reliance upon some physical relationship between the quantity being measured and the parameter of interest. In the case of fluid flow and a parallel plate-model, the physical relationship is the cubic law:

$$(2.6) \quad q = \rho g / 12\mu b^3 l$$

where

- q is the volumetric flow rate per unit length of fracture;
- $\rho$  is the density of the fluid;
- g is the gravitational constant;

$\mu$  is the dynamic viscosity of the fluid;  
 $i$  is the hydraulic gradient; and  
 $b$  is the aperture.

Equation (2.6) assumes that the fluid is incompressible and that flow is laminar. The law has been verified by several experimenters using glass plates (Lomize, 1951; Romm, 1966). If Equation (2.6) can be assumed to be valid, then measurements of the volumetric flow through individual fractures can be used to measure the mean fracture aperture with a high degree of accuracy. Yet the validity of the cubic law when applied to rough natural fractures remains an area of dispute. Experiments conducted by Sharp (1970) on rough, natural fractures suggest that the volumetric flow rate is approximately proportional to the square of the aperture, rather than to the cube.

Similar tests conducted by Iwai (1976), however, indicate the cubic law is valid even at aperture sizes as small as 10  $\mu\text{m}$ . Gale (1975) re-evaluated Sharp's data and concluded that the cubic law is valid if the aperture measured from complete fracture closure is used instead of the aperture measured from maximum observed closure.

As rough fracture surfaces never completely close, even under very high stress, the measurement of absolute aperture has never been made. Instead, residual flows observed at maximum induced closure (minimum aperture) have been assumed to follow the cubic law in order to estimate the minimum absolute aperture. Hence, the value of aperture computed from the cubic law may differ from the mean aperture.

While the flow rate is generally the easiest flow parameter to measure, flow velocity is also measurable and provides a second method for determining the aperture of fractures. By noting that the velocity is the volumetric flow rate divided by cross-sectional area perpendicular to the flow, the velocity can also be related to the fracture aperture:

$$(2.7) \quad v = \rho g / 12\mu b^2 i$$

where  $v$  is the average, true velocity of the fluid.

The velocity can be measured directly using a tracer and measuring transit times between the injection point and at least one observation point. Furthermore, because the velocity is an independent measurement of the volumetric flow rate, it provides a second estimate of the average fracture aperture.

A third measurable flow parameter which can be used to estimate fracture aperture is the transition between laminar and turbulent flow. Using the Reynolds' number concept, the upper limit of completely laminar flow is given by (Louis, 1969):

$$(2.8) \quad R_e = 2b v/v_w \approx 2300$$

where

$R_e$  is Reynolds' number;

$b$  is the aperture;

$v$  is the velocity; and

$v_w$  is the kinematic viscosity of the fluid.

The use of Equation (2.8) is limited to relatively smooth fractures with a surface roughness index (mean height of fracture asperities divided by twice the aperture) of less than 0.033 (Figure 2.12). Transition from laminar to turbulent flow is determined from a plot of the flow rate or flow velocity versus the hydraulic gradient (Figure 2.13) obtained from several measurements of the flow rate or flow velocity at several imposed gradients. Equation (2.8) is approximate and, therefore, apertures computed by this method are likely to be approximate in nature.

Pneumatic tests were used to measure fracture apertures and gas conductivities of fractures located at the Santo Nino mine and at the densely-welded tuff site, discussed in Chapter 3.

Fracture apertures have been shown to obey a lognormal distribution (Bianchi and Snow, 1969). The measurement of 256 such fractures on surface outcrops indicated that individual fracture apertures were lognormally distributed.

#### 2.2.4 Fracture Porosity

In rocks of low permeability, the effective fracture porosity can be an important determinant of the overall hydraulic conductivity. The fracture porosity is the percentage volume of fracture openings. The effective fracture porosity is the percentage volume of fracture openings which are interconnected to each other and to an exterior surface. Fracture porosity is calculated from measurements of fracture apertures and fracture density. In many cases, the fracture porosity is a minor component of the total porosity, yet it can play an important role in determining the hydraulic conductivity of a geologic medium.

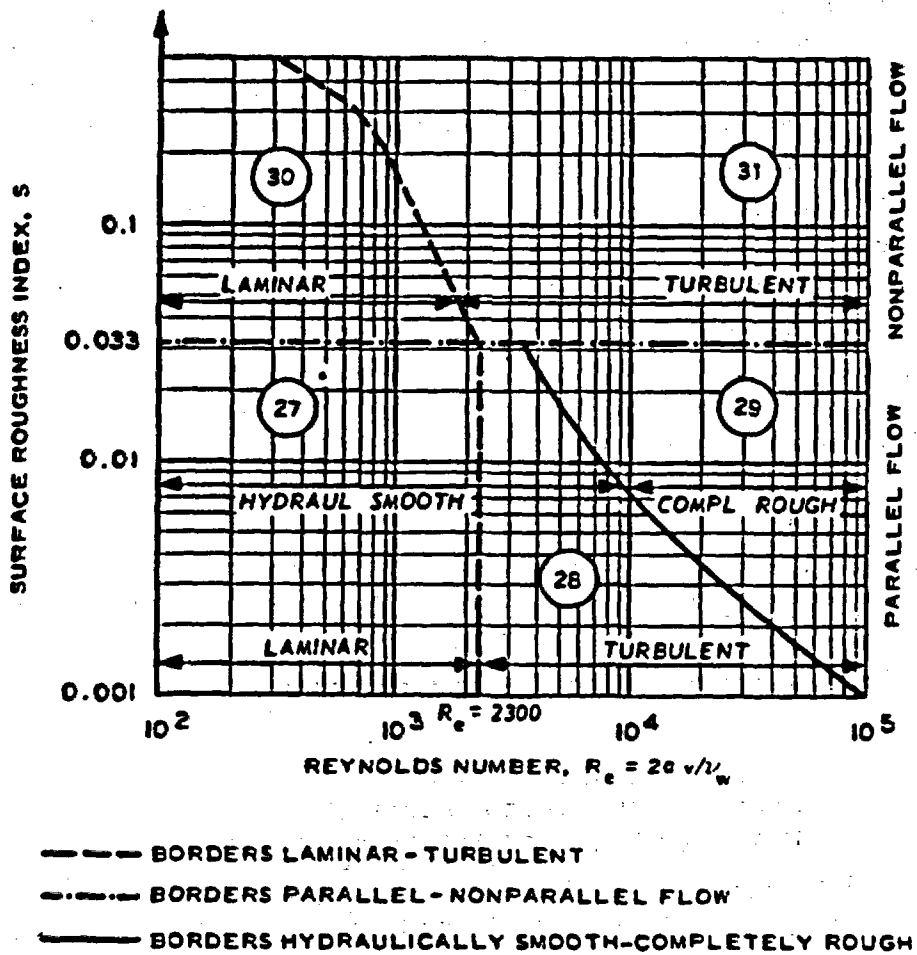
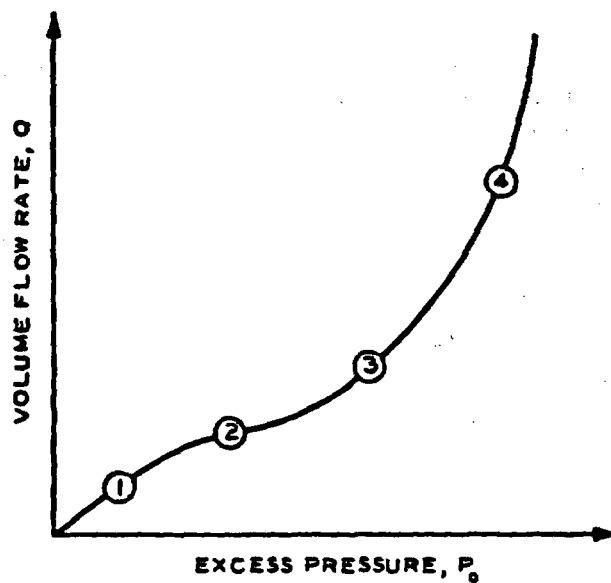


Figure 2.12 Reynolds number diagram for fracture flow.



- ZONE 1 - LINEAR LAMINAR REGIME
- ZONE 2 - TURBULENCE EFFECTS
- ZONE 3 - TURBULENCE OFFSET BY FISSURE EXPANSION, OR PACKER LEAKAGE
- ZONE 4 - PREDOMINANCE OF FISSURE EXPANSION OR PACKER LEAKAGE

Figure 2.13 Typical curve of flow rate against hydraulic gradient.

To demonstrate that the fracture porosity is normally a minor percentage of the total porosity, the fracture density of a core taken from the densely-welded unit of the Apache Leap tuff is used as an example. The fracture density is estimated to be approximately three fractures per meter. By assuming an extreme mean aperture to be 300  $\mu\text{m}$ , the fracture porosity is not more than 0.1 percent.

### 2.2.5 Fracture-Surface Characterization

As mentioned earlier, flow through rock fractures is often idealized as flow between smooth, parallel plates. Significant deviations of rough, natural fractures from an equivalent parallel plate model include:

- (1) Deviation from a planar surface (fracture waviness);
- (2) Deviation from parallel sides (aperture variation); and
- (3) Reduction-of-flow cross section (increased contact area).

Schrauf (1984) shows that existing numerical and experimental data for fracture apertures under approximately 200 to 300  $\mu\text{m}$  suggest that the magnitude of roughness and waviness effects of fracture surfaces are secondary in comparison with the effect of contact area between fracture surfaces. Iwai (1976), in a comprehensive study of water flow through a single fracture, demonstrated that the reduction of flow cross section as a result of increasing contact area was more significant. In fact, Iwai showed that the expected flow rate decreased hyperbolically as the fracture surface contact area increased. However, roughness and waviness of the fractures become more significant as apertures increase due to increased effects of turbulence and inertial forces.

#### 2.2.5.1 Specific Surface

The fracture specific surface of a rock is defined as the total fracture surface area per bulk volume of rock. Specific surface resulting from fractures may be obtained by multiplying the number of fractures per square meter by two (the number of fracture sides), and dividing by a unit depth of one meter. For the densely-welded Apache Leap tuff site, the fracture specific surface may be obtained by using an average fracture density of three fractures per square meter. The fracture specific surface is calculated to be 60,000  $\text{cm}^2$  per cubic meter. Fracture density is a three-dimensional parameter, and cannot be accurately determined from two unidirectional cores.

### 2.2.5.2 Aperture Variability

The measurement of aperture variation has rarely been done. Field measurements have been limited to direct measurement (as discussed in the previous section) of fracture apertures along exposed rock surfaces where repeated measurements along a single fracture trace give an estimate of aperture variability. Unfortunately, it is difficult to extrapolate such results to deeper in situ fractures because of the complex relationship between stress and fracture aperture. Direct measurements of fracture aperture have also been made on large lab samples containing rough natural fractures (Sharp and Maini, 1972). Fracture contact areas as a function of stress were measured by Iwai (1976) using pressure sensitive plastic on lab samples containing rough, induced fractures.

Indirect methods of measuring fracture aperture variability can only be suggested at this point. Tracer dispersion may represent one possible method if diffusion and dispersion due to other factors can be separated or ignored. Another possible method is based on the relationship between stress and fracture aperture, which can be measured either in situ or on large laboratory samples. The required assumption is that the stiffness of a fracture loaded normally is strictly a function of the contact area between the opposing fracture surfaces. If this is true, then the change in average apertures with increasing stress can be related to the change in surface area of loading or, equivalently, the percentage of the surface area lying between the incremental values of absolute aperture. Difficulties with this approach include localized modulus variations due to fracture surface coatings, weathering, or crushing of asperities during loading; all of which influence fracture stiffness.

CHAPTER 3  
ISOTHERMAL HYDROLOGIC CHARACTERIZATION

The in situ measurement of water potential in geologic media is essential for the determination of the magnitude and direction of ground-water flow. This is because the water potential is an expression of the free energy status of the water in the media. Changes in the free energy status are manifestations of the driving forces. The driving forces, in turn, are responsible for the magnitude and direction of the movement of ground water in geologic media.

In saturated geologic materials, water potentials, usually expressed in terms of potential (bars) or head (cm of water) are positive and liquid water moves from regions where the total potential is higher to regions where the total potential is lower. The measurement of fluid potential is obtained using water level elevations, and/or using pressure sensors. In unsaturated media, however, water potentials are negative and the use of standard measurement devices is inappropriate. It is the purpose of this chapter to review the determinants of the potential, and the means for measuring them.

### 3.1 Water Potential Measurement

Four components commonly contribute to the total moisture potential,  $\phi_T$ , in ground-water systems:

- Elevation or gravitational potential,  $\phi_G$ ;
- Pressure potential,  $\phi_p$ ;
- Matric potential,  $\phi_M$ , associated with capillary and adsorptive forces exerted by the rock matrix. The matric component of the total water potential determines which fractures and pores will be partially drained and also the thickness of water films along walls of drained fractures; and
- Osmotic potential,  $\phi_0$ , associated with dissolved solute concentrations within the water.

Osmotic-potential gradients and matric potential gradients are not equally effective in inducing water flow in most hydrologic situations. It has been shown (Kemper and Evans, 1963; Kemper and Rollins, 1966; Letey et al., 1969) that the relative effectiveness of osmotic-pressure gradients depends on the solid medium, types of ions present in solution, size of solute molecules relative to pore-size, water-film thickness, and electrostatic interactions between solutes and the substrate.

Letey et al., (1969) and Kemper and Rollins (1966) demonstrated that solute concentration gradients are insignificant with regard to water flow at soil moisture potentials between 0 and 15 bars suction, and can therefore be neglected for practical purposes. Only when salt concentration gradients are large and water films are very thin (e.g., near evaporating surfaces) will osmotic potentials become significant in inducing fluid movement in soils (and presumably in fractured rock).

Osmotic potentials become increasingly significant when a concentration gradient exists across a semi-permeable membrane. Kemper and Evans (1963) demonstrated that the effectiveness of the osmotic potential increases as the degree of restriction of solute movement through the membrane increases, and that osmotic-pressure and hydraulic-pressure differences are equally effective in moving water through a membrane when the solutes are completely restricted. This principle has been applied in the present study in the selection of a solute and semi-permeable membrane for use in the prototype osmotic tensiometer.

Soil scientists employ various methods to measure water potential in situ. These methods include:

- Soil moisture blocks made of ceramic, gypsum or nylon (Marshall, 1959; Richards, 1949);
- Thermocouple psychrometers (Spanner, 1951; Richards and Ogata, 1958);
- Standard tensiometers (Richards and Gardner, 1936; Richards, 1965); and
- Osmotic tensiometers (Peck and Rabbidge, 1966, 1969).

Thermocouple psychrometers and osmotic tensiometers have been evaluated in this research program primarily because these devices appear to be most readily adaptable for use in fractured rocks of low permeability. The thermocouple-psychrometer measurement range is reported to be approximately 2 to 50 bars suction (Wiebe et al., 1971). The osmotic-tensiometer measurement range is reported to be 0 to 15 bars suction (Peck and Rubbidge, 1969), although the modified device evaluated in this study is more likely limited to the range of 0 to about 3 bars suction.

### 3.1.1 Thermocouple Psychrometer

The thermocouple psychrometer is an electronic probe used to measure the relative humidity of the pure air. The water potential is related to the equilibrium vapor pressure by the expression:

$$(3-1) \quad \phi_T = R T / M_w \ln(P/P_0)$$

where

R is the universal gas constant;  
T is the absolute temperature;  
 $M_w$  is the molecular weight of water;  
P is the actual vapor pressure; and  
 $P_0$  is the saturated vapor pressure.

The water potential measured by the psychrometer is the sum of matric and osmotic potentials.

The psychrometer contains a small thermocouple, with a measuring and a reference junction. The measuring junction is moistened while the reference junction remains dry. As water evaporates from the measuring junction it cools the junction and the temperature difference between the measuring and reference junction creates a voltage. This voltage is proportional to the difference between the wet- and dry-bulb temperatures of the vapor being sampled. Cooling at the wet junction is proportional to the product of the evaporation rate and the latent heat of vaporization. The evaporation rate is primarily a function of the relative humidity of the chamber, but also varies with the diffusivity of water in air. The latent heat of vaporization, thermal conductivity and water-vapor diffusivity of air are all functions of temperature.

Errors in psychrometer readings may result from temperature fluctuations, temperature gradients, vapor-pressure gradients and variation in wet-junction size and shape. Two designs for thermocouple psychrometers have been developed to minimize these sources of errors. The two designs, a field thermocouple psychrometer and a thermocouple psychrometer sample changer, utilize two variations of the basic design described above.

The "psychrometric" method (Merrill and Rawlins, 1972; Brown and Johnson, 1976; Briscoe, 1979; and Daniel et al., 1981) involves the measurement of the temperature depression associated with the evaporation of water from wet surface of the measuring thermocouple. The thermocouple surface is initially wetted by inducing condensation through Peltier cooling; i.e., a small current (5 to 8 mA) is passed through the thermocouple for a length of time (6 to 60 seconds) sufficient to cool the thermocouple and completely wet the surface of the thermocouple. The magnitude of the temperature depression, relative to that measured by the reference electrode, is a function of the relative humidity of air surrounding the exposed thermocouple.

The second variation is the "dew point" method (Campbell et al., 1973), which utilizes circuitry within the control unit to maintain the temperature of the wetted measuring thermocouple at the dew point corresponding to the ambient relative humidity. At this temperature, moisture neither condenses on, nor evaporates from, the thermocouple. Typical response curves for the dew point, psychrometric, and combined modes of operation are illustrated in Figure 3.1.

Psychrometer response is a function of ambient temperature and pressure as well as relative humidity. Since response characteristics of individual psychrometers differ slightly, precise field measurements require prior calibration of each instrument in the laboratory. A detailed description of the calibration procedure utilized for this part of the project is outlined in Appendix A. Briefly, the calibration procedure involves a series of measurements made over salt solutions having known osmotic potentials. Measurements are repeated at several temperatures covering the range anticipated in the field. Variations in response of individual psychrometers to ambient pressure changes are insignificant and are not evaluated during the calibration procedure.

An additional aspect of psychrometer-response characteristics evaluated during the present study concerns the rate at which measuring thermocouples cool when a fixed current is applied under moisture-potential extremes. As stated previously, the effective range of the thermocouple psychrometer is about 2 to 50 bars suction. Beyond the extremes of this range, psychrometers do not respond to either dew point or psychrometric measurement methods. At the wet extreme (0 to 2 bars suction), failure is attributable to moisture evaporating from the wet-measuring thermocouple at a rate insufficient to produce a measurable temperature depression after the cooling current is terminated.

At the dry extreme (more than about 50 bars suction), the failure results from the fact that condensation cannot be induced on the measuring thermocouple by Peltier cooling. Because it is of great importance to the hydrologist to ascertain which moisture extreme exists in a given situation, we have attempted to develop a method which differentiates between very wet and very dry conditions utilizing the rate at which the measuring thermocouple cools when a fixed current is applied. The reasoning is a wet thermocouple should cool significantly slower than a dry thermocouple due to the large heat capacity of water films which condense on the thermocouple surface in response to Peltier cooling under wet conditions.

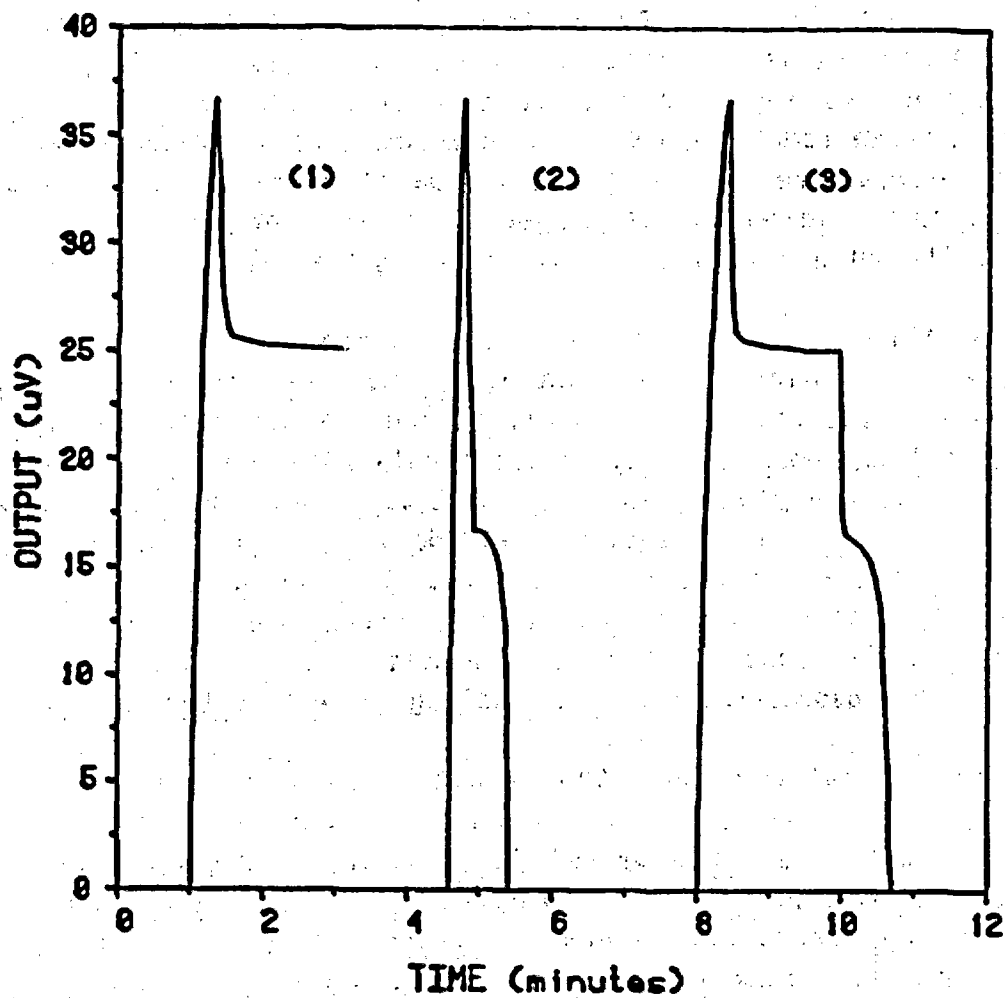


Figure 3.1 Thermocouple psychrometer response curve for dewpoint (1), psychrometric (2), and combined modes (3). Water potential is 25 bars suction. Temperature is 32.8°C.

Laboratory experiments have been conducted to ascertain whether such a distinction between cooling rates under wet and dry conditions could be made. Results obtained for 8 Merrill screen-cage psychrometers which were equilibrated over distilled water (0 bars) and a 1.6 molal NaCl solution (76 bars suction) are presented in Figure 3.2. These results suggest that a distinction can be made either by comparing cooling curves plotted from field data with corresponding laboratory calibration curves or more simply, by comparing the microvolt reading taken at a fixed time after Peltier cooling is initiated (e.g., at  $t = 30$  seconds) with corresponding values from calibration data.

When making these comparisons, it is imperative that all microvolt values be corrected to a common temperature (e.g., 25°C) using relationships suggested by the psychrometer manufacturer. Also imperative is that direct comparisons only be made between psychrometers manufactured by the same company and having the same type of protective shield (ceramic or screen). Ideally, one should compare field results for an individual psychrometer with cooling curves developed specifically for that psychrometer.

#### 3.1.1.1 Field Psychrometer

For in situ measurements of soil water potential, the thermocouple of the field psychrometer is protected by a cup-shaped shield; the shield should permit rapid vapor equilibration between the soil and the chamber. Essential components of commercial thermocouple psychrometers include a reference thermocouple (copper-constantan), a measuring thermocouple (chromel-constantan), a protective shield, a Teflon base, and a length of four-strand wire (Figure 3.3). The reference thermocouple is embedded in epoxy within the base of the instrument and is utilized to measure ambient temperature. This reference thermocouple is isolated from and remains independent of effects of changing moisture conditions.

The measuring thermocouple, supported by the Teflon base and protected by the shield, is exposed to ambient moisture conditions of the rock or soil being measured. The protective shield which surrounds the measuring thermocouple consists of either a wire screen cage or a porous ceramic cup. Ceramic shields provide greater protection, but they also inhibit vapor transport through the shield and thus require longer equilibration times during calibration and field measurement.

Psychrometer measurements are made utilizing control units/meters available from several manufacturers. These units provide the required

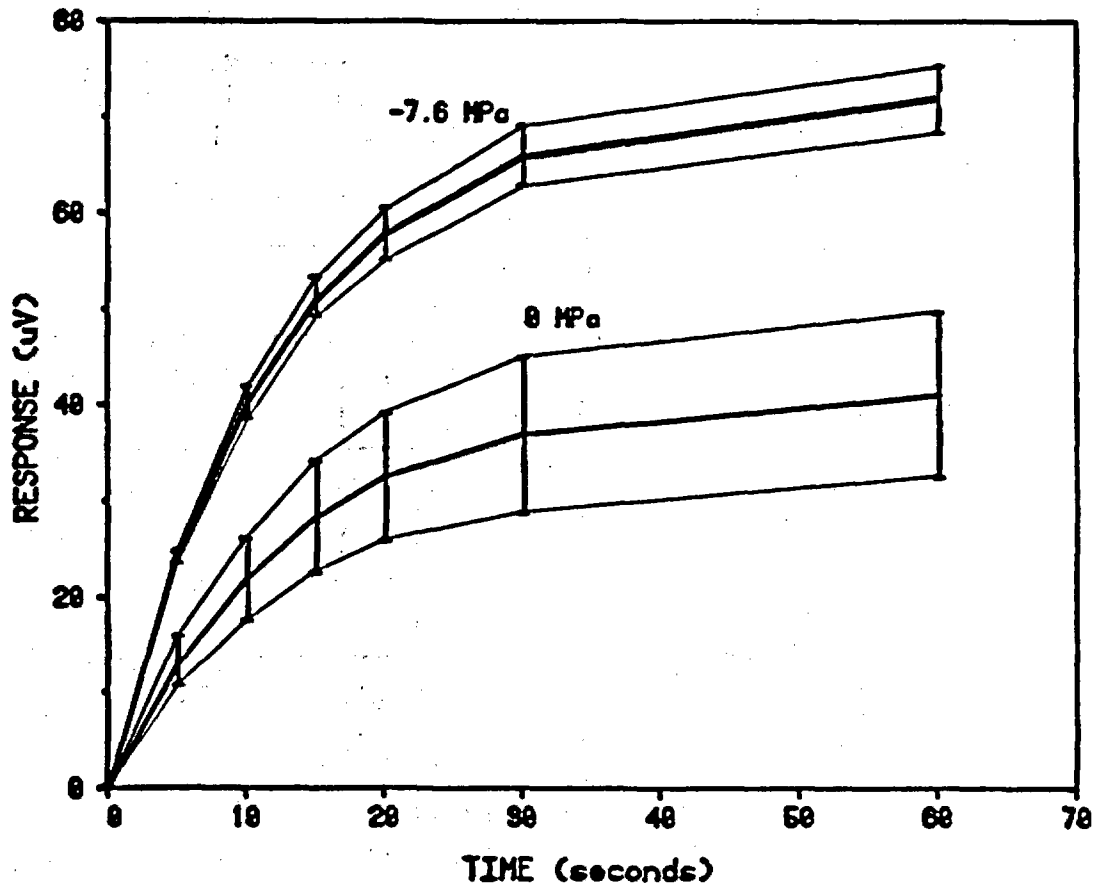
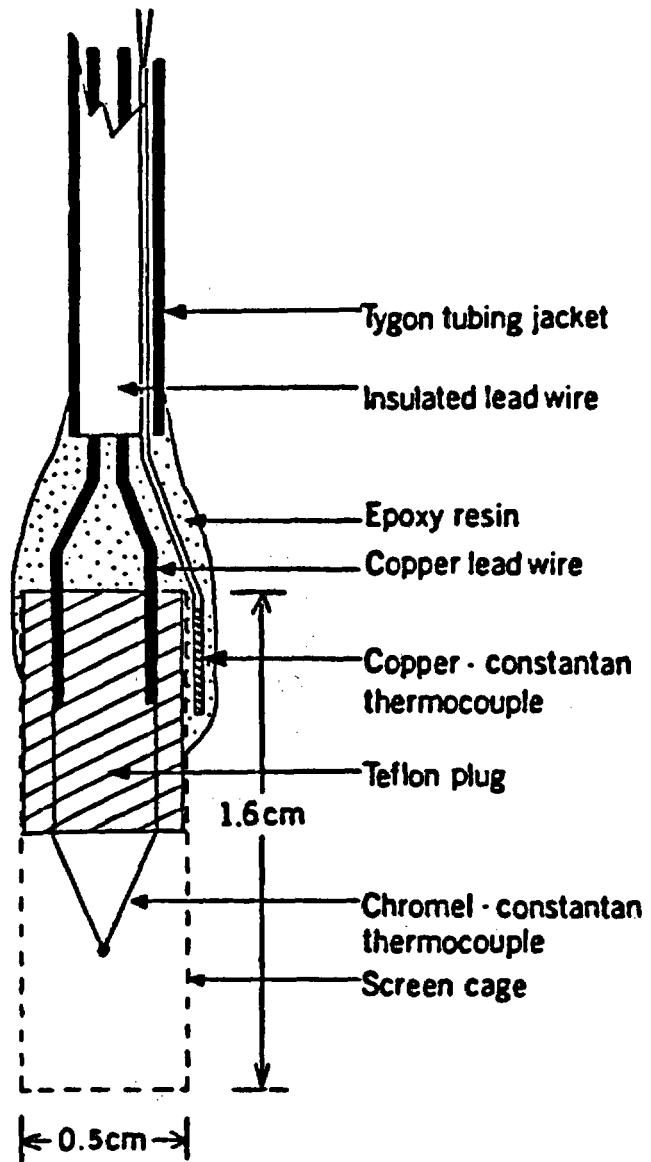


Figure 3.2 Average cooling rate curves for eight screen cage psychrometers under saturated (0 bar) and very dry (76 bar suction) conditions. Vertical bars about the mean values indicate the one standard deviation confidence region.



**Figure 3.3** Median longitudinal section of a screen-enclosed thermocouple psychrometer (after Meyn and White, 1972).

switching and cooling circuitry and signal amplification and measurement devices. Psychrometer response is read in microvolts using a built-in meter or an auxiliary chart recorder. Available control units range from relatively simple switch boxes to automated scanning/recording devices.

Thermocouple psychrometers have been emplaced for variable periods of time in seven boreholes in the Santo Nino mine, six boreholes in the Pride-of-the-West mine, three boreholes in the Queen Creek road tunnel, and one in the haulage tunnel in the Magma mine. Typically, two psychrometers have been emplaced and sealed in each borehole using inflatable packers. After an initial equilibration period, these psychrometers measure an "average" moisture potential of the rock matrix and of all open fractures which intersect the borehole. Periodic measurements have been made at one to four week intervals in an effort to quantify temporal changes in moisture conditions within each borehole.

Results obtained from the Pride-of-the-West mine and the Santo Nino mine indicate that moisture potentials for all but Borehole 3 of Pride-of-the-West are out of the psychrometers' measurement range. Psychrometric measurements obtained at the Pride-of-the-West site are summarized in Table 3.1. Results for Borehole 3, presented graphically in Figure 3.4, indicate a wetting trend (decreasing negative potentials) during the first several weeks after installation followed by essentially constant moisture conditions during the next four months. This pattern suggests that the initial wetting period may have been the result of a gradual re-equilibration of moisture conditions within the borehole after it was sealed with the packer.

Cooling rate data were obtained on several occasions in order to determine whether the psychrometer response failures in Boreholes 1, 4, 5, 6 and 8 were due to excessive moisture or excessive dryness. Microvolt readings (corrected to 25°C) recorded after a 30-second cooling period are presented in the last column of Table 3.1. Laboratory calibration data (Figure 3.5) indicate that if the 30-second reading is less than 45  $\mu\text{V}$ , then moisture conditions are probably too wet; and if the reading is greater than 60  $\mu\text{V}$ , then conditions are probably too dry.

On this basis, Boreholes 5 and 6 appear to be too wet, and Boreholes 4 and 8 appear to be too dry. Substantiation of this interpretation of conditions in Borehole 5 was obtained in July, when the packer was deflated and a significant volume of water poured out of the borehole.

-----  
**Table 3.1 Summary of thermocouple psychrometer measurements in Pride-  
of-the-West mine.**  
-----

Borehole Number	Borehole Length (m)	Date of Measurement	Psychrometer Number	Borehole Temperature (°C)	Psychrometric Response (µV)	Moisture Potential (Mpa)
1	4.4	3/22/82	M73 <sup>a</sup>	16.2	NR <sup>f</sup>	
		3/30/82	M152 <sup>a</sup>	16.3	NR	
			M73	16.3	NR	
		4/20/82	M152	16.1	NR	
			M73 <sup>b</sup>	16.3	NR	
			M152 <sup>b</sup>	16.5	NR	
3	>6.1	3/22/82	M150 <sup>a</sup>	16.7	13.7 ± 0.15	-4.01
		3/30/82	M150	16.5	13.1 ± 0.1	-3.78
		4/20/82	M150	16.5	12.1 ± 0.1	-3.49
		5/11/82	M150	16.6	12.0 ± 0	-3.46
		5/25/82	M150	16.6	12.0 ± 0	-3.45
		6/08/82	M150	16.4	12.0 ± 0	-3.49
		7/12/82	M150	16.6	12.1 ± 0.2	-3.48
		8/01/82	M150	16.6	12.0 ± 0.05	-3.45
		9/24/82 <sup>e</sup>				
4	4.0	5/11/82	M73 <sup>c</sup>	16.8	NR	
			M152 <sup>c</sup>	16.8	NR	
		5/25/82	M73	16.7	NR	
			M152	16.7	NR	
		6/08/82	M73	16.6	NR	64.0
			M152	16.6	NR	67.2
			7/12/82	M73 <sup>d</sup>	16.6	NR
M152 <sup>d</sup>	16.6	NR		67.2		

µV at  
30 sec

-----  
**Table 3.1 (continued)**  
 -----

Borehole Number	Borehole Length	Date of Measurement	Psychrometer Number	Borehole Temperature (°C)	Psychrometric Response (µV)	µV at 30 sec
5	>6.1m	4/20/82	M151 <sup>g</sup>	16.4	NR	-
		5/11/82	M151	16.9	NR	-
		5/25/82	M151	16.6	NR	-
		6/08/82	M151	16.7	NR	86.4
		7/12/82 <sup>d</sup>	M151	16.9	NR	32.9
6	-	8/01/82	M73 <sup>h</sup>	-	NR	39.5
		11/10/82 <sup>i</sup>	M152	16.5	NR	-
			M73	16.5	NR	30.9
			M152	16.7	NR	28.4
8	>6.1m	5/11/82	M153 <sup>c</sup>	16.5	NR	-
		5/25/82	M153	16.6	NR	-
		6/08/82	M153	16.8	NR	66.8
		7/12/82 <sup>d</sup>	M153	16.7	NR	68.3

- a. Psychrometers installed 3/18/82.  
 b. Borehole abandoned 4/20/82.  
 c. Psychrometers installed 4/20/82.  
 d. Borehole abandoned 7/12/82.  
 e. Packer found to be completely deflated; borehole abandoned.  
 f. NR indicates "no response".  
 g. Psychrometer installed 3/30/82.  
 h. Psychrometers installed 7/12/82.  
 i. Borehole abandoned 11/10/82.

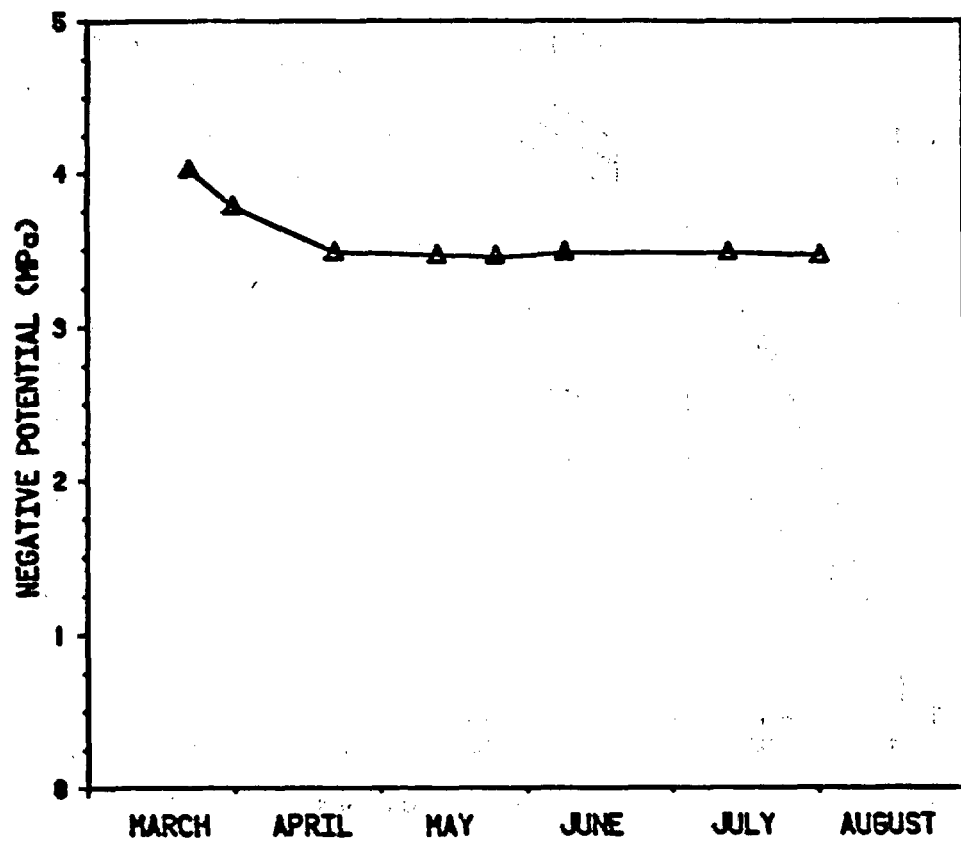


Figure 3.4. Moisture potentials measured in Borehole 3 of the Pride-of-the-West mine using Thermocouple Psychrometer 150.

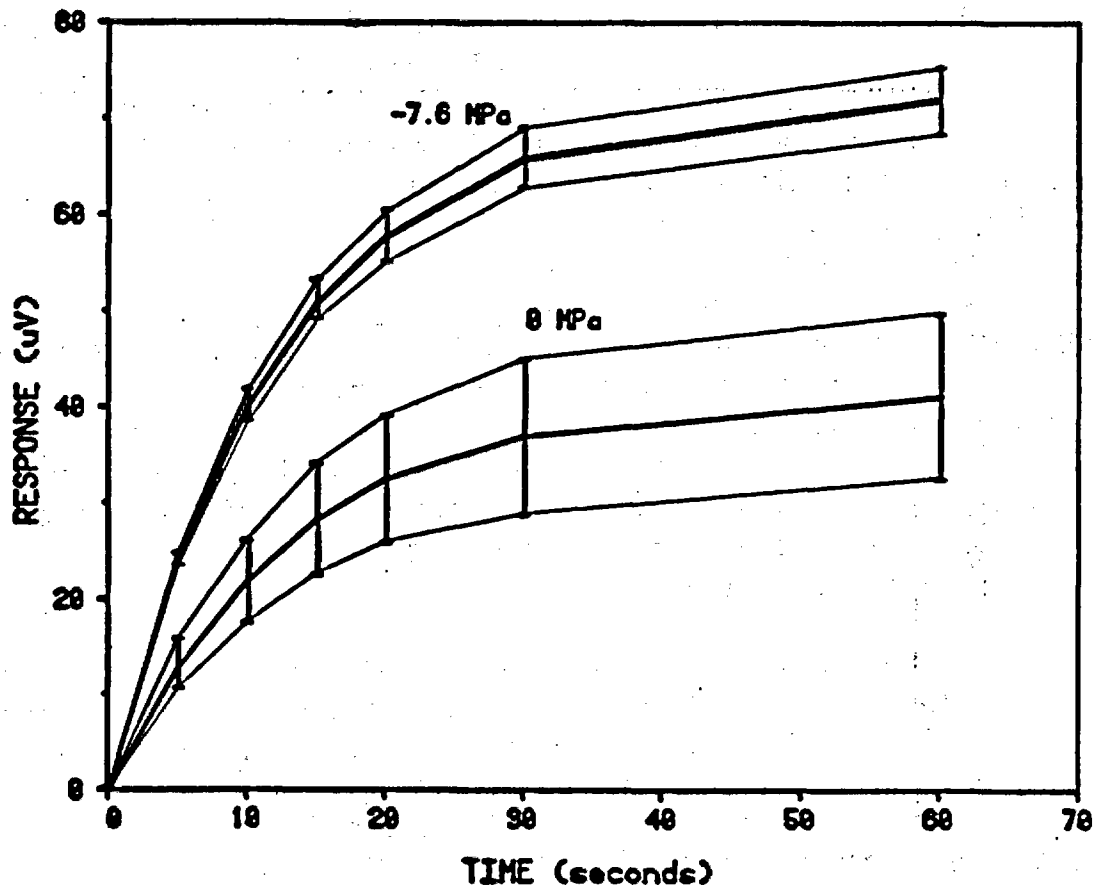


Figure 3.5 Average cooling rate curves for eight screen cage psychrometers under very wet (0 bars suction) and very dry (76 bars suction) conditions. Vertical bars represent a one standard deviation confidence region about the mean.

Indirect support of the hypothesis that Borehole 6 may be too wet is suggested by the presence of some water staining on the mine wall beneath this borehole. Neither staining nor moisture have been evident in Boreholes 4 and 8 during the course of this study.

Moisture conditions at the second field study site, the Santo Nino mine appeared to range from damp to very wet. Seven existing boreholes were instrumented with thermocouple psychrometers. Results are summarized in Table 3.2. All measurements obtained in the Santo Nino mine have been outside the effective range of the psychrometric and dew-point measurement methods. Cooling-rate data (microvolt readings at  $t = 30$  seconds, corrected to  $25^{\circ}\text{C}$ ) are presented in the last column of Table 3.2. Using the same criteria as before, Borehole D1 would be judged to be very wet, Boreholes W3, C1, and C2 would be judged to be extremely dry, and data for Boreholes D2 and W4 would be inconclusive. Data for psychrometers having a "W" preceding the numerical designation have not been included in this interpretation because those psychrometers were obtained from a different manufacturer than those which were used during laboratory calibration procedures.

Psychrometer measurements taken in the haulage tunnel at the Magma mine and the Queen Creek road tunnel east of Superior, Arizona, are made in welded tuff. The welded tuff in the haulage tunnel has remained very wet through the period of this study while tuff in the road tunnel is much dryer and has shown greater variation in moisture potential. Measurements made at the road tunnel during the first six months of 1984 are summarized in Table 3.3.

Road tunnel data for Boreholes 1 and 2 indicate significant wetting (i.e., lower potentials) between May and June sampling date. Borehole 3, located about 30 meters away from holes 1 and 2, has consistently been much wetter than the other holes and shows a slight drying trend throughout the measurement period, with the possible exception of the last date.

Comparison of results obtained from corresponding pairs of psychrometers indicates different measured potentials. These discrepancies cast doubt on the precise magnitude of water-potential measurements made using thermocouple psychrometers with the existing procedures. However, the results presented in Table 3.3 do suggest that temporal trends in moisture potential can be readily followed using this method even if the absolute values are subject to uncertainty.

-----  
**Table 3.2 Summary of thermocouple psychrometer measurements in Santo Nino mine.**  
 -----

Borehole Number	Date of Measurement	Psychrometer Number	Borehole Temperature	Psychrometric Response	$\mu\text{V}$ at 30 sec
D1	3/22/82	M76 <sup>a</sup>	10.2	NR	-
	3/30/82	M76	10.2	NR	-
	4/20/82	M76	10.1	NR	-
	5/11/82	M76	10.6	NR	-
	5/25/82	M76	10.6	NR	-
	6/08/82	M76	11.0	NR	49.0
	7/12/82	M76	11.0	NR	51.4
	7/27/82	M76	10.9	NR	40.4
	8/03/82	M5 <sup>b</sup>	11.2	NR	51.0
		M76	11.1	NR	37.6
	8/13/82	M5	11.4	NR	46.0
		M76	11.2	NR	35.9
	9/17/82	M5	11.4	NR	38.7
		M76	11.4	NR	34.8
	10/20/82	M5	11.3	NR	32.5
	M76	11.1	NR	33.6	
D2	4/20/82	M210 <sup>c</sup>	11.0	NR	-
	5/11/82	M210	11.0	NR	-
	5/25/82	M210	11.2	NR	-
	6/08/82	M210	11.3	NR	46.8
	7/12/82	M210	11.3	NR	-
	7/27/82	M210	10.9	NR	56.5
	8/03/82	M20	11.5	NR	54.3
	8/13/82	M20	11.1	NR	56.8
		M210	11.4	NR	55.6
	9/17/82	M20	11.2	NR	55.8
		M210	11.4	NR	48.2
	10/20/82	M20	11.3	NR	56.3
	M210	11.6	NR	43.9	

Table 3.2 (continued)

Borehole Number	Date of Measurement	Psychrometer Number	Borehole Temperature °C	Psychrometric Response $\mu$ V	$\mu$ V at 30 sec	
W1	3/22/82	M209 <sup>e</sup>	9.5	NR	-	
	3/30/82	M209 <sup>f</sup>	9.6	NR	-	
W3	5/25/82	M208 <sup>g</sup>	9.9	NR	-	
	6/8/82	M208	-	NR	49.5	
	7/12/82	M208	10.8	NR	64.9	
	7/27/82	M208	10.8	NR	63.2	
		M6 <sup>h</sup>	-	NR	59.5	
	8/15/82	M208	11.1	NR	66.0	
		M6	10.9	NR	55.0	
	9/17/82	M208	11.3	NR	63.2	
		M6	10.8	NR	59.2	
	10/20/82	M208	10.9	NR	51.7	
		M6	11.1	NR	55.6	
	W4	4/20/82	M210 <sup>i</sup>	10.1	NR	-
		5/11/82	M210	10.5	NR	-
5/25/82		M210	10.4	NR	-	
6/8/82		M210	10.4	NR	52.8	
7/12/82		M210	10.6	NR	46.0	
7/27/82		M210	10.9	NR	63.5	
		M2 <sup>j</sup>	11.4	NR	44.7	
8/15/82		M210	11.0	NR	57.6	
9/17/82 <sup>k</sup>		M2	11.0	NR	45.0	
C1		7/27/82	M8 <sup>l</sup>	10.6	NR	73.6
		W6 <sup>l</sup>	10.6	NR	41.7	
	8/13/82	M8	11.5	NR	71.0	
		W6	12.0	NR	-	
	9/17/82	M8	11.1	NR	76.8	
		W6	10.9	NR	41.2	
	10/20/82	M8	10.5	NR	67.6	
	W6	10.3	NR	38.1		
C2	7/27/82	M2 <sup>l</sup>	10.7	NR	61.9	
		M31	10.7	NR	69.2	
	8/13/82	M2	11.0	NR	-	
		M3	11.1	NR	-	
	9/17/82	M2	10.1	NR	58.6	
		M3	10.5	NR	61.6	
10/20/82	M2	10.5	NR	48.0		
	M3	10.9	NR	58.1		

note:

- |                                    |  |
|------------------------------------|--|
| a. Psychrometer installed 3/18/82. | g. Psychrometer installed 5/11/82.         |
| b. Psychrometer installed 7/27/82. | h. Psychrometer installed 7/12/82.         |
| c. Psychrometer installed 3/30/82. | i. Psychrometer installed 3/18/82.         |
| d. Psychrometer installed 7/27/82. | j. Psychrometer installed 7/12/82.         |
| e. Psychrometer installed 3/18/82. | k. Packer had deflated; apparatus removed. |
| f. Psychrometer removed 3/30/82.   | l. Psychrometers installed 7/12/82.        |

-----  
**Table 3.3 Moisture potential as measured using thermocouple  
 psychrometers in the dew point (DP) and psychrometric (PS)  
 modes in welded tuff at the Queen Creek road tunnel.**  
 -----

<u>BOREHOLE</u>	<u>PSYCHROMETER</u>	<u>METHOD</u>	<u>1/23/84</u>	<u>3/1/84</u>	<u>3/2/84</u>	<u>3/14/84</u>	<u>4/5/84</u>	<u>5/10/84</u>	<u>6/6/84</u>	<u>6/14/84</u>
#1	M26	DP	-	-	21.5	20.3	19.8	27.5	15.3	15.8
		PS	33.5	29.3	30.0	28.6	27.3	28.0	16.5	17.4
	M27	DP	-	-	21.8	20.9	20.0	24.0	15.5	17.0
		PS	37.5	29.8	29.8	28.5	27.1	29.1	16.8	20.8
#2	M28	DP	-	-	22.9	21.3	24.2	* 21.0	13.6	-
		PS	-	35.5	34.6	32.7	32.4	24.4	12.7	-
	M29	DP	-	-	16.4	18.7	-	* 21.9	20.0	-
		PS	-	25.0	24.5	25.1	-	26.3	22.8	-
#3	M23	DP	-	-	-	<1	<1	4.5	5.7	4.5
		PS	-	<1	-	<1	<1	6.0	8.2	6.8
	M24	DP	-	-	-	2.8	1.5	2.8	5.1	3.8
		PS	-	<1	-	3.5	<1	3.7	5.4	3.5

\*Psychrometers M28 and M29 were replaced with psychrometers M22 and M30 following the 4/8/84 readings.

### 3.1.1.2 Thermocouple Psychrometer Sample Changer

The thermocouple psychrometer sample changer (SC-10A), manufactured by Decagon Devices, Inc., Pullman, Washington, is constructed of a machined and anodized aluminum body 12.7 cm in diameter and 5.4 cm high. (Figure 3.6). The SC-10A consists of a ceramic-bead thermocouple and ten removable chromed-brass sample cups all encased in the massive aluminum housing. Samples are contained within the chromed cups and can be packed with a device which produces a conical depression for the thermocouple.

Just prior to each reading, a special sample cup with distilled water is rotated to the thermocouple, and the ceramic bead is dipped to provide the wet bulb. Voltage and temperature readings are recorded as each sample is rotated and sealed directly below the thermocouple. By sealing the sample directly below the thermocouple in an isothermal chamber, the water potential of the gas phase in the chamber is assumed to be equal to the potential of the water in the liquid phase. The voltage produced becomes stable when equilibrium is attained and is proportional to the wet-bulb temperature depression.

For subsequent calculations of water potential, a psychrometer constant for a particular thermocouple must be determined using salt solutions of known osmotic potentials. Appendix A gives a detailed explanation and the equations necessary for calculating a psychrometer constant. The water potential of a particular sample can be calculated using the equations presented in Appendix A, along with the microvolt and temperature readings of the psychrometer.

The sample cups of the thermocouple psychrometer SC-10A can accommodate samples of soil, rock, filter papers and salt solutions. Rock samples taken from the slightly-welded white unit of the Apache Leap tuff have been used in the SC-10A to calculate a moisture-release curve for the tuff.

### 3.1.2 Tensiometer

The standard tensiometer consists of a porous, ceramic cup connected by a rigid tube to a device for measuring negative pressures (vacuum gage, manometer, or transducer). The entire apparatus is filled with pure water and sealed before or after insertion at a desired depth within an unsaturated soil. During the subsequent equilibration process, dissolved solutes move through the ceramic cup and water flows out of the cup in response to a matric potential in the surrounding soil.

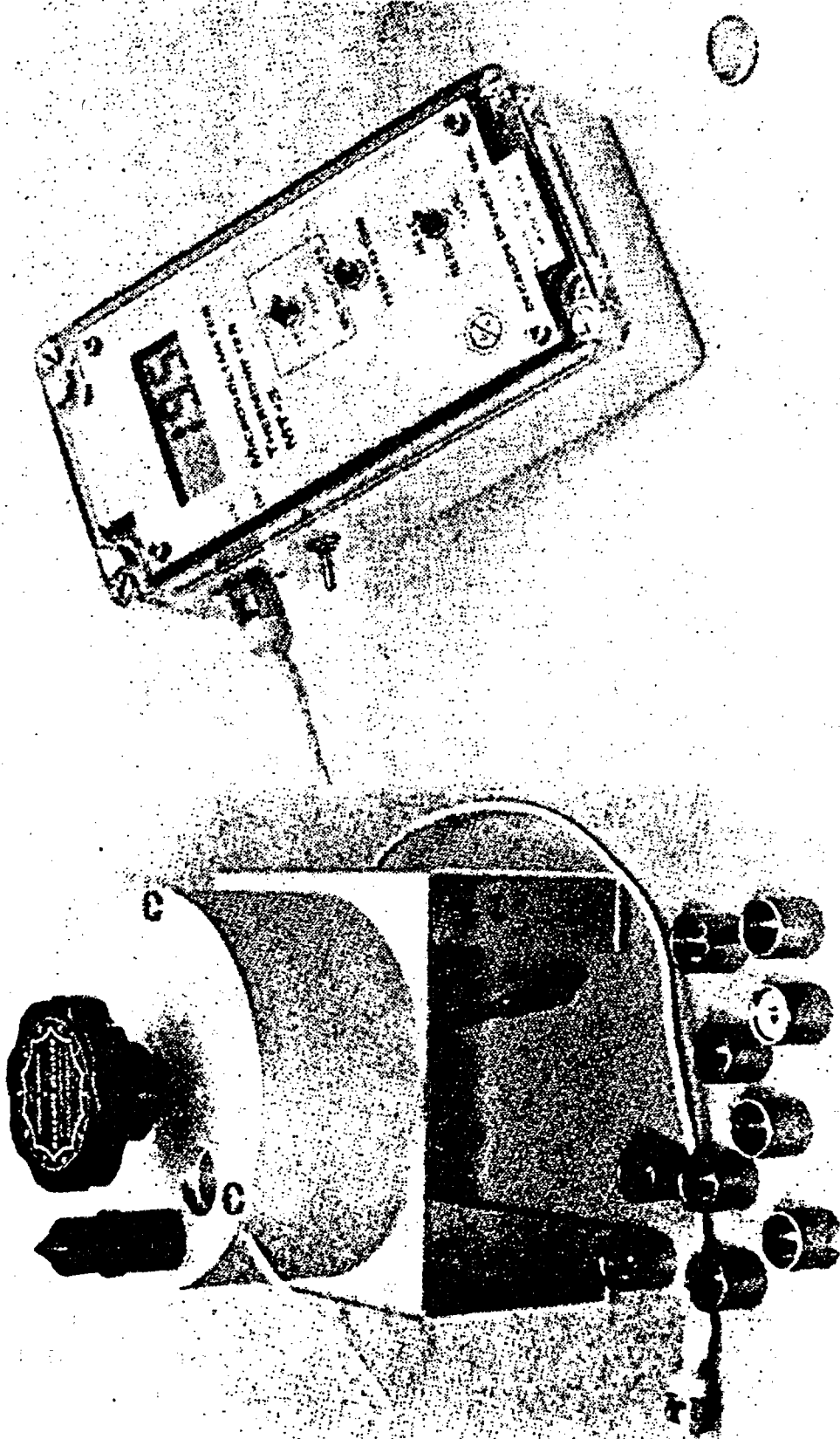


Figure 3.6 Thermocouple psychrometer sample changer, sample cups and microvoltmeter (Decagon Devices, Inc., Pullman, Washington).

At equilibrium, the negative hydrostatic pressure measured by the manometer is equal to the matric potential of the soil moisture. The osmotic component of the total moisture potential is not included in measurements made with standard tensiometers because the ceramic cup is permeable to dissolved solutes. The effective range of a standard tensiometer, 0 to about 0.8 bars suction, is limited by the fact that negative pressures are measured with reference to atmospheric pressure. To date, the standard tensiometer has not been used to measure water potentials of a rock system in boreholes. Possible modifications to the tensiometer which would increase contact between the rock walls and ceramic cup include filling the gap with silica sand or inert material.

### 3.1.3 Osmotic Tensiometer

Modifications to the standard tensiometer which increased the measurement range from 0 to 15 bars suction were first accomplished by Peck and Rabbidge (1966, 1969). Their device differed from a standard tensiometer in several ways:

- Communication between the tensiometer and soil moisture was achieved through a semi-permeable membrane supported and protected by a porous, ceramic disk;
- The tensiometer is initially filled with an aqueous solution of large organic molecules which are retained by the membrane; and
- Positive hydrostatic pressures are maintained within the device at all times.

This modified tensiometer has been termed the osmotic tensiometer. The osmotic potential created by the organic solute within an osmotic tensiometer serves to partially offset the matric potential of the surrounding soil moisture and thus reduces the amount of liquid that must flow through the membrane during equilibration.

Also, if the total potential inside the device ( $\phi_0$  and  $\phi_p$ ) is more negative than that of the matric component of the soil-moisture potential ( $\phi_M$ ), then water will flow into the device during the equilibration process and a positive hydrostatic pressure will be measured by the pressure-sensing device. The range of potentials which can be measured is increased significantly in this manner.

The membrane used in osmotic tensiometers is nearly impermeable to the organic solute but is readily permeable to the smaller inorganic solutes generally found in soil water. Consequently, this instrument, like the standard tensiometer, does not measure the osmotic component of the

total moisture potential if sufficient time is allowed for inorganic solute concentrations to equalize on either side of the membrane.

The osmotic tensiometer developed in this study differs from that utilized by previous workers. The device is intended for use in a fractured rock in which the volumetric moisture content is small. Our design incorporates a tubular membrane to provide contact between the tensiometer fluid and the wall of the borehole in which the device is installed. Hydrostatic pressure within the tensiometer is measured with a 0 to 3.5 bar transducer.

During laboratory testing, the hydrostatic pressure can be adjusted using a piston assembly controlled by a computer/data-acquisition unit. The null-type pressure control system (which may be deleted for field applications) serves to greatly decrease the length of time required for the tensiometer to equilibrate with the surrounding medium and to significantly reduce the volume of water which must be transmitted through the membrane during equilibration.

An illustration of how the prototype osmotic tensiometer appears following insertion in a borehole in fractured rock is presented in Figure 3.7. The core of the prototype (3.8 cm diameter x 91.4 cm stainless steel pipe) contains internal access tubes (0.32 cm diameter) which open to the annular space at each end of the device. A tubular semi-permeable membrane provides contact between moisture in the rock surrounding the borehole and the osmotic solution within the tensiometer. Each end of the membrane is sealed by compressing it between a flat, rubber gasket and an O-ring by bolting a circular end plate to the stainless-steel core. A thin layer of silicone sealant applied between the gasket and membrane assures complete sealing.

The prototype is evacuated prior to insertion in a borehole, and the annular space is filled with the osmotic solution after the device is in place. Filling is accomplished by applying positive pressure to the solution reservoir attached to one of the access tubes. Valves on the vacuum and inlet lines are closed after the device has been filled. During the subsequent measurement procedure, hydrostatic pressure within the tensiometer is monitored using a pressure gauge or pressure transducer attached to the inlet line.

Hydrostatic pressure increases or decreases in response to water flowing through the membrane until such time as the sum of the osmotic and hydrostatic pressures inside the tensiometer is equal to the total water potential in the surrounding rock mass. This equilibration process can

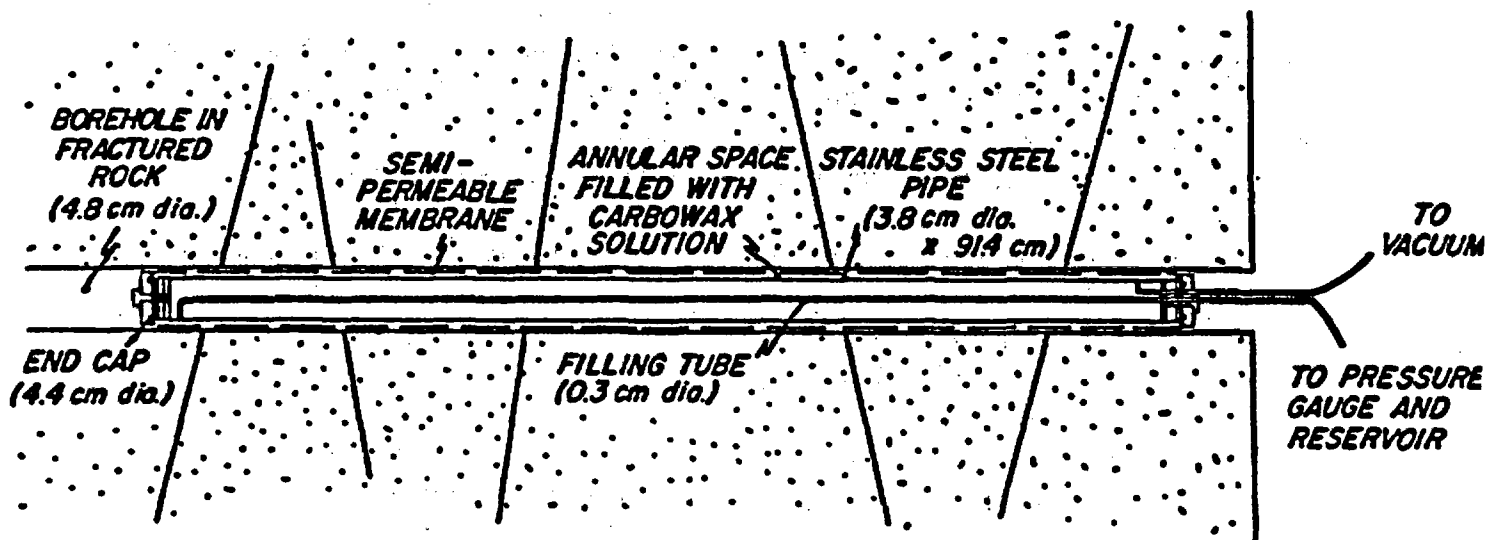


Figure 3.7 Diagram of the prototype osmotic tensiometer in a borehole in fractured rock.

be accelerated by incrementally pressurizing or depressurizing the tensiometer, manually or automatically, when significant increases or decreases in hydrostatic pressure are observed.

Development of the prototype osmotic tensiometer involved lab and field evaluations of several membrane materials and organic solutes. The following properties were considered to be important in the selection of a semi-permeable membrane:

- Maintains sufficient strength and flexibility to permit insertion into a borehole without damage and to withstand several bars of hydrostatic pressure from within;
- Readily permeable to water at low pressure gradients;
- Permeable to inorganic solutes commonly found in water within the fractured host rock;
- Completely impermeable to large organic molecules of the type used to create a known osmotic potential within the tensiometer;
- Available in tubular form with diameters approximately equal to those of test boreholes; and
- Resistant to microbial decomposition.

Detailed descriptions and evaluations of various types of membranes are presented in Appendix B. The solute molecules utilized to generate a known osmotic potential should ideally be:

- Large enough to preclude passage through the semi-permeable membrane;
- Inert with respect to the membrane material and to metals used in the tensiometer support apparatus;
- Chemically stable; and
- Resistant to microbial decomposition.

Several organic solutes have been evaluated during this study, including polystyrene sulfonic acid, polyethylene glycol, polyvinyl pyrrolidone, and polyethylene oxide. Results and descriptions for each are also summarized in Appendix B.

#### 3.1.4 Absorber Method

The absorber method uses filter papers to determine rock-water potentials in situ. The method assumes the porous materials in liquid or vapor contact with the filter paper will exchange water until the water potential of both are the same. The technique involves placing the filter paper in contact with the soil or rock, allowing it to equilibrate, and determining the water potential of the filter paper with a thermocouple psychrometer sample changer.

Gardner (1937) first proposed the water uptake by filter papers to measure soil-water potential and obtained a calibration curve for a type of filter paper. Fawcett and Collis-George (1967) modified the method, allowing the papers to equilibrate with soil samples for seven days using Whatman No. 42 filter papers treated with 0.005%  $\text{HgCl}_2$ .

McQueen and Miller (1968) noted that when filter paper is placed in direct contact with the soil, only the matric potential is measured, whereas when the filter paper is in a closed chamber on top of the soil, the matric and osmotic potentials are measured. Improving the measurement of matric and osmotic potentials, Al-Khafaf and Hanks (1974) used a modification of the method of McQueen and Miller (1968) by placing the filter paper across a rubber ring to prevent soil contact. Hamblin (1981) used Whatman No. 42 filter papers to construct a calibration curve and, comparing two different batches two years apart, found the calibration curves to be nearly identical.

To estimate in situ rock-water potentials with the filter papers, a device is being designed for use in a borehole. The device will place the filter papers in contact with the borehole wall, the water potential of the filter papers and rock wall will be allowed to equilibrate, and the filter papers will be removed. The filter papers are then quickly placed in the psychrometer cups to determine their water potential. In addition, the water content can be estimated using calibration curves. Appendix C provides additional information about this technique.

### 3.2 Water Content Measurement

Many parameters in the governing equations for the flow through unsaturated media are functions of water content. The hydraulic conductivity and the fluid potential are examples of such parameters. The objective of this section is to evaluate the ability of two geophysical methods, electrical resistivity and neutron logging, to measure in situ changes in the water content of unsaturated, low-porosity, fractured rocks.

Downhole resistivity and neutron logging are used to detect temporal variations in the water content of a quartz monzonite at the Santo Nino mine and at the Magma mine. The feasibility of using electrical resistivity and neutron logging to measure temporal changes in the water content at the quartz monzonite site is decided by:

- Comparing the relative measurements over time;
- Comparing the results of both methods; and
- Correlating the borehole measurements with surface rainfall data.

These results are then used to evaluate temporal changes in the water content at the dacitic ash-flow tuff site from the wet winter months through the dry summer months. Before this qualitative analysis can be undertaken, the physical parameters which affect each method must be evaluated.

Neutron logging has been used extensively by soil scientists to measure the water content of soils and by geophysicists to measure the saturated porosity of oil-bearing formations. The procedure uses high-energy neutrons which are emitted from a radiation source. The water content within the pore volume is calculated from the number of low-energy neutrons which are reflected by hydrogen atoms in water molecules (or in oil molecules) and counted at a detector.

Three dimensional plots of the neutron data collected at the Santo Nino field site are presented in Figures 3.8 and 3.9. Similarly, three dimensional plots of the neutron and resistivity data collected at the Magma field site are presented in Figures 3.10 and 3.11. The average apparent resistivity values for the two Santo Nino boreholes are plotted versus time in Figures 3.12 and 3.13. The average is used in these plots because only a small interval (less than one meter) was logged in each hole. For comparison, the average neutron data for the Santo Nino boreholes are also plotted in Figures 3.12 and 3.13.

Temporal variations in resistivity data can be attributed to changes in the water content of a rock. An increase or decrease in the water content of the rock can be detected by a corresponding increase or decrease in the number of thermal neutrons detected by the neutron probe. Indeed, by comparing the two dimensional plots for the Santo Nino boreholes (Figures 3.12 and 3.13), the maximum and minimum resistivity values corresponding to the minimum and maximum neutron values, respectively, can be found.

The resistivity profile for the Borehole 5.2 at the Santo Nino field site (shown in Figure 3.12) indicates that the water content of the quartz monzonite gradually decreased from the beginning of October through the end of December; then, responding to winter rain, steadily increased through February. The water content remained at this high level until the end of May. In June the water content decreased slightly, only to rebound upward in July and August.

The normalized neutron profile for Borehole 5.2 shows the same general trends. The major difference is the neutron counts did not level off in

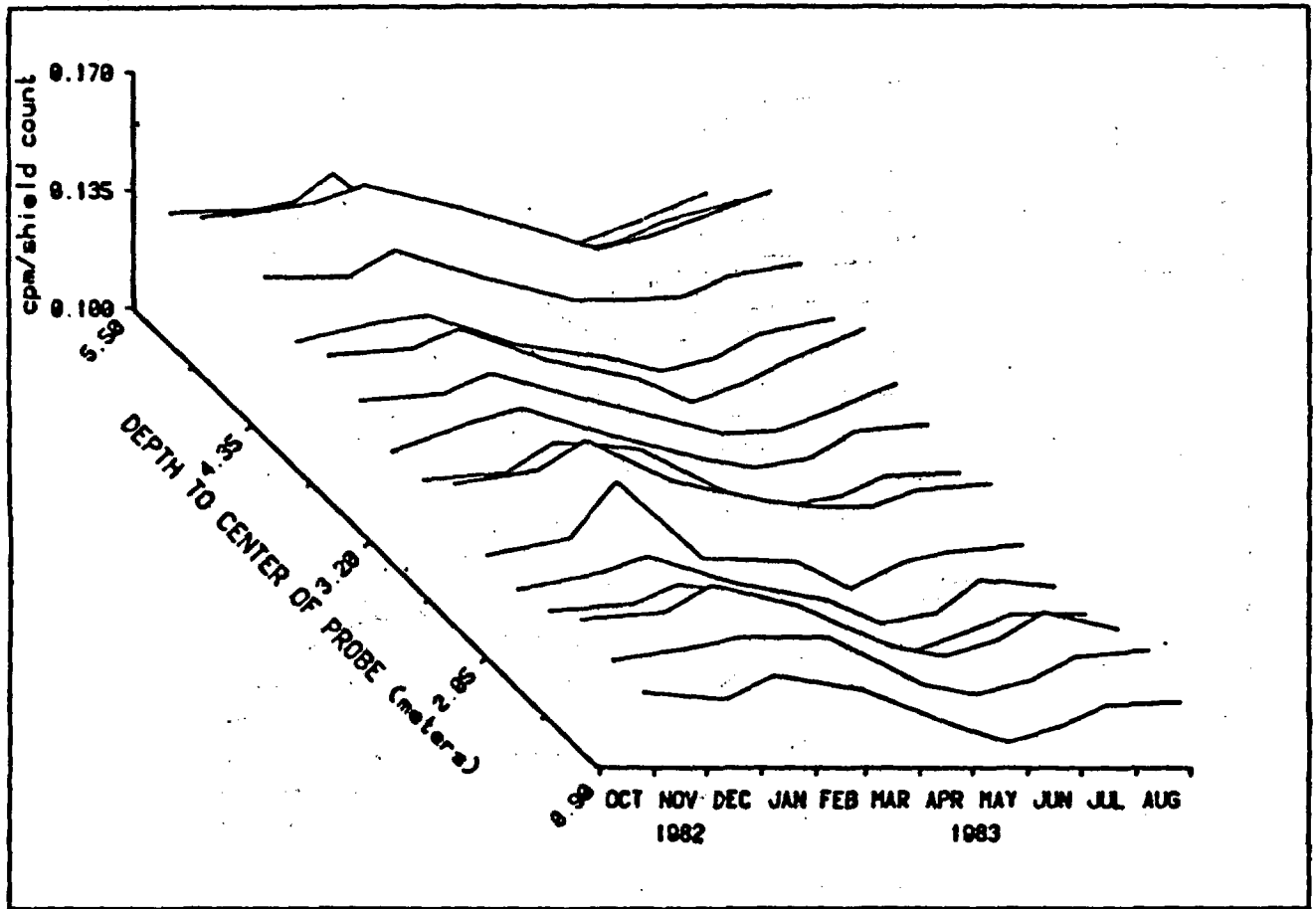


Figure 3.8 Variation in the normalized neutron data with time and space in Borehole 5.2 at the Santo Nino field site.

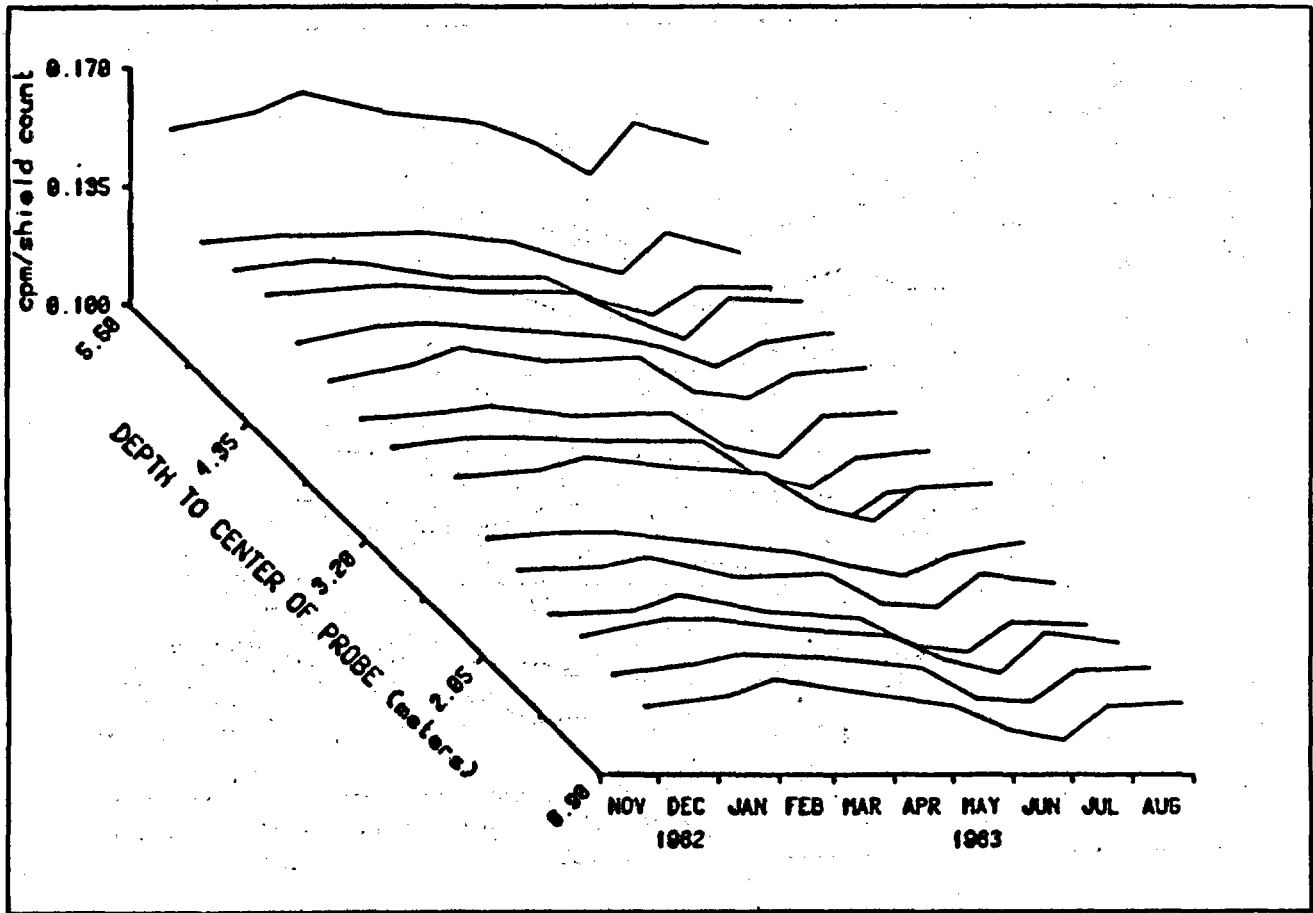


Figure 3.9 Variation in the normalized neutron data with time and space in Borehole 5.8 at the Santo Nino field site.

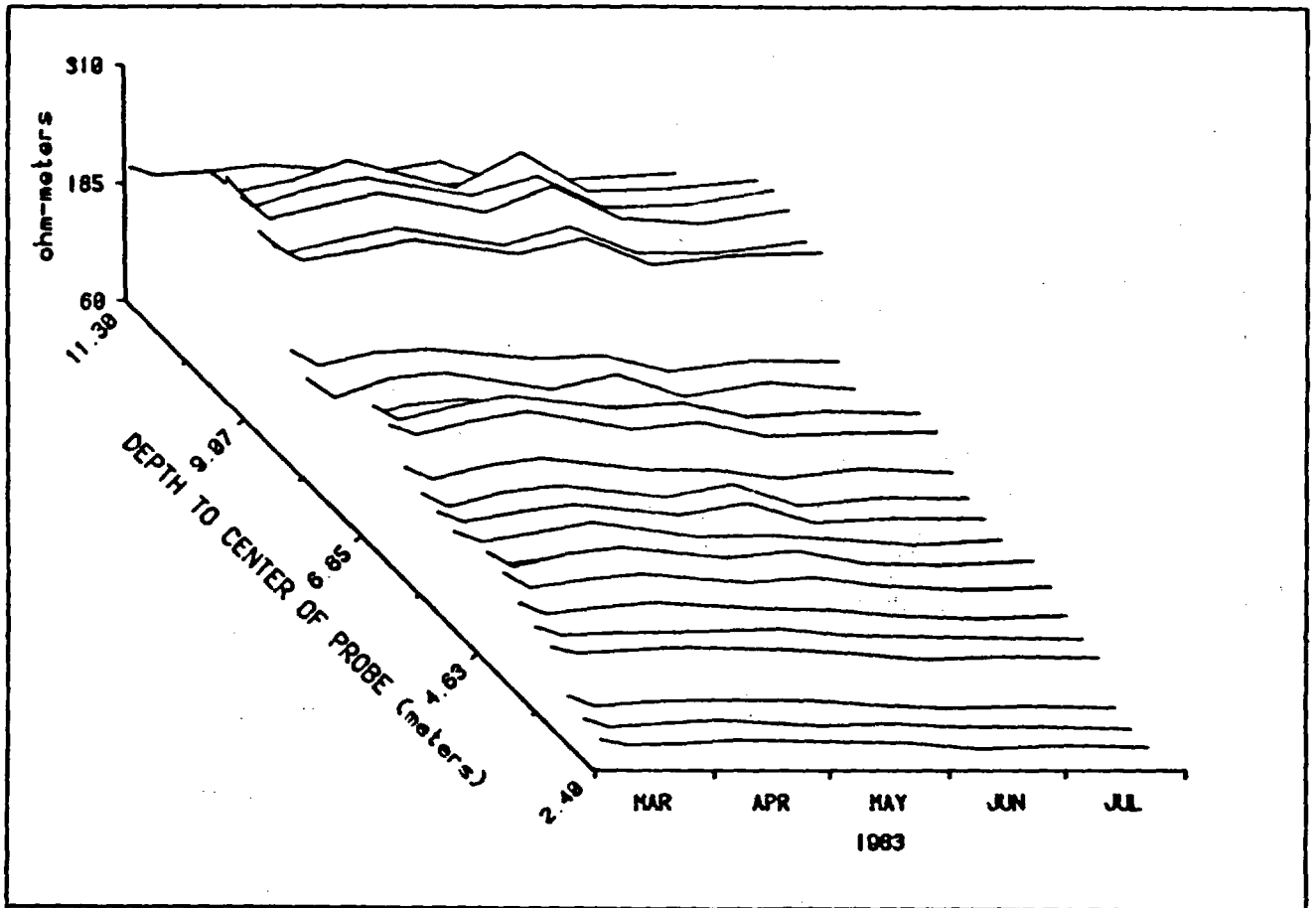


Figure 3.10 Variation in the resistivity data with time and space in upper borehole at the Magma field site.

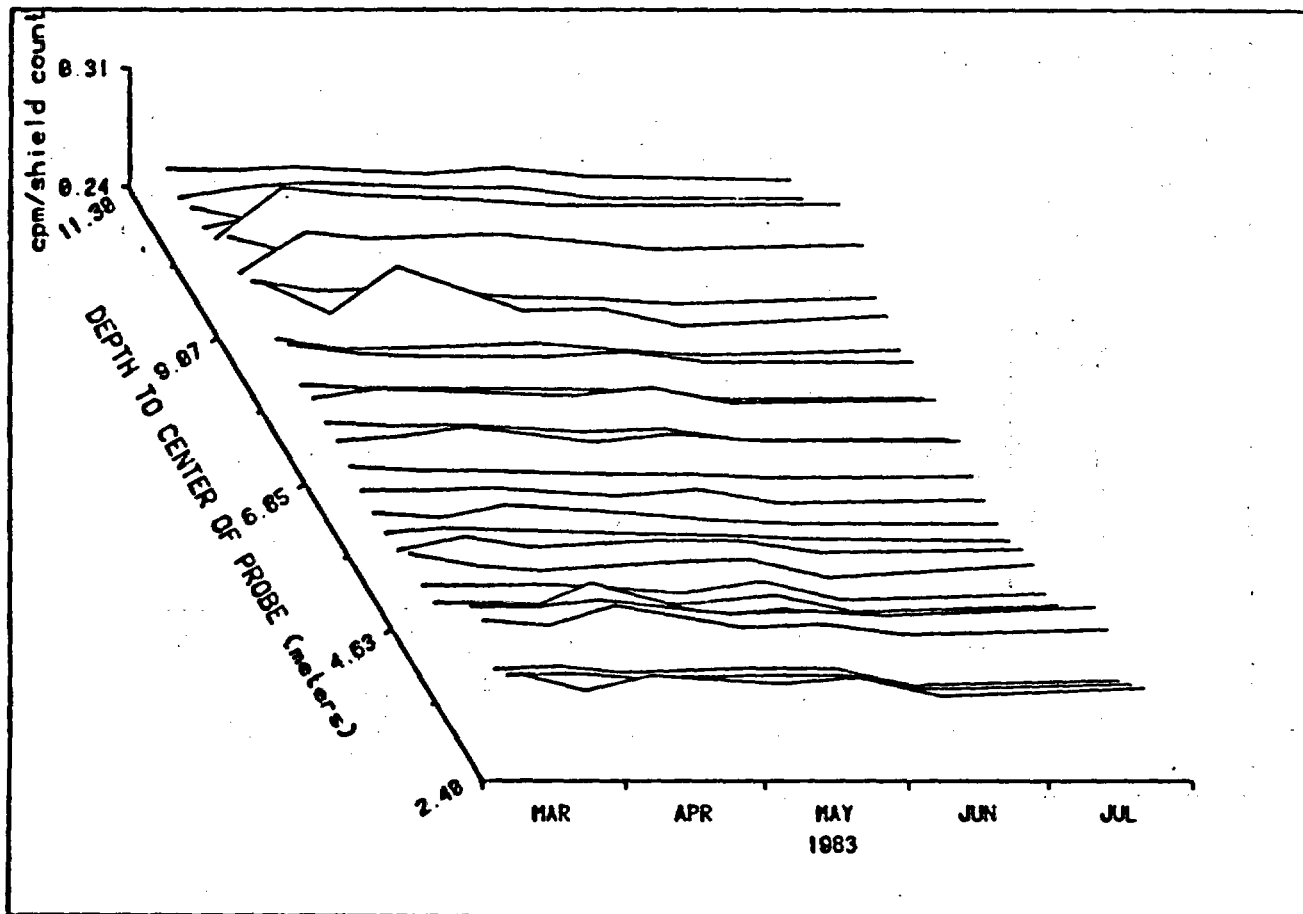


Figure 3.11 Variation in the normalized neutron data with time and space in the upper borehole at the Magma field site.

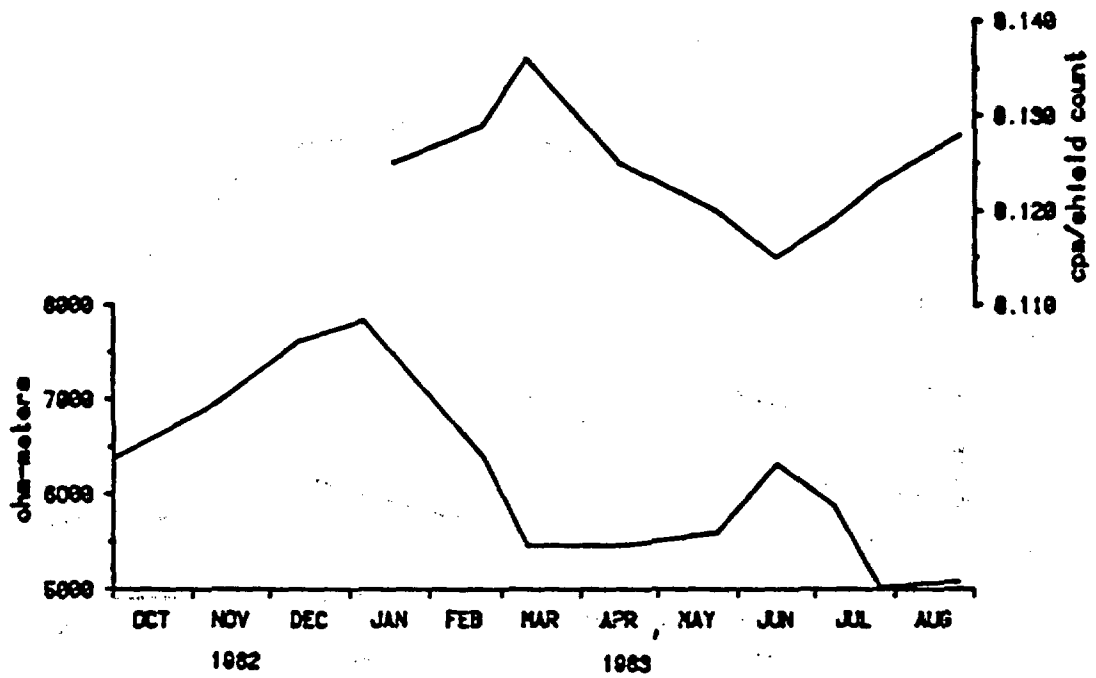


Figure 3.12 Resistivity (lower) profile and normalized neutron (upper) profile for Borehole 5.2 at the Santo Nino field site.

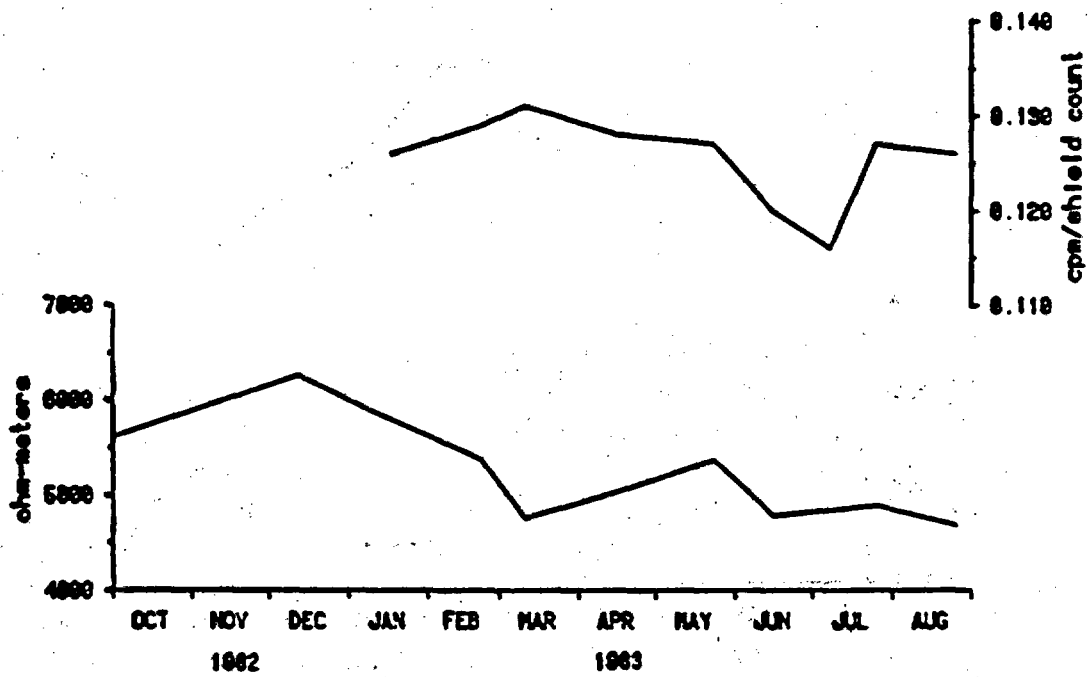


Figure 3.13 Resistivity (lower) profile and normalized neutron (upper) profile for Borehole 5.8 at the Santo Nino field site.

March and April. A possible explanation for this is the standing water in the adit (Figure 3.14) affected the resistivity measurements but not the neutron measurements. Similar trends for Borehole 5.8 at the Santo Nino field site are shown in Figure 3.13. The June resistivity data point in this figure may be in error. On this data, the wire inside a current electrode broke while the hole was being logged. Attempts to remedy the problem in the field were unsuccessful.

Besides responding similarly in time, by overlaying these profiles with the borehole water-level profile presented in Figure 3.15, it appears both methods respond to the same mechanism which controls the water level in Borehole 6.0a. In particular, the borehole water-level profile correlates remarkably well with the inverted resistivity profiles.

The similarities between the resistivity and the normalized neutron profiles for Boreholes 5.2 and 5.8, and the positive correlation between these profiles and the standing water-level profile for the Borehole 6.0a suggest that the temporal variations in the resistivity and neutron measurements recorded changes in the water content of the quartz monzonite.

The resistivity and normalized neutron profiles from the Magma borehole do not show these consistent trends. Although the resistivity profiles at 5.2 and 11.3 m are similar (Figure 3.16 and 3.17), they are not mirrored by the normalized neutron profiles. For the most part, the profiles are smooth, indicating that the water content of the rock surrounding the Magma borehole did not change significantly during the span of the survey.

In summary, two geophysical methods have been evaluated as to their usefulness in measuring the water content of unsaturated, fractured, low-porosity, crystalline rocks. The conclusion is that downhole resistivity and neutron-moisture measurement techniques are able to detect qualitative changes in the water content of these rocks. The evidence supporting this conclusion is that each method responded similarly in time, and precipitation and borehole water-level data corroborated these trends at the Santo Nino field site. Furthermore, the time lag between the surface precipitation data and the borehole data appears to be eight weeks during the dry months and less as the overburden becomes saturated. The distance between the boreholes and the surface is six meters. Similar trends were not observed at the Magma field site, where the distance between the borehole and the surface is 80 m.

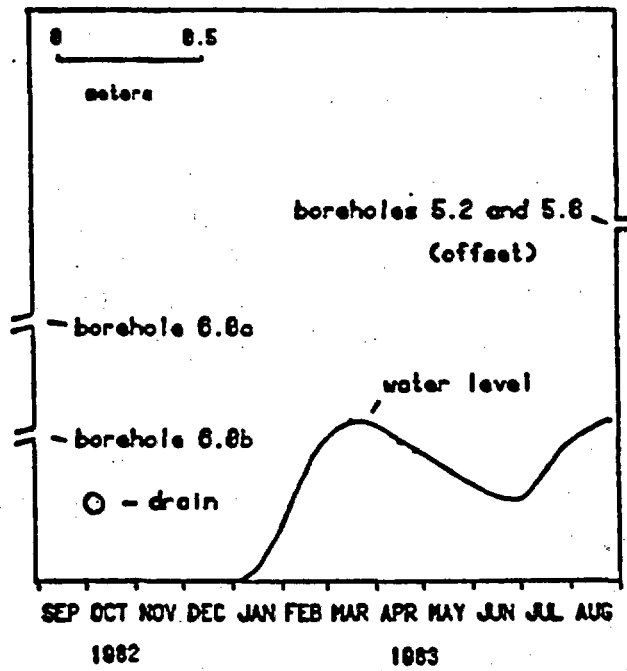


Figure 3.14 Cross-section perpendicular to the Santo Nino mine adit showing the location of boreholes and ponded water levels.

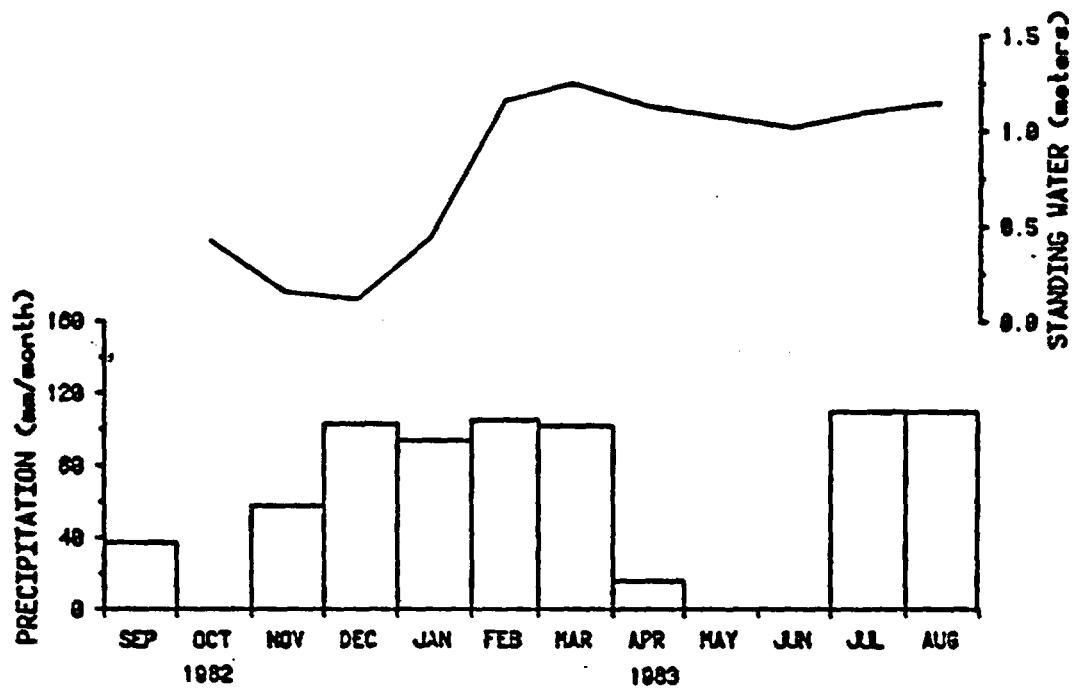


Figure 3.15 Relative water levels in Borehole 6.0a.

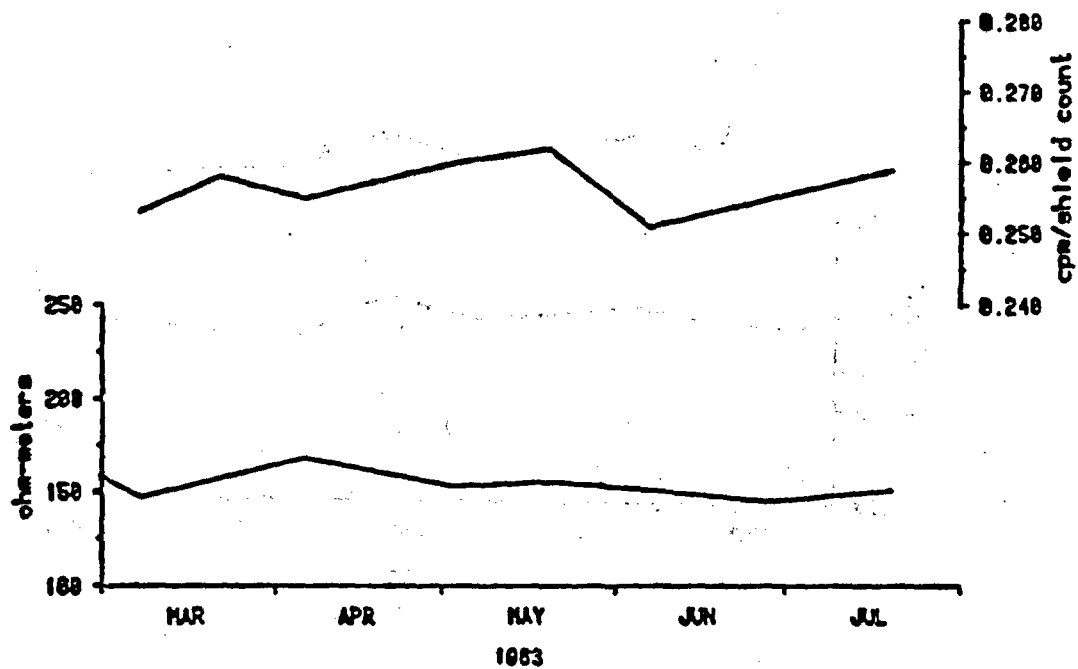


Figure 3.16 Resistivity (lower) profile and normalized neutron (upper) profile at a depth of 5.2 meters in the top borehole at the Magma field site.

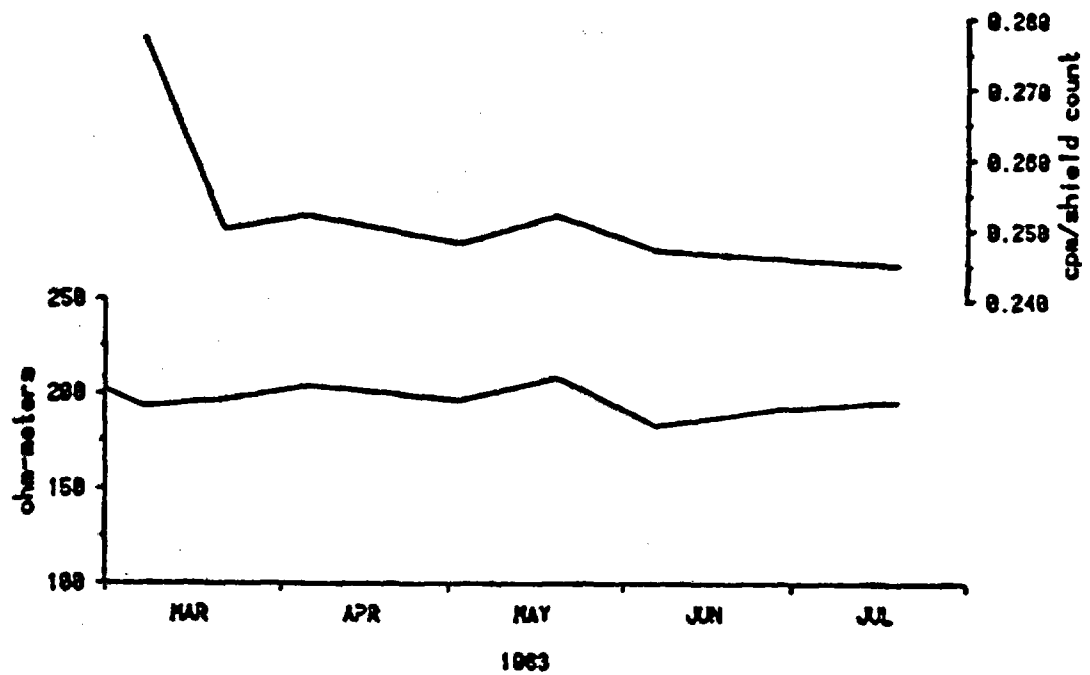


Figure 3.17 Resistivity (lower) profile and normalized neutron (upper) profile at a depth of 11.3 meters in the top borehole at the Magma field site.

How to equate the volume investigated by the resistivity and neutron methods is the most difficult problem in designing a logging program. Decreasing the spacing between the resistivity electrodes increases the effect of fractures, and increasing the spacing between the source and detector in the neutron probe necessitates preliminary calibration before an increasing or decreasing count can be related to an increasing or decreasing water content. A solution to this problem would make these tools more useful in calibrating each other. The current status is that both methods are able to detect qualitative changes in the water content of crystalline rocks.

### 3.3 Rock Matrix Hydraulic Conductivity

Normally, hydraulic conductivity varies spatially, making it difficult to evaluate by direct measurement in the laboratory or by using in situ methods. The unsaturated hydraulic conductivity is a function of the degree of saturation. Computational models are useful for calculating the unsaturated hydraulic conductivity from previously-measured, porous media, water-retention curves, or from moisture-release curves.

The most widely used model for obtaining the unsaturated hydraulic conductivity is that proposed by Mualem (1976), specifically the closed equation given by Van Genuchten (1978 and 1980). This model has been applied to unconsolidated porous media and shows excellent correlation between observed and calculated data (Van Genuchten, 1980; Yates, Van Genuchten and Warrick, 1984; Van Genuchten and Nielson 1985).

Peters et al. (1984) have applied the model to consolidated media (tuffaceous material) and have shown a good correlation between the moisture-release curve predicted by the model and the curve found from experimental data. On the negative side, they were unable to reproduce measured hydraulic conductivity values using calculated values, which may have been caused by the use of a psychrometer to define the moisture-retention curve for their samples. As will be shown, the psychrometer method lacks accuracy when defining the retention curve near saturation.

A pressure extractor has been used to define the moisture-release curve for sandstone and tuffaceous rock, with emphasis placed on the wet portion of the curve (i.e., from 0 to 1 bar suction). In addition, the measured unsaturated hydraulic conductivity has been compared to the computed value.

### 3.3.1 Mathematical Development

Two models were used to calculate the hydraulic conductivity,  $K$ . The first model, suggested by Burdine (1953), is given by:

$$(3.2) \quad K(S_e) = K_s S_e^2 \int_0^{S_e} h^{-2}(x) dx / \int_0^1 h^{-2}(x) dx$$

where

$K_s$  is the saturated hydraulic conductivity;

$h$  is the pressure head, a function of reduced water content ( $S_e$ );  
and

$S_e$  is given by:

$$(3.3) \quad S_e = (\theta - \theta_r) / (\theta_s - \theta_r)$$

where

$\theta$  is the water content;

$\theta_s$  is the saturated water content; and

$\theta_r$  is the residual water content.

Brooks and Corey (1964) adopted an expression relating the moisture content,  $\theta$ , to the pressure head,  $h$ . This expression yields a closed form solution to Equation (3.3):

$$(3.4) \quad \theta = \begin{cases} \theta_r + (\theta_s - \theta_r) (ah)^{-n} & ah > 1 \\ \theta_s & ah < 1 \end{cases}$$

where

$a$  and  $n$  are parameters to be determined from the observed moisture-release curve.

The solution for Equation (3.2) using Equation (3.4) is:

$$(3.5) \quad K(S_e) = K_s S_e^{(3+2/n)}$$

The second model, presented by Maulem (1976), is an improvement of the statistical model which was developed by Childs and Collis-George (1951). The Maulem equation is of the form:

$$(3.6) \quad K(S_e) = K_s S_e^{1/2} \left[ \int_0^{S_e} h^{-1}(x) dx / \int_0^1 h^{-1}(x) dx \right]^2$$

Van Genuchten (1978, 1980) introduced an empirical equation relating  $h$  to  $\theta$ ;

$$(3.7) \quad S_e = [1 + (\alpha h)^n]^{-m}$$

where

$h$  is positive; and

$\alpha$ ,  $n$ , and  $m$  are determined from the experimental moisture release curve.

Van Genuchten (1978, 1980) substituted Equation (3.7) into Equation (3.6), and gave a closed form solution for the later as:

$$(3.8) \quad K(S_e) = K_s S_e^{0.5} [1 - (1 - S_e^{1/m})^m]^2$$

where

$$m = 1 - 1/n;$$

$$0 < m < 1$$

and

$$n > 1$$

Equations (3.5) and (3.8) show that the unsaturated hydraulic conductivity for a porous media can be estimated from its moisture-retention curve and from the saturated hydraulic conductivity.

### 3.3.2 Numerical Implementation

A computer code developed by Van Genuchten (1985) is used to produce the best fit to observed data, which consists of a moisture-retention curve and the measured hydraulic conductivity. The program, referred to as RECT, uses least-squares optimization to estimate the parameters. The objective functions,  $E_1$  and  $E_2$ , that are to be minimized are of the form:

$$(3.9) \quad E_1(b) = \sum_{i=1}^N [\theta_i - \hat{\theta}_i]^2$$

where

$\theta_i$  is the observed water content;

$\hat{\theta}_i$  is the fitted water content, given by Equation (3.7); and

$N$  is the number of observations.

The second objective function is of the form:

$$(3.10) \quad E_2(b) = \sum_{i=1}^N [W_1[\theta_i - \hat{\theta}_i]]^2 + \sum_{i=N+1}^M [W_1 W_2 W_1[K_i - \hat{K}_i]]^2$$

where

$K_i$  is the observed hydraulic conductivity;

$\hat{K}_i$  is the fitted hydraulic conductivity;

$W_1$ ,  $W_1$ , and  $W_2$  are weighting factors designed to give more or less weight to a given set of the observed data; and

$M$  is the total number of the observed points of the retention and conductivity data.

### 3.3.3 Materials and Methods

Rocks from two different geologic formations in different parts of Arizona have been tested: Coconino sandstone from Strawberry, Arizona, and Apache Leap tuff from Superior, Arizona (Table 3.4). The Coconino sandstone was divided into two samples. The moisture-release curve and hydraulic conductivity were determined for the first sample, while only the moisture-release curve was determined for the second sample.

The moisture-release curve and the hydraulic conductivity were also determined for four Apache Leap tuff samples of which three samples were from the surface and one was collected from borehole cuttings at a depth of eight meters.

All samples were saturated by first placing the oven-dried sample in a vacuum desiccator and evacuating the air for at least two hours. Tap water was introduced into the desiccator until most of the sample was immersed in water. A continuous vacuum was maintained for 4 to 6 hours. The vacuum pump was turned off, but the desiccator was sealed and retained the vacuum for an additional 12 to 24 hours. The samples were then assumed to be fully saturated. Accordingly, the porosity of the sample was assumed to be equal to the saturated water content. Bulk density was calculated by dividing the oven-dry weight of the sample by its volume determined by geometrical measurement. The grain density is calculated from the following relationship:

$$(3.11) \quad \rho_s = \rho_B / (1 - \theta)$$

where

$\rho_s$  is the grain density;

$\rho_B$  is the bulk density; and

$\theta$  is the porosity.

The validity of this calculation relies on the degree of saturation that could be obtained. But it should be a good estimation if we consider the porosity is equal to the effective porosity (i.e., interconnected pores), and by considering the dead-end pores to be part of the solid portion of the rock.

-----  
 Table 3.4 Selective properties of rock samples.  
 -----

Sample No.	Rock Type	Diameter (cm)	Length (cm)	Porosity (%)	Bulk Density (gm/cm <sup>3</sup> )	Grain Density (gm/cm <sup>3</sup> )
S1	Sandstone	5.025	4.88	16.4	2.18	2.60
S2	Sandstone	5.025	1.5	17.5	2.16	2.62
T1	Tuff	7.63	4.84	18.6	2.10	2.57
T2	Tuff	7.63	4.81	17.8	2.11	2.57
T3	Tuff	7.63	4.84	17.8	2.12	2.57
T4	Tuff	6.32	5.04	17.1	2.14	2.58
T5	Tuff	6.32	5.01	17.0	2.15	2.59
TS1A	Tuff	-	-	20.6	1.92	2.42
TS1B	Tuff	-	-	19.8	1.94	2.42
TS2A	Tuff	-	-	19.5	2.03	2.52
TS2B	Tuff	-	-	19.3	2.03	2.52

-----

Three experimental techniques can be used to derive the moisture-release curve for the samples tested. They are the ceramic-plate extractor method, the Tempe pressure-cell method, and the psychrometer method. These methods are described in Appendix D.

The saturated hydraulic conductivity was measured using a modified Tempe Pressure-cell (Figures 3.18 and 3.19). The saturated sample is placed in the cell and confined by O-rings on the top and the bottom. The sides of the sample between the O-rings are sealed to prevent flow along the sides. The cell is filled with water and pressure applied. Outflow from the Tempe cell is collected in a graduated cylinder, and the time to collect 10 cm<sup>3</sup> is recorded. The saturated hydraulic conductivity,  $K_s$ , can then be calculated using a form of Darcy's Law.

The unsaturated hydraulic conductivity can be measured by the outflow method as outlined by Gardner (1956), Miller and Elrick (1958), and

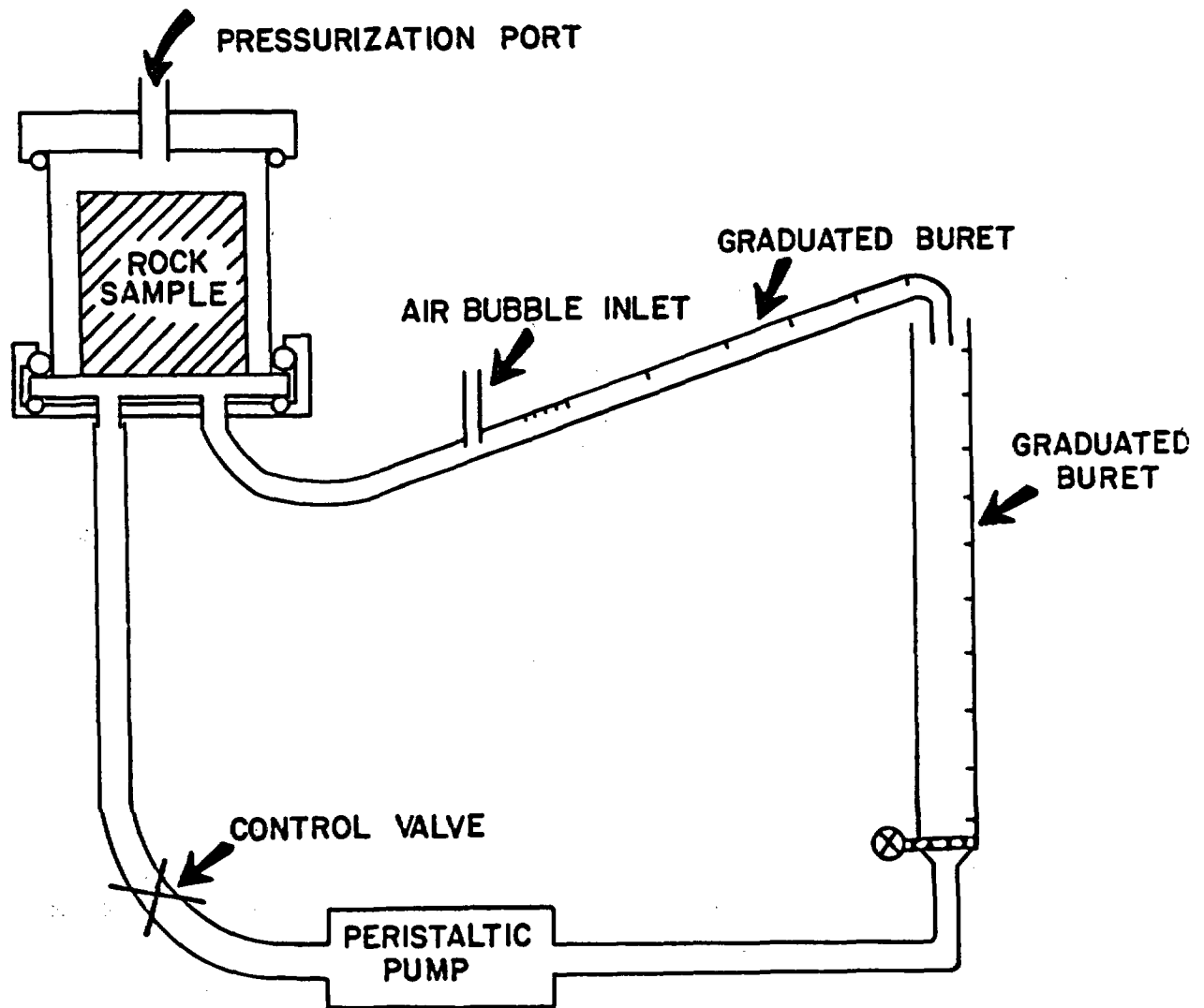


Figure 3.18 Modified Tempe pressure cell for measuring saturated conductivity,  $K_s$ . Water is forced through a saturated sample by applying air pressure. Outflow is collected and used to compute  $K_s$  by using Darcy's law. Sealant is used to prevent flow along the sides of the sample. Clay and tissue are used to improve the contact between the sample and the porous plate.

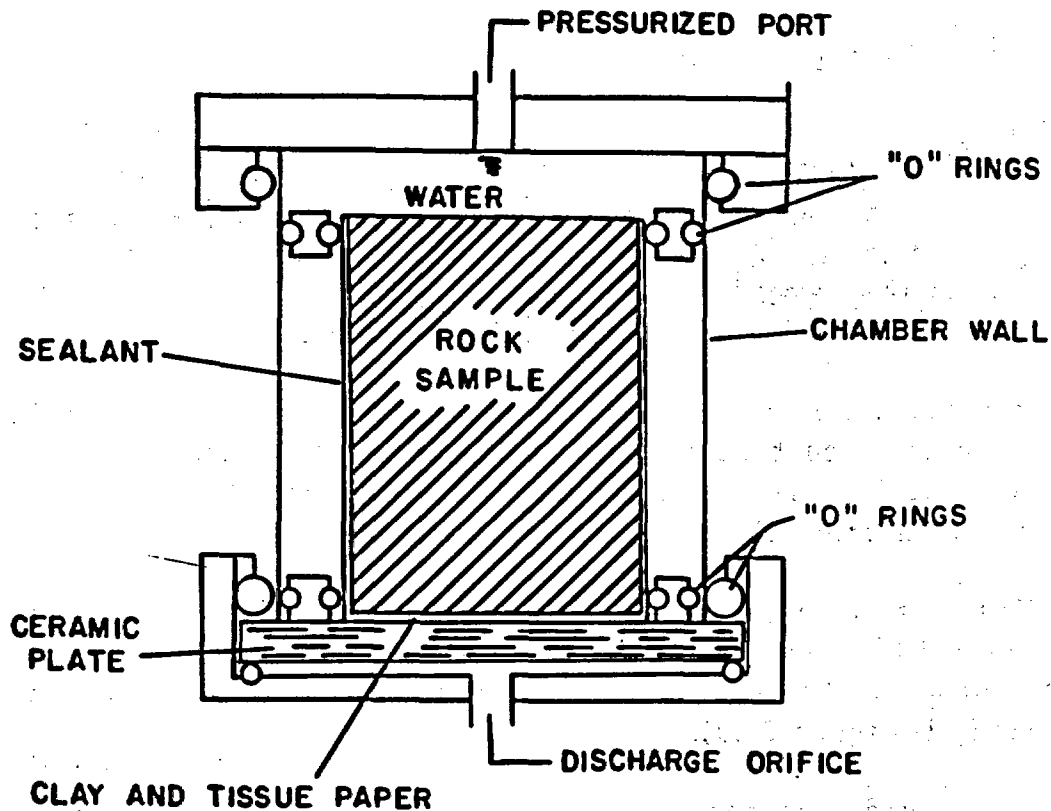


Figure 3.19 Cross-sectional view of Tempe pressure cell used to measure unsaturated hydraulic conductivity,  $K$ , by the outflow method. A saturated sample is placed in the cell and, after assuring good contact between the sample and the ceramic plate, a small increment of pressure is applied. Outflow is measured using a graduated tube after an air bubble is introduced into the system.  $K$  is calculated by plotting the flow rate against time, and then using a set of type curves.

Kunze and Kirkham (1962). The time dependence of the outflow of water from a rock sample on a porous plate in the Tempe pressure cell (see Figure 3.19) is used to determine rock diffusivity. The unsaturated hydraulic conductivity, can then be determined from the diffusivity using the equation:

$$(3.12) \quad K_s = D (\Delta\theta/\Delta P)$$

where

$$D = L^2 / (\alpha_1^2 t_{rp})$$

and

$L$  is the length of the sample;

$\alpha_1^2$  and  $t_{rp}$  are parameters determined by fitting the experimental data to a family of type curves; and

$\Delta\theta$  is the change of water content of the sample due to the application of a pressure increment  $\Delta P$ .

The outflow method assumes that the effect of gravity is negligible, and that the water content is a linear function of pressure head for the applied small pressure increments. Detailed descriptions of the method are given in original papers mentioned above.

Difficulties arise in establishing a good hydraulic contact between the sample and the ceramic plate. A thin layer of bentonite was used for that purpose; the setting being similar to that of Kunze and Kirkham (1962) (see Figure 3.19).

Another contact enhancement material examined was tissue paper. This material gave good results and did not introduce any extra measurable outflow. However, the tissue did not remain saturated for the whole range of pressure used, and weak contact resulted when high pressure was applied (0.6 bar of water or more). The best results were obtained when the tissue and very thin layer of clay were used together.

### 3.3.4 Results and Discussion

Table 3.5 presents estimates of parameters for the two models examined. The purpose of estimating these parameters is to assess the applicability of methods used to calculate the unsaturated hydraulic conductivity of geologic media. The parameters were estimated by optimization techniques presented as Equations (3.9) and (3.10).

Table 3.5 Computed parameters of rock samples using three models.

Sample No.	e Model <sup>1</sup>			e and K Model <sup>2</sup>			Brooks and Corey <sup>3</sup>		
	$\theta_r$	$\alpha$	n	$\theta_r$	$\alpha$	n	$\theta_r$	$\alpha$	n
S1	.0000	.0078	2.09	.00	.0074	2.19	.026	.0108	1.346
S2	.0325	.0034	4.92		-		.031	.0044	2.638
T1	.1092	.0010	2.232	.00	.0018	1.15	.11	.0019	1.005
T2	.0	.0017	1.314	.05	.0019	1.32	.13	.0058	1.005
T3	.0	.0007	1.426	.00	.0060	1.09	.10	.0018	1.005
T4	.0	.0133	1.084	.00	.0046	1.07		-	
TS1A	.0127	.0002	1.775		-			-	
TS1B	.0136	.0002	1.957		-			-	
TS2A	.0001	.0003	1.496		-			-	
TS2B	.0125	.0002	1.730		-			-	

<sup>1</sup> Only moisture content data optimized.

<sup>2</sup> Moisture content and hydraulic conductivity data optimized.

<sup>3</sup> Analytic function proposed by Brooks and Corey.

To verify the computational results, experimental data obtained by the outflow method were compared to the analytic expressions. Before making this comparison, however, a brief discussion of data acquisition limitations is in order. Some difficulties occurred when the outflow method was applied. Establishing good contact between the rock sample and the ceramic plate is one of the problems with this method. An uncertain contact could be overcome by using a relatively large sample and making measurements when the sample is at least 50% saturated.

Other difficulties are related to the equipment used, (i.e., the Tempe pressure cell set-up, Figure 3.18 or 3.19). A volumetric pressure-plate extractor (Soil Moisture Equipment Catalog No. 1250) may be a more suitable device to use because of the greater range of pressures available compared to the Tempe cell. Also, the precision in measuring the outflow rates is better. Problems arise when the moisture-release data are needed for pressure head as high as 15 bars. Without data points at the extremely dry end of the release curve, it is difficult to conclude which of the parameter optimization schemes is more suitable.

The models used to calculate unsaturated hydraulic conductivity were derived mainly for homogeneous, isotropic media, which is rarely encountered in the field. Most consolidated porous media are nonisotropic because the mechanics of sedimentation result in vertical compression of the medium. The assumption of isotropy for small samples, such as the samples used in this study is considered appropriate and accurate (Wyllie and Spangler, 1952). Even though it is generally assumed for this study that the rock being studied is homogeneous and isotropic, some layering of the sandstone samples was noted.

The results of tests of sandstone samples (see Figures 3.20 to 3.23) are in excellent agreement between the computational model and observed data. However, such results would not be expected when evaluating the unsaturated hydraulic conductivity for a large formation, due to heterogeneities and anisotropies.

The parameters used in the solution of the unsaturated hydraulic conductivity equations consist of a residual and saturated water-content parameters, three calibration parameters ( $\alpha$ ,  $n$ , and  $m$ ) and the saturated hydraulic conductivity. It is generally assumed that the saturated water content and the saturated hydraulic conductivity are known for the computational model. If a value of either parameter is not available, a good estimation can be obtained by the optimization scheme. In this study the saturated water content was assumed to be known because a complete saturation of the rocks' pores is probable. The measured hydraulic conductivity, however, may be incorrect due to experimental error, and so its value was obtained using the optimization scheme. Generally, the optimized value is less than the measured one. For most cases, the difference is not significant and both values fall in the same order of magnitude.

The most ambiguous parameter is the residual water content. By definition, the unsaturated hydraulic conductivity is zero when the water content is equal to the residual water content. This may be true for characterizing soil physics problems such as drainage and irrigation, but for characterizing rock of low permeability, this assumption may be inappropriate.

The present models are not able to define the unsaturated hydraulic conductivity if we assume that the water content may be less than the residual water content. It may be preferable to assume that the residual water content is always zero, and use this value as a known input parameter. In this case, the unsaturated hydraulic conductivity will be zero only if the medium is completely dry.

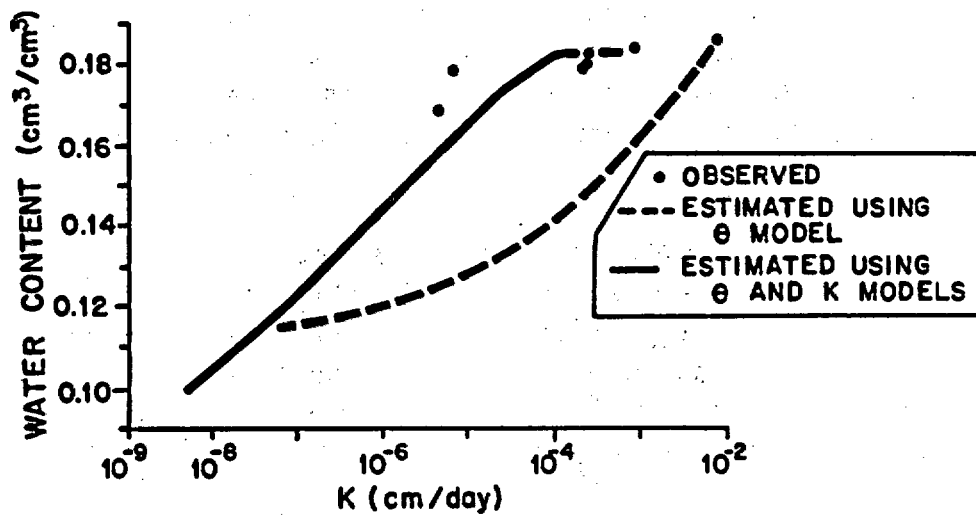
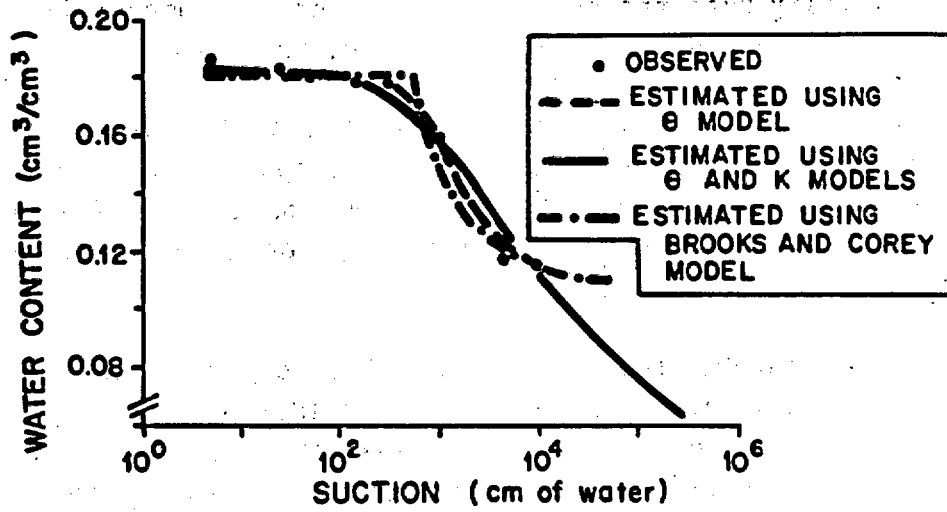


Figure 3.20 Moisture content by volume ( $\theta$ ) versus suction for the Apache Leap Tuff sample T1.

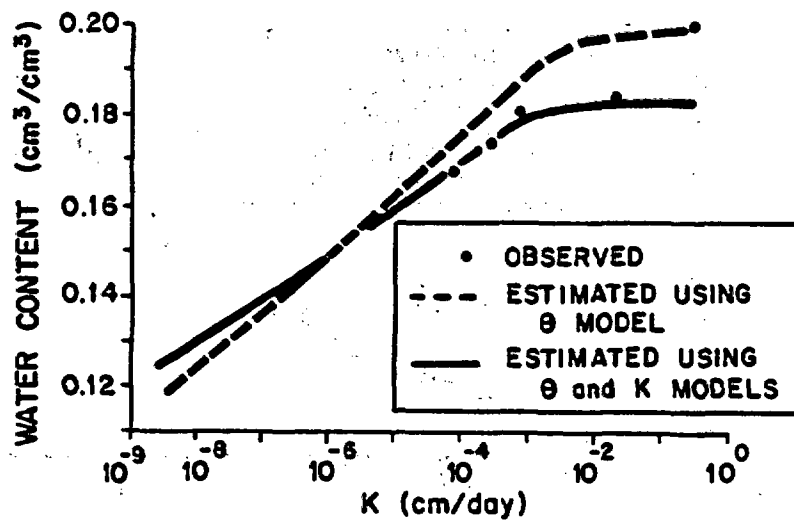
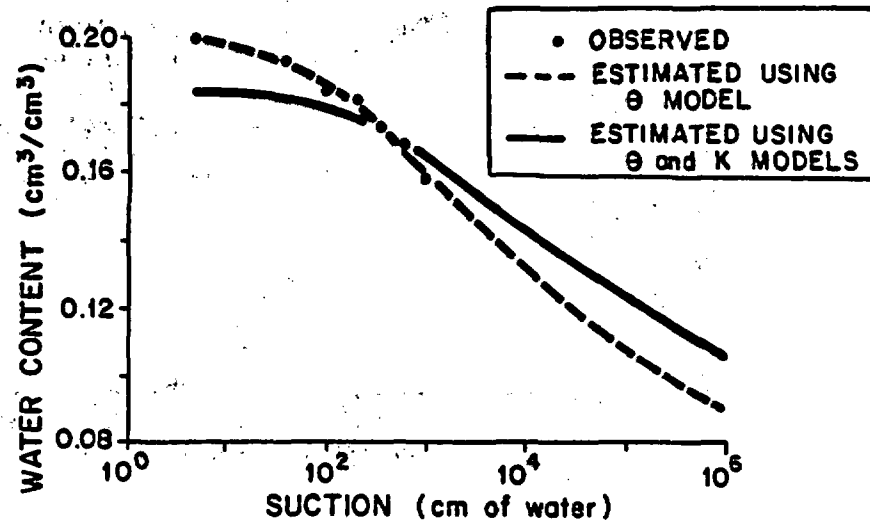


Figure 3.21 Moisture content by volume ( $\theta$ ) versus suction for the Coconino Sandstone sample T4.

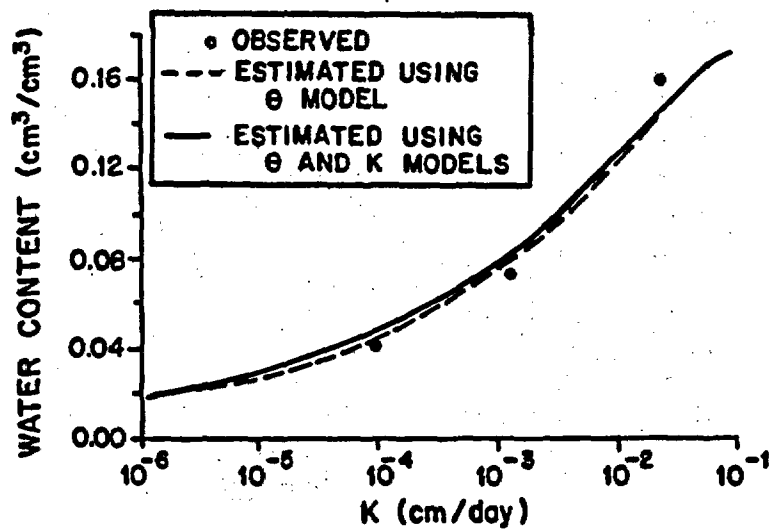
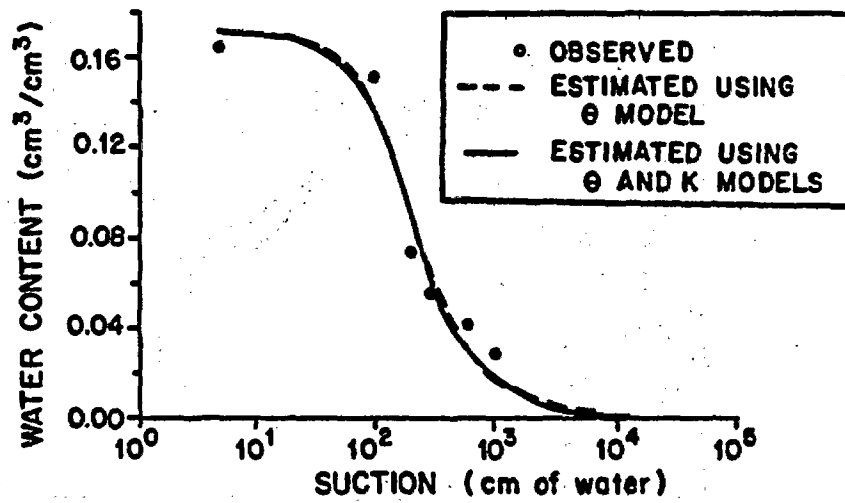


Figure 3.22 Moisture content by volume ( $\theta$ ) versus suction for the Coconino Sandstone sample S1.

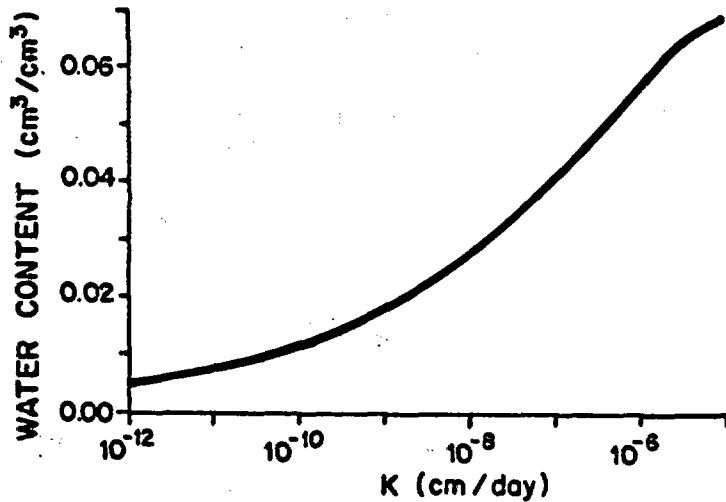
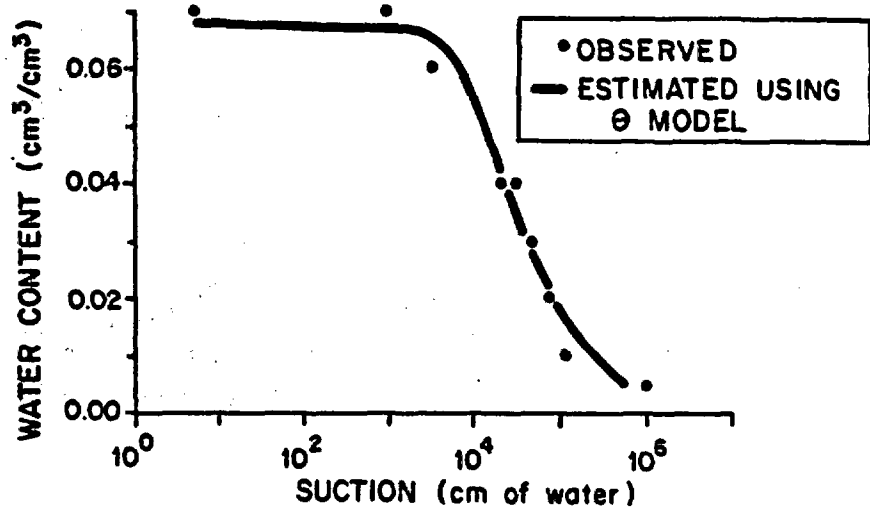


Figure 3.23 Moisture content by volume ( $\theta$ ) versus suction for the tuff sample GU4 (from Peters et al., 1984).

The reliability of the calibration parameters ( $\alpha$ ,  $m$ , and  $n$ ) depends on the precision by which the experimental data is obtained. A relationship suggested by Van Genuchten (1980) provides a good approximation of the unsaturated hydraulic conductivity and reduces the number of calibration parameters by one.

### 3.4 Fracture Permeability Using a Heat-Pulse Flowmeter

The heat-pulse flowmeter is an experimental instrument designed to detect low velocity flows by measuring the travel time of an induced heat pulse. By observing changes in the vertical flow in a borehole it is possible to locate zones of outflow which can be correlated with fractures observed in the drill core. The relative permeabilities of the fractures can be compared by observing the amount of outflow occurring. This information is useful in determining suitable areas for future testing using tracers.

Tracer tests are being used extensively in the analysis of flow in fractured crystalline rock. One of problems associated with this type of testing is the location of permeable zones in a borehole suitable for conducting tracer tests. Drill cores reveal the location and condition of fractures intersected by the borehole and the degree of weathering and mineralization observed along a fracture surface allows some speculation about the fracture permeability.

A borehole flowmeter survey was conducted at the Apache Leap site to locate permeable zones and determine their relative conductivities. By measuring changes in the vertical flow in a borehole, it is possible to identify permeable fractures and observe the amount of flow leaving the borehole. Flow velocities encountered at the Apache Leap site were far below the lower detection limit of conventional flowmeters that measure impeller rate of spin. An experimental heat-pulse flowmeter was used successfully to survey the low velocity flows at the Apache Leap site.

#### 3.4.1 Operation

The flowmeter operates by measuring the travel time of an induced heat pulse that is advected by the borehole flow. The flow sensor consists of a heater grid mounted between two thermistors inside a flow tube (Figure 3.24). A measurement is taken by sending a electric pulse through the heater grid, heating a sheet of water around it. The heated water is advected past one of the two thermistors depending on the direction of flow. The thermistors are wired in a bridge (Figure 3.25)

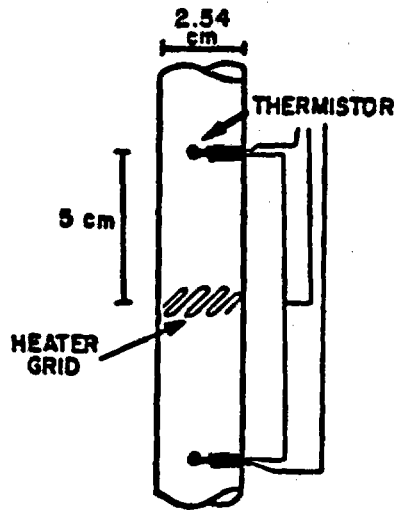


Figure 3.24 View of heater grid and thermistor inside flow tube of heat-pulse flowmeter.

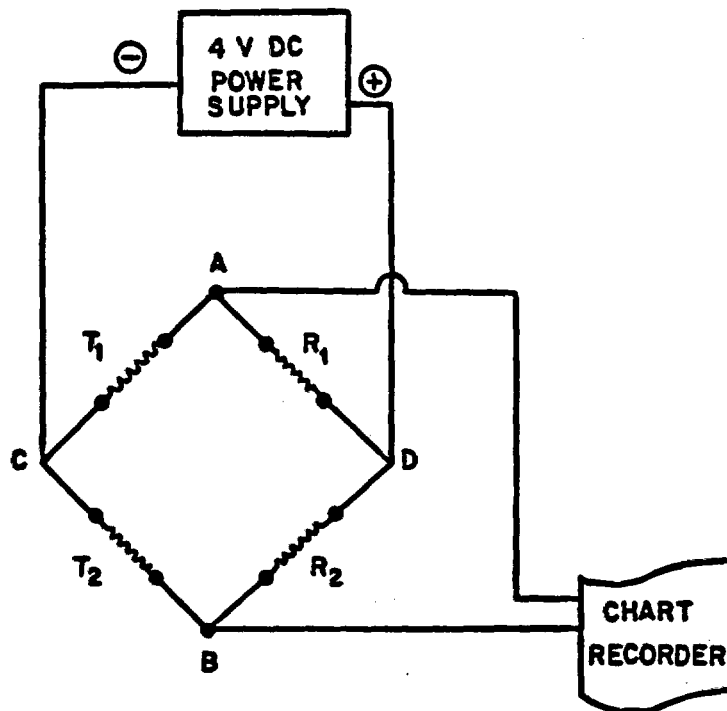


Figure 3.25 Diagram of electronic circuit used for recording temperature pulse in flowmeter.

such that a signal is produced when one thermistor experiences a temperature change not occurring at the other.

The response curve on a chart recorder (Figure 3.26) indicates direction of flow and the temporary thermal imbalance of the two thermistors. The elapsed time between the electrical pulse and the peak of the response curve is compared to a calibration graph (Figure 3.27) to determine the flow rate in the borehole.

The concept of a thermal flowmeter was first developed in 1955 by H.E. Skibitzke of the U.S. Geological Survey (Chapman and Robinson, 1962). Skibitzke used a continuous heat source mounted between two thermistors in a flow tube. The measured difference in temperature is a function of the water velocity. The instrument had a lower limit of 0.5 cm/s.

Flowmeter research is currently being conducted by A.E. Hess and F.L. Paillet of the U.S. Geological Survey, Water Resource Division. Hess (1982) has modified a heat-pulse flowmeter manufactured by Wuidart Engineering and reports an ability to measure flows down to 0.1 cm/s. Paillet has field tested the instrument and increased the sensitivity of the flowmeter by constructing a rubber skirt around the flowmeter that serves to concentrate the flow through the instrument. Laboratory calibrations using a total seal around the flowmeter increased the sensitivity for detecting flows down to 20 cm<sup>3</sup>/min. However, Paillet has noted that under field conditions, a significant amount of flow may bypass the instrument producing error in the measurements (unpublished).

Paillet's work demonstrated the need for an effective way of sealing the borehole around the flowmeter. This led to the development of the packer sealed heat-pulse flowmeter used at the Apache Leap site. The packer increased the low range sensitivity and assured a reliable seal around the instrument.

The flow-sensor tube is mounted inside a packer assembly that seals the space around the flowmeter when inflated (Figure 3.28), forcing all flow to pass through the flowtube. The flow remains constant, while the average velocity is inversely proportional to the cross-sectional area. When flow in the 10.16 cm diameter boreholes at the Apache Leap site is forced through the 2.54 cm flowtube of the instrument, the velocity in the flowtube is 16 times that of the borehole velocity. This relationship allows the measurement of very low velocity flows.

The flowmeter was calibrated by comparing known flow rates in a test column to inverse response time (Figure 3.27), i.e., the time from the

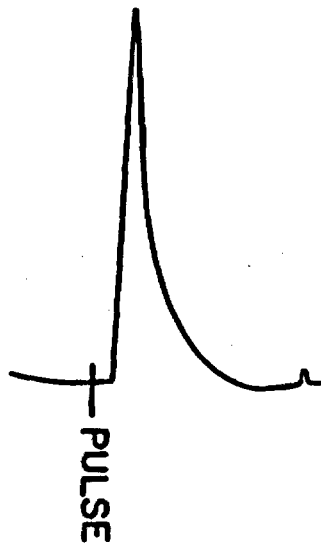


Figure 3.26 Temperature response curve showing electric pulse to heater and peak temperature difference between the two thermistors.

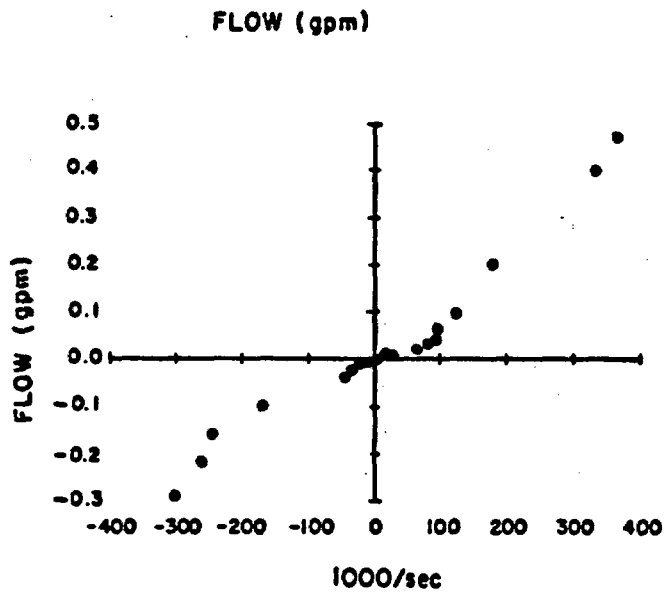


Figure 3.27 Calibration curve for the heat-pulse flowmeter.

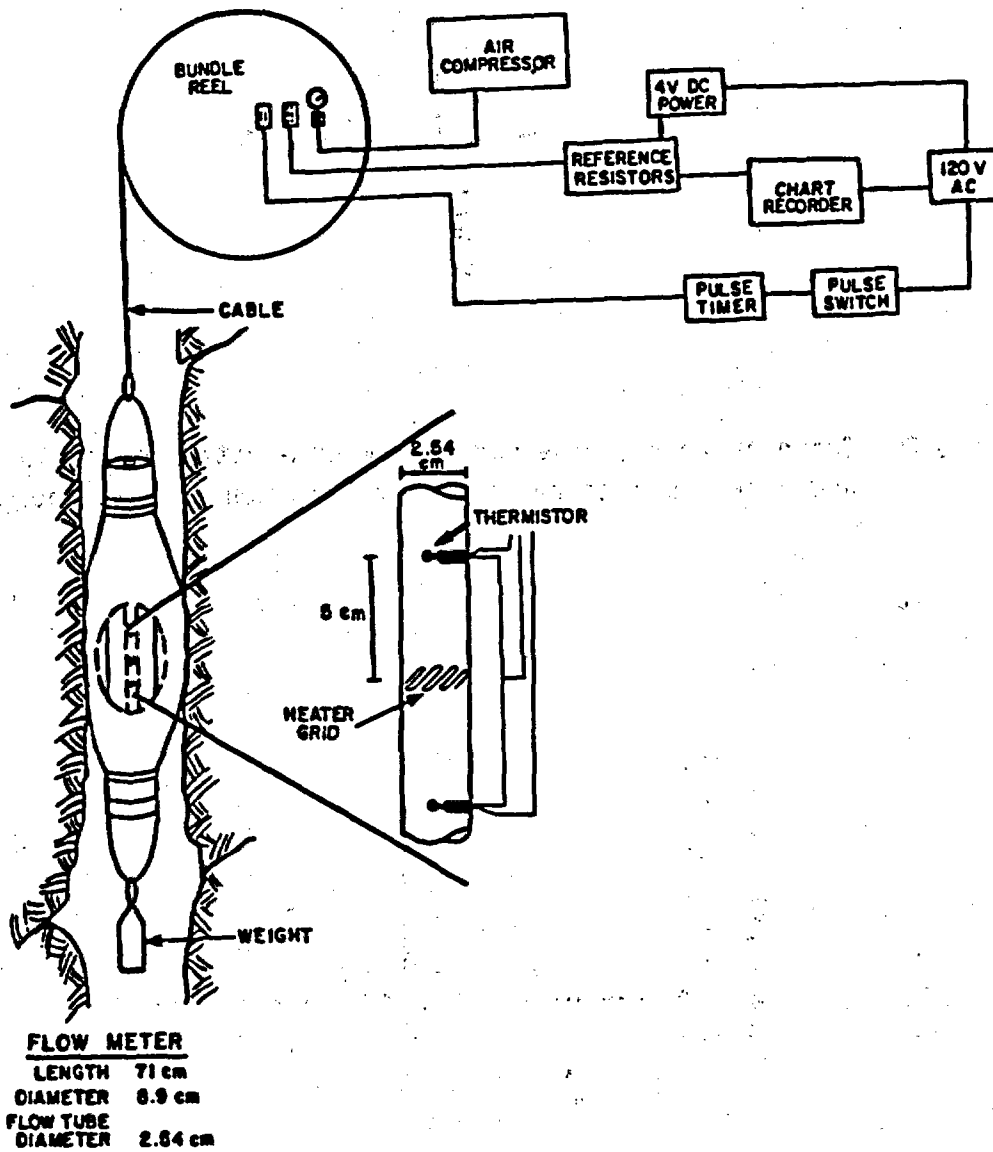


Figure 3.28 View of heat-pulse flowmeter and packer assembly. Wall roughness exaggerated.

electrical pulse until the peak temperature response. Inverse time was chosen because it linearizes and spreads the data over the optimum range of the instrument.

The effect of convection caused by the tendency of the heated water to rise, produces a non linear response for low flow rates. It also results in different-shaped curves for upflow and downflow. The effective measurement range of the packer sealed heat-pulse flowmeter is between  $40 \text{ cm}^3/\text{min}$  (0.01 gpm) and  $2000 \text{ cm}^3/\text{min}$  (0.5 gpm). At the Apache Leap site it is possible to measure borehole velocities between 0.008 cm/s and 0.4 cm/s.

### 3.4.2 Field Investigation

The Apache Leap site is located near Superior, Arizona. Three boreholes were drilled at a  $45^\circ$  angle in an attempt to intersect vertical fractures in the welded tuff. The boreholes are 10 m apart and penetrate the fractured tuff to a maximum depth of 46 m. Figure 3.29 shows the arrangement of the boreholes and the distribution of the fractures observed in the drill core.

The purpose of the flowmeter survey at the Apache Leap site was to locate and measure flow out of the boreholes. Because the boreholes are in the unsaturated zone, it was necessary to fill them with water to the top of the casing, 30 cm above the ground surface. Borehole X-3 was surveyed in one afternoon and boreholes X-2 and X-3 were surveyed the following day.

In each case the borehole was filled to the top of the casing with water and a constant head was maintained. A period of one hour was allowed for the flow rate to reach equilibrium before measurements began. The total flowrate in the borehole was monitored periodically by stopping the flow from the water source and timing the rate of fall of the water level in the casing. In each borehole, the total flow reached equilibrium within 15 minutes of filling the borehole and the flow rate remained relatively constant throughout the test. Measurements taken at the same location over a period of time also support the conclusion that the flow field near the borehole was nearly steady.

The boreholes were surveyed downhole beginning at the top just below the casing. In some cases, measurements were taken on the return trip uphole. The instrument was moved carefully in the hole to avoid altering fracture permeabilities. Measurement positions were chosen by examining the drill core logs. Measurements were taken above and below

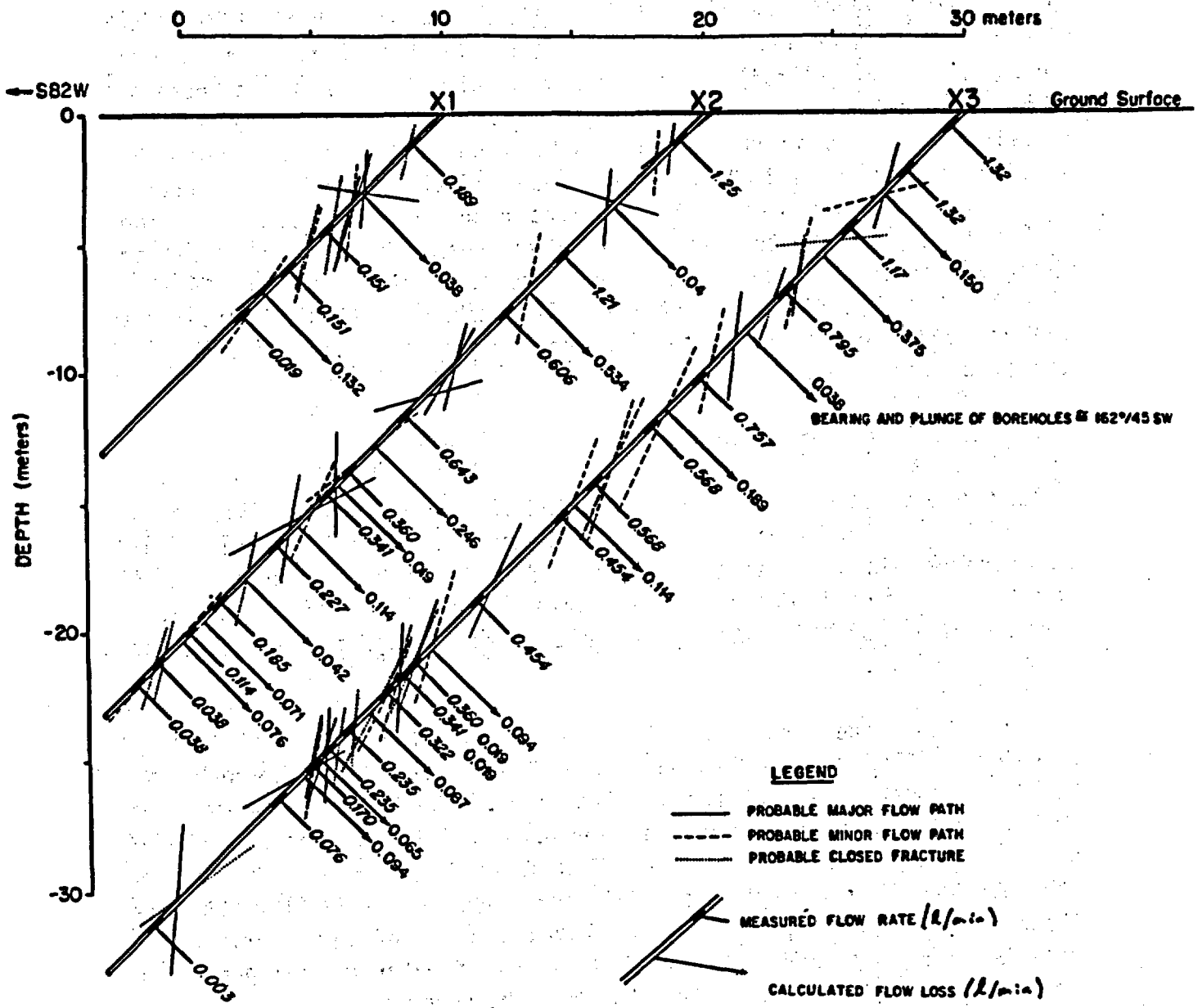


Figure 3.29 Measured flow rates and calculated flow losses for Boreholes X-1, X-2, and X-3 at the Apache Leap site.

all major fracture zones to determine if there was a change in flow. If a flow change was detected, the borehole was surveyed at closer intervals until the fracture conducting the flow was located.

Measurements were taken with the flowmeter by the following procedure. The instrument was lowered to the desired depth in the borehole and positioned to avoid blocking fractures with the packer if possible. The 60-cm packer was inflated with nitrogen or compressed air until the instrument was immobilized in the borehole. This required a pressure of about  $0.7 \text{ kg/cm}^2$  (10 psi) above the hydrostatic pressure at the depth of the instrument. Flow was measured by closing the switch to the timer causing a 0.05 second pulse of 120 volt AC current to pass through the heater coil (Figure 3.28). The movement of the heated water past a thermistor was displayed on the chart recorder. The time from the electrical pulse to the peak temperature response was also recorded using a stopwatch. Measurements were repeated until consistent results over a 5-minute period were obtained. The packer was then deflated by a release valve on the reel, the instrument moved to a new location, and the procedure repeated.

### 3.4.3 Results and Conclusions

Borehole X-3 was surveyed over a period of 5 hours, during which time 1500 liters of water was injected. A steady rate of fall of 30.5 cm/min was observed in the casing during periodic checks throughout the test. Water was observed seeping to the surface through a fracture located about 4 m west of X-3. Seepage was also noted around the concrete pad of the borehole.

The results of the flowmeter survey in X-3 (as well as for X-2 and X-1) are shown in Table 3.6 and Figure 3.30. Figure 3.29 shows the relation between flow changes and fracture locations. The highest permeability was found in a fractured zone between 6.1 m and 9.2 m. The sum of the outflows accounts for 92.9% of the flow measured just below the casing. Borehole X-2 was surveyed on the following day. A steady flow rate was observed in the casing with a water level decline of 15 cm/min. Borehole X-2 received approximately 7500 liters of water over a period of 3.5 hours. Damp soil was observed around the concrete pad of X-2.

Approximately half of the vertical flow in X-2 was seen to exit the borehole between 7.6 m and 10.7 m. There are two fractures recorded in the core log for that interval. Another interval of relatively high permeability was located between 16.2 m and 19.2 m. One fracture was observed in the drill core for that interval at 18.7 m.

-----  
**Table 3.6 Observed flow rates versus depth of observation for boreholes X-1, X-2, and X-3 at the Apache Leap site.**  
 -----

<b>Borehole X-1</b>		<b>Borehole X-2</b>		<b>Borehole X-3</b>	
<b>Downhole Flow (liters/min)</b>	<b>Depth (m)</b>	<b>Downhole Flow (liters/min)</b>	<b>Depth (m)</b>	<b>Downhole Flow (liters/min)</b>	<b>Depth (m)</b>
0.189	1.52	1.136	1.52	1.320	0.61
0.151	6.10	1.211	7.62	1.320	3.05
0.151	7.92	0.606	10.67	1.170	6.10
0.019	10.67	0.454	14.33	0.795	9.14
		0.825	14.33	0.757	13.72
		0.643	16.15	0.568	16.76
		0.360	19.20	0.568	19.81
		0.341	20.42	0.454	21.34
		0.227	23.60	0.454	25.91
		0.185	25.91	0.360	29.26
		0.114	27.43	0.341	29.87
		0.038	28.80	0.322	30.78
		0.038	29.87	0.235	32.61
				0.235	33.83
				0.170	34.90
				0.076	36.58
				0.030	43.28

-----

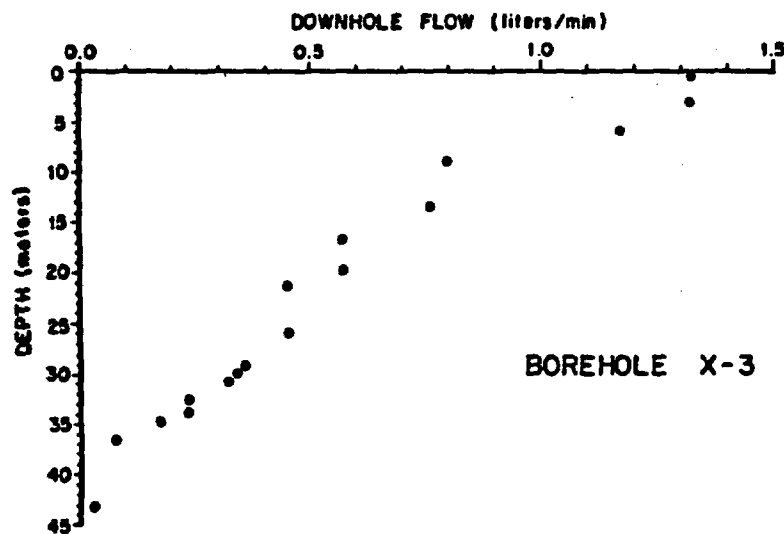
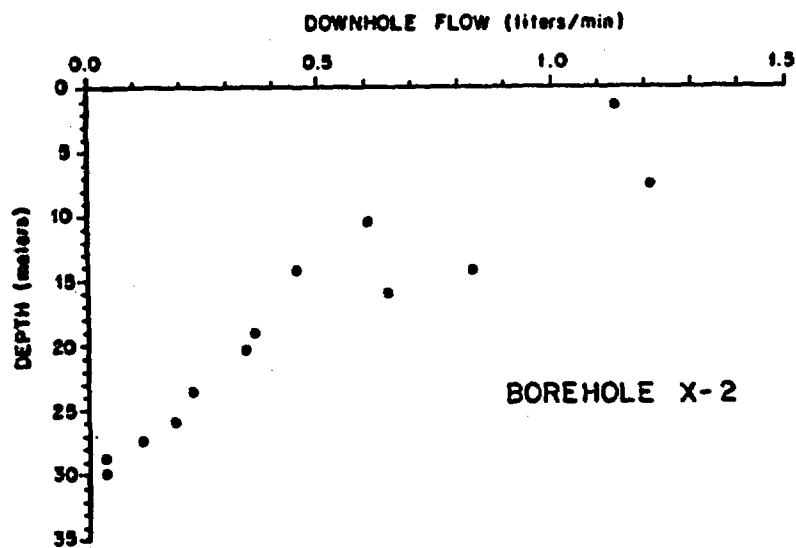
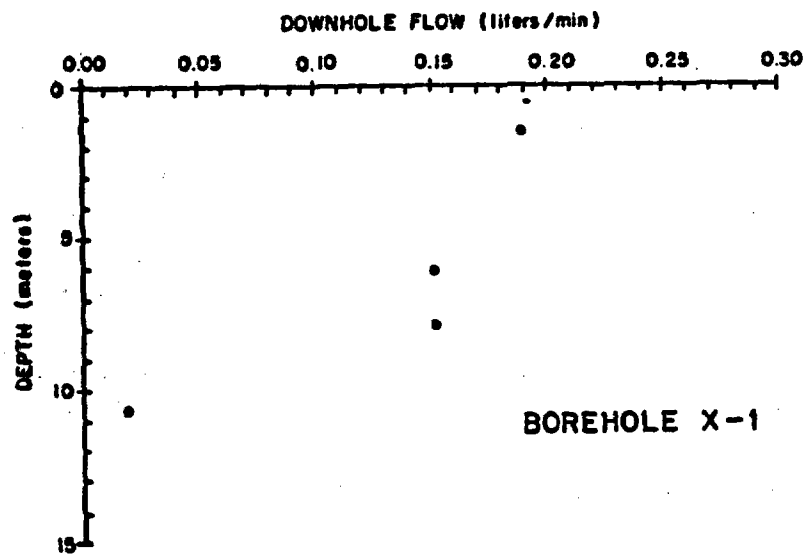


Figure 3.30 Measured downhole flows for Boreholes X-1, X-2, and X-3, plotted against vertical depth.

The rate of flow in X-1 was much lower than in the other boreholes. Water in the casing was observed to fall at the rate of 1.8 cm/min. The zone of highest discharge was between 7.9 m and 10.7 m. Two fractures were observed in the drill core for that interval. No moisture was observed at the surface around the borehole, nor in nearby fractures.

In conclusion, the flowmeter survey at the Apache Leap site successfully located permeable fractures in all three boreholes. The results of this test can be used to determine suitable zones for conducting tracer tests in future studies. Time restrictions limited this investigation to a general survey of the three boreholes. Future investigations will be required in some cases to locate the specific fractures responsible for conducting flow in an identified interval of outflow.

A discrepancy exists between the amount of flow measured in the casing by observing water-level decline and the flow rates measured in the borehole with the flowmeter. Flow rates in the casing are double those measured near the top of the borehole. The surface flow observed at X-3 and the damp soil around X-2 suggest that a significant amount of outflow may be occurring where the casing joins the borehole. Further improvements and calibration studies are needed to improve the reliability of the flowmeter at rates greater than 3 l/min (0.5 gpm). In any case, the measurements were consistent and accurately reflect the amount of flow relative to other points in the borehole.

Further analysis of the data may provide more information about the characteristics of the site. If some assumptions can be made about the hydraulic gradient around the borehole, it should be possible to calculate the apparent hydraulic conductivity of a fracture, using Darcy's law. In order to approximate the hydraulic gradient, it is necessary to estimate the borehole pressure at the fracture and the distance to the wetting front. The problem is further complicated by the fracture orientation and the effect of gravity on the shape of the flow field surrounding the borehole. A study has been proposed to model the flow field around similar boreholes in an equivalent porous medium to gain insight into the problem.

One approach to estimating the hydraulic gradient might be achieved by cross-hole testing. First, it would require locating a fracture connection between two boreholes. This could be accomplished by injecting water into a permeable interval of the borehole sealed off by packers. The flowmeter would then be used in an adjacent borehole filled with water to locate a zone of inflow. If such a connection is found, the hydraulic gradient across the fracture would be equal to the difference

in pressure between the injection borehole and the adjacent borehole divided by the estimated fracture length. The flowrate obtained by the flowmeter would then be used in Darcy's Equation to solve for the hydraulic conductivity.

The heat-pulse flowmeter has proven to be a valuable tool for conducting preliminary studies in fractured rock. It can provide information about the permeable zones in a borehole that will be useful in locating equipment in future tracer tests. Further studies hold the promise of providing additional information that will help characterize the hydraulic properties of unsaturated fractured rock.

### 3.5 Water and Air Intake on Surface-Exposed Rock Fractures

Fractures within lithic units are major contributors to fluid flow, vapor movement, and contaminant transport, particularly when matrix permeability is low. Here, the term "fracture" is defined as any discontinuity within a rock mass characterized by a small but open aperture. Fractures vary in terms of aperture, spatial extent, planar void continuity, tortuosity, and mode of occurrence. The fractures may appear in a rock mass as a result of single or multiple thermal events (i.e., heating/cooling), or geologic structural events. Distinct joint sets are commonly apparent in large rock masses and have a major influence on flow direction and velocity. Rocks of low matrix permeabilities which display high transmissivity are often characterized by spatially-dense fracture networks.

Interest in the flow behavior within unsaturated fractured rock media has been generated by the search for high-level nuclear waste repositories in unsaturated rock and by toxic waste sites located above fractured rock. These sites must provide for the long-term isolation of hazardous wastes. Hydrologic characterization of unsaturated fractured rock media is necessary because liquid phase movement may be the principal mechanism for contaminant transport.

The ability to estimate fluid intake into fractured rock media is an important part of the site characterization process because water intake at the atmosphere-earth boundary may permit or restrict the transport of contaminants at depth. The assumption that matrix flow is negligible compared to fracture flow allows observed fracture intake rates to serve as an estimate of the boundary condition of fluid flow at the atmosphere-earth interface. An accurate estimation of the potential water input to the geologic medium is a necessary precondition for the reliable simulation of subsurface unsaturated flow systems.

Little or no data have been collected from in situ experiments of water intake into individual rock fractures. Data from in situ experiments are important because previous fluid flow studies of both artificial and natural fractures have shown that the effects of applied stress on fracture conductivity are significant. Sharp (1970) examined one-dimensional flow through a single fracture in a granite porphyry under variable stress. Sharp's findings reveal that flow rate is not strictly a linear function of applied hydraulic gradient, but may vary according to inertial losses and turbulence associated with irregular boundaries along fracture walls. In a laboratory study, Schrauf and Evans (1984) show that the magnitude of fracture plane roughness and waviness is secondary to the effects of contact area between fracture surfaces for fracture apertures under 200 to 300 micrometers ( $\mu\text{m}$ ). The contact area was found to be a function of applied stress.

The fracture aperture is critical in estimating flow through fractures because of the cubic relation between aperture and flow. Iwai (1976) measured water flow rates as a function of fracture aperture in core samples of basalt, marble, and granite. Iwai's results support the cubic relation between flow rate and fracture aperture; i.e.,

$$(3.13) \quad q = - e^3 f/12 dh/dz$$

where

- q is the flow rate per unit length of fracture;
- e is the mean fracture aperture;
- dh/dz is the hydraulic gradient; and
- f is the fluidity of the liquid, computed using:

$$f = \rho g/\mu$$

where

- $\rho$  is the fluid density;
- g is the gravitational acceleration coefficient; and
- $\mu$  is the dynamic viscosity of the liquid.

The aperture calculation is useful for characterizing distributions of fracture apertures. Snow (1970) and Bianchi and Snow (1968) found that 256 fracture apertures in the Pike's Peak granite in Colorado are log-normally distributed. They measured fracture apertures by photographing fractures on outcrops treated with a fluorescent dye penetrant.

The cubic law is not free of inadequacies: fracture surface roughness,

waviness, and variable contact between fracture surfaces are arguments against the unqualified application of the cubic law when examining flow in natural fractures (Iwai, 1976; Shrauf and Evans, 1984). It is important to state, however, that preliminary models are used in this analysis because of the absence of experimental data which are required to verify a more rigorous formulation.

To investigate the adequacy of the cubic law and to demonstrate field and analytical methods for the measurement of water and air intake into individual natural fractures under ambient stress, a fractured rock infiltrometer (FRI) was designed, built and tested at a site in southern Arizona. Intake rate data collected using both water and air FRI measurements are used to calculate apparent fracture apertures. The analytic techniques used to calculate the apertures based on water and air measurements employ different governing equations and different boundary conditions. Despite the substantial differences in the two analytic techniques, results using the two methods compare favorably.

The methods presented are significant because heretofore there has not existed a technique of sufficient precision for providing estimates of potential intake of water into individual fracture segments under conditions of ambient rock stress. The field and analytic techniques described here are important for estimating water intake for a fractured rock medium of large areal extent. A statistical relation can be used as the basis of an event-based precipitation and/or streamflow model to simulate water intake into a fractured rock medium for extended simulation periods. In this manner, it is possible to vary model inputs (e.g., rainfall) for a particular fractured rock medium, allowing the prediction of intake rates for the rock medium under historical, maximal, or minimal climatic conditions.

### 3.5.1 Water Intake Method

The fractured rock infiltrometer (FRI), when used to determine water intake rates into individual fracture segments, utilizes a dual-chambered system (Figures 3.31 and 3.32) designed to minimize lateral (i.e., divergent) flow in the plane of the fracture below the interior chamber, identical to the purpose of the exterior ring of a double-ring infiltrometer. This arrangement ensures vertical flow when measuring water intake from the interior chamber.

The top of the FRI is a rectangular 6.35 mm steel plate. Welded onto the underside of the plate are two oval chambers. The two chambers are concentric to each other (one interior to the other) and both are open

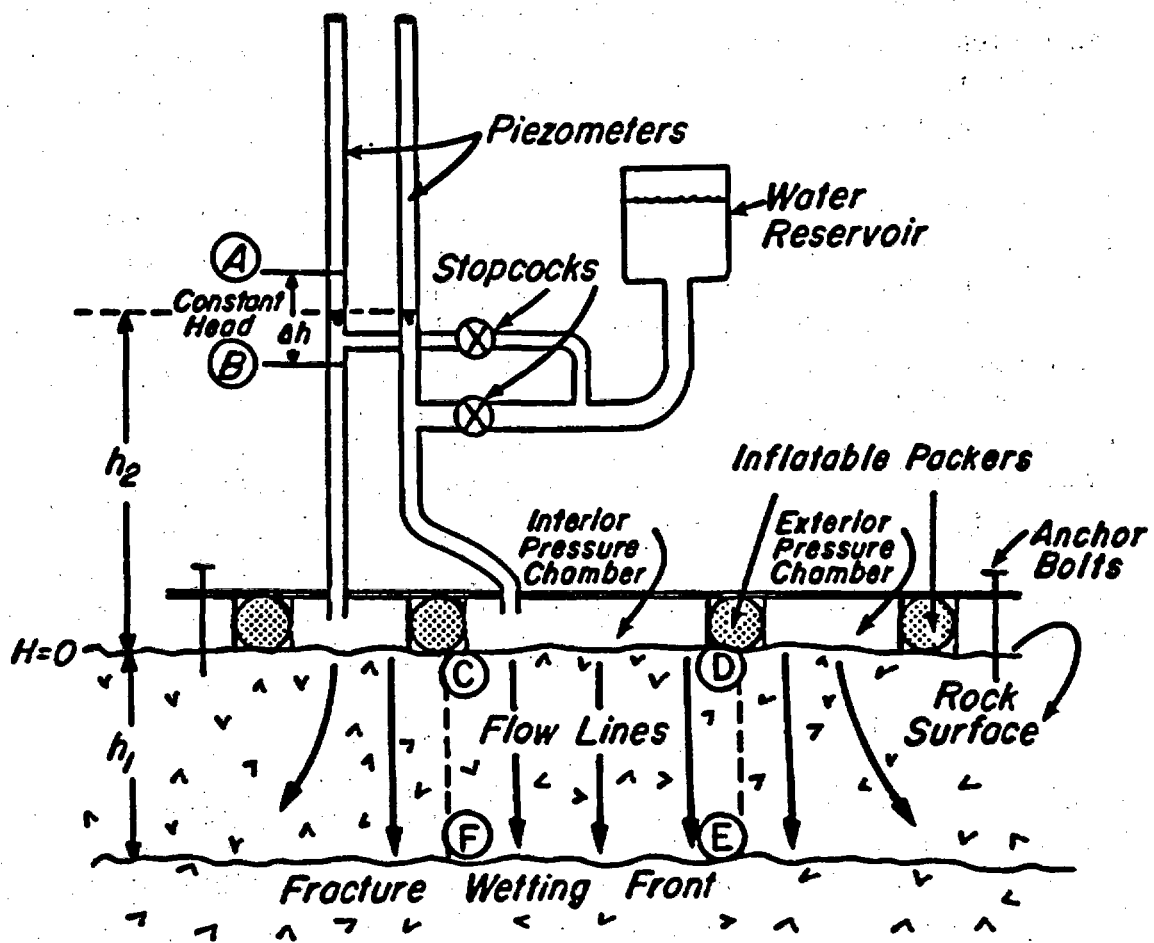


Figure 3.31 Cross-sectional diagram of the FRI, showing the apparatus as used for water intake measurements.

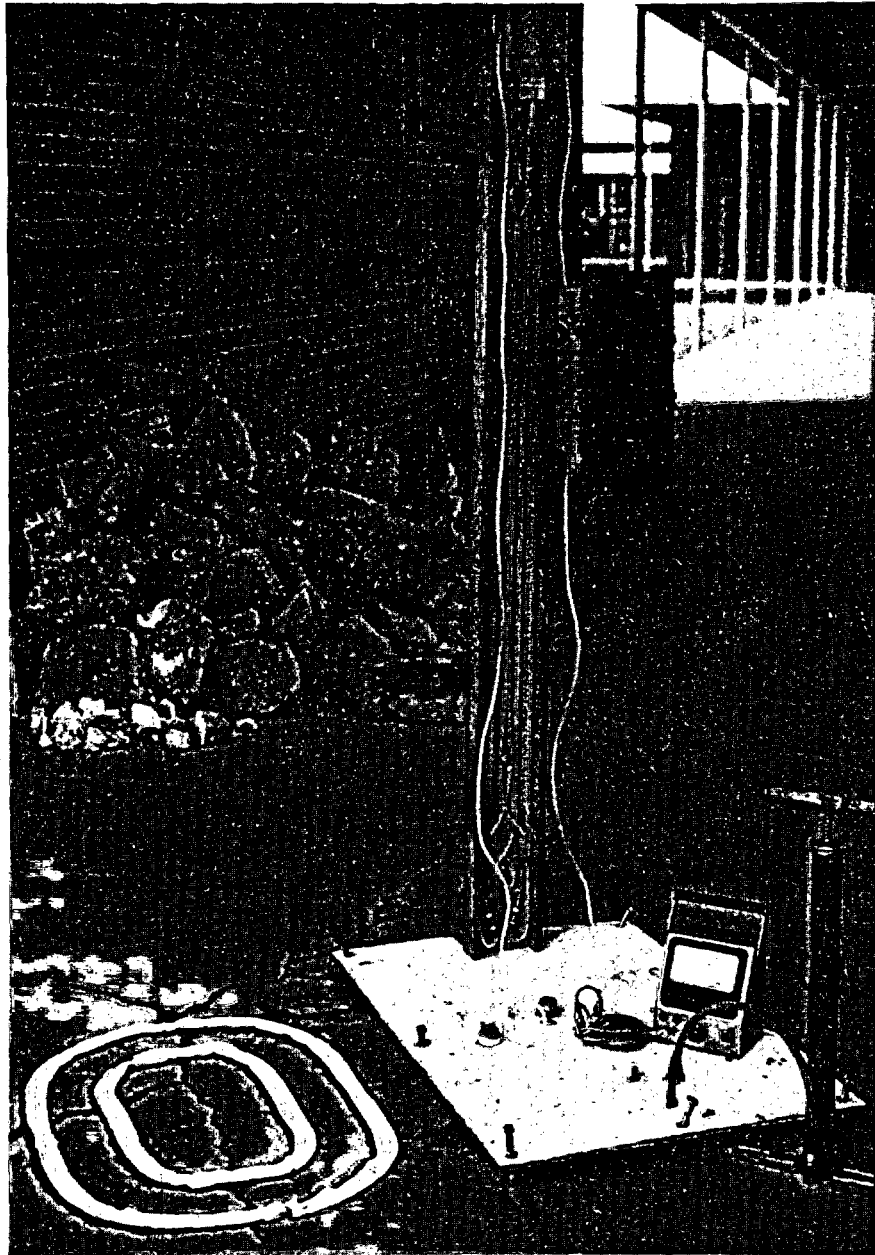


Figure 3.32 Photograph of the FRI set up over a mock fracture.

to the bottom. The interior and exterior chambers are, respectively, 41 and 61 cm in length. A dual piezometer system is used to measure intake from both chambers. A water reservoir is used maintain a constant fluid pressure at the rock surface by periodically replenishing fluid.

The FRI is secured to a rock surface using anchor bolts, with the exposed fracture aligned through the middle of the longitudinal axis of the rectangular plate. Any natural sediment or debris is left undisturbed in the fracture. To ensure a good seal between the rock surface and the FRI, the rock surface is cleaned and holes for anchor bolts are drilled into the rock with an electric hammer drill.

Inflatable packers (consisting of modified bicycle tubes) are used to seal the FRI chambers to the rock surface, and to prevent leakage from one chamber to another or to the atmosphere. During the experiment, the packers are inflated to approximately 240 kPa. Critical to a successful FRI experiment is ensuring that water does not escape from either pressure chamber between the rock surface and the bottom of the packers. A clay caulking material placed under the packers provides an air- and water-tight seal throughout the duration of FRI tests. Each experiment was tested for leaks at the rock-FRI interface by visual inspection. The presence of water exterior to the outer chamber was cause for abandonment of that experiment.

Immediately after the FRI is secured to the rock surface, the packers are pressurized. Both the interior and exterior pressure chambers are quickly filled with water through plugs on the top plate of the FRI. The water reservoir stopcocks are then opened to fill the piezometers to the level labeled A on Figure 3.31. Entrained air is allowed to escape through release valves on the FRI. As water flows into the fracture, the time interval required for the level in the piezometer (connected to the inner chamber) to reach level B is recorded. Water levels in both piezometers are then quickly replenished to level A. This process is repeated until the time interval becomes constant. Because the volume in the piezometer from level A to level B is known, a volumetric flow rate can be computed for each repetition. Water temperature is monitored throughout each FRI test with temperature sensors seated within the chambers.

To provide field tests of the FRI, a site located in undisturbed, unsaturated, relatively flat, exposed rock was required. An outcrop was selected in the Gringo Gulch Volcanics located approximately 3 km southwest of Patagonia, Arizona (Figures 1.11 to 1.14). The outcrop is a flat-topped butte composed of a fractured, densely-welded, ash-flow

tuff described by Drewes (1972) as Paleocene in age. Inspection of vertical fractures exposed at the surface reveal no single dominant fracture pattern. It is likely that a combination of fracture-inducing events, such as contraction due to cooling and tectonic events, produced the random fracture strike pattern found at the site.

Boundary conditions for the FRI water experiment below the fractured rock surface and interior chamber are assumed to be (Figure 3.31):

$$\begin{array}{ll}
 (3.14) \quad \text{Boundary C - D:} & H = h_2 \quad t > 0 \\
 \text{Boundary C - F and D - E:} & \partial H / \partial x = 0 \quad t > 0 \\
 \text{Boundary E - F:} & H = h_1 \quad t > 0
 \end{array}$$

where

- H is the hydraulic head, measured from the a reference elevation at the rock surface;
- $h_2$  is the mean applied head;
- $h_1$  is the distance from surface to wetted front;
- x is the horizontal direction; and
- t is time.

In this formulation, the boundary (E - F) is the wetting front which moves downward with time. It is assumed that the pressure head at the wetting front is atmospheric and that the air pressure ahead of the wetting front remains equal to the atmospheric pressure due to the much higher permeability of the fracture to air. In addition, the assumption is made that the fracture is initially dry and there is no air entrapment behind the wetting front.

Figure 3.33 shows a water intake curve resulting from an FRI injection test at the Patagonia field site. For the majority of the 21 FRI tests performed at the site, water intake was high at early time and progressively decayed to a steady-state value. Most of the water intake curves generated at the site are similar in shape to infiltration decay curves characteristic of soils and other porous media. Scatter in the observed water intake is attributed to the presence of silt or clay particles near the fracture entrance which affect intake rates.

Once estimates of fracture water intake rates are obtained, a physical model can be formulated which relates the time-dependent intake rate to parameters characteristic of the fractures of interest. One such parameter is the apparent fracture aperture. The ability to characterize a set of fractures by a distribution of apparent fracture apertures allows for the extension of the results obtained at a number of point measurement sites to a regional estimate of water intake.

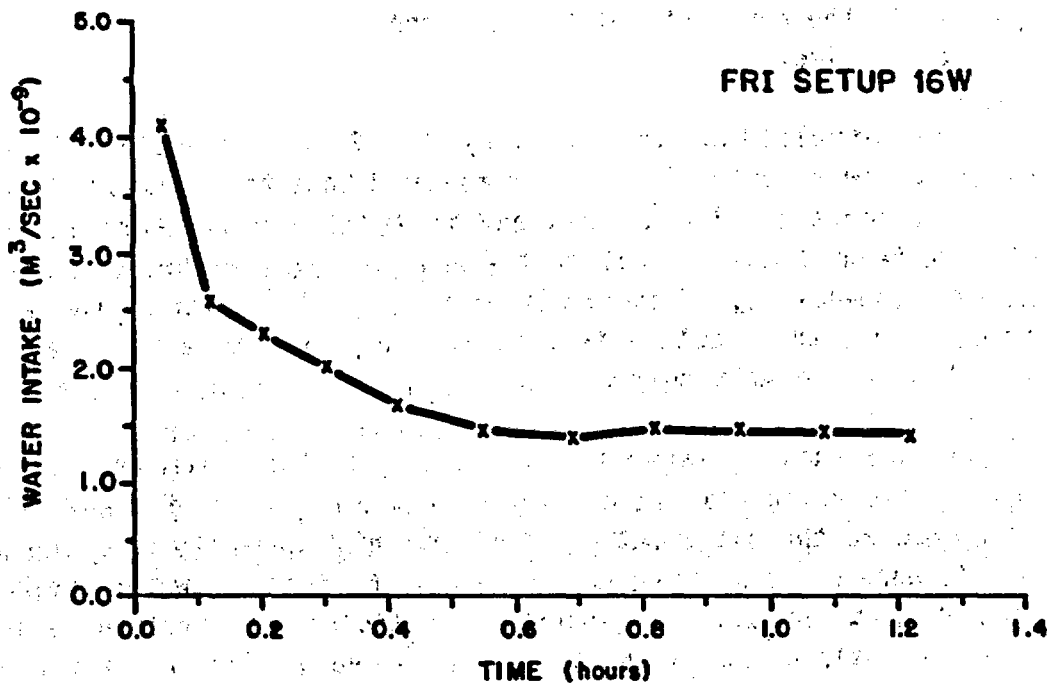


Figure 3.33 Water intake rate vs. time for a representative FRI water experiment (setup 16W).

The mathematical formulation used to compute fracture aperture assumes the fracture to be completely drained prior to each experiment. As water flows into the fracture, a wetting front moves progressively downward, completely saturating the fracture. The equation used to compute fracture apertures for the FRI water method uses the Green and Ampt (1911) formulation. Application of this approach to the FRI flow geometry yields the following relation which is derived in Kilbury (1985):

$$(3.15) \quad e_w^2 = (h_2 \ln[h_2/(h_2-h_1)] - h_1) / ft$$

where  $e_w$  is the apparent fracture aperture using water method, m.

Equation (3.15) incorporates two unknowns; the apparent fracture aperture and the depth of the wetting front. The depth of the wetting front can be obtained using the equation of continuity for a planar fracture:

$$(3.16) \quad h_1 = V / (w e_w)$$

where

$V$  is the volume of water infiltrated into the fracture; and  
 $w$  fracture length measured along the fracture in the interior pressure chamber, equal to 41 cm for the apparatus used.

Equations (3.15) and (3.16) can be coupled by assuming that the apparent fracture aperture is equal to the mean fracture aperture. Laboratory evidence (Shrauf and Evans, 1984) supports this assumption for smooth fractures. The equations may be solved using iterative procedures. An algebraic equation solver (e.g., TK Solver, Software Arts, Inc.) can be used to obtain estimates of the fracture aperture and the depth of the wetting front as a function of time.

To estimate the travel time of water in individual fracture segments, the fluid intake velocity and the depth to the wetting front can be determined as a function of time. These functions, plus the cumulative volume versus time, are shown in Figure 3.34 for a representative water experiment. Observed steady-state water intake rates and calculated fracture apertures, depths to wetting front, and fluid velocities are presented in Table 3.7 for 21 test locations at the Patagonia site.

-----  
**Table 3.7** Steady-state water intake ( $Q_w$ ), fracture aperture ( $e_w$ ), final depth to wetting front ( $h_1$ ), and fluid velocity ( $v$ ) for 21 FRI experiments.  
 -----

FRI Setup Number	Steady State Water Intake $Q_w$ ( $10^{-9}$ m <sup>3</sup> /sec)	Fracture Aperture $e_w$ ( $\mu$ m)	Final Depth to Wetting Front $h_1$ (m)	Fluid Velocity $v$ (m/hr)
1W	3.25	15.6	-2.62	1.83
2W	5.00	21.7	-7.47	2.02
3W	0.50	7.8	-1.61	0.56
4W	1.80	9.6	-2.29	1.65
5W	0.25	6.9	-1.48	0.32
6W	0.030	1.9	-0.34	0.14
7W	1.00	9.1	-1.05	0.96
8W	0.019	1.5	-0.17	0.11
9W	0.006	1.0	-0.14	0.05
10W	0.60	3.0	-0.43	1.76
11W	3.20	14.1	-1.42	1.99
12W	1.10	8.8	-0.72	1.10
13W	0.65	8.1	-1.14	0.70
14W	4.00	18.4	-2.43	1.91
15W	30.0	33.7	-2.53	7.82
16W	1.50	11.2	-1.44	1.18
17W	1.90	12.4	-1.18	1.35
18W	4.60	14.6	-0.81	3.26
19W	16.0	27.6	-2.73	5.09
20W	3.00	16.0	-3.09	1.65
21W	14.0	26.0	-2.60	4.73

-----

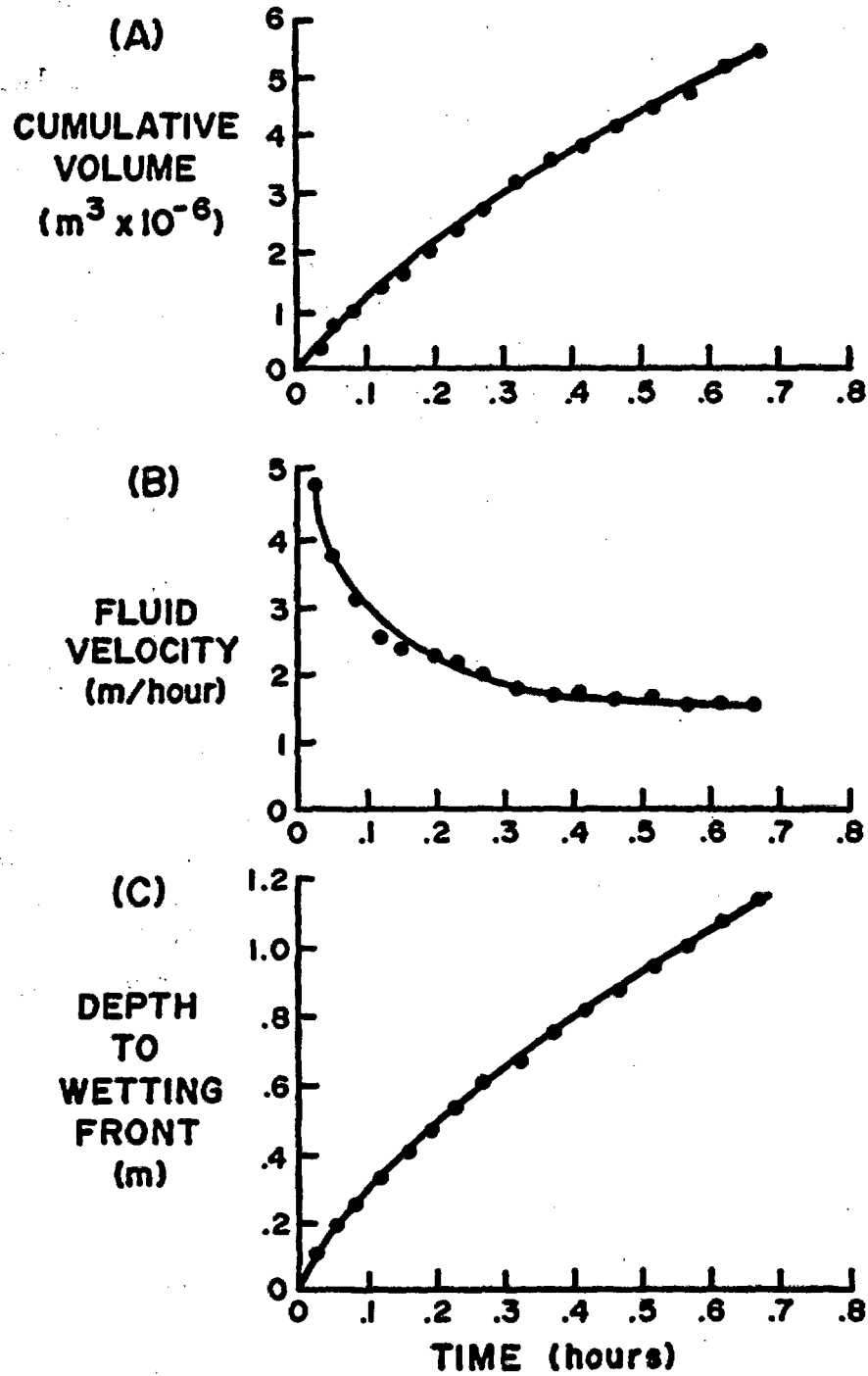


Figure 3.34 Cumulative water intake volume (A), fluid velocity (B), and depth to wetting front (C) vs. time graphs.

A log-probability plot of apparent fracture apertures for the tests reveals a straight line fit for fractures whose computed apertures are greater than 20  $\mu\text{m}$  (Figure 3.35), indicating a log-normal distribution. Fractures with apertures less than 20  $\mu\text{m}$  do not appear to belong to the same distribution. Instead, the computed fracture aperture is smaller than what the log-normal distribution would suggest. This may result because either 1) the smaller fractures are, in fact, less likely to occur, or 2) a heretofore undocumented physical process may cause a reduction in the flow rate and, hence, an under-estimation of the fracture aperture.

A Kolmogorov-Smirnov goodness-of-fit test performed on the larger aperture data failed to reject the hypothesis ( $\alpha < 0.05$ ) that the distribution of apertures is log-normally distributed. The critical test value was 0.8750 with five intervals. Uncertainties which may affect aperture calculation using Equations (3.14) and (3.15) arise from unknown boundary conditions and the validity of applying the cubic law to natural fractures. If the influence of the external pressure chamber introduces a horizontal flow component, the effective fracture length will change as the wetting front advances through the fracture. This situation will affect aperture values computed using Equation (3.15). The variability in the measured constant head level, and the fact that flow continues momentarily while the piezometer system is replenished, are considered to be the main contributors to experimental error.

Another potential error results because the boundary condition along E - F is formulated such that a zero pressure condition is present. If fractures are small, however, there will be an additional negative pressure due to capillary forces acting on the fluid front. This will result in a larger head gradient than when this force is neglected. The capillary head is computed as:

$$(3.17) \quad h_r = - 2 T / \rho g e_w'$$

where

- $h_r$  capillary pressure head;
- $T$  surface tension, 0.073 kg/s<sup>2</sup> at 25 °C; and
- $e_w'$  computed aperture which includes the capillary effect.

Table 3.8 presents adjusted depths to the wetting front and fracture aperture, along with the original estimates. The magnitude of the influence of the capillary effect is generally minor for the larger fractures, yet substantially affects the estimated fracture aperture for the smaller fractures. Because the effect tends to reduce the estimated

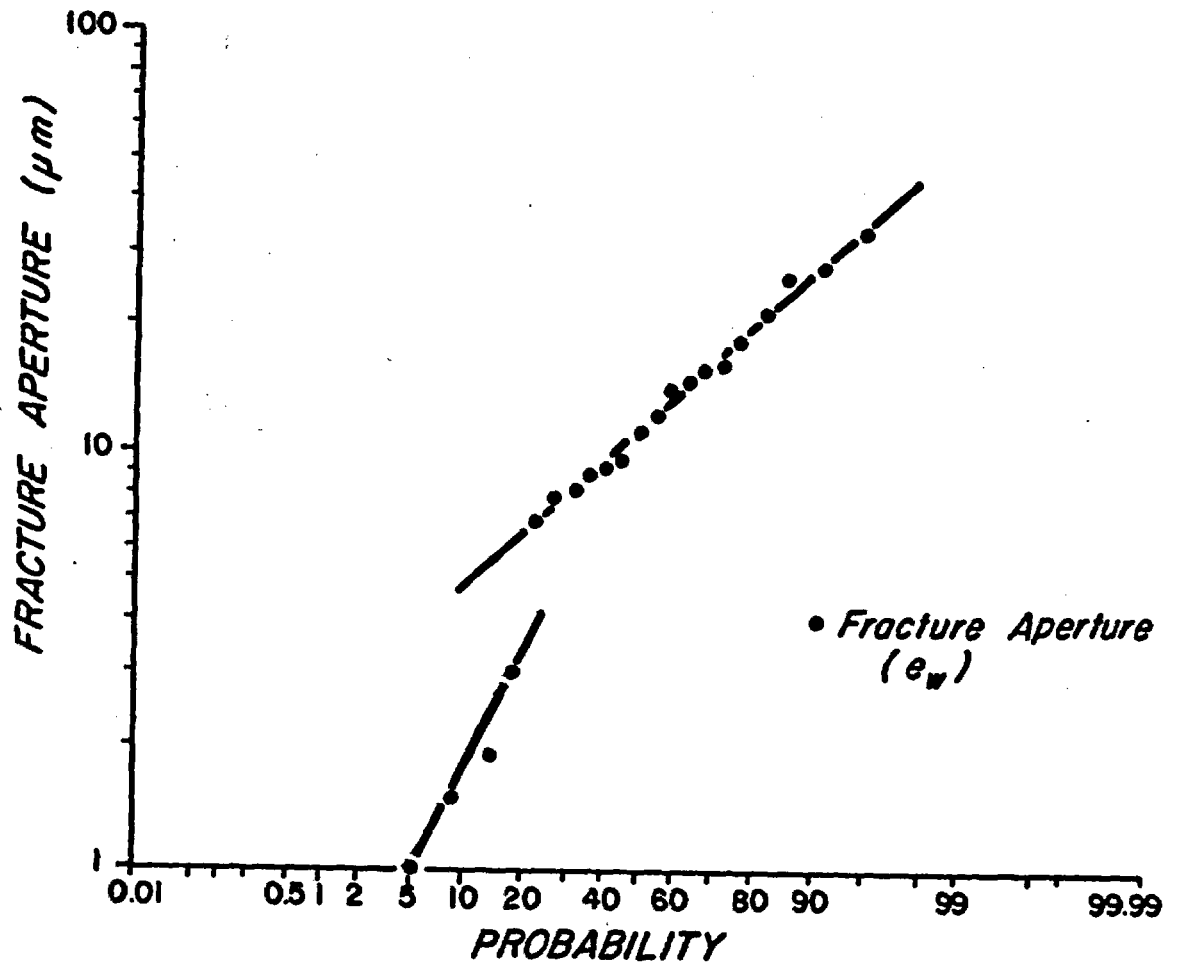


Figure 3.35 Log-probability plot of fracture apertures computed for the FRI water method.

aperture of the smaller fractures, the discontinuity of the probability distribution function (Figure 3.35) is accentuated. The probability distribution function for larger fractures is essentially unchanged.

Table 3.8 Comparison of final depth to wetting front and fracture aperture not considering the capillary effect ( $h_1$  and  $e_w$ , respectively) with values computed considering the capillary effect ( $h_1'$  and  $e_w'$ , respectively).

FRI Setup Number	WITHOUT CAPILLARY EFFECT		WITH CAPILLARY EFFECT		Percent Change in Aperture
	Elevation Head at Wetting Front	Fracture Aperture	Elevation Head at Wetting Front	Fracture Aperture	
	$h_1$ (m)	$e_w$ ( $\mu\text{m}$ )	$h_1'$ (m)	$e_w'$ ( $\mu\text{m}$ )	
1W	-2.62	15.6	-2.88	14.1	- 9.6
2W	-7.47	21.7	-7.82	20.8	- 4.1
3W	-1.61	7.8	-1.97	6.3	-19.2
4W	-2.29	9.6	-2.69	8.1	-15.6
5W	-1.48	6.9	-1.94	5.3	-23.2
6W	-0.34	1.9	-0.40	1.7	-10.5
7W	-1.05	9.1	-1.29	7.4	-18.7
8W	-0.17	1.5	-1.01	0.3	-80.0
9W	-0.14	1.0	-1.04	0.1	-90.0
10W	-0.43	3.0	-0.71	1.8	-40.0
11W	-1.42	14.1	-1.62	12.3	-12.8
12W	-0.72	8.8	-0.92	6.9	-21.6
13W	-1.14	8.1	-1.43	6.5	-19.8
14W	-2.43	18.4	-2.68	16.8	- 8.7
15W	-2.53	33.7	-2.67	31.9	- 5.3
16W	-1.44	11.2	-1.70	9.4	-14.5
17W	-1.18	12.4	-1.37	10.6	-14.5
18W	-0.81	14.6	-0.94	12.5	-13.0
19W	-2.73	27.6	-2.91	25.8	- 6.5
20W	-3.09	16.0	-3.41	14.5	- 9.4
21W	-2.60	26.0	-2.78	24.3	- 6.5

### 3.5.2 Air Intake Method

The FRI has also been used to measure air intake rates into fractures subsequently used for water intake experiments. These tests are used to:

- Provide information about air permeabilities of fractures in rock masses; and
- Augment the water intake investigation by providing a secondary means of determining fracture apertures.

Field and analytic techniques are developed to determine fracture apertures using air. Figure 3.36 shows the FRI configuration and flow geometry for the air experiment. Design for this experiment is comparable to that for water, except that a manometer system is now incorporated to measure air intake into the fracture. Also, an air reservoir (in the form of a 0.121 m<sup>3</sup> drum) is used to provide a volume of air sufficient to reduce the observed pressure changes in the manometer. In addition, the exterior and interior chambers are open to each other and are not separately pressurized.

Experiments using air were completed on individual fractures prior to conducting a water intake experiment. Procedures in this application are similar to those of the water experiment. The clay caulk is again used as a sealant. The packers are inflated to the same pressure used in the water tests. Air temperature within each chamber is recorded throughout each test. Air is pumped into the air reservoir until the manometer level rises to a level marked as level 1 in Figure 3.36(A). As air flows into the fracture, the time required for the manometer to reach level 2 is recorded. The difference between the two levels is  $\Delta h$ , and the corresponding mean head reading is  $h_c$ . The process is repeated until several constant time intervals are observed. Boundary conditions for the FRI air experiment below the fractured rock surface and interior chamber are as follows:

$$\begin{array}{lll} (3.18) \text{ Boundary B - C - D:} & p = 2 \rho g (h_c - h_a) & t > 0 \\ \text{Boundary A - B and D - E:} & \partial p / \partial y = 0 & t > 0 \\ \text{Boundary A - F' and E - F:} & p = 0 & t > 0 \end{array}$$

where

$p$  gauge pressure, kg/m-s<sup>2</sup>.

$\rho$  fluid density at ambient temperature and pressure, kg/m<sup>3</sup>.

$y$  vertical direction, m.

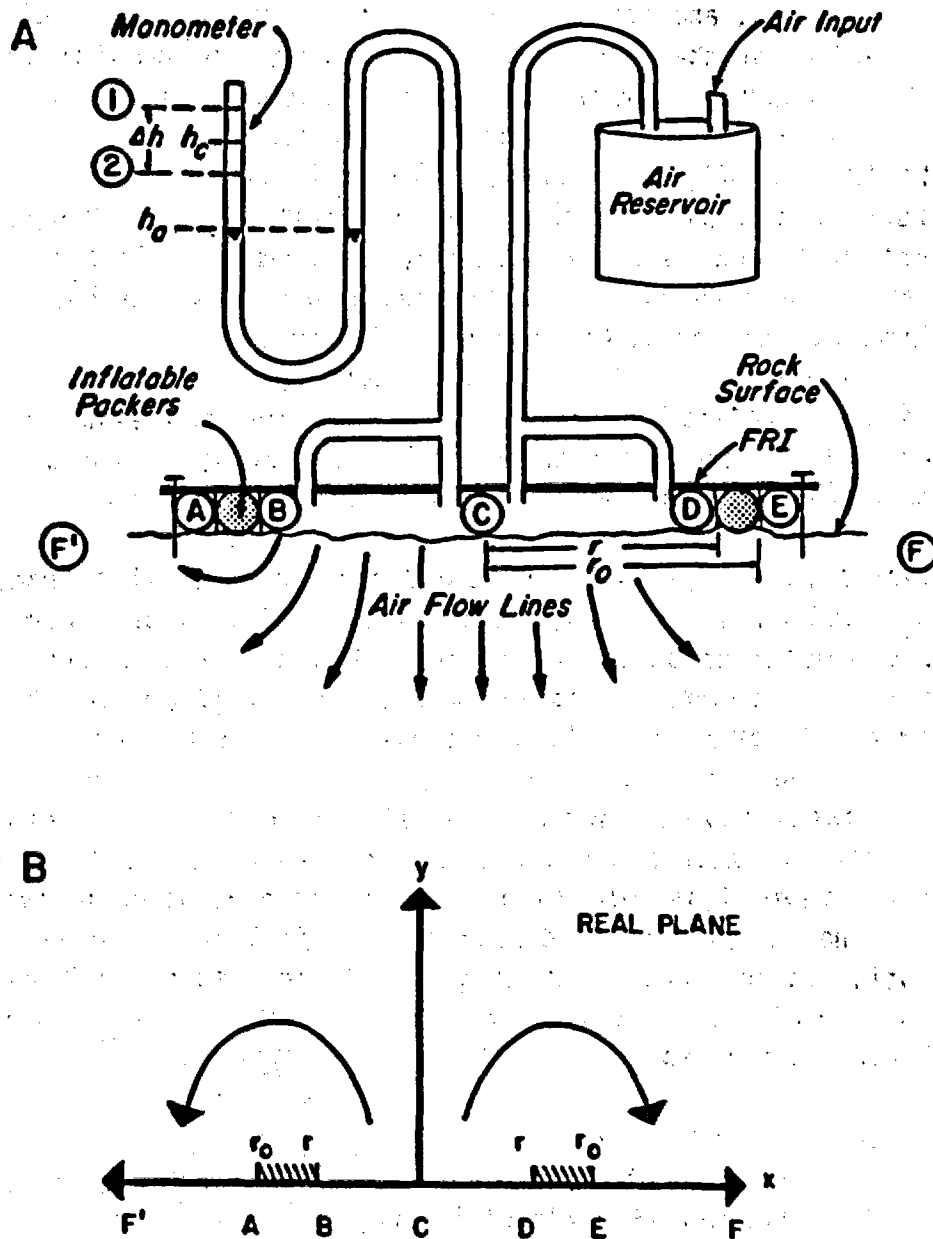


Figure 3.36 Cross-sectional diagram of the FRI as used for air intake measurements (A), and FRI geometry represented in the real plane (B).

Air experiments typically exhibit initial steady-state conditions; i.e., intake rates at early readings are usually similar to those recorded after many repetitions (Figure 3.37).

Each air test was performed using different applied pressures, thus, the air intake rate for each experiment must be standardized. For this problem, the ideal gas law was used to calculate the air intake volume at standard temperature and pressure conditions for each air test. Temperature variations during all FRI air experiments were small enough to be ignored. The fracture air intake rate was computed by dividing the intake volume by the time between pressure readings. As expected, air intake rates into fractures was consistently higher than that of water. Air intake rates are on the order of  $10^{-5}$  m<sup>3</sup>/s, while water intake rates are on the order of  $10^{-9}$  m<sup>3</sup>/s.

Aperture determination using gas intake methods may be preferable to water intake methods when exposed fractures are not vertically inclined, or in circumstances when water may not be used for geochemical, or other reasons. Schrauf and Evans (1984) examined gas flow between parallel plates at low pressure gradients and concluded that the application of the cubic law for gases yielded good estimates of the average aperture for smooth fractures. Trautz (1984) measured apparent fracture apertures in the Apache Leap Tuff near Superior, Arizona, using nitrogen gas, and found apertures ranging from 9.0 to 19.7  $\mu$ m.

The equation used for aperture calculations in the present analysis is derived by combining the cubic law, an equation of state for compressible gases, a pressure-related potential expression derived from the FRI flow geometry, and an appropriate conformal transformation. This derivation is presented in Kilbury (1985) and results in the expression:

$$(3.19) \quad e_a^3 = 6 Q_a \mu (n+1) / [P_a (K/K')] \quad (5)$$

where

- $e_a$  is the aperture computed using the air intake method;
- $Q_a$  is the volumetric flow rate; and
- $\mu$  is the dynamic viscosity;
- $n$  is the ratio of specific heats at constant volume and pressure,  $C_v/C_p$ , dimensionless. For an incompressible fluid,  $n = 0$ ; for air,  $n = 0.71$ ; and for isothermal expansion,  $n = 1$ ;
- $P_a$  air pressure at ambient temperature, kg/m-s<sup>2</sup>; and
- $K/K'$  the ratio of the complete elliptical integral to its complement for a specified modulus (see Kilbury, 1985).

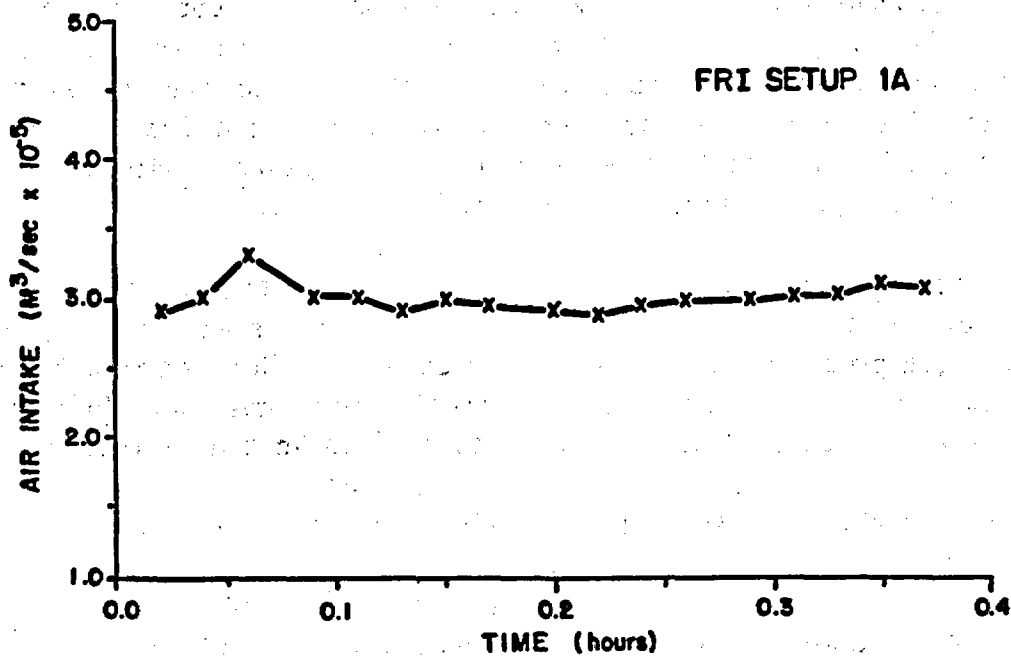


Figure 3.37 Air intake rate vs. time for a representative FRI air experiment (setup 1A).

Table 3.9 presents calculated fracture apertures for 14 FRI air tests, which replicated many, but not all, of the water tests. The calculated apertures range from 10.0 to 37.2  $\mu\text{m}$ , a range similar in magnitude to the range (1.0 to 33.7  $\mu\text{m}$ ) computed using the FRI water tests.

-----  
 Table 3.9 Fracture apertures for FRI air experiments.  
 -----

FRI setup:	1A	2A	3A	4A	5A	6A	7A
Aperture ( $\mu\text{m}$ )	28.0	14.3	10.0	32.1	17.8	29.2	37.2
FRI setup:	8A	9A	10A	11A	12A	13A	14A
Aperture ( $\mu\text{m}$ )	35.5	20.9	23.3	18.2	26.5	14.1	30.0

-----

Figure 3.38 illustrates the relative agreement between aperture results for individual fractures involving both air and water methods. The straight-line log-probability plot suggests that fracture apertures computed using the air method are log-normally distributed. The paucity of data points, however, prevents the determination of a unique probability density function.

A comparison of fracture apertures calculated by first performing an air test, followed by a water test is presented as Figure 3.39. In this assessment, the fracture is initially assumed to be completely drained and a fracture aperture is calculated using the air method. Once the air experiment is terminated, the same location is retested using water.

It is important to note that calculated fracture apertures were obtained by using different governing equations and boundary conditions. Thus, the general agreement between apertures calculated from air and water experiments provides confidence with regard to both methods of aperture calculation, and to the application of the cubic law for fluid flow in natural fractures.

To evaluate the assumption that the fracture was initially completely drained, a series of experiments were performed. Figure 3.40(A) displays a plot of the air intake rate of an undisturbed fracture.

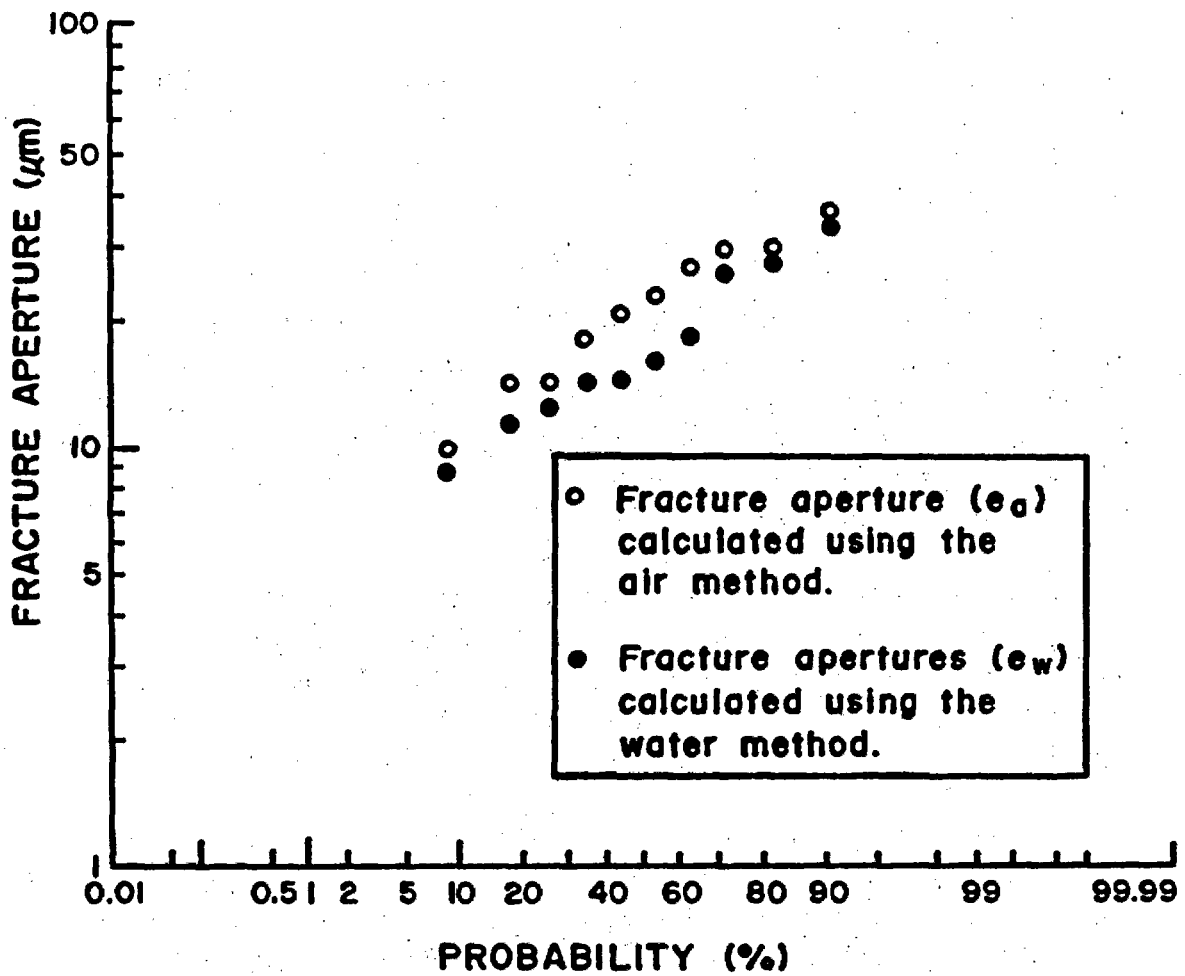


Figure 3.38 Log-probability plot of fracture apertures computed using the air and water methods on the same fractures.

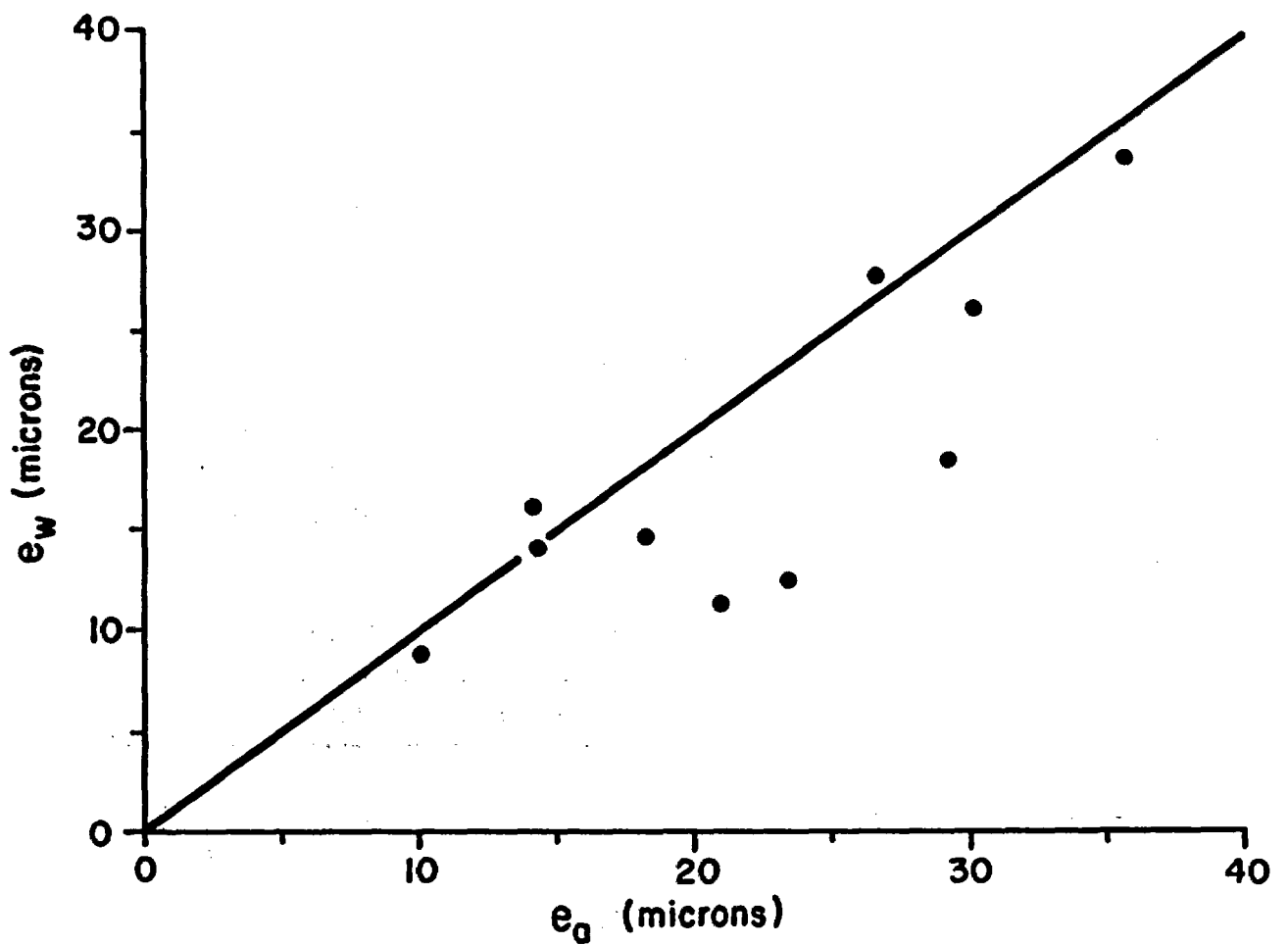


Figure 3.39 Plot of fracture apertures calculated using the water method ( $e_w$ ) vs. apertures calculated using the air method ( $e_a$ ) for the same fracture.

Figure 3.40(B) displays a plot of the water intake of the same fracture following the completion of the air intake experiment. Finally, Figure 3.40(C) displays a last experiment in which the air experiment is repeated after the completion of the water experiment. The fact that the air intake rate after the termination of the water intake experiment is initially very low, and then rises toward the pre-water intake experiment lends support to the assumption that the fracture was initially completely drained and briefly became relatively impermeable to air following a water intake experiment.

### 3.5.3 Discussion and Conclusions

The presented analytic solutions provide a description of the transient intake rate over time for prescribed external boundary conditions at fractures which intersect the earth-atmosphere interface. The solutions are for air and water. These solutions require the application of the cubic law and the estimation of fracture aperture. While the validity of the application of the cubic law to flow in natural fractures has not been fully substantiated, especially for fractures smaller than 20  $\mu\text{m}$ , the fact that calculated apertures compare favorably when two independent tests are performed (and also with other studies in similar geologic materials) increases the credibility of the technique and of the underlying assumptions.

The FRI method is an approach potentially capable of serving as an intake measurement device under an assortment of conditions. The analytic solution for the water experiment is limited to a horizontal, relatively flat, exposed rock surface, which also is required for FRI experiment procedures. The solution for air experiments is not limited to horizontal rock surfaces, however, and may be used on any flat, exposed rock surface. The use of air as a surrogate measure of hydraulic conductivity is useful when horizontal surfaces are not available, or when the use of water is contra-indicated.

### 3.6 Determination of Fracture Aperture Using Air Injection

The flow-test theory is developed for the case where two boreholes intersect a single fracture. One borehole is pressurized, forcing radial flow outward in the plane of the fracture toward the second borehole. Radial flow is a special case of a more general type of flow condition called elliptical flow. Strictly radial flow (i.e., when equipotential lines form concentric circles) will only occur when the axis of the borehole is oriented perpendicular to the fracture plane. If the borehole intersects the fracture at a nonzero angle ( $\alpha \neq 0$ ), as

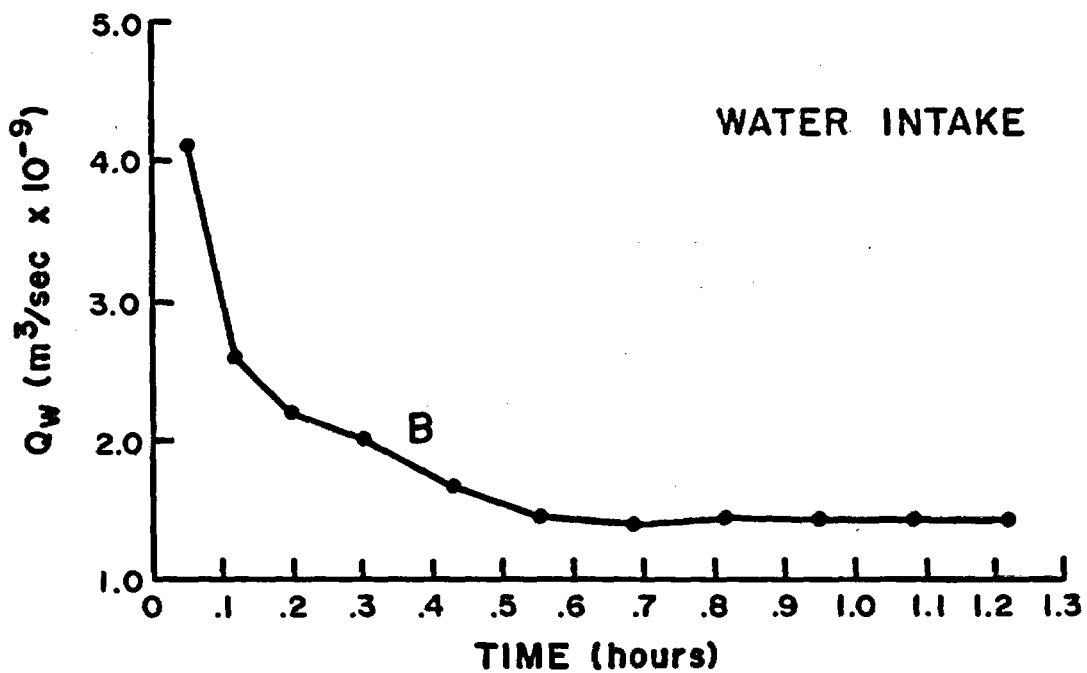
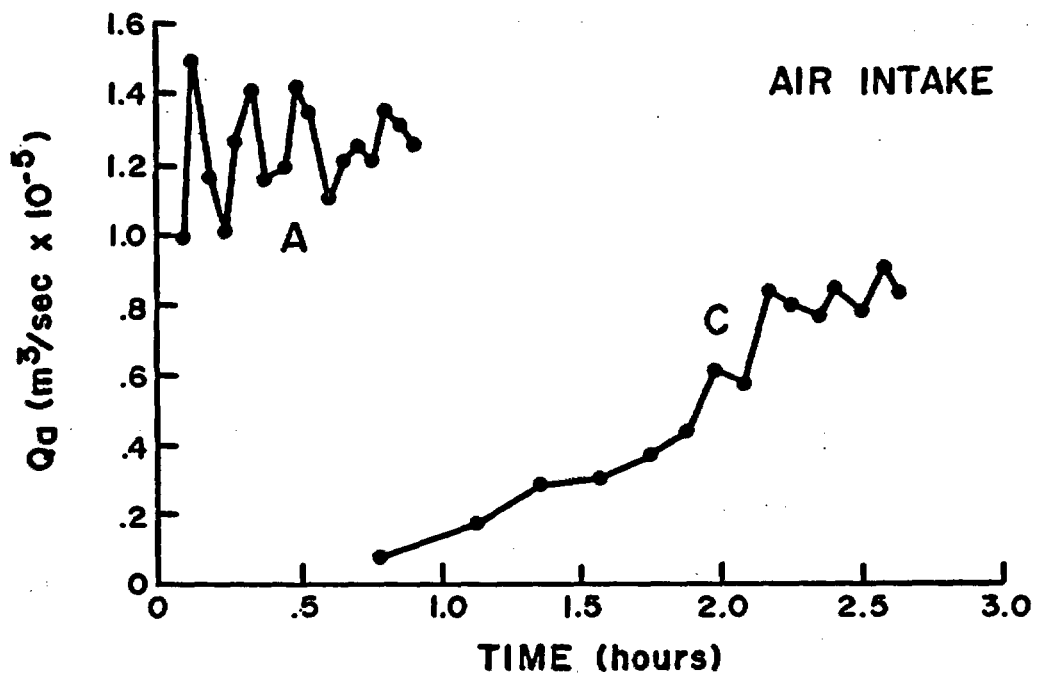


Figure 3.40 Sequential air-intake (A), water-intake (B), and air-intake (C), curves for a single fracture at the Patagonia study area.

shown in Figure 3.41, the fracture-borehole intersection trace in the plane of the fracture will be an ellipse.

The ellipse will form a constant-pressure boundary along which flow will take place. Elliptic flow can be described using the cubic law:

$$(3.20) \quad Q_m = - \frac{\pi e^3 \rho_b}{12\mu P_b} \frac{P_2^2 - P_1^2}{\ln [(a_2+b_2)/(a_1+b_1)]}$$

where

- $Q_m$  is total mass flow rate, kg/s;
- $e$  is fracture aperture, m;
- $\mu$  is dynamic viscosity, kg/m-s;
- $\rho_b$  is density of fluid at reference state b, 1.164 kg/m<sup>3</sup>;
- $P_b$  is pressure at reference state b, 0.101325 \* 10<sup>6</sup> Pa;
- $P_2$  is absolute pressure at observation borehole, Pa;
- $P_1$  is absolute pressure at injection borehole, Pa;
- $a_1$  is semimajor axis of the inner ellipse formed by the borehole-fracture plane interaction, m;
- $b_1$  is semiminor axis of the inner ellipse formed by the borehole-fracture plane interaction, m;
- $a_2$  is semimajor axis of the outer ellipse on which observation borehole lies, m; and
- $b_2$  is semiminor axis of the outer ellipse on which observation borehole lies, m.

The geometry of variables  $a_1$ ,  $b_1$ ,  $a_2$ , and  $b_2$  are presented in Figure 3.42. It may be observed that for distances far from the inner elliptical boundary  $a_2$  approaches  $b_2$ . This implies that at a given radial distance from the injected borehole, radial flow conditions will exist. The radial distance from the injection borehole necessary for this assumption depends upon the borehole-fracture plane intersection angle,  $\alpha$ . Figure 3.43 is a plot of  $a_2/b_2$  versus an average radius,  $r_{ave}$ , for various angles.

The average radius is defined as:

$$(3.21) \quad r_{ave} = (a_2 + b_2) / 2 \quad r_1$$

where

- $r_1$  is the radius of the injection borehole, m.

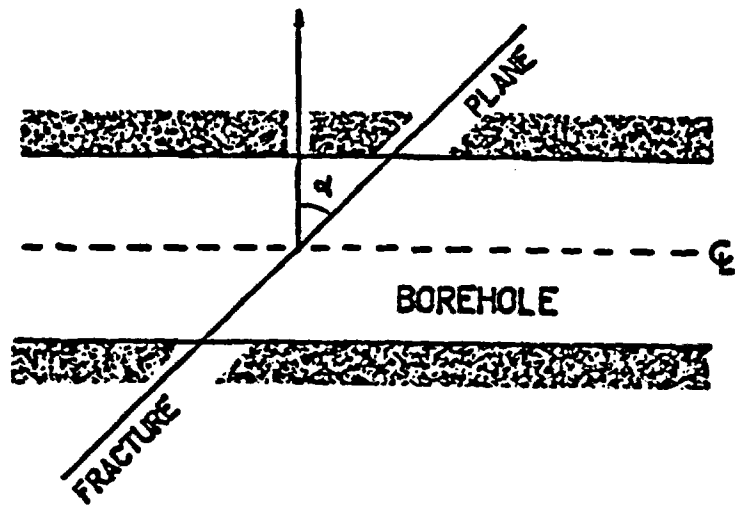


Figure 3.41 Fracture-borehole interaction angle,  $\alpha$ .

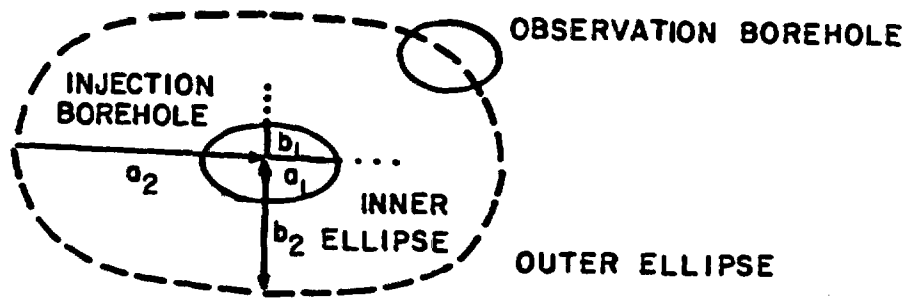


Figure 3.42 Geometric relations between injection and observation boreholes.

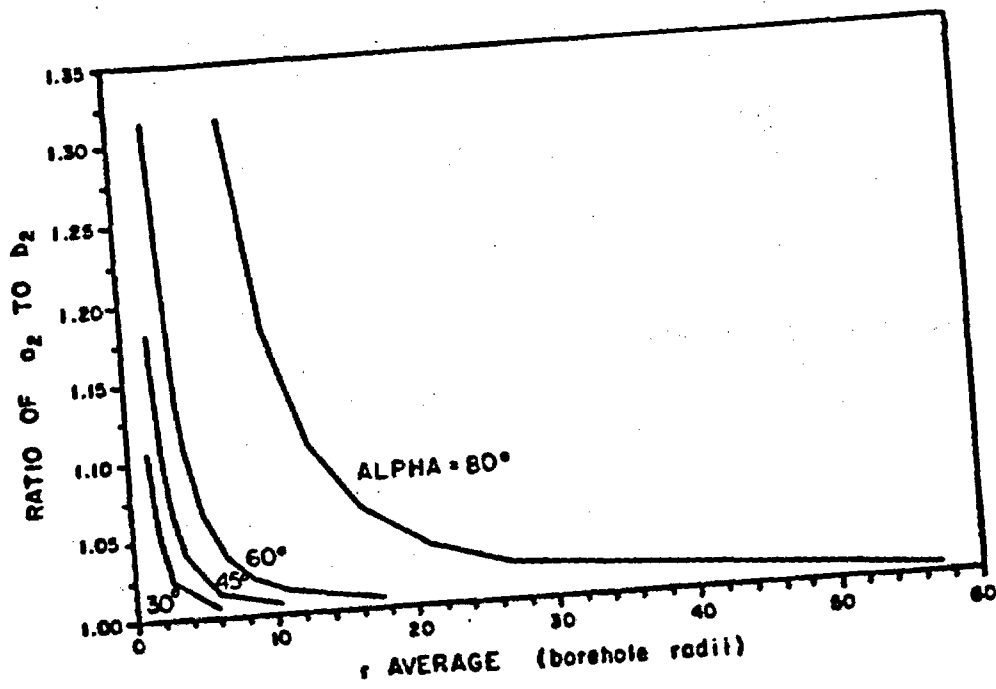


Figure 3.43  $r_{ave}$  versus  $a_2/b_2$  for different borehole-fracture plane interaction angles,  $\alpha$ .

This formulation allows the average radius of the outer ellipse (along which the observation borehole lies) to be given in terms of borehole radii instead of dimensional units. It is evident from Figure 3.43 that radial flow exists at distances greater than 57 borehole radii from the origin for all intersection angles less than 80° and  $a_2$  to  $b_2$  ratios less than 1.01. For intersection angles less than 60°, radial flow will occur at distances greater than 18 borehole radii. If the observation borehole is located within this critical radius, then Equation (3.20) can be simplified even further. By noting that  $a_2$ ,  $b_2$ , and  $r_2$  are approximately equal for a distance greater than the critical radius, and realizing:

$$a_1 = r_1 \sec\alpha \quad \text{and} \quad b_1 = r_1$$

then Equation (3.20) can be rewritten as:

$$(3.22) \quad Q_m = \frac{\pi e^3 \rho_b}{12\mu P_b} \frac{P_2^2 - P_1^2}{\ln [2r_2/r_1(\sec\alpha + 1)]}$$

where

- $r_1$  is injection borehole radius, m;
- $r_2$  is radial distance to observation hole, m; and
- $\alpha$  is borehole-fracture plane intersection angle, °.

The Teledyne-Hastings mass flowmeter was used to provide readings in standard (i.e., standard temperature and pressure)  $\text{cm}^3/\text{min}$  (SCCM). The volumetric flow rate is related to the mass flow rate using:

$$(3.23) \quad Q_m = Q_{\text{SCCM}} \rho_{\text{STP}}$$

where

- $\rho_{\text{STP}}$  is the density of the gas; a function of the standard temperature and pressure state for which the flowmeter was calibrated.

### 3.6.1 Single Hole Flow Test

When a single hole is being utilized to measure fracture aperture, there is no longer an observation borehole where  $P_2$  can be measured or easily defined. To remedy this difficulty, an undisturbed pressure head is assumed to exist at an effective radius,  $r_e$ , from the injection borehole. The effective radius corresponds to the rather ill-defined radius of influence. Outside of the effective radius, the pressure distribution

is unaffected by gas injection at the injection well. For a gas flow test, the pressure outside of the effective radius is atmospheric.

The effective radius can be determined using cross-hole flow tests. The test results from the Santo Nino and Superior Road tunnel flow experiments indicate that for fractures with apertures between 100 and 200  $\mu\text{m}$ , the effective radius is approximately 1 m for flow rates less than 500 SCCM. The borehole radius for these experiments was 0.025 m. For a borehole with a radius of 0.05 m, such as boreholes being tested near the Number 9 Magma shaft, the effective radius would be 2 m. In general, for a single-hole test with injection borehole radius equal to  $r_1$ , the effective radius  $r_e$  would be calculated using:

$$(3.24) \quad r_e = r_1 / 0.025$$

The estimate of the effective radius would be for a flow test conducted on a fracture with aperture between 100 and 200  $\mu\text{m}$  and flow rate less than 500 SCCM. The development of Equation (3.24) is given by:

$$(3.24a) \quad \frac{Q_a}{Q_b} = \frac{\frac{\pi e^3 \rho_b}{12\mu P_b} \frac{(P_2^2 - P_1^2)_a}{\ln [2r_2/r_1(\sec\alpha + 1)]_a}}{\frac{\pi e^3 \rho_b}{12\mu P_b} \frac{(P_2^2 - P_1^2)_b}{\ln [2r_2/r_1(\sec\alpha + 1)]_b}}$$

where subscripts a and b indicate the cross-hole and single-hole tests, respectively. Simplifying Equation (3.24a) yields:

$$(3.24b) \quad \frac{Q_a}{Q_b} = \frac{\ln [2r_2/r_1(\sec\alpha + 1)]_b (P_2^2 - P_1^2)_a}{\ln [2r_2/r_1(\sec\alpha + 1)]_a (P_2^2 - P_1^2)_b}$$

To maintain the same pressure drop and flow rate:

$$Q_a = Q_b \quad \text{and} \quad (P_2^2 - P_1^2)_a = (P_2^2 - P_1^2)_b$$

Equation (3.24b) can now be reduced to:

$$(3.24c) \quad \ln [2r_2/r_1(\sec\alpha + 1)]_a = \ln [2r_2/r_1(\sec\alpha + 1)]_b$$

or;

$$(3.24d) \quad (r_2/r_1)_a = (r_2/r_1)_b$$

and finally;

$$(3.24e) \quad r_{2b} = r_{1b} * (r_2/r_1)_a$$

where

- $r_{1a}$  is borehole radius of cross-hole flow test, m;
- $r_{2a}$  is known effective radius from cross-hole flow test, m;
- $r_{1b}$  is borehole radius of single-hole flow test, m; and
- $r_{2b}$  is the unknown effective radius, m.

For the application of interest,  $r_{2b}$  is equal to the effective radius,  $r_e$ . In addition,  $r_{2a}$  is equal to 1 m and  $r_{1a}$  is equal to 0.0025 m. Thus, the new effective radius can be computed for variable borehole radii (Figure 3.44).

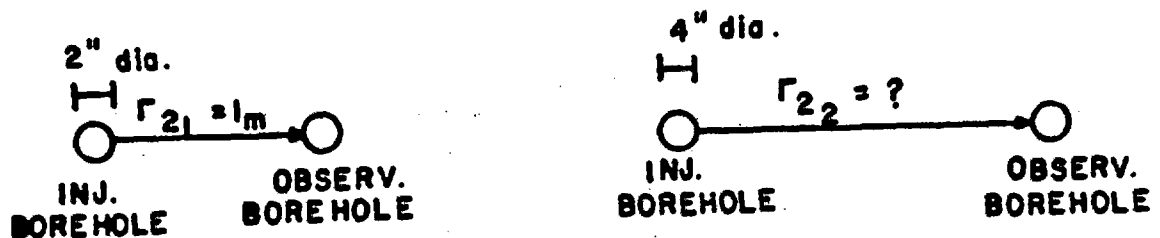


Figure 3.44 Geometric relations between radius of influence for a known case (left) and for an unknown case (right).

The analytical equation used to reduce the field data from a single-borehole flow test would be identical to Equation (3.24), except that the following relationships are utilized:

$$r_2 = r_e \quad \text{and} \quad P_2 = P_{atm} = 0.101325 \text{ mPa}$$

Thus:

$$(3.25) \quad Q_m = - \frac{\pi e^3 \rho_b}{12\mu P_b} \frac{P_{atm}^2 - P_1^2}{\ln [2r_e/r_1(\sec\alpha + 1)]}$$

Figures 3.45 and 3.46 give the pressure drop versus flow rate for fractures with varying aperture and borehole-fracture plane intersection angles of 0° (radial flow) and 60° (elliptical flow), respectively. These figures can be used by field personnel to determine the fracture aperture from a flow test. These figures were developed using Equation (3.25) with an effective radius of 2 m and injection borehole radius of 5 cm. Steady-state flow conditions must exist in order to use these figures. Also, it must be assumed that nonlinear flow conditions (i.e., nonlinear relationship between  $P_{atm}^2 - P_1^2$  and  $Q_m$ ) brought on by turbulence, water blockages or fracture opening are not exhibited.

### 3.6.2 Fracture Aperture Test Procedure

There are many direct methods of measuring fracture apertures in situ. However, a hydraulic or pneumatic test can be used to measure fracture apertures indirectly. The results of the hydraulic test are interpreted using the cubic law by relating the mass flow rate,  $Q_m$ , to the fracture aperture,  $e$ , as follows for a compressible fluid such as a gas;

$$(3.26) \quad Q_m = C e^3 \Delta P^2$$

where

- C is a constant dependent upon flow geometry and fluid properties; and
- $\Delta P^2$  is the difference between the squared injection borehole-pressure and nearby squared observation borehole-pressure.

When an observation borehole is not being utilized, the pressure is assumed to be atmospheric. Equation (3.26) can be solved for the fracture aperture:

$$(3.27) \quad e^3 = Q_m / (C \Delta P^2)$$

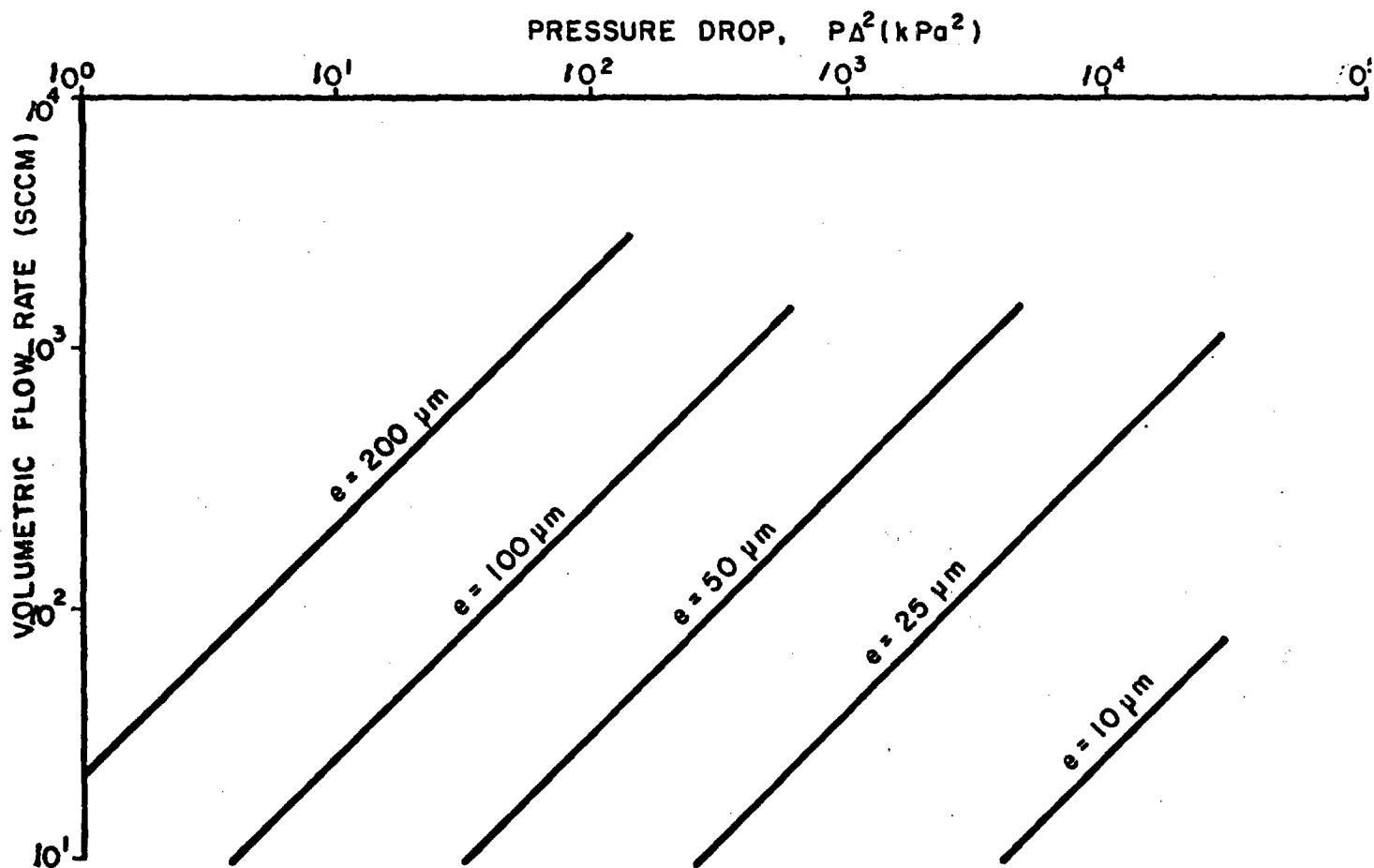


Figure 3.45 Pressure drop versus volumetric flow rate for different apertures,  $e$ . Theoretical equations using  $r_2 = 2 \text{ m}$ ,  $r_1 = 0.05 \text{ m}$  and  $\alpha = 0^\circ$ .

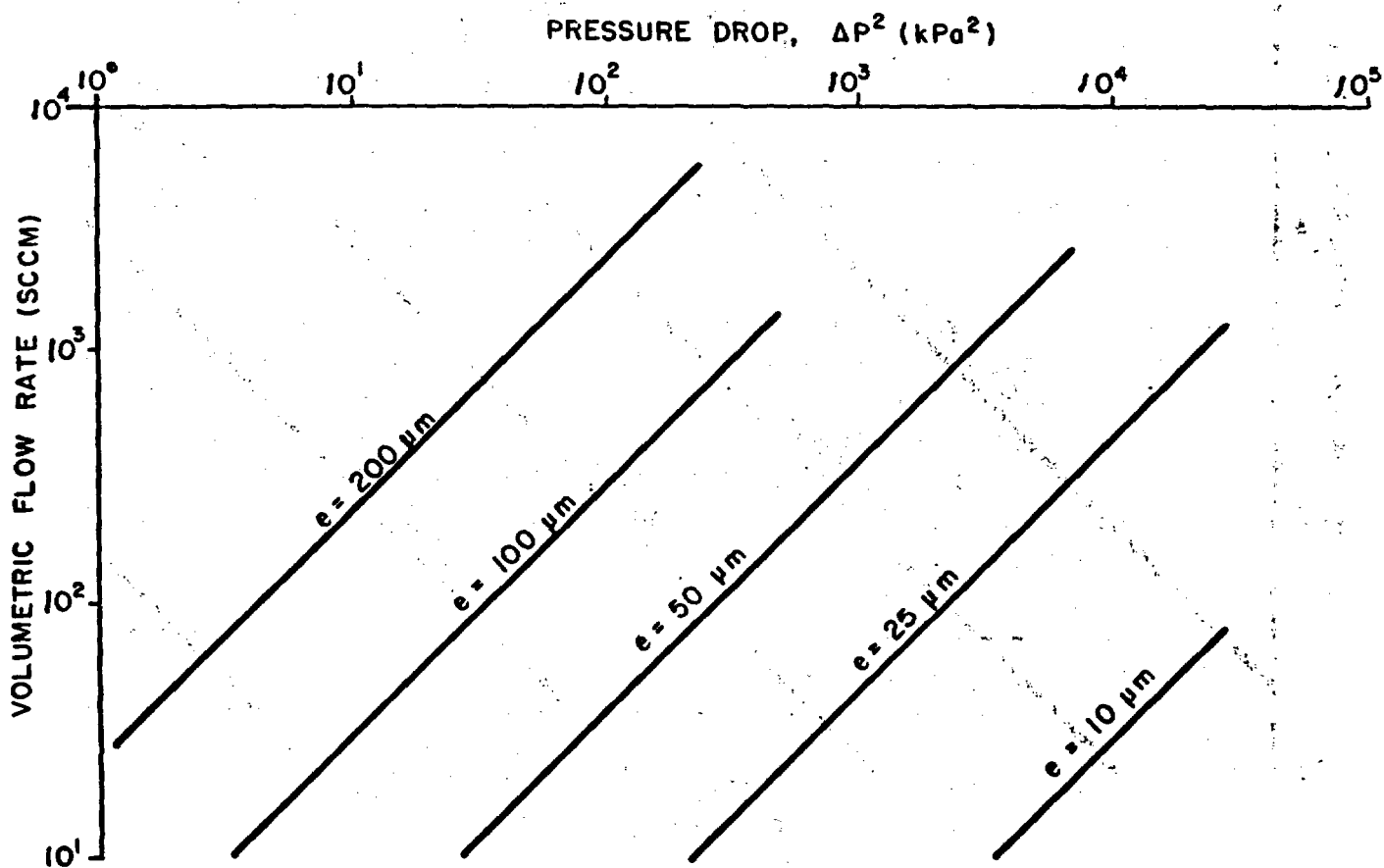


Figure 3.46 Pressure drop versus volumetric flow rate for different apertures,  $e$ . Theoretical equations using  $r_2 = 2 \text{ m}$ ,  $r_1 = 0.05 \text{ m}$  and  $\alpha = 60^\circ$ .

The mass flow rate,  $Q_m$ , is measured using mass flowmeters and the pressure drop,  $\Delta P^2$ , is measured using a mercury-filled manometer. Because the constant,  $C$ , is known, Equation (3.27) can be used to calculate the hydraulic aperture,  $e$ . The procedure for measuring  $Q_m$  and  $\Delta P^2$  is described below.

First, the packer system is assembled in a plastic or steel pipe to check the system for leaks. The packers are inflated after placing them inside the pipe which simulated a nonporous, nonfractured section of borehole. The downstream and upstream valves on the 10,000 SCCM flowmeter board are then opened (see Figure 3.47).

Gas is allowed to flow into the packer system. The flow rate should be set to the maximum of 5 volts (V) or approximately 10,000 SCCM. The pressure regulator on the nitrogen tank should read between 15 and 20 psi. The regulator should not be set any higher than 20 psi or the mercury in the manometer will be blown out of the top of the glass. If there is a leak in the packer system, the flow rate will become steady or constant after approximately 30 to 50 minutes. If there are no leaks in the packer system, then the flow rate will drop off to zero voltage. Fittings should be tightened if there are leaks and the leak test should be repeated using the same procedure and the 0-100 SCCM flowmeter.

The packer system is said to be tight (i.e., no leaks) when the maximum flow rate using the 0-100 SCCM flowmeter is less than 1 SCCM (0.05 V). A leak-detection test should be performed each time fittings are put together or loosened for transport. Leak-detection tests do not have to be performed if the injection lines and manometer lines are not tampered with when the packers are deflated or inflated during the fracture testing procedure.

-----  
 Table 3.10 Sample flow test.  
 -----

TIME	PRESSURE DIFFERENCE (cm Hg)	PRESSURE TRANSDUCER (mV)	FLOW RATE (V)	COMMENTS
14:32	60-40 = 20	19.95	0.95	- flowmeter used - temperature - no flow, flow, etc.

-----

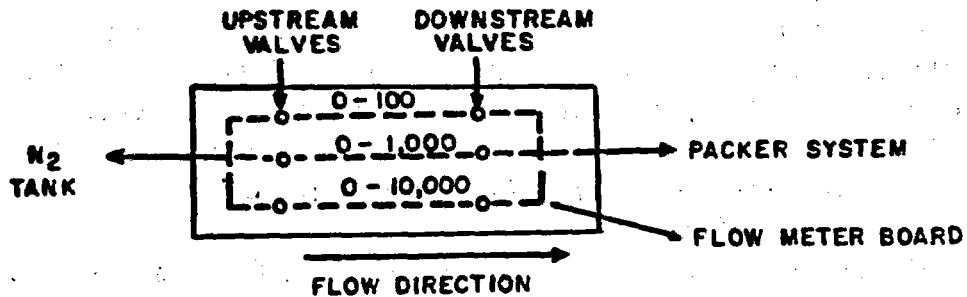


Figure 3.47 Arrangement of valves for packer system.

Once the packer system has been tested for leaks it can be used to measure fracture apertures. First, the packers are lowered in place and inflated. The borehole number, test date, depth to the middle of the injection zone length are then noted. The flowmeters are adjusted to zero flow (i.e., zero output voltage) with both the upstream and downstream valves closed.

The test is started using the 0-1000 SCCM flowmeter. The downstream valve is opened until a reading of 2 V is obtained. The system should then be allowed to come to steady state (i.e., constant pressure and flow rate). Once steady-state conditions have been reached the following information should be recorded: (1) Time; (2) Flow rate (V); (3) Pressure difference read off of manometer (cm Hg); (4) Pressure-transducer reading (mV); and (5) Any comments concerning the test. It is extremely important to note which flowmeter was used for the test.

A second data point should be taken using the same procedure. This time, also using the same 0-1000 SCCM flowmeter, the flow rate should be set at approximately 4 V output. If this cannot be achieved without increasing the injection pressure above that of the manometer range, then the flow rate should be reduced instead. After the system comes to steady state the pertinent readings should be made. Table 3.11 summarizes the testing procedure.

-----  
Table 3.11 Summary of the single-hole pneumatic testing procedure.  
-----

I. Leak Detection Test

- A. Place packers in plastic pipe.
- B. Inflate packer.
- C. Inject gas into system using 0-10,000 SCCM flowmeter.
  - 1. If flow rate becomes constant then leaks exist.
    - a. Check fittings and tubing for leaks - repeat C.1.
  - 2. If flow rate drops off to 0 then no leaks.
- D. Inject gas into system using 0-100 SCCM flowmeter.
  - 1. If flow rate becomes constant then leaks exist. Repeat C.1.
  - 2. If flow rate drops off to less than 0.05 V, no leaks exist.

II. Fracture Test

- A. Place packer at desired depth.
  - 1. Record borehole being used, depth to center of injection zone, injection-zone length, etc.
- B. Zero flowmeter.
- C. Open downstream valve.
- D. Open upstream valve until flow rate is approximately 2 V.
  - 1. Allow system to come to constant pressure and flow rate.
  - 2. Record time of day, flow rate, pressure difference from manometer, pressure transducer reading, and any comments.
- E. Open upstream valve again until 4 V output is reached.
  - 1. If flow rate reaches 4 V:
    - a. Allow system to come to steady state; and
    - b. Record information under D.1. above.
  - 2. If flow rate of 4 V cannot be reached without exceeding the range of the manometer:
    - a. Drop flow rate below 2 V;
    - b. Allow system to come to steady state; and
    - c. Record information under D.1.
- F. Deflate packers and move on to next fracture.

## CHAPTER 4 NONISOTHERMAL HYDROLOGIC CHARACTERIZATION

Geologic media near HLNW repositories will reach high temperatures as the result of heat generated by the radioactive decay of the waste (Wang et al., 1981). The resulting temperature gradients will alter the ambient-moisture flow field by changing the distribution and physical properties of water residing in the surrounding rock. This could give rise to a liquid-vapor countercurrent flow system in the rock pore space surrounding the subsurface HLNW disposal facility.

Liquid water near the repository will evaporate more readily due to the higher temperature surrounding the repository. Because water vapor density increases with increasing temperature, the thermally-induced temperature gradient will cause water vapor to diffuse away from the repository and condense where the rock is cooler. The creation of a dry zone near the repository and a wetter zone away from the repository will create a potential for flow of liquid water back towards the facility.

Temperature gradients will persist for centuries in rock surrounding a repository. Initially, liquid water will flow more slowly in this system than water vapor, in part because hydraulic conductivity falls very rapidly with decreasing water content, while vapor diffusivity increases as the rock water content decreases. For this reason, net moisture flow will initially be directed away from the repository. The flow could maintain a dry zone near the repository while simultaneously maintaining a moist zone at a greater distance from the repository where the rock is near ambient temperature. The dimensions of the flow system are to a large extent controlled by the thermal properties, the pore-size distribution, and the initial water-content distribution of the rock surrounding the repository, as well as by the intensity and persistence of the radioactive-decay heat source.

Soluble radionuclide migration toward the accessible environment will tend to be contained within the zone of the countercurrent flow system by liquid-water return flow. The high temperature zone will inhibit the release of soluble radionuclides to the accessible environment, provided the countercurrent flow system lies within the confines of the geologic medium selected for the repository.

Experimental work (e.g., Gurr, Marshall and Hutton, 1952) supports the countercurrent phenomenon, showing that a steady thermal gradient can give rise to a liquid-vapor countercurrent in closed systems of unsaturated soil materials. A number of investigations, including those

of Taylor and Cavazza (1954) and Cassel, Nielsen and Biggar (1969), have reported measuring transfer coefficients for water vapor-movement resulting from thermal gradients in various soil types.

While the countercurrent phenomenon has been established for soils, published experimental investigations of countercurrent flow systems operating in unsaturated rock are lacking. Likewise, measurements of vapor and liquid transfer coefficients for unsaturated rock are limited.

The objectives of this chapter are:

- To demonstrate the existence of the thermal countercurrent phenomenon in unsaturated rock;
- To evaluate the effect of rock type on the formation of the thermal countercurrent; and
- To present a method for estimating unsaturated flow parameters from laboratory scale heating experiments.

Axial temperature gradients have been established in sealed, unsaturated sand and rock cores and maintained until steady distributions of temperature and moisture content were observed. The laboratory experiments have been designed to permit the resulting unsaturated flow system to be modeled as a one-dimensional system.

Also, a heat source has been placed in a borehole within a fractured tuff medium. The heat source was used to establish a temperature pulse, and the resulting temperature, water content and water potential have been measured in a nearby observation borehole, as well as in the source borehole following the heating phase.

Finally, a numerical model is presented which incorporates the physical processes. The simulation model is useful for confirming observed distributions of temperature, water content and water potential at various distances from a heat source.

#### 4.1 Laboratory Experiments Using Gamma Attenuation

Bouyoucos (1915) proposed that soil water can move in response to a temperature gradient. The study by Gurr et al. (1952) of closed unsaturated soil systems subjected to a temperature gradient provided evidence of a liquid-vapor countercurrent system operating under these conditions. These investigators found that liquid water moved towards the heated end of a soil column while water vapor moved towards the cooled end.

The observed vapor flux was far greater at intermediate water contents than that predicted by a Fickian diffusion model modified for porous media. Taylor and Cavazza (1954) found that the movement of water from warm to cool regions occurred mainly in the vapor phase and was accompanied by a liquid water return flow in response to the induced, matric potential gradient.

The heat flux through a porous unsaturated rock is the result of contributions from heat conduction through the rock matrix, the pore water, the pore air, heat convection accompanying movement of pore fluids, and the transfer of latent heat (Philip and deVries, 1957). The transfer of heat by evaporation near a heat source and the subsequent vapor movement and condensation downgradient releasing the latent heat of evaporation is known as heat piping, and can transfer heat rapidly with a small temperature gradient (Grover, Cotter and Erickson, 1964).

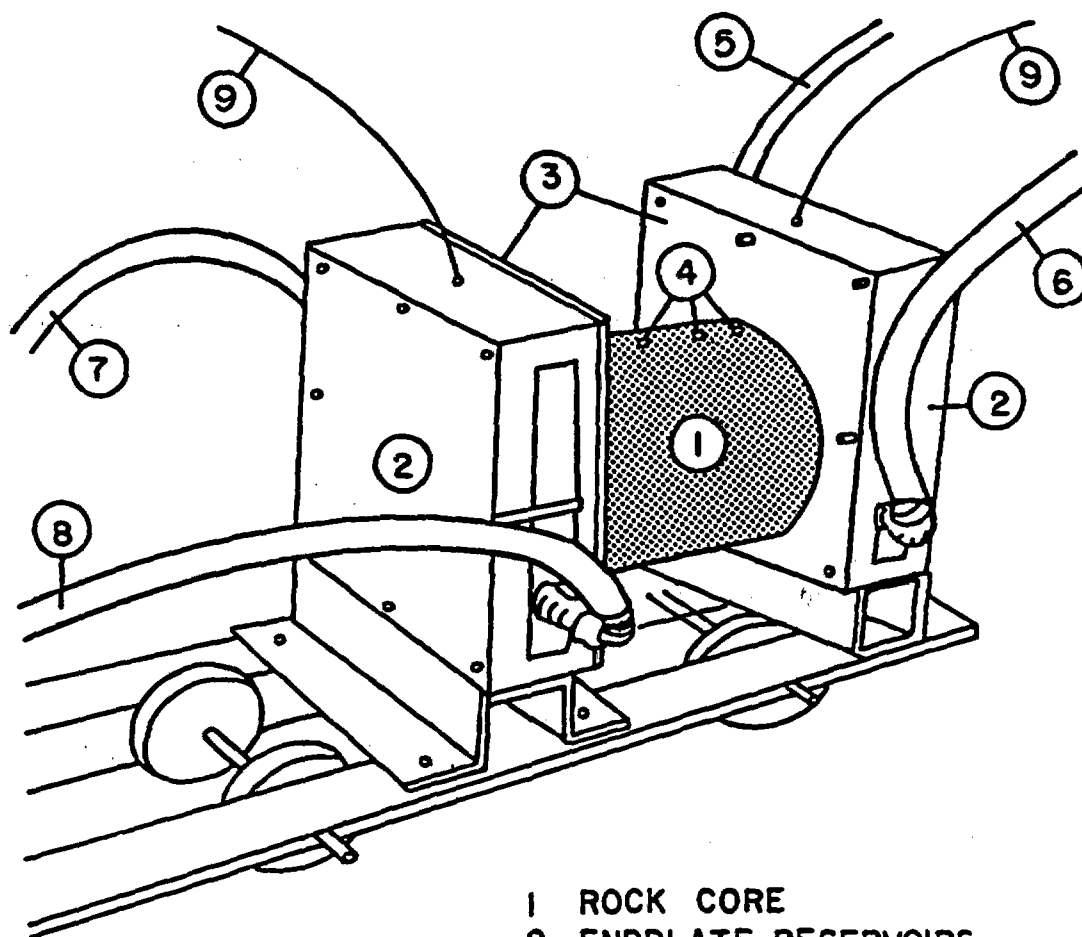
Philip and de Vries (1957) tried to reconcile the observed vapor flux rates with the theory of diffusion in unsaturated porous media. Cary and Taylor (1962) developed equations for heat and moisture transfer in unsaturated soil subjected to temperature gradients using the theory of thermodynamics of irreversible processes.

Cassel et al. (1969) measured moisture movement in response to steady temperature gradients in sealed cylinders of uniformly-packed, fine sandy loam at several different initial water contents. They observed countercurrent flow with maximum moisture transfer at intermediate, initial water contents. Their observed vapor fluxes agreed closely with that predicted by the theory of Philip and de Vries, while the Taylor and Cary expression underestimated the vapor flux in all cases.

Another experimental study (Tromble, 1973) concluded that neither the Taylor and Cary model nor the Philip and de Vries physically-based formulation was entirely successful in predicting the observed vapor flux in a closed, heated soil column.

#### 4.1.1 Equipment and Procedures

Heating experiments have been performed on a sand core and on diamond-drilled, rock core samples. The bulk density and water content of the cores were measured using gamma attenuation equipment originally built (Thames and Evans, 1968) to measure water content of soil columns during infiltration experiments. A core was mounted on a steel carriage, shown in Figure 4.1, which has an aluminum track to carry the cylindrical core sample into the path of the gamma-ray beam.



- 1 ROCK CORE
- 2 ENDPLATE RESERVOIRS
- 3 ALUMINUM ENDPLATE
- 4 THERMOCOUPLE PORTS  
(FIVE TOTAL)
- 5 PRECOOLED WATER INLET
- 6 PRECOOLED WATER OUTLET
- 7 PREHEATED WATER INLET
- 8 PREHEATED WATER OUTLET
- 9 ENDPLATE RESERVOIR THERMOCOUPLE

Figure 4.1 Heating experimental carriage.

Temperature gradients were established lengthwise along the rock cylinders. Initial, transient, and final temperature distributions in the cores were monitored by a data acquisition system. The rock cylinder in the heating carriage was wrapped with insulating material to reduce radial heat loss. A pinhole in the plastic vapor barrier coating the rock core sample helped maintain atmospheric pressure in the rock.

Gamma attenuation measurements were made periodically during a heating test until no significant gamma attenuation change could be detected. Bulk density and water content were calculated at specific locations along the length of the core using the gamma attenuation data.

The volumetric water content of a material can be obtained by passing a mono-energetic, gamma radiation beam through the material. The formula is given by Reginato and Van Bavel (1964):

$$(4.1) \quad \theta = - (\ln(I/I_0) - x \mu_r \rho_r) / (x \mu_w \rho_w)$$

where

- $\theta$  is the volumetric water content of the rock;
- $I$  is the measured beam intensity after attenuation by the porous material;
- $I_0$  is the source strength;
- $x$  is the thickness of soil material in the path of the gamma beam;
- $\mu_r$  is the gamma absorption coefficient for the porous material;
- $\rho_r$  is the dry bulk density of the porous material;
- $\mu_w$  is the gamma absorption coefficient for water; and
- $\rho_w$  is the density of the pore water.

The intensity of a gamma radiation beam ( $I$  and  $I_0$ ) is defined as the number of gamma photons counted during a given time interval. As the gamma beam from the source passes through matter, a fraction of the incident photons interact with nuclei in the matter. Most of this interaction is Compton scattering where a photon is deflected with a reduction in energy. The reduction in intensity of the gamma beam (reduction in the number of photons with energies near the 0.66 MeV peak for Cs-137) can be related to the water content or bulk density of the material mounted in the carriage using Equation (4.1). The intensity of the Cs-137 source was fixed and assumed constant for the relatively short duration of these experiments.

Radioactive decay is a random process in which the number of disintegrations occurring during a given time interval is normally distributed about a constant mean for a sufficiently intense source

(MacIntyre, 1970). This implies that the standard deviation of the number of counts occurring in a given time period is approximately equal to the square root of the mean number of counts.

The number of counts recorded for a given configuration of the experimental setup can only be increased by increasing the counting time. This indicates that if the counting time is increased by a factor of 100, the mean number of counts also increases by a factor of 100. As a consequence, the error associated with variations in the number of gamma radiation counts recorded for a set of repetitive measurements only increases by a factor of ten. The relative error (the standard deviation of a series of measurements divided by the mean number of counts) decreases with increasing mean counts. Therefore, the precision of measurement is improved by increasing the counting time.

The equipment used for gamma attenuation measurements consists of a 110 millicurie Cs-137 source enclosed in a 5-cm, thick lead shielding unit; a sodium-iodide crystal gamma detector also mounted in a lead shield; and associated electronics to process and record the detector signal. The source and detector are mounted in a heavy steel frame and separated by a 25 cm air gap through which the carriage passes carrying the core sample (Figure 4.2). All of the electronics in the detector system, consisting of an automatic, gain control amplifier; a discriminator unit; a timer; and a six digit counter, were manufactured by Harshaw Electric. The discriminator was operated in integral mode to pass a signal marking the arrival of all gamma photons with energies greater than 0.51 MeV.

Initial tests to assist in developing the experimental techniques were conducted with plexiglas columns packed with washed silica sand. A clear plexiglas column, 12.7 cm long with an inside diameter of 8.9 cm, was packed with dry sand. A solution of Schaefer water-soluble black ink in water was slowly added to the sand column until the tracer was visible throughout the column. To obtain a uniform, initial water content, the saturated sand column was placed on a 1-bar porous plate. The plate was then placed in a porous-plate moisture extractor at a pressure of 2/3 bar for a period of five days.

Upon removal from the moisture extractor, the average water content was determined gravimetrically. Aluminum endplates were fastened to the ends of the sand column with Dow RTV silicone-adhesive sealant compound. This assembly was secured to the carriage and insulation was wrapped around the column.

- 1 Power Supply
- 2 High Voltage Power Supply
- 3 Timer
- 4 Six Digit Counter
- 5 AGC Amplifier
- 6 Linear Amplifier
- 7 Gamma Detector
- 8 Lead Detector Shield
- 9 Gamma Beam Collimater
- 10 Cs-137 Gamma Source
- 11 Lead Source Shield
- 12 Aluminum Track
- 13 Endplate Reservoir
- 14 Insulation
- 15 Precooled Water Inlet Port
- 16 Precooled Water Outlet Port
- 17 Steel Frame

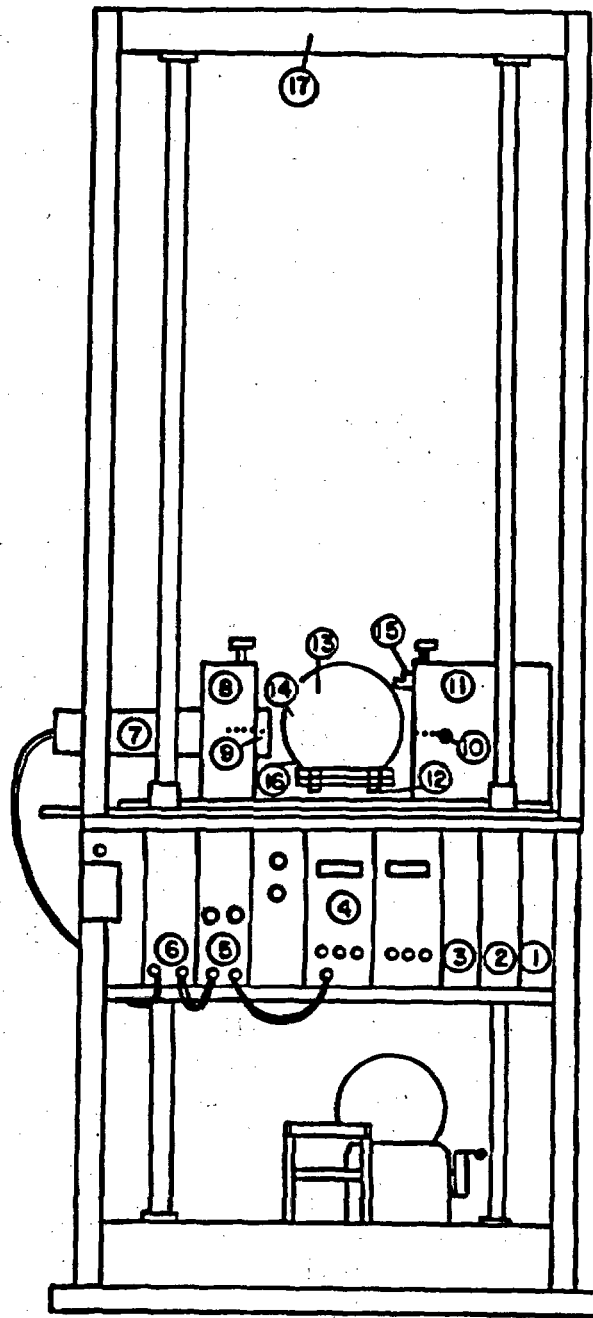


Figure 4.2 Gamma attenuation equipment.

Initial gamma attenuation measurements under isothermal conditions in the sand column were used to calculate the bulk density distribution along the column by assuming that the initial gravimetrically estimated water content was uniformly distributed. Equation (4.1) was rearranged to give the bulk density:

$$(4.2) \quad \rho_r = (-\ln I/I_0 - x\rho_w\theta u_w)/(xu_r)$$

Subsequent calculations of water content under nonisothermal conditions using Equation (4.1) were made using this bulk density distribution.

The endplate reservoirs at the hot and cold ends were maintained at temperatures of 40 and 20°C respectively for nine days. For this initial experiment, temperature sensors were placed in the sand column. Periodic measurements of water content were made over several days, until the water-content changes became small. The tracer added to the solution used to saturate the sand column was intended to trace liquid-water flow. The final distribution of tracer in the sand column was viewed at the end of the experiment by carefully scooping out half of the sand (lengthwise) in the clear plexiglas column.

Rock cores were prepared from a fine-grained sandstone, a slightly-welded ash-flow tuff, and a densely-welded ash-flow tuff. The cores (10.2 cm in diameter) were diamond-drilled from each rock sample using water as the cutting fluid. The cores were cut to a length of 12 to 13 cm with a diamond-tipped saw using an oil-based cutting fluid and washed with acetone to remove the cutting fluid. Then the rock cores were placed in a convection oven and heated for five days at 105°C. The dry cores were weighed and wrapped in plastic to prevent moisture entry. The average bulk density of the dry cores was calculated from the measured volume of the cores and their weight after drying. Each rock core cylinder was individually secured in the carriage described above. Bulk density was measured at 1-cm intervals along the length of the core by means of the gamma attenuation method.

After the bulk density measurement, individual rock cores were placed in a desiccator vessel and the vessel was evacuated for 24 hours to remove pore air. Deionized water containing 100 ppm fluorescein was released into the chamber to saturate the rock cores. Fluorescein is strongly fluorescent under ultraviolet light and is a simple but effective tracer of liquid-water movement. Vacuum was maintained during water entry so that water could infiltrate the core samples without entrapping air. Heating experiments were not performed on nonwelded ash-flow tuff cores because the samples swelled and cracked on wetting.

Previously wetted rock cores were desaturated under controlled conditions similar to those used for the sand column. However, moist bentonite clay spread on a damp filter paper was placed between the porous plate and the rock core. This improved the hydraulic contact between the somewhat curved surface of the porous plate and the flat end of the rock cylinder. A pressure of 2/3 and 1 bar, for the sandstone and the tuff, respectively, was used to reduce the water content. The cores were left for five to seven days in the moisture extractor.

After desaturation, the rock cores were sprayed with a quick-drying varnish and dipped in an air-dry, liquid plastic (PDI, Inc., Plasti-Dip) compound to prevent moisture loss during the heating experiments. Aluminum plates were fastened to each end of the rock cores with heat-conducting, water-resistant epoxy. Three holes (0.3 cm in diameter and 2 cm deep) were drilled at intervals along the length of each rock core. Thermocouple leads were inserted in these ports and sealed in place with Dow RTV silicone-adhesive sealant compound.

Water could be circulated through the endplate reservoirs over a temperature range of 1 to 100°C, measured to a precision of  $\pm 0.5^\circ\text{C}$ . Precise control of the cooled water was provided by a Forma Scientific Model 2095 bath and circulator, while the heated water was controlled by a Braun Thermomix Model 1460 heater. Average temperature in the cores was maintained near ambient temperature, 22°C, in order to reduce radial heat losses; therefore, the hot bath could not exceed 45°C.

Water containing fluorescein dye was used to saturate the rock cores. The purpose of the dye was to provide evidence of liquid-water flow. The initial tracer distribution was assumed to be strongly correlated with the initial water-content distribution. The concentration (percent by weight) of tracer in the rock should not change from the initial distribution unless it is altered by liquid water flow moving the soluble tracer.

At the end of an experiment, the rock core was cut in half, lengthwise, to observe the distribution of tracer on the face of the cut. The relative intensity of the fluorescein dye was determined along the axis of the core. In addition, the half core was sectioned and the sections pulverized. Deionized water was added to 40 gm samples of the crushed rock to make 50 ml solutions. The solutions were stirred and then allowed to sit for 24 hours before 10 ml of solution was filtered from the 50 ml samples. The filtrate from each section of the rock cylinder was ranked by the intensity of fluorescence under ultraviolet light.

Moisture-release curves were determined for samples of sandstone and tuff using the porous plate apparatus, as discussed by Richards (1969). Rock discs (five cm in diameter and two cm thick) were saturated by means of the vacuum procedure, discussed previously. The saturated discs were placed on moist filter paper and bentonite clay and set on a saturated extractor plate. An overpressure was applied until the water within the rock discs came to equilibrium with the applied pressure. The discs were then removed and their weights determined. The discs were then returned to the extractor and reweighed after two additional pressures were applied. The retained moisture versus pressure curve is the moisture release curve which can be used to find the pore size distribution for the sample.

#### 4.1.2 Results and Conclusions

Laboratory experiments were performed to determine how an imposed heat field affects the movement of liquid and vapor on three different geologic media. The media ranged from unconsolidated silica sand to a consolidated sandstone core, and finally to a welded tuff. The samples were of variable porosity and homogeneity, with the welded tuff being the least homogeneous. By varying the media, a better understanding was obtained of the physical parameters which affect the movement of fluid and vapor, as well as heat conduction, in geologic media. The extension of these results to in situ tests is reserved for Section 4.2.

The simplified experiment used to develop experimental techniques was run on a plexiglas column uniformly packed with washed silica sand. The average bulk density of the sand column was  $1.5 \text{ gm/cm}^3$  (Table 4.1), using a grain density of  $2.65 \text{ g/cm}^3$ . The average water content for the column was measured as 3.4 percent by volume and was assumed to be uniform throughout.

The experiment was initiated by applying a temperature difference of  $20^\circ\text{C}$  across the two ends of the column. Steady state was attained after nine days. A dry zone was created in the sand column extending 2.5 cm from the hot face of the column, while the water content at a point near the cold face of the sand column increased from 3.4 percent to 7.7 percent (Figure 4.3 and Table 4.1). This redistribution was caused by the vaporization and subsequent movement of water vapor from the hot end to the cold end, where the vapor condensed.

Liquid-water return flow (from the cold end to the hot end) deposited tracer in a darkened disk where the liquid flow intersected the dry zone

created by vapor movement away from the heat source. The darkened disk was concave towards the cold end, indicating that vapor flux was greater at the central axis of the sand column than along the boundaries. This suggests that radial heat loss may have occurred.

The darkened disk was tilted from a vertical plane, with the lower edge 0.5 cm closer to the hot face. A convection cell operating in the sand column would tend to enhance the axial vapor flux along the top of the horizontal column (and also liquid flow near the bottom), causing the dry zone to extend further from the hot face. This indicates that gravitational effects on moisture movement may not have been negligible.

The bulk density of the sandstone core was found to range from 2.08 to 2.20 gm/cm<sup>3</sup>, averaging 2.15 gm/cm<sup>3</sup>. The initial water content ranged from 2.4 percent to 9.9 percent (Table 4.2 and Figure 4.4). These variations indicate considerably more heterogeneities within the core than was anticipated from visual inspection. The variability also implies a large variation in hydraulic conductivity and vapor-diffusion coefficients. Because of the variability, one can expect a more complex water-content distribution over time than would develop in a homogeneous medium.

An average temperature gradient of 2.2°C/cm was established within the core, with a maximum temperature of about 36°C. The sandstone core reached steady state after twelve days of heating. Water content decreased from 4.7 percent to 2.7 percent at a point near the hot face of the sandstone core while water content increased from 7.3 percent to 9 percent at a point near the cold face. Water content decreased during the experiment at a point 11.5 cm from the cold face, stabilizing after twelve days of heating. Water content increased at a point 1 cm from the cold face, decreasing only between the first and the fifth days and between the ninth and the eleventh days. Water content near the midpoint of the core remained stable throughout the experiment.

Figure 4.5 shows the difference in volumetric water content between the intact core and sections of the core analyzed following the experiment. The intact core retained more water with much more variation in water content than did small slices of that core. This indicates that the saturated rock core was not at a uniform, initial water content.

The initial concentration of fluorescein tracer in the solution used to saturate the sandstone core was 6.0 ppm. When the core was cut in half lengthwise at the end of the experiment, no fluorescein tracer was visible using natural or ultraviolet lighting. The relative amount of

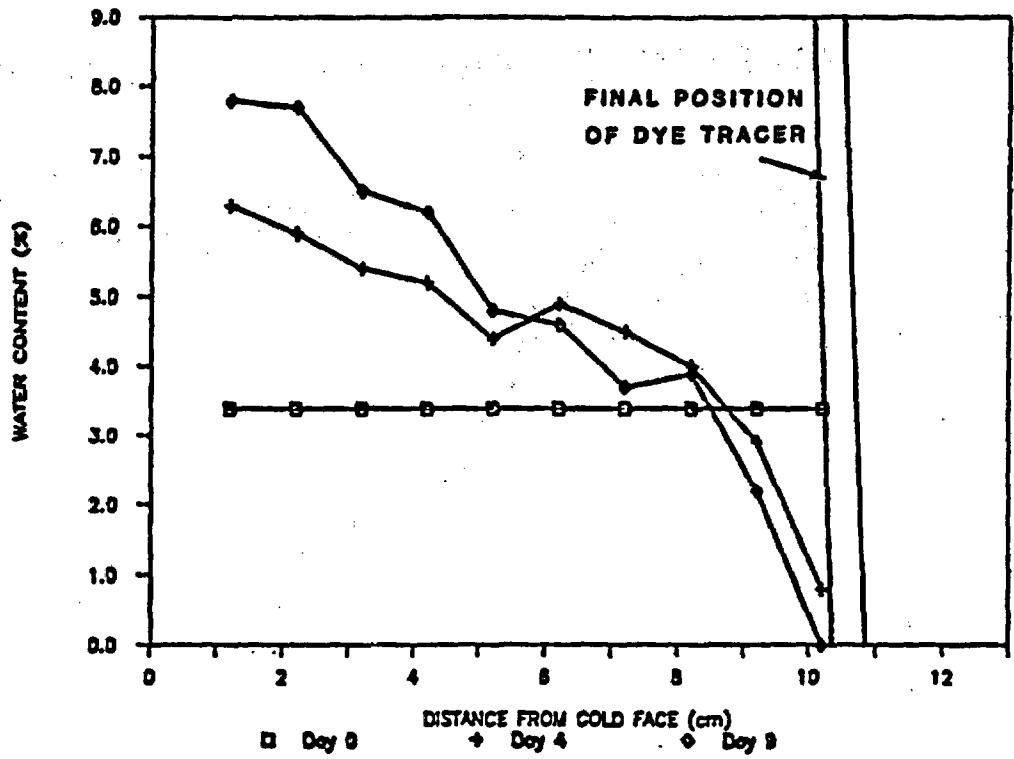


Figure 4.3 Comparison of initial and steady state water content changes for sand column.

## SANDSTONE CORE HEATING EXPERIMENT

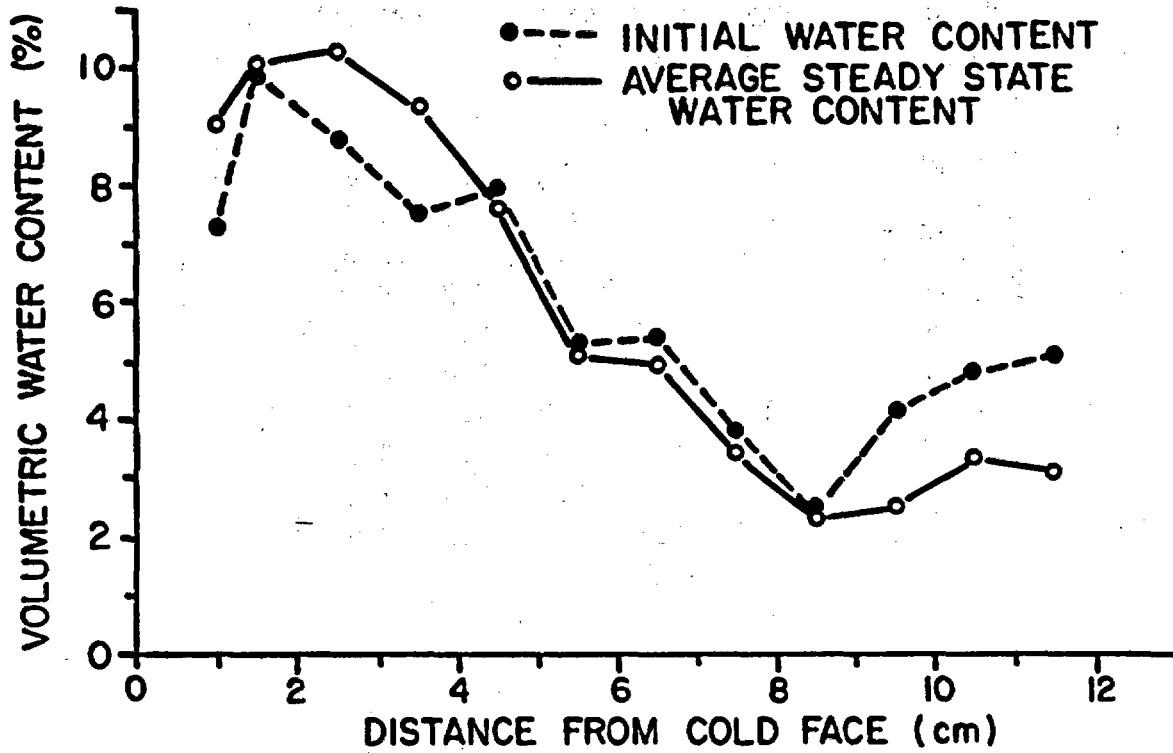


Figure 4.4 Comparison of initial and steady state water content changes for sandstone core.

-----  
**Table 4.1 Sand column countercurrent experimental results.**  
 -----

Distance (cm)	Dry bulk density (gm/cm <sup>3</sup> )	Water content (percent by volume) - Days after start of experiment -				
		0	2	4	5	9
0.0		- COLD FACE -				
1.2	1.51	3.4	4.4	6.3	6.1	7.8
2.2	1.55	3.4	3.7	5.7	5.6	7.7
3.2	1.56	3.4	3.7	5.7	5.6	7.7
4.2	1.52	3.4	3.5	4.6	5.2	6.2
5.2	1.55	3.4	3.8	5.1	5.3	4.8
6.2	1.55	3.4	3.6	4.7	5.0	4.6
7.2	1.53	3.4	3.6	4.0	4.4	3.7
8.2	1.51	3.4	3.7	3.1	2.9	3.9
9.2	1.56	3.4	2.9	2.9	2.5	2.2
10.2	1.52	3.4	2.3	0.0	0.0	0.0
12.0		- HOT FACE -				

-----

-----  
**Table 4.2 Sandstone core countercurrent experimental results.**  
 -----

Distance (cm)	Dry bulk density (gm/cm <sup>3</sup> )	Water content (percent by volume)								
		----- Days after start of experiment -----								
		0	1	3	5	7	9	11	13	16
0.0		- COLD FACE -								
1.2	2.18	7.3	8.8	8.4	8.2	8.4	9.8	8.7	9.1	9.2
1.5	2.12	9.9	9.6	9.7	9.7	9.4	9.7	9.6	10.0	9.9
2.5	2.13	8.8	8.8	9.0	9.6	8.8	9.5	9.0	10.4	9.8
3.5	2.10	7.5	7.6	8.9	9.3	8.1	8.7	8.4	9.2	9.0
4.5	2.08	7.9	7.9	7.9	7.9	7.7	7.6	7.6	7.6	7.3
5.5	2.11	5.3	5.5	5.3	5.4	5.4	5.4	5.4	5.2	5.0
6.5	2.15	5.4	5.1	5.0	4.9	5.0	4.9	4.8	4.6	5.0
7.5	2.20	3.8	3.4	3.3	3.6	3.6	3.3	6.4	3.4	3.4
8.5	2.11	2.4	2.6	2.1	2.4	2.5	2.5	2.4	2.2	2.1
9.5	2.09	4.1	2.8	2.6	2.9	2.8	2.6	2.5	2.5	2.6
10.5	2.09	4.8	3.7	3.2	3.6	3.6	3.4	3.4	3.2	3.3
11.5	2.10	5.1	4.0	3.2	3.7	3.6	3.5	3.3	3.2	3.1
12.0		- HOT FACE -								

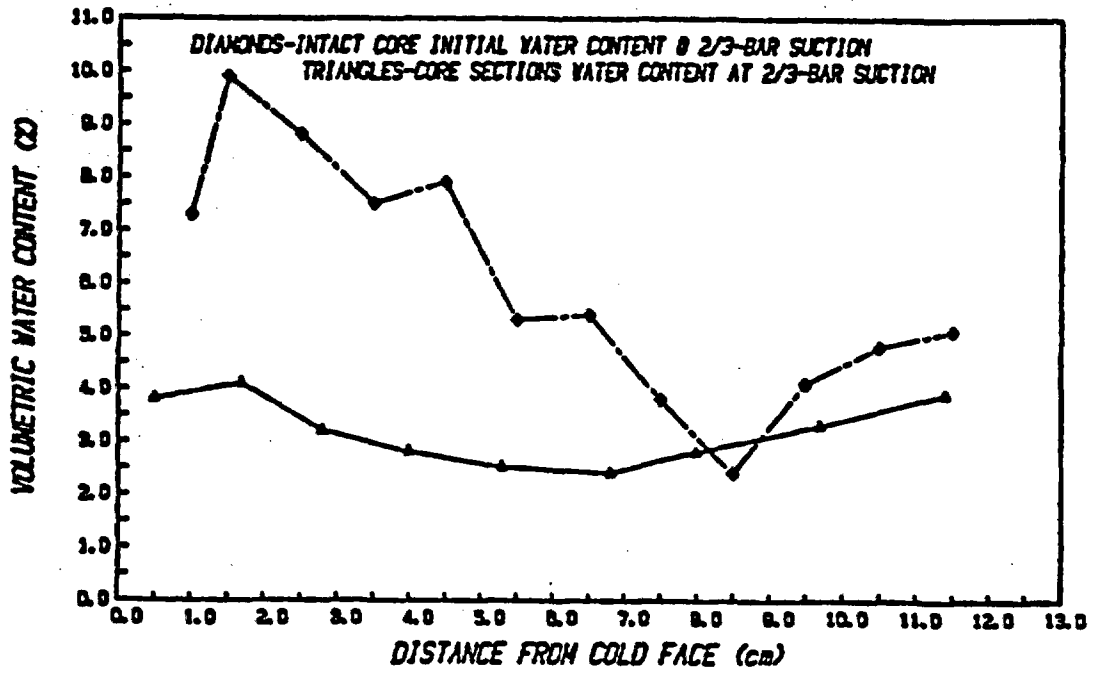


Figure 4.5 Water content of sandstone sample after application of 2/3 bar suction.

tracer found in the filtrate of crushed core sections is shown in Figure 4.6. The initial tracer distribution in the core was assumed to equal the initial water content. The concentration of the tracer in the filtrate was less than 0.1 ppm indicating that the tracer may have been adsorbed by the core.

Figure 4.6 shows that the final tracer concentration was lowest 2 to 5 cm from the cold face and highest in a zone extending from 5 to 8.5 cm from the cold face. The final tracer distribution indicates that liquid-water return flow carried the tracer from cold to warm until an obstruction to flow was encountered 8.5 cm from the cold face. Figure 4.6 also shows that a relatively dry zone existed in the initial water content distribution in this section of the core. This suggests that liquid water flowed from the cold face toward the hot face and that the return flow may have been limited by a low permeability zone resulting from the low, initial water content 8.5 cm from the cold face.

Another heating experiment was conducted on a sealed, slightly-welded tuff cylinder subjected to an average temperature gradient of  $2.22^{\circ}\text{C}/\text{cm}$ . The bulk density of the core averaged  $2.34 \text{ gm}/\text{cm}^3$  (Table 4.3). The grain density was estimated to be  $2.53 \text{ gm}/\text{cm}^3$ . The water content of the five small disks cut from the tuff sample after the experiment averaged 10.4 percent with a standard deviation of 0.2 percent water content. The range of the initial water content in the large core was greater than that of the small slices equilibrated at the same pressure, implying that the core may not have had enough time to reach equilibrium when it was removed from the moisture-extractor device.

Initial and final (i.e., after 21 days) water-content distributions are shown in Figure 4.7. The initial water content is substantially larger than the final water content at all points along the core, indicating that water was lost from the system. The figure shows that the water content in the tuff core decreased steadily throughout the experiment except at a point 0.5 cm from the cold face. The water content at that point decreased between the first and the seventh days then increased to a stable value of approximately 9.3 percent. A quasi-steady state was attained after 16 days of heating.

The water-content change is expected to be greatest near the hot face. The calculated decrease in water content during the experiment at the hot end of the core, 12 cm from the cold face, was similar to the decrease of approximately 2 percent near the middle of the core, 7 cm from the cold face (Figure 4.8). This suggests that liquid-water return flow reduced the water-content change at the hot face.

### SANDSTONE CORE INITIAL WATER CONTENT AND FINAL DYE DISTRIBUTION

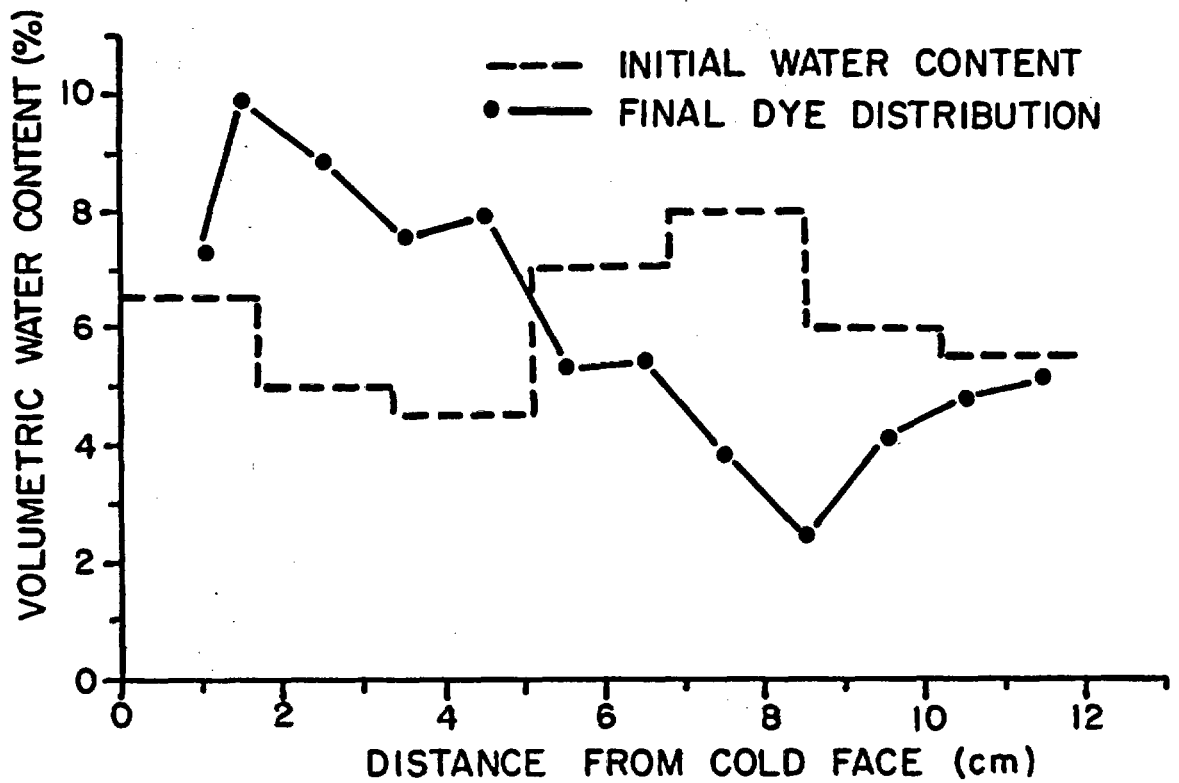


Figure 4.6 Sandstone core tracer distribution.

### TUFF CORE HEATING EXPERIMENT

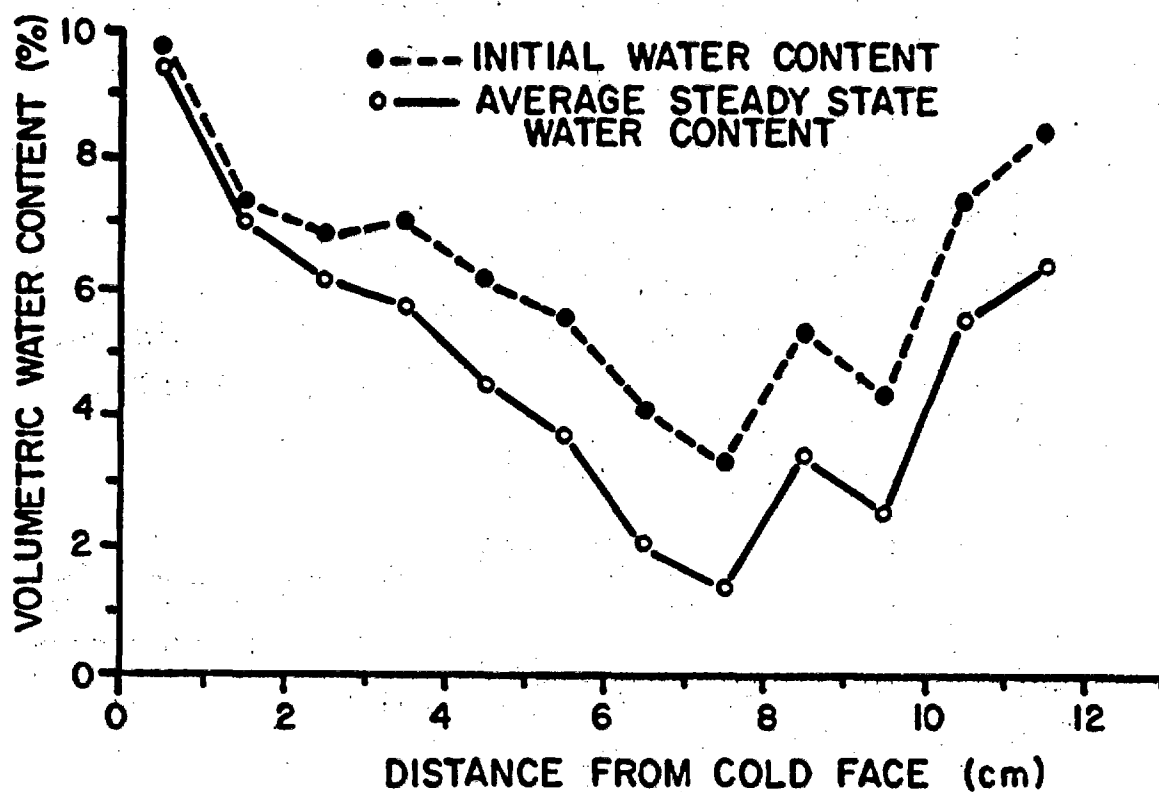


Figure 4.7 Tuff core heating experiment initial and final water content distribution.

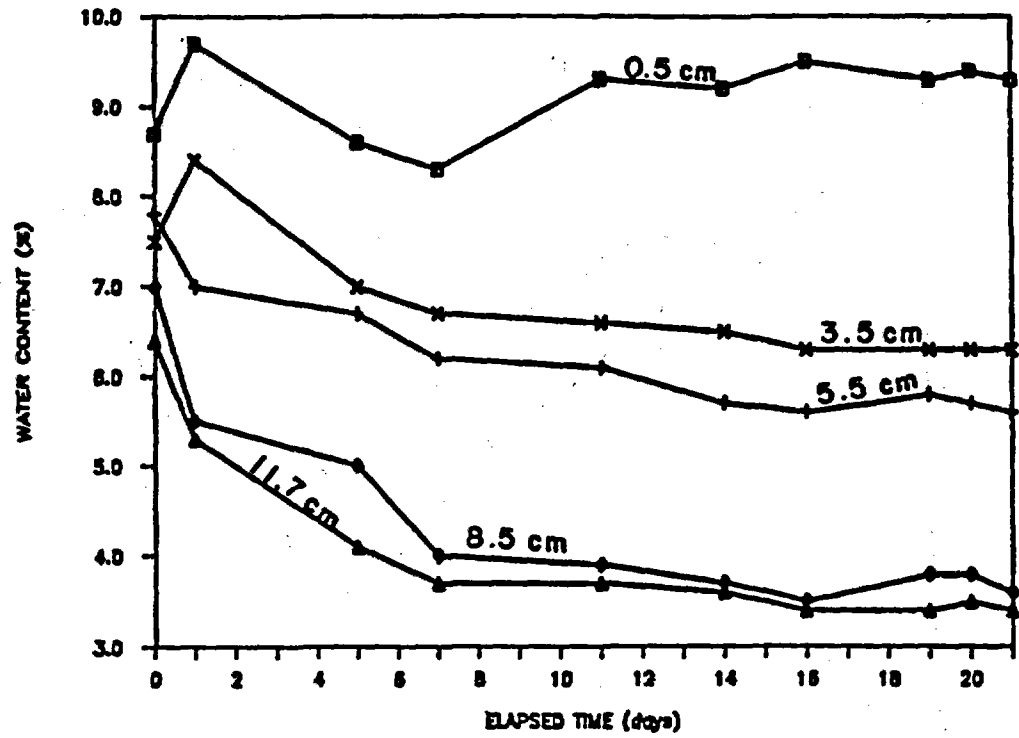


Figure 4.8 Tuff core heating experiment water content changes with time.

Table 4.3 Tuff core countercurrent experimental results.

Distance (cm)	Dry bulk density (gm/cm <sup>3</sup> )	Water content (percent by volume)									
		Days after start of experiment									
		0	1	5	7	11	14	16	19	21	
0.0		- COLD FACE -									
0.5	2.35	8.7	9.7	8.6	8.3	9.3	9.2	9.5	9.3	9.3	
1.5	2.34	6.9	7.3	6.6	6.0	6.7	6.5	6.3	7.3	6.9	
2.5	2.34	7.1	6.8	6.2	5.7	6.2	5.9	5.9	6.3	5.9	
3.5	2.33	7.8	7.0	6.7	6.2	6.1	5.7	5.6	5.8	5.6	
4.5	2.33	7.3	6.1	5.1	4.7	4.8	4.5	4.5	4.5	4.4	
5.5	2.33	7.0	5.5	5.0	4.0	3.9	3.7	3.5	3.8	3.6	
6.5	2.34	5.7	4.1	2.6	2.3	2.0	1.9	1.9	2.0	1.9	
7.5	2.35	4.7	3.3	2.3	1.6	1.5	1.4	1.2	1.4	1.2	
8.5	2.33	6.4	5.3	4.1	3.7	3.7	3.6	3.4	3.4	3.4	
9.5	2.35	6.1	4.3	3.4	2.8	2.7	2.4	2.5	2.3	2.5	
10.5	2.35	7.7	7.3	6.2	5.7	5.5	5.5	5.5	5.7	5.5	
11.5	2.35	7.5	8.4	7.0	6.7	6.6	6.5	6.3	6.3	6.3	
12.0		- HOT FACE -									

At 0.5 cm from the cold face the decrease in the water content was approximately 0.5 percent less than that observed at any other location along the axis of the core. This indicates that vapor flow from the hot end towards the cold end of the tuff cylinder reduced the water-content change at the cold face. Data on the final tracer distribution in the tuff core corroborating moisture redistribution could not be obtained.

The final temperature distributions in the tuff and sandstone cores are shown in Figure 4.9. The thermal conductivity of tuff is greater than that of water and air (Wang et al., 1983). Also the water- and air-filled pore space of this welded tuff core amount to less than 10 percent of the volume of the core suggesting that heat conduction through the solid tuff is likely to be the dominant heat-transport process. The axial temperature data for the tuff core fits a straight line, supporting this premise.

The plot of temperature versus distance from the cold face for the sandstone core is bowed downward. The temperature gradient was lower near the cold end, indicating that the greater water content at the cold

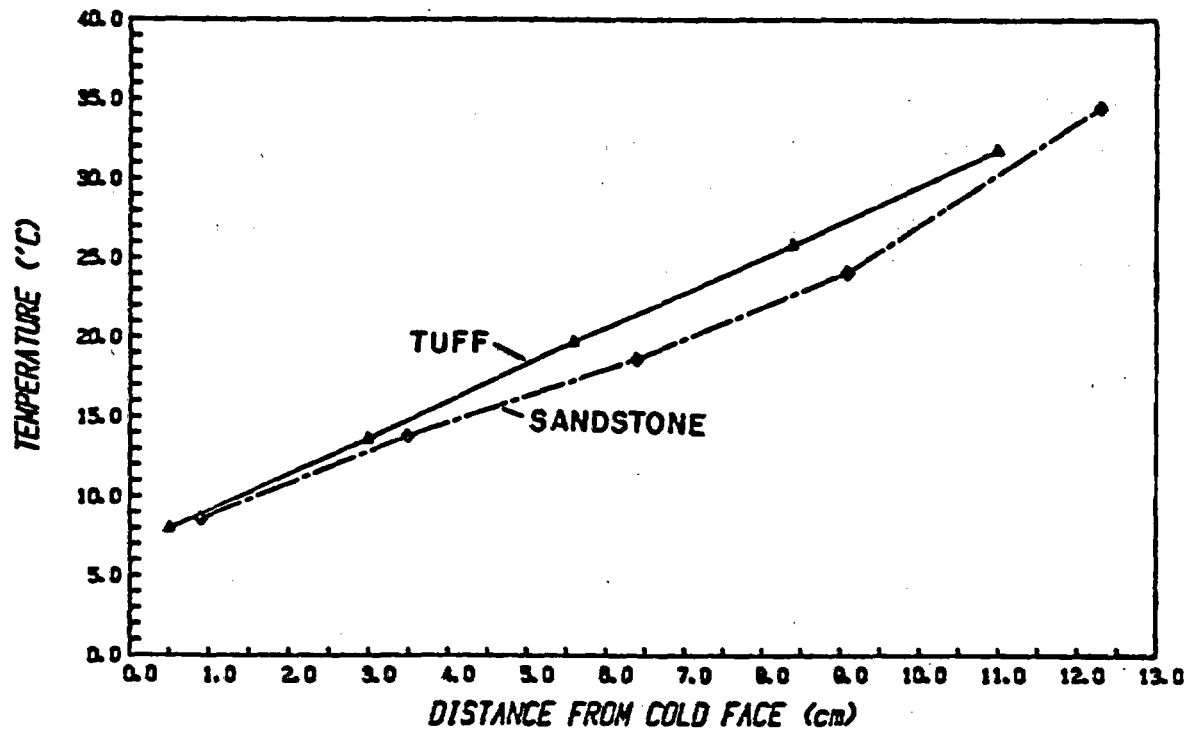


Figure 4.9 Temperature distribution at the end of tuff and sandstone heating experiments.

end significantly increased the thermal conductivity of the core. The water content near the hot end had less effect on the thermal conductivity of the core because there was less liquid water. Transfer of heat by convection and latent heat transport would also make the temperature gradient smaller at the hot end.

In conclusion, countercurrent flow has been demonstrated in heating experiments performed on an unsaturated sand column and with an unsaturated sandstone core. Results of a heating experiment performed on a tuff core also strongly indicates the presence of countercurrent flow phenomenon. The phenomenon was more pronounced in the sand column, followed by the sandstone core, and then by the tuff core.

Heating the sand column results in the creation of a dry zone extending approximately 2.5 cm from the hot face and a sizable water-content gradient with a maximum water content near the cold end. A soluble dye accumulated in a band near the hot end, providing evidence of liquid return flow and a zone of maximum evaporation.

The final distribution of tracer in the sandstone core indicates that liquid-water flow was limited by the presence of a low permeability zone, resulting in a large variation in the water content throughout the experiment. The results for the tuff sample indicates a loss of water from the system during the experiment.

The final temperature distribution observed in the tuff core suggests that conduction is the dominant heat-transport process while the final temperature distribution in the sandstone core indicates that convection and latent heat transfer also contribute to heat transport.

These experiments suggest that countercurrent flow systems might exist in the vicinity of subsurface heat sources in the unsaturated zone. The dimensions of the countercurrent flow system and the rate of moisture movement will depend upon the imposed temperature gradient, on the initial water-content distribution, and on the porosity and pore-size distribution of the surrounding medium.

It is important to note that the rock samples are more variable in water content, porosity, and hydraulic conductivity than sand columns of identical size. These heterogeneities are not always evident from visual inspections. These differences, however, may not be important for larger samples. For this reason, additional field and simulation studies are required to confirm the existence and nature of the countercurrent phenomenon in natural geologic settings.

## 4.2 Field Heating Experiment

A small scale heating experiment was conducted in the densely-welded, fractured tuff at the Queen Creek road tunnel site. The objectives of this experiment were to:

- Measure the changes in temperature caused by the addition of varied amounts of heat.
- Measure the changes in water potential and water content with time.
- Determine instrument problems and power requirements for future heating experiments.

Two nearly-parallel, horizontal boreholes (5 cm in diameter, 15 m long and 0.89 m apart), were used in this experiment (Figure 4.10). (For a description of drilling techniques used, see Appendix E.) A heating element was placed six meters into one borehole, while the adjacent hole was packed off at two locations to form an air space approximately the same distance into the borehole. Three thermocouple psychrometers were installed to monitor changes in water potential and temperature in the air space between the packers. A neutron probe was used to determine changes in the water content of the tuff in both boreholes.

### 4.2.1 Equipment and Procedures

The heating elements used in the experiments are Incoloy 800 sheathed nickel alloy elements manufactured by Dayton. The flange of each element was cut to fit into a combined element and temperature sensor holder (Figure 4.11). The holder is 4.45 cm in diameter and holds the heating element in the borehole, preventing it from coming in contact with the rock. The elements normally use 240 volt current at 60 hertz. While the elements were intended to be used while submersed in a liquid, the application here requires them to be used in air and thus, element burnout was avoided by reducing the voltage to 120 volts. This reduced the heat yield of each element to 1/4 of its potential output.

The two elements used are the 2000 and 6000-watt models, which effectively provide 500 and 1500-watt outputs for the experiments. The element lengths are 23.5 cm and 58.7 cm, respectively. The elements were powered by a field generator and controlled by a thermostat which monitored the temperature of the rock at a point midway along the heating element holder. The thermostat can be adjusted between 100 and 200°C. The thermocouple psychrometers used are manufactured by Wescor and are used in conjunction with a Wescor HR-33T dew point micro-volt meter. Each psychrometer had been calibrated for different temperatures and potentials.

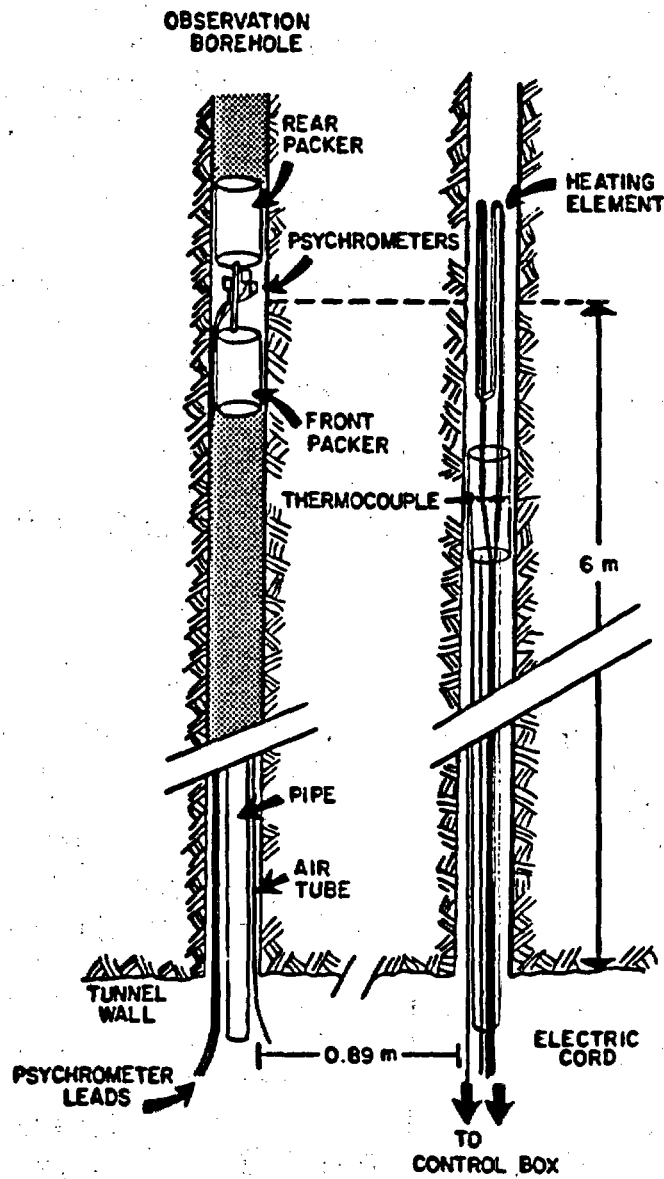


**Figure 4.10** Diagram of heating element and thermocouple located behind packer (right borehole), and packers isolating psychrometers (left borehole) at Queen Creek road tunnel site.

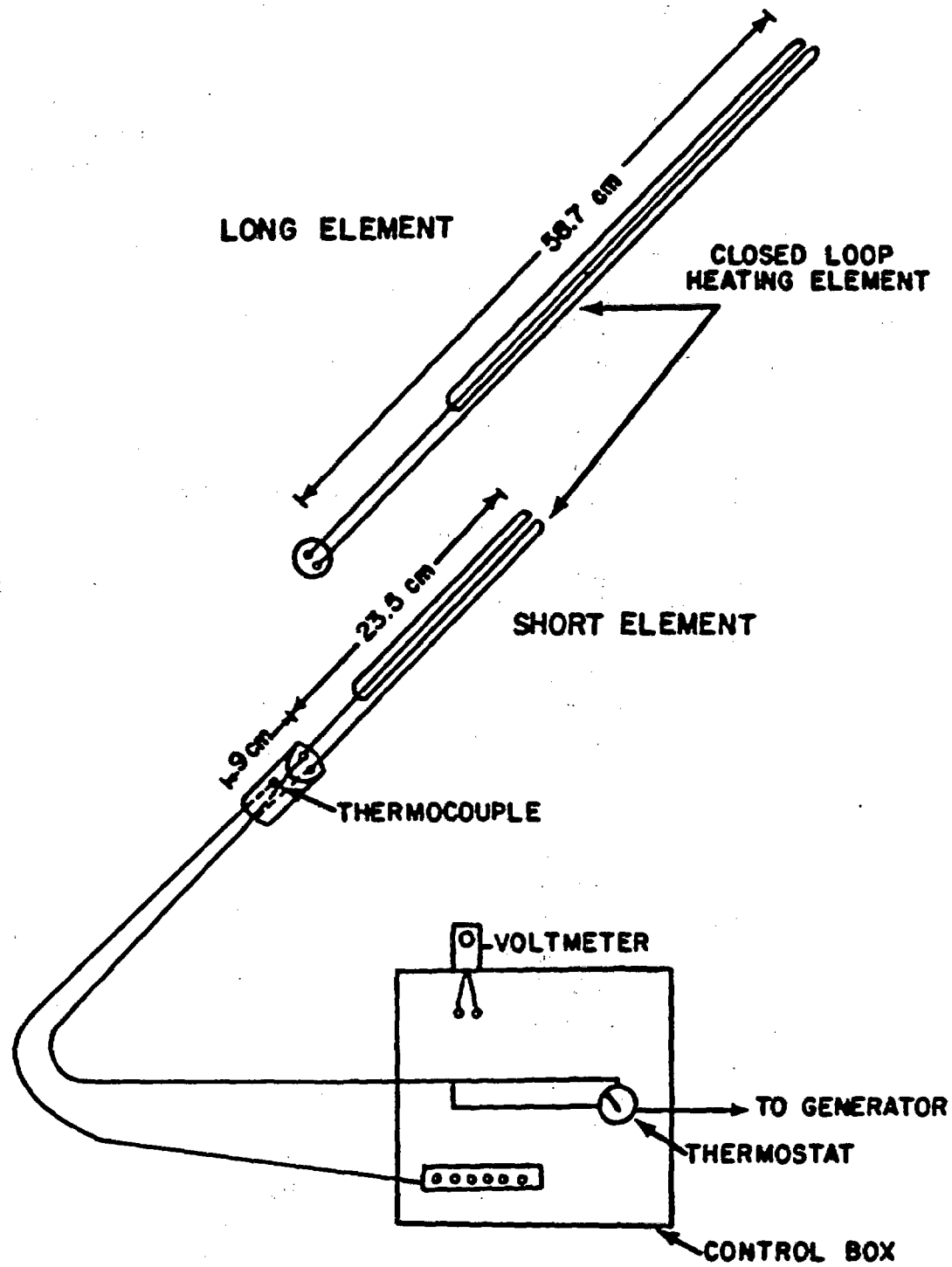


Figure 4.11 Diagram of 500 watt (short element) and 1500 watt (long element) heating units, and wiring to control box.

Bulk water content was measured using a neutron probe (Model 503, Hydroprobe, by Campbell Pacific Nuclear). The initial water content of the tuff was determined by taking three neutron probe measurements over one-minute periods at half meter intervals in the two boreholes. The psychrometers were then installed six meters into the borehole between two packers and allowed to equilibrate for four days to determine the initial water potential. The heating element and the element holder was attached to a pipe and placed in the other borehole at a depth of six meters to the middle of the heating element. Power was supplied by an electric cord running through the pipe to the element and connected to the thermostat control box. The thermocouple wire ran from the spring mechanism along the outside of the pipe to the thermostat.

Temperature and potential measurements in the observation borehole were taken hourly while the heater was operating. Heat was applied for approximately three days with the 500-watt element, then no heat was applied for four days. Finally, heat was again applied using the 1500-watt element for another four days. Neutron measurements were taken after heating to determine the change in water content. The thermocouple psychrometers and packers were removed after each heating period, neutron measurements were made, and the packers were replaced for periodic temperature and potential measurements. Periodic neutron measurements were also obtained in the heated borehole.

#### 4.2.2 Results and Discussion

In the first part of the experiment, the 500-watt element was emplaced and heated for 65 hours. The water content and water potential in the observation borehole did not change during this period, even though the temperature increased from 21.0 °C to 24.8 °C. In the heated borehole, the water content decreased in the immediate vicinity of the heating element (Figure 4.12). These results indicated that additional heat was required to obtain sizable responses in the observation borehole.

The psychrometers were left in place and a second trial was conducted, starting 103 hours after the first trial ended. During the time between the first and second heating episodes, the temperature in the observation borehole fell from 24.8 °C to 23.5 °C and the water content in the heated borehole remained the same. In the second trial, the 1500-watt element was heated for 94 hours. In the observation borehole, the water suction increased from approximately 0.25 to 9.0 bars. This change, and subsequent changes in suction after the element was turned off, are shown in Figure 4.13.

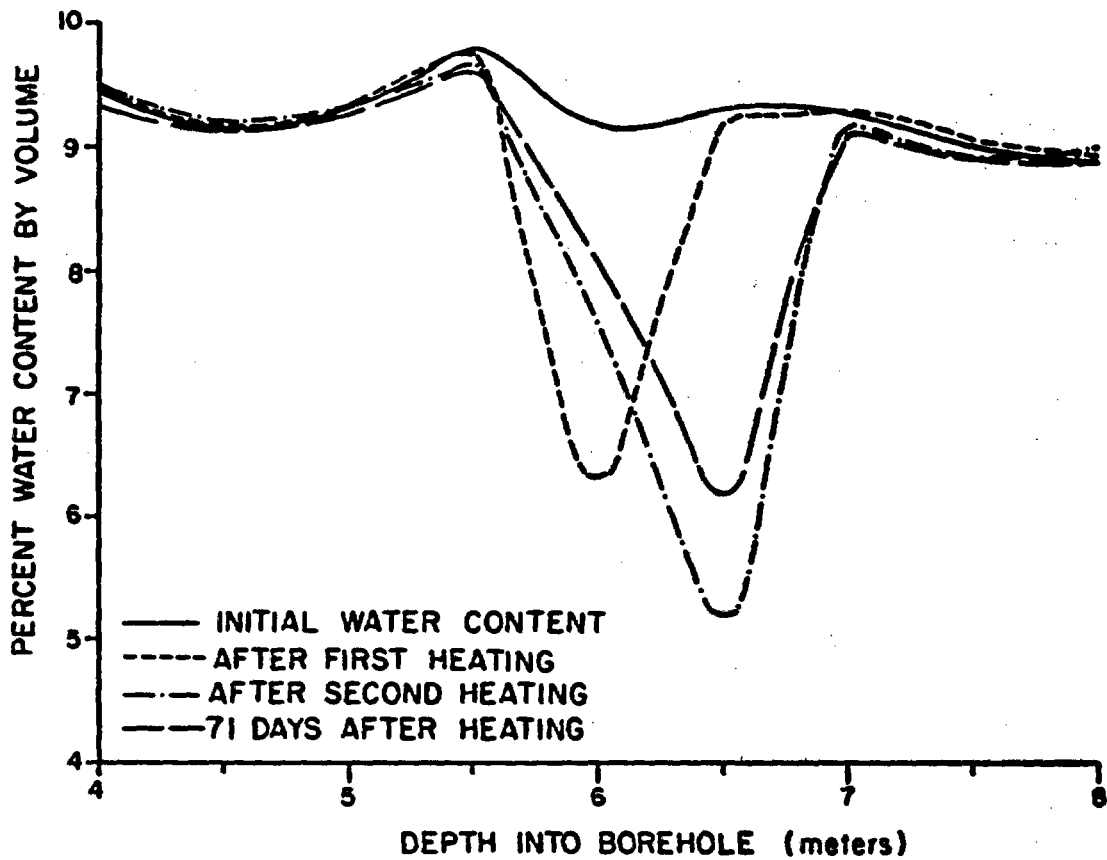


Figure 4.12 Water content against time for heating experiment in the Queen Creek road tunnel.

Data for water potential were obtained using the dew point method and the psychrometric method. The psychrometric method consistently indicated suction readings 0.5 to 1.5 bars above those determined using the dew point method. Data for Figure 4.13 were derived by averaging the values from the two methods. The psychrometer method is not considered accurate above 2 bars suction and, therefore, the initial and final measurements only provide qualitative information about changes in water potential.

The temperature in the observation borehole increased during the time of heating, from 23.5 to 29.5°C (Figure 4.14). The temperature continued to rise for 28 hours after the heating was stopped, and then gradually decreased. Temperature measurements taken in the heated borehole were made by a thermocouple attached to the element holder. At that position, the temperature of the rock increased to 90°C in 48 hours and continued to slowly rise after that to 91.5°C by the end of the heating period. After the heating was stopped, the temperature fell 9.9°C in the first 30 minutes of recovery. The sensor was then pushed further into the hole and allowed to equilibrate. One hour after the heating, the temperature of the rock adjacent to the former heating element position was 132.3°C.

During the second trial, the heating element was mispositioned by 0.36 meters, which resulted in the center of the element being located at 6.36 meters into the borehole instead of 6 meters. The results of this misplacement can be observed in Figure 4.12 which shows the change in water content in the heated borehole after heating with the 1500-watt element. The results show an increase during the second heating period near the 6-meter depth. The neutron method reflects a weighted average water content over a diameter of a few tens of centimeters (the precise diameter has not yet been determined for this site). Therefore, sharp changes in water content cannot be determined.

Seven days after the heating was stopped, the temperature in the observation borehole had dropped to 27.0 °C and the water potential had dropped to near its initial state. Although the suction had increased to approximately 9 bars during this trial no change in water content was observed. This indicates that a small change in water content can result in a large change in the suction for the range measured.

The recovery of the water content in the heated hole was very slow, as evidenced by the water content distribution after 71 days (Figure 4.12). Because wet and dry zones are located relatively close to each other

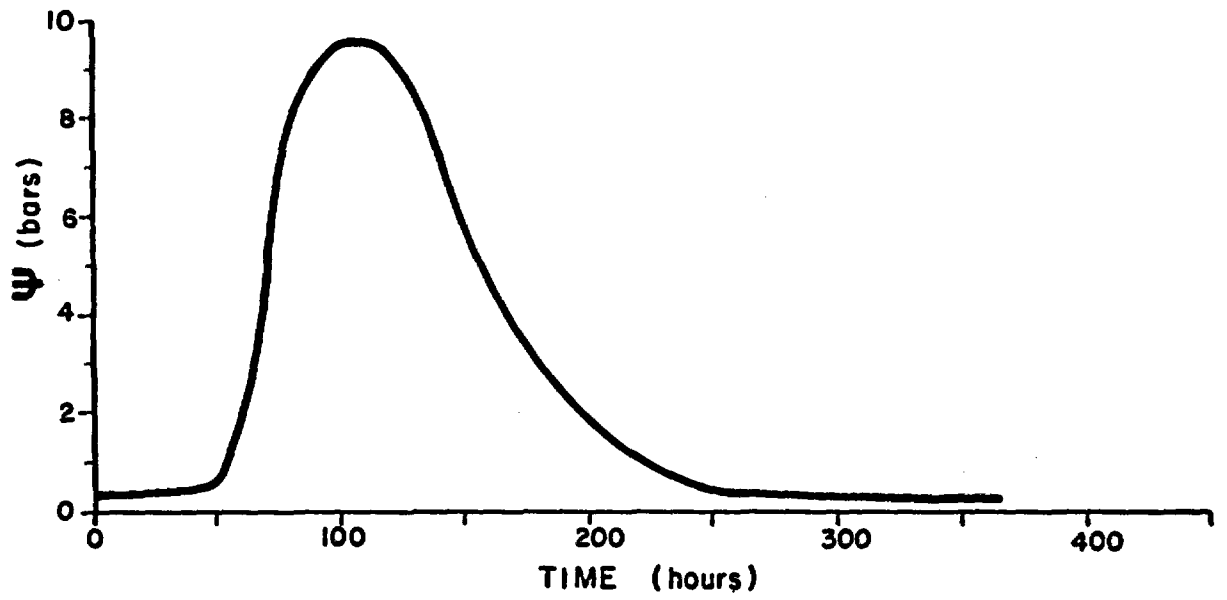


Figure 4.13 Suction against time plot for heater experiment in Queen Creek road tunnel.

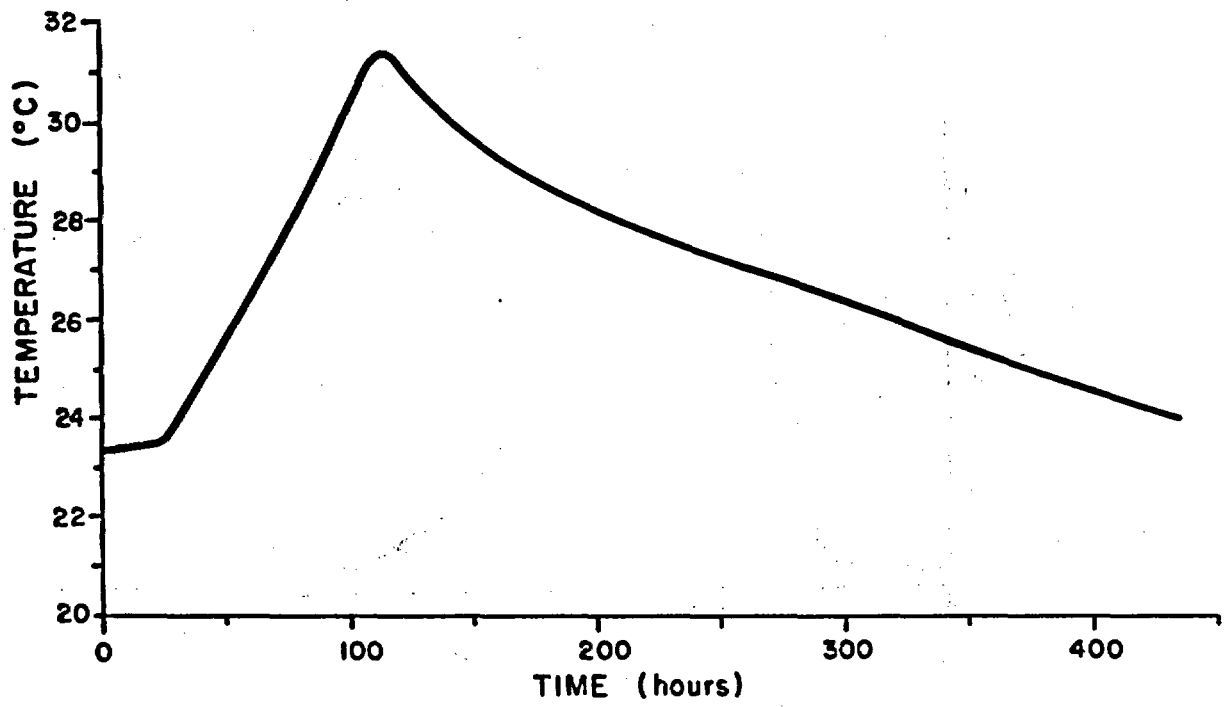


Figure 4.14 Temperature against time plot for heater experiment in Queen Creek road tunnel.

(thus forming a large hydraulic gradient), the conclusion can be made that the hydraulic conductivity of the rock is low. Another factor in the slow recovery could be that some of the water left the system as a liquid and was unavailable to re-wet the dried area.

These heater experiments have provided valuable data for the design and conduct of more elaborate experiments. Such experiments should include several observation boreholes at varying distances from the heater. Selected boreholes should be instrumented at depth intervals to measure suction and temperature distributions. Other boreholes should be designed to periodically measure water content by the neutron method. The boreholes should be packed off at all times when measurements are not being made to reduce disturbances to vapor and liquid flow.

Finally, future experiments should be run with heating episodes lasting several weeks and then allowed to recover for several months to permit temperature and water content measurements over longer time periods.

#### 4.3 Numerical Simulation

A numerical procedure is developed to demonstrate changes surrounding a heat source under conditions where the host rock may approach 100°C. Such a study involves the coupled transfer of water and heat.

The flow problem investigated is composed of five components; they are:

- Heat transfer;
- Rock-matrix water flow;
- Micro-fracture drainage;
- Vapor transfer; and
- Evaporation/condensation.

The first three processes are modeled by numerically solving analytic solutions. Vapor transfer is solved by a finite-element method (FEM) which allows temperature dependent properties to be imposed on the fracture system. Finally, evaporation and condensation are approximated by use of a psychrometric table.

The heat- and water-flow domain is illustrated in Figure 4.15. The left boundary ( $x=0$ ) corresponds to the boundary of a waste repository. At this boundary the temperature rises with time in response to radioactive decay to some peak temperature. This boundary also corresponds to a no-flow boundary for vapor, representing the impermeable repository wall.

The right boundary ( $x=d$ ) is chosen to be far enough from the repository to have a constant vapor density and temperature. That is, these parameters, at  $x=d$ , never change from their initial values. The upper and lower boundaries are symmetrical. In both cases, an imaginary, impermeable plane exists halfway between two main fractures from which liquid, rock-matrix water flows toward the fracture evaporation surface in response to water-content gradients. Finally, gravity drainage through microfractures takes place at specified points throughout the main fracture. For this study, the microfractures were taken to be uniformly distributed.

#### 4.3.1 Assumptions

Given this simplified flow geometry, the nonisothermal flow problem is mathematically formulated based on the following assumptions:

- (1) The main fracture (Figure 4.15) is considered to be horizontal, planar, and of uniform aperture. Microfractures are parallel, of equal aperture and spacing, and are normal to the main fracture. Both the main and microfractures are considered smooth. Thus, the fractures are approximated by a parallel-plate analogy.
- (2) Vapor transfer takes place solely through the main fracture air space; the air has no velocity. Implicit in this assumption is that no vapor is transported by advection, nor by thermal convection.
- (3) The liquid-film flux is negligible. Evans and Huang (1982) state that "an aperture of 1.5 microns will drain at 1-bar potential." Once it is drained, the film thickness on the fracture surface is approximately  $30 \text{ \AA}$ . In this case, the relative cross-sectional area for liquid transport in this particular fracture is 0.004 and the relative flux is  $6.4 \times 10^{-8}$  of that when saturated.
- (4) Evaporation and condensation occur instantaneously. This assumption implies that the time span over which the evaporation/condensation process occurs is small when compared to the time step taken in the computer model.
- (5) The repository wall (heat source;  $x=0$ ) can be approximated as an infinite plane in a semi-infinite solid when compared to the intersecting fracture aperture.
- (6) Heat transfer takes place by conduction only, and the air in the fracture is at the same temperature as the adjacent rock. The fracture aperture (millimeters to microns) is small compared to the plane heat source. Because of this difference the distortion on the temperature field resulting from the differing thermal properties of the fracture air/rock matrix is disregarded.

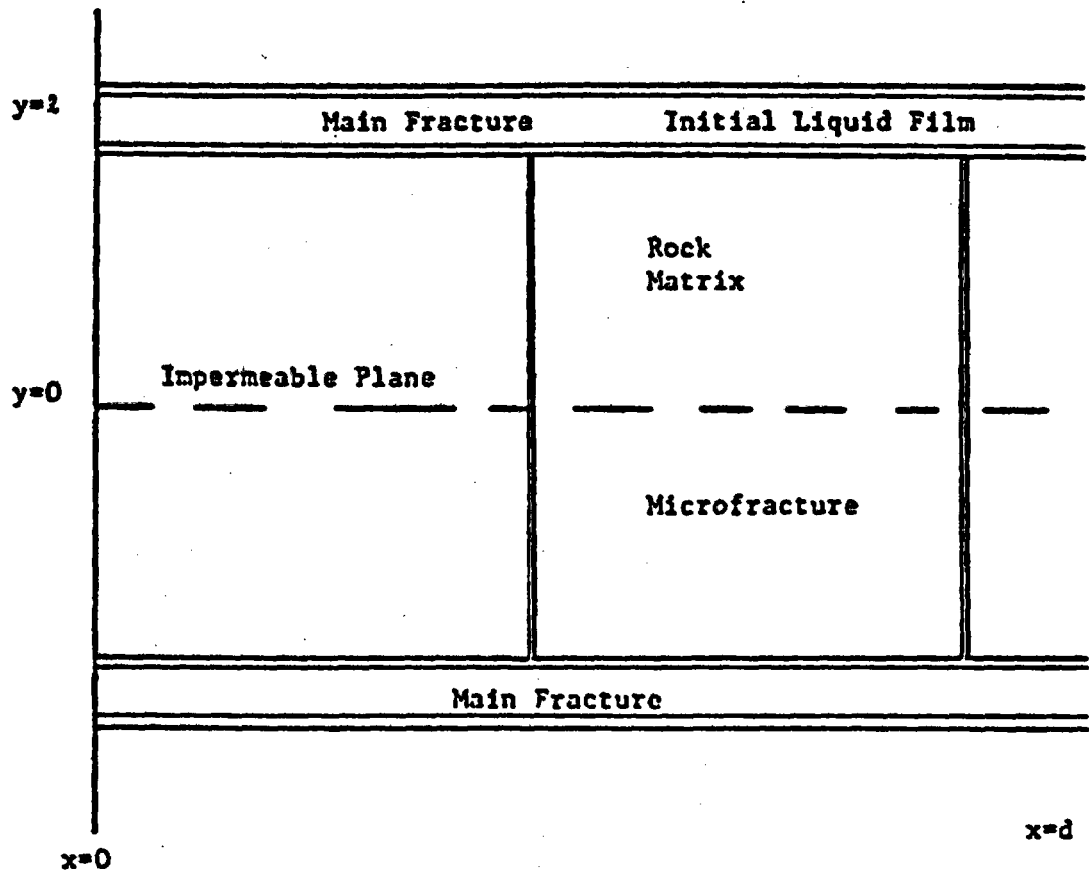


Figure 4.15 The heat and moisture flow domain.

- (7) Rock-matrix water flow perpendicular to the main fracture is in response to a water-content gradient. The temperature effect on the host-rock-water diffusivity is disregarded. The effect of the temperature gradient is neglected also because for this study no temperature gradient exists perpendicular to the main fracture. Finally, the rock-water diffusivity value presents a weighted average over the range of water contents expected.
- (8) The rock-matrix water reservoir (host rock) is bounded by two main fractures. An impermeable plane exists halfway between the two fractures. Below this plane, water flows to the lower fracture and above this plane, water flows to the upper fracture.
- (9) Water contained within the primary porosity of the rock matrix will not exude from the rock into the fracture as the result of thermal expansion.
- (10) Water drained from the main fracture by microfractures is considered to leave the system and is no longer accounted for. The fact that the drained water volume is large with respect to the water within the main fracture and small with respect to that within the microfractured rock makes this assumption reasonable.

Given these assumptions, the following mathematical models for heat transfer, water flow in the rock matrix, liquid-water drainage and vapor transfer are combined to demonstrate nonisothermal water flow.

The heat-transfer model chosen to simulate the heat produced at the repository wall consists of an infinite plane (with respect to the fracture) in an semi-infinite medium. In addition, the plane heat source has a time varying power density, which in this case decreases with time. Equation (4.3) accounts for vapor diffusion and the associated evaporation and condensation processes:

$$(4.3) \quad \partial c / \partial t = \partial [D \partial c / \partial t \partial T / \partial x] / \partial x + Q$$

where

- c is vapor density;
- t is time;
- D is diffusion coefficient for water vapor in air;
- T is temperature;
- x is a spatial variable; and
- Q is a source/sink term.

The net transfer of water is predominantly due to vapor movement, while the vapor source/sink term actually controls flow (Jackson, 1964). For the particular problem studied, Equation (4.3) is solved by the finite-

element method with boundary and initial conditions:

$$\begin{array}{lll} c = w_0 & t = 0 & 0 \leq x \leq d \\ \frac{\partial c}{\partial x} = 0 & t > 0 & x = 0 \\ c = w_0 & t > 0 & x = d \end{array}$$

where

$w_0$  is the initial, saturated vapor density determined by the natural subsurface temperature.

Each flow component is indirectly coupled through the changing temperature field resulting from radioactive waste decay. Vapor transfer is coupled through the diffusion coefficient for water vapor in air, the vapor density gradient and a source/sink term. Rock matrix water flow is coupled by means of a temperature-dependent boundary condition; namely, the condition that the fracture surface ( $y=l$ ) be dry before water flows from the rock to the fracture. That is, the liquid-film-source term for vapor transfer must be zero. Finally, microfracture drainage is coupled through the vapor-transfer-sink term. When enough water has condensed from the vapor phase to the liquid phase to cause gravity drainage, flux through the microfractures is calculated.

#### 4.3.2 Results and Discussion

A computer model of a real physical system necessarily simplifies and approximates the actual physical problem. This model is no exception. What follows is a description of the methods used to account for temperature changes, variable vapor-flow parameters, condensation/evaporation, rock-matrix water flow, and microfracture drainage. In addition, the parameters used to assess the water distribution throughout the single fracture at any time are discussed.

Changes in temperature produce changes in water-flow properties. In this investigation thermally introduced changes in vapor-flow parameters were of most interest. The diffusion coefficient for water vapor in air and the saturated vapor density are functions of temperature. New nodal diffusion coefficients and saturated vapor density are calculated by the following two temperature-dependent relationships (Childs and Malstaff, 1982):

$$(4.4) \quad D = 0.212 \left[ \frac{(T + 273)}{273} \right]^{1.808}$$

where

D is the diffusion coefficient,  $\text{cm}^2/\text{s}$ .

$$(4.5) \quad w = 1323.0 [\exp 17.17 T/(237.3 + T) (T + 273)]$$

where

w is the saturated vapor density,  $\text{g}/\text{m}^3$ .

While both D and w change with temperature, the saturated vapor density is extremely sensitive. At  $50^\circ\text{C}$ , the saturated vapor density is six times its value at  $0^\circ\text{C}$ , and at  $90^\circ\text{C}$  the increase is 87 times its  $0^\circ\text{C}$  value. These increases allow much greater amounts of water vapor in the same volume of air and will, therefore, affect the vapor-transfer process.

As vapor moves away from the repository, the temperature and saturated vapor density decrease, allowing the vapor to condense. In the model, evaporation and condensation are approximated by comparing the calculated vapor density with the existing nodal saturated value (Figure 4.16). If the computed value is greater, condensation occurs until the saturated value is equaled. Likewise, if the computed value is less than saturation, then evaporation occurs assuming there is still water to be evaporated.

The water source for evaporation is composed of two reservoirs. The first reservoir is a liquid film of thickness, h, on the fracture surface which evaporates in the manner discussed above. During this period, actual evaporation equals potential evaporation. When the liquid film is depleted, rock-matrix water moves from the host rock to the fracture evaporation surface. The water source may be supplied initially such that the liquid flux to the surface from within the rock compensates for the rate of evaporation. The duration of this period is short and determined solely by external (i.e., fracture) drying conditions. At the end of this drying period the falling-rate, supply period begins (Figure 4.17). Once the drying process has entered the falling-rate period, the external fracture conditions become relatively unimportant compared with rock-water flux parameters. Eventually, the falling-rate period decreases to zero, corresponding to the time at which the rock becomes completely dry (Berger and Pei, 1972).

The temperatures over which the vapor transport process is studied (i.e., less than  $100^\circ\text{C}$ , the boiling point of water at 1 atmosphere) ensure that liquid water will still be present in the fracture/rock-matrix flow system. Liquid water flow in the fracture has been disregarded for the reasons discussed earlier in this study (i.e.,

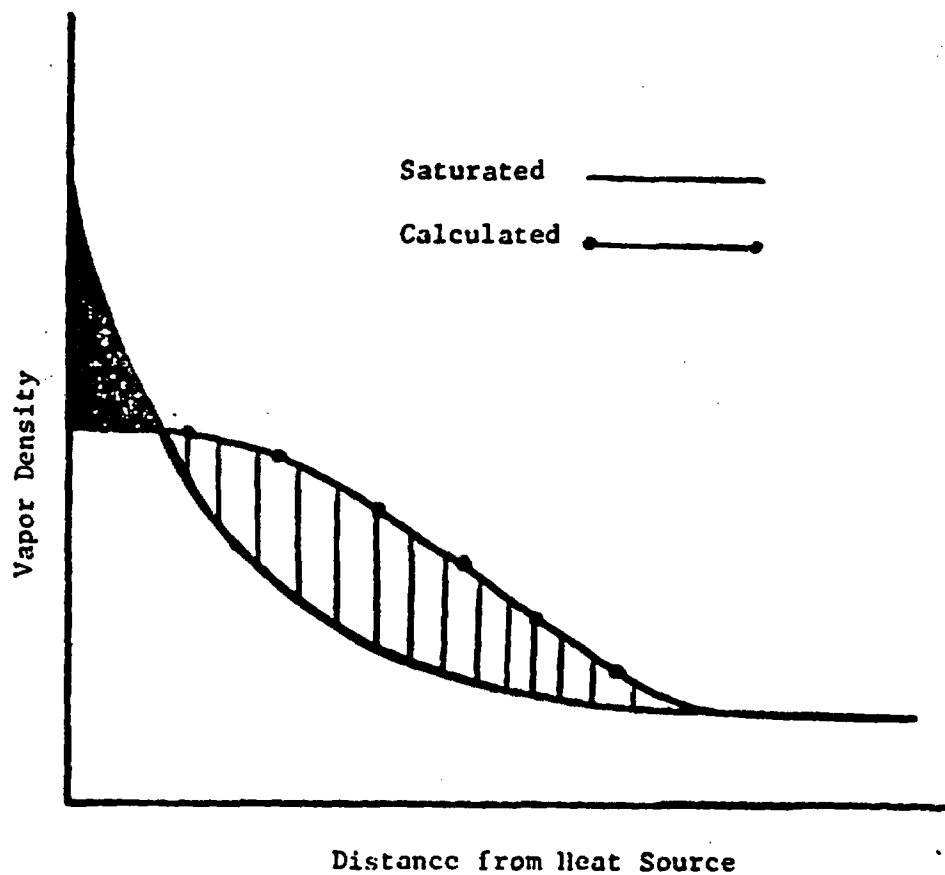


Figure 4.16 Saturated vapor density versus calculated vapor density. The shaded area represents a zone of evaporation and the hashed area a zone of condensation.

Assumption 3). Liquid water in the rock matrix flows in response to a water-content gradient. That is, the flux of water ( $q_w$ ) is assumed to correspond to:

$$(4.6) \quad q_w = - D_R \, d\theta/dy$$

The lack of data with regard to the temperature and water-content dependence of  $D_R$  does, however, limit the use of this flow theory. In zero condensation, Poiseuille drainage may be an important process. In the model, an effective aperture is used for the purpose of fracture drainage at a given node (Figure 4.18). This single drainage fracture takes into account all drainage in the space represented by a node. The amount of water drained at each node is tabulated for mass balance considerations, as it is no longer in the flow domain.

After the evaporation/condensation process has been carried out for a time step, the relative humidity for each node is calculated. The water potential can then be obtained from the relationship:

$$(4.7) \quad \psi = (R/v_w) (T + 273) \ln(H_r)$$

where

- $\psi$  is water potential;
- $H_r$  is relative humidity;
- $R$  is universal gas constant; and
- $v_w$  is molar volume of water in the fracture air space relative to water-saturated air.

The amount of liquid water on the fractured surface at a given node is assessed by means of a liquid-water ratio ( $R_L$ ). It is defined as the ratio of liquid water at some time ( $t > 0$ ) to the initial amount of liquid water present ( $S_i$ ) at the node.

$$(4.8) \quad R_L = S_t/S_i$$

In summary, for each time step ( $\Delta t$ ) the temperature distribution is determined. The diffusion coefficients and saturated vapor densities at each node are then calculated. This allows the global matrix to be constructed which is subsequently solved by a direct solution technique for new nodal compared with saturated values to determine whether evaporation/condensation, rock-matrix water flow, or drainage should occur. Finally, the relative humidity and liquid water ratio are calculated in order to assess the drying of the fracture.

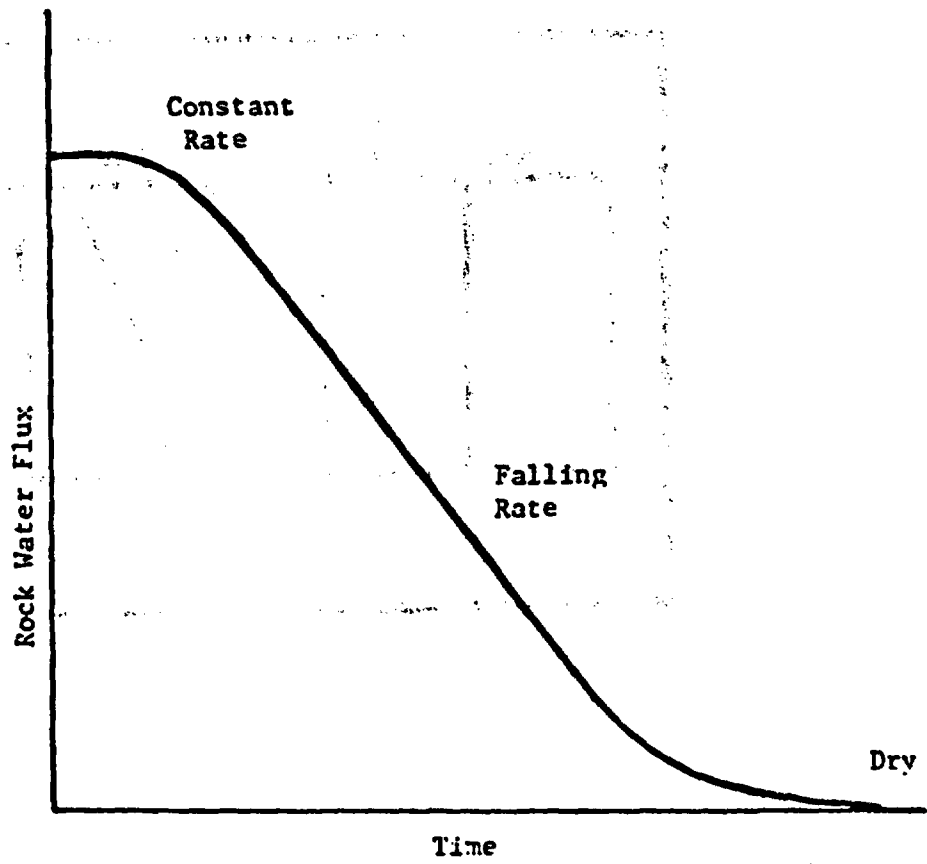
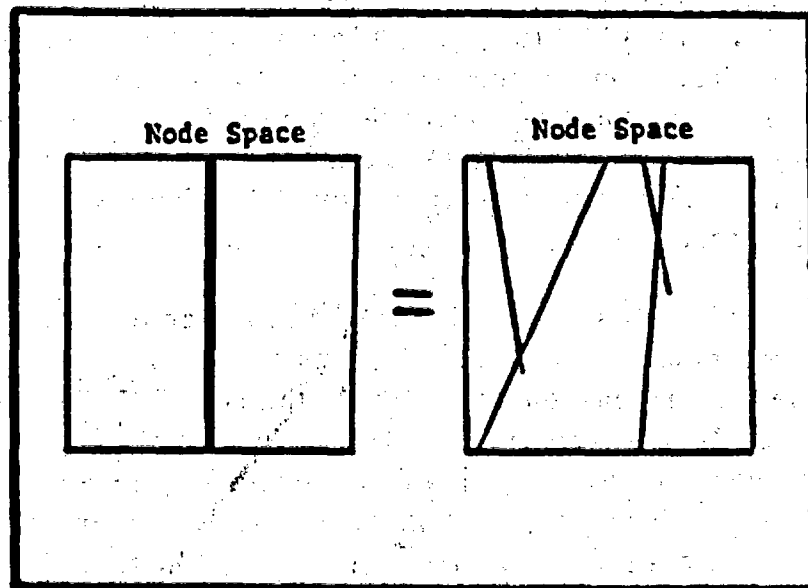


Figure 4.17 Qualitative plot of rock water flux versus time illustrating the drying process.



**Figure 4.18** Illustration of how a set of natural microfractures is replaced by an effective microfracture. The single fracture takes into account all gravity drainage for a given node space.

In conclusion, the placement of a HLNW repository in fractured rock will alter the hydrologic flow field. The most notable change will be due to the thermal energy (heat) produced by radioactive decay. A repository located in the unsaturated zone will presumably cause movement of water vapor. That is, the repository acts as a heat source, causing water to diffuse away from the heat source in the vapor phase.

This process has been modeled using a single, main fracture which provides a path for vapor diffusion away from the repository. Smaller fractures intersect the main fracture providing a mechanism for drainage. In addition, the flow of rock-matrix water to the main fracture has been accounted for. These three processes are coupled together with the repository-generated temperature field and the resulting evaporation/condensation process. Thus, using a simple flow geometry, the movement of water away from a HLNW repository was investigated.

Taking all these processes into account required several simplifications. The assumptions that the air is stationary, and that the thermal expansion of water in the rock matrix may be disregarded, are probably most critical. Certainly the effects of air movement on the degree and extent of water movement should be evaluated. The possibility of rock-water flux resulting from thermal expansion is also a flux mechanism which should be investigated further.

From the modeling investigation, one can make several conclusions. First, rising temperatures near the repository will induce vapor diffusion, and over a long enough time-span, significant quantities of water will be transported away from the repository. Model results demonstrate how temperature changes and vapor diffusion have an effect on the production of wet and dry zones in a fracture. In repository-induced, high-temperature areas, available water is evaporated; this water vapor condenses when it reaches rock near ambient conditions.

Second, the sensitivity analysis indicates that variations in initial film thickness will have only second-order influence on wet- and dry-zone alteration. Aperture and spacing of drainage fractures and the host-rock hydraulic properties will have much greater effects. The greater volume of water within the rock when compared to the fracture is the reason water movement is more sensitive to the water diffusivity. On the other hand, the drainage fractures act as a valve. Even small (micro-range) drainage fractures have the capacity to drain liquid water faster than diffusion away from the heat source. It is this difference

in transport rates that makes the water movement sensitive to the drainage mechanism.

Finally, during both heating and cooling phases, the dominant direction of water movement will be away from the repository wall. While temperatures decrease near the repository, the temperature gradient is primarily outward, i.e., away from the repository. This result could be an artifact of the boundary condition specified. In any event, the cooling process must be further evaluated before final conclusions are made with respect to HLW disposal in the unsaturated zone.

## CHAPTER 5 SOLUTE TRANSPORT

Solute transport is caused by the dissolution or suspension of a chemical in water or air and the subsequent movement of the air or water. The dissolution or suspension can occur under both saturated and unsaturated conditions. If the solubility of a given species in water is very low, only trace amounts will be transported by the flowing water or air. The volume-averaged rate of movement can be described by the expression:

$$(5.1) \quad V_s = K/n \text{ grad } (h)$$

where

$V_s$  is seepage velocity;  
 $K$  is hydraulic conductivity;  
 $n$  is effective porosity; and  
 $\text{grad}(h)$  is the gradient of total head.

Solute transport in unsaturated media is more difficult to characterize than movement through saturated systems, especially in fractured rock. In the unsaturated zone, it is possible for chemical species to move by advection in both the gas and liquid phase. The velocity, or bulk movement, in the gas and liquid phases need not be the same. Because pathways through the porous medium are irregular, different water or gas particles travel at different velocities (statistically centered about average values). These velocity differences cause the solutes flowing with the gas and liquid phases to disperse due to the mechanical action of fluid movement.

In addition to the dispersive forces associated with fluid movement, diffusion occurs due to the molecular agitation of gas and liquid particles. This force causes solutes to move from areas of high concentration to areas of low concentration. Solutes will tend to move outward from a concentrated source even in the absence of fluid movement.

In saturated media, both the dispersive and diffusive forces are often grouped together and treated as a single process called hydrodynamic dispersion. The coefficient of hydrodynamic dispersion or, equivalently, the dispersion coefficient, is written as:

$$(5.2) \quad D = D^* + \alpha V_s$$

where

- D is the dispersion coefficient;
- D\* is the coefficient of molecular diffusion;
- $\alpha$  is dispersivity; and
- $V_s$  is the average linear seepage velocity.

To describe solute transport in a three-dimensional flow field, dispersivity and the dispersion coefficient are usually divided into two expressions, one to describe spreading in the direction of flow and one to describe spreading transverse to the direction of flow.

Solute species interact with the solid matrix through which they flow. Solute particles often adsorb to the matrix by forming bonds with ions of opposite charge on the solid matrix surface. The strength of these bonds and the kinetics of the surface reactions which form them are complex. Among other things, the binding strength is dependent on the size and charge of both solute and surface species, the degree of saturation of surface bonding sites, pH, the oxidation/reduction potential, and the temperature and pressure of the system (Morel, 1983; Freeze and Cherry, 1979).

There is also a tendency for solute particles to desorb from the solid surface, allowing the solute particles to flow with the moving fluid. A state of chemical equilibrium between adsorption and desorption exists for any given surface reaction system. In practical terms, this means that at any moment some of the solute particles are bonded to the solid surface and some are free to move with the fluid gas or liquid. The net effect is to retard the movement of solutes relative to that of the fluid. This process is described by the retardation equation:

$$(5.3) \quad V_s/V_c = 1 + b/n K_d$$

where

- $V_s$  is average seepage velocity of the ground water;
- $V_c$  is contaminant velocity;
- $K_d$  is distribution coefficient;
- b is bulk density; and
- n is porosity.

Solutes which travel at approximately the same rate as the ground water have distribution coefficients close to zero and are known as conservative solutes. Solutes with finite distribution coefficients which travel at lower rates than the ground water are called nonconservative.

Other types of chemical reactions can act as attenuating factors in solute transport. Precipitation and radioactive decay are two examples. Changes in pH and the oxidation/reduction potential can favor precipitation of solutes. Other chemical reactions can also occur leading to the formation of ions not originally present in the waste source. These ions can have markedly different transport properties.

In the unsaturated zone, solutes can also travel in the gas phase by suspension or by volatilization. Of the two, the most important is volatilization, particularly in the case of many organic species. Volatilization is the process by which a molecule in solution leaves the liquid surface and escapes into the gas phase due to molecular agitation. In a closed system, this process is in balance with the opposite tendency to rejoin the liquid surface. Some fraction of a volatile species will be in the vapor phase at any given moment. A volatile species in solution in the water film surrounding grains in an unsaturated porous medium will tend to escape into the air space between grains. The volatile species is then free to flow with the air phase or diffuse by osmosis to other areas where the concentration of the volatile species is low.

## 5.1 Sampling Techniques

This section describes techniques appropriate for evaluating the movement of solutes in the liquid and vapor phases in unsaturated, fractured rock. The ability to extract fluid samples, or fluid-derived samples from the unsaturated zone is critical for identifying and quantifying the occurrence and movement of solutes. The topics to be addressed in this section incorporate potentially useful techniques for obtaining such samples.

### 5.1.1 Volatile Compounds

A volatile tracer method for monitoring water movement in the vadose zone is presented. Gaseous sampling of a volatile fluorocarbon tracer in equilibrium with the liquid phase is used to predict the rate of liquid movement. A major advantage of a volatile tracer method is that the tracer can be transported in the liquid phase and sampled in the gaseous phase, thereby eliminating the difficulty of extracting a liquid sample from an unsaturated rock formation. Presented in this section are the results from laboratory soil column tests performed to study the behavior of volatile tracers and test their suitability for measuring water percolation rates.

Volatile tracers can be used in field situations to trace the movement of water in the unsaturated zone. A preliminary field test of this technique has been performed at the Apache Leap site in fractured tuff. A volatile tracer was introduced on the surface and gas samples were recovered at depth where vertical fractures in the tuff intersected a borehole drilled at an angle of 45° from the vertical. Heavy rains made interpretation of test results difficult, perhaps due to the saturation of air-filled pores, and the dilution of injected liquids. Proposed applications at the Apache Leap site include underground cross-hole tests where a tracer is applied at depth in an upper borehole and the breakthrough is measured in a lower borehole.

The tracers selected to investigate the suitability of the volatile tracer technique were the fluorocarbon compounds bromochlorodifluoromethane (BCF), chlorodifluoromethane (F-22), and sulfur hexafluoride (SF<sub>6</sub>). Fluorocarbons are man-made compounds which were first produced in the late-1930's and are now widely used as propellants, refrigerants, and solvents. Freon-12 is the most abundant fluorocarbon in the environment and is found in the atmosphere in concentrations of up to 300 parts per trillion by volume (Weeks, 1982).

Several physical properties of fluorocarbons make them suitable for use as hydrologic tracers. One important advantage is that they are generally considered to have very low toxicities (Davis et al., 1980). Second, among all organic compounds, fluorocarbons have the lowest known surface energies and are, therefore, not likely to adsorb onto solid particles (Shafrin and Zisman, 1960). Field tests using fluorocarbons and bromide, the latter being a commonly used tracer, indicate that there is little difference in sorption between the two (Davis et al., 1980). The third major advantage of fluorocarbons is their high affinity for electrons, making them suitable for analysis using electron capture detection gas chromatography, with detection limits in concentrations as low as one part per trillion (Lovelock et al., 1973).

The use of fluorocarbons as a tracer in the saturated zone was proposed by Thompson et al. (1974) because of their low toxicity and ease of detection at small concentrations. Field studies conducted by Thompson (1979) demonstrated that fluorocarbons could be a favorable tracer in the hydrologic environment. Brown (1980) investigated fluorocarbon tracers in a saturated soil column study and found that the fluorocarbon tracers traveled slightly slower than the average water velocity. Fluorocarbons were used as a tracer in the unsaturated zone by Weeks et al. (1982) to determine gaseous diffusion parameters.

Measurements of the gas phase to indicate the presence of fluorocarbons in the liquid state has not been documented in the literature. Since this technique has never been tested, laboratory experiments were needed to study the behavior of volatile tracers in a controlled situation before field tests could be considered. Laboratory tests on soil columns indicated that several overlapping processes are involved in the transport of a volatile tracer. Computer modeling was proposed to help interpret the data from the column test to allow a more accurate prediction of water percolation rates in the vadose zone.

The primary objective of the column study and the computer simulation was to define the processes involved in the transport of a volatile compound under unsaturated conditions. In order to interpret water percolation rates using a volatile tracer technique, one must understand both gaseous tracer movement and the movement of tracer as solutes in the water phase.

Chloride was used to trace the movement of the fluorocarbon tracer in the liquid phase. Chloride was used as a tracer in the liquid phase because of the ease of measuring its breakthrough which can be accomplished by placing small electrodes in the column and measuring the electrical conductance between them. Changes in conductance relate to changes in chloride concentration. Gas samples were obtained by extracting a syringe sample of gas at the same point on the column that the chloride sampling electrodes were installed.

Data from the column test were used to calibrate a computer model. The column test provided data for both liquid and gas tracer concentrations with time. When the technique is applied in the field only gas phase concentrations will be available to use in the model. Therefore, the soil column test is vital in validating whether the computer model accurately simulates volatile tracer flow.

The Discrete State Compartment (DSC) model (Campana, 1975, Rasmussen, 1982) was used in the study because of the simplicity of the model and the ability to run the model on a microcomputer. The DSC model uses a series of cells or compartments to represent a hydrologic system. An iterative equation combines inputs, outputs, sources and sinks with a mass balance equation in order to define the flow regime for a specific cell.

The DSC model has been used to estimate solute transport through the liquid and vapor phases by using different cells to represent the

liquid, solid, and gas phases. That is, for each liquid cell there is a corresponding solid and gas cell. Interactions between the phases are modeled as exchanges between these cells. For example, the process by which a tracer evolves out of the liquid phase and into the gas phase is modeled by an exchange between the mixing cells representing the liquid and gas components.

Physical processes occurring within the soil during a tracer test which must be addressed by the computer simulation consist primarily of advection, sorption onto the soil particles, partitioning of the volatile tracer into the soil gas, diffusion of the tracer in the liquid phase, and the gas phase. Adapting the DSC model to include all of these processes and expressing the mathematical equations was done by Rasmussen (1982). Seidemann (1986) adapted the model for execution on an PC and compatible microcomputers.

Advection of the volatile tracer in the water phase is considered in the column study by the chloride ion measurements. Chloride ion is a commonly used tracer which is generally considered to be conservative and travel with the average water velocity at dilute concentrations. In the column study it was assumed that the volatile fluorocarbon compounds travel at the same rate as the water. Since the chloride ion also is known to travel at the rate as the water it can then be assumed that the chloride ion breakthrough represented the breakthrough of the fluorocarbon tracer.

Davis (1980) attempted to verify the assumption that fluorocarbons travel with the average water velocity, using bromide and several fluorocarbon tracers including BCF in a saturated, field tracer test. Little difference in tracer breakthrough was found between the bromide ion and the fluorocarbon compounds.

Predicting the movement of any tracer requires an understanding of how the compound is sorbed onto the soil media. Soil batch tests were performed to gain a quantitative knowledge of the sorptive behavior of the soil for the tracers used. Appendix F gives a detailed explanation of the experimental procedure for the batch tests. The partition coefficient is the number of moles of a tracer sorbed on to the soil per gram of soil divided by the number of moles of tracer in solution per gram of water. Sorption properties can be modeled with the DSC if the partition coefficients are known.

The same approach of using partition coefficients is used to express the relationship between the tracer in the gas phase and the tracer in the

water phase.  $K_w$  is the partitioning coefficient that represents the equilibrium of the water and gas phases and is defined as the moles of tracer per gram of water divided by the moles of tracer in a cubic centimeter of gas.

Gaseous diffusion is a transport process driven by concentration gradients and may be described by Fick's Law which, in one dimension, is expressed as:

$$(5.4) \quad F = -D_e \frac{dC}{dx}$$

where

$F$  is the mass flux per unit area;

$D_e$  is the effective gas diffusion coefficient; and

$C$  is the concentration of tracer in gas.

Indications that gaseous diffusion is occurring in the soil column would be seen in the results as a smearing or stretching out of the tracer breakthrough curve or the arrival of fluorocarbon tracer in the gas phase before the arrival of the tracer in the liquid phase. Gaseous diffusion is considered in the model by adjusting exchange volumes used in the mixing process so as to give the desired amount of diffusion.

Diffusion of the tracer in the water phase was not addressed in this problem due to added complexity and the relatively small influence the process has on the soil column system. Also neglected are processes that would produce convection in the soil gas phase. These processes include primarily temperature and barometric fluctuations which are often too small to be of significance.

#### 5.1.1.1 Selection of Fluorocarbon Tracers

Fluorocarbon compounds were selected as the first group of tracers to be tested because of the previous field work done using these compounds in both saturated and unsaturated porous media. Approximately sixteen fluorocarbon compounds have been reported in the literature. Properties of interest in selection of a tracer for this study were primarily; boiling temperature, critical temperature, solubility in water, toxicity and availability. The boiling temperature of a volatile tracer must be below the ambient temperature in order for the compound to remain a gas under test conditions.

A critical temperature of greater than 50°C is generally needed to construct a permeation device to store and release most fluorocarbons.

To create a tracer saturated water solution that will volatize fluorocarbons as it travels through the soil column, the tracer must also be partially soluble in water.

Presented in Table 5.1 is a summary of the significant properties of the most common fluorocarbons. From this list five possible tracers can be shown to fill the requirements needed for the column test: BCF, F-22, F13B-1, SF<sub>6</sub> and F-114. Of the five tracers, three (BCF, F-22, and SF<sub>6</sub>) were selected for initial testing because of their availability and their previous use by other investigators.

-----  
 Table 5.1 Properties of possible fluorocarbon tracers.  
 -----

Tracer	Formula	Boiling Temp °C	Critical Temp °C	Solubility by Wt. %	Toxicity *
F-11	CCl <sub>3</sub> F	23.82	198	.011	5a
F-12	CCl <sub>2</sub> F <sub>2</sub>	-29.79	112	.028	6
F-13	CClF <sub>3</sub>	-81.4	28.9	.009	Prob. 6
F13B-1	CBrF <sub>3</sub>	-57.75	67	.03	6
F-14	CF <sub>4</sub>	-127.96	-45.67	.0015	Prob. 6
F-21	CHCl <sub>2</sub> F	8.92	178.5	.95	4-5
F-22	CHClF <sub>2</sub>	-40.75	96	.30	5a
F-23	CHF <sub>3</sub>	-82.03	25.9	.10	Prob. 6
F-112	C <sub>2</sub> Cl <sub>4</sub> F <sub>2</sub>	92.8	278	.12	4-5
F-113	C <sub>2</sub> Cl <sub>3</sub> F <sub>3</sub>	47.57	214	.017	4-5
F-114	C <sub>2</sub> Cl <sub>2</sub> F <sub>4</sub>	3.77	145.7	.013	6
F-114B2	C <sub>2</sub> Br <sub>2</sub> F <sub>4</sub>	47.26	214.5	---	5a
F-115	C <sub>2</sub> ClF <sub>5</sub>	-38.7	80	.006	6
F-116	C <sub>2</sub> F <sub>6</sub>	-78.2	19.7	---	Prob. 6
12B1(BCF)	CClBrF <sub>2</sub>	-3.98	153.9	---	Non Toxic

\* Underwriters Classification (see Table F.2)  
 -----

### 5.1.1.2 Experimental and Computer Results

Soil column experiments were the main focus of the study to investigate the movement of volatile tracers under unsaturated conditions. Water saturated with the volatile tracer was introduced into the top of a sand column where the solution percolated downward. The fluorocarbon tracer volatilizes out of the water as the solution travels down the sand column.

Measurements of the gaseous fluorocarbon concentration through time at a fixed point were made, as well as a qualitative measurement of the chloride concentration in the liquid phase. Using these breakthrough curves of the gaseous and liquid phase, the feasibility of estimating liquid velocity by sampling only the gaseous phase can be evaluated.

Column tests were run for the three tracers at three separate flow rates in order to evaluate the behavior of each gas and to determine the suitability of each compound as a tracer in the unsaturated zone. The purpose of the test was also to determine how much of an influence gaseous diffusion has on the gas breakthrough curve. The column test will help to understand the relationship of a tracer in the soil gas to the tracer in solution with the water phase.

Figures 5.1 through 5.3 are graphs depicting breakthrough curves for selected soil column tests. All graphs show the time since the start of a test versus the dimensionless concentration  $C/C_0$ , where  $C$  is the concentration of tracer in the soil gas and  $C_0$  is the concentration of tracer initially dissolved in the water phase. The vertical line indicates the beginning of the tracer breakthrough front in the water phase as represented by the chloride concentration. Details of the procedures followed in the soil column tests run to produce the graphs are presented in Appendix F.

Figure 5.1(A) is the breakthrough curve for BCF for a fairly high water application rate of  $5 \text{ cm}^3/\text{min}$ . The first appearance of volatile fluorocarbon tracer roughly corresponds to the appearance of the chloride (Figure 5.1(B)). Results for F-22 from all three ports test are shown in Figure 5.2. The tests were run at approximately the same water application rate as the BCF test. Breakthrough of the liquid and gas phases at each port occur roughly at the same time. However, there is a sharp decrease in concentration of tracer at port number 4.

The drastic reduction in concentration is too large to be explained by dispersion of the tracer front as it moves down the column. During the

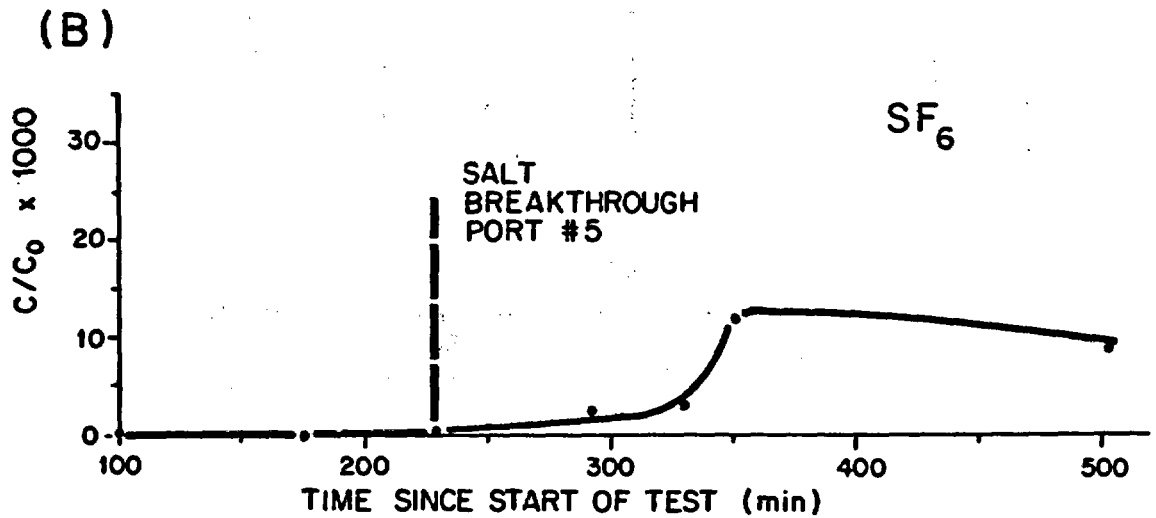
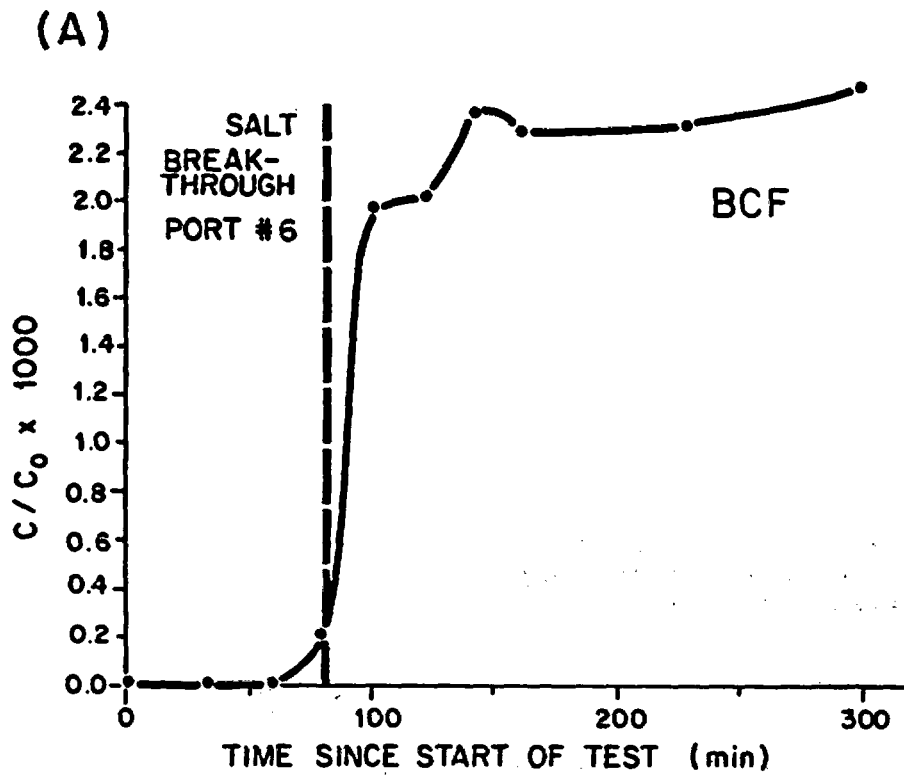


Figure 5.1 Breakthrough curves for BCF (A) and SF<sub>6</sub> (B).

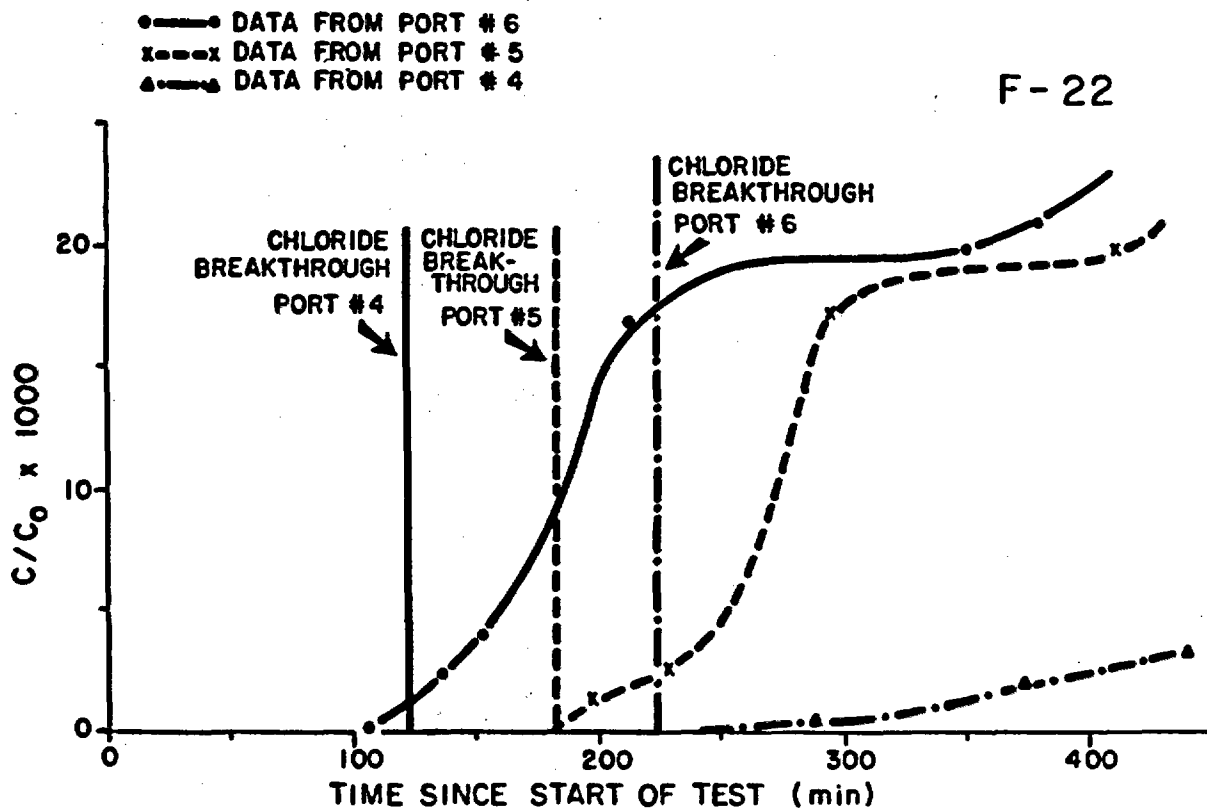


Figure 5.2 Breakthrough curves for Freon-22 test.

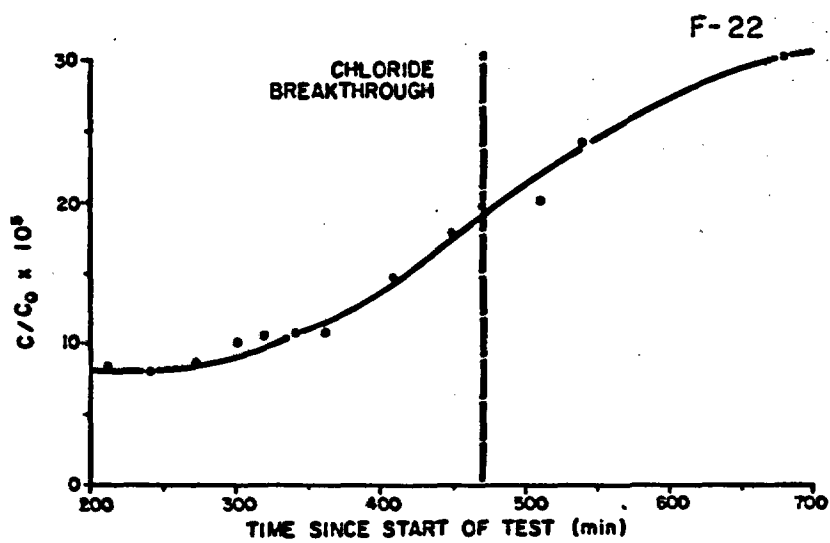
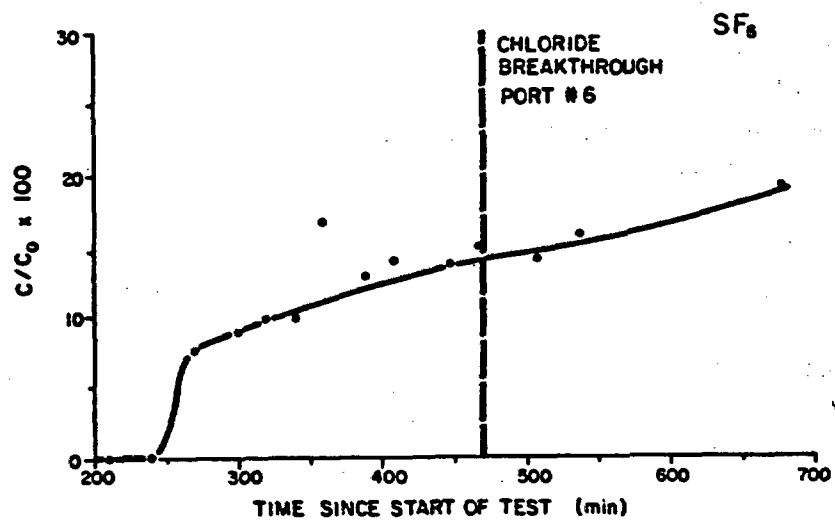
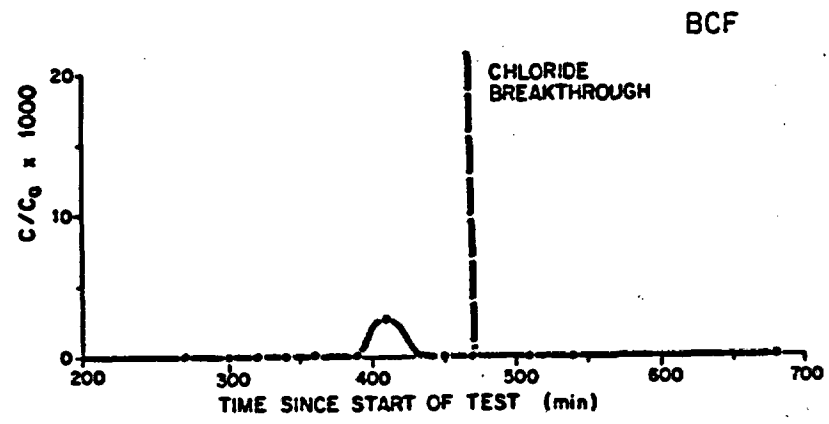


Figure 5.3 Breakthrough curves for BCF (A), SF<sub>6</sub> (B), and Freon-22 (C).

test, gas samples of  $0.5 \text{ cm}^3$  were withdrawn to obtain concentration data. The relatively large sample size did influence the concentration measurements. This was tested by conducting an experiment at the end of the tracer test when there was a large concentration of tracer left in the column. Three gas samples were withdrawn at five-minute intervals, sampling was stopped for fifteen minutes, and the concentration of tracer was allowed to recover.

The results of this test showed that the size of the tracer peak on the gas chromatograph decreased by approximately one-half. After recovering for fifteen minutes the concentration of the tracer was essentially the same as at the beginning of the test. These results suggested that air surrounding the column was pulled into the column when the gas sample was being withdrawn, thus creating a dilution effect due to sampling. To standardize the data and make interpretation easier, it became evident that the same size sample should be taken at regular intervals during the test.

Water percolation rates were decreased by a factor of fifty and the column was allowed to sit for a period of a few weeks to let the water outflow rate reach a steady state. The slower flow rate was used to increase the effects of gaseous diffusion. Graphs of breakthrough curves for all three tracers for a test which used a water application rate of  $0.083 \text{ cm}^3/\text{min}$  are shown in Figures 5.3(A), 5.3(B), and 5.3(C). In all three cases the fluorocarbon tracers appeared in the soil gas significantly ahead of the fluorocarbons dissolved in the water.

Gaseous diffusion apparently was causing the tracer in the soil gas to lead the tracer dissolved in the water. When the technique is applied in the field, sampling of the water will not be possible and therefore a direct comparison of gas breakthrough with water percolation rate will not be possible. Because of this difficulty, computer simulation has become important for assessing the suitability of the volatile tracer method.

The breakthrough curve in Figure 5.3(B) shows how the  $\text{SF}_6$  tracer concentration in the soil gas has almost leveled out by the time the front of the chloride tracer has started to breakthrough. Of all the tracers used in this study,  $\text{SF}_6$  was always the first tracer detected.  $\text{SF}_6$  exhibits highly diffusive characteristics. During one tracer test  $\text{SF}_6$  in dilute concentration in the lab atmosphere diffused into the column and forced a rerun of the test.

Another problem encountered in the soil column experiments is illustrated in Figure 5.3(C). F-22 is highly sorptive and once placed into the system it is extremely difficult to remove. Therefore, the concentration of F-22 is not zero at the beginning of the test because of a previous test using this column.

Computer modeling is needed to determine when the influence of gaseous diffusion becomes important and becomes the dominate transport process controlling concentration of fluorocarbon tracer in the soil gas. Parameters needed to run a computer simulation of the experiment may be obtained both from laboratory experiments and from the literature. The parameters required to simulate the soil column experiments using the DSC model are partition coefficients, the tortuosity of the porous media, diffusion coefficients, the bulk density and the water content.

For this study, partition coefficients describing the sorptive properties of the soil were determined from batch tests for F-22 which were obtained earlier by Thompson and Stiles (1981) for SF<sub>6</sub> and BCF. The partition coefficients describing the volatilization of tracer from the water into the soil gas were also obtained from Thompson and Stiles (1981). Tortuosity is needed to calculate the effective dispersion coefficient. Weeks et al. (1982) published a partial list of equations which can be used to calculate tortuosity. These equations are listed in Table 5.2. Tortuosities were calculated using the "wet" soil equations in Table 5.2, then averaged to give one value for tortuosity.

Bulk density and water content measurements were made using a gamma ray technique. These parameters are needed to calculate cell volumes and derive an effective diffusion coefficient. The effective diffusion coefficient was calculated using (Weeks et al., 1982):

$$(5.5) \quad D_e = t \theta_d D_{AB} / [\theta_d + (\theta_t - \theta_d) \rho_w K_w + (1 - \theta_d) \rho_s K_s]$$

where

- t is tortuosity;
- $\theta_d$  is drained porosity;
- $D_{AB}$  is molecular diffusion constant;
- $\theta_t$  is total porosity;
- $K_w$  is liquid-gas partitioning coefficient;
- $K_s$  is gas-liquid-solid distribution coefficient;
- $\rho_s$  is particle density of soil matrix; and
- $\rho_w$  is density of water.

A computer simulation was performed for the experiment where the percolation rate of water through the column was fast. In this experiment, the transport of fluorocarbon tracer was dominated by advection. Results of the DSC model are shown in Figure 5.4. The breakthrough curves for the tracer in the soil gas coincides with the breakthrough for the bulk of the water.

-----  
 Table 5.2 Partial list of published expressions relating tortuosity to air-filled and total porosity (Weeks et. al., 1982).  
 -----

Investigator	Date	Tortuosity Factor <sup>1</sup>	
		dry	wet
Buckingham	1904	$e_t$	$e_d$
Penman	1940	0.66	0.66
van Bavel	1951	0.6	0.6
Marshall	1959	$(e_d)^{0.5}$	-
Millington	1959	$(e_d)^{0.333}$	$(e_d)^{0.333} (e_d/e_t)^2$
Wesseling	1962	-	$0.9e_d - 0.1$
Grable and Siemer	1968	-	$5.25(e_d)^{2.36}$
Currie	1970	-	$(e_t)^{0.5} (e_d/e_t)^4$
de Jong and Schappert	1972	-	$0.31 - 0.59(e_t - e_d)$
Lai et al.	1976	-	$(e_d)^{4/3}$
Albertson	1979	-	$0.777 (e_d/e_t) - 0.274$

<sup>1</sup>  $e_d$  is drained porosity; and  $e_t$  is total porosity.  
 -----

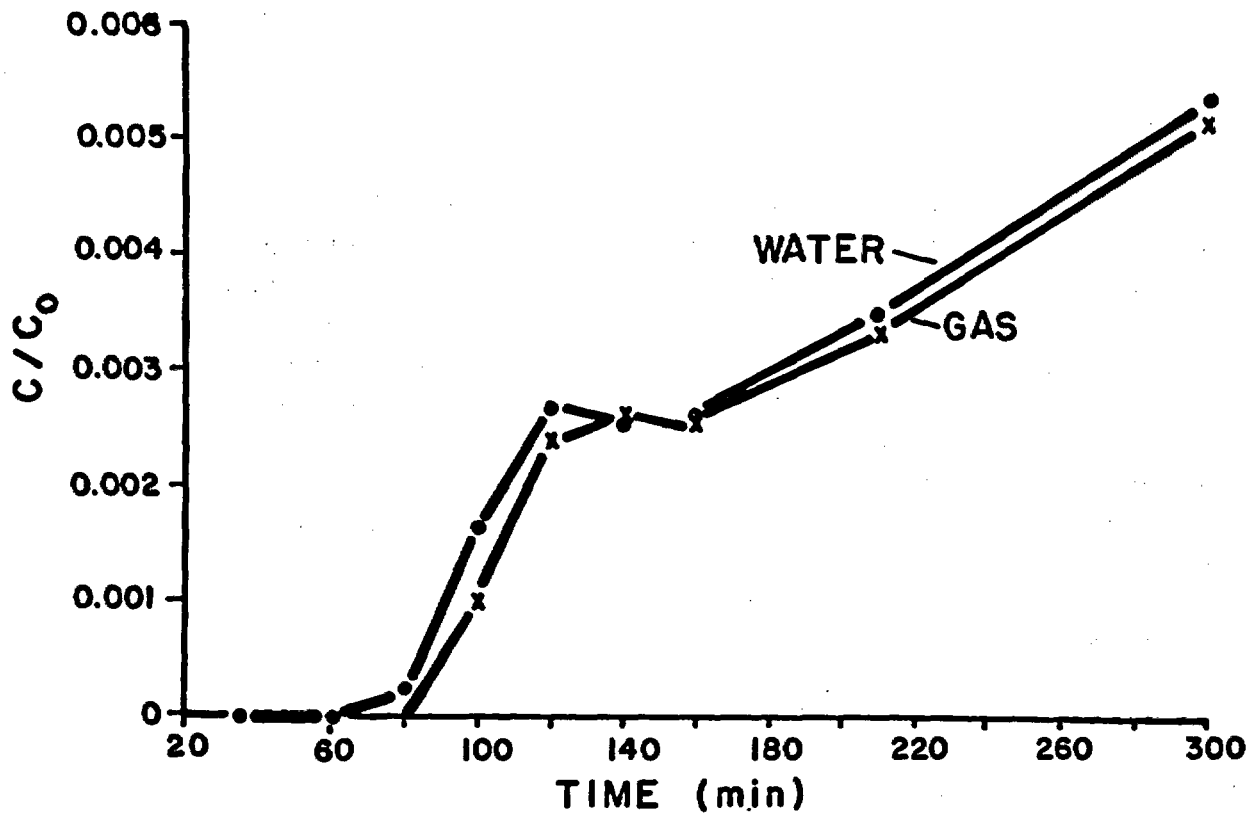


Figure 5.4 Computed breakthrough curves for fluorocarbon tracer in the soil gas and in the liquid. The close agreement between the curves indicates the suitability of vapor phase concentration as a surrogate measure of fluid concentration.

DSC results also compared well with data obtained from laboratory column experiments. Figure 5.5 illustrates a second data set and a computer simulation which generally reproduces the laboratory data. However, the predicted tracer breakthrough front is spread more than the laboratory data. Also, the observed concentration of tracer at 300 minutes is substantially less than that obtained from the computer model. Tracer front spreading in the computer model is caused by numerical dispersion and can be corrected by increasing the number of cells.

A more difficult issue is the large error between the computer model and laboratory results occurring at 300 minutes into the test. Differences between laboratory data and model results may be attributable to measurement errors or to the failure to incorporate reaction kinetics in the computer model. If measurement errors can be discounted, then several reaction kinetics can perhaps provide an explanation of the observed data. One possibility is that the rate of sorption onto the solid phase increases with time, which will cause a flattening of tracer concentration at later times, as indicated. Another possibility is that because sorption is assumed to adsorb and desorb at the same rates, then an error can be expected if the rate of desorption is slower. To address this and other issues, additional computer modeling is needed to simulate a larger variety of breakthrough curves observed in laboratory column experiments.

#### 5.1.1.3 Summary and Conclusions

Soil column studies indicate that soil gas concentrations of fluorocarbon tracers BCF, F-22 and SF<sub>6</sub> can estimate water percolation rates under certain conditions. SF<sub>6</sub> is the most mobile tracer and appears to be most suitable for field use for verifying the hypothesis that volatile tracers can be sampled in the soil gas environment. F-22 also appears suitable except it is difficult to purge from the hydrologic system. BCF may be applicable if a method for concentrating the compound in water could be developed.

Computer simulations will be used to help interpret the data from the column tests, thus allowing a more accurate estimate of water percolation rates in unsaturated media. Preliminary results from laboratory tests indicate that a field test of the volatile tracer technique should be made. If the field tests are successful, volatile tracers could provide a viable, low-cost technique for measuring water percolation rates in fractured rocks.

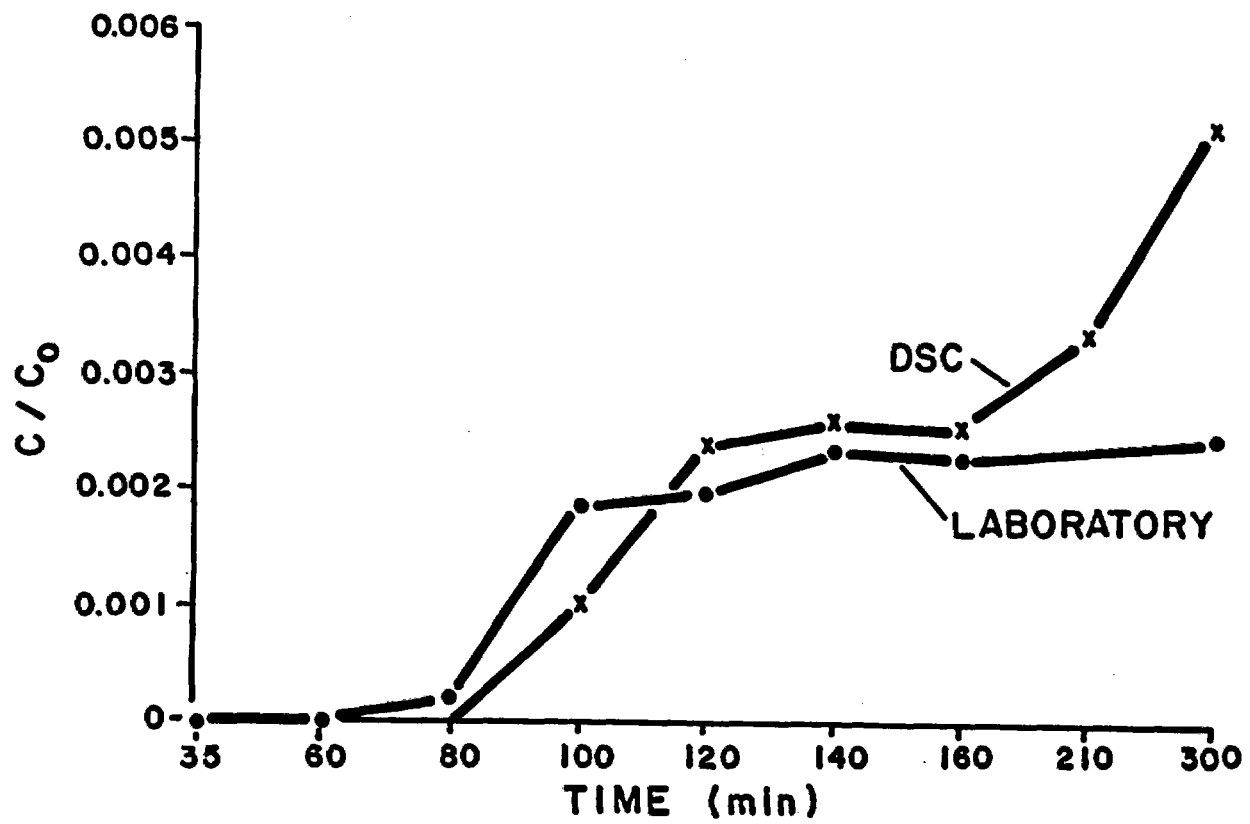


Figure 5.5 Observed and computed soil gas breakthrough curves for a fluorocarbon tracer in a column test. The two curves agree except for the last data point.

### 5.1.2 Vacuum Lysimeter

Water samples from the unsaturated zone are important for obtaining chemical data useful in subsurface characterization or monitoring programs near waste impoundments. Vacuum lysimeters have been used for this purpose in geologic media near saturation. In relatively dry media where matrix suction exceeds 300 to 400 cm of water, samples cannot be obtained using the vacuum lysimeter or other conventional methods. This is especially true for porous, fractured rock.

Results from computer simulations suggest that water samples can be obtained from relatively dry media if an existing technique is modified. The proposed methodology requires that water be injected into the area to be sampled, increasing the water content of the medium until the operational range for a vacuum lysimeter is reached. The injected water will mix with native water and eventually approach chemical equilibrium. A sample of water can then be recovered utilizing the vacuum lysimeter. Because the native water has been diluted, chemical analysis of the sample will only yield qualitative data, or perhaps semi-quantitative data, sufficient to determine the suite of dissolved constituents, tracer travel time, or the presence or absence of target compounds.

The primary element of a vacuum lysimeter is a thin-walled porous cup made of ceramic or Teflon. The porous cup is connected to a blank casing which is sealed at the top. The seal is penetrated by two access tubes which extend down to the cup. One of the two access tubes is connected to a combination vacuum/pressure pump at the surface. The pump facilitates sample collection and withdrawal. The other tube serves as a discharge tube and leads to a sample container. The components of the vacuum lysimeter are shown schematically in Figure 5.6.

Prior to use, the assembly is buried and the area about the porous cup is back-filled with a slurry of soil or 200-mesh silica sand. The slurry ensures a good hydraulic connection between the porous cup and the surrounding medium. A sample is collected by closing the discharge tube and evacuating air from the lysimeter, causing water in the surrounding medium to be drawn into the porous cup. If the medium is sufficiently wet, enough water for chemical analysis can be obtained in a few hours. To bring the water to the surface, the discharge tube is opened and air is pumped into the lysimeter. The positive pressure forces the collected water through the discharge tube into a sample container at the surface.

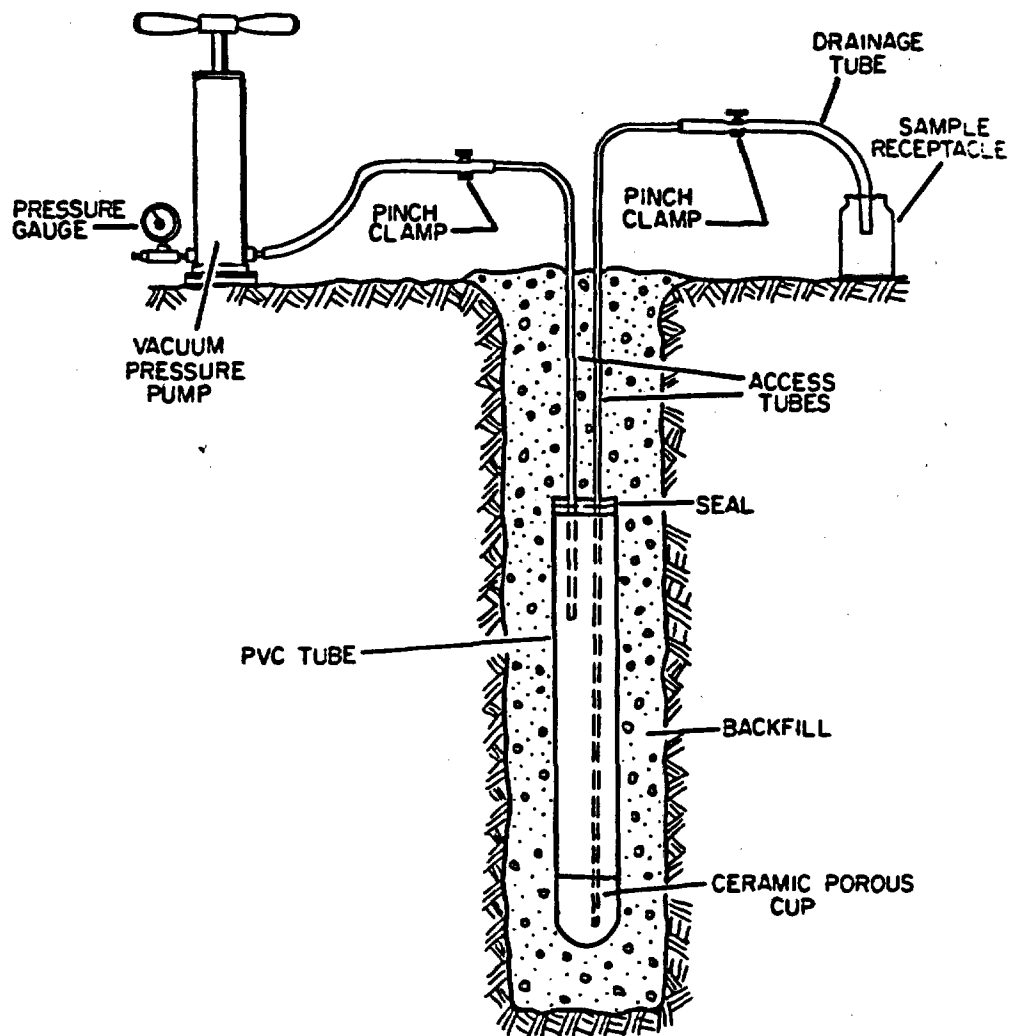


**Figure 5.6** Schematic view of parts and installation of a vacuum lysimeter. In sufficiently wet media a water sample is collected by clamping shut the discharge tube and pumping the air out of the sampler. Water flows from the soil into the sampler through the porous cup. To bring this sample to the surface, air is pumped into the lysimeter with the discharge tube open. Positive pressure forces the water to the surface through the open tube. (Figure is modified from Soilmoisture Equipment Corp. Instruction Manual)

A principal feature of the vacuum lysimeter is the micro-porous cup. Water in the surrounding medium flows into the cup due to a matric potential gradient induced by evacuating the air within the lysimeter. Theoretically, the maximum amount of suction that can be induced into the cup is equal to the atmospheric pressure (e.g., 1033 cm of water at sea level), but in practice only vacuums of 85 percent of the atmospheric pressure can be maintained. This limit restricts the operational range of vacuum lysimeters. When matric suction in the medium exceeds 85 percent of the atmospheric pressure, water can not be induced to flow into the cup. In fact, when the suction exceeds 300 to 400 cm, the rate of inflow may be too slow to be of practical use.

#### 5.1.2.1 Proposed Methodology

If a geologic medium is too dry to extract a water sample by conventional means, it still may be possible to obtain a sample if the water content in the medium is increased to the operational range of the vacuum lysimeter. One way to increase the water content, which does not require major modifications of commercially available equipment, is to inject a quantity of water through the cup into the medium immediately prior to sample collection. The injected water is allowed to mix with the pore water, and then removed.

The recovered water will represent some dilution of the native water and thus provide potentially useful chemical data. Although the samples will not yield the absolute concentrations present in undiluted water, the ratios and presence or absence of dissolved species can be obtained. This type of information may be sufficient for a variety of applications, including the determination of tracer travel time or leakage from a waste impoundment.

The modified methodology can be divided into three phases:

- The injection phase;
- The redistribution phase; and
- The recovery phase.

Many factors, some of which can be controlled by experimental design, affect the movement of water and dissolved chemicals in each phase. These are briefly discussed below.

The object in the injection phase is to inject through the porous cup a quantity of water sufficient to allow a sample to be withdrawn. The necessary quantity and injection rate depend upon the following factors which control the movement of water:

- The hydraulic conductivity of the medium;
- The degree of saturation;
- The hydraulic conductivity of the cup;
- Cup surface area; and
- The injection pressure of the water.

The first two variables are initially dictated by environmental conditions. The next two factors depend entirely upon the manufacture of the cup. A highly permeable cup is desirable to facilitate a practical rate of water injection. The last variable, injection pressure, is subject to control by the sampler.

If water is pumped into the lysimeter under sufficient positive pressure, water will flow through the walls of the porous cup into the surrounding medium. The flow rate will depend upon the magnitude of the hydraulic gradient generated and the hydraulic conductivity of the medium, which is a function of the moisture content.

The hydraulic gradient through the cup will at first be high because there is a positive pressure head inside the cup and a negative pressure head (matric suction) in the medium outside the cup. This will result in an initially large flow rate that decreases to some steady state value, and an advancing wetting front that becomes less defined with time. If the injection rate is sufficiently fast, the water content near the cup will greatly increase, perhaps even reach saturation. If the injection is sustained indefinitely, the moisture distribution about the cup will reach a steady state profile.

All injection regimes will result in the dilution of the native water. The rate at which the injected water mixes with the native pore water within the medium will depend upon the dispersive properties of the medium, the diffusion coefficients of the dissolved species, and temperature. These factors drive the chemistry of the waters in different directions. Injected water may partially displace the native water by piston flow, resulting in a gradient of chemical concentration that increases outward from the cup, whereas diffusion and dispersion will create a more uniform distribution of chemical concentrations.

During the injection phase a gradient of volumetric water content is created. In the redistribution phase, matric suction and gravity will draw water from the region surrounding the cup to adjacent, drier regions. Chemical and potential differences between the injected and native water will also be diminished by dilution.

Following injection, both redistribution and dilution will continue until respective equilibriums are established. These processes may be beneficial if the most chemically representative sample is desired. As time progresses, however, the water content may be reduced until the medium becomes too dry for sample recovery. Because of this problem, the timing of the start of the recovery phase is critically important. Under some conditions, the start of the recovery phase should commence immediately after the injection phase ceases. The ability to predict the approximate rate of redistribution and the optimal time to initiate recovery are important design parameters. Computer simulations are helpful for resolving these questions.

Although the methodology of the sample recovery phase is identical to the conventional methodology described above, the length of time that water can be drawn into the cup is constrained by the rate of water redistribution. Flow into the cup will cease when the matric suction exceeds the suction induced by applying a vacuum. If the surrounding medium becomes sufficiently dry, the flow regime may be reversed and a previously collected sample may be drawn out of the cup into the medium. Therefore, the sample must be extracted before this critical time.

Warrick and Amoozegor-Fard (1977) show analytically that a vacuum lysimeter can draw water from a radius generally less than a meter. This theoretical result suggests that it is not necessary to inject a large quantity of water to increase the moisture content of a large volume of soil. To minimize disruption of the natural flow regime, it is best to quickly bring the region adjacent to the cup (from which the sample is drawn) to near saturation by rapidly injecting a relatively small quantity of water.

#### 5.1.2.2 Computer Simulation

There are some design parameters of the vacuum lysimeter which can be optimized before the proposed methodology is used. A computer simulation is presented below which is used to predict how a representative system will respond to a specified set of conditions. The insight gained from the simulations will then be used for the design and implementation of field and laboratory experiments to test the proposed methodology.

Computer simulations can be used to predict how a system will act under a specified set of conditions and facilitate an understanding of how sensitive the system is to variation of one or more parameters. A model that has been verified to accurately simulate physical conditions can be

a powerful tool. Any number of hypothetical scenarios and methodologies can be simulated, tested and refined. The insight gained in simple problems can be applied immediately to more complex problems and the most promising results can then be checked experimentally.

A simulation of a physical system was designed to be simple yet sufficient to test whether the methodology presented above is consistent with the basic hydrologic principles. For this study the UNSAT2 variably saturated flow model (Davis and Neuman, 1983) was selected. The model solves equations of flow using a lumped-mass Galerkin finite element scheme that divides the flow region into discrete quadrilateral and triangular elements. The model can simulate axially-symmetric, three-dimensional, variably-saturated flow.

Results generated by the UNSAT2 model have been verified experimentally. The program has a restart feature which enables the user to reset input data, reset boundary conditions and continue the simulation from the end of any previously completed stage, as many times as desired. For further information the reader is referred to Davis and Neuman (1983).

Figure 5.7 shows the finite element mesh used to represent a simplified, axially-symmetric porous cup and geologic medium. The mesh overlies the right side of a vertical plane that cuts through the lysimeter. The left side of the flow system is a mirror image of the right side and is deleted for simplicity. The region contains 44 discrete triangular and quadrilateral elements defined by 42 corner nodes. The model assigns head values at nodal points based upon numerical integration of elemental areas, thus the mesh is finer near the cup where the most precise results are desired.

Although a lysimeter is shown at the left side of the mesh, it actually lies outside of the flow region. Nodal points 5, 6 and 7 represent the right wall of a cup and form the only part of the boundary where water can enter or leave the system. Flow in or out of the cup was simulated by prescribing a constant value of hydraulic head at these nodes.

When the hydraulic head is greater than that in the surrounding medium, water flows outward; when hydraulic head is less than that in the surrounding medium, water flows inward. This simplified construction eliminates the need to model the properties of the ceramic cup, instead allowing the focus to be on the variables effecting flow in the medium.

In a physical system, the head values on the cup exterior need not always be constant during injection. If the pressure inside the cup is

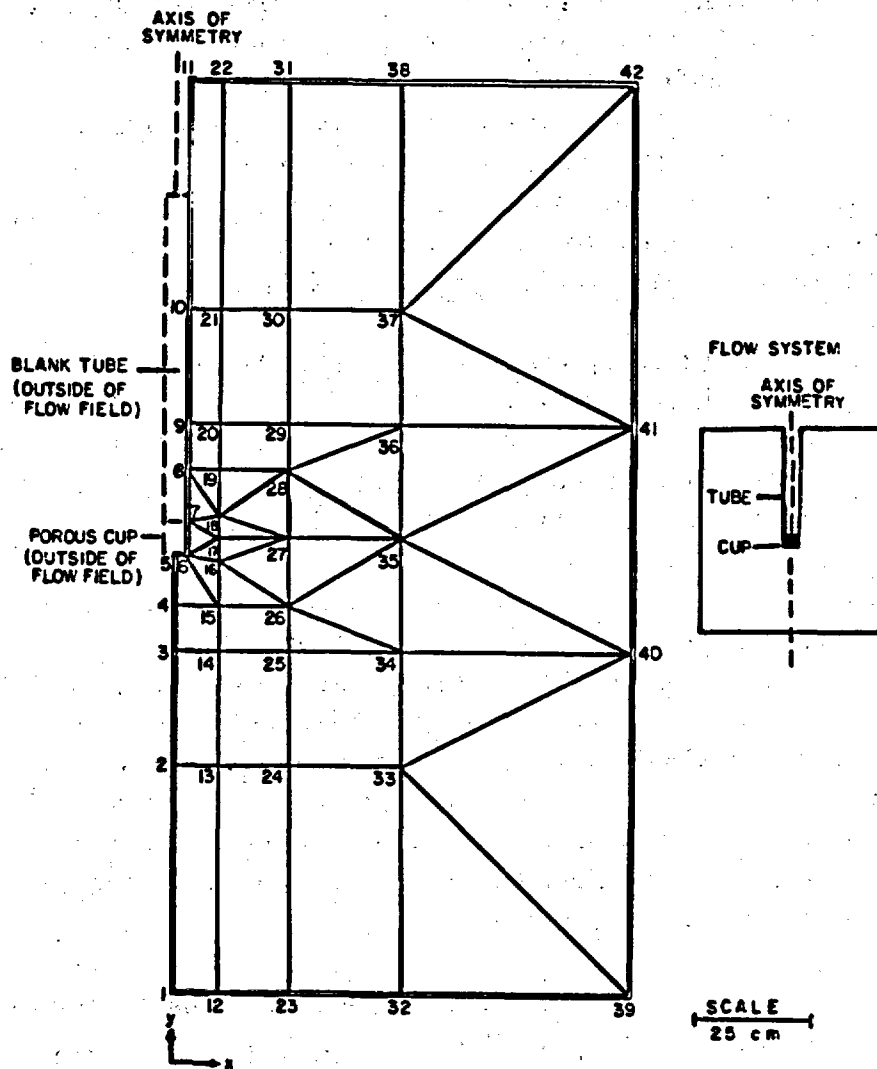


Figure 5.7 Finite element mesh. The flow field contains triangular and quadrilateral elements which are defined by the numbered corner nodes. The lysimeter shown forms part of the left side boundary, along an axis of symmetry. The region simulated is the right side of a mirrored pair.

held constant, then the head on the exterior would increase as matric suction decreases. On the other hand, if the head at the cup exterior is held constant, an identical flow regime could be generated if the pressure inside the cup is varied. In fact, this is what is assumed to happen in the simulation. In both cases the rate at which the head changes is related to the rate at which inflow through the medium changes by the hydraulic gradient.

This simplification has important consequences because it means that flow through the cup is not explicitly modeled, thus the flow rate through the system must depend entirely upon the properties of the medium. Initially, the medium is relatively dry and matric suction is high, thus the gradient of hydraulic head between the cup and the medium will be at a maximum. The rate of outflow from the cup will initially be rapid, but quickly diminish as increased water content in the medium reduces the head gradient.

Eventually, a steady state flow may be reached. Because the mass of water entering the system is conserved, the volume of flow through the medium for a given interval of time must also be equal to the volume of flow through the cup. Darcy's law can thus be used to calculate the head change across the cup required to produce the simulated flow in a given time interval. Once this is known, the magnitude of pressure that must be applied inside the cup to maintain the prescribed pressure head on the cup exterior can also be determined.

The flow region simulated contains an isotropic, homogeneous, porous soil with the properties of the Gilat sandy loam soil described in the catalogue compiled by Mualem (1976). This soil contains 55 percent fine sand and sand, 45 percent silt and clay, has a porosity of 44 percent, a saturated hydraulic conductivity of  $7.64 \times 10^{-6}$  m/s, and a bulk density of approximately  $1.45 \text{ g/cm}^3$ . The initial volumetric water content of the soil is 12.7 percent, corresponding to a saturation of 30 percent and a matric suction of 1020 cm.

The three phases of the simulation correspond to the three parts of the hypothetical methodology. In the first phase, water injection was simulated for 720 seconds. The second phase begins at this time; the injected water being allowed to redistribute for two hours. After redistribution, the restart facility of UNSAT2 was used to reset the moisture contents within the soil to conditions observed at the end of the injection phase. As a result, the simulation of the final, recovery phase immediately follows the injection phase.

Figure 5.8 is a plot of the simulated injection rate versus time. The initially high rate rapidly decreased and asymptotically approached a steady state value of approximately  $6 \text{ cm}^3/\text{s}$ . After 700 seconds the total volume of water injected (equal to the area under the curve) was  $6200 \text{ cm}^3$ . Figure 5.9 demonstrates the expansion of the wetted region with time. Three positions of the 20 percent volumetric water content isobar are shown for times equal to 30, 100 and 720 seconds respectively, defining a region of 20 percent or greater water content about the cup. The volumetric water content prior to injection was 12.7 percent. During the simulation, the maximum water content reached 30 percent (68 percent of saturation), occurring at the cup wall.

Because all water entering the system must first flow out through the cup, the inflow rate through the medium can be used to calculate the head gradient through the cup for different times. Darcy's law relates the volumetric flow rate through a medium with a hydraulic conductivity and a cross sectional area to the gradient of hydraulic head acting on the fluid. In these simulations, the assumed cup had a surface area of  $109 \text{ cm}^2$ , a hydraulic conductivity of  $8.6 \times 10^{-6} \text{ m/s}$  and a wall thickness of 0.239 cm.

Darcy's law was combined with the flow rates from Figure 5.8 to calculate the gradient of hydraulic head through the wall of the cup during discrete time intervals. Calculated values were then added to the specified values at the cup boundary, giving the hydraulic head that had to be applied inside the cup to generate the observed rate of injection during that time interval. The calculated pressures represent an average for the entire cup. (The average hydraulic head gradient through the cup is approximately equal to the average pressure-head gradient through the cup because the gravity head along any horizontal line through the cup wall is constant, and also because the cup is only 6.2 cm long.) These calculations yield the pressures which have to be applied inside the cup to generate the desired rates of injection.

For example, the simulation indicates that at time equal to 100 seconds, 3300 cm of pressure must be applied to generate the observed injection rate, which from Figure 5.10 is seen to be  $12 \text{ cm}^3/\text{s}$ . The plot shows that at early times a physical system has not been realistically simulated because the required injection pressure heads would probably exceed the breaking strength of most samplers. However, within 45 seconds physically attainable pressure heads, approximately 5000 cm of water, generate  $5,200 \text{ cm}^3$  or 82 percent of the total inflow. Thus, although requiring qualification, these data demonstrate that an appreciable flow rate can be injected through a porous cup.

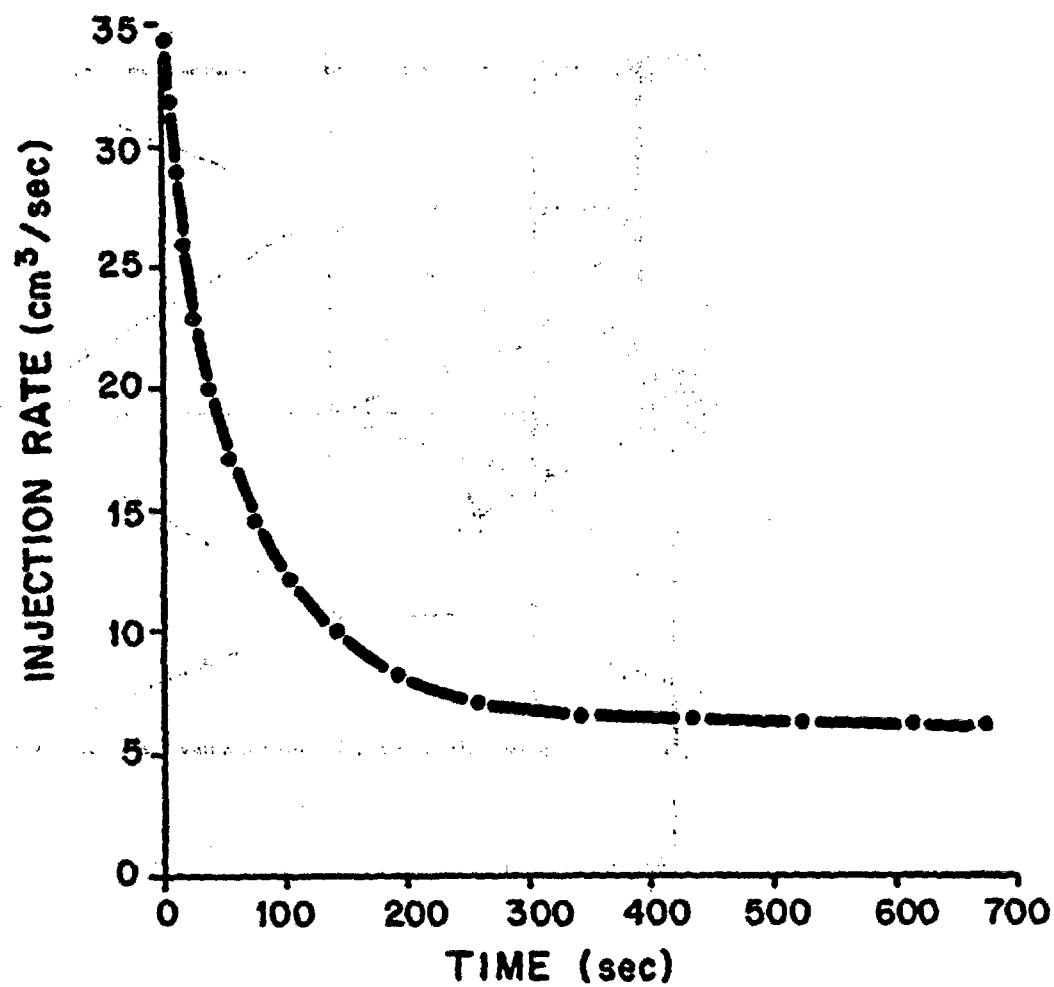


Figure 5.8 Plot of injection rate against time. The injection rate is initially rapid, then quickly decreases toward a steady state value of approximately 6 ml/sec. The area under the curve is equal to the cumulative injection volume.

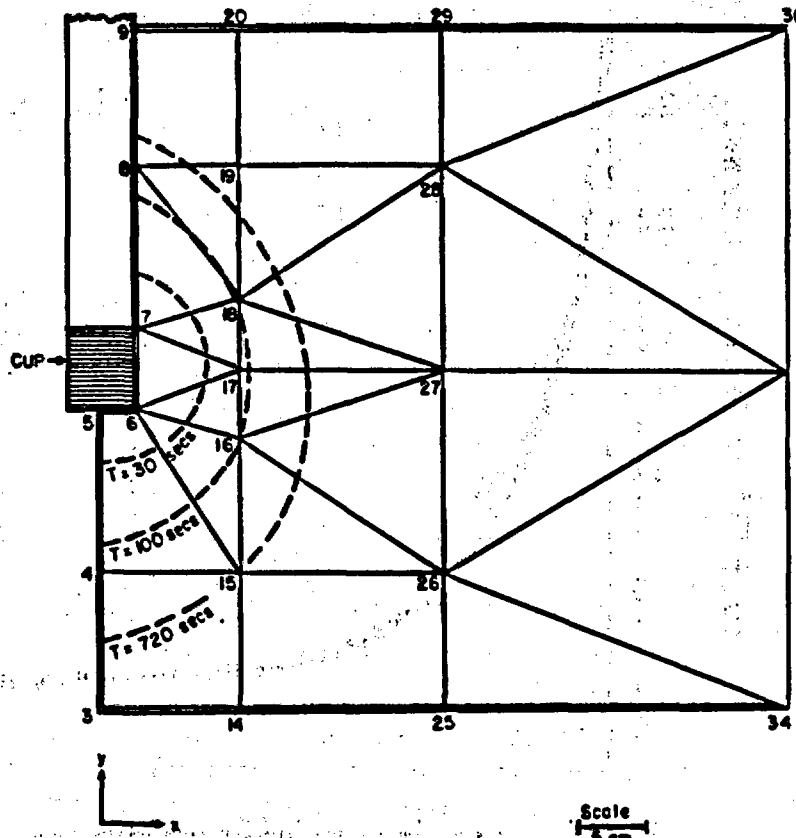


Figure 5.9 Expansion of the wetted region. Three positions of the 20 percent volumetric water content isobar corresponding to  $T = 30$ , 100, and 720 sec are shown. Each isobar defines an area of 20 percent or greater water content about the cup. Antecedent moisture content in the soil was 12.7 percent.

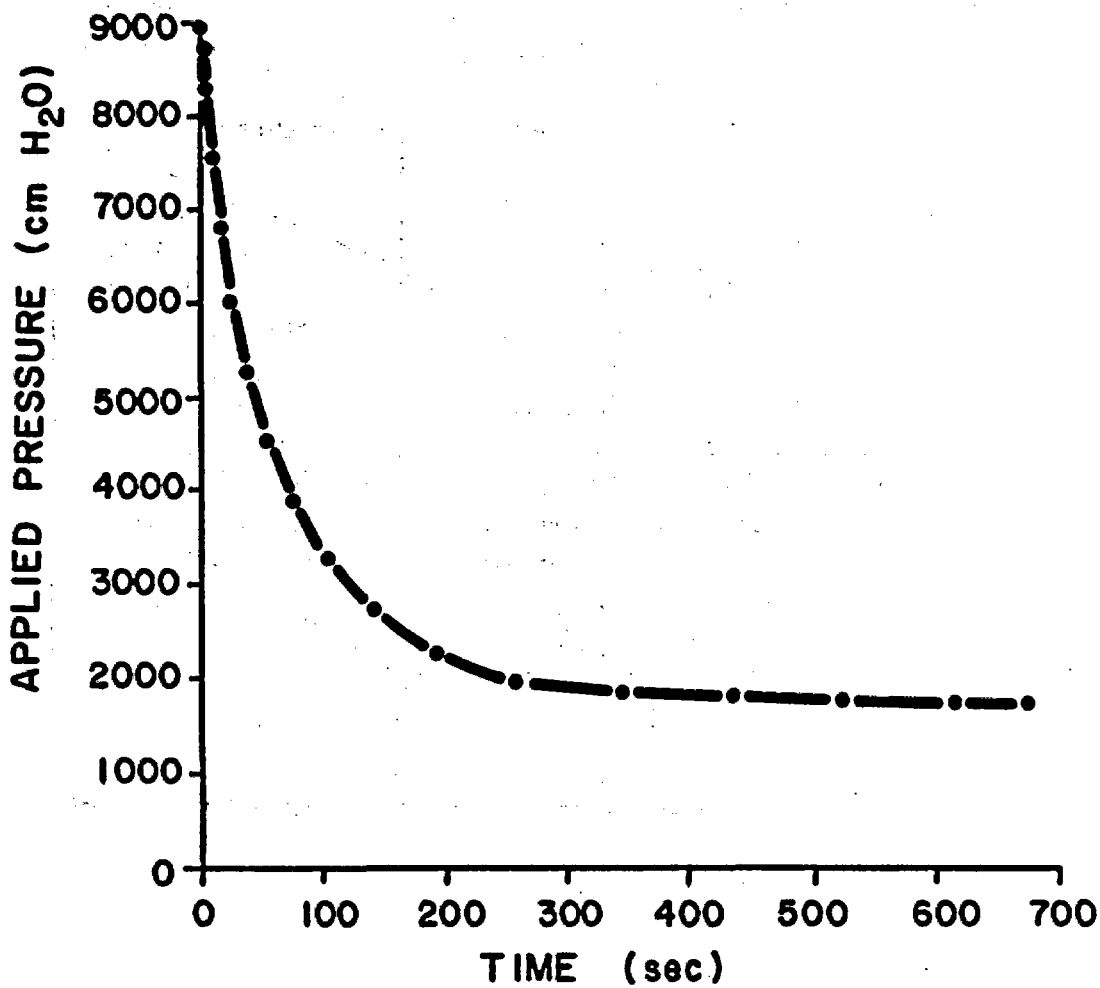


Figure 5.10 Applied pressure against time during the simulated injection phase. The magnitude of applied pressure inside the cup required to generate the simulated injection rate was calculated for different times using Darcy's law. Although pressures which may exceed the breaking strength of ceramic cups were required at times before 45 sec, this interval accounts for only 18 percent of the total flow.

In Figure 5.11 moisture profiles are shown for different times during the redistribution phase. The vertical axis corresponds to volumetric water content and the horizontal axis is a scale plot of distance along a horizontal line from the midpoint of the cup. The baseline at 12.7 percent represents the uniform water content prior to injection. Profiles are shown for three times after the end of injection, and the gradual reduction in the moisture content near the cup is indicated by progressively flatter curves. Given sufficient time, the moisture profile would begin to resemble the profile for antecedent conditions.

These data suggest that the recovery phase must be initiated within some critical time interval after injection, else little sample will be collected. The length of the interval will depend upon the medium's initial water content, and sample volume requirements.

The simulation of recovery was similar to that of injection in that constant values of hydraulic head were specified at the cup exterior. This time Darcy's law was used to calculate the magnitude of vacuum inside the cup. These results are shown in Figure 5.12. Recovery began immediately after the cessation of injection, at 720 seconds. The calculated pressures range from 436 to 811 cm of suction. These pressures are physically attainable.

Figure 5.13 is a plot of the cumulative volume of recovered water versus time. The rate at which water was drained from the medium decreased from initial values, reaching zero inflow near 1216 seconds. This is an important event for two reasons:

- The volume of recovered water reached a maximum of 146 cm<sup>3</sup>; and
- After this time, previously recovered water drained from the cup.

The recovery rate decreased because the medium's hydraulic conductivity decreased. After 1216 seconds the surrounding soil had become so dry that matric suction exceeded the applied suction, and water was drawn from the cup. The simulation thus confirms that water samples can be recovered only for some limited time period after injection. The greater the antecedent matric suction, the shorter the time interval. However, the interval can be lengthened by increasing the quantity of injected water.

### 5.1.2.3 Conclusions and Applications

The simulations described above suggest that the proposed injection-recovery methodology is appropriate for obtaining sufficient water from media that are far too dry to permit the use of conventional sampling

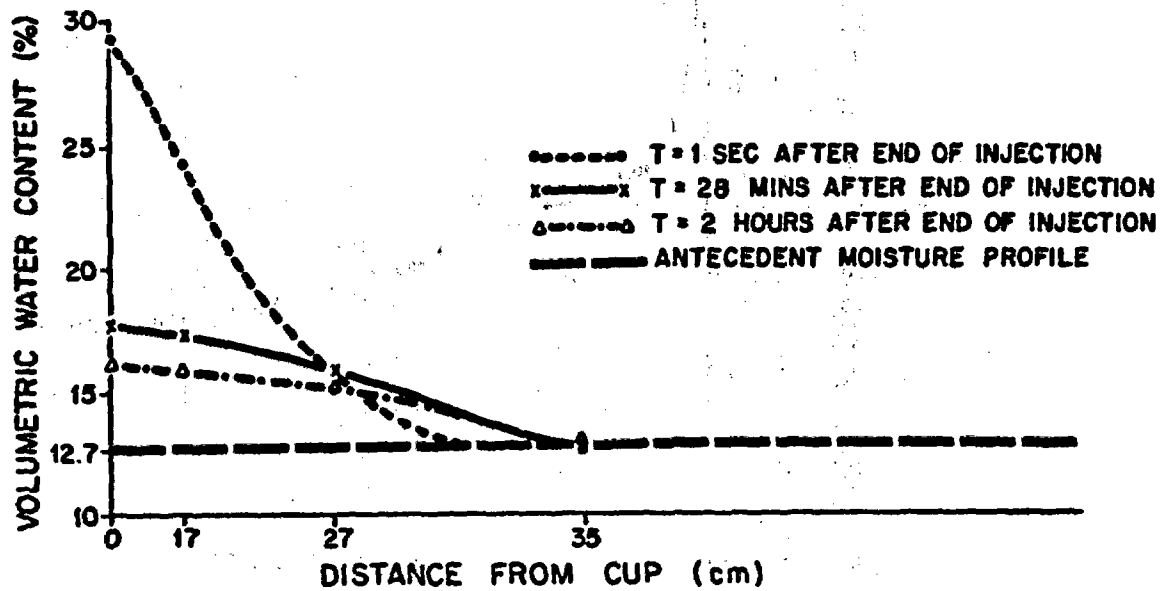
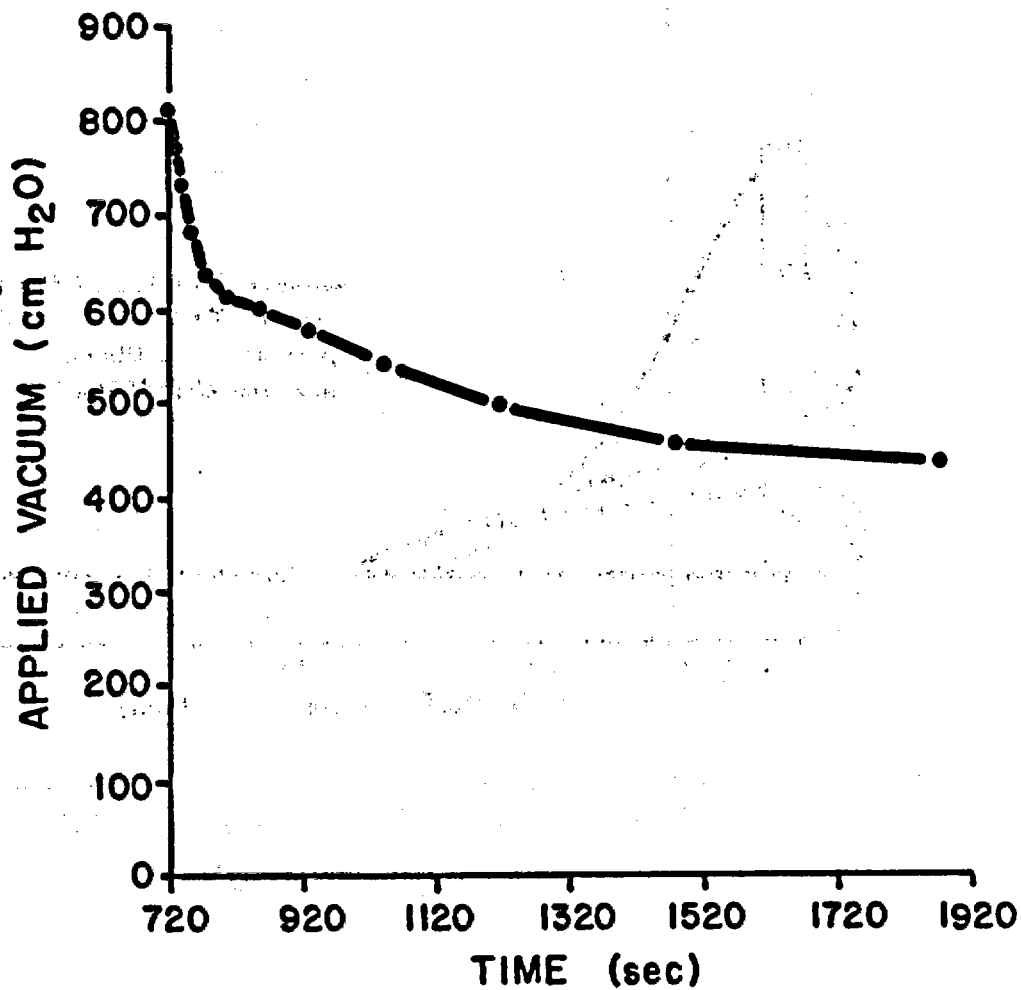


Figure 5.11 Moisture profile for three times during redistribution. The vertical axis corresponds to volumetric water content and the horizontal axis is a scale plot of node distance along a horizontal line from the midpoint of the cup. At  $T = 1$  sec after the end of injection, the gradient of moisture content is steep. With time the gradient decreases as water is drawn into unwetted areas. Given sufficient time the moisture profile would approach the shape corresponding to the antecedent moisture condition.



**Figure 5.12** Applied vacuum during the recovery phase. The magnitude of vacuum inside the cup required to generate the simulated sample recovery rate was calculated for different times using Darcy's law. All calculated values fall within practical limits. Recovery began at 720 sec.

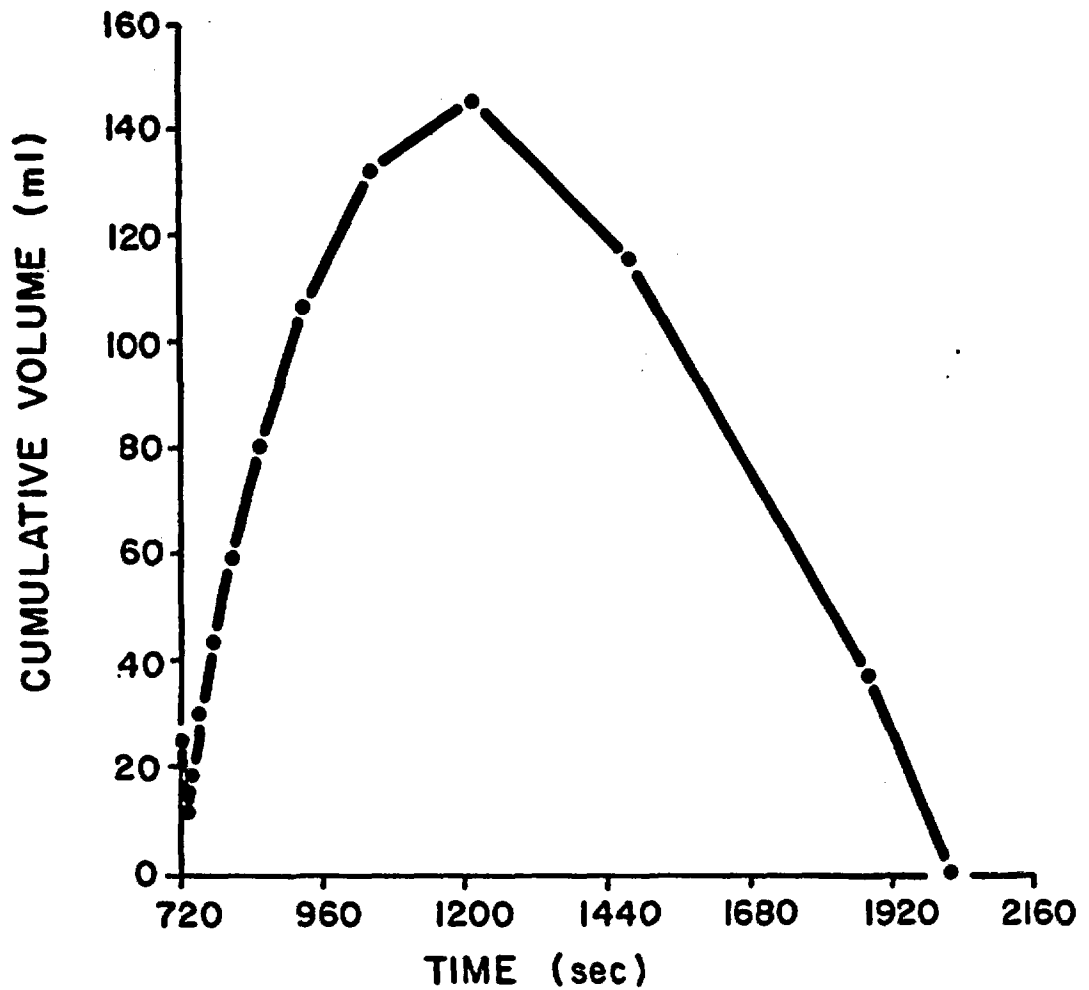


Figure 5.13 Cumulative volume of recovered water against time during the simulated recovery phase. Recovery began at 720 sec and the rate at which water drained from the soil rapidly decreased with time, as indicated by the decrease in slope. The maximum molume of recovered water was 146 ml. At times after 1216 sec, matric suction exceeded the applied suction and previously recovered water was drawn from the cup back into the soil. By 2016 sec all recovered water had been lost. It is important to collect the water sample before the gradient reverses.

techniques. The simulations also demonstrate that the timing of the injection and recovery phases is important. The recovery phase must begin and end before redistribution can reduce the moisture content near the cup below critical values. Simulations prior to sampling may therefore be useful for optimizing the timing of sampling phases.

Recovered samples may contain highly-diluted native water. The chemical data obtained from samples may therefore only be of a qualitative nature. The data may, however, be sufficient for determining the identity of dissolved constituents or the presence or absence of target compounds. Such data can be used to determine the travel time of water through the unsaturated zone to the sampling point, or detect leakage from a waste impoundment.

Qualitative data may be obtainable if the injected water contains a known concentration of some conservative tracer and none of the target compounds. The ratio of the concentration of tracer in the recovered water to its input concentration would then be related to the percent recovery of native water by

$$(5.6) \quad C_n = 1 - C_r / C_0$$

where

$C_n$  is the concentration in the native water;  
 $C_r$  is the concentration in the recovered water; and  
 $C_0$  is the concentration in the injected water.

Once the percent recovery is known the concentrations of the target compounds can then be adjusted accordingly. For repeated sampling, the same tracer could not be used again until its residual concentration in the medium had become negligible.

The results presented above are based on highly-simplified representations of a physical system. The simulation can be improved by explicitly modeling flow through the porous cup. By allowing head values on the cup exterior to change a more accurate simulation can be obtained. Optimal injection rates, injection volumes, redistribution times and recovery periods may be approximated for a variety of media, including fractured rock, as well as variable initial water contents.

The proposed methodology should be tested in a variety of geologic media and a range of initial water contents. The results of this testing should then be compared to computer simulations. A verified injection-recovery simulation would aid the design of future experiments. The

degree to which injected water displaces and dilutes matric water needs to be examined, as do the effects of repeated sampling upon the chemical and physical properties of the system. It may be possible to incorporate the results of simulations and experiments into tables and graphs that provide guidelines for applying the injection-recovery methodology in a variety of field settings.

### 5.1.3 Vapor Condensation

In this section the employment of thermoelectric cooling techniques as a method of sampling water vapor in the unsaturated zone is examined. This method makes use of the Peltier cooling effect produced by passing an electric current through a semiconductor junction. A thermocooling module is composed of a number of these junctions and is overlain by a ceramic plate, producing a surface upon which condensation of water vapor may occur when cooled to the dewpoint. When operated in a borehole in the unsaturated zone, this provides a means of collecting a sample of water vapor. The development of such sampling techniques is important for obtaining information about the mechanics of solute transport in the vapor state, which may occur either as a gas or aerosol transport process. (For more information on vapor transport mechanisms, the reader is referred to Chapter 6 of this report.)

Vapor sampling is of particular importance as it applies to the evaluation of areas under consideration for high level waste repositories where water vapor transport of radionuclides may occur. Radionuclides which have significant gas phase (including  $^3\text{H}$ ,  $^{14}\text{C}$ ,  $^{85}\text{Kr}$ ,  $^{129}\text{I}$ ) are important in the study of gaseous transport mechanisms. In the case of aerosol processes, any radionuclide which enters the environment from a failed container (including fission products and transuranic actinides) may be transported from the repository site.

The method also has potential use in conjunction with tracer tests in the unsaturated zone. An example of this is the detection of thermonuclear tritium. Before 1952, the tritium content of natural waters was in the range of 1 to 10 tritium units (1 TU = 1  $^3\text{H}$  atom for every  $10^{18}$  total H atoms). Testing of thermonuclear devices since 1952 greatly increased this value to over several hundred tritium units.

The movement of the front of highly tritiated water has been used in the area of groundwater hydrology to both date and trace the movement of water in the saturated zone. Not much is known, however, about the behavior of tritium in the vapor state in the unsaturated zone and this device could be used to gain new information in this area. Should the

tritium level in a region be found to be below detection limits, the use of artificial tritium or some volatile tracer may be considered.

The examination of the thermocooling technique will begin with a discussion of the basic principles of thermoelectricity pertaining to cooling mechanisms. This will be followed by the implementation of these techniques to collection of vapor samples, including a detailed description of the actual apparatus used in this research. Results obtained in laboratory and field testing, along with suggestions pertaining to sample collection in the field will be evaluated.

### 5.1.3.1 Principles of Thermoelectricity

The underlying factor which produces the desired cooling effect in any thermoelectric application results from the unusual properties of the semiconductor. A semiconductor is a material having an electrical resistivity intermediate between that of a metal and of an insulator. The resistivities of metals are from  $10^{-2}$  to  $10^{-6}$  ohm-cm, semiconductor resistivities are between  $10^{-2}$  and  $10^9$  ohm-cm, while insulators range upward from values of  $10^{12}$  ohm-cm. In the case of a metal, electric conduction is due to the flow of valence electrons of the atoms constituting its crystal lattice.

In the case of a semiconductor, all or nearly all electrons are tied up in bonds between neighboring atoms. This occurs with elements of Groups III and IV of the Periodic Table, such as germanium, gallium, silicon, etc. At very low temperatures (approaching absolute zero) these materials act as insulators but as temperatures increase, thermal excitation releases electrons from their interatomic bonds and the application of an electromotive force will enable the released electrons to move through the crystal. Thus, a basic property of the semiconductor is that electronic conduction increases with increasing temperature.

The bond site from which an electron has been ejected is left with a vacancy, having a net positive charge equal and opposite to the charge on the ejected electron and is referred to as a "hole". The hole produced at a particular bond site may then acquire an electron from a neighboring bond site creating a new vacancy. As this process continues the hole effectively becomes a positive charge carrier and is made to wander through the crystal in a direction opposite to that of the electron or negative charge carrier.

Under electromotive force the replacement of a vacancy by an electron will take place in the direction favored by the force and the positive

and negative charge carriers will acquire drift velocities in opposite directions. The movement of the charge carriers in opposite directions is equivalent to electric currents travelling in the same direction. The effects of the electrons and holes are additive.

In its path through the semiconductor crystal, an electron may eventually encounter a hole, whereby a recombination occurs and both charge carriers disappear. The conductivity in a semiconductor is constant under an applied current because ejections and recombinations are occurring at the same rate. Semiconductors which have an equal number of thermally produced electrons and holes are known as intrinsic semiconductors.

The addition of impurities to an intrinsic semiconductor by replacing an atom in a pure crystal lattice with an atom having a different valency has the effect of increasing the density of charge carriers in the crystal. This process of adding impurities is known as doping, and the material produced is called an extrinsic semiconductor, which is the type used in thermoelectric cooling applications.

There are two types of extrinsic semiconductors, n-type and p-type, the difference between them depending on the valency of the impurity atom added to the pure crystal. If the impurity atom has an extra electron, as in the addition of arsenic to germanium, the additional electron will have no bonding site and will be free to move about the crystal along with the thermally excited electrons.

There will, however, be no compensating positive hole produced by this electron because the positive charge is locked in place as the ion of the impurity in the crystal lattice. The impurity has thus contributed an electron without a compensating hole and is called a donor. The extrinsic semiconductor produced has the excess negative charge carriers typical of the n-type.

If the impurity is of a valency one lower than that of the pure semiconductor, as in the addition of gallium to germanium, the impurity will in this case produce a positive hole by having one less electron than it needs to complete bonding. The positive hole is then free to drift about the crystal but the complementary negative charge is locked in place in the crystal lattice as the ion of the impurity. When an impurity contributes a positive charge carrier (or hole) without a compensating negative charge carrier (or electron), it is called an acceptor and the extrinsic semiconductor produced is referred to as a p-type.

A p-n junction is formed by joining together two sections of a semiconductor material, one section of which has been doped with an acceptor impurity (forming the p-side), the other being doped with a donor impurity (forming the n-side) and in this way a thermocouple is produced.

Diffusion processes will tend to bring some of the mobile holes across the junction to the n-side, and some of the mobile electrons across to the p-side which will result in two main differences between the semiconductor material at either side of the junction. First, each side will be depleted of its normal amount of charge carriers and second, a net positive charge on the n-side and a net negative charge on the p-side occur due to the presence of the charged ions in the crystal structure which have been left behind after diffusion of the charge carriers.

The net electric charge at either side of the junction serves as a barrier to the continuing flow of charge carriers across it and creates an energy potential which the mobile charges must overcome in order to leave the region from which they diffused.

This potential energy difference occurring at the p-n junction gives rise to the thermal effect first observed by J.C. Peltier in 1834. Peltier noted that temperature change occurs in the vicinity of the junction between dissimilar conductors when a current is applied. The effect was further evaluated by Lenz in 1838 who determined that heat will be produced or absorbed at a junction between two dissimilar conductors depending on the direction of current flow. He demonstrated this by freezing water at a bismuth-junction and then melting the ice by reversing the current direction.

The Peltier effect arises because of the difference in the potential energies of the charge carriers in the materials on either side of the junction. Therefore, when a current is passed through the junction energy must be either absorbed from the surroundings (producing cooling) or released into the surroundings (producing heat) in order to maintain conservation of energy and charge. The effect is quantified by the Peltier coefficient which is a measure of the rate of heat absorption accompanying the passage of a current through a junction, given by:

$$(5.7) \quad Q = \pi_{ab} i$$

where

$Q$  is the heat absorbed (in watts);

$i$  is the current (in amps); and

$\tau_{ab}$  is the Peltier coefficient (in watt/amps). The coefficient is positive if the current is flowing from point a to point b across a junction and  $Q$  is absorbed from the surroundings.

There are three main components to a thermoelectric cooling system in any application. These include:

- The cooling module, which is composed of a number of thermocouples joined electrically in series and thermally in parallel;
- The power supply, in this case a DC source; and
- A heat sink which discharges accumulated heat energy from the system.

In the following paragraphs, the functions and subcomponents of each of these main elements will be examined more closely.

In the thermoelectric cooling module, semiconductor materials of dissimilar characteristics (n-type and p-type) are connected electrically in series and thermally in parallel in such a manner that two junctions, one hot and the other cold, are created due to Peltier cooling when a current is passed through them. The arrangement is shown schematically in Figure 5.14. The charge carriers (electrons and holes) of the n-type and p-type materials are the agents that move heat from the cold to the hot junction.

Heat is absorbed at the cold junction as the charge carriers pass through the potential energy barrier described previously and remove energy from their surroundings in order to maintain a conservation of energy. The heat is pumped to the hot junction at a rate proportional to the carrier current passing through the circuit and the number of thermocouples in the module.

A single module may contain anywhere from eight to one hundred couples. Ceramic-metal laminated plates are located at each junction and it is on these surfaces that the temperature differences are felt. The ceramic plates are separated from the thermocouple junctions by a thin, electrically insulating material that is capable of providing good thermal contact between the plate and the junction. The applied current is run through two electrical leads as shown.

Due to the natural tendency of heat to flow from a hotter to a colder region, the energy absorbed and transported to the hot junction by the electronic carriers will tend to flow back to the cold junction.

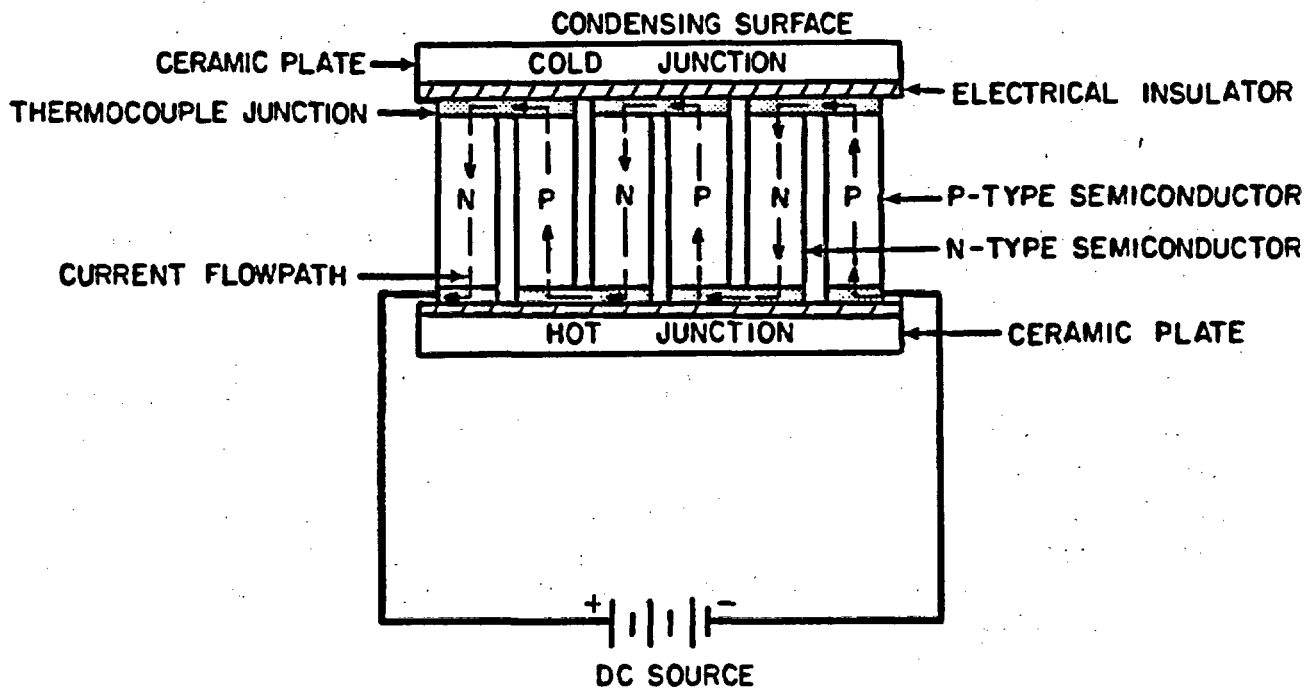


Figure 5.14 Schematic cross section of Thermoelectric Cooling Module. Semiconductor materials of dissimilar properties (n-type and p-type) are connected thermally in parallel and electrically in series so that heat is absorbed on one surface and carried to the other. The junction is formed by welding the p- and n-type semiconductor materials together. The reduction of temperature at the cold junction results in condensation of vapor on the ceramic surface. Actual size of the module used in these experiments is (3 x 3 x .4) cm.

Therefore, a method must be provided for dissipating the energy at the hot junction to colder environment or heat sink. The cooling module is only a mechanism by which energy is removed from the source to the sink the thermocouple alone does not eliminate heat. The heat sink may take on any one or a combination of three forms:

- Massive blocks of material, which must have enough mass to absorb the required amount of heat before reaching equilibrium;
- Free and forced convection-cooled fins, consisting of a finned heat sink with a blower; and/or
- A liquid cooling system requiring coolant, tubing, and a pump.

The power supply is usually the largest component in the thermoelectric cooling system. Its function is to convert the available AC (normally 120 volt, 60 cycle) to the DC required by the module.

There are a number of parameters which must be evaluated when attempting to make use of this type of cooling system in a particular application. These include:

- The total heat load (how many watts must be pumped from the heat source area);
- Module current and voltage;
- Required cold junction temperature;
- Ambient temperature; and
- Coefficient of Performance, COP, which is the ratio of the amount of heat absorbed at the cold face of the module to the electrical power supplied.

In the following section, these parameters will be assessed, and the components needed to provide them will be determined, for application of the cooling system to the condensation of water vapor as a sampling technique in unsaturated rock.

#### 5.1.3.2 Application to Vapor Condensation

The calculations made in deriving the values of the parameters mentioned above for this specific application were based on the following assumed field conditions. A 1-cm<sup>3</sup> sample of vapor condensate must be removed from a borehole (diameter 4.5 cm) in a fractured, welded tuff (it is necessary only to multiply by the number of cm<sup>3</sup> desired where larger samples are required). The interval of interest is located in the unsaturated zone where the relative humidity under natural conditions may vary from no less than 98 to 100 percent, and where the average temperature is assumed to be approximately 25°C.

The total heat load which the cooling system must remove per  $\text{cm}^3$  of condensate formed is equal to the sum of the energy required to change the temperature of the water and the energy required to condense it. This is calculated by:

$$(5.8) \quad Q_T = mC\Delta T + mH_v$$

where

$Q_T$  is the total energy required (Joules);

$m$  is the mass of water, i.e., 1 gm;

$C$  is the specific heat of water at  $25^\circ\text{C}$  (i.e.,  $4.186 \text{ J/gm}^\circ\text{C}$ ); and

$H_v$  is the heat of vaporization of water at  $25^\circ$  (i.e.,  $583.2 \text{ cal/gm}$ ).

Because the rock is close to saturation with respect to relative humidity, it is necessary to lower the temperature only slightly in order to reach the point where condensation will occur, so  $\Delta T$  is considered to be  $1^\circ\text{C}$ . Substituting these values into the equation yields  $584.2 \text{ cal}$  ( $2445.5 \text{ Joules}$ ) which is the total energy required to condense  $1 \text{ cm}^3$  of water.

There are a number of commercially available thermoelectric cooling modules which are capable of operating at this required energy level. For this application, the module chosen is produced by the Thermo Electric Cooling America Corp. (module series no. 950-71). The maximum heat load it is capable of removing is 30 watts which means it can remove the required  $2445.5 \text{ Joules}$  of heat energy in:

$$(5.9) \quad t = E/P = 2445.5 \text{ Joules}/(30 \text{ Watts}) = 81.5 \text{ sec.}$$

where

$t$  is time;

$E$  is energy; and

$P$  is power.

If the module is operated at 75 percent of its maximum capacity (i.e., 22.5 watts) to improve its coefficient of performance, the time required to condense  $1 \text{ cm}^3$  is 2 minutes. The size of the module ( $3 \times 3 \times 0.4 \text{ cm}$ ) meets the restriction set by the borehole size of 4.5 cm diameters.

Graphs are usually provided by the company for determining the module current and voltage needed to meet specific results. These plot current as a function of required heat load and the difference between ambient and cold junction temperatures, and the voltage as a function of current and temperature difference. Entering the graphs for the chosen module

with values of  $\Delta T = 1^\circ\text{C}$  and heat load (Q) of 22.5 watts yields a current of 3.25 amps and voltage of 5.5 volts. These are the values of current and voltage with which the cooling module must be supplied in order to produce the  $1 \text{ cm}^3$  of condensate in two minutes.

Once these parameters are known, the heat sink and power supply needed to provide them can be determined. The experimental apparatus is shown in Figures 5.15 and 5.16. Figure 5.15 shows a the cooling module and heat sink, and Figure 5.16 depicts the entire cooling system and sample collection method when operated in the field. When the dew point temperature is reached, condensate will form on the ceramic surface of the cooling module from which it can be collected for analyses.

An aluminum block is attached to the hot junction for removal of heat from the surface and a 0.64 cm copper tube is connected to the block, through which cold water is circulated. The entire module (other than the cold surface) is covered with a thin heat insulating material to reduce heat flow back to the cold junction by convection.

#### 5.1.3.3 Testing and Application

The apparatus was first tested in the laboratory to determine the actual amount of time required to collect a sample in comparison with the 2 minutes per  $\text{cm}^3$  of condensate as was determined by theoretical calculations. This was done by placing the module directly above a free water surface inside a sealed glass cylinder. The electrical leads and tubing for water circulation were run through a rubber stopper.

It was found that by the application of 2.25 amps (3.5 volts), the amount of time required to collect  $1 \text{ cm}^3$  of sample was actually 15 to 20 minutes. An increased current to 3.0 amps (5.0 volts) cooled the module to below freezing point and ice crystals were formed. The rate of sample collection was no greater than for the lower current. A decrease in current to 1.0 amps (2.75 volts) resulted in an increased collection time for  $1 \text{ cm}^3$  to 20 minutes.

The discrepancy between the amount of time actually required and that predicted may be explained by a failure to maintain 100 percent relative humidity conditions within the container. After removal of the initial vapor present in the space above the water, the air may remain at less than 59 percent of the free water surface. In this case, the rate of condensation will depend on vapor diffusion.

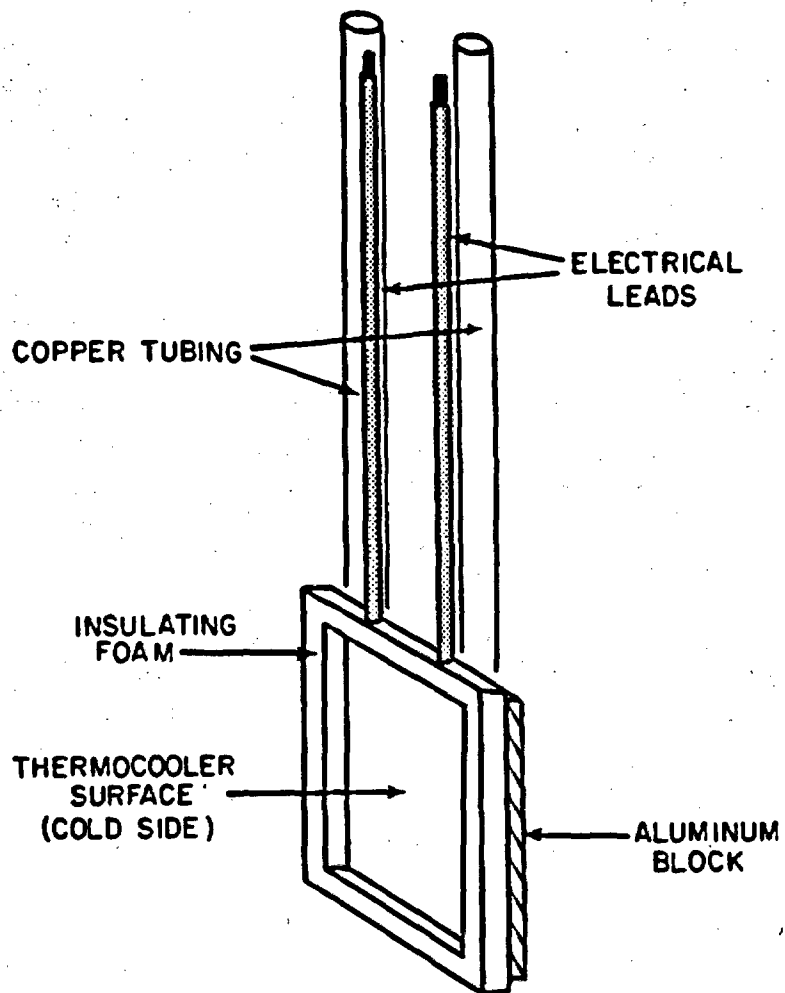


**Figure 5.15** Thermoelectric Cooling System: Current is run through leads so as to create a reduction in temperature on the exposed surface, resulting in vapor condensation. The opposite surface of the module is attached to an aluminum block heat sink. In addition, copper tubing is attached to the block and used to circulate cold water to dissipate heat.

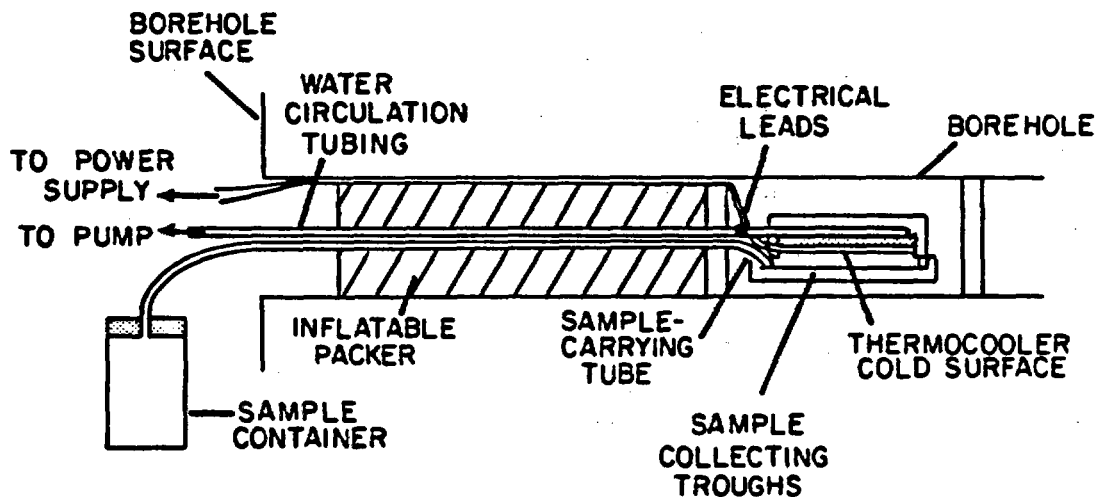


**Figure 5.16 Schematic Diagram of Proposed Field Application:** The thermocooling system is inserted into a nearly horizontal borehole attached to one end of an inflatable packer assembly, which is used to isolate the section of interest. Tubing for water circulation and for drawing off the sample are run through the center of the packer. Electrical leads run between the borehole wall and the packer and fit snugly when the packer is fully inflated. When operated, the condensate formed on the thermocooler cold side will drip off into the sample collecting trough and be carried through tubing to the sample container at the surface.

Another possible explanation may be a reduction in efficiency due to thermal convection and conduction processes in the system which are transporting heat to the cooling surface of the module. This problem is directly related to the fact that thermoelectric cooling systems are ideally designed to be operated in a vacuum, which would not be possible in an application such as this, especially in the field where it is desired to collect a sample from a system open to the environment. Therefore, a certain amount of inefficiency may be inherent to using thermoelectric cooling devices to collect vapor condensate samples from unsaturated rock.

Figure 5.16 also illustrates a possible setup for collecting the condensate in the field. A preliminary test was performed to establish the potential of using the method to collect water vapor samples in the field, and to determine what adjustments in design may be necessary. The field test site is the unsaturated densely welded tuff unit at the road tunnel near Superior, Arizona, in a road tunnel approximately 15 m from the tunnel wall. The borehole is 4.5 cm in diameter and is nearly horizontal.

The thermocooling system was inserted into the borehole attached to one end of an inflatable packer assembly which is used to isolate the section of interest. Tubing for water circulation and sample collection were run through the center of the packer. Electrical leads running between the borehole wall and the packer fit snugly when the packer was fully inflated.

At the surface, the electrical leads were attached to a DC converter which is connected in turn to a portable generator. Water was moved through the heat sink by means of a peristaltic pump which circulated the water through a cold water reservoir at the surface. When operated, the condensate formed on the thermocooler cold side dripped off into a sample collecting trough and from there it was carried through the packer center and collected in the sample container in the tunnel.

For the trial run, a current of 2.5 amps (5.0 volts) was applied. After operating the system for approximately 20 minutes, the packers were deflated and the unit was removed from the borehole. It was found that the entire cooling surface of the module was covered with ice, which when melted results in a volume of liquid condensate of slightly more than 2 cm<sup>3</sup>.

Thus, efficiency was somewhat increased in the field situation, perhaps due to the high relative humidity conditions. Improvements must be made,

however, in order to collect the large samples needed for tracer tests or detection of background tritium, within a reasonable period of time. One way in which this might be done is to connect several cooling modules together in series to condense vapor from a larger area. Temperature control may be improved by attaching a thermostatic device to the power supply so that a liquid or solid sample may be collected, depending on which is more desirable.

#### 5.1.4 Fluorescent Tracers

Fluorescent dyes are becoming increasingly popular as tracers in surface and ground water. In surface hydrology, they are commonly used in dispersion and time-of-travel studies. However, in ground water, their use has primarily been limited to studies of flow in karst systems, and in oil fields (Davis et al., 1985). They have also been used to trace soil water movement (Reynolds, 1966).

Although much has yet to be learned about the physio-chemical characteristics of various fluorescent dyes, several dyes show promise for use as tracers in unsaturated fractured rock. The dyes lissamine FF, rhodamine WT, and amino G acid all have low adsorption properties with respect to silicate materials, and would be well suited for use as tracers of fracture and matrix flow within tuffs. Other potential tracers include fluorescein, pyranine, and rhodamine B, although these are not as ideal.

Fluorescent dyes have a number of distinct advantages as tracers. Although costs vary considerably between dyes, fluorescent tracers are still relatively inexpensive due to their very low detection limits. In addition, conventional analysis techniques for fluorescence yield highly quantifiable results. Also the dyes may prove conservative as tracers in fractured rock systems due to their low adsorption characteristics.

Fluorescent dyes have some serious disadvantages as tracers, however. Many are notorious for their adsorbing onto mineral and rock surfaces. In addition, fluorescence intensity of some dyes is highly temperature and pH dependent. Similarly, high salinity levels as well as dissolved CO<sub>2</sub> also affect fluorescence intensity of certain dyes. High natural fluorescence of minerals may also limit dye use in some environments.

##### 5.1.4.1 Use in Fractured Rock

Standard analysis techniques for fluorescent tracers in surface and groundwater usually require use of a filter fluorometer. This type of

instrument is relatively simple to operate, yet provides a high degree of accuracy. However, standard filter fluorometers require dye solutions of low turbidity and of sufficient quantity to fill some type of sample compartment or cubette, and hence, their use has been primarily restricted to studies of surface water and of saturated ground-water systems. Other sampling techniques are necessary if fluorescent tracers are to be used in fractured volcanic rocks due to the relatively low flow-rates involved and consequently, the difficulties in obtaining enough sample to fill a fluorometer cubette.

A "front-surface fluorometer" would be an alternative to a standard filter fluorometer for tracer detection in unsaturated fractured rocks. The proposed instrument consists of an excitation light source (such as a xenon lamp) with a monochromator and a fluorescence detector. This device would be set up to measure in situ fluorescence along fractures, instantaneously detecting "breakthrough" when the tracer has emerged from the fracture. This technique would permit continuous monitoring of individual fractures without requiring samples to be collected and analyzed.

Alternatively, fluorescent dyes could be used to study matrix flow within tuffs in a controlled experiment. A front surface fluorometer might be used to detect the emergence of tracer from an (unfractured) block of tuff. Furthermore, actual micro-scale flowpaths could then be visually determined by cutting the block in half and observing tracer concentrations within the pores and microfractures.

The measured fluorescence intensity would depend on a variety of factors, including the design and sensitivity of the fluorometer, the characteristics of the dye used, and the distance from the instrument to the rock surface. Thus, the design challenge is to engineer a device and monitoring system which is small enough to fit into a borehole, yet is flexible and accurate enough to be used in a variety of field situations.

Once the nature of the fractured rock's background fluorescence has been determined, a tracer can then be selected. The tracer's maximum emission peak should be in a different spectral region from that of the background fluorescence of the rock and any fracture solution to be encountered by the tracer. After the dye has been selected, the proper primary and secondary filters for the fluorometer must be chosen. Filter choice should minimize background fluorescence, while maximizing sensitivity, and will depend on the excitation and emission spectra of the fluorescent tracer. The primary filter is placed between the UV

light source and the sample, and is used to select the excitation wavelength. The secondary filter should prevent unwanted wavelengths from reaching the detector, and must be chosen so as to be compatible with the primary filter. Smart and Laidlaw (1977) provide further information on the select of proper filter combinations.

Chemical characteristics of the individual dyes must also be taken into account. The pH of any fracture solution encountered by the tracer will often affect total dye fluorescence (Figure 5.17). Lissamine FF is relatively unaffected between pH 4.0 and 10.0, Rhodamine WT is affected below pH 5.0, which Pyranine fluorescence varies continuously between pH 3.0 and 11.0. In each case, the total fluorescence intensity is lower at low pH levels, and in some cases also dropped at high pH levels. Thus, pH effects must be accounted for when using fluorescent tracers.

Two other environmental factors affecting fluorescent intensities of various dyes are temperature and salinity. Although each dye behaves differently with varying temperatures, as a rule, increased temperatures will result in decreased fluorescence intensity. Increased salinity levels have also been documented to decrease fluorescence intensity in Rhodamine WT and Rhodamine B (Smart and Laidlaw, 1977).

One should carefully consider dye adsorption characteristics when choosing a tracer for use in fractured rock, due to the large amount of rock surface area contacted by the tracer per unit of water. Dye adsorption onto fracture surfaces is generally irreversible and adsorption characteristics are also a good indicator of a conservative tracer. To quantify relative adsorption rates of different dyes, Smart and Laidlaw (1977) conducted a series of tests injecting various dyes through columns of different inorganic and organic particles. Results are shown in Figure 5.18.

Three fluorescent dyes, amino G acid, lissamine FF, and rhodamine WT are good candidates for use as tracers in fractured volcanic tuff. These dyes were chosen for their low adsorption properties, as well as for their emission/excitation behavior (Figures 5.19(A) and 5.19(B)). The dye emission peaks vary from 445 nm (amino G acid) to 515 nm (lissamine FF) to 580 nm (rhodamine WT). Hence, dye choice may be tailored to a wide range of background fluorescence situations.

Perhaps the best dye for use with a front surface fluorometer would be one with an excitation wavelength in the invisible UV band, yet with an emission spectrum in the visible range. This would permit use of an invisible light UV source which would not visibly illuminate the core,

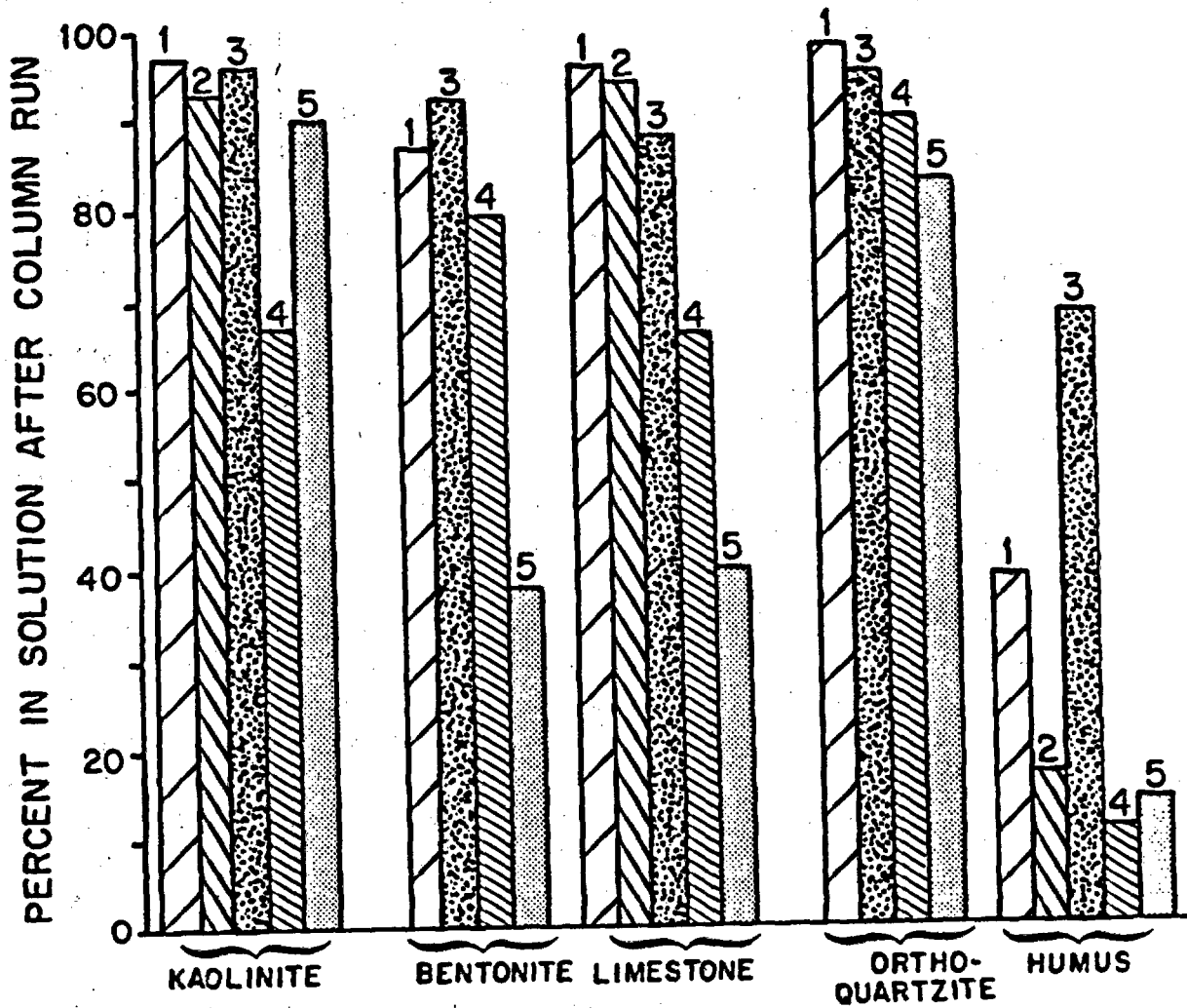


Figure 5.17 Effect of pH on fluorescence of tracer dyes.

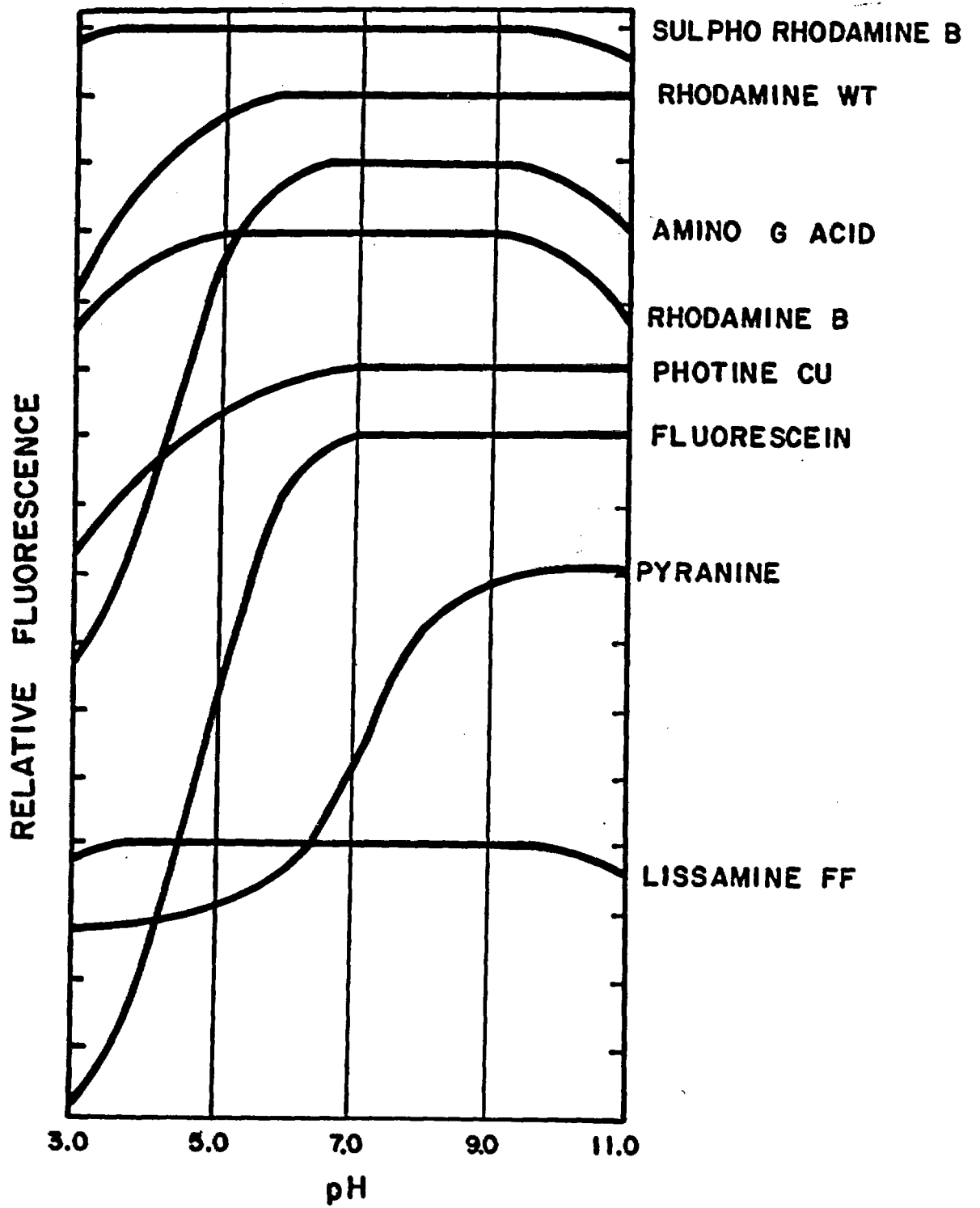


Figure 5.18 Effect of various materials on solubility of tracers.

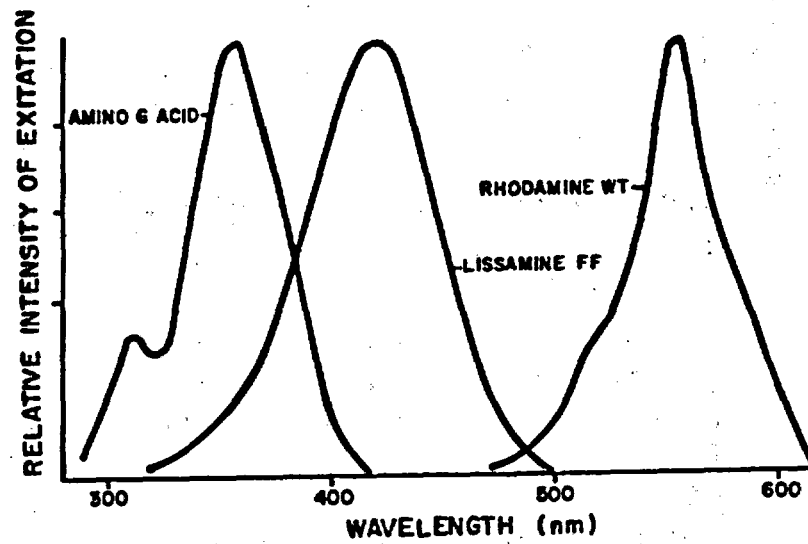
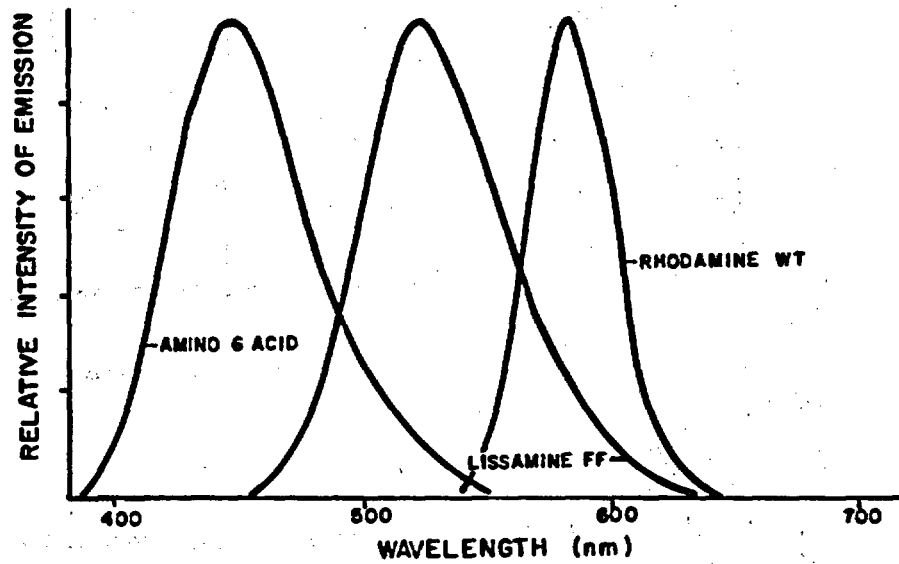


Figure 5.19 Excitation spectra of amino G acid, lissamine FF, and rhodamine WT and transmission characteristics using secondary filters (A) and primary filters (B).

and yet the dye would fluoresce in the visible range, thus greatly aiding the detection task. Amino G acid is the only dye of the three which has these characteristics.

#### 5.1.4.2 Preliminary Testing in Tuff

To determine the adequacy of fluorescent tracers for characterizing flow through fractures at the Apache Leap Site, the natural background fluorescence of the tuff had to be evaluated. Samples of tuff were pulverized into clay and silt sized particles to be evaluated under Ultra-Violet (UV) light for fluorescence. The material was observed while being irradiated first with short-wave (254 nm) UV light, then with long-wave (366 nm) UV light. The pulverized rock was observed to fluoresce under short-wave light with a deep purple color, estimated at 450 nm. Fluorescence was less intense under longwave UV light.

The fluorescence observed from the pulverized tuff was considered indicative of the average fluorescence of the rock matrix. However, fracture surface mineralogy often varies considerably from that of the average rock matrix due to trace minerals which form along the surface. In addition, because the excitation spectra of the dyes to be used in the field are at considerably higher wavelengths than the monochromatic 366 nm UV source used earlier, further evaluation was deemed necessary.

Four core samples containing representative fracture surfaces from various intervals within the boreholes at the Apache Leap Site were selected for study under UV light similar to that which might be used in a front surface type fluorometer. A black-light fluorescent bulb was chosen as a UV source because its emission spectrum closely overlapped dye excitation spectra of rhodamine WT, lissamine FF, and amino G acid.

Thus, if the samples fluoresced significantly under this source, then the dyes would have to be reevaluated as tracers. The core samples were observed in a dark room under the black-light bulb, and no obvious fluorescence was detected. Of course, the cores were visibly illuminated because the UV bulb emitted some visible light. Conventional (and more quantitative) fluorescence measurement techniques (including standard filter fluorometry and spectrofluorometry) cannot easily be used to determine background rock fluorescence due to their design for liquid samples only.

In a preliminary test, a dilute solution of the pulverized rock material was suspended in distilled water and analyzed with a Perkin Elmer fluorescence spectrophotometer (Model MPF-2A). However, the instrument

was designed for transparent liquid samples only, and the scattering effect from the suspended rock particles overwhelmed any measurable fluorescence effects.

Ideally, a front surface fluorometer should be used to measure the rock background fluorescence. This would provide an indication of both the intensity and the emission wavelength bands of the fluorescence, and from this information, a dye could be selected.

To obtain a preliminary evaluation of fluorescent tracer flow-rates within fractures, as well as to compare dye adsorption characteristics, a simple experiment was devised. Two dyes, rhodamine WT and fluorescein, were injected into separate, near-vertical fractures near the Apache Leap Site. Each fracture was traceable to a location further down the rock face, and hence, tracer travel time could be calculated once the tracer emerged from the fracture.

The fluorescein dye was injected into a fracture with an aperture of 2 to 3 mm, and breakthrough was observed 8.2 seconds later from a location 1.5 meters below, and 11.8 seconds later from another fracture 2.7 meters below. Assuming linear fractures, the average flow rate was 4.9 m/s. This high velocity reflects the large aperture of the fracture.

Breakthrough never occurred for the rhodamine WT dye in the second fracture, and this was believed due to the nature of the fracture and rock matrix into which it was injected. The rock in the immediate vicinity of the fracture appeared weathered and quite porous, suggesting the possibility that the dye became adsorbed into the matrix pores, rather than migrating down the fracture.

#### 5.1.4.3 Recommendations

Three fluorescent dyes, lissamine FF, rhodamine WT, and amino G acid, show potential for use as tracers within fractured volcanic tuffs. Of these, amino G acid may prove to be most optimal for in situ borehole testing with a front-surface fluorometer, due to its invisible UV excitation spectrum and visible UV emission spectrum. Further research is recommended into tracer types, as this may yield other dyes with good emission/excitation and adsorption characteristics.

In addition, a front surface fluorometer must be designed which is flexible enough to be used with a variety of fluorescent dyes, yet small enough in diameter to be used inside a borehole. At the same time, an automatic borehole monitoring system must be developed for use with the

fluorometer. This system should allow continuous in situ monitoring of fractures within the borehole, and would yield a variety of information on the differential flow rates through fractures of various apertures.

## 5.2 Hydrogeochemistry of Unsaturated Fractured Rock

Hydrogeochemical studies for the unsaturated zone may be used to help interpret the rate of water and solute movement over long time periods and determine flowpaths. Identifying mineralogic changes and measuring isotopic and hydration variations may also help establish the history of climatic and geomorphological processes that might affect the isolation properties of a repository setting.

For example, if the isotopic and hydration measurements of a fractured rock at a proposed repository depth reflect the strong presence of modern meteoric water, there may be a higher risk of off-site migration of contaminants. Similarly, if these results reflect the paleohydrology of a wetter climate, the proposed unsaturated zone might be inadequate as the primary buffer between infiltrating water and a water table if future climates become wetter.

### 5.2.1 Variation of Environmental Isotopes and Hydration of Authigenic Minerals

When water moves through unsaturated fractured rock of low permeability, the body of rock can be considered a dynamic system tending toward chemical and isotopic equilibrium with its environment. This process causes growth and alteration of mineral assemblages in situ (authigenesis) and is driven by the quantity and chemical/isotopic quality of present and past waters.

Additionally, the hydration and isotopic nature of fracture surfaces and rock matrix is influenced by the mineralogy of the parent rock, adsorption properties of the alteration minerals, interconnected pores and fracture apertures that regulate the quantity of water, and the temperature of the fractured rock environment.

Water is one of the most important reservoirs that control the isotopic composition and hydration of fractured rock. In extensive, open fracture systems, the ratio of water to fracture surface is quite high (water in this context meaning the total water that has flowed through a fracture, not the amount present at any instant). When water/rock ratios are high, the isotopic composition of the water imparts a

characteristic signature upon precipitating or exchanging solid phases; the change in isotopic composition of the water may be negligible.

However, as the water/rock ratio decreases the isotopic composition of the water may be markedly affected and the authigenic minerals will retain an isotopic signature similar to the parent rock. Similarly, the hydration or water that is involved in the authigenic process and becomes chemically incorporated in rock will vary according to water/rock ratios. To this end, the analysis of authigenic assemblages for their isotope ratios and hydration states can help determine the extent and source of water, both past and present, in the unsaturated zone.

#### 5.2.1.1 Stable Isotopes of Oxygen and Hydrogen as Tracers of Water/Rock Interactions

The ratios of stable isotopes of oxygen ( $^{18}\text{O}/^{16}\text{O}$ ), and hydrogen (D/H) can be used to deduce the physical and chemical changes in weathering and sedimentary environments. Fundamental information and extensive bibliographies can be found in: Taylor (1968); Lawrence and Taylor (1971, 1972); Lawrence et al., (1979); Savin (1980); Longstaffe (1983, 1984). An extension of the methodology for the growth of authigenic minerals in low temperature environments can be applied to the formation of fracture-filling minerals in unsaturated rock.

Craig (1961) demonstrated the  $\delta\text{D}$  and  $\delta^{18}\text{O}$  of meteoric water lie very close to a straight line described by:

$$(5.10) \quad \delta\text{D} = 8 \delta^{18}\text{O} + 10$$

where

$\delta\text{D}$  and  $\delta^{18}\text{O}$  are defined as ratios so that:

$$(5.11) \quad \delta_x = (R_x - R_{\text{std}}/R_{\text{std}}) \times 10^3$$

where

$$R_x = (\text{D/H})_x$$

or

$$R_x = (^{18}\text{O}/^{16}\text{O})_x$$

and

$R_{\text{std}}$  is the corresponding hydrogen or oxygen ratio in a standard (see Appendix G for further discussion).

The weathering process generally involves large quantities of meteoric water invoking high water/rock ratios. Under such conditions the isotopic nature of the parent rock was shown by Lawrence and Taylor (1972) to have little effect on the alteration weathering products.

In a weathering zone, the  $\delta D$  and  $\delta^{18}O$  of clay minerals and hydroxides forming from the alteration of igneous parent rock correlate directly with the systematic variations of  $\delta D$  and  $\delta^{18}O$  of corresponding present-day meteoric water (Lawrence and Taylor, 1971). Clay minerals of similar chemical composition which have equilibrated with different meteoric waters at the same temperature have characteristic  $\delta D$  and  $\delta^{18}O$  values that lie parallel to the meteoric water line (Figure 5.20).

Authigenic minerals derived from equilibrium precipitation with low  $^{18}O$ , continental meteoric water should have  $\delta^{18}O$  values significantly different than chemically equivalent minerals of detrital origin (e.g., minerals derived and transported from another source area), or minerals formed earlier in the diagenesis of the unit from more  $^{18}O$ -rich formation waters. Because of the dominance of oxygen atoms compared to hydrogen atoms in silicate and carbonate terrains, as water/rock interactions increase there is a noticeable shift in isotope ratio of oxygen and relatively little with respect to hydrogen.

In volcanic rocks, the glass shards which make up much of the groundmass also exhibit characteristic chemical changes when exposed to surface waters. Taylor (1968) found that the  $\delta^{18}O$  values of siliceous flows and tuffs increase as a result of isotopic exchanges with meteoric waters during hydration of the glass in a rock body. Similarly, Garlick and Dymond (1970) showed the  $\delta^{18}O$  of siliceous volcanic glass shards in deep-sea sediments increase with age due to isotopic exchanges between the volcanic glass and ocean water.

#### 5.2.1.2 Radiogenic Isotope of Strontium ( $^{87}Sr/^{86}Sr$ ) as a Tracer of Water/Rock Interactions

Rainfall, percolating waters, and ground waters at a particular site will have distinct isotopic tags. The usefulness of isotope measurements along fracture pathways is that inferences may be drawn about hydrologic sources. Also, the ratios of isotopes can quantitatively determine the degree of presence of the source and relative rates of water movement as related to the chemical equilibrium in fracture zones. Faure (1977) gives the relationship of mixtures having different  $^{87}Sr/^{86}Sr$  ratios as the equation of a hyperbola:

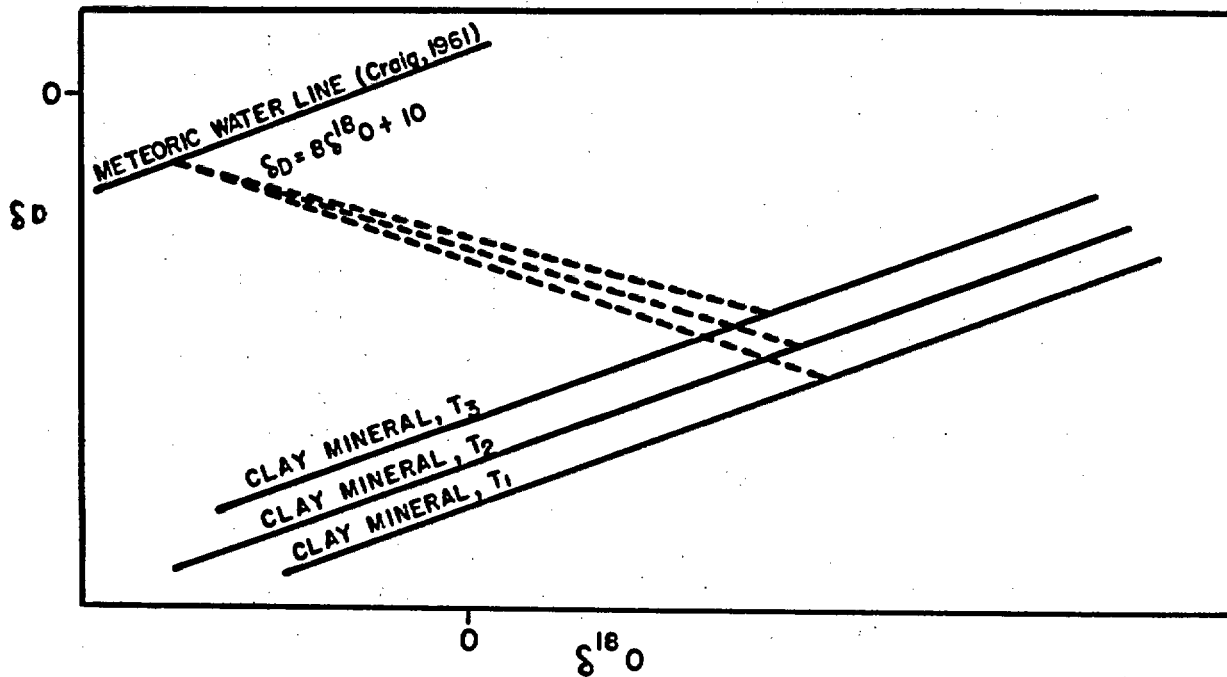


Figure 5.20 Schematic representation of  $\delta D$  and  $\delta^{18}O$  correlation of clay minerals (or other minerals such as diagenetic quartz which contains both hydrogen and oxygen) and a meteoric water source. At temperature  $T_1$  the isotopic composition of a particular clay mineral form along a line parallel to isotopic compositions of meteoric water. As temperatures increase the clay mineral line approaches the meteoric water line ( $T_3 > T_2 > T_1$ ). Dashed lines connect hypothetical meteoric water for a specific climate and latitude in equilibrium with clay at different temperatures (adapted from Savin, 1980). For extensive, open fractures, the extent and degree of meteoric water input can be determined by the correlation of the isotopic signature of the fracture-filling mineral to that of meteoric water and/or ground water for a given area.

$$\begin{aligned}
 (5.12) \quad ({}^{87}\text{Sr}/{}^{86}\text{Sr})_{\text{mixed}} &= ({}^{87}\text{Sr}/{}^{86}\text{Sr})_A (\text{Sr}_A f / \text{Sr}_{\text{mixed}}) \\
 &\quad + ({}^{87}\text{Sr}/{}^{86}\text{Sr})_B (\text{Sr}_B (1-f) / \text{Sr}_{\text{mixed}}) \\
 &= a / \text{Sr}_{\text{mixed}} + b
 \end{aligned}$$

where

a and b are constants specified by the ratio  ${}^{87}\text{Sr}/{}^{86}\text{Sr}$  in components A and B; and  
 f is the fractional influence of component A.

This mixing relationship has been used extensively to estimate the contribution of different hydrologic sources to surface waters (see Appendix G for more discussion).

In a study on the deep fracture system of the Grand Ronde basalt in Washington, Brookins et al., (1984) suggest using this mixing relationship postulating that the chemical character of fracture zones will belong to one of the three inputs and their possible mixtures:

- The fracture-filling minerals and chemistry are a result of chemical equilibrium with the parent rock;
- The fracture surface chemistry may have mineral assemblages reflecting the infiltration of percolating water; or
- The fracture-filling minerals may be similar to the chemistry of the saturated zone, suggesting a once higher static water level.

On the basis of the near agreement of the fracture-filling minerals and the basalt isotope ratios of  ${}^{87}\text{Sr}/{}^{86}\text{Sr}$ , the authors concluded relatively no mixing in the fracture zone, that is essentially no infiltration of percolating water at their depth of sampling (from 760 to 920 meters below land surface). Additional isotope analysis of K/Rb, Th/U, Rb/Sr, and K-Ar also suggest that the origin of the fracture-filling minerals is deuteritic rather than very young. Further leaching studies for total calcite or total chlorine may also help confirm the absence of deep percolation.

#### 5.2.2 Field Investigations Involving Isotopic and Hydration Analyses of Unsaturated Fractured Tuff

The core samples from the recent emplacement of the three boreholes in slightly-welded tuff at the Apache Leap site near Superior, Arizona, allow for the hydrologic assessment concerning the variation of isotopes and hydration states of unsaturated fractured tuff. The design specifications for this site required core drilling with high

percentages of core recovery in fracture areas so as to determine fracture orientation and identify major and minor flowpaths.

Detailed isotopic, hydration, and mineralogic studies of the tuff can further verify the application of this methodology and hydrologic significance. Preliminary investigations using hand sample identifications and x-ray diffractometry of the fracture-fillings at the Apache Leap site indicate a substantial amount of secondary quartz and opal with lesser amounts of calcite and smectite. Future analyses on the tuff may include:

- $\delta D$  and  $\delta^{18}O$  systematics of minerals which contain both hydrogen and oxygen;
- $\delta D$  and  $\delta^{18}O$  correlation between fracture-filling minerals and present-day meteoric water in Southern Arizona;
- Relationship between stable isotope ratios of fracture-filling minerals and mineral assemblages, both primary and secondary, found in the rock matrix;
- Variation of quartz and calcite both mineralogically and isotopically to assess temperatures of formation;
- Hydration states of the volcanic glass in the tuff to determine the relative influence of water movement in the matrix versus fractures
- $^{87}Sr/^{86}Sr$  relationship between fracture-filling minerals and the parent rock, ground water, and surface water.

Hydrogeochemical analyses emphasizing these isotopic and hydration parameters may lead to information concerning the source of water in the Apache Leap tuff and determine the applicability these measurements used as indicators of water/rock interaction in unsaturated fractured rock. Results may be useful in distinguishing primary flowpaths and defining the extent of water inputs. Additionally, ratios of stable isotopes could indicate conditions of formation of authigenic minerals and determine the relative influence of a present or a past climate.

## CHAPTER 6 CONTAMINANT TRANSPORT AS VAPOR

### 6.1 Introduction

The objective of this chapter is to identify the mechanisms and processes of transport of radionuclides as vapor which may contribute to the overall transport process and the conditions under which the mechanisms and processes are potentially important. Each transport mechanism is evaluated in terms of what conditions would permit the mechanism to be significant. The mechanism is then dismissed or identified, when possible, as a potential contributor to the transport of radionuclides in unsaturated fractured rock. Two inherently different transport processes identified are transport as a gas and transport as an aerosol. Both processes are referred to here as vapor transport.

#### 6.1.1 Radioactive Species of Interest

The nature of radionuclides placed in a HLW repository is an important factor that needs consideration when characterizing vapor transport of radionuclides. The composition of nuclear wastes to be placed in HLW repositories is varied and depends on reactor operation and the nuclear fuel cycle. Light water reactors (LWR) are the most common commercial nuclear reactors in the United States and, therefore, the most common source of high-level waste. Reprocessing of HLW will remove all the tritium, the noble gases (He, Kr and Xe) and 99.9% of the volatile elements (I and Br) (Wang et al., 1983). However, even if these species are removed initially, many will continue to be produced by the waste.

Heat emitted by spent fuel is generated by two main components, fission products and the transuranic actinides (Wang et al., 1983). During the first few hundred years after removal of nuclear fuel from a reactor, the principal contributors to heat generation are fission products such as strontium-90 and cesium-137. Subsequent to high activity by fission products, transuranic actinides and their daughters become the major contributors to heat generation. Transuranic actinides are relatively long-lived and include elements such as plutonium, americium and curium. Removal of plutonium by reprocessing will cause significant decreases in the heat generating capability of high-level waste.

Radionuclides with a significant vapor phase are not present in reprocessed fuel, hence, gaseous transport of radionuclides will not occur for this case. However, nuclear fuel reprocessing facilities for high-level waste from commercial nuclear reactors are not available in

the United States. There are no plans for construction of a reprocessing facility in the near future. Therefore, HLW repository design should consider the consequences resulting from the burial of spent fuel complete with all fission products and transuranic actinides.

Radionuclides which exist as compounds with a significant gas phase are  $^3\text{H}$ ,  $^{14}\text{C}$ ,  $^{85}\text{Kr}$  and  $^{129}\text{I}$ . The respective half-lives for the gases are 12.26 yrs, 5730 yrs, 10.76 yrs and  $1.7 \times 10^7$  (CRC Handbook of Chemistry Physics, 1974). Carbon dioxide,  $\text{CO}_2$ , and methane,  $\text{CH}_4$ , are gases that pose a potential hazard because of their possible  $^{14}\text{C}$  content. Of the volatile radionuclides,  $^{129}\text{I}$  appears to have the greatest potential as a hazard because of its toxicity and long half-life.

Radionuclides that are of interest to the study of vapor transport, therefore, include the volatile species when gaseous transport mechanisms are considered and all radionuclides, including more serious contaminants such as fission products and the transuranic actinides, when transport as aerosol is present. The particular inventory of radionuclides from a SF canister used in this study is derived from the results of SANDIA-ORIGEN (Sutherland and Bennett, 1979).

The particular species and the chemical compound of species that will be introduced into the geologic environment from a failed HLW canister will depend upon the chemistry of the geologic medium, the pore water and the radioactive waste. The complex chemical interactions between them and the chemical profile of a HLW repository have not been entirely determined and are considered only in general terms in this study.

### 6.1.2 Physical Setting

Different physical processes can contribute to vapor transport of radionuclides. Each transport mechanism requires specific conditions to be present before the mechanism can significantly contribute to the overall transport process. Vapor transport of radionuclides, therefore, has to be examined for each physical setting where any of the contributing transport mechanisms may be important.

Preliminary investigations of vapor transport indicate that some transport mechanisms may be important in the zone near the repository, while others may be important at more distant zones. Factors influencing transport mechanisms near the repository include radiation and heat generation from high-level waste. The significance of vapor transport in the zone near the repository may be the transport of radionuclides from the canister source to liquid in the matrix and in

the fractures a short distance away. Although the distance of transport may be as short as several centimeters, transport as vapor may be significant because it can supply a major transport link from the canister to zones of increased saturation at some distance (Figure 6.1).

The importance of this vapor transport link is increased because high temperatures at HLW canisters can dry the rock proximal to the waste package, restricting transport as liquid in the zone near the repository. The zone near the repository is defined as distances of centimeters to meters from the canister. Radionuclides in the zone near the repository are largely influenced by the engineering design of the canister and the nature of the waste.

Other transport mechanisms exist which are important over larger distances. (Large distances are assumed to be as great as tens of meters to hundreds of meters.) Transport mechanisms important over large distances are, in general, influenced more by the geologic medium than the nature of high-level waste buried at the repository. One notable exception is heat generated by radioactive decay at the canisters. Burial of a sufficient number of canisters along a single plane in the subsurface can exhibit thermal effects over large distances for a repository which may cover an area of many hectares.

Neither the specific repository site nor the engineering design of the repository and canister have been determined. The design of waste canisters is very important in terms of the expected magnitude of the source of radionuclides and the generation of heat and radiation at the time of emplacement and how the source varies with time after emplacement. Until the engineering design of the repository, exact inventory of high-level waste and repository site are specified, the contaminant source must be treated as a variable. Without a specified source, vapor transport mechanisms are investigated relative to other transport mechanisms when possible. Otherwise, they are investigated in general terms only.

## 6.2 Gas Movement in a Fractured Medium

The movement of gas in an unsaturated, non-isothermal, fractured medium which is located near a radioactive source can take place as a result of several different driving forces. The driving forces present in this setting include those resulting from:

- a concentration or partial pressure gradient;
- a total pressure gradient;
- a liquid or surface concentration gradient;

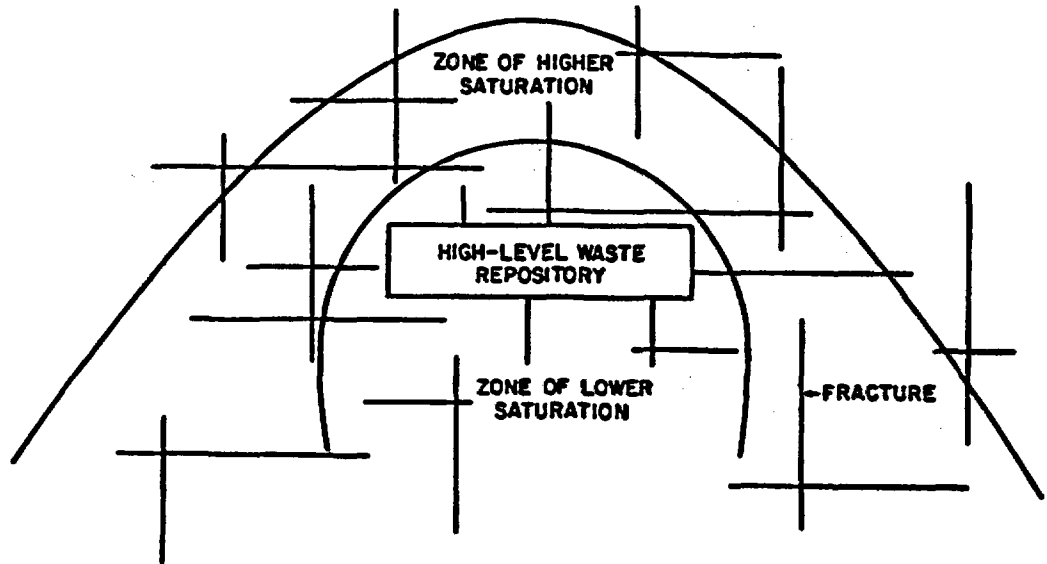


**Figure 6.1** Schematic of high-level waste repository located in fractured media illustrating thermally induced zone of lower saturation enveloped by zone of higher saturation.

- an external electrical field; and
- a thermal gradient.

Each driving force results in an associated transport mechanism. A concentration gradient can cause ordinary diffusion. Diffusion includes Knudsen flow, self-diffusion, binary diffusion and surface flow. A gradient in the total pressure can result in viscous flow which includes Poiseuille (or Couette) and slip flow. An electric field can result in forced diffusion. And finally, a thermal gradient can cause a mechanism called thermal diffusion. A brief review of the equations governing gas movement in a fractured medium is presented here.

The representation of gas movement through non-isothermal fractured media entails an examination of the problem through several possible perspectives. Similar to the examination of the transport mechanisms of saturated flow in fractured media, there is an enigma in deciding the appropriate course necessary to adequately represent the physical mechanisms which govern non-isothermal gas movement through fractured media. The major factors that dictate which approaches are feasible are the scale of the problem of interest and the availability of the technology required to apply the selected approach.

Representation of gas movement through fractured, consolidated media is a perplexing and difficult endeavor. At one extreme, consolidated unfractured rock matrix has low permeability which may be assumed to be treated as a continuum. At the other extreme is a set or several sets of fracture systems superimposed on rock matrix of low permeability.

When the orientation, spacing, aperture, and lateral extent of the fractures are regular in their nature and adequately defined, the medium can be treated as an equivalent porous medium (EPM). A dual porosity system such as this can generally be considered a continuum with a sufficiently large representative elemental volume (REV) and therefore treated with methodologies developed for porous media.

A major dilemma arises when the medium cannot be represented by a reasonably sized REV. This dual porosity system can not be treated as a continuum and methodologies designed for porous media are, in general, inadequate.

Application of the REV concept to vapor transport raises additional problems. The size of the REV required to represent a system is dependent upon the particular properties of interest of the system. As an example, a REV may be considered homogeneous in terms of gas porosity

but highly heterogeneous with respect to gas permeability. The non-isothermal effect of high-level waste at the repository and the additional pathways present in the disturbed zone are two major contributions to the heterogeneity of the system. As a result, a particular transport mechanism may have to be investigated with a REV of one size while another transport mechanism will require a REV of a different size.

Vapor transport is investigated at two scales:

- Near the repository with a single fracture characterized by a parallel plate model; and
- At a larger distance in which the system is treated as a continuum thus permitting an analysis using porous media methodologies.

The pore structure of a rock matrix may be better represented with a capillary tube model than the parallel plate model used for fractures. The use of a capillary tube model will make the rock matrix analysis analogous to continuum models used for porous media.

Gas movement can occur as gas dissolved in a fluid. However, only vapor transport as vapor flow through the air spaces in the system is considered here. The degree of saturation in fractured rock has a significant effect upon vapor transport. As a system dries out, the degree of gas porosity increases while the remaining liquid water exists at a larger negative pressure. Fractures and pore spaces saturate according to the expression:

$$(6.1) \quad \Delta P = C t \cos \alpha / r$$

where

- $\Delta P$  is the gauge pressure of the fluid;
- $C$  is a constant, dependent upon the shape of the void;
- $t$  is the surface tension of the fluid;
- $\alpha$  is the angle of contact between the solid and the fluid; and
- $r$  is the hydraulic radius.

Therefore, the amount of airspace available for vapor flow is highly dependent upon the negative pressure of the system. Vapor phase transport will be greatly diminished at small negative pressures because most voids within the medium will be saturated. It is possible that voids in the rock matrix of a dual porosity system can be saturated while at the same pressure, fractures will be unsaturated except for liquid film retained on solid surfaces by surface tension. Additionally, flow mechanisms that affect vapor phase transport in the

rock matrix are not necessarily the same mechanisms that govern vapor phase flow in rock fractures.

### 6.2.1 Ordinary Diffusion

Movement of gas through air resulting from a concentration gradient is attributed to Brownian motion of the gas molecules. This transport mechanism is referred to as ordinary (or concentration) diffusion. Gas molecules can collide with other gas molecules, with walls retaining the gas or with molecules forming a layer on the retaining pore walls. Gas movement caused by collisions between gas molecules and pore walls is referred to as Knudsen flow. Movement resulting from collisions between like molecules is referred to as self diffusion, and movement by diffusion of gas along the layer of molecules adsorbed onto the surface of the retaining pore wall is called surface diffusion. Movement resulting from collisions between molecules of different gases in response to their respective concentration gradients is binary diffusion. The direction of flux of two separate gases can either occur in the same direction or in opposite directions.

The total flux resulting from these different transport mechanisms can be written:

$$(6.2) \quad J_0 = J_k + J_{\text{self}} + J_b + J_s$$

where

- $J_0$  is the total flux;
- $J_k$  is the Knudsen flow component;
- $J_{\text{self}}$  is the self-diffusion component;
- $J_b$  is the binary diffusion component; and
- $J_s$  is the surface diffusion component.

These four transport mechanisms are grouped together because the driving force of each mechanism is a concentration (or partial pressure) gradient. If more than one gas is present in significant quantities, self diffusion is not present and only the binary term contributes to total diffusion flux. Flux resulting from self-diffusion is represented by the binary diffusion term in a binary gas system.

Of integral importance to the investigation of gas flow is the ratio of the mean free path length between molecule collisions to the distance between pore walls. This ratio is referred to as the Knudsen number,  $Kn$ . The relative importance of molecule-molecule collisions to molecule-wall collisions is indicated in the Knudsen number. The

frequency of molecule-molecule collisions exceeds the frequency of molecule-wall collisions when the distance separating pore walls is greater than the average distance between molecule-molecule collisions. Table 6.1 (from Kennard, 1938) lists for several gases the mean free path, viscosity, molecular weight and molecular diameter, all at one bar pressure and 15°C.

Pure Knudsen flow represents the limit as the Knudsen number ratio tends toward infinity. When ( $\lambda \gg b$ ), gas molecules will have greater occasion to collide with the pore walls rather than colliding with other gas molecules. When the Knudsen number decreases to about unity (i.e.,  $\lambda/b = 1$ ), either slip flow, which is a component of viscous flow, or self-diffusion becomes prominent.

#### 6.2.1.1 Self and Binary Diffusion

The flow of a single gas by self diffusion or two gases by binary diffusion occurs in response to a concentration gradient when the Knudsen number is small. Ficks first law relates the mass flux by self-diffusion and by binary diffusion of a diffusing substance which passes across a unit cross sectional area to the concentration gradient by the expression:

$$(6.3) \quad J_b = - D_{AB} \nabla c$$

where

$\nabla c$  is the total concentration gradient of species A; and  
 $D_{AB}$  is the diffusivity of species A diffusing through B.

The diffusion coefficient appears as  $D_{AA}$  and the flux as  $J_{self}$  in self diffusion. Ficks law was originally obtained empirically but has since been derived using kinetic theory and several important assumptions (Geankoplis, 1972).

Values for the diffusion coefficient vary with the type of flow mechanism and with the physical conditions of the system (i.e., temperature and pressure). Methodologies used to determine the values of the diffusion coefficient vary with the basic approach employed, either empirical or analytical, and the level of sophistication of each approach. Although experimentally determined values for diffusion coefficients are available for a variety of gases at different temperatures and pressures, values for additional gases under different conditions are not available and must be measured or predicted theoretically.

-----  
**Table 6.1 Attributes of various gases, from Kennard (1938).**  
 -----

	M	n	$\lambda$	d
H <sub>2</sub>	2.016	871	11.77	2.74
Helium	4.002	1943	18.62	2.18
CH <sub>4</sub> (methane)	16.03	1077	5.16	4.14
NH <sub>3</sub>	17.03	970	4.51	4.43
H <sub>2</sub> O	18.02	926	4.18	4.60
N <sub>2</sub>	28.02	1734	6.28	3.75
C <sub>2</sub> H <sub>4</sub> (ethylene)	28.03	998	3.61	4.95
C <sub>2</sub> H <sub>6</sub> (ethane)	30.05	900	3.15	5.30
O <sub>2</sub>	32.00	2003	6.79	3.61
HCL	36.46	1397	4.44	4.46
Argon	39.94	2196	6.66	3.64
CO <sub>2</sub>	44.00	1448	4.19	4.59
Krypton	82.9	2431	5.12	4.16
Xenon	130.2	2236	3.76	4.85
Air	28.96	1796	6.40	3.72

M = molecular weight (g/mole)  
 n = viscosity ( $10^{-7}$  dyne·sec/cm<sup>7</sup>)  
 $\lambda$  = mean free path ( $10^{-6}$ cm)  
 d = diameter ( $10^{-8}$ cm)

(From Kennard, E.H., Kinetic Theory of Gases, copyright 1938, reprinted, by permission of the publisher, McGraw-Hill.)

Diffusion of one gas into another gas can be calculated using simplified kinetic theory with the expression (Present, 1958; Bird et al., 1960):

$$(6.4) \quad D_{AB} = 1/3 \bar{v} \lambda$$

where

$\bar{v}$  is the mean gas velocity; and  
 $\lambda$  is the mean free path.

Evaluating this expression using the ideal gas law and definitions of mean free path length and mean gas velocity yields:

$$(6.5) \quad D_{AA^*} = 2/3 (k^3/\pi^3 m_A)^{1/2} T^{2/3} / (P d_A^2)$$

where

$k$  is Boltzman's constant;  
 $d_A$  is the molecular diameter of gas A;  
 $m_A$  is the mass of a molecule of gas A;  
 $T$  is the temperature; and  
 $P$  is the total pressure.

In this analysis, it is assumed that both gas A and A\* are comprised of rigid spheres of identical mass and diameter. The diffusion coefficient of two rigid spheres of unequal diameter and mass becomes:

$$(6.6) \quad D_{AB} = 2/3(k^3/\pi^3)^{1/2}(1/2m_A + 1/2m_B)^{1/2} T^{2/3} / P[(d_A + d_B)/2]^2$$

Although values calculated by Equations (6.5) and (6.6) are generally good, more accurate results can be determined by employing rigorous kinetic theory. Chapman-Enskog theory allows the calculation of the diffusion coefficient for low density gases using:

$$(6.7) \quad D_{AB} = 0.0018583 [T^3(1/M_A + 1/M_B)]^{1/2}/(P \beta_{AB}^2 \Omega_D)$$

where

$\Omega_D$  is the collision integral which is a slowly varying dimensionless function of dimensionless temperature, of  $kT/\epsilon_{AB}$  and of the intermolecular potential field for one molecule of gas A and one of B.

$M_i$  is the molecular weight of gas  $i$ ; and  
 $\beta_{AB}$  is reduced initial relative speed between molecules A and B defined by:

$$(6.8) \quad \beta_{AB} = (\mu_{AB}/2kT)^{1/2} g_{AB}$$

The parameter  $g_{AB}$  is the initial relative velocity between the colliding molecules. The term  $\mu_{AB}$  is the reduced mass defined by:

$$(6.9) \quad 1/\mu_{AB} = (1/m_A) + (1/m_B)$$

The collision integral is defined by the expression (Hirschfelder et al., 1954):

$$(6.10) \quad \Omega_D = (2\pi kT/\epsilon\beta_{AB})^{1/2} \int_0^\infty \int_0^\infty \exp(-\beta_{AB}^2 b^2) \beta_{AB}^5 (1 - \cos \alpha) b \, db \, d\beta_{AB}$$

where

$b$  is the impact parameter; and

$\alpha$  is the angle at which the molecules are deflected (Figure 6.2).

Values of the collision integrals are given for values of dimensionless temperature,  $kT/\epsilon_{AB}$ , in Table 6.2.

An alternate approach to determine the coefficient of diffusion based on kinetic theory and a correlation technique has been developed by Slattery and Bird (1958) and applied to available sets of diffusion flow data for self-diffusion and binary diffusion of dilute gases. The Slattery-Bird expression for the diffusion coefficient is written:

$$(6.11) \quad D_{AB} = [(P_{CA} P_{CB})^{1/3} (T_{CA} T_{CB})^{5/12} [(1/m_A) + (1/m_B)]^{1/2}] / P \\ \cdot a [T / (T_{CA} T_{CB})^{1/2}]^b$$

where

$P_{Ci}$  is the critical pressure for gas  $i$ ;

$T_{Ci}$  is the critical temperature for gas  $i$ ; and

$a, b$  are constants.

The diffusion coefficient is inversely proportional to pressure, increases with increasing temperature, and somewhat insensitive to the composition of the gases at low temperatures. Values for the constants  $a$  and  $b$  are derived by a least squares method and computed for two classes of mixtures (Slattery and Bird, 1958). Experimental data on mixtures containing hydrogen, helium and water plotted on a trend separate from non-polar gases. Therefore, values for  $a$  and  $b$  used when determining the coefficient of diffusion of a pair of non-polar gases are different than values of  $a$  and  $b$  used for  $H_2O$  with a non-polar gas.

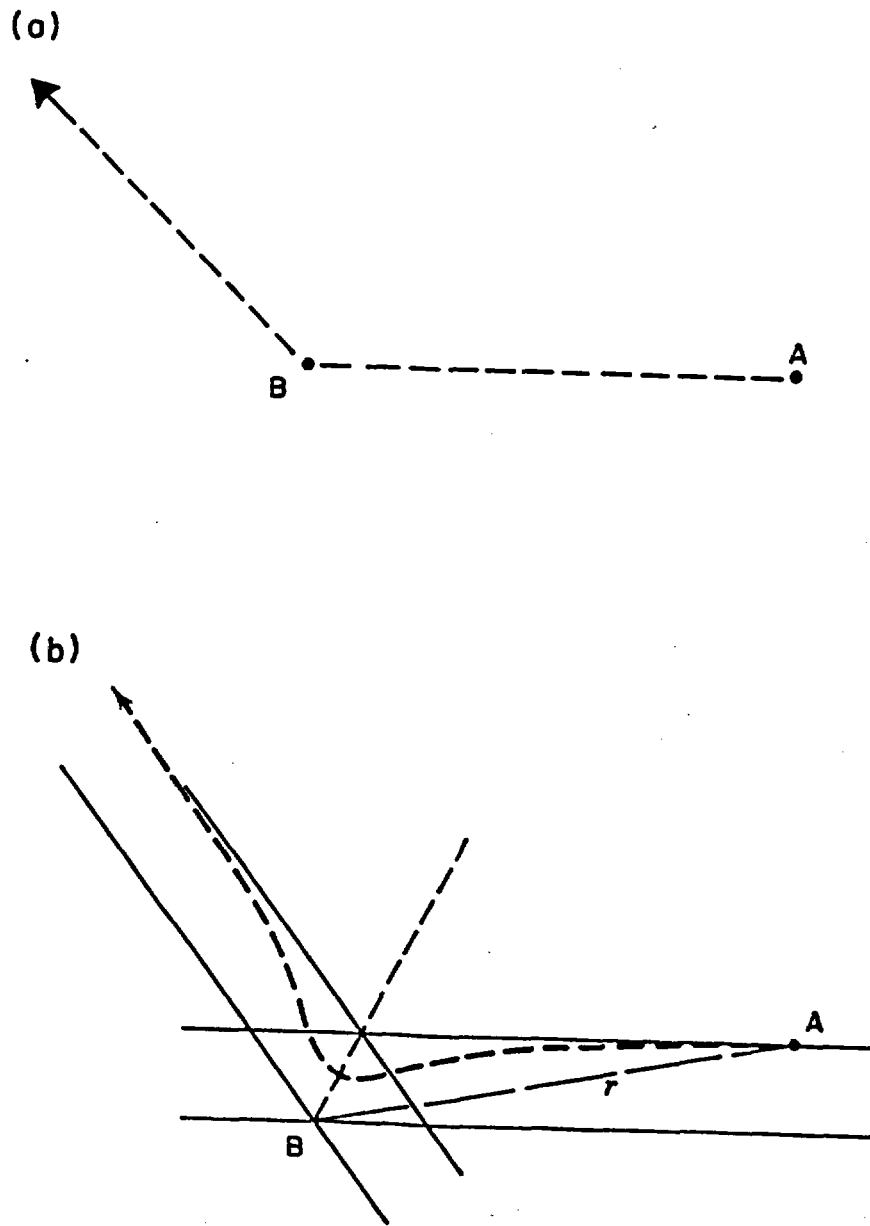


Figure 6.2 Representation of molecule-molecule interaction according to (a) simplified kinetic theory and (b) rigorous kinetic theory. Molecule A travels toward molecule B along trajectory (dotted line) (adapted from Hirschfelder et al., 1954).

(From Hirschfelder, J.O., C.F. Curtis, R.B. Bird, Molecular Theory of Gases and Liquids, copyright 1954, reprinted by permission of John Wiley & Sons, Inc.)

Table 6.2 Functions for prediction of transport properties of gases at low densities, from Hirschfelder et al. (1954).

$KT/\epsilon_{AB}$	$\Omega_{\mu} = \Omega_k^*$	$\Omega_{D,AB}^{**}$	$KT/\epsilon_{AB}$	$\Omega_{\mu} = \Omega_k^*$	$\Omega_{D,AB}^{**}$
0.30	2.785	2.662	2.50	1.093	0.9996
0.35	2.628	2.476	2.60	1.081	0.9878
0.40	2.492	2.318	2.70	1.069	0.9770
0.45	2.368	2.184	2.80	1.058	0.9672
			2.90	1.048	0.9576
0.50	2.257	2.066	3.00	1.039	0.9490
0.55	2.156	1.966	3.10	1.030	0.9406
0.60	2.065	1.877	3.20	1.022	0.9328
0.65	1.982	1.798	3.30	1.014	0.9256
0.70	1.908	1.729	3.40	1.007	0.9186
			3.50	0.9999	0.9120
0.75	1.841	1.667	3.60	0.9932	0.9058
0.80	1.780	1.612	3.70	0.9870	0.8998
0.85	1.725	1.562	3.80	0.9811	0.8942
0.90	1.675	1.517	3.90	0.9755	0.8888
0.95	1.629	1.476			
1.00	1.587	1.439	4.00	0.9700	0.8836
1.05	1.549	1.406	4.10	0.9649	0.8788
1.10	1.514	1.375	4.20	0.9600	0.8740
1.15	1.482	1.346	4.30	0.9553	0.8694
1.20	1.452	1.320	4.40	0.9507	0.8652
			4.50	0.9464	0.8610
1.25	1.424	1.296	4.60	0.9422	0.8568
1.30	1.399	1.273	4.70	0.9382	0.8530
1.35	1.375	1.253	4.80	0.9343	0.8492
1.40	1.353	1.233	4.90	0.9305	0.8456
1.45	1.333	1.215			
1.50	1.314	1.198	5.0	0.9269	0.8422
1.55	1.296	1.182	6.0	0.8963	0.8124
1.60	1.279	1.167	7.0	0.8727	0.7896
1.65	1.264	1.153	8.0	0.8538	0.7712
1.70	1.248	1.140	9.0	0.8379	0.7556
			10.0	0.8242	0.7424
1.75	1.234	1.128	20.0	0.7432	0.6640
1.80	1.221	1.116	30.0	0.7005	0.6232
1.85	1.209	1.105	40.0	0.6718	0.5960
1.90	1.197	1.094	50.0	0.6504	0.5756
1.95	1.186	1.084			
2.00	1.175	1.075	60.0	0.6335	0.5596
2.10	1.156	1.057	70.0	0.6194	0.5464
2.20	1.138	1.041	80.0	0.6076	0.5352
2.30	1.122	1.026	90.0	0.5973	0.5256
2.40	1.107	1.012	100.0	0.5882	0.5170

\* For viscosity and thermal conductivity.

\*\*For mass diffusivity.

(From Hirschfelder, J.O., C.F. Curtis, R.B. Bird, Molecular Theory of Gases and Liquids, copyright 1954, reprinted by permission of John Wiley & Sons, Inc.)

The two pairs of constants are:

non-polar pairs:  $a = 2.745 \times 10^{-4}$   $b = 1.823$

H<sub>2</sub>O with a non-polar gas:  $a = 3.640 \times 10^{-4}$   $b = 2.334$

Diffusion coefficients for the range of temperature from 30° to 250°C have been calculated for H<sub>2</sub>, Kr, CO<sub>2</sub>, I<sub>2</sub> and CH<sub>4</sub> using the Slattery-Bird formula and the Chapman-Enskog formula (Figures 6.3 to 6.7). The gases are diffused into air in making the Chapman-Enskog calculations. Standard values for the critical temperature and critical pressure of air are not available. Because of this, diffusion coefficients were determined with the Slattery-Bird formula for gases diffused into N<sub>2</sub>. The difference in diffusion coefficients calculated by each method is partially because the gases of interest are diffused into different gases.

The Chapman-Enskog expression for the diffusion coefficient for self and binary diffusion generally gives more accurate values than other methods except when the potential parameters are not experimentally determined and must be estimated from the critical properties of the gas.

In general, the Chapman-Enskog calculation technique is employed when the Lennard-Jones potential for the gas is available. The Slattery-Bird technique is used when the Lennard-Jones potential is not available but the critical temperature and critical pressure of the substance are available. However, experimentally determined diffusion coefficients are used when possible (Bird et al., 1958).

#### 6.2.1.2 Knudsen Flow

Mass flux by Knudsen flow between parallel plates separated by a distance  $b$  with a hydraulic radius of  $2b$  can be shown to equal:

$$(6.12) \quad J_{kP} = - (4/3) (2/\pi)^{1/2} b (1/RMT)^{1/2} dP/dx$$

The mass flux by Knudsen flow in a capillary tube is identical to parallel plate flow except that the cross-sectional area is  $\pi a^2$  and the hydraulic radius is  $2\pi a$  where  $a$  is the capillary radius (Figure 6.8). The mass flux of gas through a capillary, therefore, appears:

$$(6.13) \quad J_{kC} = - (4/3) (2/\pi)^{1/2} a (1/RMT)^{1/2} dP/dl$$

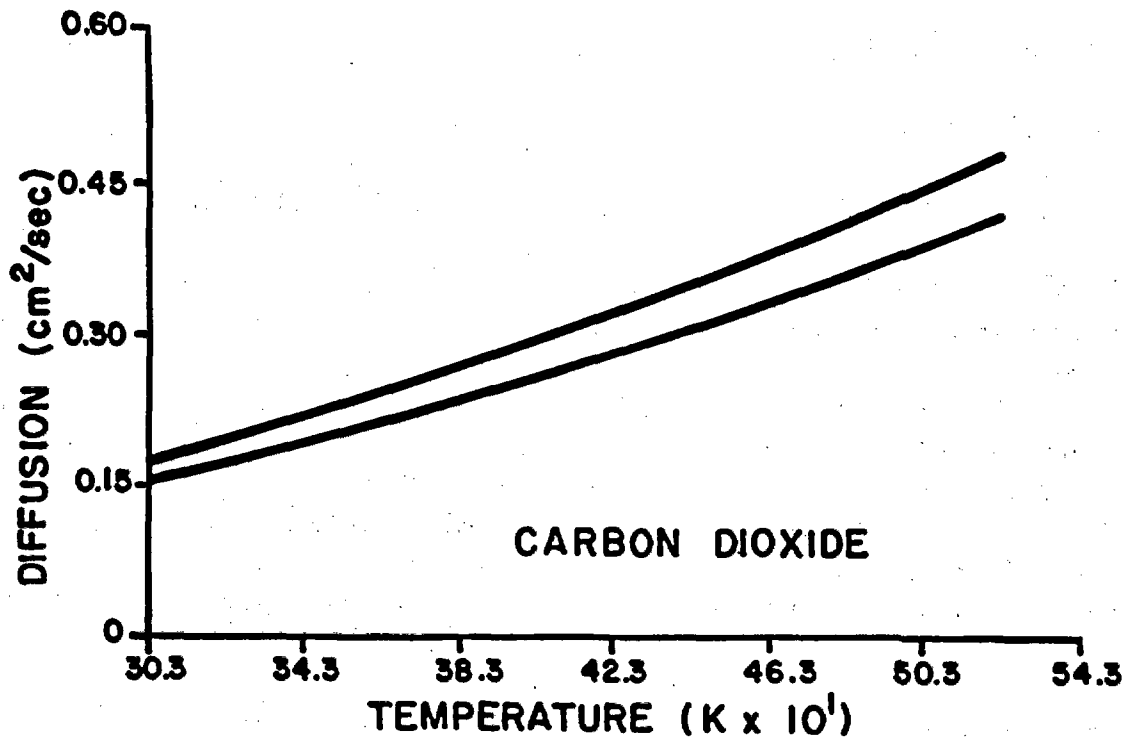


Figure 6.3 Diffusion coefficient (cm<sup>2</sup>/sec) for carbon dioxide versus temperature (°K). The top curve is determined by the Bird-Slattery method, the bottom curve is determined by the Chapman-Enskog method.

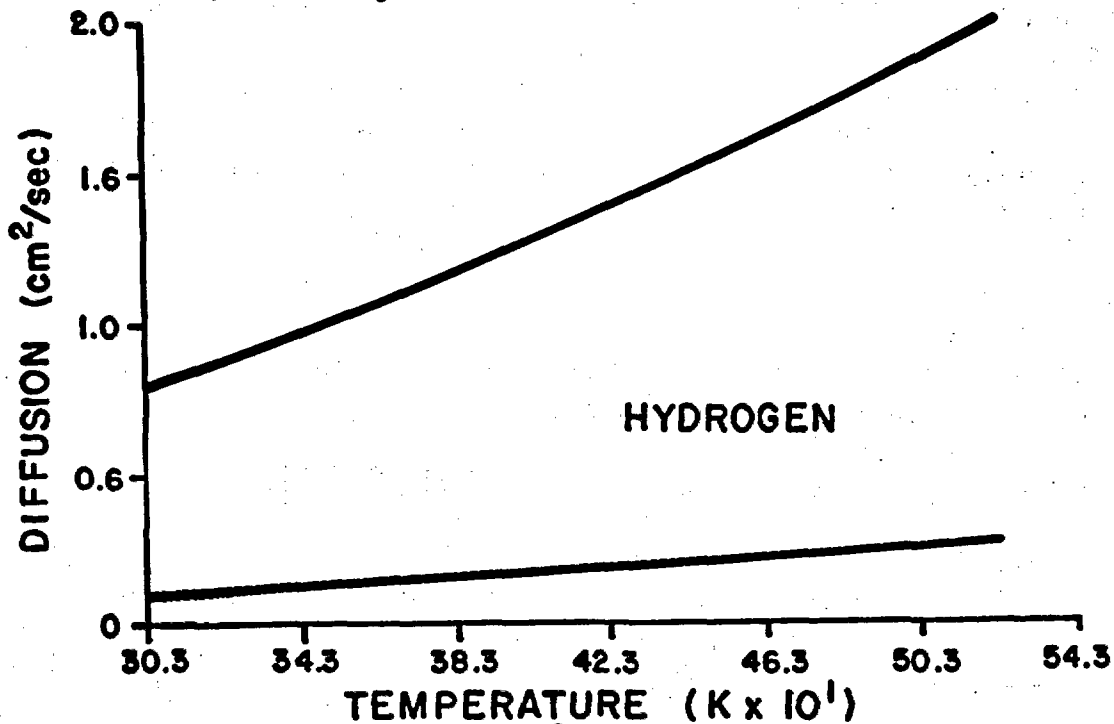


Figure 6.4 Diffusion coefficient (cm<sup>2</sup>/sec) for hydrogen versus temperature (°K). The top curve is determined by the Bird-Slattery method, the bottom curve is determined by the Chapman-Enskog method.

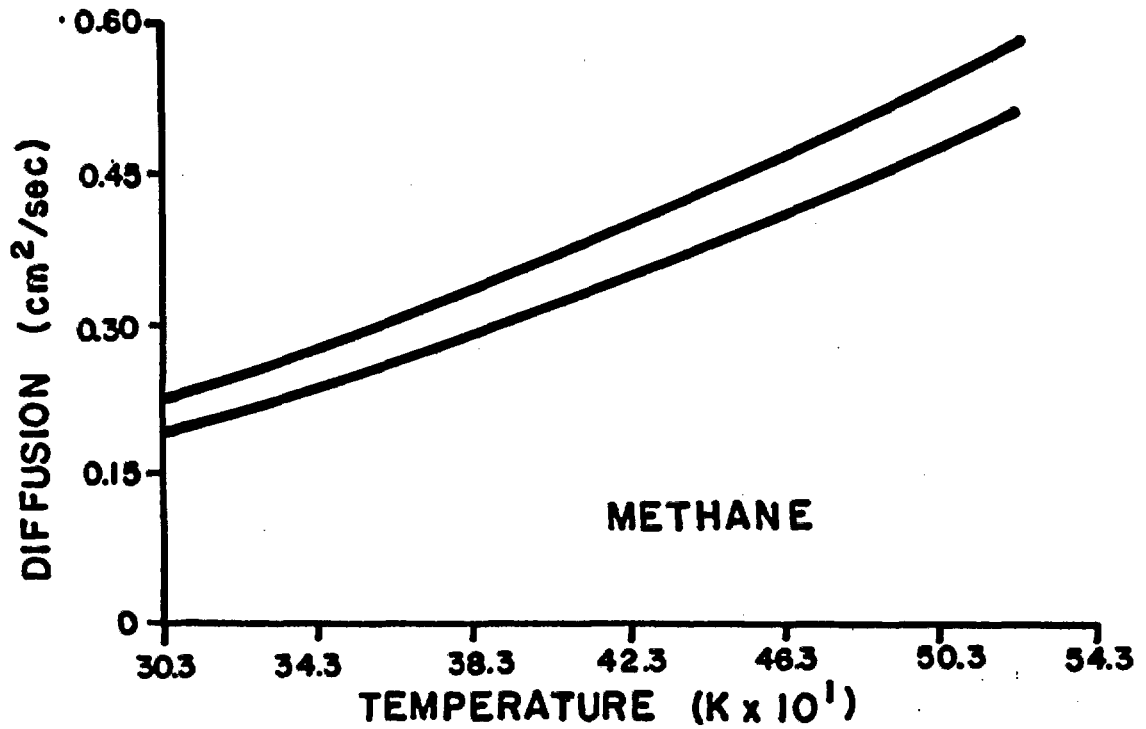


Figure 6.5 Diffusion coefficient (cm<sup>2</sup>/sec) for methane versus temperature (°K). The top curve is determined by the Bird-Slattery method, the bottom curve is determined by the Chapman-Enskog method.

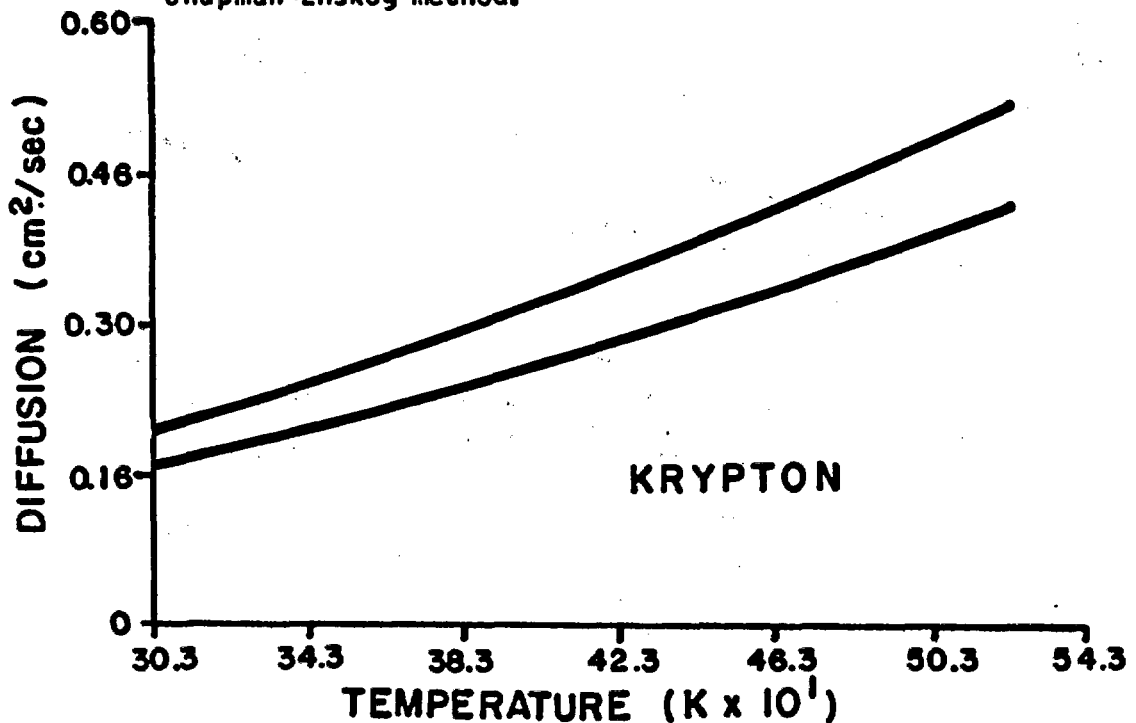


Figure 6.6 Diffusion coefficient (cm<sup>2</sup>/sec) for krypton versus temperature (°K). The top curve is determined by the Bird-Slattery method, the bottom curve is determined by the Chapman-Enskog method.

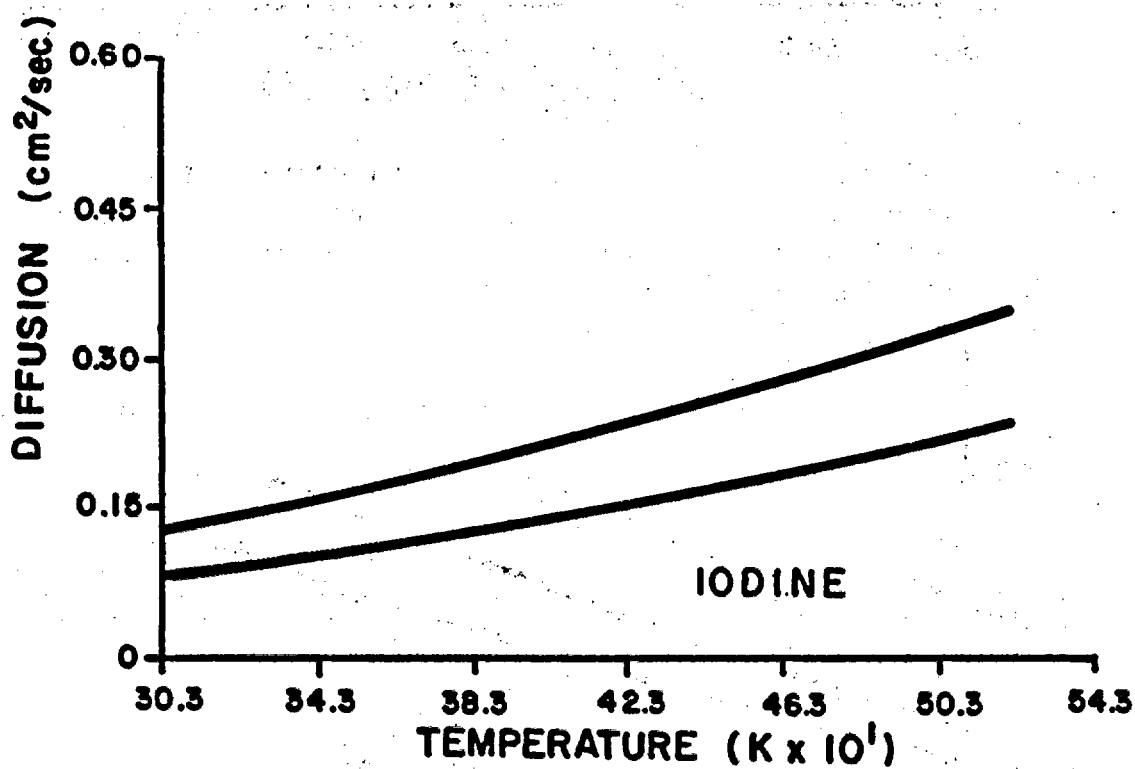
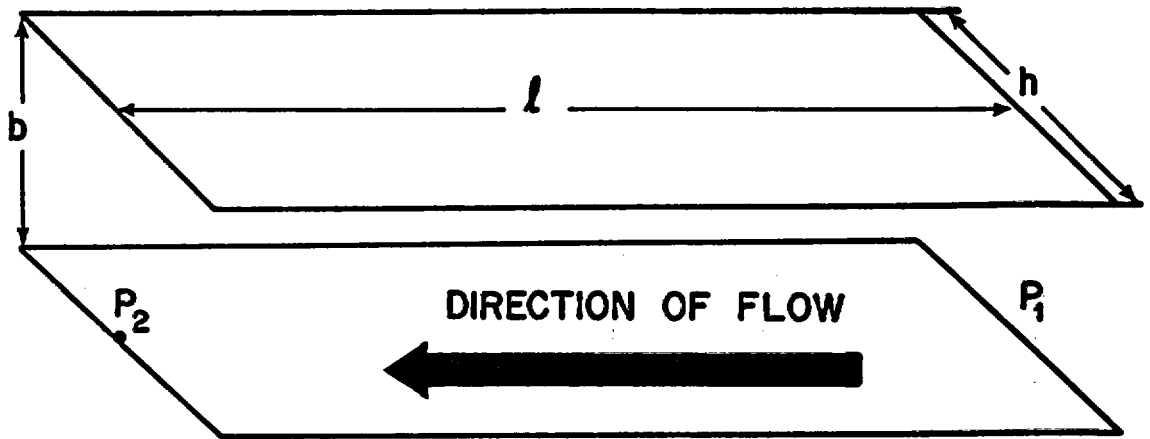


Figure 6.7 Diffusion coefficient (cm<sup>2</sup>/sec) for iodine versus temperature (°K). The top curve is determined by the Bird-Slattery method, the bottom curve is determined by the Chapman-Enskog method.



$$P_2 < P_1$$

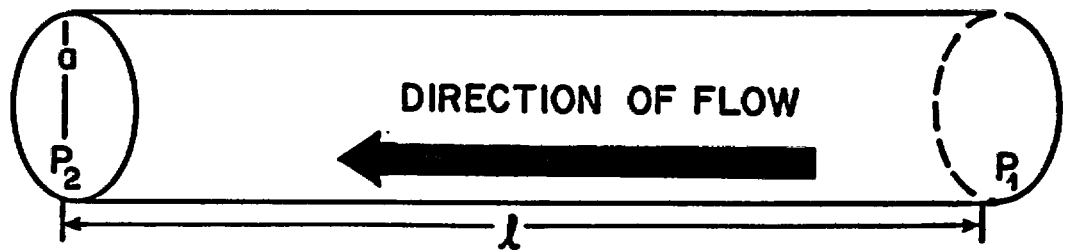


Figure 6.8 Parallel plate model (a) and capillary tube model (b) used to represent flow through an idealized fracture and an idealized porous medium, respectively.

Equation (6.12) can be expressed in a more familiar form known as Fick's law:

$$(6.14) \quad J_k = - D_K \frac{dP}{dl}$$

where the Knudsen diffusion coefficient for parallel plate flow equals:

$$(6.15) \quad D_{kp} = (4/3) (2/\pi)^{1/2} b (1/RMT)^{1/2}$$

and for capillary flow appears:

$$(6.16) \quad D_{kc} = (4/3) (2/\pi)^{1/2} a (1/RMT)^{1/2}$$

As partial pressure is increased on a flow system with a relatively high Knudsen number (i.e.,  $Kn > 1$ ) self diffusion will begin to occur. At smaller Knudsen numbers ( $Kn \ll 1$ ), a component of diffusion flow, either self or binary diffusion, increases in importance relative to Knudsen flow. Expressions have been developed to describe the transitional flow between Knudsen flow and self-diffusion.

The diffusion coefficient at the transitional region between Knudsen flow and molecular diffusion for a cylinder of infinite length under isothermal conditions is (Pollard and Present, 1948):

$$(6.17) \quad D_T = (1/3) \bar{v} \lambda [1 - (3/8) \lambda/a + 6/\lambda (\lambda/a) Q_C(a/\lambda)]$$

where  $Q_C(a/\lambda)$  is defined:

$$(6.18) \quad Q_C(a/\lambda) = \pi/16 - \pi/6 (a/\lambda) + \pi/3 (a/\lambda)^2 \\ - \pi/3(1.2264 - 3/4 \ln(2 \delta a/\lambda))(a/\lambda)^3 + \dots$$

where

$\delta$  is Eulers constant, approximately equal to 0.5772.

For the case where ( $\lambda \gg a$ ) Equation (6.17) reduces to:

$$(6.19) \quad D_T = (2/3) \bar{v} a [1 - (1.2264 + 3/4 \ln(\lambda/2 \delta a))(a/\delta) + \dots]$$

Similarly, when ( $\lambda \ll a$ ) one gets:

$$(6.20) \quad D_T = 1/3 \bar{v} \lambda [1 - (3/8)(\lambda/a)]$$

It is possible that unconsolidated rock matrix may not be adequately modeled using capillaries of infinite length. Capillaries of finite length may, in fact, better represent the flow channels through the rock matrix. The integrals from which Equations (6.17) to (6.20) are based are adapted to account for the finite length of the capillaries. It is then found that the diffusion coefficient at the transitional flow region between Knudsen flow and molecular diffusion for an isothermal system becomes (Pollard and Present, 1948):

$$(6.21) \quad D_T = (1/3) \bar{v} \lambda [1 - (3/8) \lambda/a + (6/\pi) \lambda/a Q_c(\lambda/a) - (3/2)(a/L)^2 L/\lambda [e^{-L/\lambda} \delta + L/\lambda \delta Ei(-L/\lambda)]]$$

where

$L$  is the length of the capillary; and

$Ei(-L/\lambda)$  denotes the exponential integral which is:

$$(6.22) \quad Ei(-L/\lambda) = \int_{\infty}^{-1/\lambda} -e^{-x}/x dx$$

The difference in the value of the diffusion coefficient for flow in a finite capillary and an infinite capillary becomes negligible when the half-length of the tube is greater than a few times the mean free path length.

The diffusion coefficient for Knudsen flow through a finite length capillary can be determined using Equation (6.21) when ( $\lambda \gg L \gg a$ ). This expression is written:

$$(6.23) \quad D_T = (2/3) \bar{v} a [1 - (3/4)a/L - (0.4764 + 3/4 \ln(L/2a))(a/\lambda)]$$

Upon comparing Equations (6.19) and (6.23), Knudsen flow is less through capillaries of infinite length than through capillaries of finite length. This result is supported by a graph by Massignon (1979) which illustrates a greater permeability for Knudsen flow through a short capillary than a long capillary (Figure 6.9).

A similar treatment of flow for the transition between low and high Knudsen numbers has been evaluated for parallel plate geometry by Hiby and Pahl (1952). This expression appears:

$$(6.24) \quad D_T = \bar{v} b [\lambda/3b - \lambda^2/8b^2 + (\lambda^2/2b^2) Q_p(b/\lambda)]$$

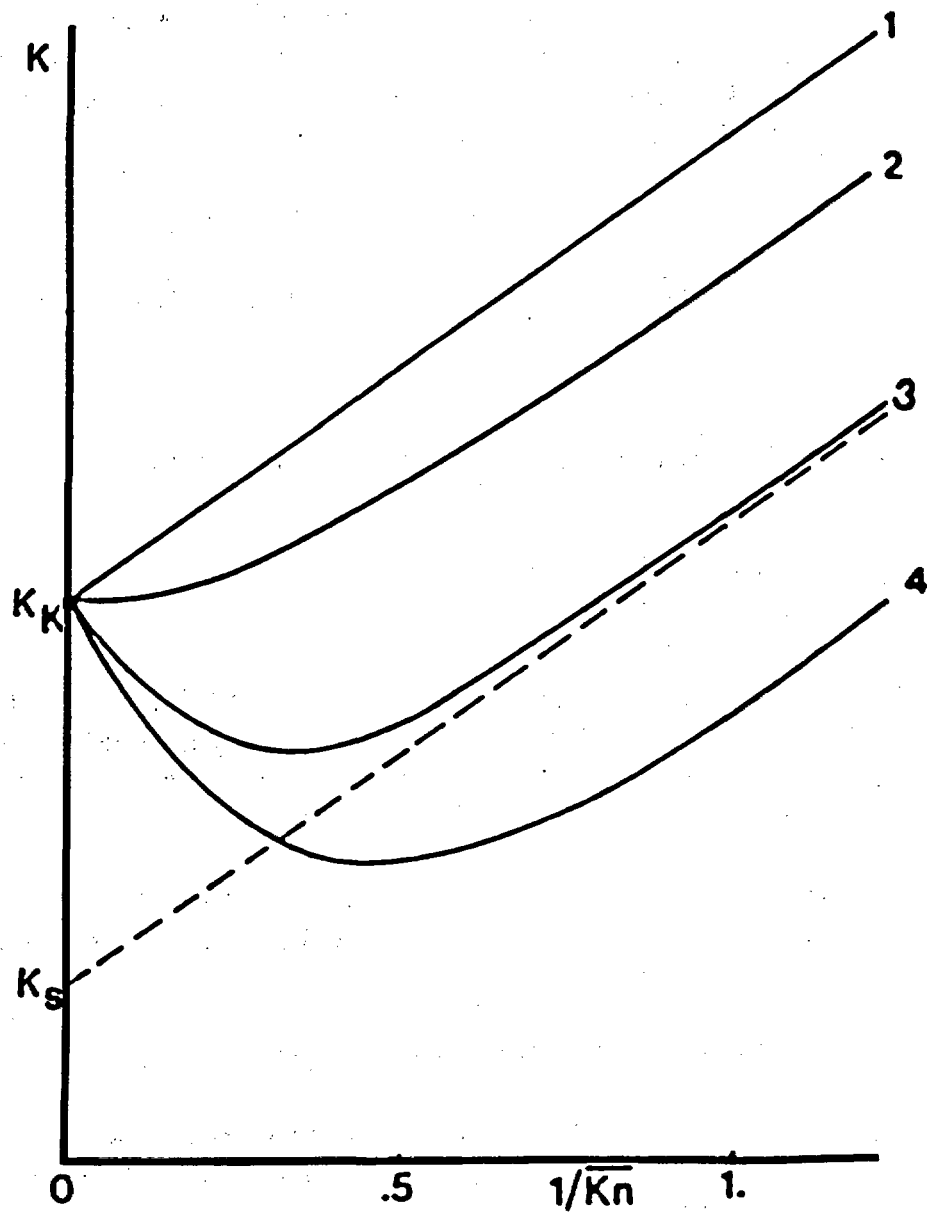


Figure 6.9 Experimental permeability,  $k$ , for different pore geometries: (1) bed of spheres; (2) short capillary ( $l = 5a$ ); (3) long capillary; and (4) parallel plates.  $k_K$  and  $k_S$  are Knudsen and slip permeabilities (from Massignon, 1979).

((From Massignon, D., Uranium Enrichment, 1979, reprinted, by permission of the author and the publisher, Springer-Verlag.)

where  $Q_p(b/\lambda)$  for parallel plate geometry is defined:

$$(6.25) \quad Q_p(b/\lambda) = e^{-b/\lambda/4} [1 - (5/3)b/\lambda - b^2/6 \lambda^2 + b^3/6\lambda^3] \\ + [(b/\lambda)^4 - 12(b/\lambda)^2]/24 E_1(-b/\lambda)$$

The diffusion coefficient is defined for a section of parallel plates of unit width. For Knudsen flow ( $\lambda \gg b$ ) Equation (6.24) reduces to:

$$(6.26) \quad D = \bar{v} b/4 (3/4 - \ln(b/\lambda))$$

When molecular diffusion predominates ( $\lambda \ll b$ ) Equation (6.24) becomes:

$$(6.27) \quad D = \bar{v} h [\lambda/3b - \lambda^2/8b^2]$$

Although probably not applicable to a fractured rock system, the diffusion coefficient for parallel plate geometry of finite extent is now calculated. The lack of applicability arises because a fracture aperture is generally several orders of magnitude less than either the length or width of a fracture in rock and edge effects can be assumed to be negligible. Nevertheless, if edge effects do exist, the following expressions are approximations of diffusion coefficients for Knudsen flow through a fracture. For most likely the case where the length of the fracture is greater than the width which, in turn, is greater than the aperture, the diffusion coefficient is expressed (Hiby and Pahl, 1952):

$$(6.28) \quad D_T = \bar{v} b/4 (1/2 + \ln(2 h/b)) \quad L \gg h \gg b$$

and for the situation where the width is greater than the length and both are greater than the aperture, the diffusion coefficient appears:

$$(6.29) \quad D_T = \bar{v} b/4 (1/2 + \ln(L/b)) \quad h \gg L \gg b$$

### 6.2.1.3 Surface Diffusion

The occurrence of surface flow (or diffusion) can greatly augment the flow of a gas through a microscopic system. A microscopic system is one in which the passageways through a medium (either fractures or capillary-like tubes) have an aperture of a magnitude of  $100 \text{ \AA}$ . Surface diffusion is parallel flow of an adsorbable gas in the presence of a concentration gradient along a surface covered with a few monolayers of an adsorbant.

Surface diffusion occurs only when the diffusing gas sorbs onto the surface of the medium through which it travels. Adsorption of gases and surface diffusion are important to gas movement when a partial layer of gases is adsorbed onto the surface of the medium or when only a few layers at most are present on the surface. If the solid surface has more than several layers of gas molecules, gas molecules adsorbed onto the surface behave as a fluid and are governed by laws of diffusion and hydrodynamics.

Ultimately, concentration can increase until the entire cross-section of a capillary is blocked by the adsorbed gas molecules. This condition is referred to as capillary condensation. Although the flux of gas transported by surface diffusion may exceed other diffusion fluxes, surface diffusion is generally less than fluid flow and therefore deemed insignificant relative to fluid flow because surface diffusion affects relatively few molecules compared to the multitude of molecules affected by fluid flow.

Adsorption can be categorized as either localized or non-localized. In the first case, adsorbed molecules take up fixed positions and are at equilibrium with the surface only when occupying adsorption sites. They may, however, move from one position to another when locally adsorbed.

Non-localized adsorption occurs when the surface has no favored positions with respect to potential energy and molecules can move about freely under stable conditions. A molecule under this condition would have the same energy at any point on a surface. Consequently, if a molecule obtained momentum in a direction parallel to the surface, it could move about freely in the absence of a lateral energy barrier. Likewise, if lateral energy barriers in the localized adsorption case have a value of  $E_a$  which is less than the kinetic energy of the molecule,  $RT$ , then molecules under localized adsorption conditions could move about laterally in a manner similar to non-localized adsorption.

Gases that exist under the above-mentioned conditions are said to possess a two-dimensional property called the spreading pressure. The spreading pressure represents the force per unit width necessary to compress the adsorbed layer of gas molecules (Gregg, 1961).

Surface diffusion at low concentrations is a two-dimensional process analogous to three-dimensional Knudsen flow because molecular collisions between pairs of adsorbed molecules are rare. Conditions which favor the existence of Knudsen diffusion ( $Kn \gg 1$ ) are also the conditions necessary for surface diffusion when an adsorbable gas is present.

The relationship between surface coverage and pressure during two-dimension surface diffusion is not adequately represented by a general isotherm. Instead, a two-dimensional form of van der Waal's equation appears to offer the best approximation for surface coverage as a function of pressure. Van der Waal's two-dimensional isotherm is written (Gregg, 1961):

$$(6.30) \quad P = K(\theta_s) \theta_s / (1 - \theta_s) \exp(\theta_s / (1 - \theta_s) - 2 a_c \theta_s / (AKT))$$

where

$\theta_s$  is the fraction of surface coverage;

$K(\theta_s)$  is a function of the heat of adsorption which will vary with  $\theta_s$ ;

$A$  is area; and

$a_c$  is a two-dimensional attraction constant analogous to the constant  $a$  in a three-dimensional form of van der Waal's equation.

Isotherms predicted by van der Waal's equation are in close agreement with experimental data for specified instances (Dacey, 1965), thus supporting the premise that two-dimensional gas behavior does exist at low coverage on uniform surfaces. Dacey determined the coefficient of surface diffusion to be the expression:

$$(6.31) \quad D_s = 1/2 \bar{v} \lambda_s$$

where the mean free path,  $\lambda_s$ , along the surface is defined as:

$$(6.32) \quad \lambda_s = 1/2 d_m c_s$$

and where

$d_m$  is the molecular diameter; and

$c_s$  is the surface concentration.

The flux resulting from surface diffusion is therefore:

$$(6.33) \quad J_s = - D_s dc_s/dx$$

Frequently, the energy barriers present at localized adsorption are greater than the kinetic energy of the gas and the gas does not diffuse in two dimensions. The movement of gas molecules in this case is referred to as activated surface diffusion and the molecules move or slip from one site to another in random walk fashion. The diffusion coefficient is related to the length of each slip by (Hill, 1956):

$$(6.34) \quad D_s = \lambda_s^2 / 2t$$

where

$\lambda_s$  is the distance between adsorption sites; and  
 $t$  is the travel time between sites calculated by the expression:

$$(6.35) \quad t = t_0 e^{E_a/kT}$$

where

$t_0$  is a property of the solid surface; and  
 $E_a$  is the potential of the barrier on the surface which must be exceeded for a molecule to change sites.

Hagashi et al. (1963) noted that  $D_s$  is dependent on surface coverage and suggest that the surface diffusion coefficient be expressed:

$$(6.36) \quad D_s = D_{s0} 1/(1 - \theta_s) \exp(-E_a/kT)$$

where  $D_{s0}$  is a gas dependent constant.

Equation (6.36) differs from Hill's formulation, Equation (6.34), because the surface diffusion coefficient increases with the degree of surface coverage instead of decreasing as Hill's equation predicts.

Although flow rates for two-dimensional surface diffusion are considerably greater than activated surface diffusion (up to  $10^5$  times greater (de Boer, 1953)), surface obstructions diminish the importance of two-dimensional surface diffusion to such an extent that activated surface diffusion is the dominant mechanism of transport at low concentrations.

#### 6.2.1.4 Total Contribution By Ordinary Diffusion

The mathematical expressions defining the contributions to concentration diffusion flux are now formulated. The total flux resulting from a concentration gradient can be represented in the expression, also presented as Equation (6.2):

$$(6.37) \quad J_0 = J_k + J_{self} + J_b + J_s$$

where the particular equation to be substituted for each contributor flux is selected based upon the nature of the gas (or gases) and the type of medium.

Table 6.3 lists all the variations of the diffusion coefficient as they appear in the text. By stating the transport mechanisms in this manner, an isothermal system is assumed when temperature is not contained in the driving force. A non-isothermal system requires that variations in temperature are accounted for when solving the appropriate equations. The non-isothermal nature of a HLW repository dictates that the driving forces resulting from temperature gradients are fully acknowledged.

Mean velocity and mean free path length are both temperature dependent variables, therefore, these two variables must be incorporated into the driving force for the non-isothermal case. Occasionally the diffusion term cannot be separated from the driving force by simple mathematical manipulation. In these cases, temperature dependent terms remain couched in the coefficient of diffusion and the equation of gas flow can not be easily factored.

Additional information is required when the driving force contains more than one variable. For example, data based upon either laboratory measurements, field measurements or computer simulations are available which provide the relationship between the spatial variation of both pressure and temperature for different scenarios of site locations and engineering designs at different times after emplacement (Wang et al., 1983; Pruess and Wang, 1985). A numerically determined curve representing the values of pressure versus temperature can be inserted into the flow equation with a complex driving force. The equations describing concentration diffusion can either be integrated analytically or numerically and solved for a particular scenario.

Expressions are presented which define the flow of gas by diffusion through fractured media for a vast range of expected flow scenarios. The selection of a flow equation (or equations) depends on the scope of the problem, the driving force present and the nature of the medium. Laboratory and field tests of gas movement can indicate which expressions best represent the medium. For example, gas-phase permeability experiments by Reda (1985) reveal an order of magnitude increase in permeability of nitrogen through densely welded tuffaceous materials as total gas pressure is decreased from 13.1 to 0.1 MPa. The mean free path between molecular collisions was increased as pressure decreased. The higher than expected flow predicted by pressure flow verified the occurrence either of Knudsen flow, slip flow or surface diffusion through micropores and the order of magnitude increase in flow rate over that predicted by pure pressure flow attests to the importance in recognizing the phenomenon.

Table 6.3 Coefficients of diffusion for the isothermal case  
(with comments), driving force is  $\nabla C$  unless otherwise noted.

$$D_{AA} = 2/3 (k^3/\pi^3 M_a)^{1/2} t^{2/3}/\rho d_a^2$$

(self diffusion, simplified kinetic theory)

$$D_{AB} = 2/3 (k^3/\pi^3)^{1/2} (1/2M_a + 1/2M_b)^{1/2} \cdot t^{3/2}/\rho [(d_a + d_b)/2]^2$$

(kinetic diffusion, simplified kinetic theory)

$$D_{AB} = 0.0018583 [t^3(1/M_a + 1/M_b)]^{1/2}/(\rho d_{ab}^2 \alpha_{Dab})$$

(binary diffusion based on rigorous kinetic theory)

$$D_{AB} = [(P^c_A P^c_B)^{1/3} (T^c_A T^c_B)^{5/12} [(1/M_a) + (1/M_b)]^{1/2}]/P \cdot a [T/(T^c_A T^c_B)^{1/2}]^b$$

(binary diffusion, kinetic theory and Slattey-Bird)

$$D_P^k = (4/3) (2/\pi)^{1/2} b(1/RMT)^{1/2}$$

(Knudsen diffusion, parallel plates, driving force is  $\nabla P$ )

$$D_C^k = (4/3) (2/\pi)^{1/2} a(1/RMT)^{1/2}$$

(Knudsen diffusion, cylindrical flow, driving force is  $\nabla P$ )

$$D_T = (1/3) \bar{v} \lambda [1 - (3/8) \lambda/a + 6/\pi(\lambda/a) Q_c(a/\lambda)]$$

(Knudsen/self-diffusion transition flow, infinite cylinder)

$$D_T = (2/3) \bar{v} a [1 - (1.2264 + 3/4 \ln(\lambda/2ga))(a/\lambda) + \dots]$$

(Knudsen/self-diffusion transition flow, infinite cylinder  $\lambda \gg a$ )

$$D = (1/3) \bar{v} \lambda [1 - (3/8)(\lambda/a)]$$

(Knudsen/self-diffusion transition flow, infinite cylinder  $\lambda \ll a$ )

$$D = (1/3) \bar{v} \lambda [1 - (3/8) \lambda/a + (6/\pi) \lambda/a Q_c(a/\lambda) - (3/2)(a/L)^2 L/\lambda [e^{-L/\lambda} + L/\lambda Ei(-L/\lambda)]]$$

(Knudsen/self-diffusion transition flow, finite cylinder)

$$D = (2/3) \bar{v} a [1 - (3/4)a/L] - (0.4764 + 3/4 \ln(L/2a))(a/\lambda)$$

(Knudsen/self-diffusion transition flow, finite cylinder  $\lambda \gg L \gg a$ )

$$D = \bar{v} b [\lambda/3b - \lambda^2/8b^2 + (\lambda^2/2b^2) Q_p(b/\lambda)]$$

(Knudsen/self-diffusion transition flow, infinite parallel plate)

$$D = \bar{v} b/4 (3/4 - \ln(b/\lambda))$$

(Knudsen/self-diffusion transition flow, infinite parallel plate  $\lambda \gg b$ )

$$D = \bar{v} h [\lambda/3b - \lambda^2/8b^2]$$

(Knudsen/self-diffusion transition flow, infinite parallel plate  $\lambda \ll b$ )

$$D = \bar{v} b/4 (1/2 + \ln(2h/b))$$

(Knudsen/self-diffusion transition flow  $L \gg h \gg b$ )

$$D = \bar{v} b/4 (1/2 + \ln(L/b))$$

(Knudsen/self-diffusion transition flow, finite parallel plate  $h \gg L \gg b$ )

$$D_s = 1/2 \bar{v} \lambda_s$$

(surface diffusion, two-dimensional, driving force is  $\nabla C_s$ )

$$D_s = \lambda_s^2 / 2 T_c$$

(surface diffusion, activated diffusion, driving force is  $\nabla C_s$ )

### 6.2.2 Viscous Flow

Laminar or turbulent flow of gas resulting from a total pressure gradient is referred to as viscous flow. Viscous flow of gas,  $J_v$ , is defined to include pressure flow,  $J_p$ , and a slip flow term,  $J_{sf}$ , (Figure 6.10) or:

$$(6.38) \quad J_v = J_p + J_{sf}$$

In this development, the governing equations which define slip flow also account for pressure flow. Thus, either  $J_p$  or  $J_{sf}$  represent a flow system but not both, so that  $J_v$  is more exactly defined by the expression  $J_p \cup J_{sf}$ .

Although turbulent flow may occur near a HLW canister at early times, total pressure will be close to one bar after about 100 years based on results by Pruess and Wang (1984). Thus, total pressure gradients are assumed to be small enough so that flow is laminar and not turbulent at later times.

#### 6.2.2.1 Pressure Flow

The governing equation for viscous flow is derived from Stokes equation. Stokes equation defines slow, laminar flow which is characteristic of Poiseuille (or Couette) flow of an incompressible fluid and is written (Neuman, 1981):

$$(6.39) \quad \rho \frac{\partial v}{\partial t} = -\nabla P + \rho g + \mu \nabla^2 v$$

where

- t is time;
- g is the acceleration of gravity; and
- $\mu$  is absolute viscosity.

Small total pressure gradients in the system permit the assumption of an incompressible fluid.

Stokes equation is solved assuming steady, one-dimensional, horizontal flow between two parallel plates separated by a distance,  $b$ , with no slip boundaries. The velocity in the direction of flow is:

$$(6.40) \quad v_x = (4z^2 - b^2)/8\mu \partial P/\partial x$$

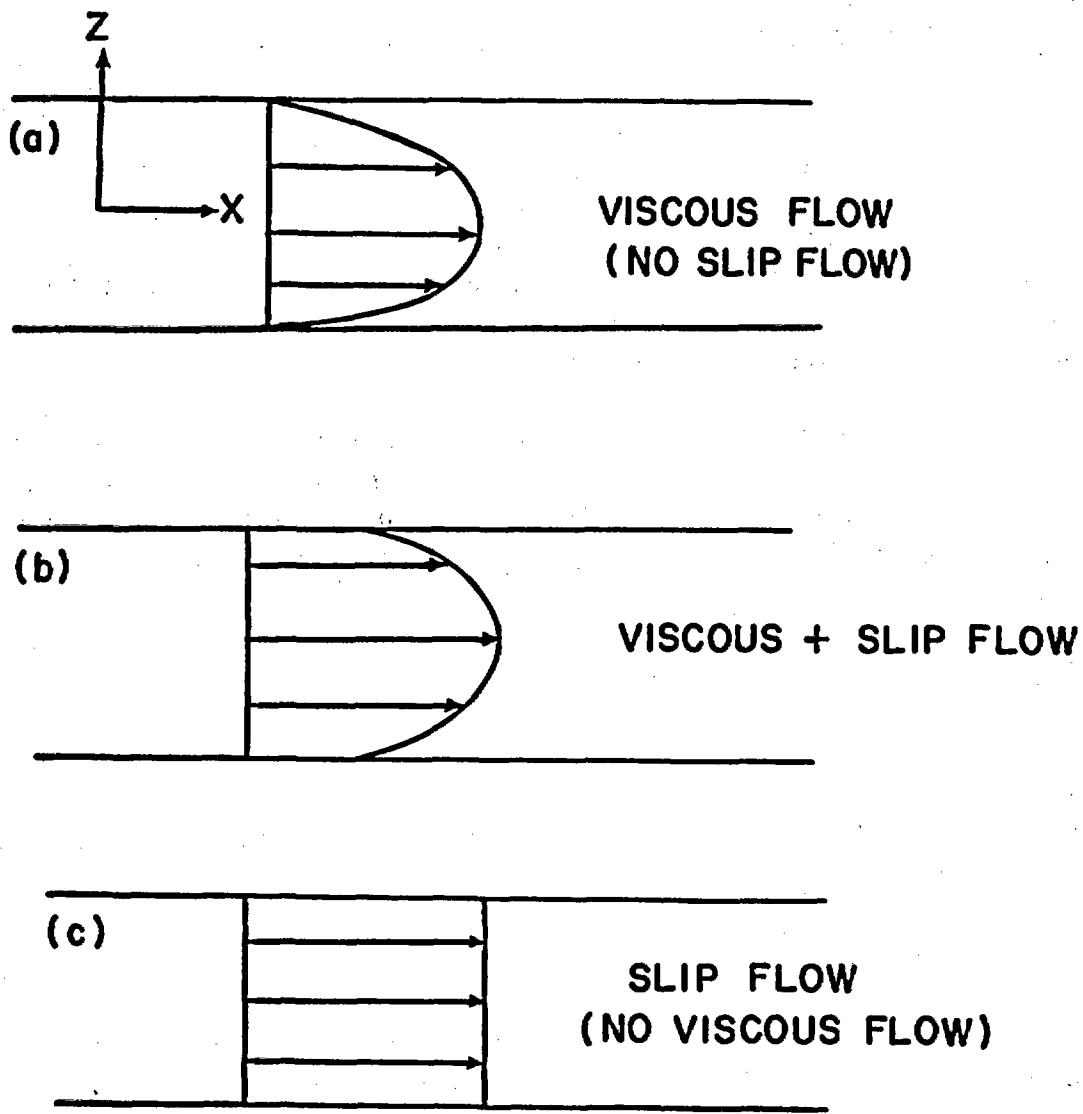


Figure 6.10 Velocity profiles of idealized gas flow through either parallel plates or capillary tube: (a) total viscous flow-no slip flow; (b) viscous and slip flow; and (c) total slip flow-no viscous flow.

Figure (6.10) illustrates the coordinate system for Poiseuille flow between two parallel plates with no slip boundaries. Velocity in the x-direction can be averaged over the entire fracture, becoming:

$$(6.41) \quad v_x^P = -b^2/12\mu \partial P/\partial x$$

The mass flux of a species can be calculated once the velocity has been determined by multiplying velocity with the density of the species of interest. If the resulting quantity is divided by the molecular weight, the mass flux caused by laminar flow can be expressed in gm-moles/cm<sup>2</sup>-sec by the expression:

$$(6.42) \quad J_L^P = -b^2 \rho/(12 \mu M) \partial P/\partial x$$

Laminar flow gas velocity through a capillary of radius, a, is determined by a similar development to that used to define parallel plate flow. Stokes equation is expressed in cylindrical coordinates with the same boundary conditions as parallel plate flow. The velocity is thus calculated to be:

$$(6.43) \quad v_x^C = -a^2/8\mu \partial P/\partial z$$

where z is the radial distance from the center line.

Likewise, the mass flux of gas by laminar flow through a capillary of radius, a, is found to be:

$$(6.44) \quad J_L^C = -a^2 \rho/(8 \mu M) \partial P/\partial z$$

Equation (6.44) can be adapted to evaluate the velocity of gas mixtures by replacing the viscosity for a single gas with the viscosity for gas mixtures,  $\mu_{mix}$ . Wilke (1950) used simple kinetic theory to calculate  $\mu_{mix}$  based upon the viscosities and molecular weights of the individual gases of the gas mixture in the expression:

$$(6.45) \quad \mu_{mix} = \sum_i^n \mu_i / [1 + 1/x_i \sum_{j \neq i}^n x_j \phi_{ij}]$$

where

$x_i$  is the mole fraction of component i of the gas mixture; and  $\phi_{ij}$  is given by the equation:

$$(6.46) \quad \phi_{ij} = [1 + (\mu_j/\mu_i)^{1/2}(M_j/M_i)^{1/4}]^{1/2} / (4/2^{1/2}) [1 + (M_i/M_j)]^{1/2}$$

### 6.2.2.2 Slip Flow

It is possible that slip flow occurs at the fracture surface-gas interface during viscous flow. Slip flow may occur when the mean free path is similar in length to the aperture of a fracture. Greater gas flow velocities will be experienced with slip flow at the boundaries than with a no-slip boundary.

The boundary layer of gas flowing next to the fracture surface is referred to as the Knudsen layer. The thickness of the Knudsen layer is of the same order of magnitude as the mean free path. The boundary condition at the fracture surface becomes:

$$(6.47) \quad v(\pm b/2) = u_0$$

where

$u_0$  is the velocity of the gas at the fracture surface-gas interface.

Gas flow velocity,  $u_0$ , at the surface of a fracture can be determined by examining momentum at the surface-gas interface. The total average viscous flow expression containing a pressure flow term plus slip flow between parallel plates is:

$$(6.48) \quad v_x^P = - [b^2/12\rho + c b/(m n \bar{v})] \partial P/\partial x$$

where

$c$  is a dimensionless term to account for discrepancies in the slip flow velocity term.

The flux term corresponding to  $v_x^P$  is:

$$(6.49) \quad J_p = -(\rho/M)[b^2/12\mu + c b/(m n \bar{v})] \partial P/\partial x$$

Similarly for capillary flow, velocity of total viscous flow appears:

$$(6.50) \quad v_x^C = - [a^2/8\mu + c a/(m n \bar{v})] \partial P/\partial x$$

The corresponding equation for flux is:

$$(6.51) \quad J_{sf}^C = -(\rho/M)[a^2/8\mu + c a/(m n \bar{v})] \partial P/\partial x$$

Expressions for slip flow also contain the pressure flow component, thus, either  $J_p$  or  $J_{sf}$  represent viscous gas flow but not both.

Concluding this section is Table 6.4 which lists the various forms of viscous flow including both pressure and slip flow.

### 6.2.2.3 Diffusion-Viscous Flow Transition

As the magnitude of the driving force varies, the nature of the transport mechanism may change. For example, if partial pressure is increased in a system where Knudsen flow is present, self-diffusion may be experienced. However, if total pressure is increased in a system where Knudsen flow is present, then slip flow may occur.

When pressure is increased in a system at low pressure where Knudsen flow is occurring, the total gas flow rate does not experience a monotonic increase. Instead, the gas flow rate will decrease to a minimum, then increase monotonically according to the physical laws that govern pressure flow as pressure is increased. This minimum in the total gas flow rate is referred to as the Knudsen minimum. The Knudsen minimum can be explained using an hypothesis fostered by Weber (1963) whereby pressure flow, slip flow, and free molecular flow are assumed to be additive. This additivity is illustrated in Figure 6.11 (from Massignon, 1979). The fact that Knudsen flow decreases at a greater rate than the increase in viscous flow (Poiseuille flow plus slip flow) causes the Knudsen minimum. Basic to Weber's hypothesis is the observation that Knudsen flow does not tend to zero as pressure is decreased.

Analogous behavior by gas flow through parallel plates is assumed to occur. Supporting this hypothesis is a graph of the relative magnitude of flow versus the inverse of the Knudsen number for several representative geometries. As is illustrated in Figure 6.11, the Knudsen minimum for flow through parallel plates (curve 4) is actually more pronounced than the minimum for flow through either a bed of spheres (curve 1), a short capillary (curve 2), or a long capillary (curve 3). The more pronounced Knudsen minimum in gas flow through parallel plates is attributed to the unique opportunity of gas molecules to travel unimpeded in two directions rather than none as in the case of the bed of spheres and only one as in the case of capillary flow before interaction with pore walls.

### 6.2.2.4 Ordinary Diffusion: Effects at Longer Distances

The significance of ordinary diffusion at a longer distances is largely dependent upon the characteristics of the rock medium through which the gas moves. Nevertheless, examination of heuristic idealized case

-----  
**Table 6.4 Equations of viscous flow.**  
 -----

$$V_x^P = - b^2 / 12\mu I_x$$

(Infinite parallel plate, Poiseuille flow)

$$J_p = - b^2 \rho / (12 \mu M) I_x$$

(Infinite parallel plate, Poiseuille flow)

$$J_p = (\bar{v} b / 4L) (\lambda e P c/b) [1.173 (P_1 - P_2) - (P_1 \ln P_1 - P_2 \ln P_2 - 2.15 (P_1^2 - P_2^2) + 0.49 (P_1^2 (\ln^2 P_1 - \ln P_1) - P_2^2 (\ln^2 P_2 - \ln P_2)))]$$

(Finite parallel plate, Poiseuille flow transitional to slip/Knudsen flow, dependent on the total pressure gradient)

$$V_p = - [b^2 / 12\mu + c b / (m n \bar{v})] I_x$$

(Infinite parallel plate, Poiseuille and slip flow)

$$J_p = - \rho / M [b^2 / 12\mu + c b / (m n \bar{v})] I_x$$

(Infinite parallel plate, Poiseuille and slip flow)

$$V_x^C = - [a^2 / 8\mu + c a / (m n \bar{v})] I_x$$

(Capillary flow, infinite capillary, slip flow)

$$J_c = - \rho / M [a^2 / 8\mu + c a / (m n \bar{v})] I_x$$

(Capillary flow, infinite capillary, slip flow)

$$V_x^C = - a^2 / 8\mu I_x$$

(Capillary flow, infinite length)

$$J_c = - a^2 \rho / (8 \mu M) I_x$$

(Capillary flow, infinite length)

where  $I_x = \partial h / \partial x$

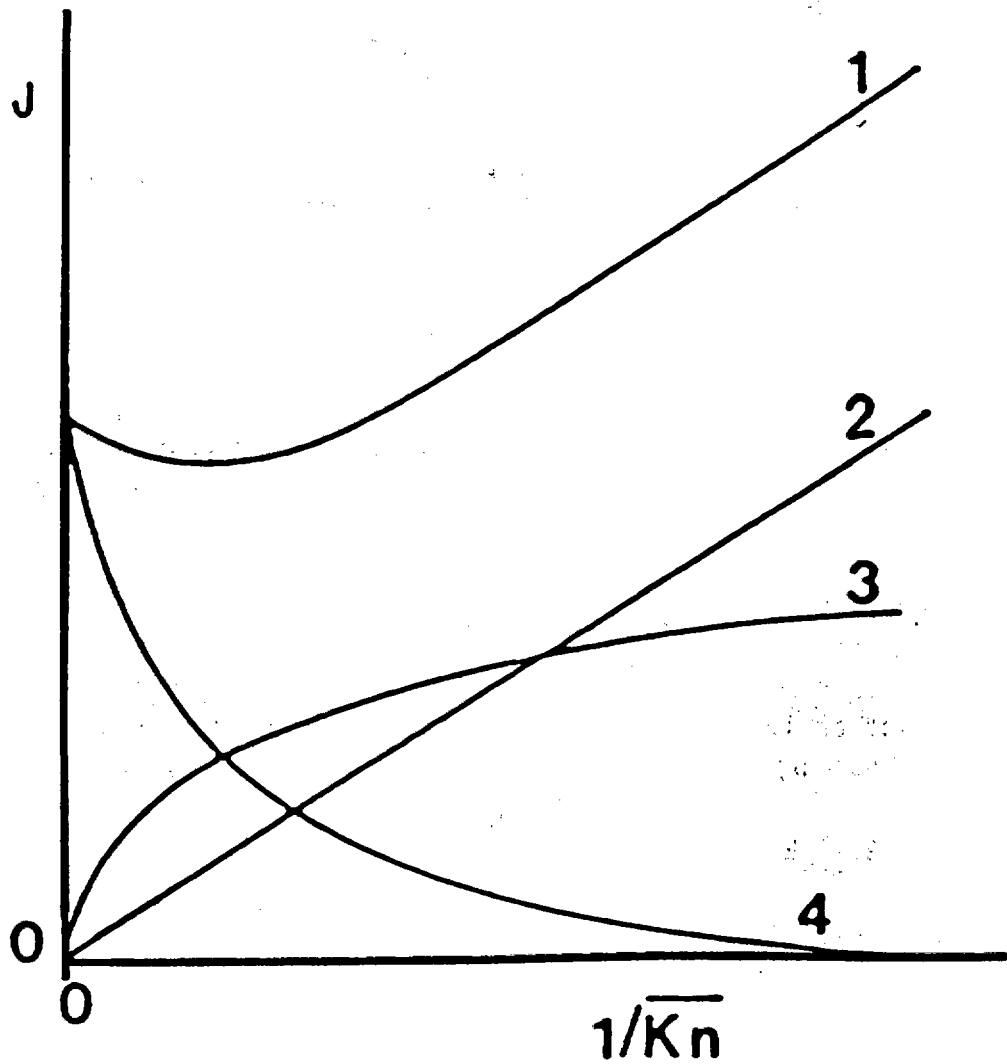


Figure 6.11 Transition from Knudsen to viscous flow through a long capillary tube as Knudsen number decreases: (1) total flow rate; (2) viscous flow; (3) slip flow; and (4) Knudsen flow (from Massignon, 1979).

(From Massignon, D., Uranium Enrichment, 1979, reprinted, by permission of the author and the publisher, Springer-Verlag.)

studies can lend valuable information concerning the importance of radionuclide transport by ordinary diffusion from a HLW canister to the accessible environment at some distance.

The equation of continuity of a gas states:

$$(6.52) \quad -\nabla \cdot J = \partial c / \partial t$$

where  $t$  denotes time.

Combining Equations (6.37) and (6.52) results in the expression:

$$(6.53) \quad D \nabla^2 c = \partial c / \partial t$$

where a constant density and isothermal medium have been assumed.

An indication of the importance of mass flux by diffusion can be gained by examining the time required for diffusive flux to approximate steady state.

For this example, an open mineshaft and borehole absent of backfill are assumed. The diffusive path is equated to a 300-m long cylindrical conduit with no retardation and an absence of convective forces. Concentration at the far end of the conduit which is located at the accessible environment is zero and contaminants that reach the far end of the conduit are immediately released. The boundary and initial conditions imposed on Equation (6.53) are therefore:

$$\begin{aligned} (6.54a) \quad c(0,t) &= 1 & z > 0 \\ (6.54b) \quad c(300,t) &= 0 & t > 0 \\ (6.54c) \quad c(z,0) &= 0 & 0 < z < 300 \end{aligned}$$

The one-dimensional analytical solution to Equation (6.53) in the  $z$ -direction is (Carslaw and Jaeger, 1959):

$$(6.55) \quad c(z,t) = \frac{2D\pi}{L^2} \sum_{i=1}^{\infty} \exp\left(\frac{-D i^2 \pi^2 t}{L^2}\right) \sin\left(\frac{i\pi z}{L}\right) \int_0^t \exp\left(\frac{D i^2 \lambda^2}{L^2}\right) c(0,t) d\lambda$$

where  $L$  is the length of the conduit.

Solving the integral in Equation (6.55) and rearranging terms yields the infinite series:

$$(6.56) \quad c(z,t) / c(0,t) = \frac{2}{\pi} \sum_{n=1}^{\infty} \sin(n\pi z/L) \frac{1}{n} [1 - \exp(-D_1^2 n^2 \pi^2 t/L^2)]$$

A diffusion coefficient of 0.15 cm<sup>2</sup>/sec is assumed which is the approximate value for either I<sub>2</sub>, Kr, CH<sub>4</sub>, H<sub>2</sub>, or CO<sub>2</sub> diffusing at through air at 300°K and atmospheric pressure. Figure 6.12 illustrates the normalized concentration, c(z,t)/c(0,t), versus distance at times 1 to 75 years. Constant diffusive flux is approached after 75 years.

The rates of contaminant emission from a HLW canister have yet to be calculated because the exact nature of waste containment is not specified. However, calculating the source term based on a specified release rate of waste to the accessible environment is possible when several assumptions are made. The proposed release rate to the accessible environment is 1000 curies (Ci) per 1000 metric tons of heavy metal (MTHM) over a 10,000 yr period for any gamma- or beta-emitting radionuclide (40CFR191). This is an average of 0.0001 Ci/yr per MTHM at a constant release rate.

In the first case analyzed, the source term is calculated for gas diffusion through a 300 m long cylindrical conduit that is 35 cm in diameter and abuts a canister containing approximately 0.5 MTHM. This quantity of high-level waste translates to an allowable constant release rate of 1.6 x 10<sup>-12</sup> Ci/sec per canister. At steady state, the diffusive flux from a beta- or gamma-emitting radionuclide in the canister will be 1.6 x 10<sup>-15</sup> Ci/cm<sup>2</sup>-sec at the accessible environment.

It is assumed that no decay or retardation occurs, the coefficient of diffusion is constant, and that 100% of the flux from the canister is released to the accessible environment through a 35 cm diameter borehole. An additional assumption made in this calculation is that once a canister is breached, the entire canister cladding is deemed inoperative and contaminants are introduced into the geologic medium over 100 percent of the total surface area of the canister.

The diffusive flux per unit area from the surface of a canister is calculated to be 3.9 x 10<sup>-18</sup> Ci/cm<sup>2</sup>-sec. Once the diffusive flux at the canister surface is known, the concentration of gas at the surface of the canister is determined using Fick's law as 7.8 x 10<sup>-13</sup> Ci/cm<sup>3</sup>.

One curie is emitted by approximately 5770 g of <sup>129</sup>I. A concentration of 7.8 x 10<sup>-13</sup> Ci/cm<sup>3</sup> corresponds to 4.5 x 10<sup>-9</sup> g/cm<sup>3</sup> of <sup>129</sup>I. Therefore, an average concentration greater than 4.5 x 10<sup>-9</sup> g/cm<sup>3</sup> of

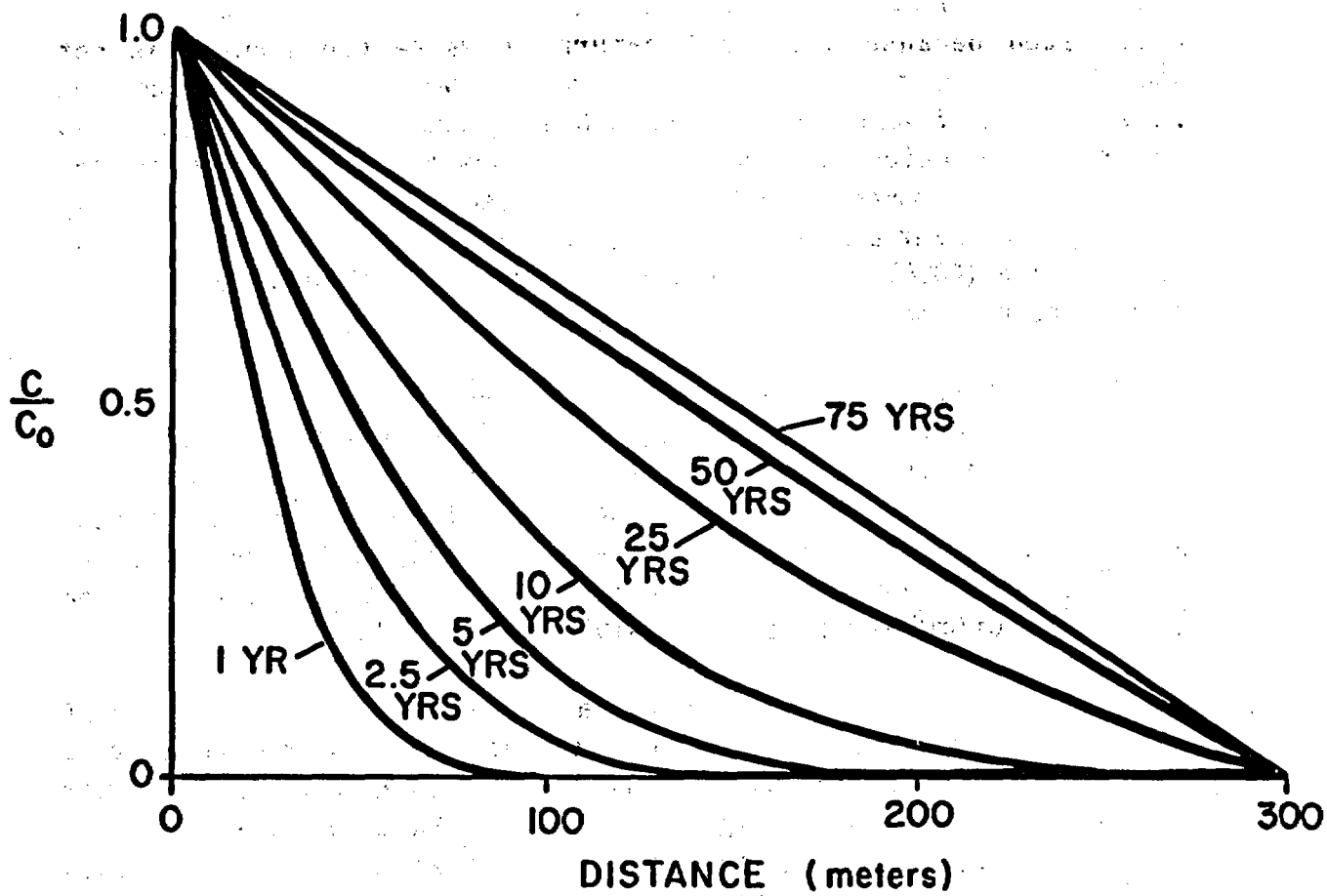


Figure 6.12 Diffusive flux versus normalized concentration for a 300 m long cylindrical conduit at time 1 to 75 years.

$^{129}\text{I}$  over the entire surface area of the canister will exceed the proposed release rate of  $1.6 \times 10^{-18}$  Ci/sec at the accessible environment for the conditions given.

A second case study analyzes ordinary diffusion from a repository overlain with a 300 m thick layer of homogeneous unsaturated fractured rock. The rock matrix is considered an equivalent porous medium with a constant effective gas porosity. The repository is assumed to cover a 1 x 2 km area and contain about 50,000 MTHM (100,000 canisters). The time to approach steady state in this case would be slightly greater than the 75 years required in the first case study.

Equation (6.37), when accounting for porosity and tortuosity, becomes (Weeks et al., 1982):

$$(6.57) \quad J = - T_t n D \nabla c$$

Tortuosity,  $T_t$ , can be related to the drained porosity,  $n$ , by the empirically derived expression (Millington, 1959):

$$(6.58) \quad T_t = n^{1/3}$$

An equivalent porous medium with a drained porosity of 10% will have a calculated tortuosity of 0.46. Therefore, the rate of diffusive flux through the rock would be 4.6% of the diffusive flux through an open borehole of similar cross-sectional area for the same concentration gradient.

Each canister will influence an average planar area of  $2.0 \times 10^5$  cm<sup>2</sup> if 100,000 canisters are uniformly spaced over a 2 km<sup>2</sup> area. It is assumed that no retardation has occurred, the coefficient of diffusion is constant and equals 0.15 cm<sup>2</sup>/sec, and that 100% of the flux of beta- or gamma-emitting radionuclides at the canister is released through a  $2.0 \times 10^5$  cm<sup>2</sup> area at the accessible environment.

Since the proposed allowable release rate of a beta- or gamma-emitting radionuclide from each canister is an average of  $1.6 \times 10^{-12}$  Ci/sec, the flux will be  $7.9 \times 10^{-18}$  Ci/cm<sup>2</sup>-sec to the accessible environment at steady state. The flux at the surface of a canister will be  $3.9 \times 10^{-18}$  Ci/cm<sup>2</sup>-sec. An average concentration of less than  $1.7 \times 10^{-11}$  Ci/cm<sup>3</sup> is necessary over the entire surface of a canister ( $4.1 \times 10^5$  cm<sup>2</sup>) to meet the proposed standards. If the radionuclide is  $^{129}\text{I}$ , a concentration of  $1.7 \times 10^{-11}$  Ci/cm<sup>3</sup> corresponds to a concentration of  $9.7 \times 10^{-8}$  g/cm<sup>3</sup> of  $^{129}\text{I}$ .

There is a lack of definitive design and analysis of the characteristics of high-level waste, the canister, and associated engineering barriers. The rate and chemical nature of high-level waste exposed to the geologic medium after canister failure has not been specified. However, the preceding analysis indicates that steady-state diffusive flux at the accessible environment is attained in a relatively short period of time for two extreme cases. The analysis also suggests source term limits at the canister that should not be exceeded if gaseous  $^{129}\text{I}$  is released.

### 6.3 Forced Diffusion

Mass flux of a gas by forced diffusion is, under most conditions, considered insignificant. However, gamma radiation emitted during decay of high-level waste can induce an electric field caused by Compton scattered electrons which in turn can create conditions conducive to forced diffusion. The magnitude of the resulting electric field and the related forced diffusion of an ionized gas through the air space of a partially saturated fracture will depend upon the physical characteristics of the high-level waste and the repository site. As first approximations, the electric field created in a rock mass and air is investigated.

The mass flux (ions/cm<sup>2</sup>-sec) of gas resulting from forced diffusion caused by an electric field can be expressed as (MacDaniel and Mason, 1973):

$$(6.59) \quad J = n v_d$$

where

$n$  is the number density of ions (ions/cm<sup>3</sup>);  
 $v_d$  is the drift velocity (cm/sec).

An electric field is classified as a low energy field if it has an intensity less than 1500 V/cm at atmospheric pressure (MacDaniel and Mason, 1973). In a low energy field, the drift velocity of ions along the field lines is proportional to the electric field as described in the expression:

$$(6.60) \quad v_d = K E$$

where

$E$  is the electric field (V/cm);  
 $K$  is the mobility (cm<sup>2</sup>/V-sec).

The mobility term,  $K$ , is a proportionality factor and is a measure of the ease at which an ion can move through a gas. It is related to the diffusion coefficient by the expression:

$$(6.61) \quad K = e D / (k T)$$

where

- $e$  is the ionic charge (coulombs);
- $D$  is the diffusion coefficient ( $\text{cm}^2/\text{sec}$ );
- $k$  is the Boltzmann constant (joules/ $^\circ\text{K}$ ); and
- $T$  is the temperature ( $^\circ\text{K}$ ).

The value of mobility can be assumed constant when the field energy is low. A value of 2 ( $\text{cm}^2/\text{V-sec}$ ) is reasonable for many ions in air (McDaniel and Mason, 1973).

The Compton current creates a displacement of electrons away from the canister. This sets up an electric field which causes a return flow of conduction electrons. The electric field grows in strength until the return flow exactly balances the Compton current. The electric field is related to the return flow (or current density),  $j$  (amps/ $\text{cm}^2$ ), and the resistivity of the medium,  $\rho$  (ohms-cm), by Ohm's law which can be expressed as:

$$(6.62) \quad E = \rho j$$

Although the Compton current is not governed by Ohm's law, the return flow is, and Equation (6.62) can be used to calculate the electric field. Current density is by definition related to the current,  $I$  (amps), by the expression:

$$(6.63) \quad j = I/A$$

where

- $A$  is area ( $\text{cm}^2$ ).

The electric field enveloping a HLW canister can, therefore, be determined if current density and resistivity are known.

The Compton effect results from an interaction of a photon with either a bound or free electron in the absorbing material. The resulting preferential movement of the emitted electrons away from the photon source creates the Compton current. A Monte Carlo algorithm has been

written to record the movement of photons, which are emitted by a high-level waste canister. Each photon is followed from collision to collision keeping track of its energy losses and the Compton electrons emitted. A history is terminated when the photon's energy becomes too small to cause further Compton scattering. The simulation program, COMPMC, follows a sufficient number of histories to account for the random nature of photon interactions.

The waste package is characterized as an infinite line source. Thus, end or edge effects are ignored. A further assumption made in this simulation is that the HLW canister is located in a homogeneous isotropic medium. This assumption simplifies the procedure employed in tracking individual photons. However, once the Compton current is calculated along with the accompanying electric field, partially drained fractures which intersect the canister can be superimposed onto the system in order to investigate forced diffusion of vapor. The effect of the canister upon photon transport, however, has not been considered. For the conservative case, it is assumed that the canister has failed.

The effective range (net displacement) of the Compton electron is determined by a separate computer routine, SR, which uses the streaming ray method (Filippone et al., 1980; and Woolf et al., 1986) to solve the electron transport equation. The effective range depends on the electron energy and the medium through which it is traveling. For the rock mass case, the effective range of electrons through a hypothetical material (with properties resembling the weighted-average properties of an unsaturated tuff, that is, atomic number of 33 and atomic mass of 68) is calculated at a total of 27 different electron energies. A graph of the effective range of an electron is plotted versus electron energy in Figure 6.13. Three second-order polynomials are used to fit a smooth curve through the data in a spline-like fashion. Therefore, after each collision, the radial distance travelled by each electron can be calculated. Following convention, we have expressed distances in  $\text{g/cm}^2$  units. Dividing these units by the rock bulk density provides a distance in cm. The most energetic electron considered (20 MeV) will thus have a range of 0.1 cm.

There is no analytic solution available to validate the full extent of COMPMC (which is based upon exact transport theory), that is, to calculate the radial density of collisions between anisotropically scattered photons and particles in the medium. However, an analytic solution based upon the diffusion theory approximation is available to calculate diffusion of isotropically scattered photons emitted from an infinite line source.

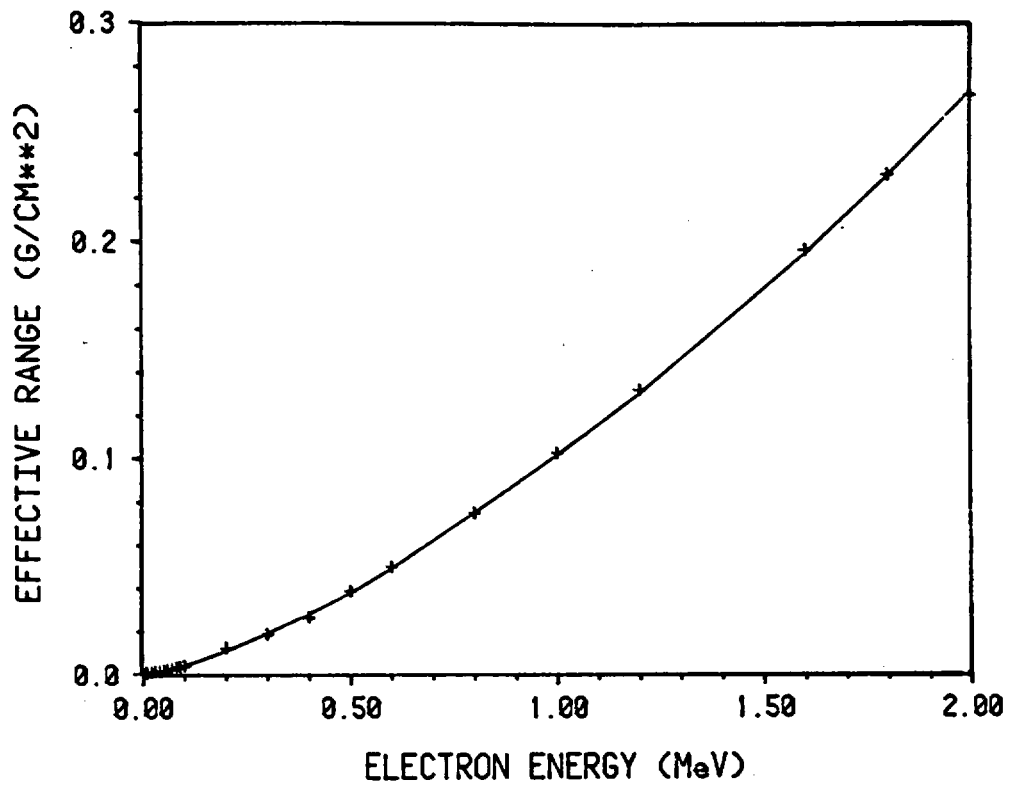


Figure 6.13 Effective range of electrons in tuff versus electron energy level.

In general, photons emitted from a line source will not propagate in a manner resembling diffusion because of their preferential outward movement. However, with isotropic scattering, diffusion theory agrees well with transport theory except near sources and sinks. Therefore, by making the collisions isotropic and maintaining the photon energy at 1 MeV, it should be possible to make the results of the COMPMC code agree well with those predicted by one speed diffusion theory in regions away from the line source. The one speed diffusion theory solution to this problem can be expressed analytically (Lamarsh, 1966):

$$(6.64) \quad N_c = \mu r K_0(r/L)/(2 \pi D)$$

where

$N_c$  is the collisions per unit length;

$\mu$  is the absorption coefficient;

$r$  is the radial distance;

$K_0$  is the zero-order Bessel function of the second kind; and

$L$  is a parameter referred to as the diffusion length.

The diffusion coefficient is defined here by the expression:

$$(6.65) \quad D = 1/3\mu$$

The normalized radial collision density determined from the results of COMPMC is compared with the analytical solution to the diffusion equation. As is illustrated in Figure 6.14, there is a discrepancy between the results near the line source where diffusion theory does not adequately represent the initial preferential outward movement apparent in the results from COMPMC. However, after the region where the initial collisions occur and beyond where outward preferential movement is significant, the results from COMPMC and the diffusion equation are close. The Compton current density,  $j(r)$ , is formally given by the expression:

$$(6.66) \quad j(r) = \iiint \sigma(\Omega^*, E^*, \Omega, E) \Omega R_{eff} \phi_e(r, \Omega', E') e \, dE \, d\Omega \, dE^* \, d\Omega^*$$

where

$\sigma(\Omega^*, E^*, \Omega, E)$  is the differential cross section for producing a Compton electron of direction  $\Omega$  and energy  $E$  from a photon of direction  $\Omega^*$  and energy  $E^*$ ;

$R_{eff}$  is the effective range of electron of energy  $E$ ; and

$\phi_e(r, \Omega, E)$  is the gamma flux (photons per unit solid angle, per unit area, per unit energy).

CURRENT DENSITY AT 0.30 MeV

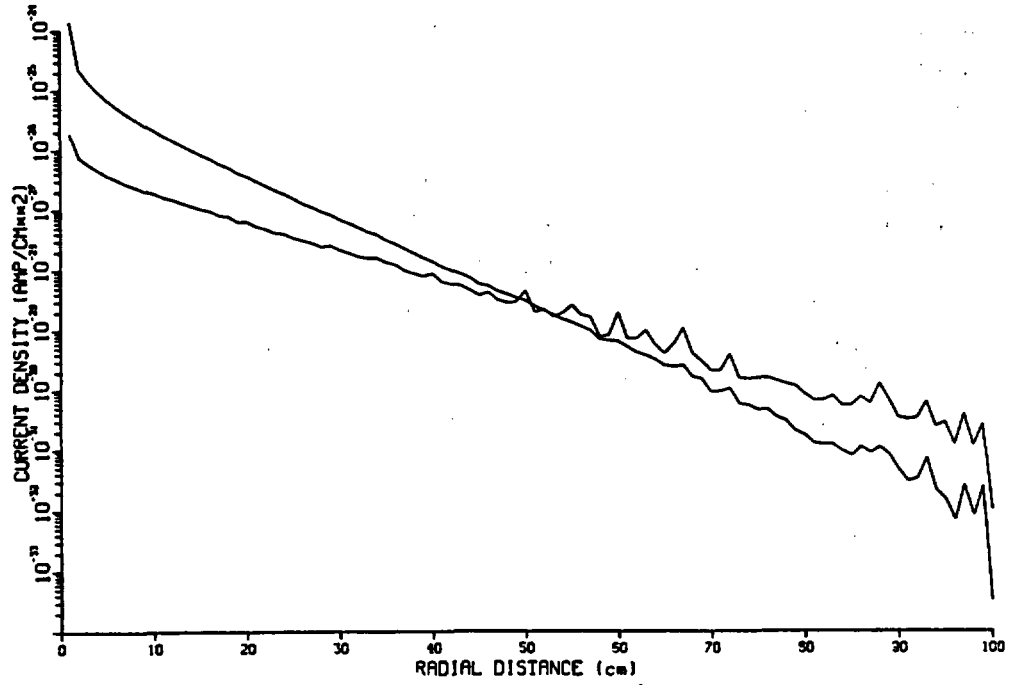


Figure 6.14 Electric current density in tuff from a 0.30 MeV photon emitted from an infinite line source. Values for  $e$  indicate accuracy relative to magnitude of current density.

Only the radial component of the current density vector is of interest and is recorded in the appropriate radial annulus as a scalar,  $j$ .

The gamma ray source employed in COMPMC is normalized so that any HLW inventory can be represented and examined in terms of the resulting electric field, drift velocity and forced diffusion caused by emitted photons. The particular gamma ray source used in this analysis is based on the radionuclide inventory of a single fuel assembly of defense high-level waste from a light water reactor predicted using the SANDIA-ORIGEN code (Sutherland and Bennett, 1979). It is assumed that spent fuel from a pressurized water reactor is immobilized in a matrix and placed in a canister without reprocessing.

COMPMC determines the Compton electric current density per photon per second at a designated initial photon energy. The distribution in energy of the source photons is determined using results from a summary of the gamma spectrum (photons/sec) per fuel assembly (as described above) at 100, 300, 1000, 10000, and 100,000 years after emplacement. Values of the gamma-spectrum at discrete energy levels for all photons originating in the structural material, actinides, and fission products of the fuel assembly are listed in Table 6.5. The electric current density caused by Compton scattered electrons in a dry tuff are calculated using the gamma ray source defined in this table.

-----  
 Table 6.5 Summary of gamma spectrum (photons/sec) per fuel assembly  
 (structural materials + actinides + fission products)(from  
 Sutherland and Bennett, 1979).  
 -----

MeV	Time (years)				
	100	300	1,000	10,000	100,000
0.30	2.4E13	1.8E13	7.8E12	1.1E12	5.6E10
0.63	1.6E14	1.8E12	2.5E11	1.1E11	1.4E10
1.10	1.4E11	7.6E10	7.2E10	3.7E10	9.8E09
1.55	5.6E06	3.2E06	1.8E07	7.6E08	6.1E09
2.75	1.3E09	1.3E09	1.3E09	1.2E09	6.9E08

-----

An error estimate of the values of current density at each radial mesh interval is determined to indicate the accuracy of the resulting normalized values. The Central Limit Theorem determines the probability that the difference between the Monte Carlo approximation for current density,  $j$ , and the true value of the current density,  $\langle j \rangle$ , is less than a given  $\epsilon$ . This theorem is stated as:

$$(6.67) \quad P(|j - \langle j \rangle| < \epsilon) \rightarrow (2/\pi)^{1/2} \int_0^{(\epsilon n^{1/2})/s_d} \exp(-t^2 / 2) dt$$

where

$n$  is the number of histories; and  
 $s_d$  is the standard deviation.

The right hand side of Eq. (6.67) is referred to as the confidence level. In this work it is assigned the conservative value of 0.9. Thus, 90% of the values for the current density determined by COMPMC should be accurate to  $\pm\epsilon$  of their true value. The values of current density and  $\epsilon$  determined for a 90% confidence level are plotted versus radial distance in Figure 6.15 for energy 1.55 MeV. Figures for the other energy levels listed in Table 6.5 are similar to this one.

The electric current density is determined at several radial annuli for discrete gamma ray energies for each of the five time periods. The total electric field enveloping the HLW canister is the summation of the five contributing electric field values determined at the five discrete energy levels. The resulting quantities are plotted versus radial distance at 100, 300, 1000, 10000, and 100,000 yrs in Figure 6.16. A value of  $10^6$  ohm-cm is assigned to the resistivity of dry tuff in this calculation (Telford et al., 1976).

Ion drift velocities can be determined from Figure 6.16 when mobility is known. An assumed mobility of  $2 \text{ cm}^2/\text{V-sec}$  indicates drift velocities will be less than about  $10^{-6} \text{ cm/sec}$  in fracture air spaces superimposed onto the rock matrix even at early times proximal to the canister.

A second scenario is investigated for the potential of forced diffusion in air near a HLW canister. The importance of forced diffusion in a significantly large air space proximal to a canister will exceed that for the case where the canister is completely encapsulated in rock mass. Significant air spaces around a canister can occur in large fractures in the disturbed zone around the canister borehole. These fractures can be induced by a thermal load caused by the canister, by mechanical loading and unloading of stress in the rock or by dissolution of the rock

CURRENT DENSITY AT 1.55 MeV

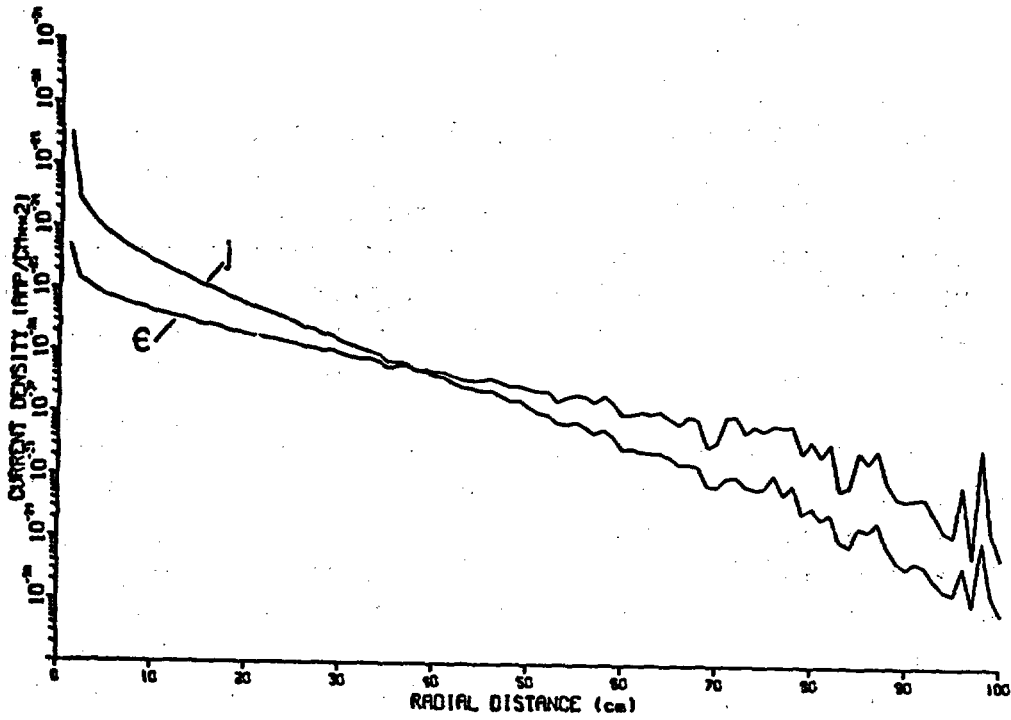


Figure 6.15 Electric current density in tuff from a 1.55 MeV photon emitted from an infinite line source. Values for  $\epsilon$  indicate accuracy relative to magnitude of current density.

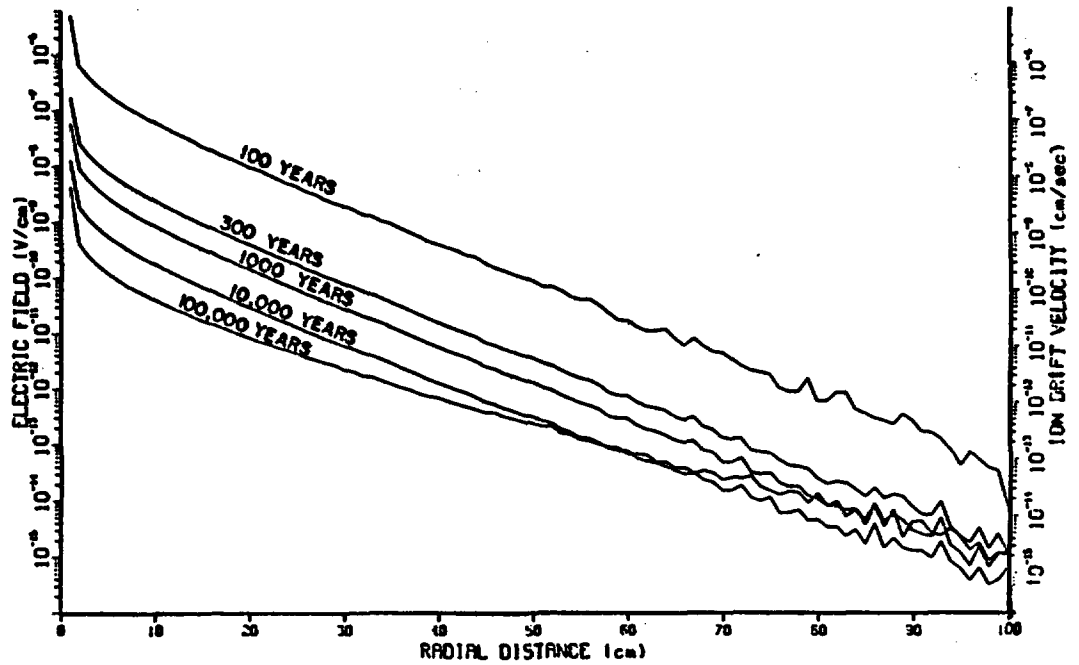


Figure 6.16 Electric field intensity (left axis) and ion drift velocity (right axis) in tuff at 100, 300, 1000, 10,000 and 100,000 years versus radial distance from an infinite line source. Resistivity of tuff is  $10^6$  ohm-cm, mobility is  $2 \text{ cm}^2/\text{V-sec}$ .

matrix. Large air spaces can also occur where a borehole intersects highly fractured rock. Leaving the borehole absent of backfill has been suggested (Fernandez and Freshley, 1983) as a means of reducing liquid flow under conditions of negative pressures.

COMPMC and SR are used to predict the current density in air by the same methodology used for the rock mass model. SR is used to calculate the effective electron range/electron energy relationship for electrons travelling through air. The weighted average atomic mass of air has an assigned value of 28.9 and the atomic number has the value of 14.2 in these calculations. As in the case of the rock mass model, the coefficients for three second-order polynomials are calculated from 23 data points to approximate the effective electron range/electron energy relationship. Figure 6.17 illustrates the computed values of effective electron range versus the electron energy and the associated approximating polynomials.

COMPMC determines current density in air for the same five energy levels of the gamma ray source given in Table 6.5. The variable  $e$  is calculated at a 90% confidence interval for each energy level. As an example, the values of current density and  $e$  are plotted versus radial distance and illustrated in Figure 6.18 for the case of 1.55 MeV gammas.

Current density edge effects near the canister are more pronounced for air than for rock mass. Additionally, the radial falloff of the current density is substantially less in air than in the rock mass. Although Figure 6.18 shows a maximum distance of 100 cm, the current density was actually calculated out to 400 cm through air with a continuing gradual decrease in current density observed.

A value of  $10^{-15}$  (mhos/cm) for electrical conductivity of air is taken from atmospheric measurements recorded immediately following lightning flashes (Krider and Musser, 1982). Here we ignore the fact that the radiation-induced ionization may alter conductivity.

The electric field resulting from the current densities is illustrated in Figure 6.19 calculated at periods of 100, 300, 1000, 10000 and 100,000 years. Drift velocity is 250 cm/sec at a distance of 10 cm from the canister 300 years after emplacement with an assumed mobility of 2  $\text{cm}^2/\text{V}\cdot\text{sec}$ . If the design period of a HLW canister is 300 years, sizable air spaces at the canister wall may occur by this time. Ionic drift velocities as large as 1000 cm/sec are possible at small distances (1-3 cm) from the canister. Forced diffusion can provide an important transport link if ion density is sufficiently large.

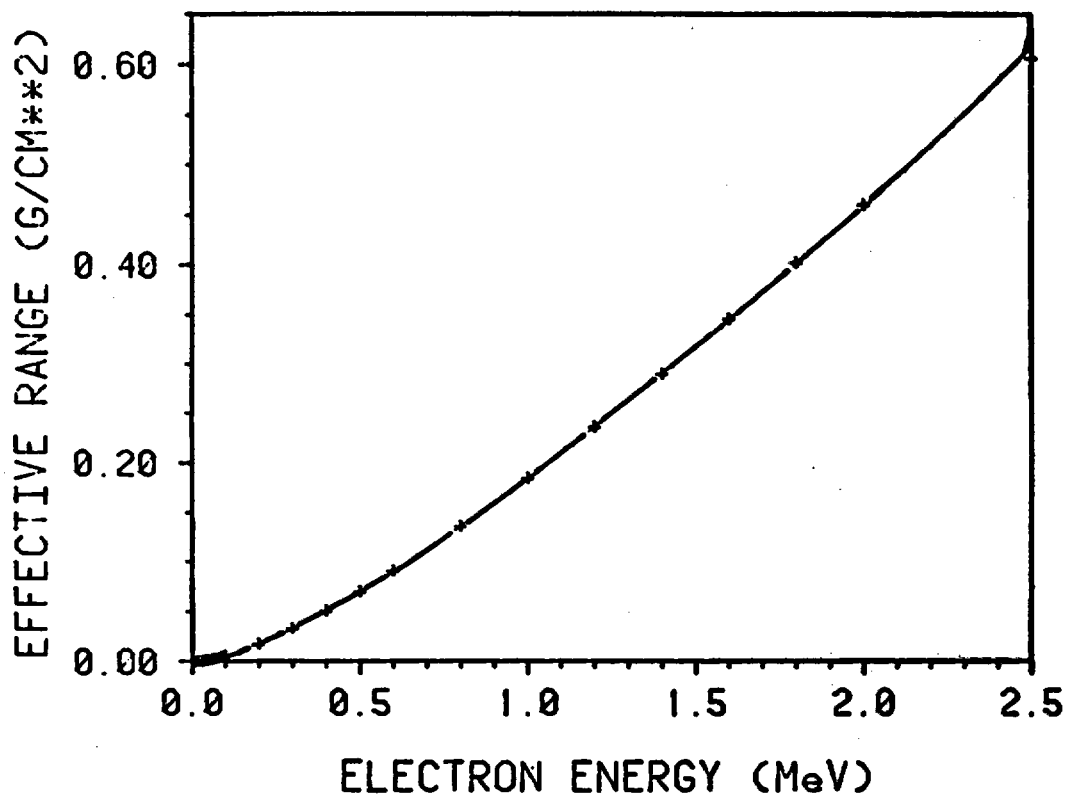


Figure 6.17 Effective range of electrons in air versus electron energy level.

CURRENT DENSITY AT 1.55 MeV

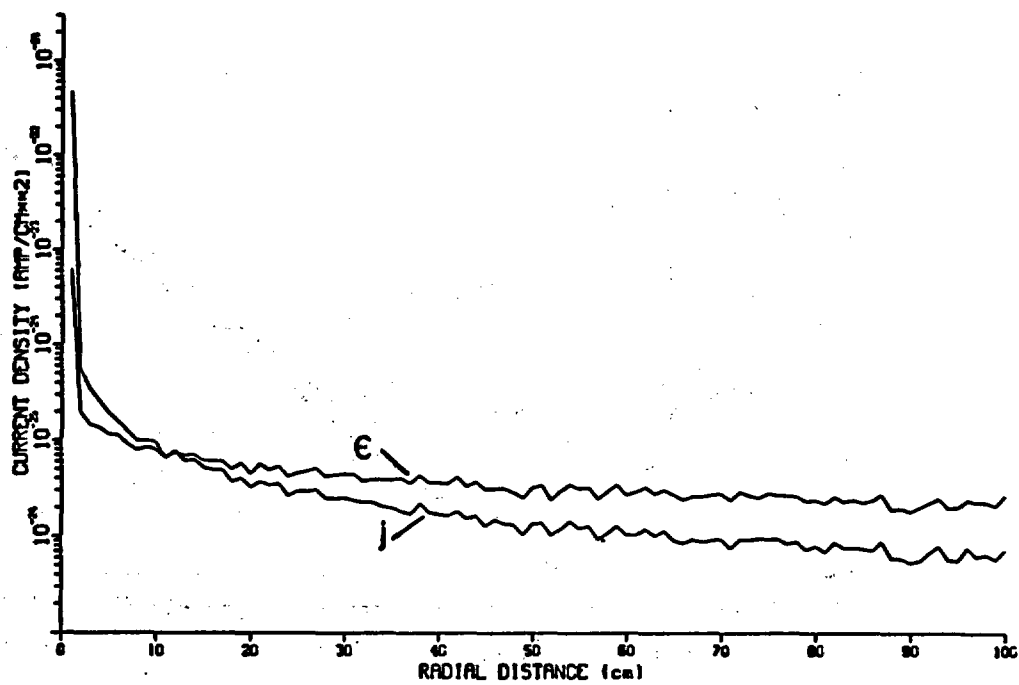


Figure 6.18 Electric current density in air from a 1.55 MeV photon emitted from an infinite line source. Values for e indicate accuracy relative to magnitude of current density.

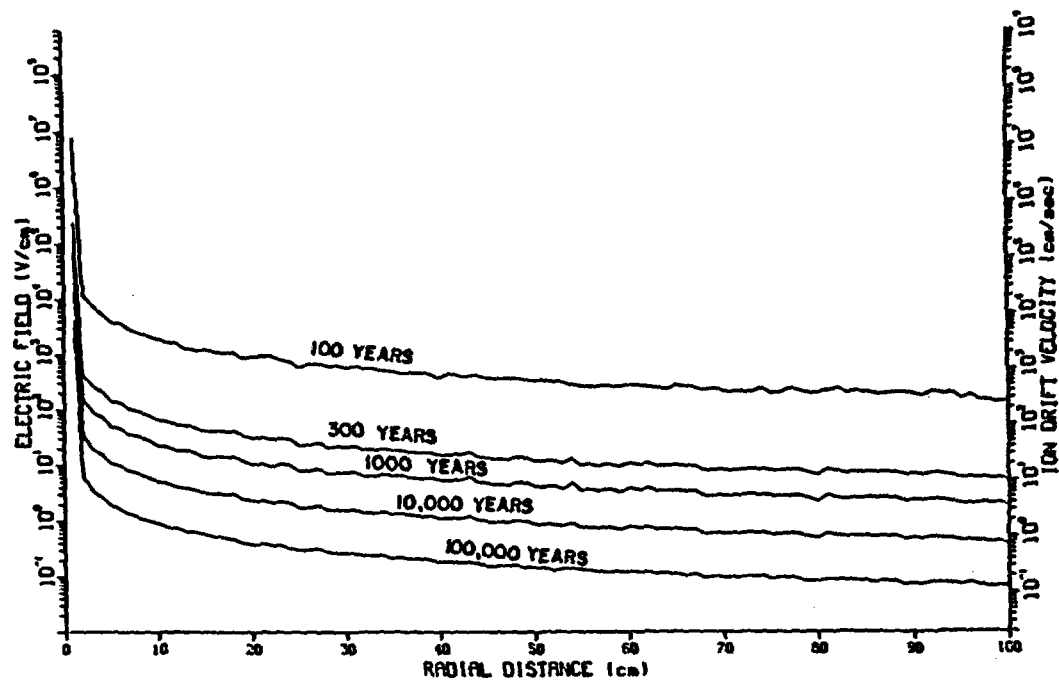


Figure 6.19 Electric field intensity (left axis) and ion drift velocity (right axis) in air at 100, 300, 1000, 10,000 and 100,000 years versus radial distance from an infinite line source. Resistivity of air is  $10^{15}$  ohm-cm and mobility is 2 cm/V.

Electric fields with an order of magnitude of intensity as indicated in Figure 6.19 can only be expected in air. Any solid material present in the electric field will tend to short circuit the return flow of electrons thereby lowering the field intensity. Additionally, photon energies will be diminished by any canister cladding.

Ion density is the most difficult variable in Equation (6.59) to determine. Its value depends on two basic parameters, the density of airborne radionuclides and the fraction of the radionuclides which are ionized. Airborne radionuclide density depends on several factors indirectly (such as temperature, matric potential, degree of fracturing and geochemical composition of the water and the rock mass) and directly on the vapor pressure of the species of interest and their thermodynamic and kinetic properties.

Determination of the fraction of airborne radionuclides which are ionized is a difficult parameter to calculate. Assessment of the significance of forced diffusion can not be accomplished until the equilibrium ion density as a function of the ionization potential of high-level waste and the ion recombination rate are determined.

#### 6.4 Aerosol Transport

A possible contributor to radionuclide vapor transport in the zone near the repository is a mechanism that produces an aerosol in the airspace of a partially saturated fracture. An aerosol originating from rock water would contain any soluble contaminant which could then be transported by diffusion or pressure flow. A physical system near a HLW canister that could bring about aerosol formation is driven by a mechanism referred to as countercurrent or a heat pipe. The reader is referred to Chapter 4 in this document for a more complete discussion of the countercurrent phenomenon.

The thermal regime at a HLW repository will consist of temperatures at the immediate site rising to between 100° and 450°C in the first 100 to 200 years after waste emplacement (Wang et al., 1983). During the heating phase, the rock matrix and any saturated or partially-saturated fractures proximal to the repository will dry out. A thermal pulse will extend outward from the source with time. The temperature of the repository will decrease to near the pre-emplacment ambient temperature over a cooling phase lasting up to 10,000 years. When the temperature of the medium surrounding the repository decreases to below 100°C, the rock matrix and fractures will rewet to some degree.

A liquid film of a specified minimum thickness and ample air space overlying the liquid film is required for aerosol production to occur. Therefore, aerosol production and transport are confined to rock fractures and will not occur in the rock matrix. Only individual fractures and fracture systems are of interest in the investigation of aerosol transport.

Heat emanating from the repository will increase the temperature of the water film proximal to the repository and vaporize the liquid water. Water film closer to the repository will become thinner causing a movement of the liquid film toward the repository by larger negative pressures. The force of gravity acting on liquid water film in a vertical fracture located above the HLW repository would enhance flow toward the repository while upward film flow in a vertical fracture located below the repository would be inhibited.

Water vaporized near the heat source will diffuse outwardly from the repository, condensing in fractures at a distance where the temperature is lower. The resulting vaporization-condensation and liquid film movement illustrated in Figure 6.20 and is referred to as countercurrent (Dhir and Catton, 1982) or as a heat pipe (Cotter 1965). The heat pipe is a highly efficient mechanism which dissipates heat away from a heat source. This mechanism has been observed theoretically (Evans, 1982; Pruess and Wang, 1984; Eaton et al., 1985) and in the laboratory (Gurr et al., 1952; Matthews, 1985).

The countercurrent process enhances the desirability of repository placement in the unsaturated zone because movement of liquid film water toward the repository could detain any radionuclides introduced into the geologic environment by a breached or failed canister. A possible disadvantage of the above-mentioned setting is vapor movement of radionuclides away from the repository in the air space of a partially-saturated fracture. Any physical process which contributes to vapor transport of radionuclides in a gaseous phase will also contribute to the transport of aerosol.

A bubble created in the liquid film by gas desorption which bursts at the surface of a liquid film has the capability of introducing aerosol particles into the air space of a partially-saturated fracture. A bursting bubble can eject hundreds of droplets away from the surface of the liquid with initial horizontal velocities as high as 800 cm/sec (MacIntyre, 1972). Aerosol droplets vary in size and have a composition similar to the composition of the top few monolayers on the surface layer of the liquid film. Any solute present in the liquid can be

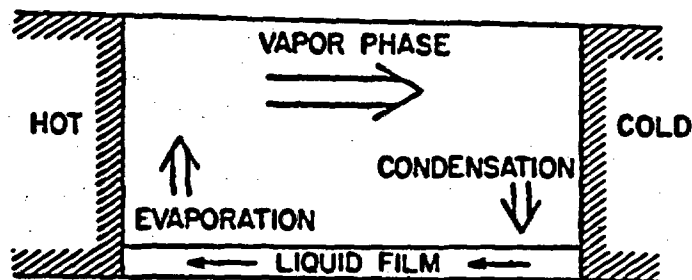


**Figure 6.20** Schematic of countercurrent (or heat pipe). Liquid film moves toward heat source in response to gradient in negative pressure and vaporizes. The vapor moves away from heat source in response to pressure or concentration gradient and condenses at lower temperature.

ejected into the airspace. This includes heavier molecules such as the transuranic actinides. The physics that govern the inception, growth, movement and bursting of a bubble are discussed in greater detail in the following sections.

#### 6.4.1 Nucleation

Bubble nucleation is the process in which molecules cluster together to form the nucleus from which a bubble may grow. Nucleation can be categorized into two basic processes: 1) homogeneous nucleation which occurs in a pure liquid, and 2) bubble inception which occurs on an impurity in a liquid or is caused by radiation acting on the liquid, referred to as heterogeneous nucleation (Apfel, 1971).

#### 6.4.2 Solubility of Gas in Liquids

The solubility of gas in liquid is important in the phenomenon that results in the introduction of an aerosol to the airspace of a partially saturated fracture. The solubility of a gas in liquid is dependent on the prevailing pressure and temperature at the canister. Gas phase pressure also depends on whether the canister remains wet at higher temperatures. Values for gas pressure are calculated by Pruess and Wang (1984) using a numerical model called TOUGH to simulate transport of unsaturated ground water and heat. Although total gas pressures exceed 5 bar for selected cases at early time (less than 20 yrs), the gas pressures asymptotically approach one bar after 50 yrs. The maximum canister surface temperature considered by Pruess and Wang is about 175°C. Because later times are of greater interest in this study, gas pressure is assumed to be one bar. Additionally, the effect of gas pressures greater than one bar on many of the processes is not known.

Temperature, however, will change dramatically both spatially and temporally at a HLW repository. The relationship between temperature and solubility is not a simple function and depends upon the particular gas/liquid system considered. Temperature/solubility relationships also vary differently over different ranges of temperature.

An empirical relationship relating gas solubility and temperature is determined by Cleaver and Han (1980). Gas solubility data for a given gas are regressed against temperature to obtain the constants of an equation of the form:

$$(6.68) \quad \ln X_2 = A_1 + A_2/(T/100) + A_3 \ln(T/100) + A_4 (T/100)$$

A scaling factor of 1/100 is used to make all the parameters of similar magnitude. Values for the coefficients in Equation (6.68) for krypton, hydrogen, nitrogen and oxygen dissolved in water are listed in Table 6.6. The fourth coefficient is used in only one approximating equation. Values of mole fraction solubility versus temperature are plotted in Figure 6.21 for nitrogen and oxygen gases as an example.

-----  
 Table 6.6 Coefficients for Equation (6.68) to determine the solubility of gases in water (from Cleaver and Han, 1980).  
 -----

System	A <sub>1</sub>	A <sub>2</sub>	A <sub>3</sub>	A <sub>4</sub>
Krypton and water	-61.1802	82.3244	21.5757	
Hydrogen and water	15.2051	-33.3273	-28.9664	5.5265
Nitrogen and water	-55.0165	69.2199	18.7292	
Oxygen and water	-54.0411	69.8961	18.5541	

-----  
 (Reprinted with permission from Thermodynamics of Aqueous Systems with Industrial Application, ACS Symposium Series 133, 1980, American Chemical Society.)  
 -----

#### 6.4.3 Gas Desorption

Liquid film on a fracture surface will flow toward a HLW canister according to the physics of a heat pipe and result in an increase in the temperature of the liquid film as it approaches the heat source. Increased temperatures of the film will decrease the solubility of gases that constitute air (basically nitrogen and oxygen) in the liquid. The liquid film will supersaturate with the gases until the stress imposed on the system in the form of added heat is annulled. Desorption of supersaturated gases and restoration of equilibrium to the system will annul the stress.

Desorption can be accomplished by two distinct mechanisms: 1) quiescent desorption which is the phase transition of dissolved gas at a liquid-gas interface, and 2) bubble desorption which is the nucleation and growth of gas bubbles (Pasiuk-Bronikowski and Rudsinski, 1981). A distinct difference exists between gas bubbles and vapor bubbles. Vapor bubbles occur when a liquid is superheated and the liquid changes phase

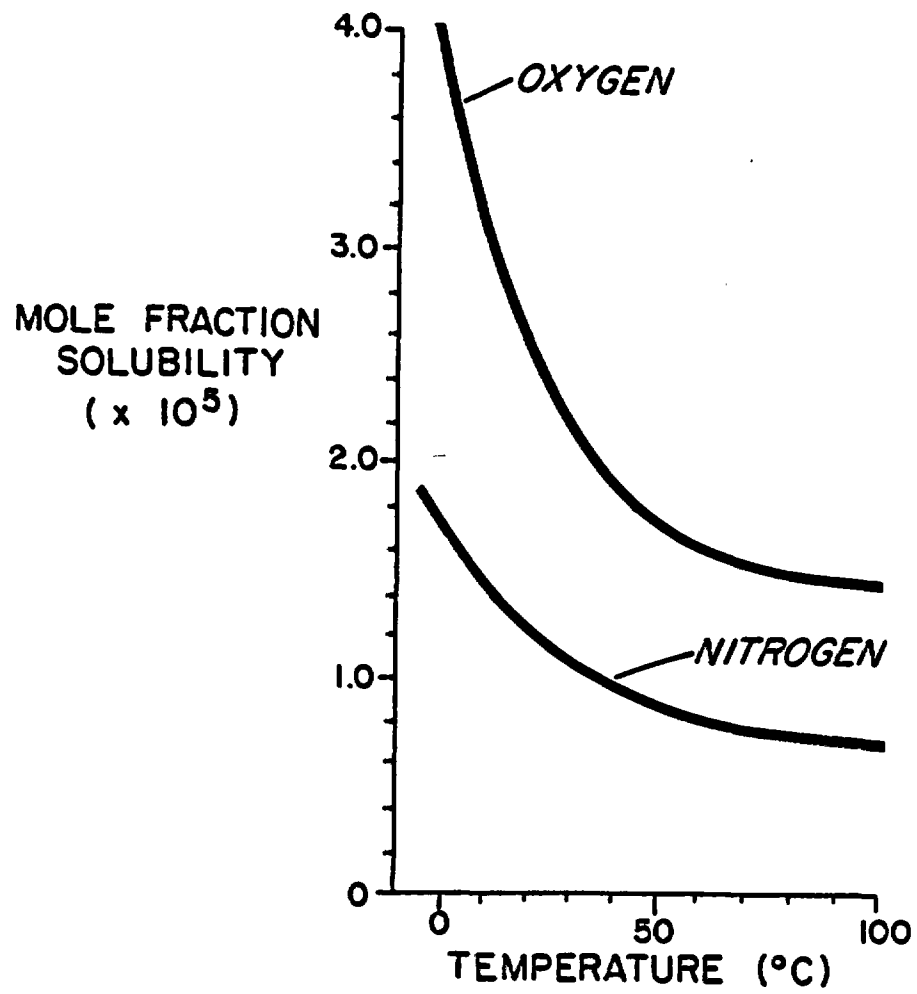


Figure 6.21 Mole fraction solubility of oxygen and nitrogen in water versus temperature.

creating bubbles, while gas bubbles result from gas desorbing out of a liquid. Gas supersaturation is defined as the bulk gas concentration in excess of the saturation concentration of the gas.

The distribution of the amounts of gas desorption between quiescent and bubble desorption is critical to aerosol formation. There will be no aerosol production and therefore no aerosol transport in the absence of bubble desorption. The inception of bubbling is contingent on several factors, namely the rate of desorption and the purity of the system.

The liquid film on a fracture surface will have particulate matter suspended in the liquid. Fracture surface roughness and the suspended particulate matter will supply numerous nucleation sites. Nucleation sites can also be supplied by the process of radiolysis (Norman and Spiegler, 1963). Radioactive material from a HLW canister is capable of producing an assortment of radiation types. Radiation passing through water creates a thermal spike which expands explosively, producing pressure waves. Surface tension of water breaks the pressure wave into discrete regions of water vapor, hydrogen and oxygen gas. Hydrogen and oxygen gas are therefore produced by the radiolysis of water. The resulting microbubbles can act as nucleation sites in a supersaturated solution.

The type of radiation impinging on water molecules affects the quantity of radiolytic products. Burns and Sims (1981) irradiated water with five different radiation types ( $^{60}\text{Co}$ -gamma, protons,  $^4\text{He}$ ,  $^{14}\text{N}$  and  $^{20}\text{Ne}$  ions). A significant range in amounts of radiolytic products ( $\text{OH}$  radical,  $\text{HO}_2$  radical,  $\text{H}_2$  and  $\text{H}_2\text{O}_2$ ) was observed. It appears that the type of radioactive waste buried in a canister will affect the available number of nucleation sites produced by radiation.

#### 6.4.4 Diffusion Process and Bubble Growth

The growth of a spherical bubble from a point of inception with a negligible radius occurs by diffusion of gas across the bubble wall from excess gas absorbed in the liquid. Subsequent to nucleation, the dynamics of gas bubble growth are governed by the physical laws of motion. The diffusion of gas from liquid into the bubble obeys Fick's law of diffusion where  $D$  is the diffusion of gas in the liquid. The size of the gas bubble and rate of bubble growth are related to pressure in the liquid by equations of viscous flow. Simply stated, the pressure of the gas in the bubble provides the force for bubble growth. The driving force is countered by inertia and viscosity of the fluid and surface tension of the bubble wall.

#### 6.4.5 Aerosol Phenomenon

The rupture of a bubble at the surface of the ocean is the principal mechanism of particulate transfer from sea to air (MacIntyre, 1972). The same mechanism can introduce aerosol droplets into the air space of a partially-saturated fracture. A bubble at the air-liquid film interface will burst as a result of evaporation in a millisecond or less, ejecting droplets into the airspace above the liquid film. The top several monolayers of liquid of which the bubble cap is composed can be of different composition than the liquid film as a whole.

One possible cause of compositional differences are concentration gradients which form in the liquid film. The addition of a solute to the liquid film causes a difference in the resulting surface activity (McBain and Davies, 1927; and Bloch and Luecke, 1972). A solute that lowers the surface activity will diffuse toward the liquid-air interface (Taylor and Glasstone, 1931). Organic molecules are an example of this. Inorganic molecules increase surface activity and tend to diffuse away from the liquid-air interface. The top one or several monolayers at the surface of the liquid film can, therefore, be more concentrated with solutes that lower the surface tension of the liquid than the average concentration of the liquid.

The significance of higher concentration surface monolayers arises when a gas bubble bursts at the liquid-air interface. At the moment before a bubble bursts, the bubble wall interfacing with the airspace of the fracture is composed of the top one or several monolayers of the liquid film. Bubble wall fragments ejected into the airspace contain a higher concentration of the solute than a volume average of the liquid film. The amount of solute contained within aerosol droplets is increased by this phenomenon.

The phenomenon of a bubble bursting at the surface of the liquid film, therefore, provides a vehicle to eject hundreds of aerosol droplets of various sizes into the airspace of the fracture provided the proper physical conditions exist at a HLW site necessary for the bubble phenomenon to occur. Larger aerosol droplets (diameter  $> 10^{-6}$  cm) will fall back into the liquid film because of gravity. Smaller droplets, however, will remain suspended in the airspace at least momentarily. The production of aerosol droplets will increase as the liquid film flows toward the HLW repository because of added heat and reduced solubility of gas in the liquid film. A concentration gradient of droplets in the airspace will occur. Diffusion will transport the aerosol from a region of high concentration (near the HLW repository) to

a region of lower concentration (away from the HLW repository). Aerosol droplets will remain suspended in the airspace until either diffusion results in their reabsorption into the liquid film or until the droplets reach a fully saturated section in the fracture and are then reabsorbed.

The mean life time,  $\bar{t}$ , of a particle between two neutrally charged walls is (Fuchs, 1964):

$$(6.69) \quad \bar{t} = b^2/12 D$$

where

b is the aperture between the walls; and  
D is the diffusion coefficient.

Thus, in a one micrometer wide fracture, the mean life time of a particle is about  $2.8 \times 10^{-9}$  sec where the diffusion coefficient has an assumed value of  $0.3 \text{ cm}^2/\text{sec}$ . A bubble fragment ejected at  $800 \text{ cm}/\text{sec}$  can travel an average of  $2.2 \times 10^{-6} \text{ cm}$  before resorbing onto the liquid film on the fracture surface. Similarly, the mean life of a particle in a fracture with aperture of 1 mm is  $2.8 \times 10^{-3}$  sec during which time a particle can travel 2.2 cm.

The liquid film on fracture surfaces, however, can provide likely pathways for the return flow of electrons traveling in response to Compton scattered electrons. Fracture surfaces will not be electrically neutral and the above expression, Equation (6.69), will not be valid for ionized aerosol particles. A particle with a negative charge will repel, to some degree, reabsorption onto the fracture surfaces and will possibly travel further while airborne. However, a positively charged ion will be attracted to a fracture surface and sorbed.

#### 6.4.6 Analysis of Aerosol Formation at Repository Conditions

The prospect of aerosol formation at expected conditions at a HLW repository located in unsaturated fractured rock as proposed in this work has been analysed (Smith et al., 1985). Arguments used are based on 1) the expected physical conditions in fractured rock at a HLW repository and 2) an analytic diffusion model for supersaturation of air in water.

A critical parameter affecting the potential for bubble formation in fractured media is fracture aperture. Fractures with an aperture less than  $250 \mu\text{m}$  are incapable of providing the needed space required for gas bubble formation under any possible conditions.

If sufficiently rapid desorption of gas in the liquid film occurs in a time of an order of magnitude less than about ten minutes, then liquid film velocities would be about 2 cm/min for an assumed temperature gradient of 5°C/cm. Liquid film velocities as large as 2 cm/min are expected near a HLW canister during the operation of a heat pipe in regions proximal to the source of heat. Temperature gradients in this section of the heat pipe, however, are very small and the required rate of gas desorption will not occur. Large liquid film velocities may be experienced in vertical fractures above a HLW canister at extreme conditions. The phenomenon of bubble formation and hence aerosol formation, however, should not exist under expected conditions.

Processes other than bubble formation, however, may furnish a mechanism for aerosol formation on fracture surfaces. One possible mechanism is the rupture of thin liquid films. The properties of thin films are different from those of the bulk phase (Sheludko, 1966). Thin films (i.e. 50-500 Å) can rupture and, although the mechanisms of rupturing are not entirely understood, aerosol droplets may be ejected into the airspace of a partially saturated fracture during this process.

Thin film rupturing and other unidentified physical processes can provide a mechanism of aerosol formation. Because of the potential importance of aerosol transport (i.e. movement as vapor of actinides and other non-volatile contaminants), further analysis of aerosol formation is required.

### 6.5 Free Convection

A potential transport mechanism of gas through non-isothermal fractured rock at large distances is convective flow. The driving force of convective flow at a HLW repository is caused by the temperature gradient. Convective gas flow results from thermally induced density differences or buoyancy in the gas.

Representing convective gas flow mathematically is a complicated endeavor but can be made manageable by invoking several standard assumptions. Foremost is Boussinesq's approximation which states that fluid density variations are negligible except in buoyancy (Lapwood, 1948). Another assumption is that the thermal characteristics of the medium are considered constant and independent of temperature. Density is assumed to vary linearly with temperature.

The equations of balance of mass, momentum and energy which govern convective flow can be expressed in dimensionless terms, one of which is

the Rayleigh number. The Rayleigh number is the ratio of buoyancy to viscous retardation and, when sufficiently large for a given system, is a strong indicator that convective flow will occur.

A HLW repository in unsaturated fractured rock may be as large as 1 x 2 km in lateral extent at a depth of 300 m. The fractured rock mass overlying the repository can be considered either an equivalent porous medium or a consolidated rock mass with distinct fracture sets or zones. An evaluation of each can be made using dimensionless Rayleigh numbers.

Lateral spacing of canisters along the plane of the repository is assumed to be small enough relative to the magnitude of the repository depth (300 m) that the lower boundary can be considered to be of uniform temperature. Thus, edge effects and a non-uniform heat source are not considered.

Convection is classified as free, forced or a mixture of the two. The difference between forced and free convection is that an external hydraulic force is the driving force of forced convection. Free convection is driven by a contrast in gas or fluid density (referred to as buoyancy). Free convection is assumed even though gas leaves the system at ground level. An equal amount of gas is introduced into the system at the lower sections of the convective cells but is not introduced by external hydraulic forces.

Lapwood (1948) calculated the minimum Rayleigh number necessary for free convective flow to occur in a homogeneous porous medium. This minimum Rayleigh number is referred to as the critical Rayleigh number,  $Ra_{cr}$ , and has a value of  $4\pi^2$ . If the Rayleigh number exceeds the critical Rayleigh number, a thermal disturbance in the system can theoretically induce convective flow. Otherwise, the disturbance will die out.

The rock mass overlying a HLW repository can be treated as an homogeneous equivalent porous medium, a layered equivalent porous medium or a consolidated medium with discrete fractures zones as illustrated in Figure 6.22. The propensity for convective gas flow to occur in each scenario is investigated. A first approximation of convective gas flow is made by treating the overlying rock mass as an homogeneous equivalent porous medium.

Conservatively, the rock mass is assumed dry. Thus, the air intrinsic permeability of the rock mass equals the intrinsic permeability. The Rayleigh number is calculated for a range of reasonable scenarios at a HLW repository. A list of values for the variables needed to determine

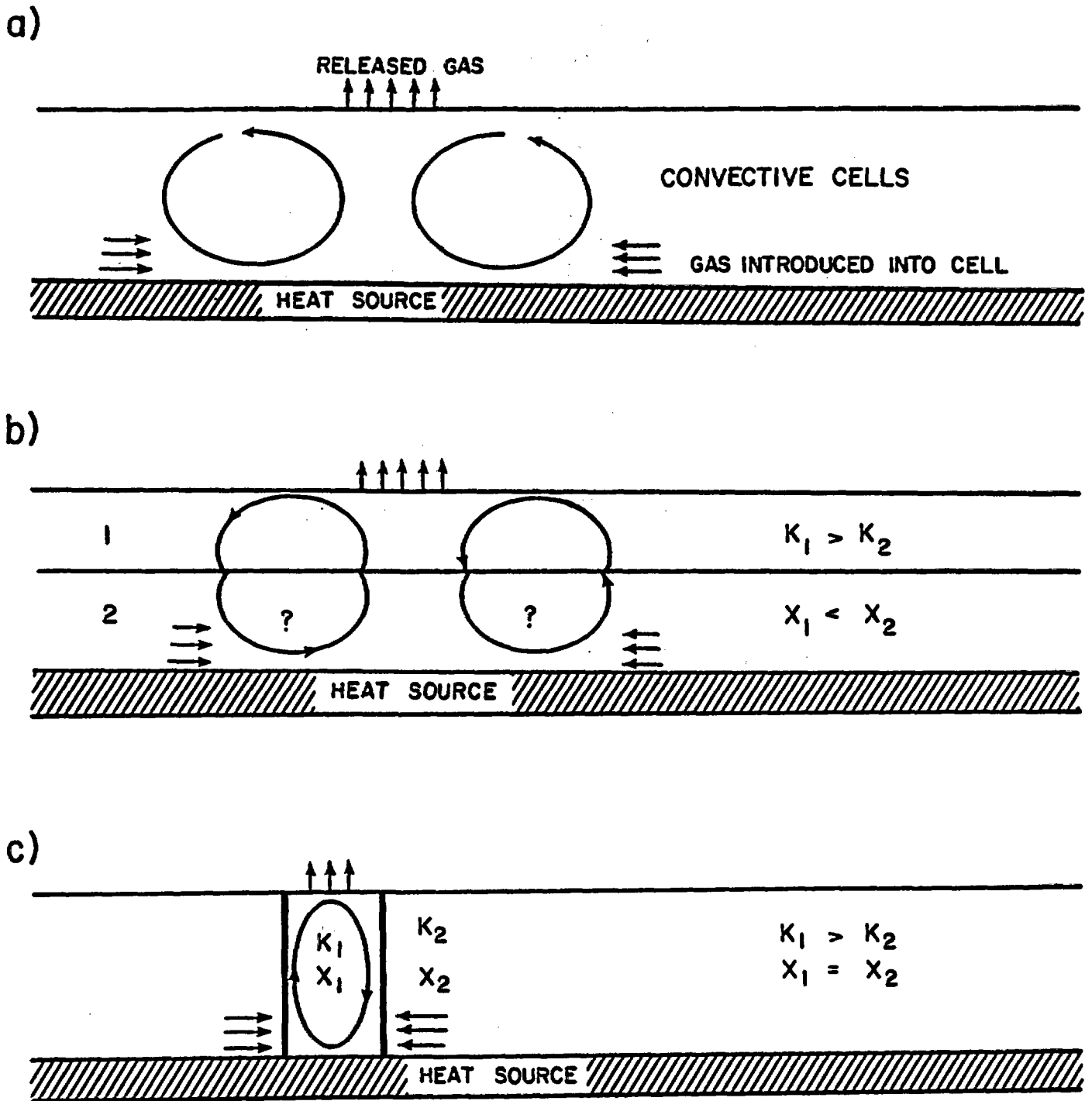


Figure 6.22 Three idealized cases of free convective flow: (a) homogeneous equivalent porous medium; (b) layered equivalent porous medium; and (c) zone of fractures or piped flow model. Arrows denote direction of gas flow.  $k$  is intrinsic permeability and  $x$  is thermal conductivity.

the Rayleigh number is presented in Table 6.7. The variables are assumed to be spatially and temporally constant.

The values assumed for most variables are reasonable for a wide variety of physical settings and have only minor changes in value over the entire range of possible HLW repository settings. Two major exceptions are the temperature difference between ground level and a repository at a depth of 300 m depth and, most importantly, the intrinsic air permeability of the rock mass overlying the repository. The difference in temperatures between the repository and ground level can be less than 100°C to as much as 400°C. Intrinsic permeability can range from  $10^{-11}$  to  $10^{-14}$  cm<sup>2</sup> (Wang et al., 1983). The limits of the Rayleigh number for these values are  $3.2 \times 10^{-5}$  for a temperature difference of 100°C and intrinsic permeability of  $10^{-14}$  cm<sup>2</sup>, and 0.13 when the temperature difference is 400°C and the intrinsic permeability is  $10^{-11}$  cm<sup>2</sup>. The largest conceivable Rayleigh number of 0.13 is more than two orders of magnitude less than the critical Rayleigh number required for free convection to occur.

The rock mass above the HLW repository is treated as a layered porous medium when making a second approximation of convective gas flow. A stratum of welded tuff will usually underlie a layer of nonwelded tuff as a consequence of the cooling history of volcanic flows. The physical

-----  
Table 6.7 A list of values assigned to the variables needed to  
determine the Rayleigh number (from Wang et al., 1983).  
-----

k	= $10^{-11}$ to $10^{-14}$ cm <sup>2</sup>
$\rho_0$	= 0.0012 g/cm <sup>3</sup>
g	= 980 cm/sec <sup>2</sup>
$\beta$	= $2.7 \times 10^{-3}$ to $3.7 \times 10^{-3}$ °C <sup>-1</sup>
$\Delta T$	= 100 to 400°C
D	= 30,000 cm
$\mu$	= $2 \times 10^{-4}$ g/cm-sec
$c_v$	= 0.16 cal/°C-g
$\lambda_{\text{eff}}$	= $3.24 \times 10^{-3}$ cal/cm-sec-°C (at 10% porosity)
$\lambda_{\text{air}}$	= $6.3 \times 10^{-5}$ cal/cm-sec-°C
$\lambda_{\text{welded tuff}}$	= $3.24 \times 10^{-3}$ cal/cm-sec-°C
$\lambda_{\text{nonwelded tuff}}$	= $1.444 \times 10^{-3}$ cal/cm-sec-°C

-----

properties of welded tuff can vary significantly from those of a nonwelded tuff. Therefore, modeling the rock mass as a two layer system of layers with different properties instead of a uniform block may better represent the actual system.

Convective gas flow in layered porous media exhibits anisotropic properties as compared to isotropic behavior through a homogeneous medium. The Rayleigh number representing a layered porous medium has to account for the anisotropic behavior. The Rayleigh number for a layered system is defined in terms of effective vertical intrinsic permeability and thermal conductivity.

The Rayleigh number for the two layered system described above using parameter values listed in Table 6.7 and the effective vertical values for intrinsic permeability and thermal conductivity is  $2.8 \times 10^{-6}$ , seven orders of magnitude less than the critical Rayleigh number.

The flow of gas through fractured rock can also be analyzed for the case in which gas flow occurs through a series of high permeability fracture zones separated by zones of low gas permeability. A piped flow model is one which has zones of high and low permeability. The potential of piped or channel flow through high gas permeability zones has been evaluated by Donaldson (1970) for a hot-water geothermal system. If all other variables are held constant,  $Ra_{CR}$  is solely a function of the aspect ratio,  $S_p$ , of the high permeability column (width/height).

$Ra_{CR}$  has been evaluated for several different values of the aspect ratio. An aspect ratio of 10/300 portrays a vertical flow channel 10 m wide and 300 m high. This corresponds to a  $Ra_{CR}$  value of about 8900. Similarly, flow channels of widths 50 m, 100 m and 300 m equate with values of 374, 105, and 39.4, respectively for  $Ra_{CR}$ . When the aspect ratio is unity, the value for  $Ra_{CR}$  conveniently degenerates to  $4\pi^2$  (39.4) when the aspect ratio is unity which is the value for the critical Rayleigh number given by Lapwood for free convection in a porous medium.

In order to have convective flow, the presence of flow channels and low gas permeability zones require the system to exist under conditions of higher Rayleigh numbers than would be necessary for a system with uniformly distributed flow paths (i.e., an equivalent porous medium). The occurrence of narrow zones of high gas permeability rather than large zones of uniform moderate permeability can be impediments to the formation of convection cells at a HLW repository.

Free convective flow of gas in the rock mass above the repository has been analyzed for three simplified scenarios. The conservative case has been assumed where possible, however, the assumptions of negligible edge effects and uniform heat source are not conservative. Nonetheless, because of the low magnitude of the computed Rayleigh numbers for the three cases, convective flow of gas above a HLW repository is not expected for scenarios with conditions similar to those investigated. Since actual HLW repository settings are expected to have conditions similar to the three case studies, free convection is not believed to be a potential contributor to the transport of radionuclides as vapor at large distances.

#### 6.6 Thermal Diffusion and Thermophoresis

Thermal diffusion and thermophoresis are the movement of vapor in response to a thermal gradient. Thermophoresis is the result of gas molecules impinging on particles from opposite sides with different mean velocities (Fuch, 1960). Thermal diffusion usually refers to thermally induced movement of gas molecules. However, it has been applied to the analysis of movement of larger particles (as large as micrometer size particles) through angstrom size gas molecules (McDaniel and Mason, 1973). Although the two expressions refer to the same physical process for at least some size scales, thermal diffusion is based on rigorous kinetic theory while thermophoresis is defined by determining the net momentum imparted to a particle by molecular collision.

The effect of thermal diffusion or thermophoresis is generally small, however, significant quantities can be moved when the thermal gradient is steep and conditions are favorable. One major condition necessary for either thermal diffusion or thermophoresis to be significant is that gas molecules and airborne particles are of widely varied sizes. Particles among other particles of similar size will not respond (by moving) to a thermal gradient whereas large particles among smaller sized particles can respond at the same conditions. It is possible that radionuclide transport by thermal diffusion or thermophoresis is significant at distances near a HLW canister.

Thermal diffusion is examined using rigorous kinetic theory by Hirschfelder et al., (1954). A brief description of their first approximation of the thermal diffusion coefficient is presented here. Next, the theory of thermophoresis from Fuch (1960) based on conservation of momentum is summarized. An assessment of particle or gas molecule movement is then performed using the analysis of Fuch.

The flux,  $j_t$ , resulting from thermal diffusion can be stated:

$$(6.70) \quad j_t = - D_A^t \nabla \ln T$$

where  $D_A^t$  is the thermal diffusion coefficient.

The driving force is the gradient of the natural log of temperature and not the gradient of temperature. Thus, sufficiently large differences in temperature must be present for the driving force to be appreciable.

The thermal diffusion coefficient is a difficult parameter to determine and is usually defined in terms of the thermal diffusion ratio  $k_t$ . The relationship between these two is expressed:

$$(6.71) \quad D_A^t = (n^2/\rho) M_A M_B D_{AB} k_t$$

The thermal diffusion ratio is related to two other commonly used parameters, the thermal diffusion factor  $\alpha_t$  and the Sorret coefficient  $\alpha_{\text{Sorret}}$ , by the following expressions (Bird et al., 1960):

$$(6.72) \quad k_t = \alpha_t x_A x_B$$

where

$x_i$  is the mole fraction of gas  $i$  and:

$$(6.73) \quad k_t = \alpha_{\text{Sorret}} x_A x_B T$$

One other important property pertaining to thermal diffusion coefficient is defined:

$$(6.74) \quad \sum_i D_i^t = 0$$

As one gas flows from a cooler region to a warmer region, the other gas will move in the opposite direction in a binary system.

As was stated earlier, thermophoresis is the result of gas molecules impinging on airborne particles from opposite sides with different mean velocities. The difference in mean velocities is a consequence of an imposed thermal gradient.

Fuch (1964) presents an analysis of the importance of thermophoresis relative to the resistance of a gas from molecular and hydrodynamic particle motion. For molecules of radius less than the mean free path

( $r \ll \lambda$ ) the net force resulting from a difference in momentum caused by the thermal gradient is defined:

$$(6.75) \quad F_T = - 32 r^2 B_a \overline{T/15v}$$

where

$B_a$  is the translational part of the thermal conductivity of the gas which equals  $K_n/m$ .

Equation (6.75) can be approximated by the expression:

$$(6.76) \quad F_T = 4 r^2 \Delta T \lambda P/T$$

However, a more complicated physical process occurs when ( $r \gg \lambda$ ). The force resulting from a thermal gradient is referred to as photophoresis and is determined for spherical particles by the expression:

$$(6.77) \quad F_T = - 3 \pi n^2 r R \Delta T/p M$$

where  $R$  is the gas constant.

Forces caused by a thermal gradient are countered by resistance forces on molecules and particles. Molecular resistance occurs when ( $r \ll \lambda$ ) and hydrodynamic resistance occurs when ( $r \gg \lambda$ ). Resistance at atmospheric pressure (with  $\lambda = 6 \times 10^{-6}$  cm) is, therefore, a result of molecular forces for molecules with radius less than about  $10^{-6}$  cm. Molecular resistance for the case when the mass of the particle is sufficiently greater than the mass of the gas molecules is stated by:

$$(6.78) \quad F_M = - (4/3) \pi \lambda n m \overline{v} r^2 v_p$$

where

$n$  and  $m$  are the concentration and mass of gas molecules; and  $v$  is their mean velocity.

Molecular resistance of particles with radii greater than the free mean path is calculated using Stokes equation:

$$(6.79) \quad F_M = - 6 \pi n r v_p$$

Velocity of the particle caused by thermophoresis,  $v_p$ , for the case when ( $r \ll \lambda$ ) is determined by:

$$(6.26) \quad v_p = - 3 \lambda \overline{v} \Delta T/[8(1 + \pi f/8)T]$$

where

$f$  is the fraction of molecules reflected diffusely by the particle.

Likewise, the particle velocity for ( $r \gg \lambda$ ) is:

$$(6.80) \quad V_p = - [3 B_a n \Delta T] / [2(2 B_a + B_i) \rho T]$$

where

subscript  $a$  denotes the larger molecules or particles; and  
 $i$  denotes the smaller parent gas molecules.

In general, gas molecules or particles with radius exceeding  $10^{-6}$  cm will not remain airborne because the force of gravity will attract them downward until they sorb onto a surface. Thus, Equation (6.78) is used to determine the thermophoresis force which is countered by molecular resistance. This analysis is calculated at 500°K since elevated temperatures at a HLW canister should average about this temperature for an extended time period. The thermal gradient is assumed to have the extreme value of 100°K/cm and pressure is assumed to be atmospheric ( $10^6$  dynes/cm<sup>2</sup>). The force generated by thermophoresis is calculated as  $-4.8 \times 10^{-12}$  dynes/molecule.

Molecular resistance requires additional information for determination. Particle velocity is determined for the case ( $r \ll \lambda$ ) using Equation (6.79) and is found to equal  $1.9 \times 10^{-2}$  cm/sec. When reflection is diffuse ( $\lambda = 1$ ), gas density is  $2.4 \times 10^{19}$  molecules/cm<sup>3</sup> and the mass of a molecule of air is about  $5 \times 10^{-23}$  g, then molecular resistance is determined to be  $-5.9 \times 10^{-12}$  dynes/molecule.

Based on the above mentioned theory and assumed parameter values, this analysis indicates that the force upon a molecule created by thermal diffusion is approximately equal to molecular resistance. A thermal gradient of 100 °K/cm, therefore, is not sufficient to cause movement of particles by thermophoresis under these conditions.

An exception to this scenario occurs when the fracture walls are not electrically neutral and particles which are negatively ionized are repelled from surfaces. Negatively charged particles with diameter greater than  $10^{-6}$  cm can remain airborne and since the force caused by increases with particle size, some movement of larger particles away from the heat source (HLW canister) may result from thermophoresis. Equation (6.78), however, suggests that a return flow of gas molecules results from particle movement induced by a thermal gradient perhaps nullifying any net mass transport.

The magnitude of mass flux of radionuclides caused by thermophoresis can not be ascertained until gas density and the size distribution of the airborne radionuclides (either as gas molecules or as aerosol particles) are known. Additionally, the preliminary results from evaluating the importance of thermophoresis should be verified by calculating the first approximation of thermal diffusion for the region where thermal diffusion and thermophoresis overlap, that of large particles or molecules moving through substantially smaller molecules, and comparing the results produced by each approach.

## 6.7 Discussion and Summary

The objective of this study has been to identify and examine potential mechanisms of radionuclide transport as vapor at a HLW repository located in unsaturated fractured rock. The transport mechanisms and processes of interest have been investigated at two distances: near the repository; and at greater distances. In general, in the zone near the repository transport mechanisms are controlled by the nature of the high-level waste and design of the waste package, while at greater distances, transport mechanisms are controlled by the geologic medium.

Transport mechanisms or processes potentially important at larger distances include ordinary diffusion, viscous flow and free convection. Ordinary diffusion includes any diffusion process driven by a concentration gradient. These are self and binary diffusion, Knudsen flow and surface diffusion. Pressure flow and slip flow comprise viscous flow. The driving force of viscous flow is the total gas pressure gradient.

A parameter useful in the examination of ordinary diffusion and viscous flow is the Knudsen number,  $Kn$ , the ratio of the mean free path length of a gas molecule to the aperture of the pore space. Greater flow of gas is observed by Knudsen flow and slip flow than the flow of gas predicted by self diffusion and pressure flow, respectively, when the Knudsen number is large, that is,  $Kn > 1$ . The mean free path length of a gas molecule in air at atmospheric pressure is about  $6 \times 10^{-6}$  cm. Thus, Knudsen flow and slip flow are important when the apertures of pores are less than about  $6 \times 10^{-6}$  cm. An order of magnitude increase in mass flow in a welded tuff has been observed over the flow predicted by pressure flow (Reda, 1985). This increase is attributed to either Knudsen flow, slip flow or surface diffusion. Therefore, these transport mechanisms must be considered when investigating gas flow through welded tuff.

Free convection is the movement of a fluid (or gas) in response to a difference in density. As a large-distance transport mechanism, free convective flow may be possible in fractured rock overlying a HLW repository. A HLW repository of sufficiently large lateral extent can create an artificial high temperature layer causing a density contrast in the gas which permeates the interconnected air space of the rock. The density contrast in the gas can result in free convection cells. The Rayleigh number, which is a dimensionless parameter measuring the ratio of buoyancy forces relative to viscous resistance, is a useful indicator as to whether convection cells will occur. Free convection will result from a thermal disturbance when the Rayleigh number representing the system exceeds a critical threshold (usually  $4\pi^2$ ).

Three idealized scenarios representing the rock mass overlying a HLW repository are investigated as to their propensity for the formation of free convection cells: 1) a homogeneous equivalent porous medium with uniform properties; 2) a two layer system with each layer treated as a homogeneous porous medium, each with uniform properties; and 3) vertical zones of high fracture density and hence higher permeability separated by zones of lower permeability. The Rayleigh number of each scenario was calculated based on reasonable and conservative rock and gas properties. In each case the Rayleigh number was significantly less than the critical Rayleigh number of  $4\pi^2$  (all Rayleigh numbers were at least two orders of magnitude less than the critical Rayleigh number).

The individual cases investigated were not conservative because the heat source at the HLW repository was assumed uniform and edge effects were not considered. Further analysis is required to insure that this preliminary conclusion is also valid for the conservative case where a non-uniform heat source and edge effects are considered.

Transport mechanisms important in the zone near the repository include ordinary diffusion, viscous flow, plus several mechanisms whose driving forces arise from the non-isothermal, radioactive nature of high-level waste. These mechanisms include forced diffusion of ionized vapor particles, aerosol transport, thermal diffusion and thermophoresis.

An additional driving force in the zone near the repository is one resulting from an electric field. Ionized particles will move in response to an electric field if the intensity of the electric field is sufficiently large and the particles are relatively mobile.

Gamma ray emission by high-level waste can create an electric field by Compton scattering. Gamma rays of a specific range in energy (0.03 to

10.0 MeV) result in Compton scattering upon collision with particles located along their pathway. A photon of lower energy and an electron are scattered during the collision. The collision causes a preferential outward movement of electrons resulting in a charge displacement. A return flow of electrons results to counter this displacement, thus inducing an electric field. The resulting electric field can cause movement of any ionized mobile particle. This particle or gas molecule movement is referred to as forced diffusion.

Two limiting cases were investigated for their potential of forced diffusion: 1) a HLW canister located in a rock mass and 2) a HLW canister located in air. The two cases are thought to approximate the range of conditions at a HLW canister.

The effect of partially saturated fractures on the electric field in the rock mass case is neglected even though the importance of ion movement through the fractures is examined. Air spaces may occur near the surface of a HLW canister as a result of several different effects (i.e., large fractures, open boreholes, canister cladding failure, etc.), hence, the justification for the second case.

Ion densities are dependent upon the physical and geochemical properties of the waste, rock mass, and rock water and are not yet known. The importance of ion flux caused by forced diffusion can not be assessed until these quantities are specified. Ion drift velocities in air, however, can be predicted for both cases with assumed values for ion mobility. Electric field intensity and ion drift velocities do not exceed about  $10^{-6}$  V/cm and  $2 \times 10^{-6}$  cm/sec in unsaturated fractures superimposed onto the rock mass in the first case. The electric field intensity in air, however, is as large as 50 V/cm and the ion drift velocity is 100 cm/sec within 10 cm of the canister surface 300 years after emplacement.

A more realistic scenario needs to be analysed to better simulate actual repository conditions. This scenario would include minor air spaces proximal to the waste package with nearby rock surfaces capable of providing electron pathways that could partially short-circuit the electric field. Forced diffusion as a mechanism of transport can not yet be dismissed based on the results predicted by this investigation.

Radionuclide transport as an aerosol is a potentially important mechanism in the zone near the repository. Radionuclides in high-level waste with a significant vapor phase include  $^3\text{H}$ ,  $^{14}\text{C}$ ,  $^{85}\text{Kr}$  and  $^{129}\text{I}$ . Only these radionuclides are expected as gases. Aerosol particles,

however, can contain any soluble radionuclide present in the solution from which the aerosol is produced. The formation of a heat pipe proximal to a HLW canister can provide an opportunity for aerosol production. The liquid film on a fracture surface moves toward the source of heat (waste canister) in response to matric potential and surface forces, is vaporized at higher temperatures, then moves away from the heat source until it condenses at lower temperatures. The decrease in gas solubility in the liquid film as temperature rises in the moving liquid may cause bubbling, which in turn introduces aerosol droplets into the airspace overlying the liquid film.

Aerosol generation, however, requires specific conditions to be present at the canister. Sufficiently thick liquid film thicknesses in conjunction with sufficiently large air spaces must be available for bubble growth and rupturing to occur. Fracture widths of less than several hundred micrometers are too narrow for the formation of bubbles and thus can not provide a setting for aerosol production. Additionally, temperature increase in the liquid film must occur rapidly so that gas desorption will result in gas desorption by bubbling rather than quiescently.

In the situation where bubbling occurs and an aerosol is produced, the airborne particles will move in response to any driving force acting on the airspace. Typical driving forces include pressure and concentration gradients. Other driving forces, however, may be present. For example, ionized particles will respond to an external electric field resulting from Compton scattering or any other cause.

Airborne ionized particles will repel any similarly charged surfaces and move toward an area of opposite charge. The return flow of electrons which move in response to forced diffusion will seek the path of least resistance, one probable pathway being the liquid film on fracture surfaces, thereby negatively charging fracture surfaces. The significance of this process is that negatively charged particles will, on the average, remain airborne longer and thus travel farther than positively or neutrally charged particles in the presence of forced diffusion. Positively charged particles will move quickly to the negatively charged surfaces and resorb without traveling a significant distance. In this respect, the electric field may aid the containment of contaminants.

High temperatures and related thermal gradients can occur at waste canisters during decay of high-level waste, thus, creating significant thermal gradients. Movement of gas molecules or particles in response

to a thermal gradient is another potential transport mechanism in the zone near the repository. The transport mechanism resulting from thermal gradients is generally referred to as thermal diffusion when gas molecules are concerned and as thermophoresis when larger sized particles are of interest. Although different theoretical arguments are used to explain each mechanism, the resulting movement is not significant unless widely varying sized molecules or particles are present.

The force caused by thermophoresis was calculated for a particle near a HLW canister. Only particles with radii less than  $10^{-6}$  cm were considered because larger particles would respond to the force of gravitational and move downward until sorbing onto a surface or a liquid film. If an extreme thermal gradient of  $100^{\circ}\text{C}/\text{cm}$  is assumed, this force is calculated to be the same order of magnitude as the counter force caused by molecular resistance. However, negatively charged surfaces will suspend negatively charged particles in an airspace as was previously mentioned. The force of repulsion can overcome the force of gravity and in this case larger particles can remain airborne and move in response to thermal gradients (the larger particles move away from the source of heat). The force from thermophoresis is directly proportional to particle size, thus an order of magnitude increase in the diameter of a particle increases the thermophoresis force by an order of magnitude which would then exceed the force of resistance for the above-mentioned case. Mass flux from this case or any other case by thermophoresis has not been estimated because particle and gas molecule densities and size distributions are not known at this time.

Several radionuclide transport mechanisms and processes have been individually introduced and investigated. Additional transport mechanisms however, may exist which do not fit into any of the earlier mentioned categories. These additional transport mechanisms or processes include any other process or coupled process not yet discussed which may occur at possible repository conditions. Furthermore, the significance of an individual transport mechanism may be augmented by forces other than the major driving force of the transport mechanism.

A chart with the four major gradients (head, concentration, temperature and electric potential) and fluxes (water, elements in solution, heat and electric current) aids in illustrating additional possible transport mechanisms (Figure 6.23, from de Marsily, 1985). Also included in Figure 6.23 are off-diagonal entries referred to as phenomenological coefficients. These are the proportionality constants relating the gradients to the different fluxes.

Gradients of Fluxes of	Head	Concentration	Temperature	Electric potential
Water	DARCY	Chemical osmosis	Thermal osmosis	Electro osmosis
Elements in solution	Ultrafiltration	FICK	Soret (Thermal Diffusion Thermophoresis)	Electro-phoresis (Forced Diffusion)
Heat	Thermal filtration	Dufour	FOURIER	Peltier
Electric current	Rouse	Sedimentation current	Sebeck or Thompson	OHM

Figure 6.23 Chart of major gradients and fluxes with off diagonal phenomenological coefficients (from de Marsilly, 1985).

The intensity of the electric field was predicted during investigation of forced diffusion. Until ion density is determined, the flux of airborne ions resulting from diffusion caused by an electric field can not be established. It is predicted, however, that the intensity of a Compton current induced electric field can be  $10^2$  V/cm or larger in an air environment immediately proximal to a HLW canister at times up to 1000 years.

An electric field intensity of this magnitude is large enough to warrant investigation of other transport mechanisms fueled by electric potential gradients. An example is electrophoresis, which is the movement of ionized particles suspended in a fluid induced by an imposed electric field. Electrophoresis could occur in the liquid film on a fracture surface. This mechanism is analogous to forced diffusion of ionized particles suspended in air.

A prediction of the intensity of a Compton current induced electric field in the liquid film on a fracture surface was not determined in this study. The scenario is complicated because any additional pathway for returning electrons (such as liquid films or fracture surfaces) short-circuits the electric current and reduces the intensity of the electric field by an undetermined amount. Since the electric field intensity for this case is unknown, the magnitude of electrophoresis can not be predicted. Electrophoresis if important, however, will only be a phenomenon in the zone near the repository because Compton scattering occurs only within this region.

Surface diffusion may also be affected by gradients other than concentration. In general, the importance of surface diffusion becomes appreciable when gas sorbed on a solid surface is limited to a few layers. The driving force of surface diffusion is a gradient in concentration of the sorbed gas. However, the driving force of particles or molecules along the surface can be augmented or impeded by the presence of other gradients. Gradients in temperature or electric potential need to be coupled with surface diffusion to ascertain the complete significance of the surface flow of contaminants.

In the zone near the repository, vapor transport mechanisms and processes, either individually or coupled with other transport mechanisms, can provide a significant means of transport from a failed canister to the geologic medium and possibly as far as the zone of higher saturation enveloping the canister or repository region (Figure 6.1). From the point where vapor transport ceases importance, other transport mechanisms, both in the vapor phase or in liquid phase, can

transport contaminants outward to the accessible environment. Although the distance at which the vapor transport is significant may be as short as several centimeters, mass flux by vapor transport could be an important, if not the most important, means of transport across this gap. Any investigation of transport mechanisms and processes within the zone near the repository will depend on engineering design.

Radionuclide transport by ordinary diffusion and viscous flow are also potentially important at a larger distance. Characterization of the geologic medium and adequate gas flow modeling is necessary to ascertain the importance of radionuclide transport as vapor at this distance.

The issues brought forth and discussed in this study are believed to be important factors that must be addressed in the assessment of the specific engineering design (vapor transport near the repository) and site selection (large distance vapor transport) of a potential HLW repository.

## CHAPTER 7 DISCUSSION AND CONCLUSIONS

A number of practical and reliable methods are available to determine the porosity, pore-size distribution, and specific surface of a rock matrix. While the determination of total matrix porosity is a standard procedure, the determination of the interconnected, or effective, matrix porosity, is more difficult. The combined use of mercury infusion and nitrogen adsorption methods for estimating the pore-size distribution within a rock sample appears to provide consistent results. These results are difficult to verify, however, for very small pores.

Cost and destructive effects of sampling limit the amount of rock fracture data that can be measured directly from surface exposures or underground workings. Despite this, a relatively large amount of data on fracture orientation, density, aperture and spacing has been collected at field sites.

The utility of field information is further limited by the difficulties inherent in interpolating between the limited fracture exposures visible on the surface and in a small number of shafts and boreholes. Additional information can be obtained using indirect measurements and the application of statistical models. Indirect methods depend upon assumed relationships between the physical quantity being measured and the parameter of interest. Use of statistical models is dependent on acceptance of a number of simplifications. Due to a lack of experimental data, a consensus has not been reached as to which of the assumed relationships or probability models are most appropriate.

In situ methods to measure water potentials in the unsaturated zone include:

- o Soil moisture blocks made of ceramic, gypsum or nylon;
- o Thermocouple psychrometers;
- o Standard tensiometers;
- o Osmotic tensiometers; and
- o Filter paper absorbers.

Thermocouple psychrometers have an effective range of 2 to 50 bars suction, but may provide erroneous readings as a result of temperature fluctuations and gradients, vapor phase gradients, and variations between individual psychrometers. Two variations of the psychrometer design, the field thermocouple psychrometer, and the thermocouple psychrometer sample changer, have been developed to minimize these errors.

The standard tensiometer has an effective range of 0 to 0.8 bars suction, and has not (to date) been useful for measuring water potentials of a rock media in boreholes.

The osmotic tensiometer, a modification of the standard tensiometer, utilizes an organic solute within the device to increase the measurement range to 15 bars suction. The original design has been modified for use in fractured rock with low volumetric water contents. Various organic solutes and semi-permeable membrane combinations have been evaluated in laboratory and field settings.

The absorber method uses filter papers to determine water potentials in situ. A device has been designed to allow a filter paper to be placed in hydraulic contact with rock in a borehole. Because of the low water holding capacity of the filter paper, the method should equilibrate rapidly. Once the filter paper has equilibrated, it is removed from the borehole and its moisture potential determined using a thermocouple psychrometer sample changer.

Two geophysical techniques, electrical resistivity and neutron moisture logging, enable the determination of in situ changes in water content of unsaturated rock of low porosity. Temporal changes in both resistivity and neutron data reflect water content changes in the host rock. When the two methods are used together, the measurements provide greater accuracy.

A heat-pulse flowmeter has been developed utilizing two thermistors and a heater grid within a standard packer assembly. The unit is used to measure low velocity fluid flow within a borehole. A general flowmeter survey at the Apache Leap field site successfully located permeable fractures at all three boreholes. Additional analysis of the flowmeter data can provide the apparent hydraulic conductivity of a fracture using Darcy's law. This analysis would be facilitated by using cross-hole testing.

A fractured rock infiltrometer has been designed, constructed, and tested for the purpose of measuring water and air intake at the atmosphere-earth surface. The measurement of intake rates can be used to calculate fracture apertures. The water intake method is limited to horizontal, relatively flat, rock surfaces. The air intake method can be used on any exposed rock surface.

Air injection techniques may be used to determine fracture apertures in single boreholes by assuming an effective radius beyond which the pressure is unaffected by gas injection. The cubic law allows the determination of the effective aperture under steady-state flow conditions, and also assuming linear flow. Single pneumatic tests utilizing mass flowmeters, a mercury manometer, and a packer can be used to estimate a fracture aperture in situ in a single borehole.

By using a simplified flow geometry, the movement of water vapor away from a heat source in a fractured media has been modeled. It is shown that a counter-current is formed, which is caused when evaporation and condensation processes result in the diffusion of water vapor away from the heat source, and in the formation of wet and dry zones within the medium surrounding the heat source. Sensitivity analyses indicate that fracture aperture and spacing, and hydraulic properties of the host rock are the most influential factors affecting wet and dry zone formation. During both heating and cooling phases, the dominant direction of water movement will be away from the repository.

The production of a counter-current phenomenon has been demonstrated in heater experiments performed in a laboratory. Results of experiments on cores of three different geologic media (sand, sandstone, and tuff) indicate the effect is most pronounced in unconsolidated sand columns, followed by sandstone cores, and least pronounced in a welded tuff core. The use of a soluble dye injected into the sand column provided evidence of liquid return flow. The dye accumulated in a band near the heated end of the column after steady state moisture potentials had been achieved in the column. The final distribution of tracer in the sandstone core indicated that the liquid flow was limited by the presence of low-permeability zones in the heterogeneous medium.

In general, the counter-current experiments in the laboratory suggest that the size of the flow system and the rate of moisture movement will depend on the imposed temperature gradient, the initial water content distribution, porosity and pore size distributions, and the degree of homogeneity of the medium.

A heating experiment was conducted in a densely-welded fractured tuff at the Queen Creek road tunnel site. The field experiment provided information valuable to the planning and design of larger experiments within the same unit. It was determined that the emplacement of more observation boreholes at varying distances from the heat source will be required. In addition, the instrumentation of selected boreholes for measuring suction and temperature distributions should be made in

boreholes sealed throughout the experiment. Specific boreholes should be designated for water content measurement using the neutron method. Also, longer time periods should be allowed for heating and cooling of the system.

Soil column tests have indicated that soil gas concentrations of three fluorocarbon tracers, BCF, F-22, and SF<sub>6</sub>, can be used for estimating water infiltration rates. The method is suitable when infiltration rates are relatively rapid, or the medium is nearly saturated. In both cases gaseous diffusion will be slow in comparison to solute advection. Computer modeling is necessary to determine when gaseous diffusion dominates advective flow. SF<sub>6</sub> is shown to have characteristics most valuable for field applications.

Vacuum lysimeters are shown to be an effective tool for sampling water from the unsaturated zone. Normally, the lysimeter is effective only when the potential within the unsaturated zone is wetter than one bar suction. A modification of the standard methodology is proposed to overcome this shortcoming. This modification entails an initial injection phase, in which water of known chemical composition is injected in the zone around the lysimeter. After the water is allowed to mix with native waters, a sample is recovered. The procedure has been demonstrated at an achievable injection pressure.

Thermoelectric cooling using a semi-conductor has been demonstrated. The process, which takes advantage of Peltier cooling, is used to condense and to collect samples of water vapor in an unsaturated medium. It is shown that the knowledge of the optimal voltage to be applied is required.

The possible application of fluorescent dyes as tracers in fractured rock is discussed. Three dyes have particular usefulness; Lissamine FF, Rhodamine WT, and Amino G acid. Of these three dyes, Amino G acid may prove to be most useful for borehole testing. A front surface fluorimeter is required for field measurements, because conventional fluorimetry techniques are designed for liquid samples only. An automatic borehole monitoring system is recommended. The system would provide continuous, in situ measurements and yield information on differential flow rates through fractures of variable aperture.

The identification of mineralogic changes and isotopic and hydration variations may be helpful in establishing the history of climatic and geomorphological processes which affect isolation properties of a repository. Results of the determination of these isotopic and

hydration parameters may be used to distinguish primary flow paths and defining the extent of water inputs. Ratios of stable isotopes, such as  $^{87}\text{Sr}/^{86}\text{Sr}$ , could indicate conditions of formation of authigenic minerals and determine the relative influence of a present or past climate.

Contaminant transport as vapor will be controlled by the design and construction parameters of the repository. No general conclusions can be made about relevant processes until a design is presented. A discussion of processes of potential influence is presented at two scales: One scale in which the factors in the immediate vicinity of the repository are considered; and a second scale at a greater distance from the repository. In the zone immediately surrounding the repository, ordinary and forced diffusion may dominate. Ionized particles will move in response to electric fields generated by the radioactive decay of the waste. Transport processes at greater distances will depend on the geologic setting, as well as on coupled processes. Other processes which will affect contaminant transport as vapor at both scales include; ordinary diffusion (including self and binary diffusion, Knudsen flow, and surface diffusion), viscous flow from a pressure gradient, forced diffusion, aerosol transport, free convection, and thermal diffusion.

CHAPTER 8  
LIST OF PUBLICATIONS

8.1 Published Articles

- Evans, D.D., and C. Huang., 1983, "Role of Desaturation on Transport Through Fractured Rock", in Role of the Unsaturated Zone in Radioactive and Hazardous Waste Disposal, p. 165-178.
- Evans, D.D., 1983, Unsaturated Flow and Transport Through Fractured Rock - Related to High-level Waste Repositories, U.S. Nuclear Regulatory Commission, NUREG/CR-3206, 231 pp.
- Huang, C., and D.D. Evans, 1984, A 3-dimensional Computer Model to Simulate Fluid Flow and Contaminant Transport Through a Rock Fracture System, U.S. Nuclear Regulatory Commission, NUREG/CR-4042, 109 pp.
- Schrauf, T.W., and D.D. Evans, 1984, Relationship Between the Gas Conductivity and Geometry of a Natural Fracture, U.S. Nuclear Regulatory Commission, NUREG/CR-3680, 131 pp.
- Green, R.T., and D.D. Evans, 1985, "Radionuclide Transport as Vapor Through Unsaturated Fractured Rocks", in IAH Memoires of Congress on Hydrology of Rocks of Low Permeability, Tucson, Az., 17(1):254-266.
- Rasmussen, T.C., C. Huang, and D.D. Evans, 1985, "Numerical Experiments on Artificially-generated, Three-dimensional Fracture Networks: An Examination of Scale and Aggregation Effects", in IAH Memoires of Congress on Hydrology of Rocks of Low Permeability, Tucson, Az., 17(2):676-682.
- Kilbury, R.K., T.C. Rasmussen, D.D. Evans, and A.W. Warrick, 1986, "Water and Air Intake of Surface-exposed Rock Fractures in Situ", Water Resour. Res., 22(10):1431-43.
- Schrauf, T.W., and D.D. Evans, 1986, "Laboratory Studies of Gas Flow Through a Single Natural Fracture", Water Resour. Res., 22(7):1038-1050.
- Green R.T., and D.D. Evans, 1986, Radionuclide Transport as Vapor Through Unsaturated Fractured Rock, U.S. Nuclear Regulatory Commission, NUREG/CR-4654.

## 8.2 Papers Accepted for Publication

Green, R.T., W.L. Filippone, and D.D. Evans, 1985, "Effect of Electric Fields on Vapor Transport Near a High-level Waste Canister", in Proceedings of International Symposium on Coupled Processes Affecting the Performance of a Nuclear Waste Repository, Lawrence Berkeley Laboratories.

## 8.3 Presented Papers

Cullinan, S.R., C. Huang, and D.D. Evans, 1982, "Non-isothermal Vapor Transport in a Single Unsaturated Rock Fracture", Abstract in EOS, 63(45):934, 1982.

Evans, D.D., R.C. Trautz, J.W. Andrews, and D.E. Earp, 1983, "Water Flow in Unsaturated Fractured Rock: A Case Study", Abstract in EOS 64(18):228.

Earp, D.E., D.D. Evans, and C. Huang, 1983, "An Osmotic Tensiometer for Measuring Pressure Head in Unsaturated Fractured Rock", Abstract in EOS, 64(18):228.

Huang, C., and D.D. Evans, 1983, "Modeling Flow in Unsaturated, Fractured Rock Formations with Application to Nuclear Waste Repositories", Abstract in EOS, 64(18):229.

Schrauf, T.W., and D.D. Evans, 1983, "Laboratory Studies of Gas Flow Through a Single Natural Fracture", Abstract in EOS, 64(45):704.

Green, R.T., and D.D. Evans, 1984, "Radionuclide Transport as Vapor Through Unsaturated Fractured Rock", Abstract in EOS, 65(45):881.

Kilbury, R.K., T.C. Rasmussen, and D.D. Evans, 1985, "Water Intake Across the Atmosphere-earth Boundary Into a Fractured Rock System", Abstract in EOS, 66(18):266.

Nicholson, T.J., and D.D. Evans, 1985, "High Level Radioactive Waste Repository Site Characterization: Unsaturated Zone", Abstract in EOS, 66(18):269.

Rasmussen, T.C., and D.D. Evans, 1985, "Three-dimensional Computer Modeling of Discrete Fracture Networks: Application to Unsaturated Media", Abstract in EOS, 66(18): 275.

### 8.3 Presented Papers (Continued)

Green, R.T., W.L. Filippone, and D.D. Evans, "Effect of Electric Fields on Vapor Transport Near a High-level Waste Canister", in Proceedings of International Symposium on Coupled Processes Affecting the Performance of a Nuclear Waste Repository, Lawrence Berkeley Laboratories, September 18-20, 1985.

Rasmussen, T.C., and D.D. Evans, 1985, "Three-dimensional Computer Model of Discrete Fracture Networks Incorporating Matrix Diffusion", Abstract in EOS, 66(46).

### 8.4 Theses Completed

Andrews, Jon W., 1983, Water Content of Unsaturated, Fractured, Crystalline Rocks from Electrical Resistivity and Neutron Logging, University of Arizona, Department of Hydrology and Water Resources.

Brown, Steve R., 1986, Estimation of Net Recharge Through Thick Unsaturated Zones by Profile Modeling of Saturated Flow Dynamics, University of Arizona, Department of Hydrology and Water Resources.

Cullinan, Steve R., 1983, Non-Isothermal Vapor Transport in a Single Unsaturated Rock Fracture, University of Arizona, Department of Hydrology and Water Resources.

Rahi, Khayyun, 1986, Hydraulic Conductivity Assessment for a Variably-Saturated Rock Matrix, University of Arizona, Department of Hydrology and Water Resources.

Roberts, Mary, 1986, Volatile Fluorocarbon Tracers for Monitoring Water Movement in the Unsaturated Zone, University of Arizona, Department of Hydrology and Water Resources.

Schrauf, Todd W., 1984, Relationship Between the Gas Conductivity and Geometry of a Natural Fracture, University of Arizona, Department of Hydrology and Water Resources.

Trautz, Robert C., 1984, Rock Fracture Aperture and Gas Conductivity Measurements In Situ, University of Arizona, Department of Hydrology and Water Resources.

### 8.5 Dissertations Completed

Green, Ron T., 1985, Transport of Radionuclides as Vapor in Unsaturated Fractured Rock, University of Arizona, Department of Hydrology and Water Resources.

### 8.6 Theses in Progress

Amter, Steven, Injection-Recovery Techniques for Vacuum Lysimeter Sampling in Highly Unsaturated Media, University of Arizona, Department of Hydrology and Water Resources.

Amutis, Rikki, The Application of Thermoelectric Cooling Techniques to Sampling and Detection of Solutes in Unsaturated Fractured Rock, University of Arizona, Department of Hydrology and Water Resources.

Anderson, Ingrid, Measurement of Unsaturated Rock-Water Potential In Situ, University of Arizona, Department of Hydrology and Water Resources.

Davies, Bill, Measurement of Thermal Conductivity and Diffusivity in an Unsaturated, Welded Tuff, University of Arizona, Department of Hydrology and Water Resources.

Goering, Tim, Use of Fluorescent Dyes as Tracers in Unsaturated, Fractured Rock, University of Arizona, Department of Hydrology and Water Resources.

Matthews, Daniel, Thermally Induced Counter-Current Flow in Unsaturated Rock, University of Arizona, Department of Hydrology and Water Resources.

Weber, Dan, Mineralogic, Isotopic and Spatial Properties of Fractures in an Unsaturated, Partially-Welded Tuff near Superior, Arizona, University of Arizona, Department of Hydrology and Water Resources.

### 8.7 Dissertations in Progress

Rasmussen, Todd Christian, Fluid Flow and Solute Transport Through Three-Dimensional Networks of Variably-Saturated Discrete Fractures, University of Arizona, Department of Hydrology and Water Resources.

CHAPTER 9  
REFERENCES

- Adar, E., 1985, "Quantification of Aquifer Recharge Distribution Using Environmental Isotopes and Regional Hydro-Chemistry", Ph.D. Dissertation, University of Arizona, Tucson, Arizona.
- Al-Khafaf, S. and R.J. Hanks, 1974, "Evaluation of the Filter Paper Method for Estimating Soil Water Potential", Soil Sci., 114(4):194-199.
- Angino, E.E., 1972, "High-Level and Long-Lived Radioactive Waste Disposal", Science, 198:885-890.
- Apfel, R.E., 1971, "A Novel Technique for Measuring the Strength of Liquids," Journal of the Acoustic Society of America, Vol. 49, No. 1, p145-155.
- Archie, G.E., 1942, "The Electrical Resistivity Log as an Aid in Determining Some Reservoir Characteristics", Trans. AIME, 146:52-62.
- Baecher, G.B, Lanney, N.A. and H.H. Einstein, 1977, "Statistical Description of Rock Properties and Sampling", in Proc. 18th U.S. Symp. Rock Mech., p. 501.1-501.8.
- Baker, R.C., 1962, "The Geology and Ore Deposits of the Southeast Portion of the Patagonia Mountains, Santa Cruz Country, Arizona, Ph.D. Dissertation, University of Michigan, Ann Arbor.
- Barton, C.M., 1977, "A Geotechnical Analysis of Rock Structure and Fabric in the CSA Mine, Cobor, New South Wales", CSIRO Aust. Div Appl. Geomechanics Tech. Paper, 24:30.
- Bear, J., 1979, Hydraulics of Groundwater, McGraw-Hill.
- BenBarka, A.M., 1982, "Aspects of Aquifer Test Error Analysis", Masters Thesis, University of Arizona, Tucson, Arizona, 188 pp.
- Benjamin, J.R. and C.A. Cornell, 1970, Probability, Statistics, and Decision for Civil Engineers, McGraw-Hill Book Company.

- Berge, D. and D.C.T. Pei, 1972, "Drying of Hygroscopic Capillary Porous Solids - A Theoretical Approach", Int. J. Heat Mass Transfer, 16:293-302.
- Bianchi, L. and D.T. Snow, 1969, "Permeability of Crystalline Rock Interpreted from Measured Orientations and Apertures of Fractures", Annals of Arid Zones, 8(2):231-235.
- Billeaux, D., B. Feuge, and S. Gentier, 1984, "Etude Theorique et en Laboratoire du Comportement d'une Fracture Rocheuse sous Contrainte Normale", Rev. Fr. Geotech, in press.
- Bird, R.B., W.E Stewart, and E.N. Lightfoot, 1960, Transport Phenomena, John Wiley and Sons, New York, 780p.
- Black, C.A., D.D. Evans, J.L. White, L.E. Ensminger, F.E. Clark, and R.C. Dinauer, 1965, Methods of Soil Analysis, Part 1, American Society of Agronomy, Inc., No. 9, Madison, Wisconsin.
- Bloch, M.R. and W.L. Lueke, 1972, "Geochemistry of Ocean Water Bubble Spray," Journal of Geophysical Research, Vol. 77, No. 27.
- Bosen, G.F., C.J. Phetteplace, and L.J. Ybarrondo, 1967, "The Where and Why of Thermoelectric Cooling", Borg-Warner Thermoelectrics, Dept. of Borg-Warner Corp., Des Plaines, Illinois, 47 pp.
- Bouyoucos, C.J., 1915, "Effect of Temperature on the Movement of Water Vapor and Capillary Moisture in Soils", Soc. Agri. Res., 5:141-172.
- Brace, W.F., A.S. Orange, 1968, "Further Studies The Effects of Pressure on the Electrical Resistivity of Rocks", J. Geophys. Res., 73:5407-5420.
- Brace, W.F., A.S. Orange, and T.R. Madden, 1965, "The Effects of Pressure on the Electrical Resistivity of Water-Saturated Crystalline Rocks", J. Geophys. Res., 70:5669-5678.
- Bridges, M.C., 1975, "Presentation of Fracture Data for Rock Mechanics", 2nd Australian-New Zealand Conference on Geomechanics, Brisbane, p. 144-148.
- Briscoe, R., 1979, "Effective Use of Thermocouple Psychrometers in Measurement of Water Potential", Presented at Annual Meeting of Agronomy Society of America, Fort Collins, CO, Aug. 3.

- Brookins, D.G., M.T. Murphy, and H.A. Wollenberg, 1984, "Strontium Isotopic Study of Fracture-Filling Minerals in the Grande Ronde Basalt, Washington", in Scientific Basis for Nuclear Waste Management, VII, G.L. McVay, ed. Elsevier Science Publishing Company, New York, P. 843-850.
- Brooks, R.H. and A.T. Corey, 1964, "Hydraulic Properties of Porous Media", Hydrology Paper (3), Civil Engineering Dept., Colorado State Univ., Fort Collins, CO.
- Brown, J.D., 1980, Evaluation of Fluorocarbon Compounds as Ground Water Tracers: Soil Column Studies, Unpublished Ms. Thesis, University of Arizona, Tucson, Arizona.
- Brown, R.W. and R.S. Johnston, 1976, "Extended Field Use of Screen Covered Thermocouple Psychrometer", Agronomy J., 68:995-996.
- Burdine, N.T., 1953, "Relative Permeability Calculations From Pore-Size Distribution Data", Petr. Trans., Am. Inst. Mining Metall. Eng., 198:51-77.
- Burns, W.G. and H.E. Sims, 1981, "Effect of Radiation Type in Water Radiolysis," Journal of Chemistry Society--Faraday Transactions, Vol. 77, p2803-13.
- Call, R.B. et al., 1976, "Estimation of Joint Set Characteristics from Surface Mapping Data", 17th U.S. Symposium on Rock Mechanics, p. 2b2-1 to 2b2-9.
- Campana, M.E., 1975, Finite State Models of Transport Phenomena in Hydrologic Systems, Unpublished Ph.D Dissertation, University of Arizona, Tucson, Arizona.
- Campbell, E.C., G.S. Campbell, and W.K. Barlow, 1973, "A Dewpoint Hygrometer for Water Potential Measurement", Agri. Meteorology, 12:113-121.
- Carpenter, E.W. and G.M. Habberjam, 1956, "A Tripotential Method of Resistivity prospecting", Geophysics, 21:455-469.
- Carlsaw, H.S. and J.C. Jaeger, 1959, Conduction of Heat in Solids, Oxford University Press.

- Cary, J.W. and S.A. Taylor, 1962, "Thermally Driven Liquid and Vapor Phase Transfer of Water and Energy in Soil", Soil Sci. Am. Proc., 26:417-420.
- Cassel, D.K., D.R. Nielsen, and J.W. Biggar, 1969, "Soil-Water Movement in Response to Imposed Temperature Gradients", Soil Sci. Soc. Am. Soc., 33:493-500.
- Chapman, H.T. and A.E. Robinson, 1962, "A Thermal Flowmeter for Measuring Velocity in a Wall", USGS Water Supply Paper, 1544-E E-1, E-2.
- Childs, E.C. and N. Collis-George, 1950, "The Permeability of Porous Material", Proc. Roy. Soc., London, A:201, 392-405.
- Childs, S.W and G. Malstaff, 1982, "Seasonal Thermal energy storage Program", Prepared for Battelle Northwest Laboratory, Contact No. DE-AC06-76RLO 1830.
- Churchill, R.V., 1960, Complex Variables and Applications, 2<sup>nd</sup> Edition, McGraw-Hill Book Co., Inc., New York.
- Cleaver, H.L. and C.H. Han, 1980, Thermodynamics of Aqueous Systems with Industrial Application, ed. S. A. Newman, ACS Symposium Series 133, American Chemical Society, Wash. D.C., p. 513-536.
- Corey, J.C., S.F. Peterson and M.A. Wahat, 1971, "Measurement of Attenuation of  $^{137}\text{Cs}$  and  $^{241}\text{Am}$  Gamma Rays for Soil Density and Water Content Determinations", Soil Sci. Soc. Am. Proc., 35:215-219.
- Cotter, T.P., 1965, "Theory of Heat Pipes," LA-3246-MS.
- Craig, H., 1961, "Isotropic Variation in Meteoric Water", Science, 133:1702-1703.
- Crank, J., 1956, The Mathematics of Diffusion, Oxford University Press.
- CRC Handbook of Chemistry and Physics, 1974, 54<sup>th</sup> ed., CRC Press.
- Dacey, J.R., 1965, "Gas Adsorption," Industrial and Engineering Chemistry, 57(6).

- Daniel, D.E., J.M. Hamilton, and R.E. Olson, 1981, "Suitability of Thermocouple Psychrometers for Studying Moisture Movement in Unsaturated Soils", Permeability and Groundwater Contaminant Transport, ASTM, STP-746, Philadelphia.
- Davis, L.A. and S.P. Neuman, 1983, "Documentation and User's Guide: UNSAT2 - Variably Saturated Flow Model (Including Four Example Problems)", Final Report, NUREG/CR-3390, Prepared for the Division of Waste Management, Office of Nuclear Material Safety and Safeguard, U.S. Nuclear Regulatory Commission, Washington, D.C.
- Davis, S.N., Campbell, D.J., Bentley, H.W. and T.J. Flynn, 1985, "An Introduction to Groundwater Tracers", Cooperative Agreement Number CR810036, US EPA.
- Davis, S.N., G.M. Thompson, H.W. Bentley and G. Stiles, 1980, "Groundwater Tracers -- A Short Review", Ground Water, 18(1):14-23.
- Dayal, R., Sweitzer, D., and R. Davis, 1983, "Wet and dry cycle leaching: aspects of releases in the unsaturated zone", NRC Nuclear Waste Geochemistry.
- Decagon Davices, Inc., 1983, Operation's Manual for SC-10A Thermocouple Psychrometer - Sample Changer, Decagon Devices, Inc., Pullman, Washington.
- deBoer, J.H., 1968, The Dynamic Character of Adsorption, Oxford, N.Y., 240p.
- de Marsily, G., 1985, "An Overview of Coupled Processes with Emphasis on Geohydrology," International Symposium on Coupled Processes Affecting the Performance of a Nuclear Waste Repository, Lawrence Berkeley Laboratory.
- Dhir, V.K., and I. Canton, 1982, "Boiling in a Porous Bed," Applied Scientific Research, Vol. 38. No. 1, p69-76.
- Donaldson, L.G., 1970, "The Simulation of Geothermal Systems with a Simple Convection Model," Geothermics, Special Issue 2.
- Drewes, H., 1972, "Cenezoic Rocks of the Santa Rita Mountains, Southeast of Tucson, Arizona", U.S. Geol. Survey Prof. Paper 746.

- Drost, W., D. Klotz, A. Koch, H. Moser, F. Neumair and W. Rauert, 1968, "Point Dilution Methods of Investigation Groundwater Flow by Means of Radioisotopes", Water Resources Res., 4:125-146.
- Duffin, W.J., 1980, Electricity and Magnetism, 3rd ed., McGraw-Hill Book Company, London.
- Duiguid, J.O. and Reeves, M., 1977, "A comparison of mass transport using average and transient rainfall boundary conditions", Finite Elements in Water Resources, Gray, W. G., Pinder, G. F., and Brebbia, C. A., (Eds.), Pentech Press, London.
- Dunlop, H.F., H.L. Bilhartz, E. Schler, and C.R. Bailey, 1949, "The Relation between Electrical Resistivity and Brine Saturation in Reservoir Rocks", Trans. AIME, p. 186.
- Eaton, R.R., N.E. Bixler and D.C. Reda, 1985, "Coupled Hydrothermal Flows of Liquid and Vapor in Welded Tuff: Numerical Modeling of Proposed Experiment," International Symposium on Coupled Processes Affecting the Performance of a Nuclear Waste Repository, Lawrence Berkeley Laboratory.
- Endo, H.K., J.C.S. Long, C.R. Wilson, and P.A. Witherspoon, 1984, "A model for investigating transport in fracture networks", Water Resour. Res., 20(10):1390-1400.
- Evans, D.D. and A.W. Warrick, 1970, "Time in Transit of Water Moving Vertically for Ground Water Recharge", Proc. South-western and Rocky Mountain Division of AAAS.
- Evans, D.D. and C. Huang, 1982, "Role of Desaturation on Transport Through Fractured Rock", in Proceedings AGU Symposium, Role of the Unsaturated Zone in Radioactive and Hazardous Waste Disposal.
- Evans, D.D., 1983a, Unsaturated Flow and Transport through Fractured Rock Related to High-Level Waste Repositories, NUREG/CR-3206.
- Evans, D.D., 1983b, "Unsaturated Flow and Transport through Fractured Rock Related to High-Level Waste Repositories", NRC Progress Report, 2nd Quarter.
- Evans, D.D., 1983c, "Unsaturated Flow and Transport through Fractured Rock Related to High-Level Waste Repositories", NRC Progress Report, 3rd Quarter.

- Everett, L.G. and L.G. McMillion, 1985, Operational Ranges for Suction Lysimeters, Report for U.S. Environmental Protection Agency, Environmental Monitoring Systems Laboratory, Las Vegas, Nevada.
- Fatt, I., 1956, "The Network Model of Porous Media: Dynamic Properties of Networks with Tube Radius Distributions", Trans. AIME, 207:164-177.
- Faure, G., 1977, Principles of Isotope Geology, Wiley Interscience, New York, pp. 460.
- Fawcett, R.G. and N. Collis-Georgye, 1967, "A Filter Paper Method for Determining the Moisture Characteristics of Soil", Aust. J. Exp. Agri. Anim. Husb., 7:162-167.
- Fernandez, J.A. and M.D. Freshley, 1984, Repository Sealing Concepts for the Nevada Nuclear Waste Storage Investigations Project, SAND83-1778.
- Filippone, W.L., S. Woolf and R. Lavigne, 1980, "Particle Transport Calculations with the Method of Streaming Rays," Nuclear Science Engineering, Vol. 11, p119.
- Freeze, R.A., 1971, "Three-dimensional, transient, saturated-unsaturated flow in a groundwater basin", Water Res. Res., 7(2):347-366.
- Freeze, R.A. and J.A. Cherry, 1979, Groundwater, Prentice Hall, p. 404-408.
- Friedman, I., and J.R. O'Neil, 1977, "Compilation of a table isotope fractionation factors of geochemical interest," In Data of Geochemistry, M. Fleisher (ed.), U.S. Geological Survey Prof. Paper, 440-K, sixth edition.
- Fritton, D.D., 1969, "Resolving Time, Mass Absorption Coefficient and Water Content with Gamma-Ray Attenuation", Soil Sci. Am. Proc., 33:651-655.
- Fritz, P., and J. Fontes, 1980, Handbook of Environmental Isotope Geochemistry, Vol 1: The Terrestrial Environment, Elsevier Scientific Publ. Co., Amsterdam.
- Fuchs, N.A., 1964, The Mechanics of Aerosols, MacMillan, New York.

- Gale, J.E., 1975, "A Numerical Field and Laboratory Study of Flow in Rocks with Deformable Fractures", Ph.D. Dissertation, University of California, Berkeley.
- Gardener, R., 1937, "A Method of Measuring Capillary Tension of Soil Moisture Over a Wide Moisture Range", Soil Science, 43:238-277.
- Gardener, W.R., 1956, "Calculation of Capillary Conductivity from Pressure Plate Outflow Data", Soil Sci. Soc. Am. Proc., 20:317-320.
- Garlick, G.D. and H.P. Taylor, Jr., 1971, "Oxygen Isotope Exchange between Volcanic Materials and Ocean Water", Geol Soc. Am. Bull., 81:2137-2142.
- Geankoplis, C.J., 1972, Mass Transport Phenomena, Ohio State University Bookstores, Columbus, Ohio.
- Gish, O.H. and W.J. Rooney, 1925, "Measurement of Resistivity of Large Masses of Unsaturated Earth", Terrestrial Magnetism Atmos. Electricity, 30:161-188.
- Glaastone, S., 1953, Textbook of Physical Chemistry, D. Van Nostrand Company, New York.
- Goodman, R.E., 1976, Methods of Geological Engineering in Discontinuous Rocks, West Publishing, New York.
- Green, W.H. and G.A. Ampt, 1911, "Studies on Soil Physics: I. Flow of Air and Water Through Soils", J. Agr. Sci., 4:1-24.
- Gregg, S. J. and K.S.W. Sing, 1967, Absorption, Surface Area, and Porosity, Academic Press, London.
- Gross, B.M., 1965, "Compton Current Polarization in Gamma-Irradiated Dielectrics", J. Appl. Phy. 36(5):1635-41.
- Grover, G.M., T.P. Cotter, and G.F. Erickson, 1964, "Structures of Very High Thermal Conductance", J. Appl. Phys., 35:1990-91.
- Gurr, C.G., T.J. Marshall, and J.T. Hutton, 1952, "Movement of Water in Soil Due to a Temperature Gradient", Soil Sci., 74:335-345.

- Guyod, H., 1944, "Fundamental Data for the Interpretation of Electric Logs", Oil Weekly, 155:38.
- Habberjam, G.M., 1979, "Apparent Resistivity Observations and the Use of Square Array Techniques", in Geoexploration Monographs Series 1, No. 9, ed. S. Saxov and H. Flathe, Gebruder Borntraeger, Berlin.
- Hagashi, K., H. Ito and J. Oisho, 1963, "Surface Diffusion Phenomena in Gaseous Diffusion, (I)," Journal of the Atomic Energy Society of Japan, Vol. 5, No. 10.
- Hamblin, A.P., 1981, "Filter-Paper Method for Routine Measurement of Field Water Potential", J. of Hydrology, 53:355-360.
- Hardin, E., N. Barton, D. Ling, M. Board, and M. Voegelé, 1981, "A Heated Flatjack Test Series to Measure the Thermomechanical and Transport Properties of In Situ Rock Masses", Terra Tek Report TR81-88, Terra Tek Inc., Salt Lake, Utah.
- Harr, M.E., 1962, Groundwater and Seepage, McGraw-Hill Book Co., Inc., New York, p. 286.
- Hearn, P.P., W.C. Steinkampf, M.C. Burns, and Z.E. Brown, 1985, "Oxygen Isotope Geothermometry of Secondary Minerals in the Columbia River Basalt", Washington State Abstr., in Proceedings, Am. Geophys. Union Conference.
- Hecht, M.E. and R.W. Reeves, 1981, The Arizona Atlas, University of Arizona Press, Tucson.
- Hengstenberg, J., and E. Schuch, 1952, "Molecular Weight Determination of Polyvinylpyrrolidones By Means of Osmotic Pressure and Light-Scattering Measurements", Dic Makromolekularc Chemie, 7:236-258.
- Hess, A.E., 1982, A Heat Pulse Flowmeter for Measuring Low Velocities in Boreholes, USGS Water Resource Division, Open File Report 82-699.
- Hiby, J.W. and M. Pahl, 1952, "Der Einfluss von Zweierstossen auf die Molekulare Gasstromung," Z. Naturforschg., Vol. 7a, p524-533.
- Hill, T.L., 1956, "Surface Diffusion and Thermal Transpiration in Fine Tubes and Pores," Journal of Chemical Physics, Vol. 25, No. 4.

- Hillel, D., 1971, Soil and Water, Academic Press.
- Hillel, D., 1982, Introduction to Soil Physics, Academic Press, p. 110-113, 238-243.
- Hirschfelder, J.O., C.F. Curtis and R.B. Bird, 1954, Molecular Theory of Gases and Liquids, John Wiley and Sons, New York, 1219p.
- Hoefs, J., 1980, Stable Isotope Geochemistry, Springer-Verlag, New York, 208 p.
- Hoenig, A., 1978/79, "Electric Conductivity of a Cracked solid", Pore and Applied Geophysics, 117:690-710.
- Holden, A., 1964, Conductors and Semiconductors, Bell Telephone Laboratory, In., 134 pp.
- Howard, K.W.F., and J.W. Lloyd, 1979, "The Sensitivity of Parameters in the Perman Evaporation Equations and Direct Recharge Balance", J. of Hydrology, 41:329-344.
- International Society for Rock Mechanics, Commission on Standardization of Laboratory and Field Tests, 1978, "Suggested Methods for the Quantitative Description of Discontinuities in Rock Masses", Int. J. Rock Mech. Min. Sci. and Geomech. Abstr., 15:319-368.
- Iokuchi, H., 1965, Electrical Condition in Solids, Dover Publications, Inc., 56 pp.
- Iwai, K., 1976, "Fundamental Studies of Fluid Flow through a Single Fracture", Ph.D. Dissertation, Univ. of Calif., Berkeley.
- Jackson, P.D., D.T. Smith, and P.N. Stanford, 1978, "Resistivity-Porosity-Particle Shape Relationships for Marine Sands", Geophysics, 43:1250-1268
- Jackson, R.H., 1964, "Water Vapor Diffusion in Relative Dry Soil: I. Theoretical Considerations and Sorption Experiments", Soil Sci. Soc. Am. Proc., 28:172-176.
- Jakubick, A.T. and V. de Korompay, 1982, "Monitoring the Permeability of the Near-Field Interface of Underground Openings".

- Johnson, H.M., 1961, "A History of Well Logging", Soc. Prof. Well Log Analysts, Symposium 2.
- Jones, J.W., 1983, "Structural, Hydraulic, and Geophysical Properties of Granite near Oracle, Arizona", Masters Thesis, University of Arizona, Tucson, Arizona, 140 pp.
- Jury, W.A. and J. Letey, Jr., 1979, "Water Vapor Movement in Soil: Reconciliation of Theory and Experiment", Soil Sci. Am. Proc., 43:823-827.
- Kafri, U. and J. Ben Asher, 1978, "Computer Estimates of Natural Recharge Through Soils In Southern Arizona, USA", J. of Hydrology, 38:125-138.
- Keith, S.J., 1981, "Stream Recharge in the Tucson Basin and Its Implications For Groundwater Management", M.S. Thesis, University of Arizona, Tucson, Arizona.
- Keller, G.V., 1971, "Electrical Studies of the Crust and Upper Mantle", in The Structure and Physical Properties of the Earth's Crust, ed. J.G. Heacock, Geophysical Monograph 14.
- Keller, G.V., 1968, "Electrical Prospecting for Oil", Quart. J. Colo. Sch. Mines, 63(2).
- Keller, G.V., 1966, "Electrical Properties of Rock and Minerals", in Handbook of Physical Constant, ed. S.P. Clark, Geol. Soc. Am. Mem. 97:546-577.
- Keller, G.V., 1953, "Effect of Wettability on the Electrical Resistivity of Sand", Oil and Gas J., 51(65).
- Keller, G.V. and F.C. Frischknecht, 1966, Electrical Method in Geophysical Prospecting, Pergamon Press, New York.
- Kemper, W.D. and N.A. Evans, 1963, "Movement of Water as Effected by Free Energy and Pressure Gradients: III Restriction of Solutes by Membranes", Soil Sci. Soc. Am. Proc., 27:485-490.
- Kemper, W.D. and N.A. Robins, 1966, "Osmotic Efficiency Coefficients Across Compacted Clays", Soil Sci. Soc. Am. Proc., 30:529-534.
- Kennard, E. H., 1938, Kinetic Theory of Gases McGraw-Hill, New York,

- Khell, C., 1971, "Analysis of Error in Logging Parameters and their Effect on Calculated Water Saturation", Soc. Prof. Well Log Analysts, Symposium 12.
- Kilbury, Richard K., 1984, "Water intake at the Atmosphere-earth interface in a fractured rock system near Patagonia, Arizona", M.S. Thesis, University of Arizona, Tucson, Arizona.
- Kimball, B.A., R.D. Jackson, R.J. Reginato, F.S. Nakayama, and S.B. Idso, 1976, "Comparison of Field Measured and Calculated Soil-Heat Fluxes", Soil Sci. Soc. Am. Proc., 40:18-25.
- Knapp, R.B., 1975, "An Analysis of the Properties of Fractured Crystallines Rocks", M.S. Thesis, University of Arizona, Tucson.
- Kreamer, D.K., 1982, "In Situ Measurement of Gas Diffusion Characteristics in Unsaturated Porous Media by Means of Experimentals", Unpublished Ph.D. Dissertation, University of Arizona, Tucson.
- Kreamer, D.K., 1983, "Proposed Greater Confinement Disposal Tracer Test Plan for Reynolds", Electrical and Engineering Company, Las Vegas, Nevada.
- Kreamer, D.K., E.P. Weeks and G.M. Thompson, 1984, "A Field Technique to Measure the Tortuosity and Effective Porosity for Gaseous Diffusing of Materials in the Unsaturated Zone", Unpublished paper.
- Krider, E.P. and J.A. Musser, 1982, "Maxwell Currents Under Thunderstorms," Journal of Geophysical Research-0 A, Vol. 87, No. C13, p1171.
- Kruseman, G.P., and N.A. DeRidder, 1970, "Analysis and Evaluation of Pumping Test Data", Int. Inst. for Land Recl. and Improv., Bulletin 11, Wageningen.
- Kunze, R.J. and D. Kirkham, 1962, "Simplified Accounting for Membrane Impedance in Capillary Conductivity Determination, Soil Sci. Soc. Am. Proc., 26:421-426.
- Lagerwerff, J.W., G. Ogata, and M.E. Eagle, 1961, "Control of Osmotic Pressure of Culture Solutions with Polyethylene Glycol", Science, 133:1486-1487.

- Lamarsh, J.R., 1966, Introduction to Nuclear Reactor Theory, Addison-Wesley, Reading, Mass.
- Lapwood, E.R., 1948, "Convection of a Fluid in a Porous Medium," Proceedings of Cambridge Philosophical Society, Vol. 44.
- Lawrence, F.J., J.I. Drever, T.F. Anderson, and H.K. Brueckner, 1979, "Importance of Alteration of Volcanic Material in the Sediments of Deep Sea Drilling Site 323: Chemistry,  $^{18}\text{O}/^{16}\text{O}$  and  $^{87}\text{Sr}/^{86}\text{Sr}$ ", Geochim. et Cosmochim. Acta, 43:573-588.
- Lawrence, J.R. and H.P. Taylor, Jr., 1971, "Deuterium and Oxygen-18 Correlation: Clay Minerals and Hydroxides in Quaternary Soils Compared to Meteoric Waters", Geochimica et Cosmochimica Acta, 35:993-1003.
- Lawrence, J.R. and H.P. Taylor, Jr., 1972, "Hydrogen and Oxygen Isotope Systematics in Weathering Profiles", Geochimica et Cosmochimica Acta, 36:1377-1393.
- Lee, K.N., 1980, "A Federalist Strategy for Nuclear Waste Management", Science, 208:679-684.
- Letey, J., W.D. Kemper, and L. Noonan, 1969, "The Effect of Osmotic Pressure Gradients on Water Movement in Unsaturated Soil", Soil Sci. Soc. Am. Proc., 33:15-18.
- Leverett, M.C., 1939, "Flow of Oil-Water Mixtures through Unconsolidated Sands", Trans. AIME, 132:149-171.
- Lomize, G.M., 1951, Flow in Fractured Porous Rocks, Moscow.
- Long, J.C.S., J.S. Remer, C.R. Wilson, and P.A. Witherspoon, 1982, "Porous Media Equivalents for Networks of Discontinuous Fractures", Water Resour. Res., 18(3):645-658.
- Longstaffe, F.J., 1983, "Stable Isotope Studies of Diagenesis in Clastic Rocks", Geoscience Canada, 10:43-58.
- Longstaffe, F.L., 1984, "The Role of Meteoric Water in Diagenesis of Shallow Sandstones: Stable Isotope Studies of the Milk River Aquifer and Gas Pool Southeastern Alberta", AAPG Memoir, 33:81-98.

- Louis, C., 1969, "A Study of Groundwater Flow in Jointed Rock and Its Influence on the Stability of Rock Masses", Rock Mech. Res. Rep. 10, Imperial College, London.
- Lovelock, J.E., 1971, "Atmospheric Flourine Compounds as Indicators of Air Movement", Nature, 230:370.
- Lovelock, J.E., 1972, "Atmospheric Turbidity and Trichlorofluoromethane Concentrations in Rural Southern England and Southern Ireland", Atmos. Environ., 6:917-925.
- Lovelock, J.E., and R.J. Maggs, 1973, "Halogenated Hydrocarbons In and Over the Atlantic", Nature, 241:194-196.
- MacIntyre, F., 1972, "Flow Patterns in Breaking Bubbles," Journal of Geophysical Research, Vol. 72, No. 27.
- MacIntyre, J.L., 1970, "Soil Density Measurement by Transmitted Gamma Radiation", M.S. Thesis, University of Arizona, Tucson, Arizona.
- Mahtab, M.A., D.D. Bolstad, J.R. Alldredge, and R.J. Shanley, 1972, "Analysis of Fracture Orientations for Input to Structural Models of Discontinuous Rock", USBM, Report 7669.
- Mahtab, M.A., D.D. Bolstad, and R.R. Pulse, 1973, "Determination of Attitudes of Joints Surveyed with a Borescope in Inclined Boreholes".
- Mansell, R.S., L.C. Hammond, and R.M. McCurdy, 1973, "Coincidence and Interference Corrections for Dual-Energy Gamma Ray Measurements of Soil Density and Water Content", Soil Sci. Soc. Am. Proc., 37:500-504.
- Marshall, T.J., 1959, "Relations between Water and Soil", Commonwealth Agricultural Bureau, Farnham Royal, England, p. 99.
- Massignon, D., 1979, "Gaseous Diffusion," in Uranium Enrichment, ed. by S. Villani, Springer-Verlag, New York.
- Matthews, D.W., 1986, Thermally Induced Countercurrent Flow in Unsaturated Rock, M. S. Thesis, University of Arizona.

- McBain, J.W. and G.P. Davies, 1927, "An Experimental Test of the Gibb's Adsorption Theorem," Journal of the American Chemical Society, Vol. 49, p2230-2257.
- McClellan, H., 1948, "Core Orientation by Graphical and Mathematical Methods.", AAPG Bull., 32(2):262-282.
- McDaniel E.W., and E.A. Mason, 1973, The Mobility and Diffusion of Ions in Gases, John Wiley, New York.
- McElwee, C.D., 1980, "Theis Parameter Evaluation from Pumping Tests by Sensitivity Analysis", Ground Water, 18(1):56-105.
- McHenry, J.R., 1963, "Theory and Application of Neutron Scattering in the Measurement of Soil Moisture", Soil Science, 95:294-307.
- McMahon, B.K., 1974, "Design of Rock Slopes Against Sliding on Pre-existing Fractures", Proc. 3rd Congr. Int. Soc. Rock Mechanics, 2:803-808.
- McQueen, I.S. and R.F. Miller, 1968, "Calibration and Evaluation of a Wide-Range Gravimetric Method for Measuring Moisture Stress", Soil Sci. Soc. Am. Proc., 106:225-231.
- Meinzer, O.E., 1942, Hydrology, Dover Publications, Inc., New York.
- Merrill, S.D. and S.L. Rawlins, 1972, "Field Measurement of Soil Water Potential with Thermocouple Psychrometer", Soil Sci. Soc. Am. Proc., 13:102-109.
- Meyn, R.L. and R.S. White, 1972, "Calibration of Thermocouple Psychrometers: A Suggested Procedure for Development of Reliable Predictive Model", in R.W. Brown and B.P. Van Haveren (eds.), Psychrometry in Water Relations Research, Utah State University, P. 56-63.
- Miller, E.E. and D. Elrick, 1958, "Dynamic Determination of Capillary Conductivity Extended for Non-Negligible Membrane Impedance", Soil Sci. Soc. Am. Proc., 22:483-486.
- Millington, R.J., 1959, "Gas Diffusion in Porous Media", Science, 130:100-102.

- Milly, P.C.D. and P.S. Eagleson, 1980, "The Coupled Transport of Water and Heat in a Vertical Soil Column Under Atmospheric Excitation", Dept. of Civil Eng., Massachusetts Institute of Technology, Cambridge, Massachusetts, Technical Report No. 258..
- Milly, P.C.D., 1982, "Moisture and Heat Transport in Hysteretic, Inhomogeneous Porous Media: A Matric Head-Based Formulation and a Numerical Model", Water Resources Res. 18(3):489-498.
- Milly, P.C.D., 1984a, "A Linear Analysis of Thermal Effects on Evaporation From Soil", Water Resources Res., 20:1075-1085.
- Milly, P.C.D., 1984b, "A Simulation Analysis of Thermal Effects on Evaporation From Soil", Water Resources Res., 20:1087-1098.
- Miyamoto, S., A.W. Warrick and H.L. Bohn, 1974, "Land Disposal of Waste Gases: I. Flow Analysis of Gas Injection Systems", J. Environ. Quality, 3(1):49-55.
- Montezzer, P., 1982, Ph.D. Dissertation in Preparation, Colorado School of Mines.
- Montezzer, P. and W.E. Wilson, 1984, "Conceptual Hydrologic Model of Flow in the Unsaturated Zone, Yucca Mountain, Nevada", U.S. Geological Survey, Water-Resources Investigations, Report 84-4345, p. 36-43
- Morel, F.M., 1983, Principles of Aquatic Chemistry, Wiley and Sons, New York, 446 p.
- Morgan, W.B. and S.J. Pirson, 1964, "The Effects of Fractional Wettability on the Archie Saturation Exponent", Soil Prof. Well Log Analysts, Symposium 5.
- Morse, J.G., 1976, "Rainfall Infiltration Characteristics For a Semi-Arid Watershed Soil", M.S. Thesis, University of Arizona, Tucson, Arizona.
- Moskowitz, B.M., 1977, "Numerical Analysis of Electrical Fluid and Rock Resistivity in Hydrothermal Systems", M.S. Thesis, University of Arizona, Tucson.
- Mualem, Y., 1976, "A New Model for Predicting the Hydraulic Conductivity of Unsaturated Porous Media", Water Resour. Res., 12(3):513-522.

- Mualem, Y., 1976, "A Catalogue of the Hydraulic properties of Unsaturated Soils", Research Project 442, Technion, Israel Institute of Technology.
- Nakano, M. and T. Miyazaki, 1979, "The Diffusion and Nonequilibrium Thermodynamic Equations of Water Vapor in Soils Under Temperature Gradients", Soil Sci., 128:184-188.
- National Oceanic and Atmospheric Administration, 1982, Climatological Data of Arizona, 86.
- National Oceanic and Atmospheric Administration, 1983, Climatological Data of Arizona, 87.
- Nelson, P., B. Paulsson, R. Rachiele, L. Anderson, T. Schrauf, W. Hustrulid, O. Duran, and K.A. Magnusson, 1979, "Preliminary Report on Geophysical and Mechanical Borehole Measurements at Stripa", LBL-8280.
- Nelson, P. and W.E. Glenn, 1975, "Influence of Bound Water on the Neutron Log in Mineralized Igneous Rocks", Soil Prof. Well Log Analysts, Symposium 16.
- Neuman, S.P., 1981, Course Notes on Subsurface Fluid Dynamics, University of Arizona.
- Nofziger, D.L., D. Swartzendruber and L.R. Ahuja, 1973, "Crusting and Swelling Effects on Water Infiltration into Soil", Technical Report No. 28, Water Resources Research Center, Purdue University.
- Norman, A. and P. Spiegler, 1963, "Radiation Nucleation of Bubbles in Water," Nuclear Science and Engineering, Vol. 16, p213-217.
- Norton, D. and R. Knapp, 1977, "Transport Phenomena in Hydrothermal Systems: The Nature of Porosity", Am. J. Sci., 277:913-936.
- Parkhomenko, E.I., 1967, Electrical Properties of Rocks, ed. and tran. G.V. Keller, Plenum Press, New York.
- Pasiuk-Bronikowski, W. and K.J. Rudzinski, 1981, "Gas Desorption from Liquids," Chemical Engineering Science, Vol. 36, p1153-1159.

- Peck, A.J., 1960, "Change of Moisture Tension with Temperature and Air Pressure: Theoretical", Soil Sci., 89:303-310.
- Peck, A.J. and R.M. Rabbidge, 1966, "Soil Water Potential: Direct Measurements by a New Technique", Science, 151:1385-1386.
- Peck, A.J. and R.M. Rabbidge, 1969, "Design and Performance of an Osmotic Tensiometer for Measuring Capillary Potential", Soil Sci. Soc. Am. Proc., 33:196-202.
- Penman, H.L., 1940, "Gas and Vapor Movements in the Soil, 1, The Diffusion of Vapors Through Porous Solids", J. Agri. Sci., 30:437-462.
- Peters, R.R., E.A. Klavetter, I.J. Hall, S.C. Blair, P.R. Heller, and G.W. Gee, 1984, "Fracture and Matrix Hydrologic Characteristics of Tuffaceous Material from Yucca Mountain", Nye County, Nevada, Sandia Report SAND84-1471.
- Peterson, D.W., 1968, "Zoned Ash-Flow Sheet in the Region around Superior, Arizona", in Southern Arizona Guidebook III, ed. S.R. Tittley, Geol. Soc. Am., p. 215-222.
- Peterson, D.W., 1961, "Dacitic Ash-Flow sheet Near Superior and Globe, Arizona", Ph.D. Dissertation, Stanford University, Palo Alto.
- Philip, J.R. and D.A. deVries, 1957, "Moisture Movement in Porous Materials Under Temperature Gradients", Trans. Am. Geophys. Union, 38(2):222-231.
- Pickens, J. F., and W.C. Lennox, 1976, "Numerical Simulation of Waste Movement in Steady Groundwater Flow Systems", Water Resour. Res., 12:171.
- Pinder, G.F. and W.C. Gray, 1977, Finite Element Simulation in Surface and Subsurface Hydrology, Academic Press.
- Pollard, W.G. and R.D. Present, 1948, "On Gaseous Self-diffusion in Long Capillary Tubes," Physical Review, Vol. 73, No. 7, p762-774.
- Porter, G.R. and J.E. Carothers, 1970, "Formation Factor-Porosity Relation Derived from Well Log Data", Soil Prof. Well Log Analysts, Symposium 11.

- Pratt, H.R., H.S. Swilfs, W.F. Brace, A.D.Black, and J.W. Handin, 1977, "Elastic and Transport Properties of an In Situ Jointed Granite", Int. J. Rock Mech. Min. Sci. and Geomech. Abstr., 14:35-45.
- Present, R.D., 1958, Kinetic Theory of Gases, McGraw-Hill, 280p.
- Priest, S. D., and J. A. Hudson, 1976, "Discontinuity Spacings in Rock", Int. J. Rock Mech. Min. Sci. and Geomech. Abstr., 13:135-148.
- Pruess, K., Y.W. Tsang and J.S.Y. Wang, 1985,"Modeling of Strongly Heat-Driven Flow in Partially Saturated Fractured Porous Media," Proceedings of the International Association of Hydrogeologists 17<sup>th</sup> Congress, Tucson, Arizona.
- Pruess, K., J.S.Y. Wang, 1984, "TOUGH - A Numerical Model for Nonisothermal Flow to Study Waste Canister Heating Effects," Material Research Society Symposium Proceedings, Vol. 26.
- Rasmussen, T.C., 1982, "Solute Transport in Saturated Fractured Media", M.S. Thesis, University of Arizona, Tucson.
- Reda, D.C., 1985, "Slip-Flow Experiments in Welded Tuff," International Symposium on Coupled Processes Affecting the Performance of a Nuclear Waste Repository, Lawrence Berkely Laboratory.
- Reginato, R.J. and C.H.M. Van Bavel, 1964, "Soil Water Measurement with Gamma Attenuation", Soil Sci. Soc. Proc., 28:721-724.
- Reynolds, E.R.C., 1966, "The Percolation of Rainwater Demonstrated by Fluorescent Dyes", J. of Soil Science, 17(1):127-132.
- Richards, L.A., Ed., 1969, "Diagnosis and Improvement of Saline and Alkali Soils", USDA. Handbook No. 60.
- Richards, L.A., 1958, "Methods of Measuring Soil Moisture Tension", Soil Science, 128:1089-1090.
- Richards, L.A. and W. Gardner, 1936, "Tensiometer for Measuring the Capillary Tension of Soil Water", Am. Soc. Agronomy J., 28:353-358.
- Richards, L.A. and G. Ogata, 1958, "Thermocouple for Vapor Pressure Measurement in Biological and Soil Systems at High Humidity", Science, 128:1089-1090.

- Richards, S.J., 1965, "Soil Suction Measurement with Tensiometers", in C.A. Black (ed.), Method of Soil Analysis, American Society of Agronomy, Madison, Wisconsin, p. 153-163.
- Robertson, A., 1970, "The Interpretation of Geological Factors for Use in Slope Theory", in P.W.J. van Rensburg (ed.), Planning Open Pit Mines, Balkema, Cape Town, South Africa, p. 55-71.
- Rodermund, C.G., R.P. Alger, and J. Tittman, 1961, "Empty-Hole Logging Programs for Reservoir Evaluation", Soil Prof. Well Log Analysts, Symposium 2.
- Rollins, R.C., M.G. Spangler, and D.K. Kirkham, 1954, "Movement of Soil Moisture Under a Thermal Gradient", Highway Research Board Proc., 33:492-508.
- Romm, E.S., 1966, Flow Characteristics of Fractured Rocks, Nedra, Moscow.
- Ross, C.S. and R.L. Smith, 1961, "Ash-Flow Tuffs - their Origin, Geologic Relations, and Identification", USGS Prof. Paper, 366.
- Rowe, D.N. and C.M. Bhandari, Modern Thermoelectrics, Prentice-Hall, 157 pp.
- Rushton, K.R., and C. Ward, 1979, "The Estimation of Groundwater Recharge", J. of Hydrology, 41:345-361.
- Russell, A.D., and G.M. Thompson, 1983, "Mechanisms Leading to Enrichment of the Atmospheric Fluorocarbons in Groundwater", Water Resour. Res., 19(1):57-60.
- Savin, S.M., 1980, "Oxygen and Hydrogen Isotope Effects in Low-Temperature-Mineral-Water Interactions: in P. Fritz and J.C. Fontes, eds., Handbook of Environmental Geochemistry, The Terrestrial Environmental, 1:283-327.
- Schrauf, T.W. and D.D. Evans, 1984, "Relationship Between the Gas Conductivity and Geometry of a Natural Fracture", Nuclear Regulatory Commission, Washington D.C., NUREG/CR-3680.
- Schumberger, 1972, Log Interpretation, Volume 1, Principals.

- Schwartz, F.W., 1975, "On Radioactive Waste Management: An Analysis of Parameters Controlling Subsurface Contaminant Transfer", J. of Hydrology, 27:51-71.
- Schwartz, F.W., 1977, "On Radioactive Waste Management: Model Analysis of a Proposed Site", J. of Hydrology, 32:257-277.
- Schwartz, F.W. and K. Muchlenbach, 1979, "Isotope and Ion Geochemistry of Groundwaters in the Milk River Aquifer, Alberta", Water Resour. Res., 15:259-268.
- Sears, F.W. and M.W. Zemansky, 1973, University Physics, 4th ed., Addison-Wesley Publishing Company Inc., Menlo Park, California.
- Seidemann, R.H., in progress, Vertical Diffusion of Volatile Organics in Unsaturated Porous Media, unpublished Ms. Thesis, University of Arizona, Tucson, Arizona.
- Sellers, W.D. and R.H. Hill, 1974, Arizona Climate, University of Arizona Press, Tucson.
- Shafrin, E.G., and W.A. Zisman, 1960, "Constitutive Relations in the Wetting of Flow Energy Surfaces and Theory of the Retraction Method of Preparing Monolayers", J. Phys. Chem., 64:519-524.
- Shanley, R.J. and M.A. Mahtab, 1974, "A Computer Program for Clustering Data Points on the Sphere", USBM, Info. Circular 8624.
- Sharp, J.C., 1970, "Fluid Flow Through Fissured Media", Ph.D. Dissertation, Imperial College, London.
- Sharp, J.C. and Y.N.T. Maini, 1972, "Fundamental Considerations on the Hydraulic Characteristics of Joints in Rock", Proc. Symp. on Percolation through Fissured Rock, Int. Soc. Rock Mech., Stuttgart, No. TI-F.
- Sheludko, A., 1966, Colloid Chemistry, Elsevier, New York.
- Skibitze, H.E., 1955, "Electronic Flowmeter", U.S. Patent, (2):225-728.
- Slattery, J.C., and R.B. Bird, 1958, "Calculation of the Diffusion Coefficient of Dilute Gases and the Self-diffusion of Dense Gases," AIChE J., Vol. 4, No. 2, p137-142.

- Smart, P.L. and I.M.S. Laidlaw, 1977, "An Evaluation of Some Fluorescent Dyes for Water Tracing", Water Resour. Res., 13(1):15-33.
- Smith, D.M., C.D. Updegraff and E.J. Bonano, 1985, "A Preliminary Assessment of Radionuclide Vapor Phase Transport in Unsaturated Tuff," SAND DE-AC04-76DP00789.
- Smith, L., 1984, Lecture Notes, Professor of Geology and Hydrology, Dept. of Geology and Geophysics, University of Utah, Salt Lake, Utah.
- Smith, L. and F.W. Schwartz, 1984, "An Analysis of the Influence of Fracture Geometry on Mass Transport in Fractured Media", Water Resour. Res., 20(9):1241-52.
- Snow, D.T., 1968, "Rock Fracture Spacings, Openings, and Porosities", J. Soil Mech. and Found. Div. Proc. ASCE, 94(SMI):73-91.
- Snow, D.T., 1969, "The Frequency and Apertures of Fractures in Rock", Int. J. Rock Mech. Min. Sci., 7:23-40.
- Soil Moisture Equipment Corp., DATE, "Engineering Details: Hydraulic Conductivity of Porous Ceramics, P.O. Box 30025, Santa Barbara, California.
- Soil Moisture Equipment Corp., DATE, "Operating Instructions for the Model 1920 Pressure-Vacuum Soil Water Sampler", P.O. Box 30025, Santa Barbara, California.
- Sorooshian, S. and V.K. Gupta, 1985, "The Analysis of Structural Identifiability: Theory and Application to Conceptual Rainfall-Runoff Models", Water Resour. Res., 21(4):487-495.
- Spanner, D.C., 1951, "The Peltier Effect and its Use in the Measurement of Suction Pressure", J. Exp. Botany, 2:145-168.
- Stetten, O., et al., 1975, "Recent Developments in the Interpretation of Data From Joint Surveys in Rock Masses", 6th Reg. Conf. for Africa on Soil Mech. and Found., 9(2):7-26.
- Sutherland, S.H. and D.E. Bennett, 1979, "Defense High-Level Waste and Spent Fuel Characterization for Geologic Waste Repositories", Sandia Report, SAND79-0172.

- Taylor, H.P., 1968, "The Oxygen Isotope Geochemistry of Igneous Rocks", Contr. Mineralogy and Petrology, 19:1-71.
- Taylor, H.S. and S. Glasstone, 1951, Treatise on Physical Chemistry, Vol 2, van Nostrand, New York.
- Taylor, S.A. and L. Cavazza, 1954, "The Movement of Soil Moisture in Response to a Temperature Gradient", Soil Sci. Soc. Am. Proc., 18:351-358.
- Telford, W.M., L.P. Geldart, R.E. Sheriff, and D.A. Keys, 1976, Applied Geophysics, Cambridge University Press, Cambridge.
- Terzaghi, R.D., 1965, "Sources of Error in Joint Surveys", Geotechnique, 15:287-304.
- Texas Nuclear Corporation, 1968, Nuclear-Chicago Model 5810 Subsurface Moisture Probe.
- Thames, J.L. and D.D. Evans, 1968, "An Analysis of the Vertical Infiltration of Water into Soil Columns", Water Resour. Res., 4:817-828.
- Thompson, G.M., and G.K. Stiles, 1981, Final Evaluation of Six Fluorocarbon Compounds for Use as Ground Water Tracers, Report for Environmental Sciences Division, Oak Ridge National Laboratory.
- Thompson, G.M., and J.M. Hayes, 1979, "Trichlorofluoromethane in Groundwater -- A Possible Tracer and Indicator of Groundwater Age", Water Resour. Res., 15(3):546-554.
- Thompson, G.M., J.M. Hayes, and S.N. Davis, 1974, "Fluorocarbon Tracers Hydrology", Geophys. Res. Lett., 1(4):177-180.
- Tittman, J., 1956, "radiation Logging", in Fundamental of Logging, University of Kansas Petroleum Engineering Conference.
- Trautz, R., 1984, "Rock Fracture Aperture and Gas Conductivity Measurements In Situ, M.S. Thesis, University of Arizona, Tucson, Arizona
- Tromble, J.M., 1973, "Thermal Gradients and Water Transfer in Unsaturated Soil", Ph.D. Dissertation, University of Arizona, Tucson, Arizona.

- Van Genuchten, M.Th., 1978, "Calculating the Unsaturated Hydraulic Conductivity with a New Closed-Form Analytical Model", Water Resource Program, Dept. of Civil Engineering, Princeton University, N.J., Research Report 78-WR-08.
- Van Genuchten, M. Th. and D.R. Nielsen, 1985, "On Describing and Predicting the Hydraulic Properties of Unsaturated Soil", Annales Geophysicae 3(5), in press.
- Van Genuchten, M. Th., 1980, "A Closed-Form Equation for Predicting the Hydraulic Conductivity of Unsaturated Soils", Soil Sci. Am. J., (44):892-898.
- Van Nostrand, R.G. and K.L. Cook, 1966, "Interpretation of Resistivity Data", USGS Prof. Paper, 499.
- Waldron, L.J., and T. Manbeian, 1970, "Soil Moisture Characteristics of Osmosis with Polyethylene Glycol: A Simple System with Osmotic Pressure Data and Some Results," Soil Sci, 110:401-404.
- Wang, J.S.Y., C.F. Tsang, N.G.W. Cook, and P.A. Witherspoon, 1979, "A Study of Regional Temperature and Thermohydrological Effects of an Underground Repository for Nuclear Wastes in Hard Rock", LBL-8271, Lawrence Berkeley Laboratory, Berkeley, California.
- Wang, J.S.Y., C.F. Tsang, N.G.W. Cook, and P.A. Witherspoon, 1981, "A Study of Regional Temperature and Thermohydrologic Effects of an Underground Repository for Nuclear Wastes in Hard Rock", J. Geophys. Res., 86:3759-3770.
- Wang, J.S.Y., D.C. Mangold, R.K. Spencer, and C.F. Tsang, 1983, "Thermal Impact of Waste Emplacement and Surface Cooling Associated with Geologic Disposal of Nuclear Waste", US NRC, NUREG/CR-2910, LBL-13341.
- Warrick, A.W. and A. Amoozergar-Fard, 1977, "Soil Water Regimes Near Porous Cup Water Samplers", Water Resour. Rec., 13:203-207.
- Weast, R.S., (Ed.), 1975, Chemical Rubber Company Handbook of Chemistry and Physics, CRC Press, Inc, Cleveland, Ohio, 773 pp.
- Weast, R.C., (Ed.), 1980, Chemical Rubber Company Handbook of Chemistry and Physics, CRC Press Inc., Boca Raton, Florida, E:34-36.

- Weber, S., 1963, "The Connection Between the Laminar Flow of Pure Gases Through Tubes and the self-Diffusion Coefficient," AERE-Trans 946.
- Weeks, E.P., D.E. Earp, and G.M. Thompson, 1982, "Use of Atmospheric Fluorocarbons F-11 and F-12 to Determine the Diffusion Parameters of the Unsaturated Zone in the Southern High Plains of Texas", Water Resour. Res., 18:1365-1378.
- Wenner, F., 1912, "The Four Terminal Conductor and the Thomson Bridge", US Bur. Standards Bull., 8.
- Wescor Inc., 1979, Instruction Manual for Wescor HR-33T Dew Point Microvoltmeter, Wescor Inc., Logan UT.
- Wiebe, H. H., G.W. Campbell, W.H. Gardner, S.L. Rawlins, J.W. Cary, and R.W. Brown, 1971, "Measurement of Plant and Soil Water Status", Bulletin 484, Utah Agri Exp. Stn., Logan, Utah.
- Wilke, C.R., 1950, "A Viscosity Equation for Gas Mixtures," Journal of Chemical Physics, Vol. 18, No. 4.
- Williams, J. and C.F. Shaykewich, 1969, "An evaluation of polysthylemeglycol (P.E.G.) 6,000 and P.E.G. 20,000 in the osmotic control of soil water potential," Canadian J. Sol. Sci., 49:347-401.
- Winsauer, W.O., H.M. Shearin Jr., P.H. Masson, and M. Williams, 1952, "Resistivity of Brine Saturated Sands in Relation to Pore Geometry", Bull. Am. Assoc. Pet. Geologists, 36:253-277.
- Woolf, S., W.L. Filippone, B.D. Ganapol, and J.C. Garth, 1986, "Electron Transport Computational Methods for a Plane Source Embedded in an Infinite Medium," to appear in Nuclear Science Engineering.
- Wyllie, M.R.J. and M.B. Spangler, 1953, "Application of Electrical Resistivity Measurements to Problem of Fluid Flow in Porous Media", Bulletin, Am. Assoc. of Petroleum Geologists, 36(2):359-403.
- Zanback, C., 1977, "Statistical Interpretation of Discontinuity Contour Diagrams", Int. J. Rock Mech. Min. Sci. and Geomech. Abst., 14:111-120.

Zimmer, P. W., 1963, "Orientation of Small Diameter Drill Core",  
Econ. Geol., 58:1313-1325.

Zur, B., 1966, "Osmotic Control of the Matric Soil Water Potential: I.  
Soil Water System", Soil Sci., 102:394-398.

## APPENDIX A THERMOCOUPLE PSYCHROMETERS

This appendix contains detailed descriptions for methods employed during laboratory calibration of thermocouple psychrometers for subsequent use in field studies. The discussion is based on experience gained during the first year of this research project and on information presented primarily in the instruction manual for the Wescor HR-33T Dew Point Microvoltmeter (Wescor, 1979), and a Utah State University Bulletin (Wiebe et al., 1971).

Thermocouple psychrometers are used to determine moisture potential indirectly by measuring temperature phenomena (dew point temperature and temperature depression associated with evaporation) which are functions of the relative humidity of the environment in which the psychrometers are placed. The relationship between relative humidity and moisture potentials, presented in Section 3.1.1, can be used to interpret psychrometer readings.

Each psychrometer, however, will produce slightly different responses to identical moisture potentials, due to variability in thermocouple characteristics. Thus, although it is possible to approximate the relationship between moisture potential and psychrometer response using theoretical and empirical equations (Wiebe et al., 1971; Wescor, 1979), it is necessary to define response characteristics of individual psychrometers through a calibration routine if precise field measurements of moisture potential are required.

Psychrometer response (as measured using a microvoltmeter) is a function of temperature as well as moisture potential. Consequently, the calibration procedure described in this section involves a series of measurements made over a range of temperatures and potentials likely to be encountered in field situations. The calibration procedures for the standard thermocouple psychrometer as well as the thermocouple psychrometer sample changer (SC-10A) are included in this section.

### A.1 Equipment

Equipment used during the calibration procedure includes a constant temperature water bath, water-tight calibration chambers, a microvoltmeter-control unit, a switch box (optional), a strip chart recorder (optional), a stop watch, and a series of salt solutions having known osmotic potentials.

The refrigerated water bath should be a type in which water is circulated with a pump (as opposed to a magnetic mixing device) and which is capable of accurately maintaining temperatures below ambient to within  $\pm 0.1^{\circ}\text{C}$  over a period of several hours. The bath should be large enough to hold the required number of calibration chambers, as well as a minimum of the first 7-10 cm of psychrometer lead wire protruding from the calibration chamber. Water baths which employ magnetic mixing devices are undesirable because electromagnetic pulses can interfere with microvolt readings.

Calibration chambers can be purchased commercially (J.R.D. Merrill Specialty Equipment, Logan, Utah) or constructed from a variety of materials. Chambers can hold single or multiple psychrometers. The primary requirement is that no vapor sources or sinks be present other than those provided by the calibration solution. Interior surfaces should be smooth Teflon, high quality stainless steel, or brass. Glass, rubber and acrylic surfaces should be avoided as they tend to absorb water (Wiebe et al., 1971). Chamber size and geometry ideally should be similar to that of the anticipated field situation. Because this generally is impractical, small cylindrical chambers are commonly used.

It is desirable to maximize the free liquid surface area within the chamber and to minimize the volume of air surrounding the psychrometer in order to facilitate rapid vapor equilibration. It is important when purchasing or constructing a calibration chamber that the chamber dimensions be compatible with those of the psychrometers which are to be calibrated. Psychrometer diameters and psychrometer lead wire diameters vary between brands, and difficulty may be encountered in obtaining a water-tight seal if a psychrometer is placed in an incompatible chamber.

Microvoltmeter-control units can be purchased from several sources including Wescor, Inc. and J.R.D. Merrill Specialty Equipment (both firms have headquarters in Logan, Utah). Some units are suitable for measurements using both psychrometric and dew point modes, while others lack the internal circuitry required for dew point measurements. Available units range in complexity from relatively simple manual devices to automated scanning units.

Switchboxes provide a useful, but not essential, means of connecting multiple psychrometers to a single microvoltmeter-control unit. Switchboxes are incorporated in some control units, while other manufacturers sell optional devices. Various types of connectors are available for attaching psychrometers to switchboxes; a switchbox should be selected which is compatible with the type of psychrometer used.

Output from a microvoltmeter-control unit can be fed into an optional strip chart recorder to provide a visual record of psychrometer response curves. These curves can be diagnostic in identifying problems (e.g., dirty thermocouples) as well as providing a record of the shape, slope, and width of response plateaus corresponding to psychrometric and dew point values. Use of a strip chart recorder is desirable during calibration procedures, although it is possible to obtain the required readings directly from the microvoltmeter. The latter method is more practical for field measurements in situations where electrical power must be obtained from batteries or where additional equipment would be cumbersome.

The series of known potentials required for the psychrometer calibration procedure is generated using salt solutions having known osmotic potentials. Sodium chloride (NaCl) or potassium chloride (KCl) solutions are typically used. Several milliliters of solutions can be used to form a free liquid surface in the bottom of the calibration chamber or, as is recommended by some authors (Wiebe et al., 1971 and others), the interior walls of the calibration chamber can be lined with filter paper which is subsequently soaked with the salt solution.

The latter method increases the surface area from which evaporation can occur and thereby reduces equilibration times. However, our experience suggests that a small "matric potential" can be imparted by the filter paper if it does not remain fully saturated during the calibration procedure. The presence of an unquantified matric potential introduces an error to the calibration. This possible error can be avoided if a free liquid surface at the bottom of the chamber is used to provide the evaporation surface instead of the filter paper.

Osmotic potentials of the calibration solutions should cover the range of moisture potential values anticipated in the field. The range typically encompasses the entire effective measurement range (2 to 50 bars suction) of thermocouple psychrometers. Consequently, we recommend using four solutions having potentials of approximately 2, 10, 25 and 50 bars suction. Osmotic potentials associated with various NaCl or KCl concentrations are determined by using the following equations (based on Raoult's law and Kelvin's law, respectively):

$$(A.1) \quad e / e_0 = 55.556 / (55.556 * 0_s)$$

$$(A.2) \quad e = R T / V \ln(e/e_0) = 0.4617 T \ln(e/e_0)$$

where

- $O_s$  is osmolality;
- $e/e_0$  is relative humidity;
- $e$  is osmotic potential;
- $V$  is the volume; and
- $T$  is absolute temperature.

Osmolality values corresponding to various KCl and NaCl concentrations can be obtained from standard chemical references (e.g., CRC Handbook, Chemical Rubber Company, 1981). Alternatively, Wiebe, et al., (1971), provides direct conversion of NaCl and KCl concentrations to corresponding osmotic potentials at 25°C. Since osmotic potential is a function of temperature, unique values must be calculated for each calibration temperature-solute concentration combination.

## A.2 Procedures

Psychrometric measurements can be made using either; 1) the dew point method, 2) the psychrometric method, or 3) a combination of both. The psychrometric method is based on measurement of the temperature depression of a wet thermocouple caused by the evaporation of water from its surface. The dew point method is based on the maintenance (by electronic means) of wet thermocouple temperature at a value at which water will neither condense on nor evaporate from the thermocouple under ambient humidity and temperature conditions. The dew point method has greater sensitivity than the psychrometric method and is less sensitive to changes in ambient temperature. However, either method may at different times appear to be the better choice, depending on experimental conditions and circumstances (Wescor, 1979). If the dew point method is to be used, it is necessary to obtain a microvoltmeter-control unit which incorporates the electronic circuitry required for the method.

General calibration and measurement procedures for the dew point and psychrometric methods are outlined below. The reader is referred to the owner's manual for the instrument being used to obtain more specific information regarding the proper procedures for use of that instrument. Typical response curves for the dew point, psychrometric, and combined modes are illustrated in Figure A.1.

### A.2.1 Dew Point Method

Prior to calibrating psychrometers for the dew point method, it is first necessary to experimentally determine cooling coefficients ( $\pi_v$ ) for

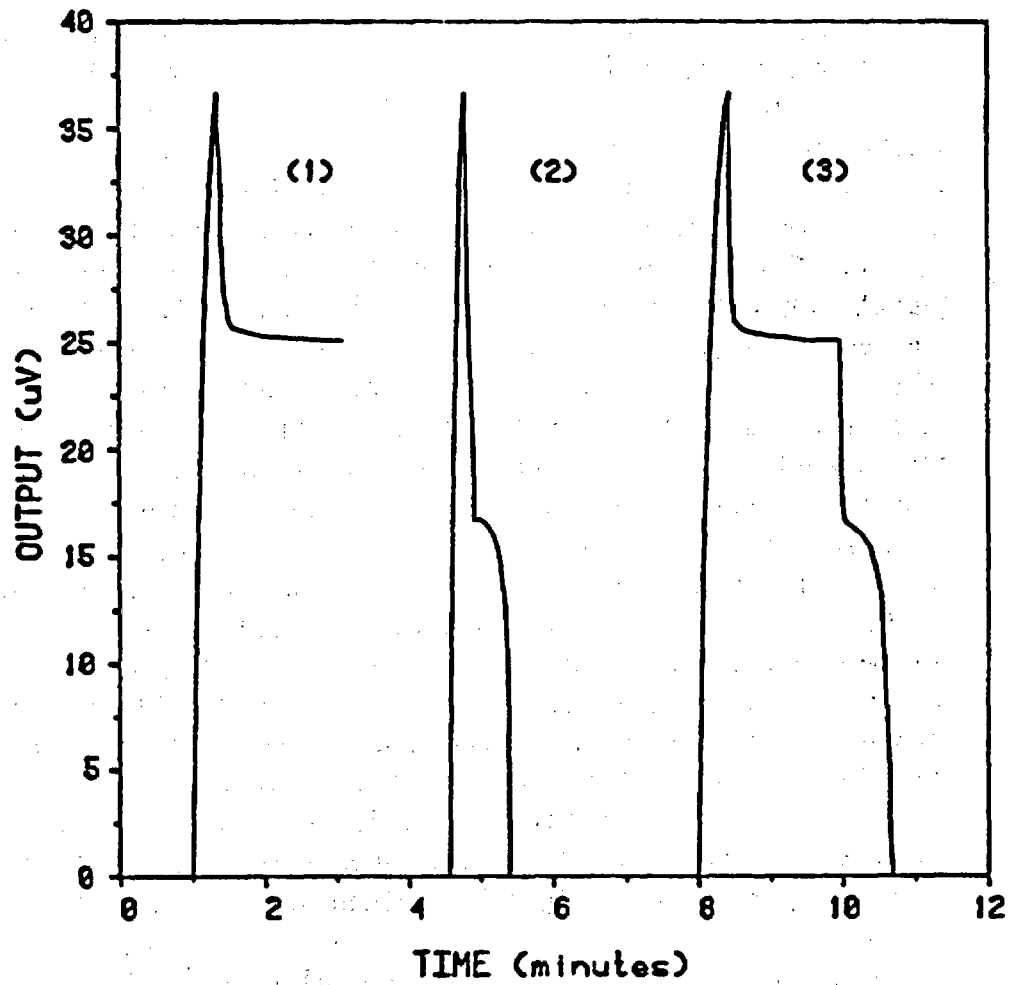


Figure A.1 Thermocouple psychrometer response curves for (1) dew point, (2) psychrometric, and (3) combined modes. Water potential is 25 bars suction and temperature is 32.8°C.

individual psychrometers. The cooling coefficient is defined as the maximum junction temperature depression which results from the passage of a specified nominally optimum cooling current through the junction under dry conditions (Wescor, 1979). Once the  $\pi_v$  has been determined for a given psychrometer, it then is possible to adjust the electronic gain of the microvoltmeter-control unit prior to making dew point measurements so that experimental results will not be influenced by dissimilarities in response characteristics of individual thermocouple junctions.

Cooling coefficients are determined after the psychrometers have been allowed to equilibrate under dry conditions (less than 90% relative humidity). An empty ice chest serves as an excellent constant temperature-constant humidity chamber for this purpose. The measurement procedure involves applying a cooling current to a psychrometer for a short period of time (10 seconds is adequate) and then adjusting the electronic gain of the control unit until the microvolt reading holds at a constant value between 15 and 30 $\mu$ V. The corresponding cooling coefficient is then determined by pressing a button on the instrument and reading a value from the microvolt meter. It is recommended that a minimum of three  $\pi_v$  values and corresponding ambient temperature values be obtained for each psychrometer over a period of several hours. The  $\pi_v$  values should be corrected to a common temperature (e.g., 25°C) using a relationship recommended by the psychrometer manufacturer, and an average  $\pi_v$  for each psychrometer should then be calculated.

Psychrometer response is affected by cleanliness of the measuring thermocouple. Deposits of salt or organic matter on the thermocouple reduce measurement accuracy and prolong re-equilibration time required between successive measurements. It is therefore recommended that the measuring thermocouple be cleaned prior to use with a zero-residue organic solvent and several rinses of distilled-deionized water (see manufacturer's recommendations in this regard). The psychrometer should then be dried thoroughly by blowing clean air over its surface and/or allowing it to set overnight in a clean dry environment.

Psychrometers are then sealed within calibration chambers containing a salt solution with a known osmotic potential. The volume of solution used should be adequate to completely cover the bottom of the chamber and to ensure that changes in salt concentrations resulting from subsequent evaporation of water during the equilibration process will not be significant. Psychrometers having ceramic shields and some types of screen cage psychrometers are reported to be submersible directly in the calibration solution. We recommend, however, that all screen cage

psychrometers be suspended above the liquid surface in order to minimize the possibility of contaminating the measuring thermocouple with salt.

Calibration chambers containing psychrometers are then submerged in a constant temperature water bath to a depth which is sufficient to completely cover the chambers and, if possible, at least 10 cm of the psychrometer lead wires protruding from the chambers. Thermal and vapor conditions are then allowed to equilibrate within the chambers. The required duration of the equilibration period will depend on the type of psychrometers being calibrated and on the size and type of calibration chamber employed. The proper duration is determined by making a series of measurements over a period of several days until sequential measurements produce the same readings.

Figure A.2 illustrates results of psychrometric and dew point measurements over a 48-hour period following placement of four initially dry screen cage psychrometers in individual calibration chambers containing a 2.51 MPa NaCl solution. Results suggest that a minimum of 24-48 hours may be required for initial equilibration using this type of psychrometer and calibration chamber. Less time is required following a subsequent adjustment of the water bath temperature or a change in the salt solution within the chamber (assuming the chamber is only opened briefly when replacing solutions). We conservatively allow 48 to 72 hours for initial equilibration, at least 12 hours for re-equilibration following a change in water bath temperature, and at least 24 hours following replacement of the salt solution within the chamber.

Previous calibrations, conducted using smaller calibration chambers purchased commercially, required much shorter equilibration periods (on the order of 2 to 4 hours). For this reason use of commercial chambers appears to be preferable if the calibration process must be carried out within a limited time frame.

Dew point measurements can then be made following detailed procedures specified in the instruction manual for the particular microvoltmeter-control unit being used. The procedures typically include:

- Measuring the calibration chamber temperature using the reference electrode located within the psychrometer base;
- Calculating and setting the appropriate cooling coefficient;
- Zeroing the microvoltmeter;
- Applying a cooling current to the measuring thermocouple for a fixed interval of time; and
- Recording the microvolt reading corresponding to the dew point plateau (see Figure A.1).

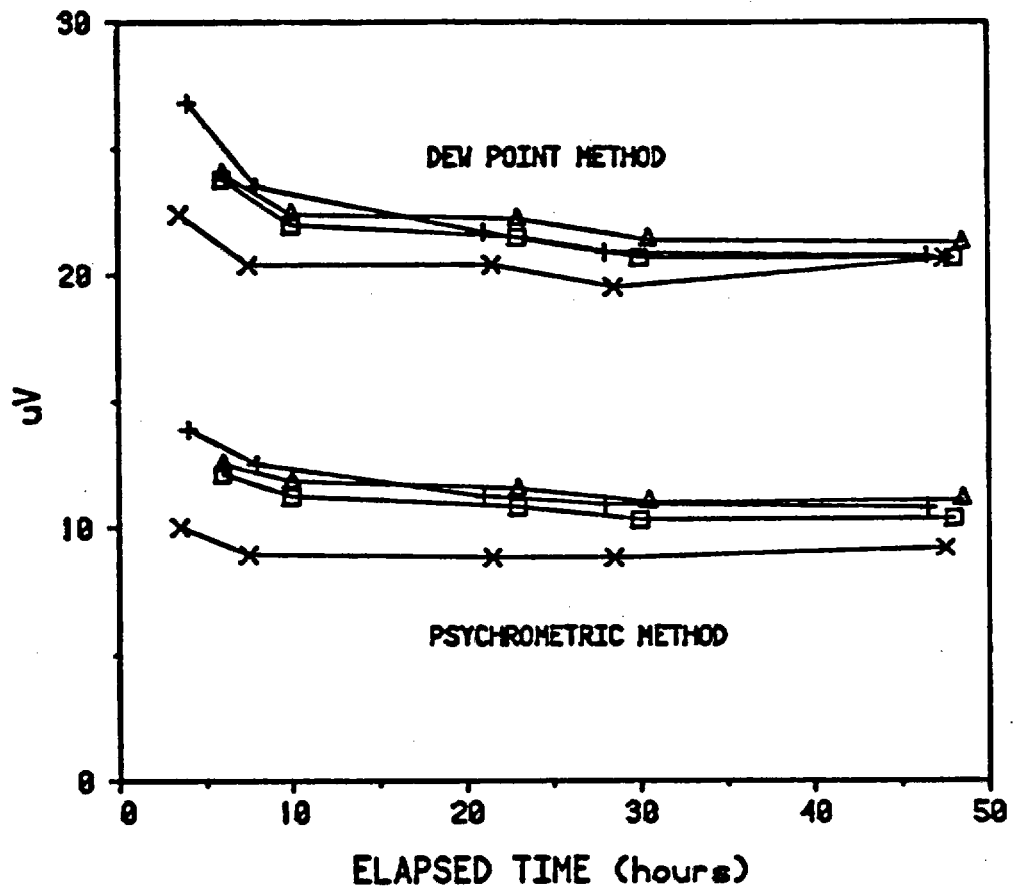


Figure A.2 Equilibration curves for four initially dry screen cage psychrometers placed in calibration chambers containing a 25 bar NaCl solution.

Three or four readings should be obtained using each psychrometer for each solute-temperature combination. The optimum duration of cooling current for a particular potential measurement is initially determined by trial and error. Typically 5 to 6 seconds are sufficient for potentials in the range of 0.2 to 0.5 bars suction, 10 to 15 seconds are sufficient for potentials near midrange (approximately 25 bars suction), and 30 to 40 seconds or more may be required for solutions having large osmotic potentials (near 50 bars suction).

If the cooling current duration is too short, the measuring thermocouple surface will not be thoroughly wetted and reproducibility of measurements will be poor. If the duration is too long, an inordinate period of time will be required for the thermocouple to dry between readings. Once the proper cooling duration has been determined for a given potential range, it should be used for all subsequent calibration and field measurements within that range.

After all psychrometers have been calibrated for a given temperature-osmotic potential combination, then the water bath temperature should be reset at a new value. We recommend that measurements be made at 3 or 4 temperatures spanning the range of values likely to occur in the field.

After making measurements, remove the calibration chambers from the water bath, carefully open the chambers, discard the salt solution, thoroughly clean, rinse, and dry the chamber base, fill the base with the next salt solution, and reassemble and resubmerge the chambers. Completing this step in a short period of time will serve to reduce the required re-equilibration period. Repeat these procedures 3 or 4 times using salt solutions having osmotic potentials adequately covering the potential range from about 0.2 to 50 bars suction. If four solutions are used, and four temperature values are checked for each temperature, then the resulting 16 data points will adequately define a calibration curve for each psychrometer. The calibration procedure can be simplified somewhat if the anticipated range of field temperatures and potentials is small or if less accurate field measurements are acceptable.

#### A.2.2 Psychrometric Method

Measurements made using the psychrometric method do not require the determination or setting of cooling coefficient ( $\mu V$ ). Calibration steps outlined in the preceding section otherwise remain valid for the psychrometric method, except that the measurement of interest is the microvolt plateau corresponding to depression of the thermocouple

temperature caused by evaporation of water from the thermocouple surface (see Figure A.1). Refer to the appropriate instruction manual for more detailed measurement procedures.

### A.2.3 Combined Method

Dew point and psychrometric measurements can be made sequentially with some microvoltmeters simply by switching the meter controls to the psychrometric measurement position following completion of the dew point measurement. All procedures remain unchanged from those described in the section on dew point measurement methods. Use of the combined method is recommended for field measurements because it provides two estimates of moisture potential from a single procedure.

### A.3 Data Analysis

Because psychrometer response is a function of temperature as well as potential, it is necessary to either plot calibration data on three-dimensional axes to obtain a "calibration plane" for each psychrometer or to combine two parameters (e.g., response-potential) and plot the resulting values against the third parameter to obtain a calibration curve. Computer programs have been developed (Meyn and White, 1972), to analyze calibration data in a three-dimensional sense. It is simpler, however, to combine response and potential data as a single parameter and to plot results against temperature on a two-dimensional graph. The latter method has been utilized in this study and is summarized below.

- Calculate mean dew point and psychrometric response value (in  $\mu\text{V}$ ) for each solution-temperature combination evaluated during the calibration procedure.
- Calculate osmotic potential values (in bars) for each solution-temperature combination using the equations presented previously (Raoult's Law and Kelvin's Law).
- Divide each mean dew point and psychrometric response value by the appropriate osmotic potential value. Express results as  $\mu\text{V}/\text{bar}$ .
- For each psychrometer, plot all  $\mu\text{V}/\text{bar}$  values against corresponding temperature values. Psychrometric method results should plot as a straight line. Dew point method results should plot nearly horizontally. Individual data points lying a significant distance away from the apparent dew point and psychrometric calibration lines should be ignored because they probably indicate that the calibration system had not reached temperature or vapor equilibrium at the time that the measurements were made. This situation could be caused by a leak in the calibration chamber or by insufficient equilibration times.

- Calculate linear regression equations using temperature and  $\mu\text{V}/\text{bar}$  values judged to be reliable in the previous step. Use these equations to accurately plot the slope and intercept of the calibration lines for each psychrometer for the dew point and psychrometric methods.
- Subsequently, the calibration lines derived in the previous steps can be used to calculate moisture potential values (in bars) corresponding to temperature and microvolt data gathered in the field.

The entire data analysis procedure outlined above can be readily accomplished using a computer, although an appropriate program has not been developed during the present study.

#### A.4 Thermocouple Psychrometer Sample Changer: Calibration

The psychrometer SC-10A can be calibrated for measurement of water potentials in the dry range (i.e., 70 bars suction) and also for water potentials near saturation (i.e., 0 bars suction). The procedure requires the determination of a unique psychrometer constant for a particular thermocouple, as well as temperature corrections.

##### A.4.1 Calibration Procedure at Low Water Potential

Calibration for low water potential can be accomplished with saturated salt solutions. The solutions are made by adding an excess of the salt to water, and allowing the solutions to stand for a few days to equilibrate. There should always be excess salt in the solution. Water potentials and water activities (or relative humidity) of several saturated salt solutions are given in Table A.1. Calibration can be accomplished with a single solution, but additional solutions provide a check and increase confidence in the measurement.

Select at least one salt which is near the range of water activity-potential of the samples and prepare the saturated solution as just described. When the solutions are ready, fill one or more cups about half full (about 1 ml) and place them in the sample changer. Make sure no solution splashes on the top or outside surfaces of the cup. Be very careful not to splash or slop solutions when you rotate the SC-10A selector knob. After the calibration solutions are loaded, put distilled water in cup 0.

Once all of the samples are loaded, wait 15-20 minutes for temperature equilibrium and then rotate the selector to position zero and raise the

water reservoir cup to wet the thermocouple. Then lower the cup, rotate the selector to the calibration solution and seal the chamber. If the chamber humidity is lower than the humidity in the sample changer (generally the case for low activity solutions) the microvolt reading will increase to a maximum, hold that value for a time (determined by the humidity of the chamber), and then decrease to zero as water disappears from the thermocouple.

The reading is taken as the highest steady value obtained. At higher sample humidities, the microvolt reading starts high and decreases exponentially toward a steady value, which it generally attains within 5-10 minutes. The reading is the steady value attained. After reading the microvolt output, determine and record the chamber temperature. Repeat the wetting and reading procedure for each of the other calibration solutions and record their microvolt readings and temperature. After calibration, remove the sample cups, wash and dry them.

#### A.4.2 Calibration Procedure at High Water Potential

The procedure already presented for measurement of low water activity potentials can generally be used at high activity as well. For high water potentials, use calibration solutions from Table A.2 rather than those in Table A.1. Also, it is a good idea to use filter paper in the sample cups, as outlined below, to speed equilibrium.

An alternative calibration procedure for high water activity potential consists of obtaining a calibration curve such as the one shown as Figure A.3, using KCl or NaCl solutions given in Table A.2. The calibration curve is useful for converting microvolt readings to water potential and is a good check on your technique with the psychrometer. The scatter of the points from a line will give some idea of how accurate the readings on unknown samples are likely to be. In addition to the calibration curve, it is often useful to run standards along with samples. The calibration of the psychrometer is temperature dependent, and will shift if the thermocouple becomes contaminated. A couple of calibrating solutions in the range of water potentials of the unknown samples will allow a check as the unknowns are being read, and will improve the reliability of the readings.

The first step in the calibration procedure is to make up the calibration solutions. For a typical calibration, a minimum of 5 solutions are required at concentrations of 0.1, 0.3, 0.5, 0.7, and 1.0 molal. The calibration solutions may be put in bottles with their own droppers, or in flasks and a single dropper used for all. If a single

Table A.1 Water potentials and water activities of selected saturated solutions at 20°C. To find water activities at other temperatures, see Greenspan (1975).

Salt Solution	Water Potential kJ/kg or MPa	Water Activity
LiCl	-294.35	0.113
MgCl <sub>2</sub>	-149.38	0.331
Mg(NO <sub>3</sub> ) <sub>2</sub>	-82.24	0.544
NaCl	-37.99	0.755
KCl	-21.77	0.851
KNO <sub>3</sub>	-7.47	0.946

Table A.2 Water potentials-activities of KCl and NaCl solutions at 20°C. To find water potentials at other temperatures use  
 $OP_T = OP_{293} T/293$

Concentration Moles/kg	Bars or J/kg x 10 <sup>-2</sup>		Water Activity	
	NaCl	KCl	NaCl	KCl
0.05	-2.32	-2.32	0.99828	0.99828
0.10	-4.54	-4.52	0.99664	0.99666
0.02	-9.01	-8.88	0.99335	0.99344
0.30	-13.49	-13.26	0.99006	0.99023
0.40	-17.93	-17.60	0.98681	0.98705
0.50	-22.42	-21.90	0.98353	0.98391
0.60	-26.99	-26.22	0.98021	0.98076
0.70	-31.59	-30.61	0.97687	0.97758
0.80	-36.18	-35.01	0.97356	0.97440
0.90	-40.87	-39.31	0.97018	0.97130
1.00	-45.58	-43.72	0.96680	0.96813

dropper is used, be sure to rinse it with the new solution several times before filling the cup with that solution to prevent changes in the solution concentration. It is also useful to include a distilled water sample to give a zero reading. Table A.2 gives the water potentials of KCl and NaCl solutions of various molalities. For potentials not shown, linear interpolation will give values with sufficient accuracy.

Best accuracy is obtained at high water potential if the walls of the sample cups are covered with the sample. The calibration should therefore be run with the walls of the cups covered. This is done by cutting filter paper strips 12 mm wide x 45 mm long to place around the walls of the cups. Make sure the filter paper is no closer than 1mm to the top of the cup, or solution will move up the cup walls and damage the thermocouple assembly. Use only enough calibration solution to wet the filter paper and cover the bottom of the cup.

Relatively small errors in solution concentration which result from evaporation of water from the solution in the psychrometer cup or transfer of water or salt from one solution to another in the dropper can cause measurable errors in the psychrometer calibration. Once all of the calibrating solutions have been loaded, fill the small well in the water source for the measuring junction, and place it in position zero. When all of the solutions and the psychrometer water source are in the sample changer, you will need to wait some time for temperature equilibrium. Twenty to thirty minutes should be adequate. During equilibration, the selector should be set so that the thermocouple is over the driest sample to minimize the possibility of condensation on the thermocouple mount.

When temperature equilibrium has been achieved, turn the selector to position zero and lift the lever to place water on the measuring junction. Then bring down the lever, turn the selector to position 1, and seal the chamber by again lifting the lever. The microvolt meter reading should decrease rapidly, and finally reach a constant value. At water potentials in the 0 to 4 bar suction range (water activities in the 1 to 0.99704 range), a constant reading may take ten minutes or longer. At lower water potentials, 2 to 3 minutes should be adequate. In any case, it will be obvious when equilibrium is reached because the reading will stay constant.

When the reading is stable, record it and the psychrometer temperature, and then go on to the next sample. It is a good idea to rewet the thermocouple before each reading, though, at high water potentials the

thermocouple will generally hold enough water for several readings. Rewet the thermocouple in position zero, and then go to position 2 and seal the chamber. Repeat this procedure for all of the calibration solutions, then remove and wash the cups from the SC-10A.

Calibration data should be plotted as in Figure A.3. As indicated in the figure, points should lie on a smooth line over the entire range of water potentials. Departures of calibration points from a smooth line indicate problems either in calibration procedure or in the equipment.

For very careful work, calibration should be checked against one or two known potential activities each time a sample is run. Less demanding work will not require this frequency of calibration, as long as room temperature remains constant. The psychrometer output increases about 2-1/2 percent per degree as temperature increases.

#### A.4.3 Calibration Equations and Curves

A calibration curve such as Figure A.3 (for low activity solutions) and Figure A.4 (for high activity solutions) can be produced from the microvolt readings and used to convert microvolt measurements to water potential for a particular temperature. However, it is more convenient to use the psychrometer equation. To use the equation, a psychrometer constant must be determined for the psychrometer. The psychrometer constant ( $g$ ) is calculated from

$$(A.3) \quad g = e'_w - a_w e' / (T_a - T_w)$$

where

$T_a - T_w$  is calculated from the microvolt reading, assuming that the thermocouple output is  $60 \mu\text{V}/\text{C}$ ;

$a_w$  is the water activity (relative humidity) of the calibration solution; and

$e'$  is the saturation vapor pressure, calculated from

$$(A.4) \quad e' = \exp (52.57633 - 6790.4985 / T_k - 5.02808 \ln(T_k))$$

where

$T_k$  is the Kelvin temperature read during calibration.

A simple calibration program can be used to calculate the psychrometer constant ( $g$ ) as well as the water activity and water potential of a sample. To calculate the water activity or relative humidity of a sample, use the equation:

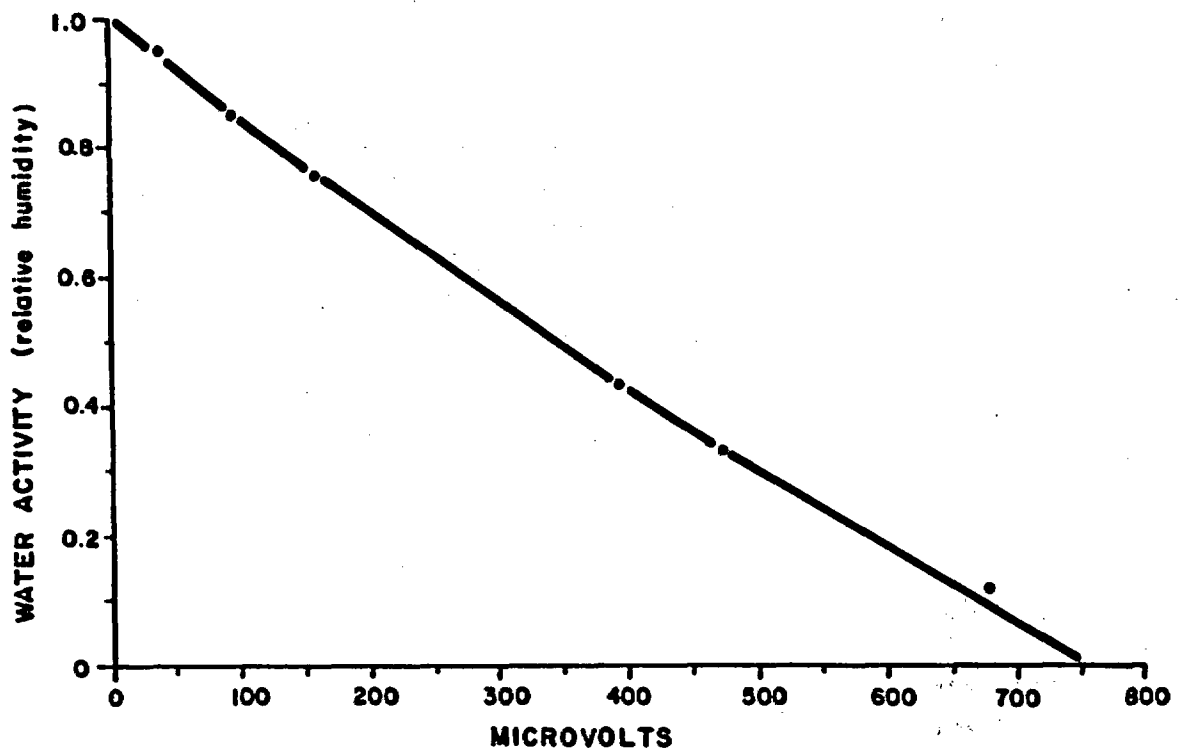


Figure A.3 Calibration curve for low water potential readings using saturated salts for calibration.

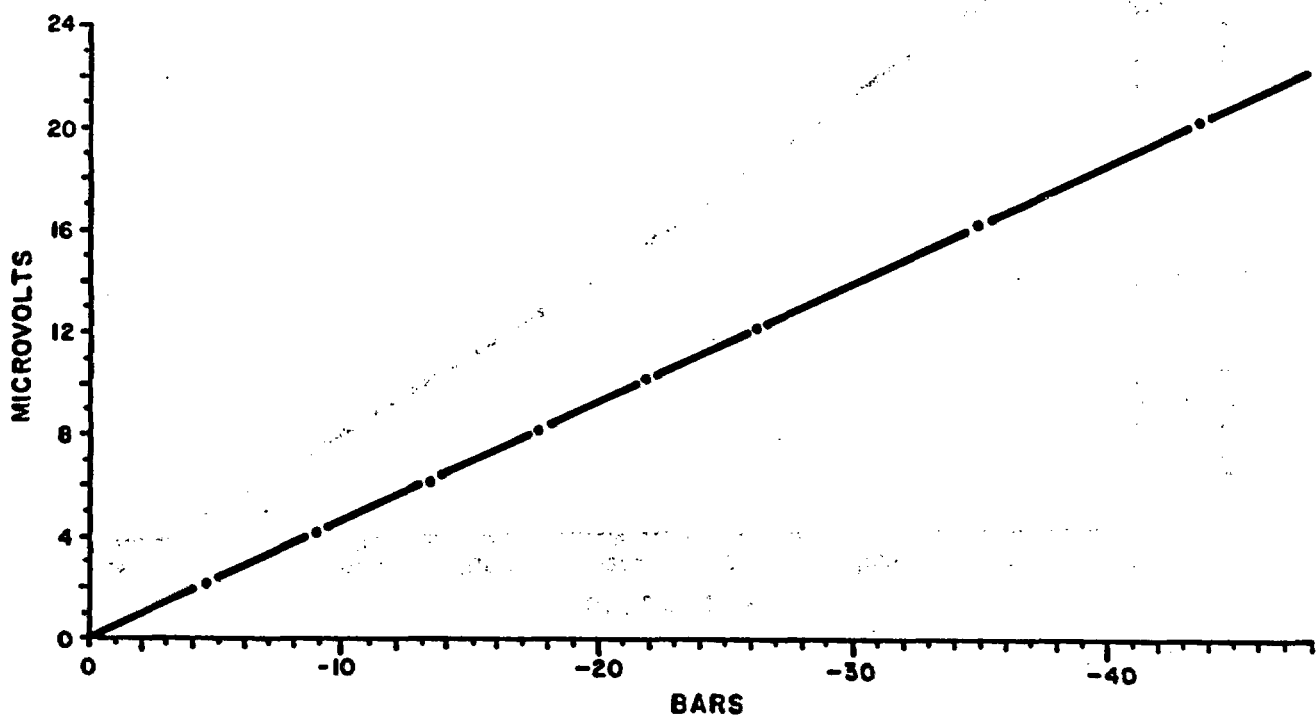


Figure A.4 Calibration curve for high water potential readings using saturated salts for calibration.

$$(A.5) \quad a_w = e_w' - g(T_a - T_w) / e'$$

The water potential is related to the water activity (i.e., relative humidity) by the equation:

$$(A.6) \quad WP = R T / M \ln(a_w)$$

where

WP is the water potential;

R is the gas-constant;

T is the Kelvin temperature;

M is the molecular weight of water; and

$a_w$  is the water activity of the sealed chamber.

## APPENDIX B OSMOTIC TENSIO METER

This Appendix contains detailed descriptions and evaluations of various types of membranes and organic solutes used when testing the osmotic tensiometer. Membrane and solute combinations have been examined in the laboratory using a variety of manufactured cylinders (PVC pipe, cloth tubes and concrete blocks) to simulate a borehole. Laboratory methods for determining the osmotic potential of a solution, the moisture potential in a soil, and the water potential of a block of tuff are presented in this Appendix. Results and interpretations of the field tests at the Santo Nino mine site are included.

### B.1 Membranes

The membranes used to retain the organic solute of the osmotic tensiometer should ideally be:

- Strong and flexible;
- Readily permeable to water and impermeable to large organic molecules;
- A tubular form with a diameter equal to the borehole; and
- Resistant to microbial decomposition.

Polysulfone ultrafiltration membrane (Osmonics, Inc., Minnetonka, MN) showed promise initially, but was subsequently rejected. This membrane exhibited good water permeability characteristics, and retained 85 to 95 percent of a large organic molecule (polystyrene sulfonic acid, 70,000 mw) and 48 to 59 percent of an inorganic salt (KCl) when a solution containing these substances was forced through the membrane under a positive pressure.

Polysulfone ultrafiltration membrane is available only in sheet form on a paper backing. Testing was discontinued after repeated unsuccessful attempts to seal the seam formed when the flat membrane was rolled into a tubular form for use in the prototype osmotic tensiometer. Leaks invariably occurred along the seam, regardless of the sealant used, when positive hydrostatic pressures were generated within the prototype.

Several tubular membranes made of regenerated natural cellulose exhibited acceptable properties through numerous lab and field experiments. One type (Spectra/Por 4) has a molecular weight cutoff of 12,000 to 14,000 and is available in a diameter (47.6 mm) identical to that of boreholes drilled at our field study sites.

A second type (Spectra/Por 1) has a more favorable molecular weight cutoff, 6,000 to 8,000, but the available diameter (63.7 mm) closest to that of the boreholes is too large for practical use with the prototype tensiometer. A third membrane, Visking dialysis membrane, is available in 5.1 cm diameter tubular form and was used during several experiments conducted near the end of this research project.

Another membrane, (Spectra/Por 5) made with a paper base, has an extremely high wet strength with a molecular weight cutoff of 12,000 - 14,000 and diameter of 41.4 mm. Preliminary experiments with the paper base membrane gave very slow transport of water through the membrane even when positive pressures of 1 bar were applied making it unsuitable for use with the osmotic tensiometer.

Spectra/Por and Visking tubular membranes are made of regenerated cellulose. Because the membrane is a gel when wet, some enlargement or flexibility in pore size can be expected when mechanical strain is applied. Also, because the membrane excludes large molecules by mechanical sieving, some change in solute retention characteristics can be expected if the membrane is stretched. Once the membrane has been wetted, it should not be allowed to dry out again. Otherwise, the porosity will change and pinholes may form.

The molecular weight cutoff for the membranes is defined on the basis of 90 percent retention of globular protein over a 24-hour period. Retention efficiency will vary depending on the structure and chemical characteristics of a particular solute.

Linear long-chain molecules will pass through the membrane much more readily than a coiled or spherical molecule of similar molecular weight. Also, because each manufacturer defines the molecular weight cutoff differently, complete or nearly complete retention of a solute can only be achieved if the solute molecule is significantly larger than the specified molecular weight cutoff.

Cellulose acetate membranes are susceptible to attack by microorganisms. Eventual breakdown of the membrane and leakage of the solute can be expected unless an effective toxin is added to the osmotic solution used to fill the tensiometer.

The most suitable tubular membranes are Spectra/Por 4 dialysis tubing (distributed by Spectrum Medical Industries, Inc., Los Angeles, CA) and Visking dialysis membrane (distributed by Teepak, Danville, IL). Problems were encountered with both membranes in that hydrostatic

pressure within the tensiometer gradually decayed during many experiments.

Possible explanations for this decay include solute leakage through small holes in the membrane or a reduction in the effective osmotic potential gradient across the membrane either as a result of the movement of large organic molecules through the membrane or the buildup of a layer of less concentrated solution along the inside of the membrane as water flowed inward. The latter possibility was discounted by results of experiments in which fresh solute was periodically purged through the tensiometer with no measurable change in the trend of gradual pressure decay.

Use of a cloth tube to protect the membrane during insertion into boreholes did not eliminate the problem. Consequently, it is believed that the pressure decay is caused by migration of solute molecules through the membrane.

## B.2 Solutes

The solute used to generate a known osmotic potential should be:

- Large enough to preclude passage through the semipermeable membrane;
- Inert with respect to the membrane material and to metals used in the tensiometer;
- Chemically stable; and
- Resistant to microbial decomposition.

The solutes evaluated during this study include; polystyrene sulfonic acid (PSSA), polyethylene glycol (Carbowax), polyvinyl pyrrolidone (PVP), and polyethylene oxide (PEO).

### B.2.1 Polystyrene Sulfonic Acid (PSSA)

The relationship between the concentration of polystyrene sulfonic acid (PSSA) and osmotic potential was determined by the freezing-point depression method using an Advance Instruments Osmometer Model 31 (Advanced Instruments, Inc., Newton Highlands, MA). Results summarized in Figure B.1 suggest an essentially linear relationship over the range 0 to 3.5 bars suction, with slight deviation from linearity occurring before 6.9 bars suction.

Magnitudes of the osmotic potential values presented here are probably inaccurate because the freezing-point depression method was subsequently

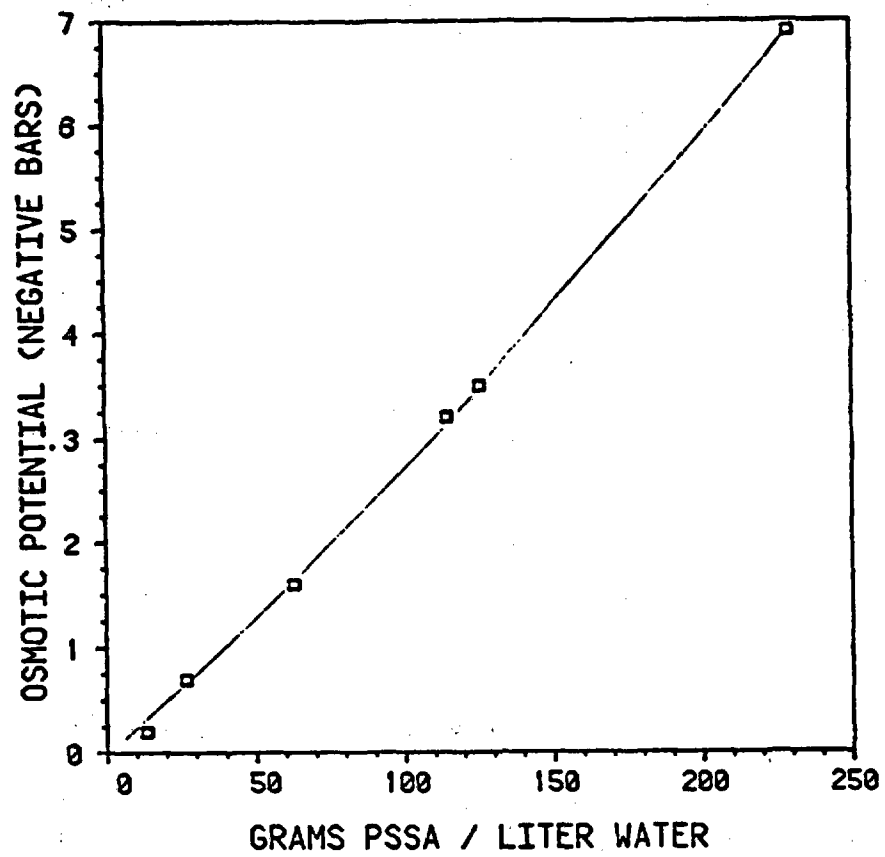


Figure B.1 Calibration curve for 70,000 mw Polystyrene sulfonic acid.

shown to be invalid for measuring osmotic potentials of solutions of high molecular weight compounds. Later results showed that the method significantly overestimated osmotic potentials corresponding to given concentrations.

PSSA solutions were initially utilized in lab experiments in which a motorized piston assembly was utilized to facilitate total potential equilibration in the experimental apparatus. PSSA solutions caused significant corrosion of stainless steel and rubber parts within the piston assembly, and use of this solute was subsequently discontinued for this reason.

Calibration curves relating osmotic potential to concentration were developed for PSSA with a molecular weight of 70,000. Osmotic potentials in the range 0 to 7 bars suction were obtained, but use of this solute was discontinued due to corrosion of stainless steel and rubber tensiometer components.

### B.2.2 Polyethylene Glycol (Carbowax)

Polyethylene glycol is commonly referenced by its trade name Carbowax (manufactured by Union Carbide). Carbowax consists of long-chain polymers of ethylene oxide and has the formula  $\text{HOCH}_2(\text{CH}_2\text{OCH}_2)_n\text{CH}_2\text{OH}$  where  $n$  is the average number of oxyethylene groups.

Carbowax polymers are available in numerous molecular weights between 200 and 20,000. All molecular weights are soluble in water although the range of osmotic potentials obtainable with relatively low viscosity solutions is reduced when larger molecular weight polymers are utilized.

Calibration curves relating osmotic potential to Carbowax concentration in aqueous solutions are available for molecular weights of 6,000 (Zur, 1966; Waldron and Manbeian, 1970; Williams and Shaykewich, 1969) and 20,000 (Williams and Shaykewich, 1969; Peck and Rabbidge, 1969).

A practical limit to the maximum osmotic potential obtainable with these solutions is about 15 bars suction. Stability of Carbowax solutions can be enhanced by adding antioxidants such as hydroquinone or butylated hydroxy anisole (0.05 to 0.1 percent).

Carbowax solutions were used in experiments designed to measure moisture potential in a small block of welded tuff and in soil samples, to measure the osmotic potential of other solutions, and to determine response characteristics of the prototype osmotic tensiometer.

Carbowax is available in many molecular weight polymers and has been used extensively by previous workers to create known osmotic potentials over the range 0.5 to 15 bars suction. A 20,000 mw Carbowax polymer was utilized during many early experiments in this project. Use was discontinued in favor of a larger molecule, PVP (40,000 and 360,000 mw), in an effort to alleviate a pressure decay problem.

### B.2.3 Polyvinyl Pyrrolidone (PVP)

PVP has a less linear and more rigid structure than Carbowax and is available in a wider range of molecular weights. PVP, of the general form  $(C_6H_3NO)_n$ , was initially developed for use as a blood plasma expander. As a result, most published research results relate to this particular application.

Concentration vs. osmotic potential curves for aqueous solutions are not available in the literature and limited data published by Hengstenberg and Schuch (1952) pertain to solutions several orders of magnitude more dilute than those required for purposes of this study. PVP is currently classified as a suspected carcinogen agent and caution should be exercised in its use. Experiments conducted during this study utilized 40,000 and 360,000 molecular weight polymers. A practical limit to osmotic potentials obtainable using PVP appears to be about 2 bars suction.

Like the Carbowax solutions described above, pressure decay problems were also encountered in lab and field experiments with the 40,000 mw PVP polymer. The range of osmotic potentials that could be created using a larger 360,000 mw polymer was limited to 0 to slightly less than 2 bars suction because the viscosity of more concentrated solutions made them impractical for use in the prototype tensiometer.

Another disadvantage of use of PVP are potential health hazards associated with inhalation of dry powder used to make aqueous solutions.

### B.2.4 Polyethylene Oxide (PEO)

PEO is the preferred solute despite the fact that pressure decay problems have been encountered. PEO is available in a variety of molecular weights; 200,000 mw PEO was utilized during this study. PEO has the general formula  $(-CH_2CH_2O-)_n$ . The maximum osmotic potential obtainable using 200,000 mw is about 3 bars suction. PEO poses no known health risks and its availability in a 200,000 mw polymer permitted a

wider range (0 to about 3 bars suction) of osmotic potentials to be created in reasonable nonviscous solutions.

Problems with the membrane weakening and developing holes may be prevented by doubling the membrane or by covering the membrane with a protective mesh. Mesh of various size openings (1-5000  $\mu\text{m}$ ) and made of polyester, nylon, polyethylene, polypropylene, stainless steel and Teflon, are presently available (Spectrum Medical Industries, Inc., Los Angeles, CA). A strong, inert mesh may be able to protect the cellulose membrane as it is transported in and out of the borehole. Possible modifications to the design of the osmotic tensiometer may assist in the prevention of leakage of solutes through the membrane.

### B.3 Experimental Apparatus

Several types of experimental apparatus were utilized during lab phases of this research. Small plexiglass cells served as osmometers, and the prototype osmotic tensiometer was tested in concrete block, a length of PVC pipe, a cotton cloth tube, and a porous ceramic pipe. The rationale for the use and design of each apparatus is summarized below.

#### B.3.1 Osmometer

Cylindrical plexiglass cells (Figure B.2) separated by a single thickness of semipermeable membrane were used to determine the osmotic potential of various solutions. The membrane was supported by a porous glass disk. One side of the apparatus (the side in contact with the membrane) was filled with the osmotic solution, sealed, and connected to a pressure transducer, taking care that no air remained trapped in the system. The other side was partially filled with distilled water.

During the process of potential equilibration between the two sides, water flowed through the membrane into the osmotic solution until the positive hydrostatic pressure in that cell was equal in magnitude to the negative osmotic potential of the solution. Thus, the total potential on both sides of the membrane is zero at equilibrium. Experiments of this type were repeated using various concentrations of solutions containing different organic solutes in order to define a concentration vs. osmotic potential calibration curve for each solute.

#### B.3.2 Concrete

Several experimental setups were utilized to test the prototype osmotic tensiometer under controlled laboratory conditions. The first of these

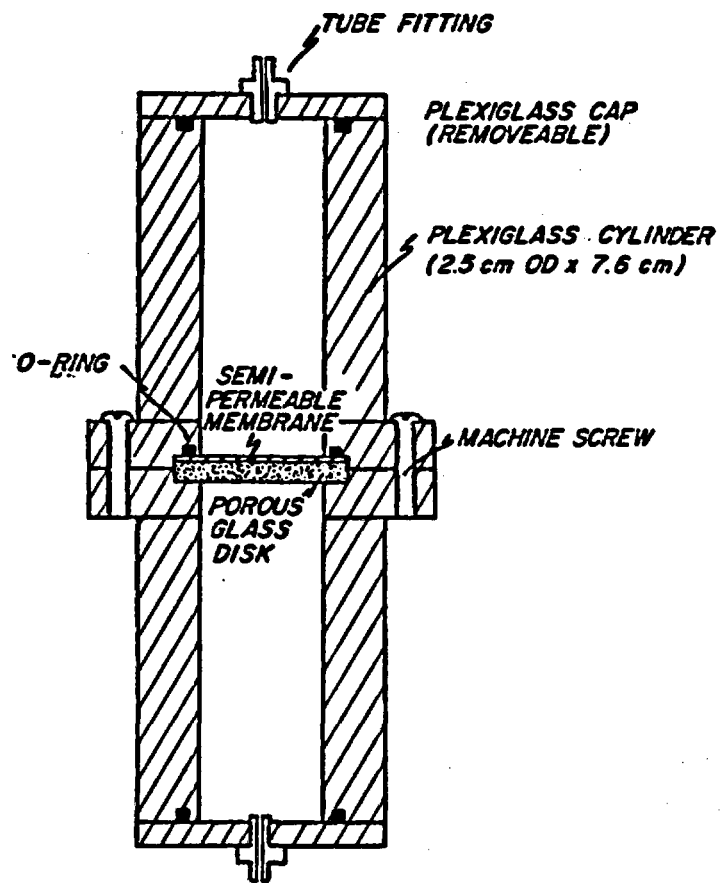


Figure B.2 Diagram of plexiglas cells used to determine osmotic potentials of aqueous solutions.

was a block of concrete containing a 4.75-cm diameter borehole. By inserting the prototype in the borehole and then submerging the entire concrete block in water, it was possible to simulate saturated conditions in a natural fractured rock.

By subsequently allowing the block to dry, it was possible to observe response of the tensiometer under changing moisture conditions. Use of the block also provided useful experience in developing techniques for inserting, filling, and draining the prototype in a borehole. This apparatus left one variable, the osmotic potential of the water in the concrete matrix, unknown and uncontrollable. Consequently, use of the concrete block was abandoned in favor of a piece of PVC pipe.

### B.3.3 PVC pipe

A submerged length of PVC pipe about 10-cm longer than the prototype and having an internal diameter approximately the same as that of boreholes at the field sites permitted insertion of the prototype in a system in which the osmotic and matric potentials of the outer system were known to be zero. The disadvantage of the system was that water flow into and out of the tensiometer only occurred through a small ring of membrane at either end of the device; the major portion of the membrane surface area remained unusable after the membrane was inflated against the inner surface of the impermeable PVC pipe.

### B.3.4 Cloth tube

Insertion of the prototype in a cotton cloth tube, also having a diameter equal to that of the borehole, and then submerging the device in water permitted maximum flow of water through the entire membrane surface area. Another advantage of this system was that air bubbles trapped under the membrane could be seen and, consequently, the filling technique was modified to preclude future air entrapment. Leak tests of fittings, welds, and o-ring seals were possible by placing a colored tracer in the solution used to fill the submerged tensiometer or by filling the tensiometer with compressed air instead of liquid.

A disadvantage of using this experimental setup to determine the osmotic potential of various solutions was that the cloth tube and membrane stretched significantly as water flowed into the tensiometer in response to the osmotic potential gradient. Substantial dilution of the internal solution and reduction of the effective osmotic potential gradient across the membrane resulted.

### B.3.5 Ceramic pipe

Porous ceramic pipe having an internal diameter of 4.75 cm and a wall thickness of approximately 0.3 cm provided an excellent rigid, porous support for testing the osmotic tensiometer under a variety of conditions. Insertion of the ceramic pipe containing the tensiometer in a larger diameter (15 cm) horizontal plexiglass pipe, partially filled with water (Figure B.3) permitted creation of a series of known external moisture potentials between 0 and 0.8 bar suction through the application of measured negative air pressures in an overlying airspace.

The osmotic potential of a given solution could be easily determined with this setup by submerging and monitoring the equilibrium hydrostatic pressure within the tensiometer. The accuracy and response characteristics of the tensiometer could be observed by applying a series of known negative air pressures to the airspace overlying the water and monitoring the resulting changes in hydrostatic pressure within the tensiometer. Ideally, the observed changes in hydrostatic pressure should be identical to the air pressure changes and the rate of re-equilibration following such changes should be rapid enough to verify the usefulness of the tensiometer for measuring moisture potentials in the field under changing conditions.

The major disadvantage of this experimental setup is that the range of negative external potentials that can be created (0 to about 0.8 bar suction) using a vacuum apparatus is much less than the range of potentials likely to be encountered in field situations.

### B.4 Laboratory Experiments

A laboratory experiment was conducted very early in this study in which a small prototype osmotic tensiometer was inserted in a borehole in a block of saturated tuff. The prototype was about 15 cm in length, was constructed using PVC pipe, and utilized a polysulfone ultrafiltration membrane. The reference solution was a Carbowax solution having an osmotic potential of 1 bar suction.

In duplicate experiments, equilibrium hydrostatic pressures of 0.27 and 0.28 bars were obtained, implying that the total moisture potential in the saturated tuff was 0.75 to 0.760 bars suction. The validity of these results is questionable because subsequent experiments using fluorescein dye to detect leaks showed considerable leakage along the seam running the length of the membrane. The seam was formed where the sheet membrane had been rolled into tube.

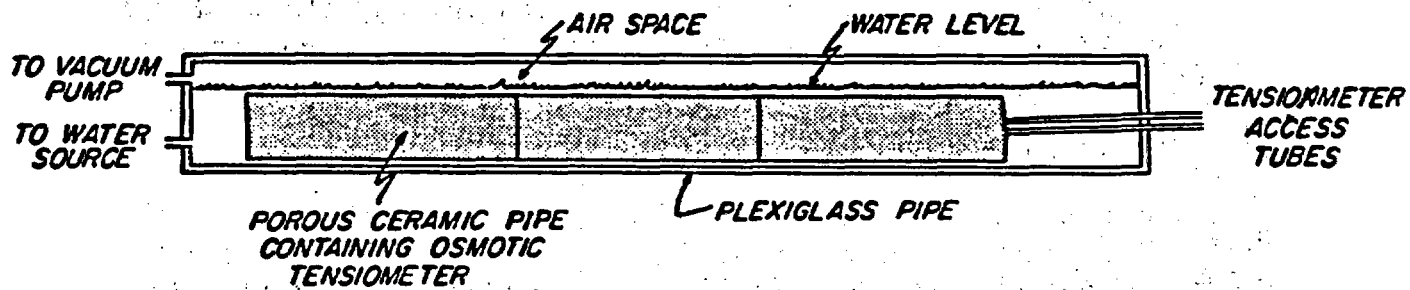


Figure B.3 Diagram of apparatus used to assess osmotic tensiometer response characteristics under variable external potentials.

Use of the polysulfone ultrafiltration membrane was discontinued following repeated failures in attempts to form a leakproof seam. Additional attempts to measure moisture potential in the tuff samples were not made because of the stainless steel prototype tensiometer which was completed at this time was much longer than the tuff sample.

Ten experiments were conducted using the osmometer shown in Figure B.2. A 135 gm/liter Carbowax solution was placed in one cell (in contact with the membrane) and distilled water was placed in the other side. The mean equilibrium osmotic potential for this solution was 1033 cm suction. Three similar experiments utilizing a 79 g/l solution yielded an equilibrium osmotic potential of 0.331 bars suction.

A series of four experiments were then run in which the 135 g/l Carbowax solution was placed in the other. An equilibrium hydrostatic pressure of about 0.7 bars was anticipated on the basis of the osmotic potentials reported above. However, values of 0.425, 0.82, 0.81, and 0.5 bars were obtained instead. The disparity of these results and the fact that gradual but significant pressure decays were observed in two experiments, suggests that some movement of Carbowax molecules through the semipermeable membrane separating the solutions was occurring.

The accuracy of water potential measurements using the osmotic principle was assessed by creating a known matric potential in soil samples and then measuring the potential using Carbowax solutions having known osmotic potential. "Known" matric potentials were created by subjecting initially saturated soil samples (contained in one side of the plexiglass test apparatus) to measured air pressures for several days.

A cellulose acetate membrane supported on a porous glass plate prohibited air flow directly out of the apparatus but permitted water to flow out until the potential of the remaining water was equal to the applied air pressure. Sand, clay loam, and sand loam soils were used. After the soil matric potential had stabilized, a Carbowax solution having a known osmotic potential was placed in the cell opposite the soil sample. As equilibrium conditions were reached, the sum of the measured hydrostatic pressure and known osmotic pressure should have been equal to the matric potential of moisture in the soil sample.

Results, summarized in Figure B.4, generally follow the expected one-to-one relationship between "known" matric potential and measured matric potential (i.e., the sum of the measured hydrostatic pressure and osmotic potential within the tensiometer). Scatter in the data is

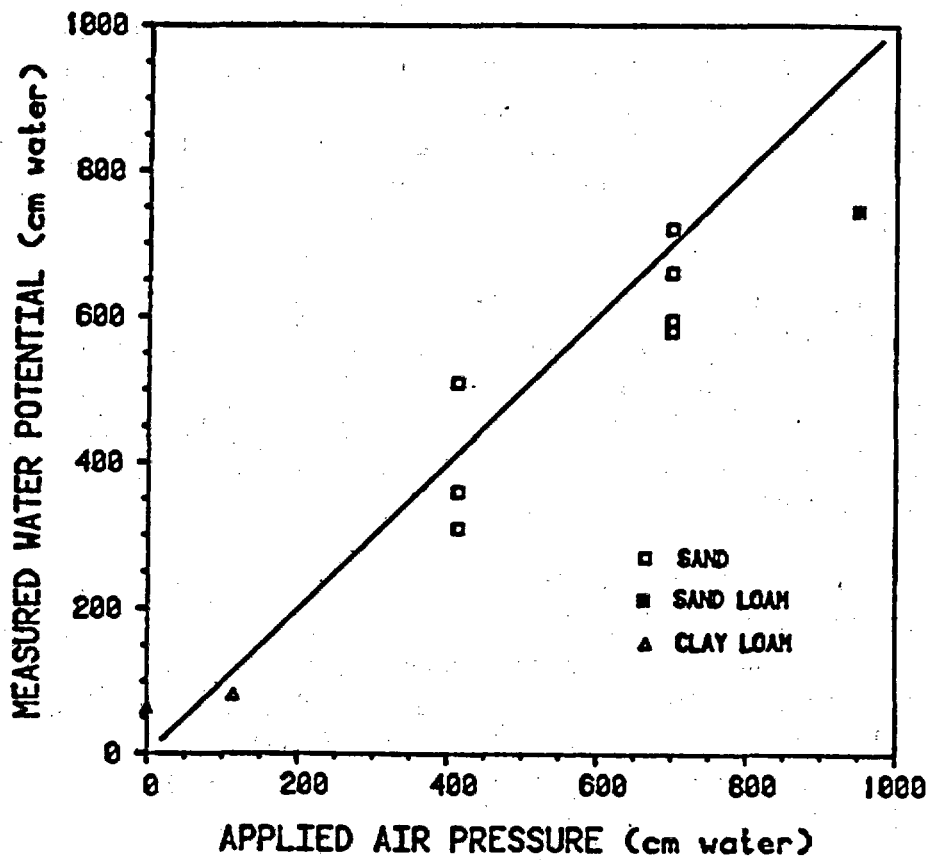


Figure B.4 Summary of water potentials measured in lab experiments in which soil samples were previously brought to a specified moisture potential by applying a known pressure for 48 hours.

probably due as much to inaccuracies in the specified matric potentials created using the air pressure method as it is to inaccuracies in the osmotic tensiometer method itself. Hydrostatic pressure data for many of these experiments drifted downward with increasing time, again suggesting leakage of Carbowax through the membrane and a consequent reduction in the osmotic pressure gradient across the membrane.

The full scale prototype osmotic tensiometer was described previously and is illustrated in Figure B.5. Response characteristics under saturated conditions were evaluated when the device was inserted in a cloth tube, a borehole, a concrete block, and a length of PVC pipe. Results are summarized below:

A cotton cloth tube (5 cm diameter) was slipped over the tensiometer and the apparatus was submerged in water in an attempt to monitor instrument response under conditions where we were sure that no external potentials would come into play. The cloth tube simply served as a "borehole" in this experiment. Instrument response over a 12.5 day period is shown in Figure B.6.

The pressure buildup during the first 20 hours corresponded to a period in which the cloth membrane and cloth tube expanded to a diameter of about 6.5 cm. The hydrostatic pressure plateau reached after about 48 hours (0.31 to 0.315 bars suction) agrees with the osmotic pressure value (0.331 bars suction) determined for the same Carbowax solution (78 g/l) using the plexiglass cylinders.

Dilution of the Carbowax solution by inflowing water undoubtedly occurred during the first 20 hours while the membrane was expanding. The gradual pressure decay which occurred during the last 10 days of the experiment was probably due to leakage of Carbowax through the membrane. This problem was exacerbated in this experiment by the stretching of the membrane noted above and the widening of pores which occurred in conjunction with the stretching.

Other lab experiments were then conducted using a block of concrete submerged in tap water. A borehole in the concrete permitted insertion of the prototype and measurement of moisture potentials under saturated conditions. Rigidity of this borehole alleviated previous problems associated with membrane stretching.

Figure B.7 illustrates response of the tensiometer (containing a 1 bar suction Carbowax solution) when placed in the saturated concrete block. Abrupt pressure changes in the early portion of the response curve were

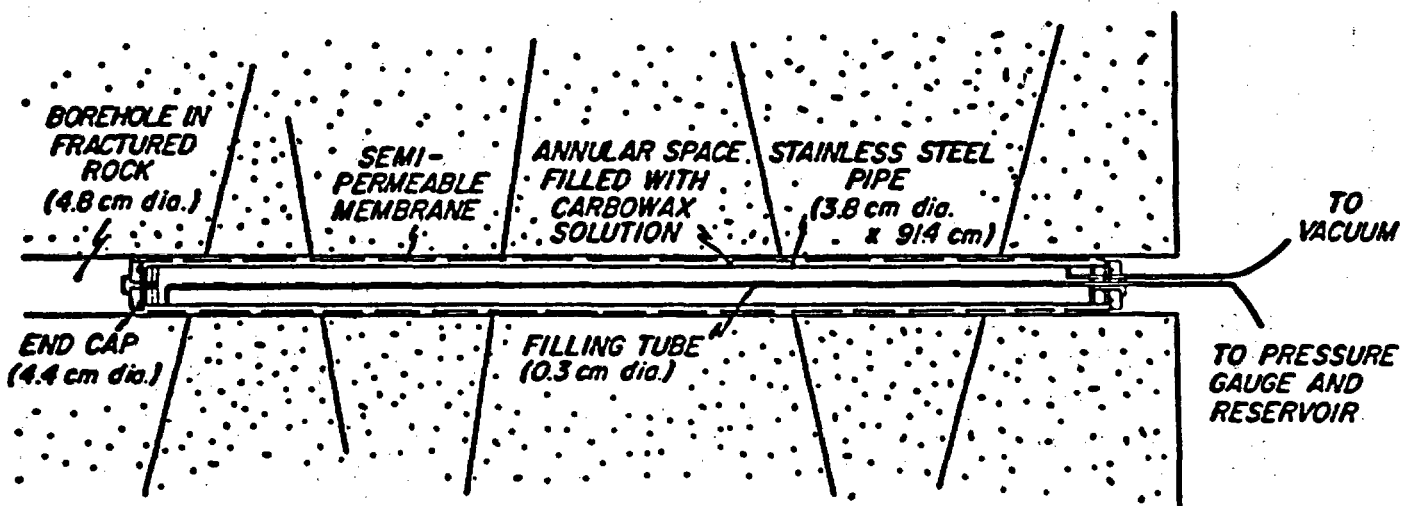


Figure B.5 Diagram of the prototype osmotic tensiometer in a borehole located in fractured rock.

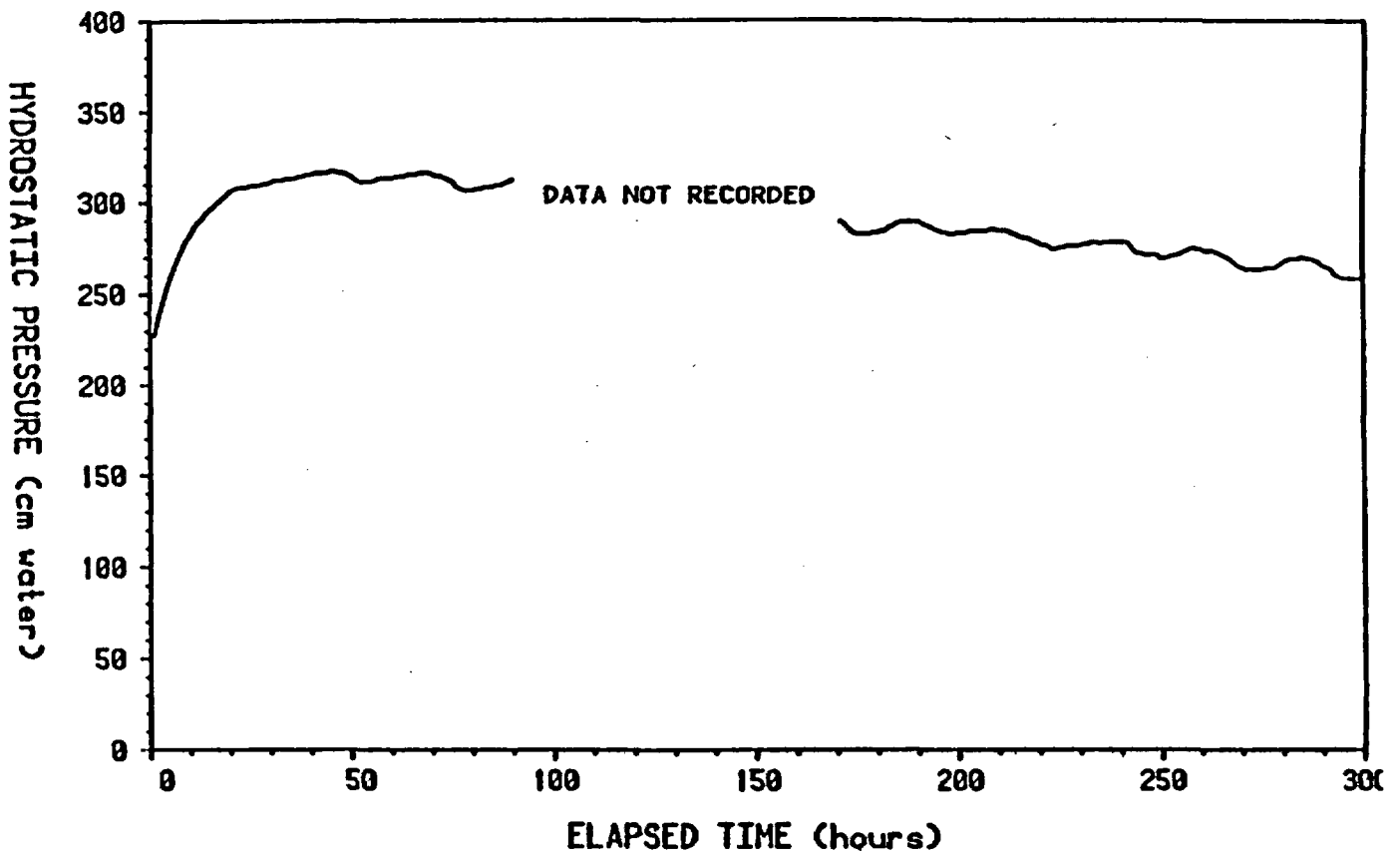


Figure B.6 Tensiometer response curve for an experiment in which the prototype containing a Carbowax solution was inserted in a simulated borehole made of cloth and submerged in water.

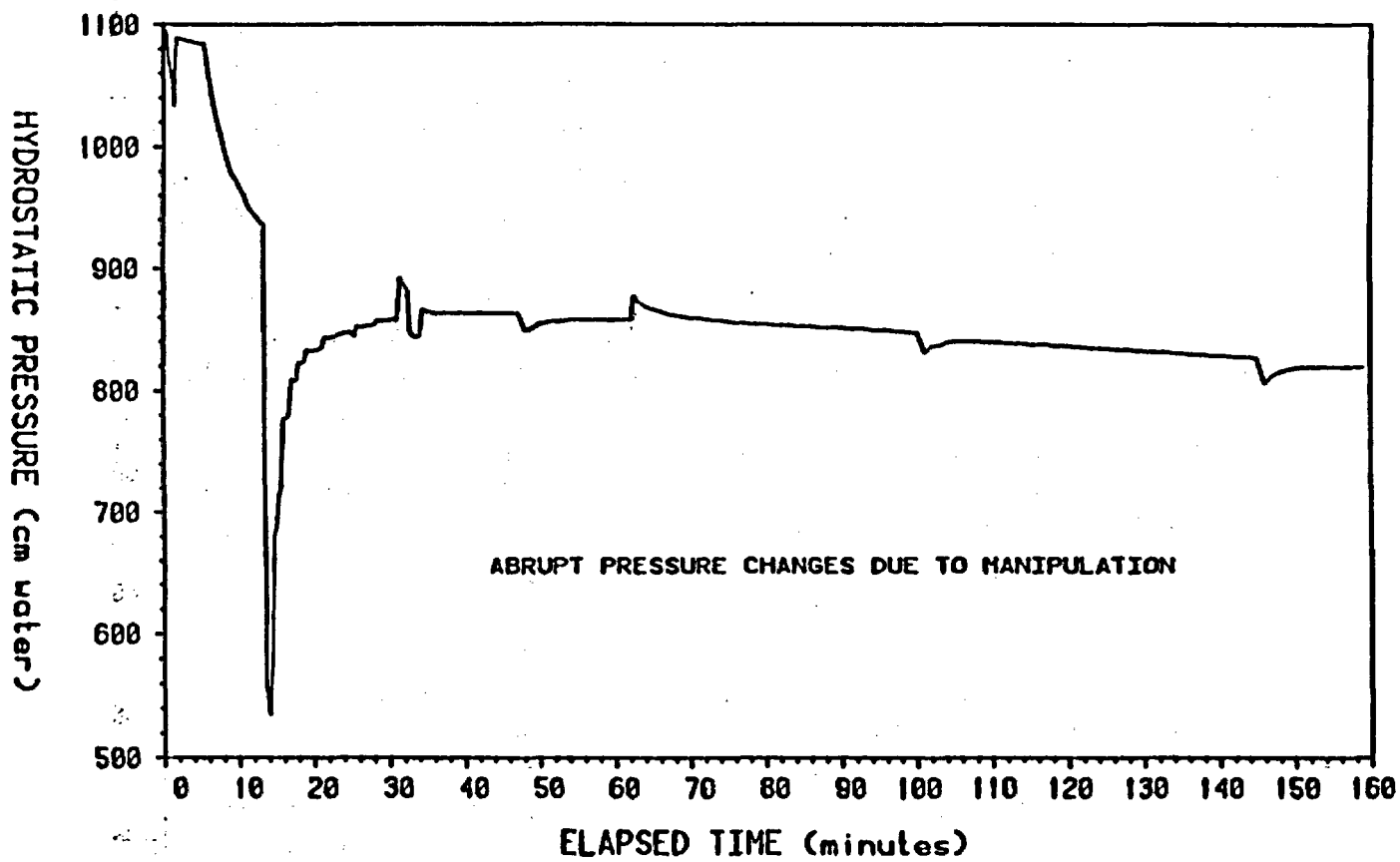


Figure B.7 Tensiometer response in saturated concrete with manual pressure adjustments to facilitate equilibrium.

caused by manually adjusting the pressure in an attempt to shorten the equilibration period and thus minimize the exchange of water through the membrane.

An apparent equilibrium plateau was achieved in less than 40 minutes using the manual nulling procedure. The equilibrium hydrostatic pressure (0.86 bars suction) implies a total moisture potential in the concrete of about 0.17 bar suction. This value is reasonable, although the gradual decline in hydrostatic pressure during the last 120 minutes of the experiment is disturbing.

The pressure decline appears to be associated with an actual decrease in the apparent external moisture potential because the rate of decay remains constant despite the manual introduction of small pressure increases and decreases (see small blips in response curve). Carbowax leakage could again explain the observed decline.

Three additional tests were conducted in saturated concrete using different Carbowax concentrations (i.e., different osmotic potentials) were performed to determine the accuracy of total moisture potential values obtained in initial field and laboratory tests. We anticipated that pressure response curves thus obtained under identical moisture conditions should be offset by values equal to known differences in osmotic potentials of the three Carbowax solutions.

Solutions having potentials of 1, 2, and 5 bars suction were utilized. Results, presented in Figure B.8 were disturbing in that equilibrium hydrostatic pressures of less than 0.5 bar were obtained for all three solutions. These results may imply either that the total moisture potential of the saturated concrete was much lower than anticipated or that the instrument was not responding properly.

The possibility that the saturated concrete was in fact exerting a strong negative potential was tested by sealing thermocouple psychrometers in the borehole as a means of obtaining independent total moisture potential measurements. Results obtained after 9 days and 17 days suggest that the total potential may have been within the range of 1 to 2 bars suction. These results must be interpreted with caution, however, because the accuracy of psychrometric measurements is uncertain in this potential range.

A second method used to isolate the cause of the pressure decay phenomenon was to insert the tensiometer in a piece of PVC pipe (having internal dimensions equal to those of the borehole in the concrete

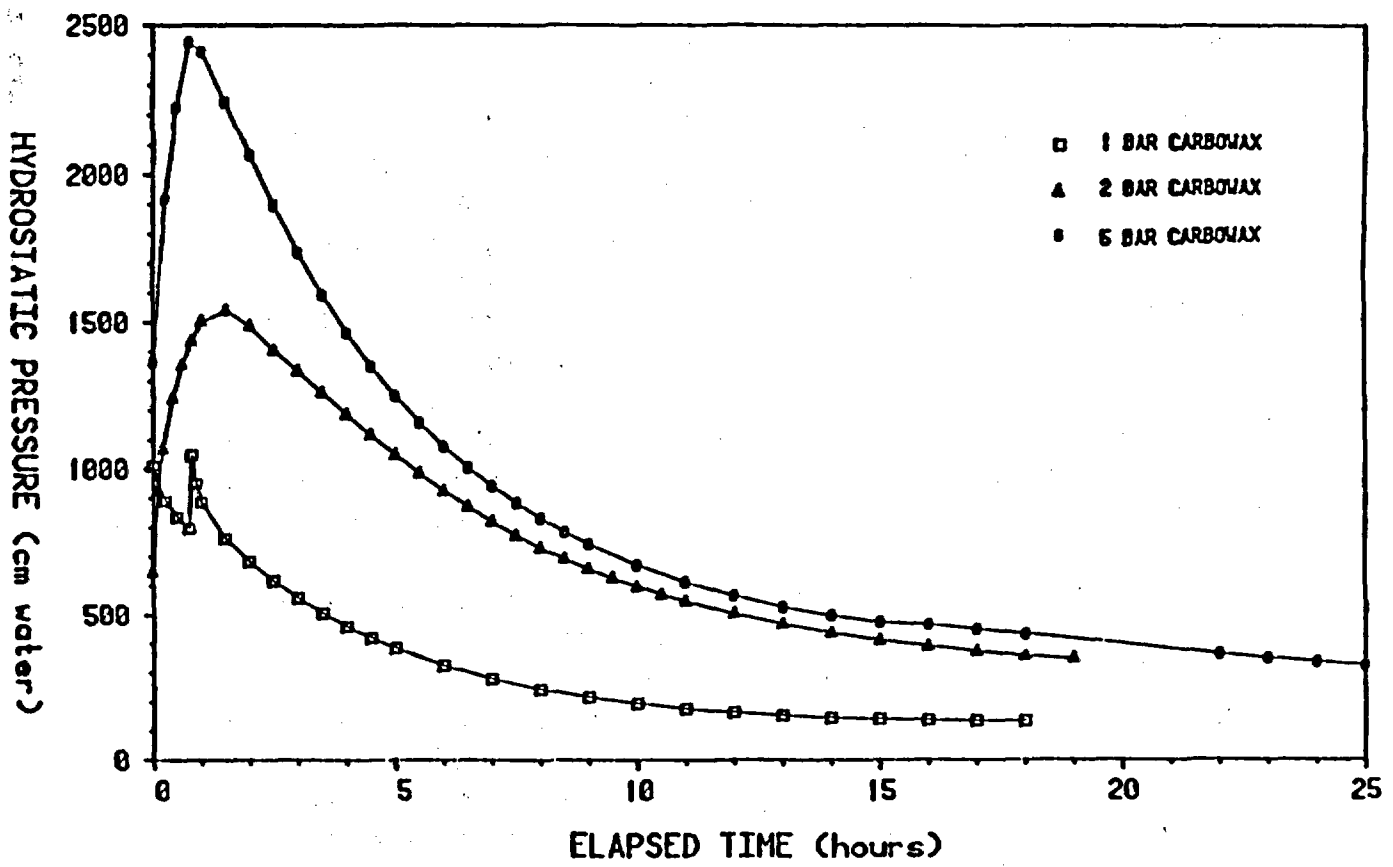


Figure B.8 Tensiometer response in saturated concrete for three different internal osmotic potentials.

block) and then submerge the entire system in water. Assuming that PVC pipe exerts neither matric nor osmotic potentials, then the equilibrium hydrostatic pressure in the tensiometer should have been equal in magnitude (and opposite in sign) to the osmotic potential of the Carbowax solution.

Results of this test, presented in Figure B.9 show a continuous, gradual hydrostatic pressure decay, and indicated that the tensiometer was not responding properly. One possible explanation is the migration of Carbowax molecules through the membrane. Such migration would progressively reduce the concentration gradient across the membrane and would explain the pressure decay observed during laboratory experiments.

## B.5 Field Experiments

### B.5.1 Field Test of Carbowax

Water potential measurements were made in two boreholes in unsaturated, fractured granodiorite at the Santo Nino field site using Spectra/Por 4 dialysis tubing and a 1 bar suction Carbowax solution. Figure B.10 illustrates the resulting response curves.

The initial increase in pressure noted in the curve for Borehole 5.8 is probably due to temperature equilibration (the borehole temperature was higher than that of the Carbowax initially used to fill the device). The response curve for Borehole 5.2 does not show an initial pressure increase because temperature equilibration occurred during a previous measurement in that hole.

A response curve for the previous event is not included because early time data were not recorded. Both response curves included in Figure B.10 indicate gradual pressure decay with time. The experiment in Borehole 5.8 was terminated before equilibration had occurred but the curve for Borehole 5.2 eventually reached an apparent equilibrium value of about 0.2 bars suction, which implies a total moisture potential in the fractured grandiorite equivalent to about 0.8 bars suction. This value was considered reasonable at the time of the measurements were made, but was subsequently judged unreliable due to Carbowax leakage.

### B.5.2 Field Test of PVP

Field measurements were made at the Santo Nino mine in September 1983 using the osmotic tensiometer filled with 40,000 mw PVP solutions. In Borehole 5.8, the hydrostatic pressure decayed from an initial value of

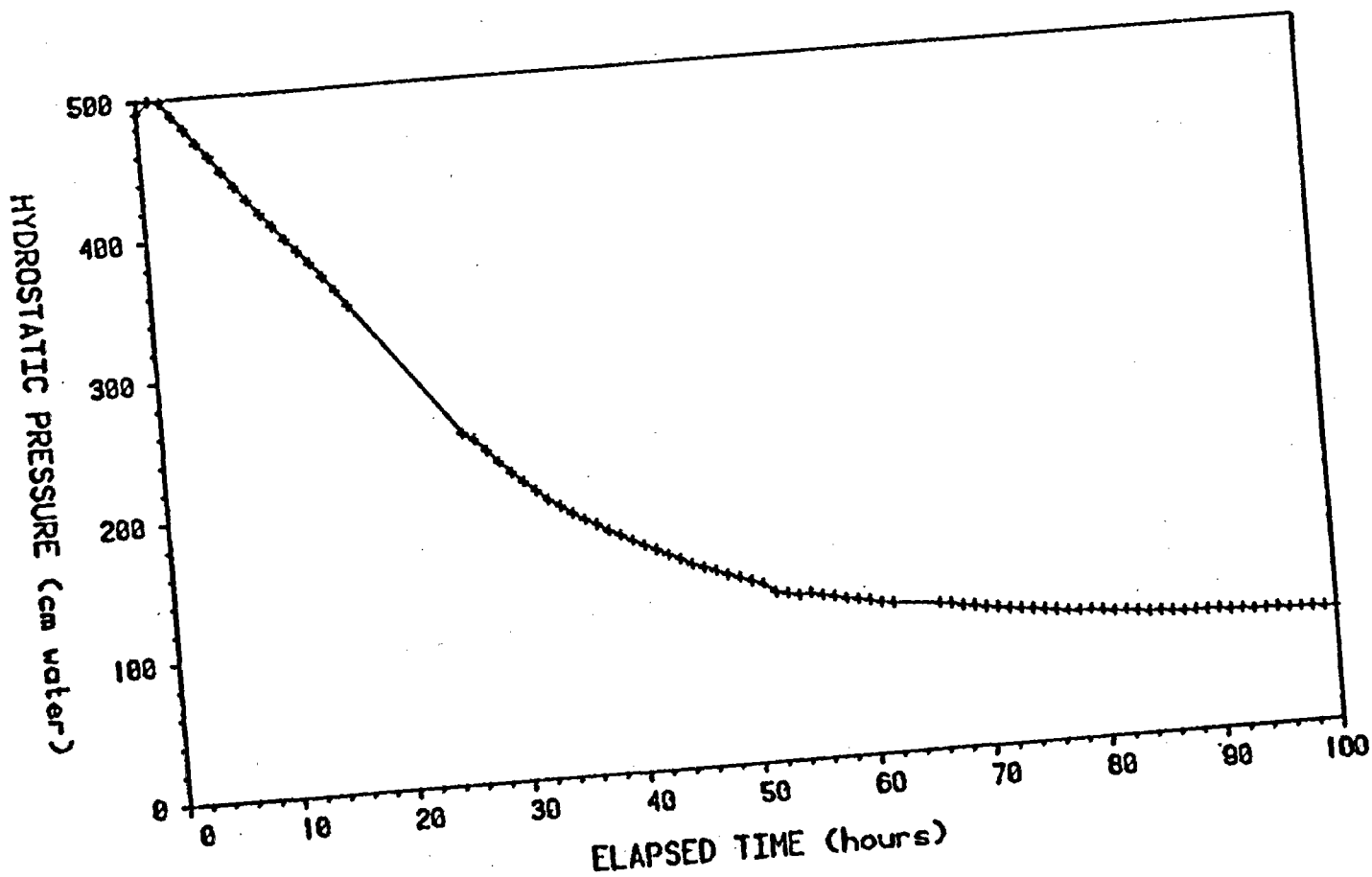


Figure B.9 Tensiometer response in PVC pipe submerged in water.

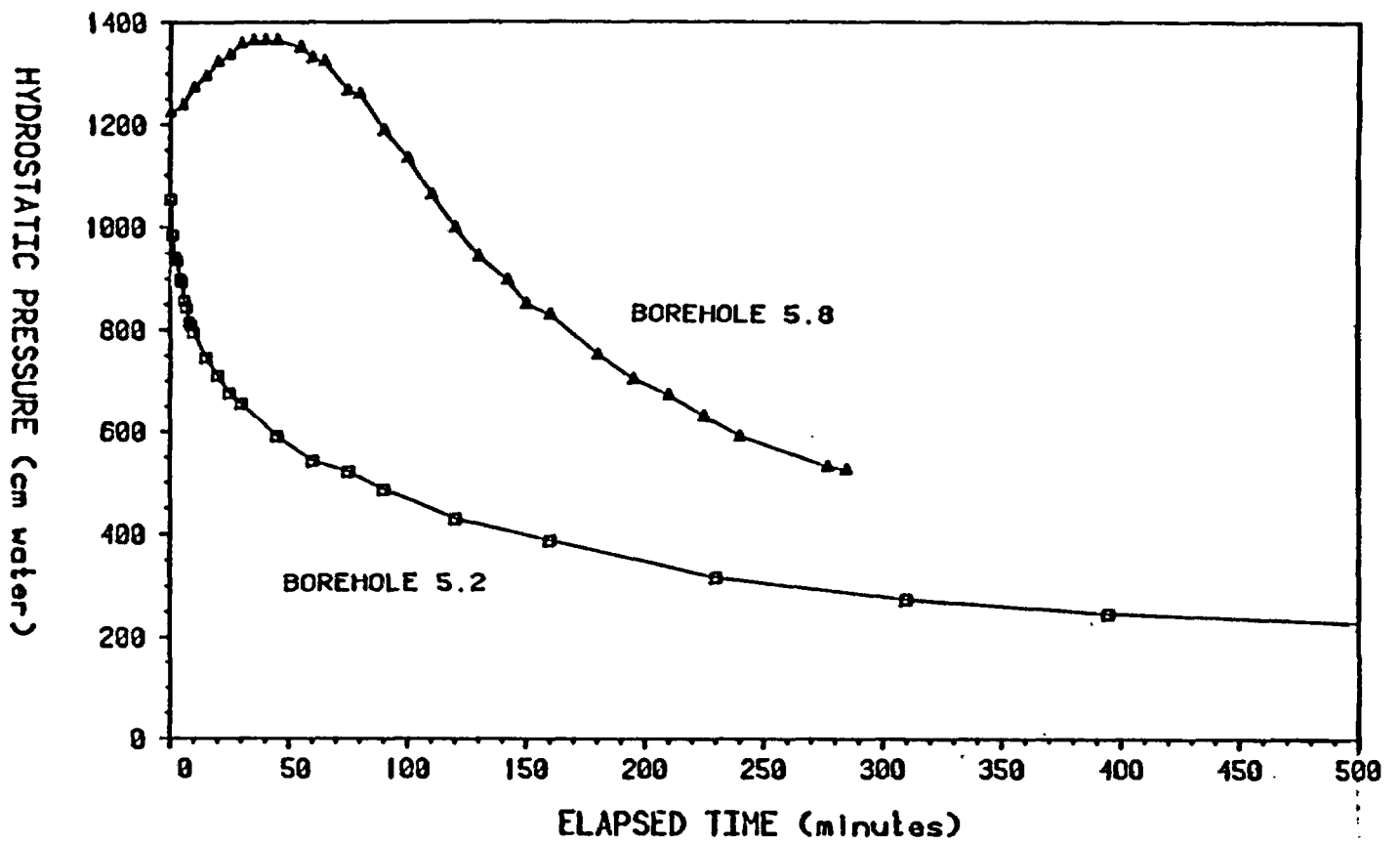


Figure B.10 Tensiometer response curve in fractured granodiorite at the Santo Nino mine. Tensiometer contained a Carbowax solution.

1.29 bar suction (the pressure used to force the PVP solution into the tensiometer) to less than 0.2 bars in about 40 minutes.

This implied that the moisture potential in the borehole was more negative than the osmotic potential of the PVP solution inside the tensiometer (1.88 bars suction). Visual observation of the borehole supported this interpretation as no moisture was visible on the borehole walls and the rock matrix appeared to be dry.

The osmotic tensiometer was subsequently inserted into Borehole 28.3 in an area of the mine where moisture was present on the borehole wall and the granodiorite matrix appeared to be wet. The tensiometer was filled with a PVP solution having an osmotic potential of 1.15 bars suction.

The resulting response curve is presented as Figure B.11. The sharp pressure drop at 7 hours was manually induced to verify that equilibrium had been approximated at that time. The curve suggests that the equilibrium hydrostatic pressure for the system was between 0.35 and 0.38 bars suction.

This result implied that the moisture potential in the fractured granodiorite was approximately 0.785 bars suction, which appears to be a reasonable value. However, in light of subsequent laboratory and field experiments, it is uncertain whether the apparent equilibrium value obtained was real or was due to a leakage problem.

### B.5.3 Field Test of PEO

A field test was conducted in Borehole 28.3 at the Santo Nino mine in June 1984. Spectra/Por 4 dialysis membrane and a 180 g/liter PEO solution were utilized. A protective cotton tube was slipped over the membrane prior to inserting the prototype in the borehole. After the prototype had been filled with the PEO solution, hydrostatic pressure within the device was monitored over a period of 6 days.

Data for the first 24 hours are presented in Figure B.12. Hydrostatic pressure initially increased to a plateau value of 2.31 bars. This plateau, which remained constant ( $\pm .001$  bars) for about 2-1/2 hours, corresponds to the osmotic potential of the PEO solution used to fill the tensiometer. This value is not related to the moisture potential of the host rock; rather it resulted from the flow of water from the initially wet protective cloth tube into the tensiometer (i.e., the tensiometer was initially subjected to artificially saturated conditions).

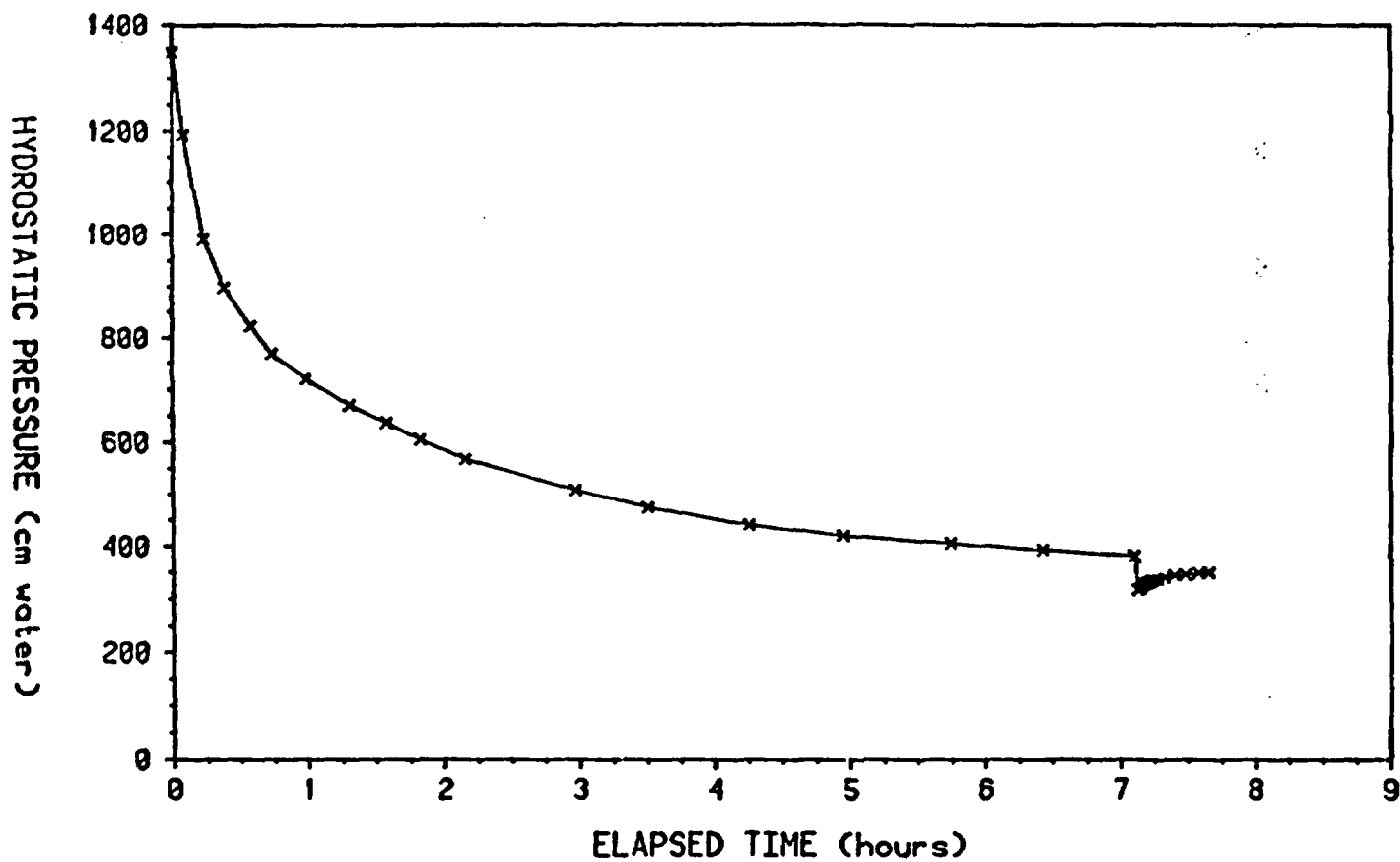


Figure B.11 Response curve for osmotic tensiometer in Borehole 28.3 at the Santo Nino mine. Tensiometer contained a 40,000 mw PVP solution with an osmotic potential equal to 1 bar suction.

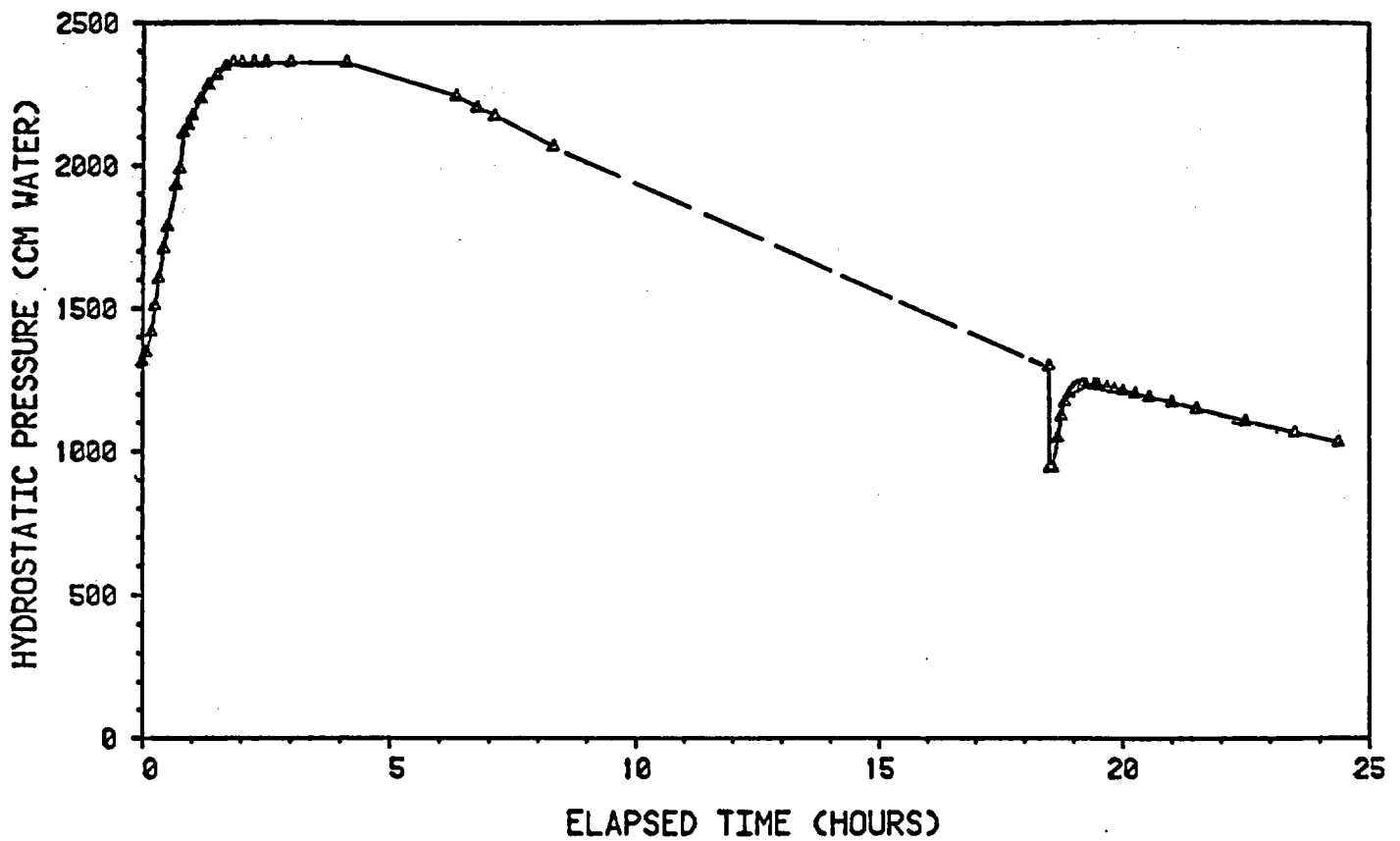


Figure B.12 Response curve for osmotic tensiometer in fractured granodiorite at the Santo Nino mine, Borehole 28.3. Tensiometer was filled with a 200,000 mw PEO solution having an osmotic potential equal to 2.41 bars suction. Pressure drop at 28.5 hours was manually induced.

The ensuing hydrostatic pressure decay was initially interpreted as reequilibration of moisture conditions to their original undisturbed value, but the rate and extent of pressure decay during the next 20 hours cast doubt on the validity of these measurements.

The sharp pressure drop at 18 hours and subsequent recovery was due to an intentional release of a few drops of liquid from the tensiometer. Data for days 2 through 6 are not plotted. The hydrostatic pressure within the tensiometer decayed to less than 0.2 bars during this period, suggesting an unreasonably low moisture potential in the host rock of about 2.15 bars suction.

When the tensiometer was removed from the borehole on the sixth day, a random array of more than a dozen small stains on the protective cloth tube verified that PEO leakage had occurred through small pinholes in the membrane during the measurement period. Even though the utmost care had been taken during the initial insertion of the tensiometer into the borehole, it was concluded that the leakage occurred through existing imperfections in the membrane material.

APPENDIX C  
ABSORBER METHOD FOR MOISTURE POTENTIAL DETERMINATION

This Appendix describes four techniques for the determination of the moisture potential within variably saturated geologic media. All techniques employ a fluid absorber, in most cases a piece of filter paper.

C.1 Ceramic Plate Extractor Method

A ceramic plate extractor (Soil Moisture Equipment Corporation, Santa Barbara, CA) has been used to simulate in situ water potentials in rock and soils. The extractors are limited to a pressure range of 0 to 15 bars suction. Experiments using the ceramic plate extractor involve placement of saturated filter papers on a saturated ceramic plate held within the extractor vessel.

The inner walls of the vessel can be covered with wet paper towels to increase the humidity within the vessel. The vessel is sealed and a pressure applied by means of a nitrogen tank. After a period of at least 24 hours, the pressure is released and the filter papers are quickly put into the sample chambers of the thermocouple psychrometer SC-10A. Assuming equilibrium, the water potential of the filter papers are equal to the amount of applied pressure. Various types of buffers and arrangements of filter papers were made in attempts to mimic applied pressures and increase accuracy of the psychrometer readings.

The ten experiments using this method have been performed with saturated Schleicher and Schuell No. 589 filter papers on a saturated ceramic plate extractor. The filter papers were placed on the ceramic plate with a "buffer" of another filter paper wrapped around them. The results from these experiments are presented in Figure C.1.

Experiments 8, 9, and 10 include columns of saturated silty loam soil on the ceramic plate along with the filter papers. In these experiments, the filter papers and soil samples were placed in separate chambers of the psychrometer to determine their water potentials. Experiments 2, 3 and 5 show the filter papers at higher water potentials (wetter range) than the value of the pressure within the extractor vessel. This discrepancy may be due to an inadequate equilibration time for these samples.

Experiments 4 and 6 through 10 show the filter papers at drier potentials than would be expected from the amount of pressure applied.

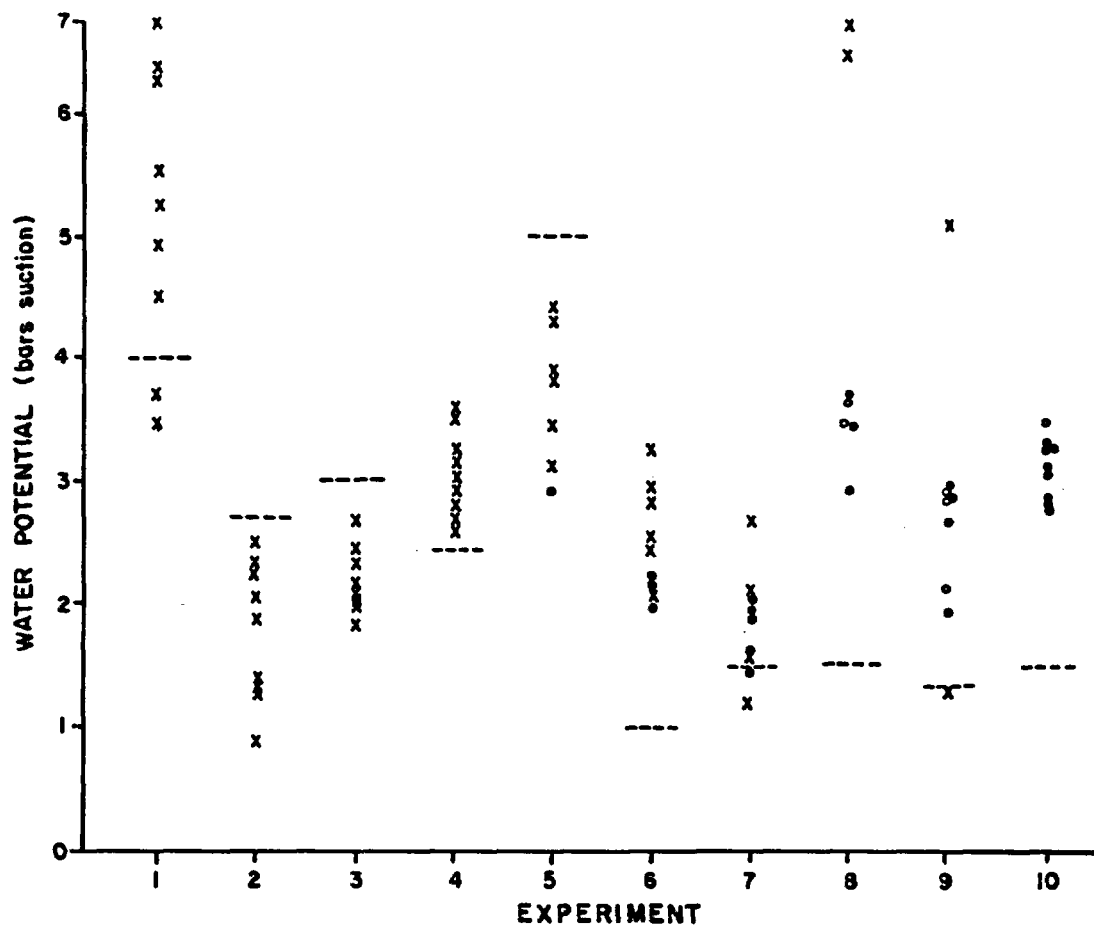


Figure C.1 Results using Schleicher and Schwell filter papers with buffers on a ceramic plate extractor: (x) indicates a single filter paper with a filter paper buffer; (o) indicates a double filter paper with filter paper buffer; (o) indicates analyses performed on a silty loam soil; and (- -) indicates the pressure applied to the ceramic plate.

The samples included with experiments 8 through 10 also give values of lower water potentials than the applied pressure.

Even though the values do not match the applied pressure exactly, the water potentials of the soil samples are very similar to the water potentials of the double filter papers with the filter paper buffers. The deviation of the samples from the applied pressure may be due to evaporation of water from the filter paper while equilibrating in the vessel or when transferring the filter papers to the psychrometer cups.

For Experiments 1 to 10, the walls of the vessel were not covered with saturated paper towels which would have increased the humidity of the chamber and reduce evaporation losses. Still, the theory behind the absorber method is to equilibrate filter papers with porous material or rock at a particular water potential. Experiments 8 through 10, showing good similarity between soil and filter paper, support the absorber method as a feasible approach to measuring water potential.

## C.2 Equilibration of Filter Papers with Soil Samples

Al-Khafaf and Hanks (1974) suggested another method for equilibrating filter papers with soil samples. The method shows the relationship of the predicted water potential of the filter papers as a function of contact with the soil. The method involves equilibrating a soil sample on a ceramic plate extractor and placing the soil in a sample can with filter papers below and above the soil (Figure C.2).

The filter papers are pretreated with a solution of cycloheximide to inhibit bacterial degradation. A rubber cylinder is placed on top of the soil with the filter papers positioned across the cylinder to prevent contact with the soil. This raised filter paper is in vapor contact with the unsaturated soil and measures osmotic and matric potential. The filter paper, in good contact with the soil, only measures the matric potential.

The sample cans are sealed and placed in a constant temperature room to equilibrate. After several weeks the filter papers and a small amount of soil are placed in the cups of the thermocouple psychrometer sample changer to determine their water potentials. Results are presented in Figure C.3.

Experiments 1 and 2 used a sandy loam soil and were set on a porous plate for 72 hours at 2.58 bars of pressure. Experiment 1 appears to simulate the applied pressure very well but calibration results showed

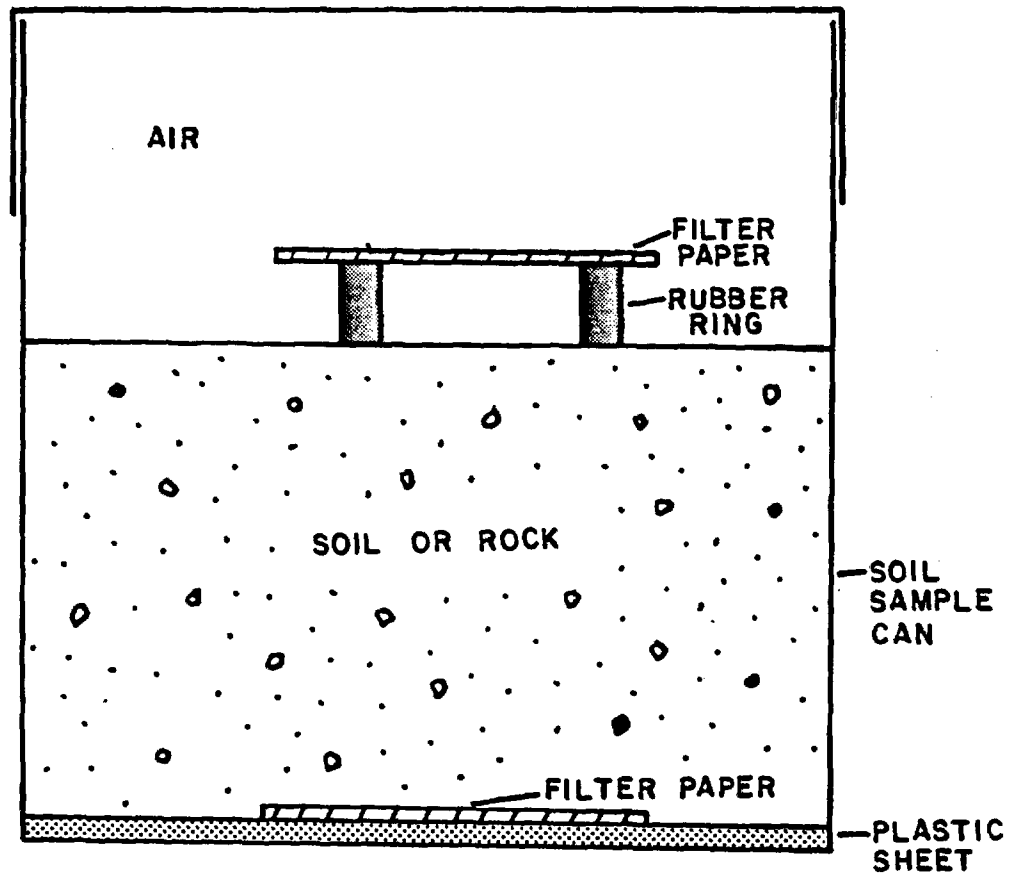


Figure C.2 Cross sectional diagram of experiment used to measure matric potential of soil or rock using a filter paper in good contact (lower), and matric plus osmotic potential using a filter paper not in direct contact (upper).

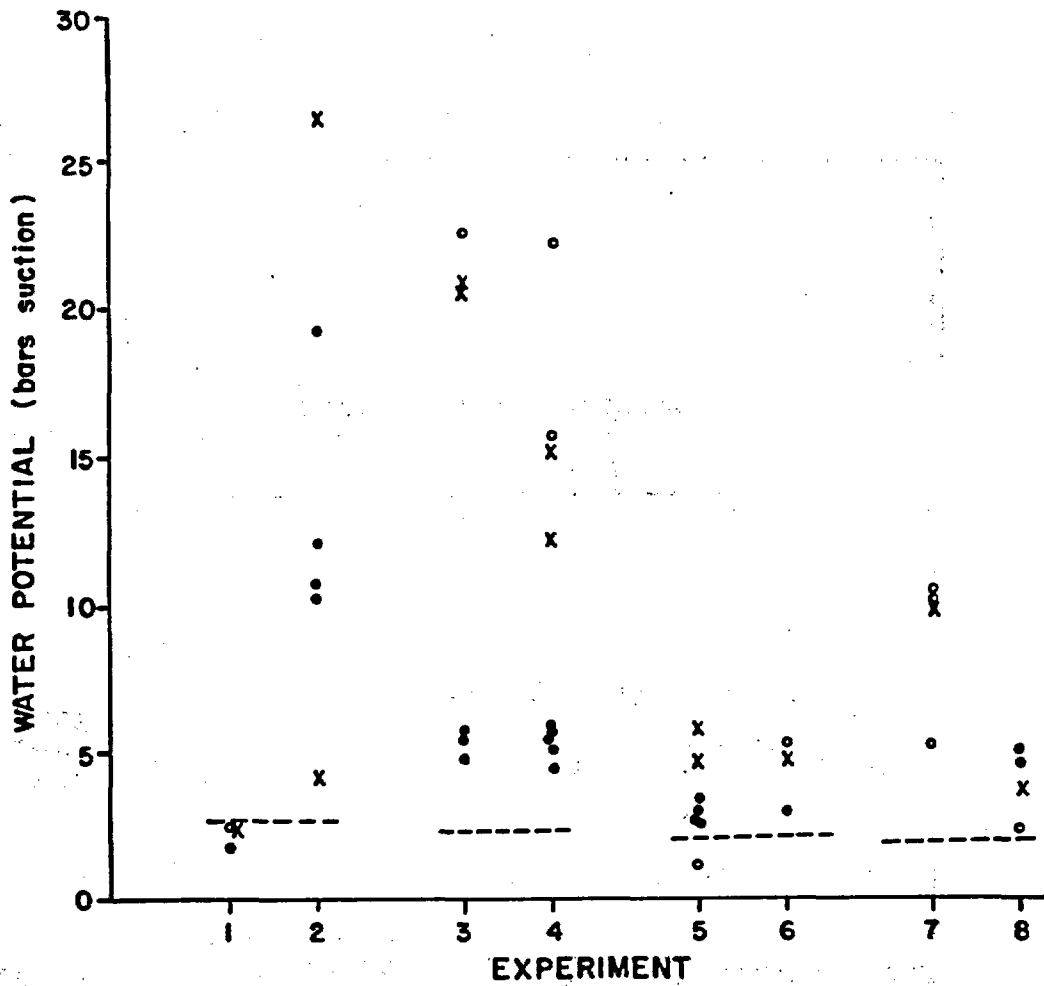


Figure C.3 Results using soils equilibrated on a ceramic plate extractor and filter papers sealed in a sample can in vapor: (•) indicates the soil potential; (+) indicates filter papers in good contact with the soil; (o) indicates filter papers in a sample can in vapor; and (- -) indicates the pressure applied to the soil. Experiments 1 and 2 were performed on a sandy loam, 3 through 6 on a clay loam, and 7 and 8 on a silica sand. The upper data points for experiment 7 are from a disturbed sample.

the thermocouple was not operating properly. The end results from Experiment 2 gave very low water potentials which could be due to the long period of time the sample was left on the ceramic plate allowing evaporation to take place.

A clay loam was used for Experiments 3 to 6. Experiments 3 and 4 were from the same run of the ceramic plate lasting 54 hours at 2.48 bars of pressure. After 8 days of equilibration the water potential of the soil was approximately 5.5 bars suction and the water potential of the filter papers was much less (approximately 21 bars suction). A sample from the same ceramic plate was left for an additional week of equilibration and the filter papers in good contact absorbed a noticeable amount of water which increased the water potential to 12.2 and 15.1 bars suction.

Experiments 5 and 6 show much less scatter of water potential readings where the filter papers in good contact are two bars lower in potential than the soil. The filter paper in vapor contact with soil in Experiment 5 is in error due to condensation on the lid of the sample can wetting the filter paper. The samples that equilibrated for 19 days were very similar in water potential as those left for an additional week of equilibration.

Experiments 7 and 8 used silica sand which was subjected to 2 bars of pressure for 46 hours. The sample can of Experiment 7 was transported which disturbed the sample. This disturbance greatly affected the water potential readings of that experiment. The results from this method suggest that soil samples subjected to pressures of 1 to 3 bars for 24 hours should be left to equilibrate for approximately 20 days. Soil samples should remain undisturbed in a constant temperature room.

Previous authors studying the filter paper method have used various types of filter papers; McQueen and Miller, Al-Khafaf and Hanks used Schleicher and Schuell No. 589, while Hamblin, and Fawcett and Collis-George used Whatman No. 42. To test the variability among different types of filter papers, the filter papers described above were placed on the ceramic plate, a pressure applied, and their water potentials determined in the psychrometer SC-10A. Whatman No. 42, Schleicher and Schuell No. 589, and Millipore filter papers were used in the experiment.

The filter papers which simulate the pressure applied in the extractor vessel with the least amount of variability are the Whatman No. 42 filter papers. Because of this uniformity, the Whatman filter papers were used for most of the experiments.

### C.3 Moisture Release Curves for Filter Papers

Calibration curves relating the water content and water potential of filter papers have been constructed by Fawcett and Collis-George (1967) and Hamblin (1981) for Whatman No. 42, and McQueen and Miller (1968) and Al-Khafaf and Hanks (1974) for Schleicher and Schuell No. 589.

A calibration curve, using similar methods suggested by previous authors, was constructed for Whatman No. 42 filter papers. The volumetric water content is defined using gravimetric weighing, while the water potential is determined by:

- The thermocouple psychrometer; and
- The ceramic plate extractor.

The first method involves wetting the filter papers, which are placed along the inner circumference of the psychrometer sample cups. The cups are placed in an oven at 105°C to dry slightly, cooled for a few minutes, weighed, and quickly placed in the psychrometer vessel to determine the water potential of the filter papers. The procedure is repeated until a range of water potential (e.g., 1 to 3000 bars) has been defined.

The second method does not use the psychrometer but assumes that the pressure applied to the filter papers in a ceramic plate extractor is equal to the water potential of the filter paper. The filter papers are saturated and placed on a saturated porous plate and a pressure applied for approximately 24 hours. The pressure is released and the samples are quickly transferred to small vials and weighed.

The process is repeated using a 15 bar ceramic plate extractor for a potentials from 1 to 15 bars suction and a Tempe pressure cell for filter papers near saturation, e.g., 0.1 to 1.0 bars suction. The use of the ceramic plate extractor is limited on the dry side of the curve by the plate capabilities (0 to 15 bars) and on the wet end by the accuracy of the experimental methods.

Figure C.4 presents results obtained using the two methods and compares them to the calibration curve of Fawcett and Collis-George (1967). Method A shows inconsistent values in the range of 0 to 2 bars suction. This is attributed to the limited ability of the thermocouple psychrometer to measure water potentials near saturation.

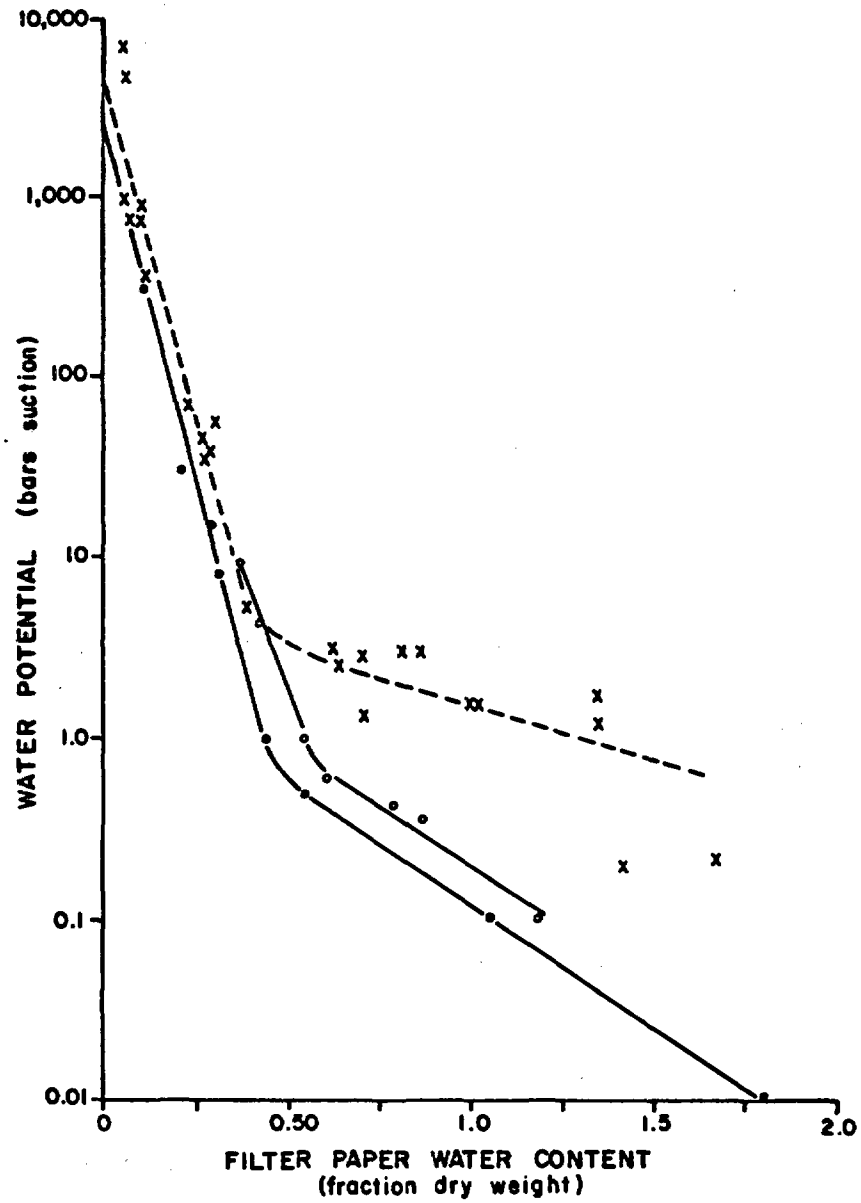


Figure C.4 Moisture release curves obtained from: (•) Fawcett and Collis-George curve; (x) psychrometer; and (o) ceramic plate.

#### C.4 Equilibration of Filter Papers with Rock Samples

For the experiments presented in this section, sandstone and welded tuff slabs of 0.65 cm to 12.5 cm thickness and a diameter of 5.0 cm were used. The rock slabs, saturated in a vacuum dessicator, were placed on a ceramic plate extractor with a pressure equivalent to a desired water potential.

After equilibration with the applied pressure, the rock slabs were placed in soil sample cans with filter papers between each slab. The cans were then sealed and placed in a styrofoam box in a constant temperature room, allowing for equilibration between the rock slabs and the filter papers.

Several weeks later, the water potential of the papers was determined after the filter papers were removed from between the rock slabs and quickly placed in the sample cups of the thermocouple psychrometer. The results of this method are presented in Figure C.5.

Calculating the water content (percent of dry weight) of the filter papers and rock slabs provided insight concerning the discrepancies between the water potential of the filter papers and the pressure applied to the soil and rock samples.

Experiments 2 and 3, using filter papers between the welded tuff, gave very low potentials (drier than applied pressure) which could be due to the rock samples not equilibrating with the applied pressure, or possibly the rock slabs were not initially fully saturated. Sandstone samples, unlike welded tuff, readily absorb water when saturated under negative pressures.

Conversely, when positive pressure is applied, the sandstone also release water more easily than the welded tuff. The results from Experiments 6 to 10 show this relationship; filter papers between sandstone slabs as compared with welded tuff slabs more closely imitate the pressure applied to the rock.

By calculating the water content of the filter papers, plotting the data, and comparing the data with the calibration curve, a judgement can be made concerning the source of error. The error may result from:

- The filter papers are not in equilibrium with the rock slabs;
- The inaccurate readings of the psychrometer; or
- The rock samples are not in equilibrium with the pressure applied.

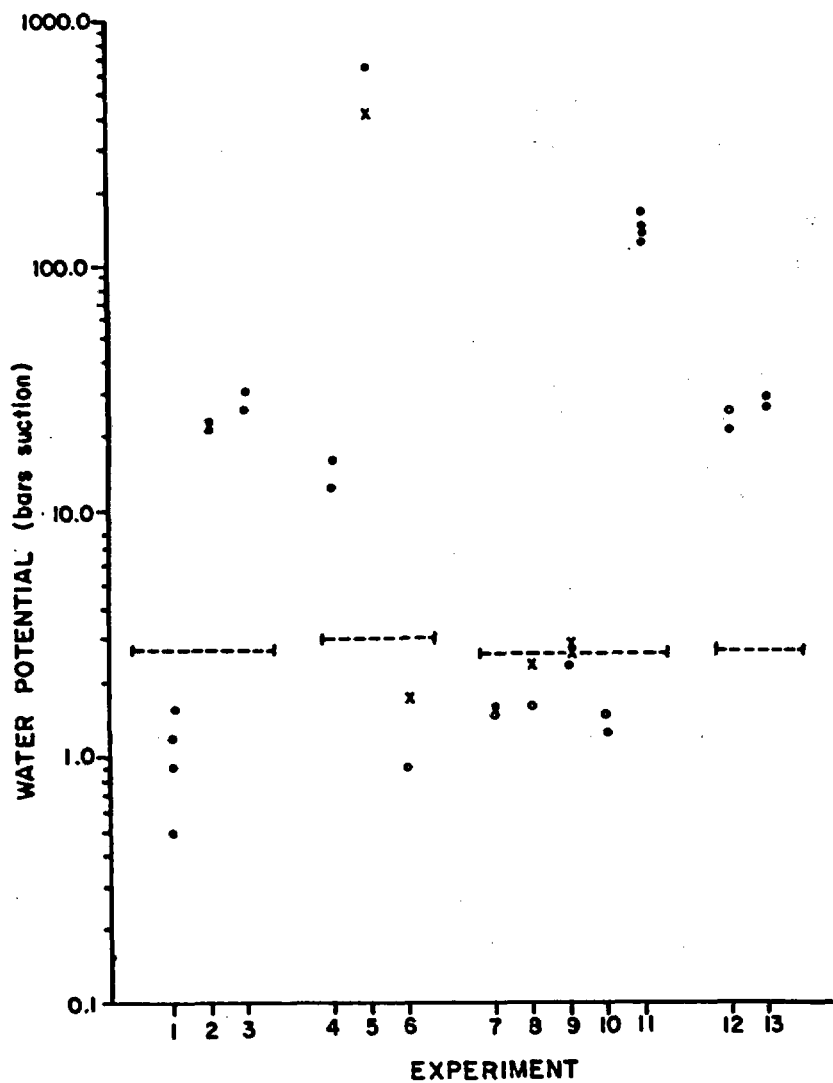


Figure C.5 Three types of filter paper; (x) Millipore, (•) Whatman No. 42, and (o) Scheicher and Schuel, were placed between sandstone or welded tuff slabs. The rock slabs were saturated and placed on a ceramic plate extractor to induce a matric potential. The applied potential is noted by (- -). The rocks were placed in sample cans with filter papers between the rocks. 22 to 36 days were allowed for equilibration. The filter papers were removed and placed in the thermocouple psychrometer to evaluate their water potential.

For example, Experiment 5 showed water potentials of filter papers of 423 and 650 bars suction while the applied pressure was only 3 bars on the sandstone slabs. Experiment 6 had the same applied pressure with water potentials of filter papers of 0.9 and 1.7 bars suction.

Although there is a large variance of water potentials of filter papers for similar samples, when the filter paper water content was calculated and the data plotted on the moisture release curve (Figure C.4), the two extreme values both correlate well with the calibration curve. Thus, the rock slabs in Experiment 5 were not in equilibrium with the applied pressure but of much lower water potential which was correctly estimated with the filter papers and psychrometer. The average water content, percent of dry weight, was evaluated for the sandstone slabs of Experiments 5 and 6. Sandstone of Experiment 5 has an average water content of 0.12 percent, and Experiment 6 yielded an average water content of 1.85 percent, dry weight. The large differences in water content are consistent with the water potential differences. Thus, the error is not due to the filter papers, but is related to the sandstone slabs. Experiment 5 slabs were not sufficiently saturated prior to equilibration in the ceramic plate extractor.

In Figure C.5, the results of this method, in which both water content and water potential of the filter papers were known, a moisture release curve of the filter papers was plotted along with the calibration curves from Figure C.4. The filter papers of water potentials drier than 2 bars suction fit the calibration curve very well. Increased scattering of results occur at water potentials near saturation (i.e., 0 to 2 bars suction). The scattering is attributed to the inability of the thermocouple psychrometer to measure water potentials near saturation.

The good correlation between the water potential of filter papers equilibrated with rock slabs and the calibration curve prove that the absorber method is a valid approach to measuring water potentials drier than 2 bars suction. Other methods, such as the osmotic tensiometer, are being developed to measure water potentials near saturation.

APPENDIX D  
LABORATORY DETERMINATION OF MOISTURE RELEASE CURVES

This Appendix presents three methods for the determination of moisture release curves in the laboratory.

Pressure Plate Extractor: To prepare samples for use on a ceramic plate extractor, samples are oven-dried, weighed, saturated, and the saturated weight recorded. The samples are then placed on a saturated 15-bar ceramic plate. To assure good contact between the samples and the ceramic plate, 1 to 3 gm of bentonite clay is placed between the sample and the ceramic plate. The ceramic plate and samples are sealed inside the extractor vessel and a positive pressure is applied within the vessel using a tank of pressurized nitrogen gas. As the pressure increases in the vessel, water in the saturated rock sample moves out of the sample through the ceramic plate and is collected in a burette outside the vessel.

When the water level in the burette remains constant for several hours, the sample is assumed to be in equilibrium with the applied pressure. The pressure is then released and the samples are removed from the vessel and immediately weighed. The samples are resaturated, again placed in the pressure vessel, and the procedure repeated until the desired range of pressure head (suction) values are determined. The range of pressure evaluated is limited by the properties of the ceramic plate (i.e., a 15-bar pressure plate is limited to the range of from 0 to 15 bars suction).

Tempe Pressure Cell: Used to measure the saturated hydraulic conductivity and the moisture release curve for the range of 0 to 10 bars suction. This method is presented in Gardner (1956).

Psychrometer Method: The moisture release curve for several tuff samples were defined using a thermocouple psychrometer SC-10A (Decagon Devices Inc., Pullman, WA). All samples were vacuum saturated, cleaned of free water, weighed, and placed in a vapor-tight chamber in the thermocouple psychrometer. After approximately one hour, during which time the samples were allowed to equilibrate thermally, the water potential of the sample was indirectly measured with the small thermocouple psychrometer. The samples were removed, oven-dried at 105°C for 5 to 10 minutes, allowed to cool and weighed again. This process was repeated for different degrees of saturation. Moisture content was determined gravimetrically, and the water potential was determined with the thermocouple psychrometer.



## APPENDIX E DRILLING TECHNIQUES

Boreholes provide access into the host rock for observation of fracture spacing, aperture, and orientation, for insertion of probes for measuring various parameters (e.g., neutron probe, electrical resistivity probe, thermocouple psychrometer, and osmotic tensiometer), and for possible future mass and heat flow experiments. Existing boreholes may be utilized where possible, but more information can be obtained by coring new holes at locations selected specifically to meet the requirements of planned experiments.

### E.1 Santo Nino Mine and Queen Creek Road Tunnel Sites

It is desirable when drilling in unsaturated fractured rock to minimize the disturbance of existing moisture conditions. At the Santo Nino mine, we initially drilled with air as a coolant to avoid introducing water into the rock mass. However, we were forced to abandon this approach because excessive heat was generated in the drilling process. When drilling at the lowest drill advance speed (600 revolutions per 2.5 cm bit advance) and with frequent stopping and starting of the drill, the heat caused excessive wear of the drill bit and possibly resulted in drying of the host rock.

Subsequent drilling was conducted using water to cool the bit and flush cuttings out of the borehole. This method invariably forced water into open fractures which intersected the borehole, but probably did not cause significant wetting of the rock matrix due to the extremely low permeability of the granite. Sufficient time must be allowed after drilling and flushing a borehole with water to allow re-equilibration of "natural" moisture conditions prior to conducting planned experiments.

During the Santo Nino mine and Queen Creek road tunnel drilling projects, a column-mounted high speed, rotary diamond drill was used. The drill was powered by a double-helical air motor (with air requirements equal to  $0.011 \text{ m}^3/\text{sec}$  per hp), had variable bit rotation speeds (0 to 1800 rpm), variable bit advance rates (200, 300, 450, and 600 revolutions per 2.5-cm bit advance), and a capacity depth rating of 300 m.

Diamond drill bits (which conform to Diamond Core Drill Manufacturers Association AW size standards) and core barrel were utilized, providing a borehole diameter of 4.8 cm and a core diameter of 2.89 cm. Required accessory equipment included an air compressor, air and water line and

hose, air line lubricator, drill rod, pin to pin couplings, water pump, and mounting column.

At the Santo Nino mine, a total of eight boreholes were drilled vertically into the mine ceiling and at various angles into the mine walls to orient the holes orthogonal to major joint sets. Holes were drilled in pairs (50 cm apart) to depths of approximately 6 meters. Cores were taken in 1.5 meter lengths. Core orientation was maintained to a maximum possible depth by scribing a vertical line on the mine wall through the center of the borehole prior to the onset of drilling.

A total of four horizontal boreholes, ranging in depth from 15.0 to 16.0 meters, were drilled at the Queen Creek road tunnel site. These boreholes were also installed in parallel sets of two. Borehole 1 was adjacent to Borehole 2, and Borehole 3 was adjacent to Borehole 4. A distance of approximately 30 meters separates the two sets from each other in the road tunnel. Boreholes 1 and 2 are located 0.89 m from each other, and a distance of 0.91 m separates Boreholes 3 and 4.

All of the boreholes discussed above were cored using a 1.97 meter long Christensen AWD4 conventional core barrel. The hole size cut by the impregnated diamond bit was 4.8 cm in diameter and the core produced was 2.89 cm in diameter. The AW borehole diameter (4.8 cm) was selected because it is large enough to facilitate the insertion of probes needed for future experimental work without creating large air space volumes which might adversely affect measurements. Boreholes were drilled in parallel pairs to facilitate determination of fracture orientation and to provide access for possible future tracer and/or gas flow experiments.

Core orientation is essential for subsequent determination of the spatial orientation of fractures intersecting the core. However, orientation of the core is difficult to preserve during the drilling process if a conventional core barrel is used. Some success in orienting the cores was obtained by marking the core stub at the start of each shift. This method produced between 1.0 and 4.5 meters of oriented core by matching successive core pieces.

Orientation was often lost when highly fractured areas were encountered or when grinding of the core due to overcoring occurred. Re-establishment of orientation was attempted by marking the core stub at the bottom of the hole, but this was rarely successful or considered reliable.

## E.2 Apache Leap Site

To preserve core orientation, cores from the three boreholes at the Apache Leap site were scribed with an orienting tool. The boreholes are inclined at an angle of  $45^\circ$  from the vertical and are offset from each other by a vertical distance of 10 meters. The boreholes vary in length from 18.3 meters for the uppermost (X-1), to 46.6 meters for the lowermost (X-3), with the intermediate borehole (X-2) having a length of 32.6 meters. This design allows for the monitoring of fluid and solute flow in both the horizontal and vertical directions.

The wire line diamond drilling, contracted to Muncy Drilling, Inc., Phoenix, Arizona, used Longyear manufactured surfaces set HQ oversized corebits; a stabilizer fitted to the hole size was run on top of the core barrel to hold the hole straight. The drilling equipment consisted of a Longyear model 38 drill adapted for angle and vertical drilling and a 1000 gallon water tank that provided the water used as the drilling fluid. The scribe orienting tool used to preserve core orientation is manufactured by Allied Machine Works, Phoenix, Arizona.

The two shallowest boreholes (X-1 and X-2) were drilled using a specially made HQ oversized diamond bit, 10.2 cm in diameter, and a standard HQ core barrel, 1.5 m long and 6.4 cm in diameter. The deepest borehole (X-3) was drilled to a borehole length of 13 m with these same specifications, however, due to excessive wearing of the bit, a standard HQ oversized bit 9.9 cm in diameter was used to drill the remaining 33.6 meters. The HQ size drilling was selected to minimize breakage of the core in the core barrel and thus preserve fracture orientation. Core recovery for the three boreholes averaged 95 percent.

APPENDIX F  
LABORATORY METHODS INVESTIGATING VOLATILE TRACERS

The laboratory methods described in this Appendix were used to determine whether gaseous sampling of a volatile fluorocarbon tracer, in equilibrium with the liquid phase, can be used to predict the rate of liquid redistribution (i.e., the liquid travel time). A major advantage of a volatile tracer method is that the tracer can be transported in the soluble phase and sampled in the gaseous phase, thereby eliminating the difficult process of trying to extract a liquid sample from an unsaturated rock formation.

### F.1 Gas Chromatography

Fluorocarbon compounds were used as hydrologic tracers in both the laboratory and field experiment. These compounds are man-made, first produced in the late-1930's. They are used as propellants, refrigerants, and solvents. A list of their physical properties is given in Table F.1. Table F.2 gives an explanation of the toxicity group classification.

Fluorocarbons were chosen because they:

- Are generally considered to have a low toxicity;
- Have low surface energies, therefore are not likely to adsorb onto soil particles; and
- Have a high affinity for electrons making them suitable for analyses using electron capture detection gas chromatography, which can detect fluorocarbons at concentrations as low as one part per trillion.

BCF, F-22, and SF<sub>6</sub> were selected for initial testing. Factors in selection of these compounds were:

- A boiling temperature greater than the ambient air temperature;
- A critical temperature greater than 50°C; and
- They are partially soluble in water.

Critical to the use of fluorocarbon tracers is the development of an analytical procedure for determining fluorocarbon concentrations using a gas chromatograph. For this study, a Hewlett-Packard 5700A Series gas chromatograph was used with a Carbopack 1% SP1000 column. Because SF<sub>6</sub> has a very fast elution time, a low column temperature was used. The low temperature, however, retarded the late eluting peaks, requiring an increased time interval between sampling and decreasing the sampling frequency. A sample chromatogram is presented in Figure F.1.

-----  
 Table F.1 Properties of possible fluorocarbon tracers.  
 -----

Tracer	Formula	Boiling Temp °C	Critical Temp °C	Solubility Wt. %	Toxicity *
F-11	CCl <sub>3</sub> F	23.82	198	.011	5a
F-12	CCl <sub>2</sub> F <sub>2</sub>	-29.79	112	.028	6
F-13	CClF <sub>3</sub>	-81.4	28.9	.009	Prob. 6
F13B-1	CBrF <sub>3</sub>	-57.75	67	.03	6
F-14	CF <sub>4</sub>	-127.96	-45.67	.0015	Prob. 6
F-21	CHCl <sub>2</sub> F	8.92	178.5	.95	4-5
F-22	CHClF <sub>2</sub>	-40.75	96	.30	5a
F-23	CHF <sub>3</sub>	-82.03	25.9	.10	Prob. 6
F-112	C <sub>2</sub> Cl <sub>4</sub> F <sub>2</sub>	92.8	278	.12	4-5
F-113	C <sub>2</sub> Cl <sub>3</sub> F <sub>3</sub>	47.57	214	.017	4-5
F-114	C <sub>2</sub> Cl <sub>2</sub> F <sub>4</sub>	3.77	145.7	.013	6
F-114B2	C <sub>2</sub> Br <sub>2</sub> F <sub>4</sub>	47.26	214.5	---	5a
F-115	C <sub>2</sub> ClF <sub>5</sub>	-38.7	80	.006	6
F-116	C <sub>2</sub> F <sub>6</sub>	-78.2	19.7	---	Prob. 6
12B1 (BCF)	CClBrF <sub>2</sub>	-3.98	153.9	---	Non Toxic

-----

\* Underwriters Classification, see Table F.2.

-----  
Table F.2 Underwriters' laboratories' classification of comparative  
life hazard of gases and vapors. (From Handbook of Chemistry  
and Physics, Chemical Rubber Company, 1979-80)  
-----

Group	Definition
1	Gases or vapors which in concentrations of the order of 1/2 to 1 percent for duration of exposure of the order of 5 minutes are lethal or produce serious injury. Example: Sulfur dioxide
2	Gases or vapors which in concentrations of the order of 1/2 to 1 percent for durations of exposure of the order of 1/2 hour are lethal or produce serious injury. Examples: Ammonia, Methylbromide
3	Gases or vapors which in concentrations of the order of 2 to 2-1/2 percent for durations of exposure of the order of 1 hour are lethal or produce serious injury. Examples: Carbon tetrachloride, Chloroform
4	Gases or vapors which in concentrations of the order of 2 to 2-1/2 percent for durations of exposure of the order of 2 hours are lethal or produce serious injury. Examples: Dichloroethylene, Methylchloride, Ethylbromide
4-5	Appear to classify as somewhat less toxic than Group 4. Example: Methylene chloride
5a	Gases or vapors much less toxic than Group 4 but more toxic than Group 6. Example: Carbon dioxide
5b	Gases or vapors which available data indicate would classify as either Group 5a or Group 6. Examples: Ethane, Propane
6	Gases or vapors which in concentrations up to at least about 20 percent by volume for durations of exposure of the order of 2 hours do not appear produce injury. Example: Many Refrigerants

-----

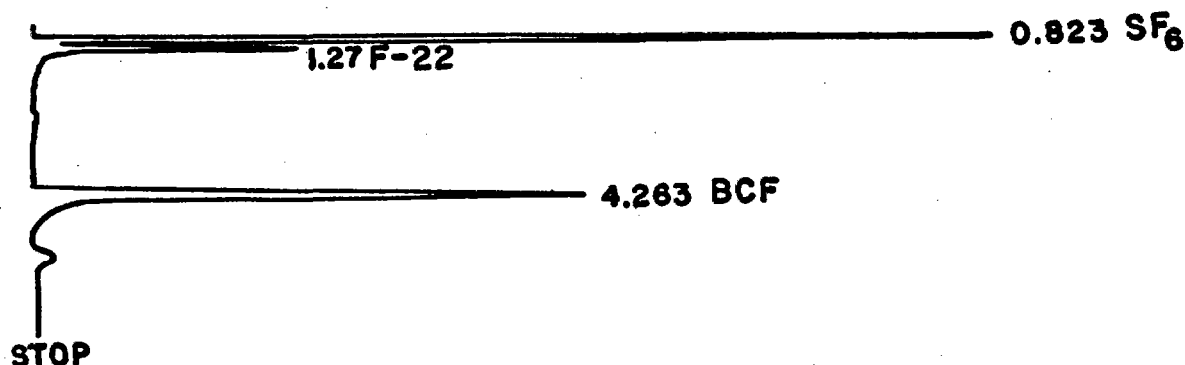


Figure F.1 Sample chromatogram showing the three fluorocarbon tracers used in study. Analyses were performed using a Hewlett-Packard 5700A series gas chromatograph with a Carbopack, 1 % SP1000 column at 60°C.

Each tracer must be calibrated to ensure that there is a linear relationship between area counts on the chromatogram and the concentration of the tracer. Calibrations must also be made every time the chromatograph is used because changes in electron capture detector sensitivity and column sensitivity can occur. Each test requires that five, point calibrations be made. In addition, a correlation coefficient (which describes the degree of linear relation between two variables) between area counts and concentration must exceed 0.98. Usually, this value was not too difficult to attain.

Tracer standards were prepared differently for each fluorocarbon gas. BCF standards were prepared by Matheson Gas Company at a concentration of 1 ppm. This standard was injected directly into the gas chromatograph. No pre-made standards were available for F-22 and SF<sub>6</sub>. Standards were made for F-22 by following EPA standard method Number 601. This method requires that a 10 ml flask be filled with approximately 9.8 ml of methanol and weighed.

After weighing, pure F-22 gas is slowly syringe injected into the methanol, the syringe needle being held just above the methanol surface. The flask is re-weighed to determine the amount of F-22 caught in the sample. Finally, the flask is filled to the 10 ml line with methanol, shaken lightly but not stirred and transferred to an air-tight vial. The methanol solution is then injected into the gas chromatograph.

SF<sub>6</sub> standards could not be prepared in the manner described above. Instead, 250 ml air-tight glass canisters with septums were used to prepare SF<sub>6</sub> standards. The canisters were cleaned and nitrogen purged while oven-dried. One microliter of pure gas was injected into the sealed canisters. After eight hours syringe samples of standard were extracted through the septum and injected into the gas chromatograph.

Napheon tubing, which allows water and other polar molecules to diffuse out of the tubing, was required because water samples degrade the sensitivity of the column.

### F.2 Batch Test Procedure

In order to quantify the tracer sorptive behavior of a particular soil, K<sub>s</sub> values must be known. BCF and SF<sub>6</sub> tracers have been studied and partition coefficients have been published (Kreamer, 1982). Distribution products for F-22 had to be determined for this study. To accomplish this, stainless-steel canisters with injection ports for tracer introduction were used. These canisters were filled with a known amount of soil so that the exact amount of air space within the air tight canister was known. Tracer gas was introduced into the soil canisters and allowed to equilibrate.

After equilibration, syringe samples of soil were removed and injected into the gas chromatograph. K<sub>s</sub> values can be calculated because the amount of tracer gas injected is known and the concentration of the tracer in the soil gas is measured. The entire test procedure is summarized in Table F.3. A K<sub>s</sub> value determined for F-22 using Highland wash soil with 10 percent water content was 0.659 cc gas/gm solid.

### F.3 Column Test Procedure

The experimental set up of the soil column is shown in Figure F.2. The column used for the volatile tracer study was 200 cm in length, 10.4 cm in diameter, and made out of glass. A glass column was used to reduce sorption. Because fluorocarbon compounds readily adsorb to Teflon and other plastics, these materials were avoided during the test.

-----  
**Table F.3 Procedure for batch test determination of distribution coefficients.**  
 -----

- Remove volatile organics from soil by purging canisters with nitrogen a 150°C for three days.
- Leave nitrogen gas in containers at atmospheric pressure to simulate subsurface pressure conditions.
- Syringe inject water into canister. Water should be purified by purging with helium for 24 hours.
- Let water equilibrate for 24 hours in canisters.
- Inject tracer into canister through foil septums to avoid adsorption on the Teflon septums, making sure that the injection syringes are clean by heating in an oven at 50°C.
- Let canisters equilibrate for 8 hours.
- Syringe inject a portion of the soil gases into the gas chromatograph using a clean syringe.
- Replace foil septums on canister, purge with nitrogen and restart.

-----  
 Highland Wash sand was used to fill the column. The sand was passed through a Number 5 screen and then funneled into the glass column using a tremy tube. The tremy tube was used to help avoid layering of the soil during packing. The soil is primarily a medium- to fine-grained sand. A sieve analysis of the soil is presented in Table F.4.  
 -----

-----  
**Table F.4 Sieve size analysis for the sand used in the column study**  
 -----

Sieve Number	Sieve Size	Amount Passing
5	4. mm	100 percent
10	2.	86
14	1.4	74
30	0.6	29
60	0.25	3
120	0.125	0.3
200	0.075	0.0

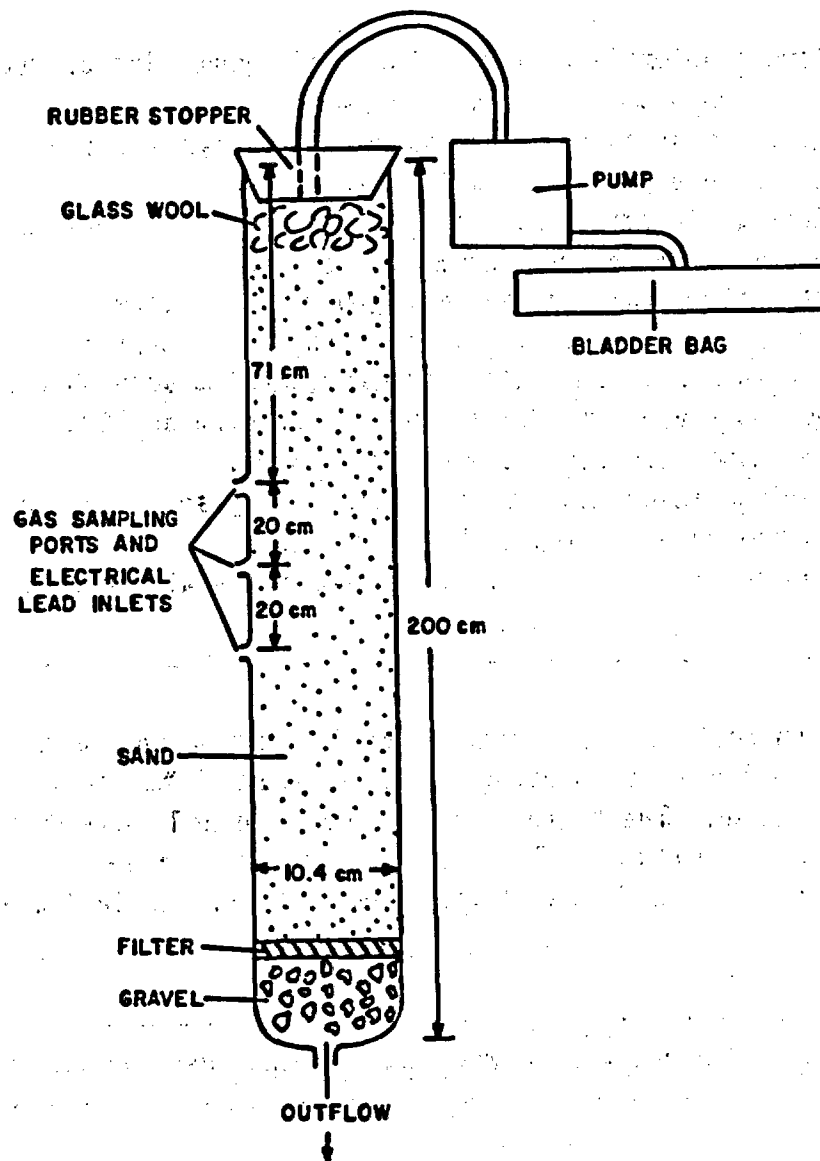


Figure F.2 Diagram of soil column test apparatus. Glass column was necessary in order to reduce sorption. Three sampling ports were used to extract gas samples. These ports were also used to take resistivity measurements needed to obtain chloride ion measurements. Chloride ion was used to monitor the movement of the water. The volatile tracer and chloride ion solution was introduced into the system using a Teflon bladder bag which collapsed as water was pumped out of the bag, thus keeping the system air-tight.

Water was pumped through the column using a peristaltic pump connected to a closed water reservoir. When the outflow of water at the bottom of the column reached a steady-state condition, tracer water was substituted in the system. A Teflon bladder bag was used to store the volatile tracer. As tracer was withdrawn during the test the bag collapsed. The tracer delivery system was air tight and did not allow for the tracer to volatilize before percolating into the column.

A tracer solution was prepared depending on the type of tracer used. BCF tracer solution was made by bubbling a 1 ppm standard through a covered vial of methanol for at least eight hours. The methanol concentrated the volatile gas in a soluble phase more effectively than water. This achieved higher concentrations in the initial tracer solution. F-22 and SF<sub>6</sub> tracer solutions were prepared by bubbling pure gas into 10 ml of methanol. All tracers that were concentrated in the methanol were then diluted with water. Commonly, 10 ml of methanol was used per 1000 ml of water.

The test procedure is presented as Table F.5.

-----  
Table F.5 Procedure for soil column test.  
-----

- Turn on peristaltic pump and measure outflow.
  - Let water percolate until the outflow rate of water at the bottom of the column becomes constant.
  - Prepare tracer standards.
  - Calibrate standards on gas chromatograph.
  - Take gas samples from each port to obtain initial concentration of tracer before test starts.
  - Take resistivity measurements to get background values for chloride concentration.
  - Substitute tracer water into column system.
  - Take sample of tracer solution just before tracer water percolates into column.
  - Take resistivity measurements at regular intervals.
  - Take periodic gas samples from column using a syringe.
-

#### F.4 Computer Modeling of Laboratory Experiment

When this technique is used in the field, sampling of the water will not be possible, therefore, there can be no direct comparison of the gas breakthrough with water percolation rate. By using a computer model and the breakthrough curve of the volatile tracer simulation of the water percolation rate is possible.

The discrete state compartment (DSC) model was used because of its simplicity and the ability to run the model on a microcomputer. Dr. Eugene S. Simpson of the University of Arizona originally proposed the DSC model uses a series of cells or compartments to represent a hydrologic system. An iterative equation combines cell inputs, sources and sinks with a masses balance equation in order to generate a flow system:

$$(F.1) \quad S(n) = S(n-1) + [BRV(n) * BRC(n)] - [BDV(n) * BDC(n)] \pm R$$

where

- S is the mass, or amount, of tracer in the cell;
- BRV is the boundary recharge volume, or input volume, of water in the cell;
- BRC is the boundary recharge concentration, or input concentration, of tracer in the cell;
- BDV is the boundary discharge volume, or output volume, of water from the cell;
- BDC is the boundary discharge concentration, or output concentration, of tracer in the cell;
- R is the source/sink term within the cell; and
- n is the iteration number.

Advection is formulated using a mixing cell algorithm. The DSC model allows for two types of mixing, the first being the simple mixing cell (SMC) approach. At each time step the SMC method water output from the preceding cell completely mixes with the contents of the current cell. Incoming water to the cell is accommodated by expanding the cell walls. After complete mixing, the walls contract and discharge a volume equal to the volume which entered. The algorithm consists essentially of input-mix-output where the boundary discharge concentration is calculated using:

$$(F.2) \quad BDC(n) = [S(n-1) + [BRC(n) * BRV(n)]]/[VOL + BRV(n)]$$

where VOL is the volume of the cell.

The second scheme that the DSC model uses to treat advection is called the modified mixing cell (MMC). The MMC algorithm assumes that at each iteration incoming water displaces an equal volume of cell water and the the incoming cell water mixes with the remaining water in the cell. Boundary discharge concentrations are calculated using

$$(F.3) \quad BRD(n) = S(n-1)/VOL$$

The MMC algorithm produces less numerical dispersion and, therefore, creates a sharper tracer front than the SMC. The choice of algorithm depends on the shape of the tracer front being simulated.

The partition coefficient is incorporated into the model by changing the cell volume in such a way as to assure that after mixing, the tracer is distributed proportionally between a cell representing the solid phase and a cell representing the liquid phase as dictated by the partition coefficient. The relationship between cell volumes is:

$$(F.4) \quad VOL_S = K_d * \rho_b/n * VOL_L$$

where

- $VOL_S$  is the equivalent cell volume of the solid;
- $K_d$  is partition coefficient between solid and liquid;
- $\rho_b$  is bulk density of soil;
- $n$  is porosity; and
- $VOL_L$  is the equivalent cell volume of the liquid.

The exchange volume,  $xv$ , needed to model gaseous diffusion can be obtained using:

$$(F.5) \quad xv = D_e \Delta t / \Delta x^2$$

where

- $\Delta t$  is time step; and
- $\Delta x$  is distance across a cell.

Parameters needed to run the DSC model are: partition coefficients, tortuosity of the porous media, diffusion coefficients, bulk density, and water content. These parameters were obtained from both laboratory experiments and from the literature.

## F.5 Field Experiment and Conclusions

An experiment was performed to apply volatile tracer sampling in the field, but no valid results were obtained because of the weather conditions. Results from the laboratory indicates the field experiments should work. BCF, F-12, and SF<sub>6</sub> tracers all could be used to estimate percolation rates in the laboratory experiments.

Conditions best suited for volatile tracer sampling are ones where water percolation rates are not extremely slow and/or the medium is close to saturation, thus slowing down the process of volatilization and thereby slowing down gaseous diffusion.

APPENDIX G  
ISOTOPE GEOCHEMISTRY IN  
LOW TEMPERATURE, WATER/ROCK INTERACTIONS

This Appendix contains a brief summary of the basic principles used in isotope geochemistry as applied to methods for the investigation of the isotopic and mineralogic nature of fracture surfaces and the rock matrix. The following discussions are based on more detailed comments and analyses given in: Faure (1977); Hoefs (1980); Friedman and Oneil (1977); and Fritz and Fontes (1980).

### G.1 General Characteristics of Isotopes

Isotopes of a particular element have the same number of protons (atomic number) but have different numbers of neutrons (atomic weight). For example, oxygen has two predominant isotopes found in nature,  $^{16}\text{O}$  with an atomic weight of 16, and  $^{18}\text{O}$  with an atomic number of 18. Isotopes of particular interest in hydrology are stable isotopes or isotopes that occur naturally and are not part of a radioactive decay sequence.

Radiogenic isotopes, which are isotopes that are products of a radioactive decay sequence but do not themselves decay, along with radioactive isotopes or isotopes undergoing radioactive decay, have less importance in hydrogeochemical investigations. Stable isotopes are used to understand sources of water or processes involved in the evolution of a water source. Radiogenic isotopes and radioactive isotopes measure age and sometimes can be used to define or infer geologic source areas.

### G.2 Stable Isotopes

Isotopes of a particular element have the same number of protons and thus will behave similarly in chemical reactions. However, differences in chemical properties of an element arise from the minute differences in mass. These mass effects cause isotopic fractionation, or isotope ratios of an element in a particular phase or state to be different if a phase shift occurs. For example, the  $^{18}\text{O}$  to  $^{16}\text{O}$  ( $^{18}\text{O}/^{16}\text{O}$ ) isotopic ratio in snow will be different from the vapor from which it condensed. Mass difference effects are most pronounced in the lighter elements.

Stable isotope values are reported using differences expressed in parts per thousand ( $\text{‰}$ , or  $\delta$ ) which is the quantity actually measured on isotope ratio mass spectrometers. Differences between a sample and a standard can be measured far more precisely than absolute values. For example, the  $\delta$ -value is defined for oxygen as:

$$(G.1) \quad \delta = ((^{18}O/^{16}O)_{\text{sample}} - (^{18}O/^{16}O)_{\text{standard}}) / (^{18}O/^{16}O)_{\text{standard}}$$

For oxygen and hydrogen isotopes the internationally accepted standard is standard mean ocean water (SMOW) (Craig, 1961). A sample with a  $\delta^{18}O$  value of +10 is enriched in  $^{18}O$  (i.e., is greater in  $^{18}O/^{16}O$ ) by 10 per mil, or 1 percent, relative to SMOW. A negative  $\delta$ -value signifies the sample is depleted in the heavy isotope relative to the standard.

Quantitative determination of isotopic values in hydrogeochemical systems are only possible if chemical equilibrium exists or if the kinetics of the reaction process are fully understood. The principle of the conservation of mass applies to isotope fractionation and any isotopic exchange reaction can be described by a temperature-dependent equilibrium constant, normally called the isotopic fractionation factor,  $\alpha$ . The isotopic fractionation factor for oxygen between two species, A and B, is given as:

$$(G.2) \quad \alpha_{A/B} = (^{18}O/^{16}O)_A / (^{18}O/^{16}O)_B$$

In terms of quantities measured by mass spectrometry ( $\delta$ -value) this expression becomes:

$$(G.3) \quad \alpha_{A/B} = (1000 + \delta A^{18}O) / (1000 + \delta B^{16}O)$$

### G.3 Stable Isotope Variations in Water

The isotope ratios of D/H (deuterium to hydrogen) and  $^{18}O/^{16}O$  have wide but systematic variation in fresh water ( $\delta^{18}O = -50$  to 0;  $\delta D = -400$  to 0). The isotopic behavior of most fresh water can be described by the meteoric water line (Craig, 1961), as:

$$(G.4) \quad \delta D = 8 \delta^{18}O + 10$$

This linearity results from evaporation and condensation cycles. For example, as water evaporates there is preferential removal of the light isotope to the vapor phase causing an enrichment of the heavy isotope in the liquid phase.

The isotope fractionation factor increases with decreasing temperature. Water initially evaporated from oceans becomes more depleted in the heavy isotope as air masses move toward higher latitudes and/or move inland, away from coasts. Along with temperature, latitude, and continental effects causing systematic variations in precipitation,

increasing altitude causes depletion of heavy isotopes as air masses move over mountain ranges.

One reason for the altitude effect is the progressive rainout of weather fronts as they move over the windward sides of mountain ranges. Mathematically, this dependency of  $\delta^{18}O$  and  $\delta D$  on latitudes and altitudes can be described by a Rayleigh-type distillation process; whereby freshwaters become depleted in the heavier isotope at high latitudes and altitudes.

#### G.4 Radiogenic Isotopes

Radiogenic isotopes have not been widely used in water studies because they normally occur as heavier elements and undergo insignificant isotope fractionation. Additionally, many of these isotopes are less abundant in nature and would not prove economical in hydrogeochemical investigations where large numbers of routine analyses are required. However, strontium isotope dating and tracer studies have been used with success in low temperature hydrogeologic processes.

The element strontium has four stable isotopes ( $^{84}Sr$ ,  $^{86}Sr$ ,  $^{87}Sr$ ,  $^{88}Sr$ ). One of these,  $^{87}Sr$ , is radiogenic; being the daughter product of the decay of  $^{87}Rb$ . Hence  $^{87}Sr$  exhibits variations due to (1) amount of rubidium, and (2) residence time in the reservoir. Variations of  $^{87}Sr$  are analyzed and compared to  $^{86}Sr$  concentrations as  $^{87}Sr/^{86}Sr$ ; analyses are done on solid-source mass spectrometers.

$^{86}Sr$  is chosen as a useful reference because of its relative abundance to that of  $^{87}Sr$  and its measurability can be measured accurately. Because source areas have different concentrations of rubidium and thus different production of  $^{87}Sr$ , the  $^{87}Sr/^{86}Sr$  ratio has been used in hydrogeology to trace source areas in both marine and fresh water.

#### G.5 Isotope Geochemistry and Rock/Water Interactions

The isotopic composition of a mineral is a function of the temperature and the isotopic composition of its environment. In surface and near-surface geologic settings, temperatures are normally low and rock/water interactions are significant. In these environments, isotopic exchange between most minerals and water is slow except when chemical or physical parameters change.

In hydrogeochemical investigations, isotopic techniques can be used to determine the water/rock ratio under present and, perhaps, past climatic

conditions. They may also be used to help decipher the source of the hydrologic input. Where the amount in the water is higher than in the surrounding rock, the isotopic composition of the water will not change significantly. However, where water/rock ratios are low, the isotopic composition of the water may be substantially altered and the authigenic minerals will more closely reflect the isotopic composition of the parent rock. Results from investigations such as these allow for constraints to be imposed on the timing of alteration as well as temperatures of formation.

**BIBLIOGRAPHIC DATA SHEET**

NUREG/CR-4655

SEE INSTRUCTIONS ON THE REVERSE.

2. TITLE AND SUBTITLE

Unsaturated Flow and Transport Through Fractured Rock  
Related to High-Level Waste Repositories  
Final Report -- Phase II

3. LEAVE BLANK

4. DATE REPORT COMPLETED

MONTH YEAR

October 1986

6. DATE REPORT ISSUED

MONTH YEAR

May 1986

5. AUTHOR(S)

T. C. Rasmussen, D. D. Evans

7. PERFORMING ORGANIZATION NAME AND MAILING ADDRESS (Include Zip Code)

Department of Hydrology and Water Resources  
University of Arizona  
Tucson, AZ 85721

8. PROJECT/TASK/WORK UNIT NUMBER

9. FIN OR GRANT NUMBER

B7291

10. SPONSORING ORGANIZATION NAME AND MAILING ADDRESS (Include Zip Code)

Division of Engineering  
Office of Nuclear Regulatory Research  
U.S. Nuclear Regulatory Commission  
Washington, DC 20555

11a. TYPE OF REPORT

Technical

b. PERIOD COVERED (Inclusive dates)

12. SUPPLEMENTARY NOTES

13. ABSTRACT (200 words or less)

In response to high-level radioactive waste repository licensing needs of the U.S. Nuclear Regulatory Commission, this report examines and provides insights into physical characteristics and methodologies for performance assessment of candidate sites in unsaturated fractured rock. The focus is on the ability of the geologic medium surrounding an underground repository to isolate radionuclides from the accessible environment. Media of interest are consolidated rocks with variable fracturing, rock matrix permeabilities, contained water under negative pressure, and air-filled voids. Temperature gradients are also of interest. Studies present conceptual and theoretical considerations, physical and geochemical characterization, computer modeling techniques, and parameter estimation procedures. Radionuclide transport pathways are as solutes in groundwater and as vapor through air-filled voids. The latter may be important near a heat source. Water flow and solute transport properties of a rock matrix may be quantified using rock core analyses. Natural spatial variation dictates many samples. Observed fractures can be characterized and combined to form a fracture network for hydraulic and transport assessments. Unresolved problems include the relation of network hydraulic conductivity to fluid pressure and to scale. Once characterized, the matrix and fracture network can be coupled. Reliable performance assessment requires additional studies.

14. DOCUMENT ANALYSIS -- a. KEYWORDS/DESCRIPTORS

contaminant transport, electric heater tests, fractures, ground water, nuclear waste, radionuclide, repository site selection, solute transport, volcanic tuff, unsaturated media, unsaturated zone

b. IDENTIFIERS/OPEN-ENDED TERMS

15. AVAILABILITY STATEMENT

Unlimited

16. SECURITY CLASSIFICATION

(This page)

Unclassified

(This report)

Unclassified

17. NUMBER OF PAGES

18. PRICE

**UNITED STATES  
NUCLEAR REGULATORY COMMISSION  
WASHINGTON, D.C. 20555**

**OFFICIAL BUSINESS  
PENALTY FOR PRIVATE USE, \$300**

**SPECIAL FOURTH-CLASS RATE  
POSTAGE & FEES PAID  
USNRC  
WASH. D.C.  
PERMIT No. G-67**